Efficient Solid State Power Amplifiers: Power Combining and Highly Accurate AM/AM and AM/PM Behavioural Models with Application to Linearisation

by

Paul Owen Fisher

Bachelor of Engineering (with Distinction),
Royal Melbourne Institute of Technology, Australia, 1981

Master of Engineering (Radio Frequency),
The University of Adelaide, Australia, 2003

Thesis submitted for the degree of

Doctor of Philosophy

in

Electrical and Electronic Engineering
The University of Adelaide

2017

Supervisors:

Dr Said Al-Sarawi, School of Electrical & Electronic Engineering

Associate Professor Dr Chris Coleman, School of Electrical & Electronic Engineering

Dedicated to my family.
To my dear wife Jan, daughter Laura and son Owen.
Also to my mother Gwladys and father Walter.
I enjoyed the journey!

Contents

Abstract

Radio Frequency (RF) Power Amplifiers (PAs) are a major contributor to modern communication systems, both in terms of being an enabling technology as well as having the most impact on overall system availability, linearity and power consumption. In order to achieve the most optimum system outcome there needs to be an appropriate method for selecting the most suitable RF PA design approach, as well as being able to select the most appropriate RF PA output device, based on a range of varying requirements, specifications and technologies. The ability to perform these tasks quickly, with improved accuracy, using existing available device data, with minimal or no further device testing and from a range of existing and emerging technologies would provide RF PA designers with significant benefits.

The investigations and research provided in this thesis consider a range of existing and emerging RF PA technologies and power combining methods and compares them via a new selection and design methodology developed in this thesis. The new methodology builds on modern design and statistical approaches including manufacturing options that enable an appropriate technology to be selected for Solid State Power Amplifier (SSPA) design. In addition to hard design specifications, the current thesis also considers less tangible specifications, such as graceful degradation, time to market and ease of use, as well as alternative design approaches, such as fuzzy logic approaches.

With a suitable technology approach determined, a selection of a suitable RF output device(s) is considered. As the demand for new communication services continues to increase, requiring tighter specifications and reduced product delivery time scales, then the ability to accurately and quickly compare available RF PA devices from a range of device technologies or devices from different manufacturers, at both the system and component level, makes such a selection paramount. In this thesis, simple memoryless (Amplitude Modulation/Amplitude Modulation (AM/AM) only) and Quasi-Memoryless (QM) Behavioural Models (BMs) (AM/AM combined with Amplitude Modulation/Phase Modulation (AM/PM)) are reviewed, extended and improved upon, with up to 20 dB Normalised Mean Squared Error (NMSE) modelling improvement achieved over a range of technologies, allowing effective RF PA device

selection using these newly developed simple and fast models. This thesis uses recent existing accurate and powerful semi-physical memoryless BMs, suited to RF PA devices, and develops and extends their use for QM modelling. The trade-off from the improvement in the overall accuracy is some further simple processing steps. Furthermore, this thesis also provides a comparison of other models, presented in the literature. The improved simple RF PA device models and extension techniques presented in this thesis show, via simulation and measurement, that the new models are suitable for use over a wide range. Linearisers improvements, linked to the accuracy improvements of the proposed models of this thesis, are also investigated, showing further benefits from this research.

Physically based simple QM BMs are also used to model thermal and bias network memory effects, which are becoming more relevant to modern communication services that use wider bandwidths, enabling the impacts of RF PA device memory effects to be determined and compared.

The feasibility of the developed models and improvements are also utilised in the simulation of a low cost RF PA linearisers. With the trend to smaller localised low cost and power RF mobile wireless repeater cells being away from larger more expensive and complex hardware, used to perform linearisation, this thesis presents a trade-off between complexity and linearisation performance and demonstrates, through modelling and simulation, that 8-10 dB improvement in linearisation performance is achievable with the use of the newly developed models.

Statement of Originality

I certify that this work contains no material which has been accepted for the award of any other degree or diploma in my name, in any university or other tertiary institution and, to the best of my knowledge and belief, contains no material previously published or written by another person, except where due reference has been made in the text. In addition, I certify that no part of this work will, in the future, be used in a submission in my name, for any other degree or diploma in any university or other tertiary institution without the prior approval of the University of Adelaide and where applicable, any partner institution responsible for the joint-award of this degree.

I give consent to this copy of my thesis, when deposited in the University Library, being made available for loan and photocopying, subject to the provisions of the Copyright Act 1968.

I also give permission for the digital version of my thesis to be made available on the web, via the University's digital research repository, the Library Search and also through web search engines, unless permission has been granted by the University to restrict access for a period of time.

Signed

Date

Acknowledgments

Never has so much been owed by so **FEW** to so **MANY**!

With apologies to Sir Winston Churchill, but I think that he may understand, although there has never been any human conflict throughout this journey!

My part time Ph.D. journey formally commenced in 2005, but really it started before this in 1999, yes last century, however I will get to that.

It took me 6 months of negotiations with my previous employer, Codan Limited, to be able to gain their support and let me embark on this journey. Without this support I would not have been able to commence my journey, so I acknowledge and thank them, particularly Peter Charlesworth, then General Manager of Engineering, and Peter Chaplin, then Satellite Communications Group Product Development Manager. At that time my Ph.D. topic was centred around high power solid state power amplifiers aligned with satellite earth terminals which was a part of the business of Codan at that time.

However within 12 months I had changed employment from Codan Limited to RF Industries (RFI) and with RFI's business associated with Land Mobile Radio and cellular band repeater products my focus needed to be different. Many thanks to Scott Magee for allowing me to join RFI and continue with my Ph.D. studies. Thanks also to the management and staff of RFI, Andrew Lesty, Graham Zacher, Jim Hider and Mark Mezzapica, who have all supported me in various ways over my Ph.D journey, in terms of financial, time or resource support. I could not have completed this Ph.D.without their support.

Changing employment, to a company with a different technical focus, and to a different more responsible role necessitated that I took a leave of absence from my studies. I was afforded 2 years leave of absence (LOA) to establish myself at my new company and I very much appreciate and thank the staff at the University of Adelaide Graduate Centre for assisting me with the LOA at this time.

Following the recommencement of my studies I re-focused my topic to be aligned with the business of my new employer. I was now looking at RF power amplifiers, behavioural modelling and linearisers, relevant to the products that RFI design and

manufacture. Throughout the initial period of my Ph.D. studies my Principal Supervisor, Associate Professor Chris Coleman, encouraged and supported me through all of the twists and turns that my journey had taken to this point. At times, when Chris was overseas for extended periods, my then Co-Supervisor Professor Andrew Parfitt, then with the University of South Australia and now Provost and Senior Vice-President of The University of Technology Sydney, stepped into Chris's role and seamlessly picked up from Chris and continued to encourage, support and direct me along the Ph.D. path. My association with both Chris and Andrew commenced in 1999, when I commenced a part-time Master of RF Engineering at the University of Adelaide that Andrew had set-up and started and that Chris had taken over. Without these two gentlemen I would absolutely never have been able to commence my Ph.D. journey. I acknowledge and thank both Chris and Andrew for their help, support and patience with my Ph.D.

Following Chris's retirement in 2012/13, and with Chris now acting as my Co-Supervisor, Dr Said Al-Sarawi took over the role as my Principal Supervisor. At that point I was struggling with the re-focusing to my new topic but Said provided me with the confidence to see the path to the end point and guided me along that path. It is safe to say that I would not have been able to complete and submit my Ph.D. thesis without Said's overwhelming assistance, guidance, knowledge and good humor, so I am truly indebted to him for his faith and support in me.

I would also like to acknowledge and thank others within the School of Electrical and Electronic Engineering being; Mr. Stephen Guest for arranging facilities and helping with administration from what he would perhaps have considered to be a "Ghost" Ph.D. student due to the part time, and at times very part time, nature of my Ph.D. studies and also to the previous School's Head of Department Professor Cheng-Chew Lim for his patience and support of my part time Ph.D. Thanks also to Dr Amir Ebrahimi for sharing his Latex skills with me.

My Ph.D. journey has not been academic alone. Outside of my work and academic life my family have always supported me. Thanks to my Mum, Gwladys, and Dad, Walter, for continually asking - "How is the Ph.D. going?" and encouraging me. Thanks to my daughter Dr Laura Fisher who continually supported and asked about my progress and at times gave me the hurry up when needed and to my son Owen Fisher, who in recent times I have been able to discuss some of my coding with. I have enjoyed these "hurry ups" and discussions and they have proved very helpful.

To my beautiful wife Jan you have always supported all of my endeavors and have always had confidence in my ability to complete this journey, even when I myself have had doubts. I love you so much and I am indebted to you for this constant support of me, thank you so much.

Throughout my journey I have learnt a lot about my topic(s) and believe that I have made some contributions to my field. However the most important thing that I have learnt is how well I have been supported and guided by both my family, work colleagues and those within the School of Electrical and Electronic Engineering at The University of Adelaide.

My sincere thank you to everyone.

Thesis Conventions

Typesetting

This document was compiled using LaTeX2e. TeXnicCenter was used as the text editor interfaced to LaTeX2e. Inkscape and Word were used to produce schematic diagrams and other drawings.

Referencing

The Institute of Electrical and Electronic Engineers (IEEE) referencing and citation style has been adopted for this thesis.

System of units

The units comply with the international system of units recommended in an Australian Standard: AS ISO 1000–1998 (Standards Australia Committee ME/71, Quantities, Units and Conversions 1998).

Spelling

Australian English spelling conventions have been used, as defined in the Macquarie English Dictionary (A. Delbridge (Ed.), Macquarie Library, North Ryde, NSW, Australia, 2001).

Acronyms, Symbols, Variables and Constants

Acronyms

2-D 2-Dimensional

3-D 3-Dimensional

3^{rd} **IMD** Third Order IMD

ACI Adjacent Channel Interference

ACLR Adjacent Channel Leakage Ratio

ACPR Adjacent Channel Power Ratio

AE Average Error

AlN Aluminium Nitride

AM/AM Amplitude Modulation/Amplitude Modulation

AM/PM Amplitude Modulation/Phase Modulation

AFP Amplitude Fitting Parameter

BJT Bipolar Junction Transistor

BM Behavioural Model

CMOS Complementary Metal Oxide Semiconductor

CPW Co-Planar Waveguide

CST Computer Simulation Technology

CW Continuous Wave

DFSS Design For Six Sigma

DPD Digital PreDistoration

DSBW Dielectric Slab Beam Waveguides

DUT Device Under Test

EBGS Electromagnetic Band-Gap structure

EMC Electro-Magnetic Compatibility

EMXT Electro-Magnetic Crystal Structure

E-pHEMT Enhancement-mode pseudomorphic High-Electron-Mobility-Transistor

E-plane Electric field vector plane

FET Field Effect Transistor

FFT Fast Fourier Transform

FMEA Failure Mode Effects Analysis

FOM Figure Of Merit

GaAs Gallium Arsenide

GaN Galliun Nitride

GHz gigahertz

HFSS High Frequency Structure Simulator

InGaP Indium Gallium Phosphide

InP Indium Phosphide

HBT Heterojunction-Bipolar-Transistor

HEMT High Electron Mobility Transistor

HFET Heterojunction FET

HFSS High Frequency Structure Simulator

HIES High Impedance Electromagnetic Surfaces

H-plane Magnetic field vector plane

IC Integrated Circuit

IMD Inter-Modulation Distortion

IMFET Internally Matched Field Effect Transistor

IMPATT IMPact ionisation Avalanche Transit-Time

LDMOS Laterally Diffused Metal Oxide Semiconductor

LSCF Least Squared Curve Fitting

LTCC Low Temperature Co-fired Ceramic

MEMS Micro Electro-Mechanical System

MESFET Metal Semiconductor Field Effect Transistors

MMI Multi-Mode Interference

MMIC Monolithic Microwave Integrated Circuit

MGS Modified Generalised form of the Saleh model

NMSE Normalised Mean Squared Error

NPR Noise Power Ratio

N/W Network

P1dB 1 dB Gain Compression Point

PA Power Amplifier

PAE Power Added efficiency

PAPR Peak to Average Power Ratio

PBGS Photonic Band Gap Structure

PCB Printed Circuit Board

PD PreDistorter

PDQ Planar Dielectric-Slab Quasi-Optical

PEC Perfect Electric Conductor

PEP Peak Envelope Power

PFP Phase Fitting Parameter

PMC Perfect Magnetic Conductor

PRLC Parallel Resistor-Inductor-Capacitor

QFD Quality Function Deployment

QM Quasi-Memoryless

QO Quasi-Optical

R Resistance

RBW Resolution Bandwidth

RF Radio Frequency

RF APD RF analog predistortion

RF PA RF power amplifier

RSS Root Sum Squared

Si Silicon

SiC Silicon Carbide

SIW Substrate Integrated Waveguide

SMT Surface Mount Technology

SP Specification Parameter

SLL Saturation Limit Level

SSPA Solid State Power Amplifier

SSG Small Signal Gain

TE Transverse Electric

TEM Transverse Electro-Magnetic

TM Transverse Magnetic

TWTA Traveling Wave Tube Amplifier

UC-EBG Uni-Planar Electromagnetic Band-Gap Surface or Structure

UC-PBGS Uni-Planar Compact PBG Surface or Structure

VVA Voltage Variable Attenuator

VVPS Voltage Variable Phase Shifter

WBG Wide Band-Gap

WCDMA Wide-band Code Division Multiple Access

Symbols

A ampere

dB decibel

dBc dB relative to the carrier

dBm dB-milliwatts

DC Direct Current

ϵ_r Dielectric Constant

K kelvin

kHz kilohertz

LC Inductor Capacitor

λ_g Guide Wavelength

λ_0 Freespace Wavelength

m metre

mA milliAmps

mm millimetres

MHz megahertz

ms millisecond

μ**m** micrometre

nF nanofarad

nH nanohenry

nJ nanojoule

ns nanosecond

Ω ohm

μ**s** microsecond

V volt

W watt

Variables

C_{th} thermal capacitance

P_{in} input power

P_{out} output power

P_{sat} saturated output power

R_{th} thermal resistance

Constants

π Ratio of a circle's circumference to its diameter = 3.14159265359

Publications

Journal Articles

[1] **P. O. Fisher** and S. F. Al-Sarawi, "An Optimised Segmented Quasi-Memoryless Nonlinear Behavioral Modeling Approach for RF Power Amplifiers," in *IEEE Transactions on Microwave Theory and Techniques*, vol. PP, no. 99, pp. 1-12, 2017. DOI: 10.1109/TMTT.2017.2723010

Conference Articles

[1] **P. O. Fisher** and S. F. Al-Sarawi, "A New Figure of Merit Methodology for Power Amplifier Combining Technologies," in *International Conference on Electronic Devices, Systems and Applications, ICEDSA*, Ras Al Khaimah, U.A.E., Dec., 2016, pp. 1–4. DOI: 10.1109/ICEDSA.2016.7818493

[2] **P. O. Fisher** and S. F. Al-Sarawi, "Memoryless AM/AM Behavioral Model for RF Power Amplifiers," in *3rd IEEE Asia-Pacific World Congress on Computer Science and Engineering, APWC on CSE*, Nadi, Fiji, Dec., 2016, pp. 131–138. DOI 10.1109/APWC.on.CSE.2016.29

[3] **P. O. Fisher** and S. F. Al-Sarawi, "Analog RF predistorter simulation using well-known behavioral models," in *10th IEEE International Conference on Industrial Electronics and Applications, ICIEA*, Auckland, New Zealand, June, 2015, pp. 1667–1671. DOI: 10.1109/ICIEA.2015.7334377

[4] **P. O. Fisher** and S. F. Al-Sarawi, "Improving the accuracy of SSPA device behavioral modeling," in *International Conference on Information and Communication Technology Research, ICTRC*, Abu Dhabi, U.A.E., May, 2015, pp. 278–281. DOI: 10.1109/ICTRC.2015.7156476

[5] **P. Fisher**, "Nonlinear behavioral model extraction of RF power amplifier devices from manufacturer's data," in *20th IEEE International Conference on Electronics, Circuits, and Systems, ICECS*, Abu Dhabi, U.A.E., Dec., 2013, pp. 593–596. DOI: 10.1109/ICECS.2013.6815484

List of Figures

List of Tables

Chapter 1

Introduction

THIS chapter provides a brief introductory background to Solid State Power Amplifier power combining and the need for a design methodology, enabling selection of the most appropriate power combining technology solution, considering both well defined and less well defined outcome requirements. It also discusses the need for simple but accurate behavioural models that allow for fast RF PA output device selection. The use of these simple behavioral models associated with simple RF predistortion linearisersis also discussed. It also explains the objectives and motivations behind the presented research. Original contributions from this research as presented in this thesis are highlighted and finally the structure of the thesis is presented.

1.1 Introduction

This thesis considers methods for selecting and designing RF and microwave SSPAs, in order to achieve higher output powers, as well as improved accuracy models and methods to assist in the selection of suitable devices, from a range of technologies, for applications over a range of frequencies and for linearisation purposes.

In their simplest form RF and microwave SSPAs consist of an active device with input and output matching and bias networks that are typically integrated on a printed circuit board assembly that is contained within a suitable enclosure having suitable RF input and output and biasing / control interfaces. Depending on the power requirements appropriate thermal management maybe required, possibly an integral or externally mountable heatsink. The assumption might be that to obtain higher output powers then just the active device would require changing to provide the required increase in output power. For an extremely simple, low frequency or low output power increase this may be the case. In the vast majority of cases only replacing the active device is not suitable for obtaining higher output powers and other techniques are required to meet the increased requirements for higher output power.

Modern communication systems, in both the commercial and defence sectors, are requiring ever greater capacity and coverage, with RF and / or microwave PAs becoming crucial elements in defining RF output power and spectral purity. In addition, requirements such as power consumption, thermal requirements, size and cost are significantly impacted by RF and / or microwave PAs, so there has been a focus on PAs in these areas. In order to obtain higher output powers, at ever increasing frequencies, with tougher constraints on power consumption, operating environments and also with the drive for lower costs and reduced time to market the demand for these requirements has pushed the research related to PAs in the area of power combining at different levels, namely:

Chip Level: Where several chip level devices are combined together in order to form higher output powers, with a a limitation being power dissipation capacity and the frequency of operation being determined by chip size,

Circuit Level: Combining requiring the interconnection of devices via transmission lines with line losses limiting the number of devices thus limiting power outputs, the physical size of these interconnecting networks and also resonant effects of

the networks limiting bandwidths. More recently a large body of research has been focused in the area of,

Spatial or Quasi-Optical: Power combining in order to address some of these factors. Spatial or QO power combining has demonstrated a potential use of a large numbers of active devices for power combining to achieve high output powers into the millimeter wave region.

A comparative analysis between well established and more recent SSPA combining techniques is also presented. Based on this analysis, a new Figure Of Merit (FOM) methodology is presented that can form part of a process to optimise SSPA design within the constraints of service, technology and performance requirements. Also, this formalises the process of determining the most appropriate SSPA design path, from the earliest stages, based on the above constraints as well as providing a detailed technology comparison to allow optimum technology selection.

For the RF PA designer there are many techniques and methods for designing RF PAs, however with the increased number of available devices spanning a wider range of technologies and to meet new modulation scheme requirements on ever shrinking product to market time scales, being able to select suitable RF output devices, that meet these demanding requirements, necessitates the need for simple device behavioural modelling that be applied at the system level thus allowing the RF PA designer to make a suitable choice to meet their design requirements.

Behavioural models and an accuracy improvement segmentation technique are presented in this thesis and offer the RF PA designer straight forward paths to assist in making these RF PA device selections. A range of existing simple BMs are reviewed and an new quasi-memoryless AM/PM model is introduced based on a recent more accurate memoryless AM/AM model that is semi-physically based. This becomes a very powerful tool for the RF PA designer, as existing manufacturer's data or simple additional testing, if required, can readily be used to create the BM. A segmentation method, to enhance the BMs accuracy, at the expense of some additional processing and number of parameters, for both AM/AM and AM/PM models is introduced that further assists this process. The new models are also compared and are shown to be suitable over a wide range of current technologies further enhancing their usefulness.

Finally an envelope predistortion lineariser scheme, using low cost integrated analog components is proposed and simulated. Integrated logarithmic amplifiers and phase

detectors are used to sample the input and output signals before and after the RF PA to measure the complex gain and phase information, which is used to control an integrated pre-distorter Integrated Circuit (IC) that contains adjustable gain and phase components within a single IC package. Comparisons of a range of well-known and developed RF PA behavioural models are evaluated to determine the most suitable behavioural model for this linearisation scheme, including the RF PA driver and memory effects. All component models are based on parameters extracted from readily available device datasheets for the driver and RF PA, thus minimizing the need for extra measurements.

1.2 Research Motivations and Objectives

The motivations and objectives of this thesis are as follows.

The previous section highlighted the need for power combining techniques to meet the emerging need for high power output stages. In the literature a wide range of techniques are developed, however a comprehensive overview of the different techniques seems to be missing, hence the need to provide an overview of the different approaches to power combining techniques.

Even after considering the different power combining techniques, a number of Figure's of Merit exist that are commonly used to highlight specific power combining parameters that would be suited for an application requirement. Nonetheless, a Figure of Merit approach for evaluating a suitable technology for a range of requirements is lacking in the literature. Hence the need for a design methodology that allows such a technology comparison.

Considering that a wide range of power combining techniques rely on the use of SSPA devices, the need to accurately model such devices becomes a paramount, especially if such modelling can be achieved using readily available design parameters from manufacturer's datasheets, with no or minimal need to perform extra measurements. Such developments will allow an accurate and fast system level modelling and will be of interest for RF PA designers as a tool to compare devices over a range of technologies, however such modelling approaches are lacking from the literature and in some cases modelling approaches are technology specific. This highlights the need to explore current modelling approaches and find out how these can be improved without

compromising the model simplicity. Such improvements can have significant benefits in building high performance but low cost linearisers.

A significant portion of RF PA modelling in the literature is memoryless behavioural modelling with limited accuracy, but the question regarding obtaining further RF PA modelling accuracy still stands, also if there is a more systematic approach that can be used to further improve the accuracy of both quasi-memoryless and memoryless behavioural modelling. In addition, would it be possible to develop a generic model that allows behavioural modelling of different amplifier technologies without compromising either the speed and accuracy of these models.

To provide the most accurate quasi-memyless behavioural model, derived from an existing accurate memoryless behavioural model and further enhance its accuracy through the use of an optimised segmentation method, again with the aim of allowing RF PA designers the ability to quickly select RF PA devices knowing the they can use a simple, fast accurate model to do this. This has also been applied to a memoryless model. To also show that the new model and techniques can be used over a range of technologies by comparing the performance with other existing quasi-memoryless and memoryless models. To show the benefits of the new model and techniques in terms of linearisation benefit.

To further improve the performance of a communication system, there is a need to operate the amplifier at its highest efficiency, however such improvement will compromise the amplifiers' linearity. In the literature a number of techniques are used to improve amplifier linearity and some of these rely on using expensive hardware to perform this needed linearisation. However in some applications the focus is more on a good compromise between the performance and system cost. The digitial approach does not lend itself to low cost applications and an alternative would be to use analog predistorters. However, such an approach would require the use of efficient and accurate modelling techniques to facilitate that. In the literature a number of these approaches are developed, however the performance seems to be moderate. Hence there is a need to investigate a better approach for linearisation.

1.3 Contributions

Based on the highlighted research gaps in the previous subsection, the aim of this subsection is to highlight how the current work is aimed at addressing these research gaps. A summary of these contributions are given below

Chapter 2: Provides a comprehensive updated review of available power combining technologies for solid state power amplifiers. These technologies cover a broad range of frequencies and methods.

Chapter 3: Based on the previous chapter's review of a range of power combining technologies this chapter provides a new method based around a Figure of Merit approach in order to select the most appropriate power combining technology and design from both a range of well defined and less well defined requirements and specifications.

Chapter 4: Details improvements to existing behavioral models and provides an extension to an AM/PM model, expanding the AM/PM performance characteristic range for RF PA devices. A technique for extending existing data into an RF PA device's saturation region is introduced and existing model comparisons are shown.

Chapter 5: Provides a comprehensive review of memoryless and quasi-memoryless behavioural models over the last 40 years and identifies more suitable models for the PA designer. The development of a new AM/PM model, based on a more accurate AM/AM model, is provided as well as a straightforward segmentation method that provides even further modelling accuracy improvements.

Chapter 6: Simulation of low cost analog based lineariser using improved amplifier behavioural models with performance comparisons.

1.4 Thesis Overview

A visual overview of the organisation of this thesis is shown in Fig. 1.1, where the initial research started by focusing on the power combining aspects of a communication system, then shifted to the core element of these power combining modules which is the solid state power amplifier. This has then followed by behavioural modelling followed by applications to linearisers.

Chapter 2: Reviews Solid State Power Amplifier combining techniques and technologies over a broad range of frequencies and achievable power levels and discusses the various trade-offs for each.

Chapter 3: As a follow on from Chapter 2, introduces the concept of a Figure of Merit based design methodology for the selection of the most appropriate technology and design approach in order to be able to achieve the most appropriate SSPA solution for not only a range of hard specifications but also including a range of less tangible requirements as well as service and reliability requirements. A case study for this methodology is provided.

Chapter 4: Moves to aspects of behavioural modeling approaches and improvements that allow PA designers to quickly and accurately model and compare PA output devices as an aid to selecting the most suitable device for a particular application. The modeling approach focuses on being able to extract models from readily available data via manufacturers data sheets of straight forward further testing. Also presented is a physics based approach to the modelling of device memory effects.

Chapter 5: Derives a new quasi-memoryless AM/PM model, from a more accurate existing AM/AM memoryless model, and demonstartes its applicability over a range of current wireless device technologies. Also developed is a straight forward segmentation modeling approach, using this new AM/PM model, resulting in improved accuracy. Discontinuity effects from this segmentation approach are discussed and show to be insignificant for a current digital modulation scheme. Further the use of this model and segmentation approach show improvements in modelling 3^{rd} IMDs. Again this new model and segmentation approach is focused on allowing the PA designer to be able to quickly asses a range of PA output devices over a range of frequencies.

Chapter 6: Provides a simulation of low cost analog based lineariser using improved amplifier behavioural models with performance comparisons.

Chapter 7: Provides a conclusion for this thesis and also discusses future possible research directions.

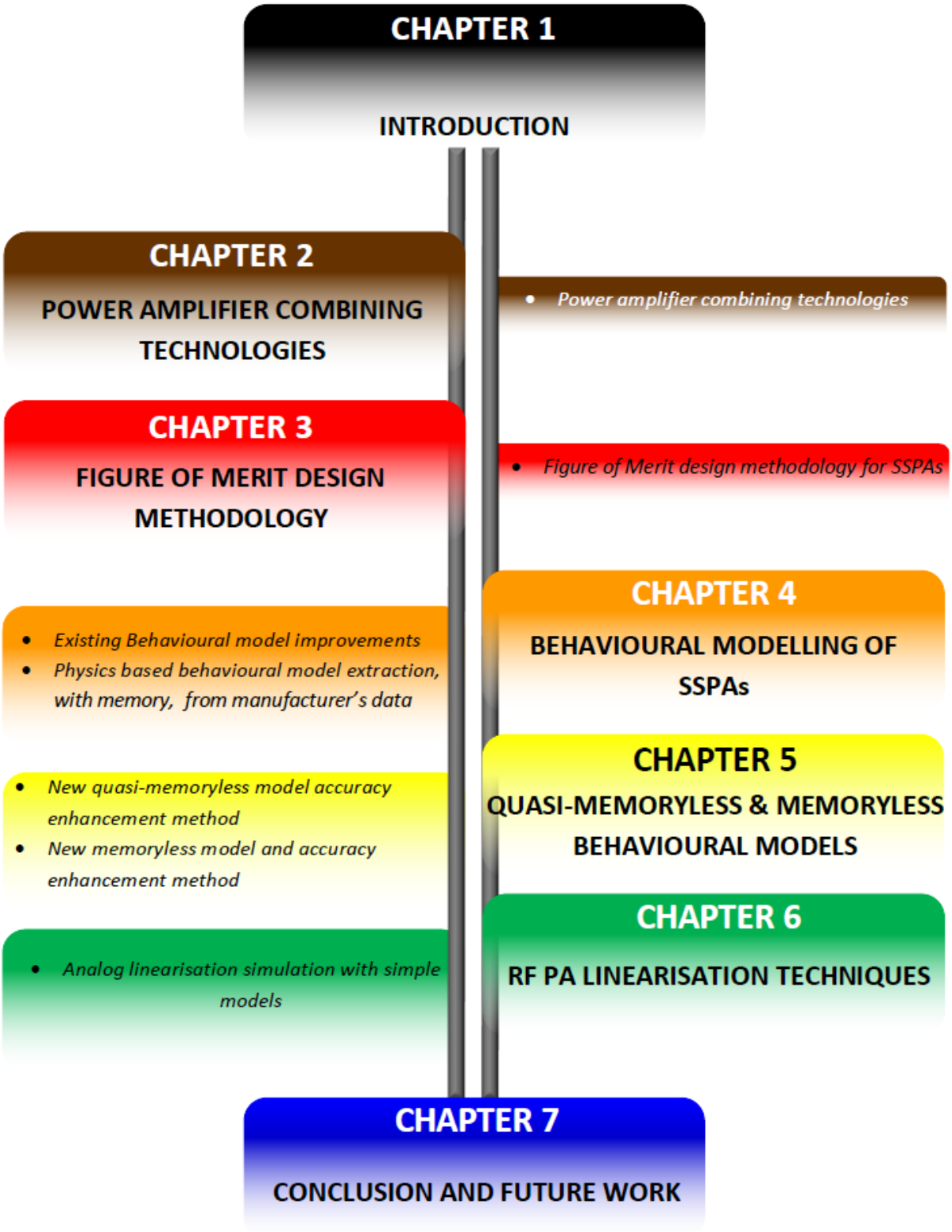

Figure 1.1. Thesis overview.

Chapter 2

Power Amplifier Combining Technologies

IN order to obtain higher RF output powers, PAs have employed various power combining techniques. For example, corporate tree and chain as well as N-way Wilkinson and radial line combiners, with, more recently, spatial and Quasi-Optical (QO) power combining techniques showing increased potential for obtaining higher output powers, particularly at higher microwave and millimeter wave frequencies. Both spatial and QO combining techniques are being researched as they offer increased output power at higher frequencies due to limitations in more established conventional techniques.

Although spatial combining and QO techniques offer the potential for more power at higher frequencies there are several areas that can be enhanced. Numerous spatial combining and QO technologies exist but a design methodology that ensures the best possible design outcome is not apparent. This chapter will review and provide a preliminary comparison of spatial and QO combining technologies, as well as more established combining technologies, indicating that further research is required in order to provide an appropriate power combining design methodology that delivers a best SSPA outcome.

2.1 Introduction

As the demand for commercial and military communication systems increase, there is a continuing need for SSPAs, operating at microwave and millimeter wave frequencies, that have higher output powers and efficiencies with reduced size, cost and thermal load while maintaining or improving reliability. The requirement for higher power means that there is considerable motivation for research activities to be undertaken at both device and amplifier module level. Beyond basic active device improvements, higher power is obtained by using passive power-combining techniques at monolithic chip, packaged device and amplifier module level.

Power amplifiers use combining networks in order to achieve higher output power levels as demonstrated by Russell [1] and Chang and Sun [2] as shown in Fig. 2.1 of Section 2.2.1. This figure shows many different combining techniques that are available for microwave and millimeter wave frequencies. Combining active devices to form higher power SSPAs at microwave frequencies is performed by a number of means with corporate dividing / combining being an established, widely used method and spatial or QO combining being a newer technique with increasing potential for achieving higher output powers at higher frequencies.

Although spatial combining and QO techniques can provide more power at higher frequencies, by using many active devices to overcome the one off higher loss associated with spatial combining, there are several areas that can be further enhanced.

This chapter will review and compare many different power amplifier-combining technologies, particularly spatial and QO combining technologies.

The Background Section 2.2 reviews the available literature, discusses current technology and highlights technical aspects that require further research.

Section 2.3 discusses technology related to Electromagnetic Band-Gap structures (EBGSs) in more detail.

2.2 Combining Technologies

2.2.1 Introduction

The many different combining techniques that are available for microwave and millimeter wave frequencies are shown in Fig. 2.1. This it is an expansion and update of the figures given by Chang and Sun [2] pp. 99 and Navarro and Chang [3] pp. 72.

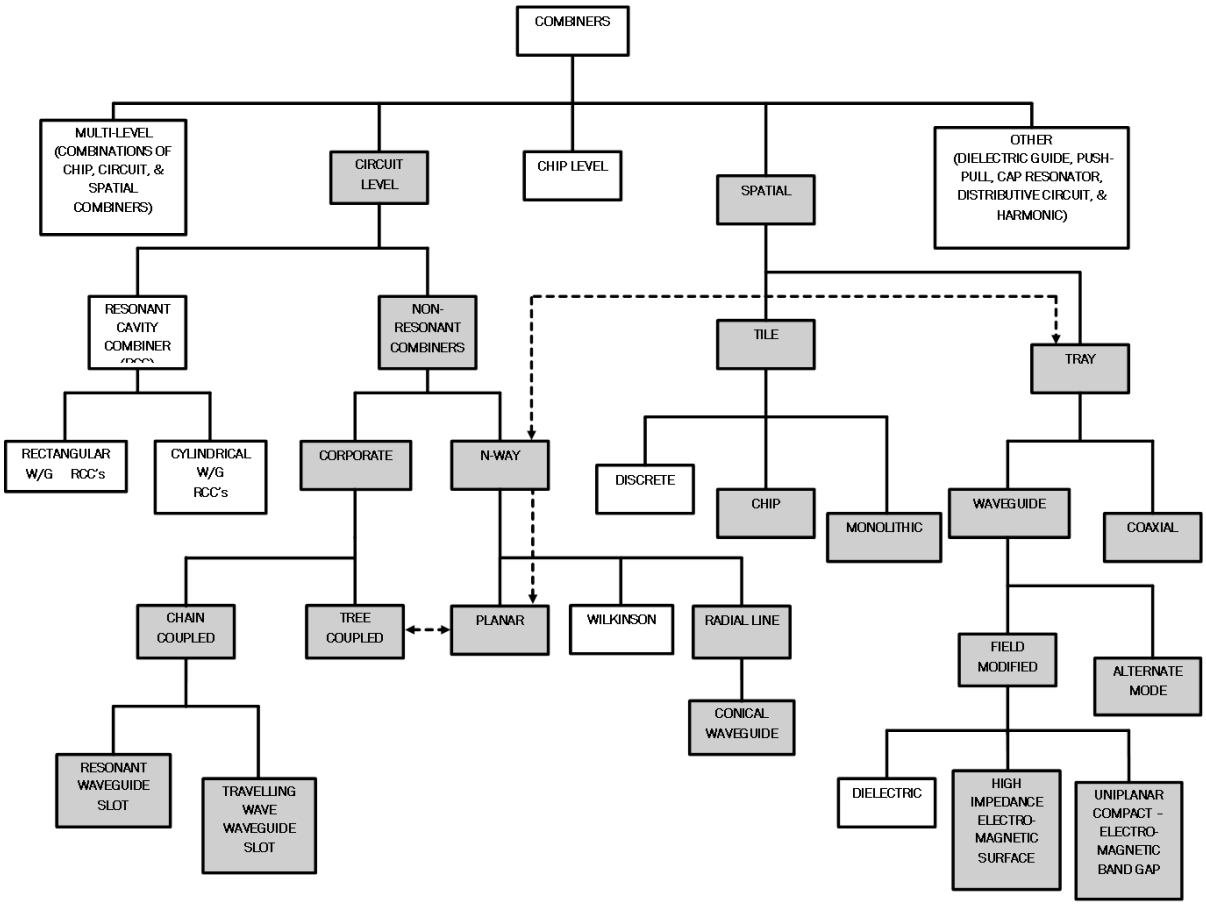

Figure 2.1. Methods of power combining. The dotted lines indicate the crossover between circuit level and spatial combining at the N-way non-resonant combiner and tray spatial combiner level.

This chapter will provide background about the shaded areas as shown in Fig. 2.1 and will focus on spatial combining technologies because of its' potential for higher output powers with increasing device numbers compared to other combining technologies.

This background introduction will briefly describe and compare corporate and spatial combining with more detailed discussions and comparisons in following sections.

Corporate combining networks either use a tree structure of two-way adders, with the adders being directional couplers, hybrids, or Wilkinson combiners or a chain structure. A schematic for a tree structure corporate combiner is shown in Fig. 2.2. It can

be seen that to combine eight separate amplifier modules that seven separate dividers and seven separate combiners are required. Thus N combining stages are required to combine $2N$ amplifiers using $2N - 1$ combiners. For the schematic shown in Fig. 2.2, $N = 3$. A fixed loss is associated with each divider and combiner, and interconnecting transmission line. However a point is reached where the benefits of combining multiple amplifiers will diminish due to the significant power loss associated with the dividers / combiners and interconnecting transmission lines.

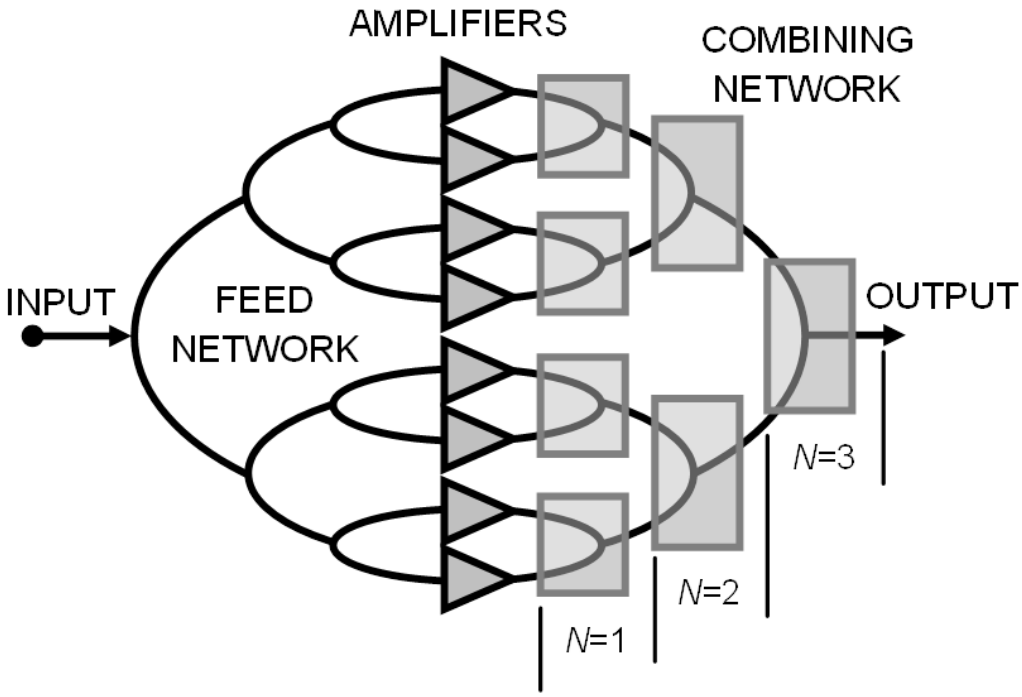

Figure 2.2. Corporate power combiner block diagram.

The number of active devices that can be combined before the combiner and transmission line connection losses become dominant is around 16 devices assuming combiner and transmission line losses of 0.1 decibel (dB) per section, as shown in Fig. 2.3. As expected, the number of stages will be less if each stage has a higher associated loss, [4].

Spatial power combiners use arrays of distributed active devices, which radiate freely into space. Synchronisation between active devices is accomplished via mutual coupling between the devices, external circuit networks or an open resonator. When the array is synchronised through the modes of an open resonator the power combining is termed to be QO because of similarities with optical Fabry-Perot laser applications. Combining in free space avoids ohmic and dielectric losses, as a result radiation losses are reduced for large enough arrays. Multi-moding problems are avoided so large

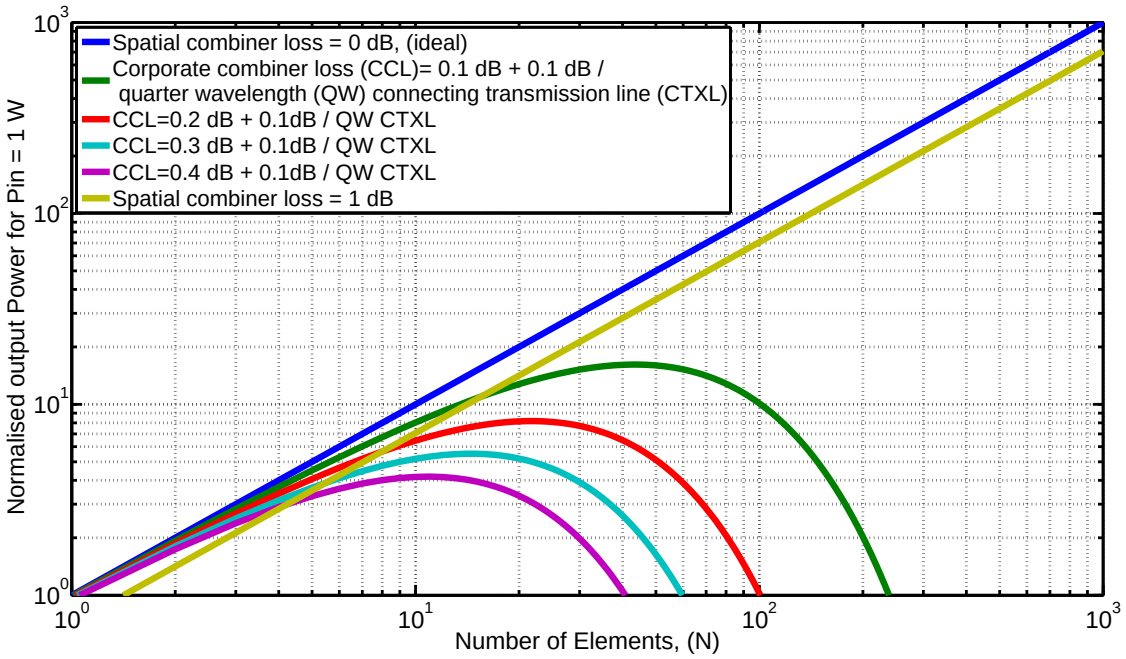

Figure 2.3. Ideal, spatial and corporate combiner network comparison. Ideal, spatial and corporate combiner network, normalised to an input of 1 W, relative to an ideal spatial combiner output power versus number of elements.

numbers of devices can be used. As spatial or QO combining occurs in free space the individual active devices are essentially active integrated antennas. A block diagram for a spatial divider / combiner is shown in Fig. 2.4. Here there is an initial Spatial combiner fixed loss associated with the divider / combiner so a minimum number of devices for dividing / combining is required in order for this technique to be viable. Beyond this point however, greater benefit is achieved in terms of output power improvement. The point where these benefits are achieved, in terms of number of devices used, is shown in Fig. 2.3 and occurs at around 16 elements for a 0.1 dB corporate combiner / divider loss.

So it can be seen that spatial or QO combining offers potential for improved output powers at higher frequencies. More details about corporate combining and spatial or QO techniques and technologies are provided in the following sections. Some historical background is also provided.

From this introduction it can be seen that there are alternative technologies that can be used for power combining and that essentially technology selection is based around

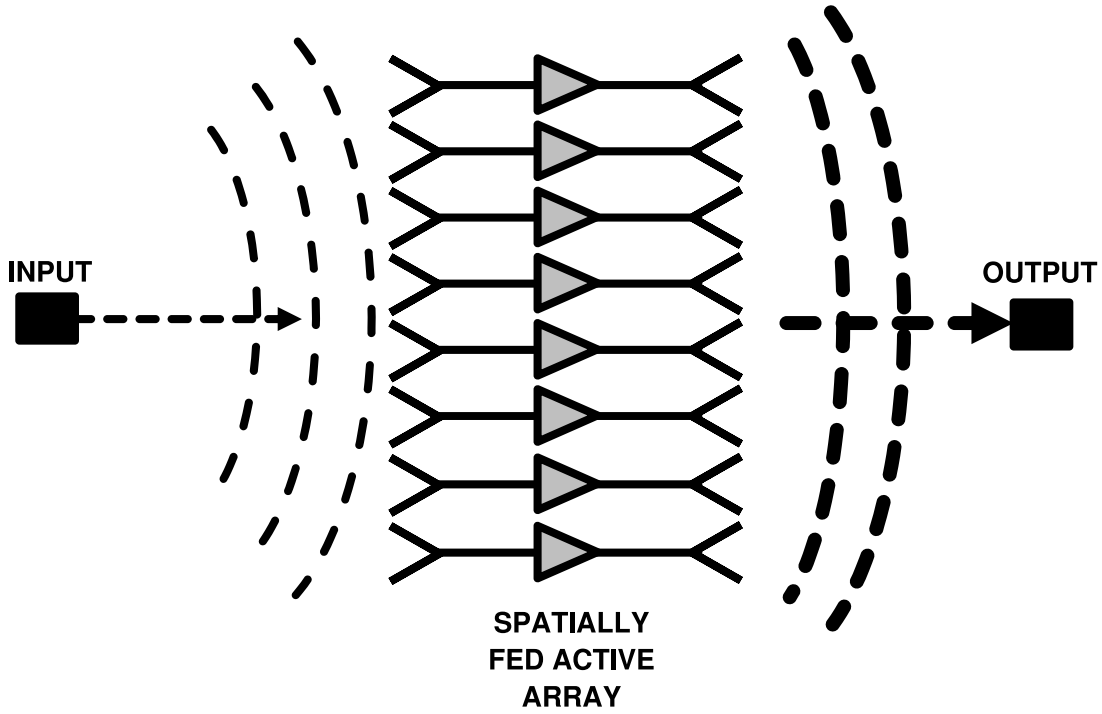

Figure 2.4. Spatial combiner block diagram.

being able to optimise, and maximize, the outcomes of particular specified parameters for a particular service type. Discussions relating to the methodology required to do this will be proposed in Section 3.1.

2.2.2 Corporate Combining Networks

Discrete Level Corporate Combining

As an example of a corporate combining network used in an SSPA, Figs. 2.5 (a) and (b) , show a Codan Limited [5] 40 watt (W) Ku-Band[1] high power SSPA module. Fig. 2.5 (a) shows the input-dividing network, which uses -3 dB, 90° hybrids, as power dividers, that are implemented in microstrip form at the circuit level. The dividers are fed by 3 stages of increasing power, Internally Matched Field Effect Transistors (IMFETs). Following the microstrip dividers are four amplifiers formed by using two cascaded IMFET stages. These cascaded IMFET stages transition from microstrip into Electric field vector plane (E-plane) waveguide and the transitions are evident on the right hand side of Fig. 2.5 (a). The output combining section, shown in Fig. 2.5 (b), consists of a waveguide step bend, a small length of waveguide and then two 3 dB, 90° hybrids,

[1] 14.0 to 14.5 gigahertz (GHz)

this time implemented in waveguide in order to minimise output losses. These combine the four outputs into two and then another waveguide combiner combines the two outputs into one output.

It can be seen that this type of combining is relatively complex and is quite large (230 millimetres (mm) x 170 mm). The advantages are that the high power IMFETs that are used can be easily mounted so that there is a minimum path to heatsinking thus minimising IMFET temperatures and improving reliability. High power IMFETs are typically constructed using Metal Semiconductor Field Effect Transistorss (MESFETs).

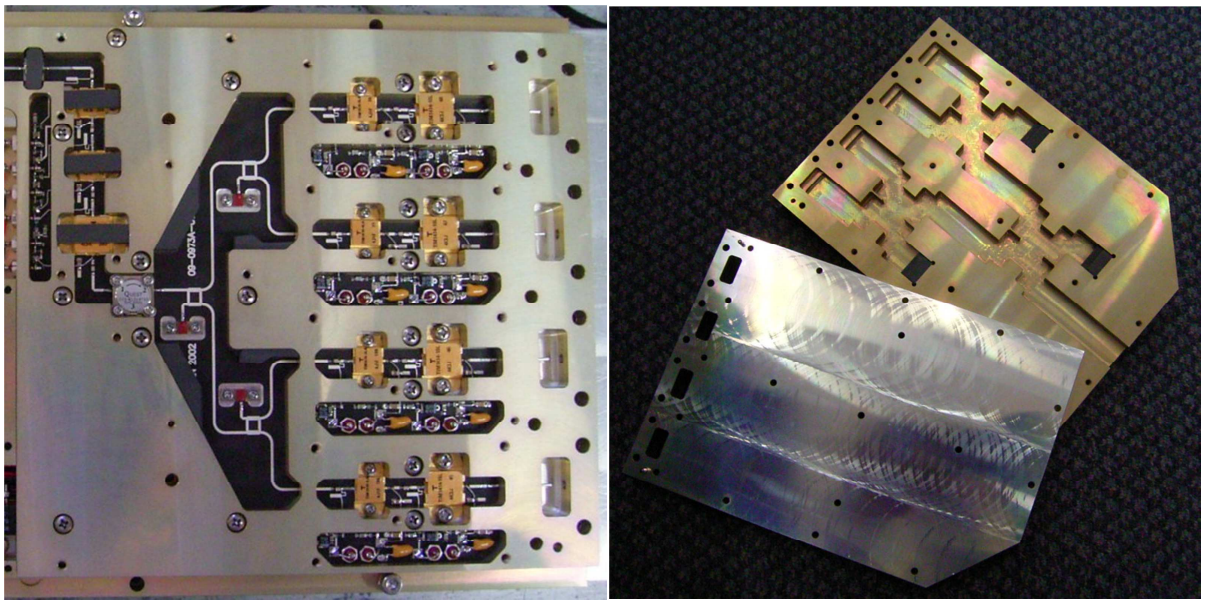

Figure 2.5. Codan Limited 40 W Ku-Band SSPA. (a) Codan Limited 40 W Ku-Band microstrip dividing / waveguide combining network and (b) Codan Limited Ku-Band 4 way E-plane waveguide (WR75) power combiner, from [5].

Chip Level Corporate Combining

At a more integrated level from discrete corporate combining, chips are also combined using corporate combining networks. This is typically done for IMFET based amplifiers where certain output power chips, which are a parallel combination of many microwave Field Effect Transistors (FETs) are combined together in one package. The chips are soldered to a pedestal across the center of the IMFET package. This package is made from good thermal conductivity (118 W/metre (m)-kelvin (K)) Beryllium Copper that is Gold plated. The divider and combiner networks are connected to the chips through input and output matching networks via Gold wire bonds. The divider / combiner networks are of microstrip form with an Alumina substrate used having

a Dielectric Constant (ϵ_r) of 9.8 in order to keep the networks as small as possible and maintaining bandwidth as large as possible. The packages are then covered with either a metal or ceramic cover, which is soldered to the surrounding metal, or plated ceramic, surrounding walls. Typical sizes for a 60 W RF output IMFET at C-Band[2] are 17.5 mm (l) x 25.4 mm (w) x 6 mm (h) dissipating 150 W of Direct Current (DC) power (10 volts (Vs) at 15 amperes (As)) at the 1 dB Gain Compression Point (P1dB) giving a Power Added efficiency (PAE) of around 30%. Typical internal construction for an IMFET Walker [6] is shown in Fig. 2.6. An additional C-Band high power IMFET example can be found at Toshiba [7]. One of the requirements / disadvantages for this assembly is the need to provide adequate heatsinking due to the high thermal density of these devices.

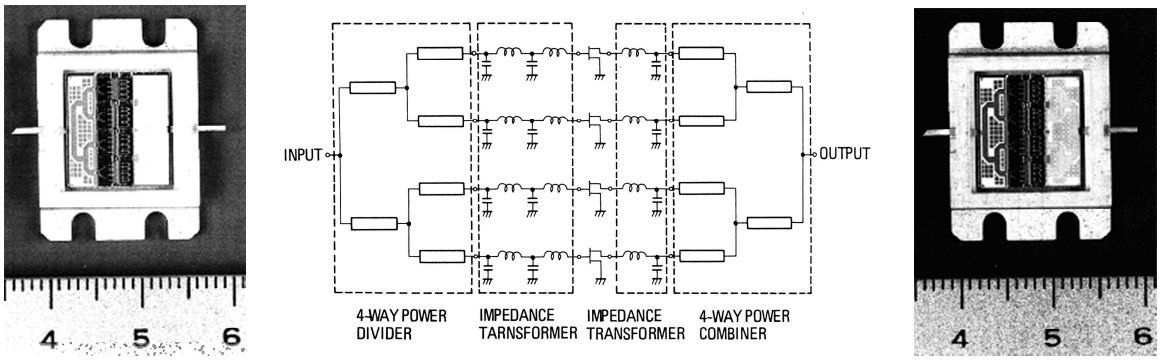

(a) (b) (c)

Figure 2.6. Fujitsu FLM4450-25D IMFET. Fujitsu's FLM4450-25D IMFET, showing the 4 chips of 4 FETs and (a) Input dividing / impedance transforming networks, (b) overall schematic of the IMFET, and (c) output impedance transforming / combining networks, from Walker [6].

Monolithic Level Corporate Combining

Corporate combining is also used at the monolithic level. Here the combining network is integrated with the active devices during device fabrication. Fig. 2.7 shows a three section high power amplifier Mimix [8], implemented as a Gallium Arsenide (GaAs) Monolithic Microwave Integrated Circuit (MMIC), that uses corporately combined individual FETs, in a 2, 4, 8 combination in order to achieve a gain of 21 dB with a typical saturated power of 40 dB-milliwatts (dBm) (10 W) over the frequency range from 8.5 to 11 GHz. This device operates at 8 V and 4.2 A typical, with a power added efficiency of

[2] 5.85 to 6.75 GHz

around 30%. The size of this chip is 4.29 mm(w) x 4.94 mm(l) x 0.11 mm(h). However it needs to be bonded to a substrate and requires wire bonding for the RF and DC connections. Losses also limit the number of devices that can be combined in this form. Another example at 23 GHz is given at Triquint [9].

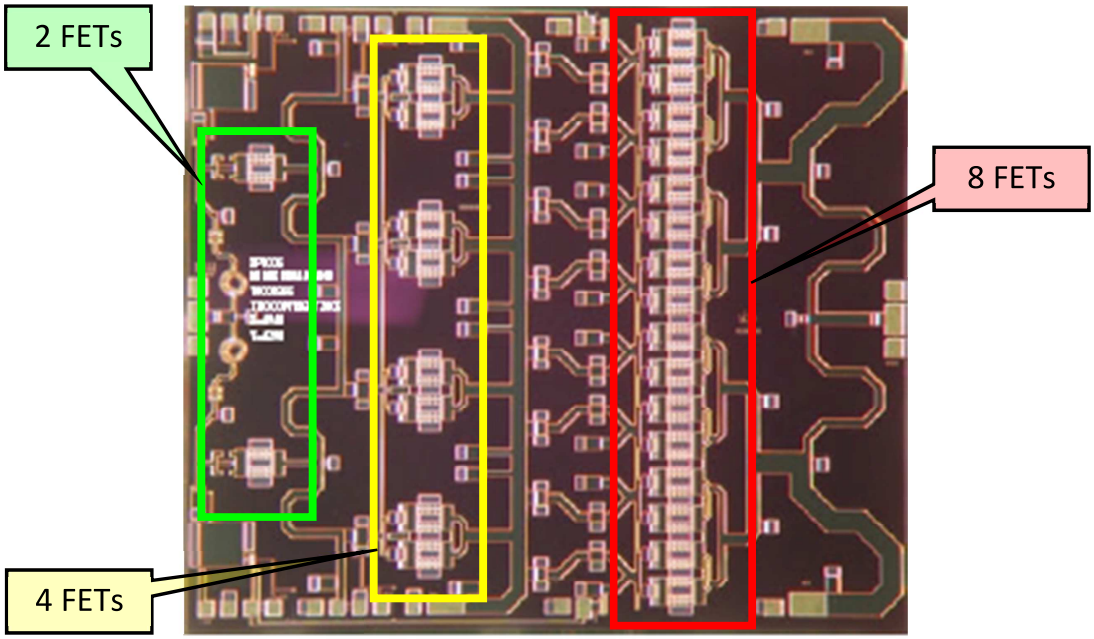

Figure 2.7. Mimix XP1006 monolithic chip combined power amplifier. Photograph of a monolithic level high power amplifier using corporate divider / combiner networks combining 8 devices, from Mimix [8].

2.2.3 Spatial / Quasi-Optical Combining Concept

Spatial or QO combining, DeLisio and York [4], Wang *et al* [10] and Huang and Dou [11], use the proper phasing of many active radiating elements to combine power in free space. An early demonstration of antenna based power combining was described in Staiman [12] in 1968 using 100-transistor amplifiers giving a gain of 4.75 dB and a power output of 100 W at 410 megahertz (MHz). QO techniques were proposed as a means of obtaining higher output powers at millimeter wave frequencies due to the limitations of conventional type power combining techniques by Mink [13] in 1986.

Spatial combining provides enhanced RF efficiency by coupling the active devices to large aperture guided beams or waveguide modes. Combiner losses are independent of the number of devices because all devices are in parallel and combining takes place in free space in low-loss waveguides. The losses are as a result of coupling between the

active devices and free space (antenna efficiency or transition losses) and are typically in the range of 1 to 2 dB depending on the frequency of operation. However once these losses are overcome then more devices can be used to obtain higher output powers without the limitations of other combining methods.

QO generally means an electronic system that uses higher-order beam guiding components, i.e. like optical lenses and mirrors. Spatial combining uses circuit based feed networks and QO uses wave based feed networks, i.e. fields in a waveguide. Spatial or QO combining has been researched as an alternative method of active device combining that offers large scale power combining without the limiting losses of divider / combiner transmission line networks, DeLisio and York [4].

Fig. 2.8 shows a comparison between corporate and spatial combining efficiency versus the number of devices for various losses. It can be seen that beyond about 30 to 32 devices that spatial combining has the advantage over corporate combining in terms of combiner efficiency. Other comparisons related to the effects of increasing the number of devices, for example thermal issues, will be discussed later.

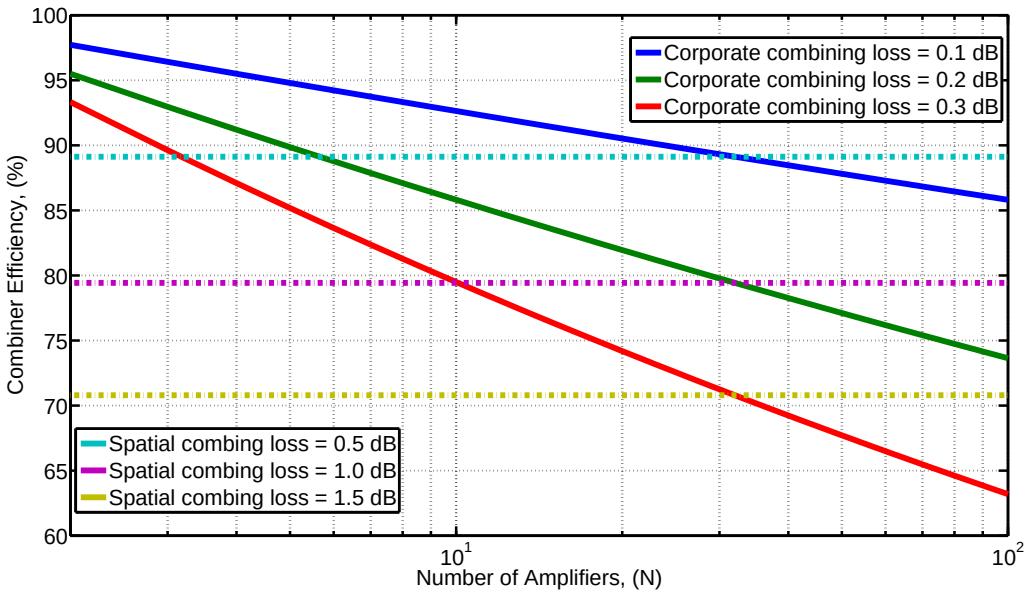

Figure 2.8. Comparison of corporate versus spatial combining efficiency. Comparison of combining efficiency versus number of elements for various corporate and spatial combining losses.

2.2.4 Spatial / Quasi-Optical Combining Methods

The two methods generally used for spatial combining are tile and tray spatial combining as shown in Fig. 2.9. The difference between the two is that in the tile approach the incident propagating wave on the tile is normal to the surface of the array whereas for the tray approach the incident propagating wave is tangential to the array surface. Each technique will be discussed separately.

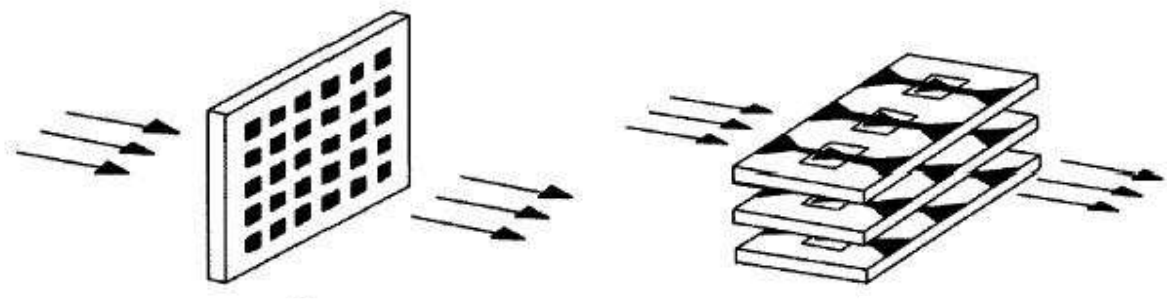

Figure 2.9. Tile and tray combined amplifiers. Tile (a) and tray (b) combined amplifiers, from DeLisio and York [4].

2.2.5 Tile and Tray Spatial Combining

The tile approach consists of an incident wave propagating normal to the planar surface of the tile and for the tray approach an incident wave propagates tangentially to the planar surface of the tray.

Tile Spatial Combining

There are two different architectures within the tile approach. These are the grid and the active array, DeLisio and York [4]. Both techniques will be discussed. Tile spatial combining consists of a planar layer that has a 2-Dimensional (2-D) array of interconnected devices, either discrete, chip or of monolithic form. electro-magnetic energy is coupled into and out of these active tiles via large aperture guided beams or modes within waveguide structures [4]. Tile spatial or QO combiners were originally implemented with discrete, packaged active devices and soft / flexible Printed Circuit Boards (PCBs) as demonstrated by Kim *et al* [14]. These were tested in the far field; refer to Section 2.2.5. This then progressed to active individual chip devices and finally to fully monolithic active substrate arrays or tiles [15]. However heat generated

by the large number of active devices requires efficient thermal power extraction techniques and currently this is not optimum, Pajic and Popovic [16], as heat removal is only achieved in the tile approach through conduction via the edges only. In addition, this approach requires the use of heat spreaders. Other limitations of the tile approach are; (i) bandwidth is limited due to the use of small resonant input and output dipole antennas and also the need for input and output polarisers, that are required to maintain good in/out isolation, thus preventing oscillations and (ii) gain and power per cell is limited due to small cell size, [4].

Grid Amplifier (Unit Cell $< \lambda_o$/2) Grid amplifiers are formed by the parallel combination of active devices, typically FETs, connected together in the same plane. The grid amplifier uses a differential connection of two FETs that have a common source connection. The FET's gates are connected to input dipole antennas in one orientation (polarization) with the FET's drain outputs connected to another set of dipoles in an orthogonal orientation (polarization), as shown in Fig. 2.10. Appropriate drain and gate tracks are provided to allow stable biasing for the FETs.

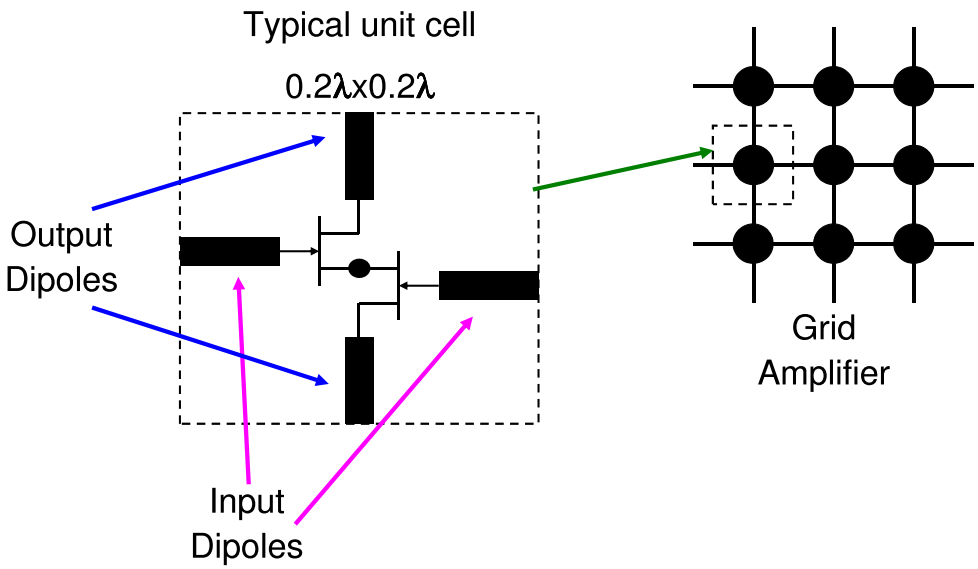

Figure 2.10. Grid amplifier. Caltech grid amplifier, left element details, right assembled into grid form, adapted from DeLisio and York [4].

Active Array Tile Spatial Combining (λ_o/2 $<$ Unit Cell $< \lambda_o$) Active arrays differ from the tile approach because larger unit cells that contain more conventional antennas, like patches or slots, form the active array. The larger cell size allows higher gain

and power multistage MMICs to be integrated into the array thus enabling higher gain and power arrays to be formed. An example is given in Section 2.2.5.

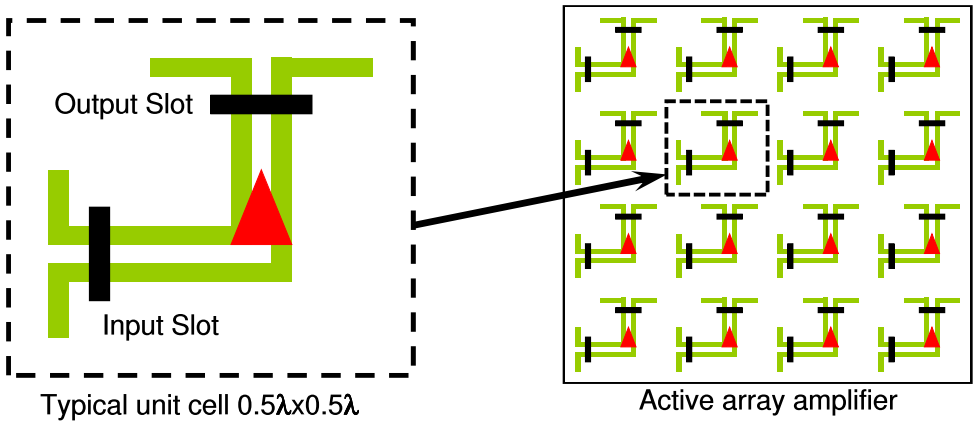

Figure 2.11. Active array amplifier. Active array amplifier, left individual cell, right combined as an array, adapted from DeLisio and York [4].

Packaging Tile Spatial Combiners Early QO amplifiers were originally measured in the far fields between horn antennas [14]. This approach was useful for laboratory characterization but the high path losses meant that this technique was not suitable for practical purposes. QO amplifiers have also been tested with dielectric lenses [15], but the focusing causes a non-uniform power distribution across the plane of the amplifier and this configuration is very bulky. Planar lens amplifiers that use appropriate phase delays across the amplifier array to focus the power have also been used, see Section 2.2.7 and also DeLisio and York [4].

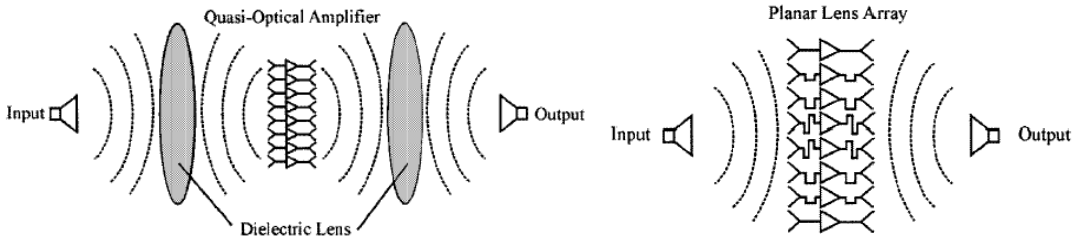

Figure 2.12. Quasi-Optical amplifier - Free-space. left, using a dielectric lens-focused system and right, a planar lens array from DeLisio and York [4].

However a more practical and usable grid amplifier needs to be appropriately housed in a structure that will allow electro-magnetic energy to transition from standard waveguide and be evenly distributed across the amplifier array input and then efficiently collected at the output for further transmission following amplification. For larger arrays

that would be operating in oversized waveguide then sidewall loading may be needed to ensure a uniform array illumination. The housing must also provide appropriate mechanical support for the grid amplifier as well as providing heatsinking for the heat that is generated from the active grid amplifier. Examples of these various packaging structures are shown in the following sections.

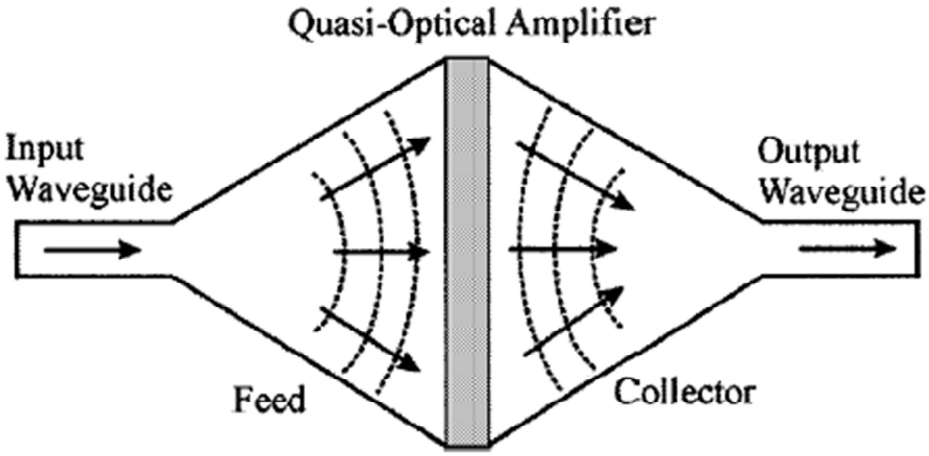

Figure 2.13. Quasi-Optical amplifier - Enclosed. QO amplifier in an enclosed waveguide structure from DeLisio and York [4].

Discrete Level Tile / Grid Spatial Combining Originally grid amplifiers were demonstrated using discrete packaged devices as a proof of concept [14]. They have been included here to describe the concept and are used for comparison. The grid amplifier described here used 50 discrete packaged Fujitsu Semiconductor FSC10LG MESFETs connected as differential pairs in a 5 x 5 grid. These devices were mounted on 2.54 mm thick Roger's Duroid substrate (ϵ_r = 10.5) with input and output polarisers used to complete the grid amplifier as shown in Fig. 2.14 . Details of the FET's connection are shown in Fig. 2.14 (b). The grid amplifier assembly is then supported in free space between an input and output horn antenna as shown in Figs. 2.15 and 2.16.

Chip Level Tile / Active Array Spatial Combining To further improve on the performance of discrete grid amplifiers, construction of a chip level tile combiner has resulted in a higher level of integration. An example of this construction is a 45-element array that has been formed by using microstrip patch antennas feeding a driver chip level amplifier that is mounted on a 0.254 mm thick carbon steel plate developed by Harvey *et al* [18]. The outputs of all of the driver chips are fed to the corresponding high power

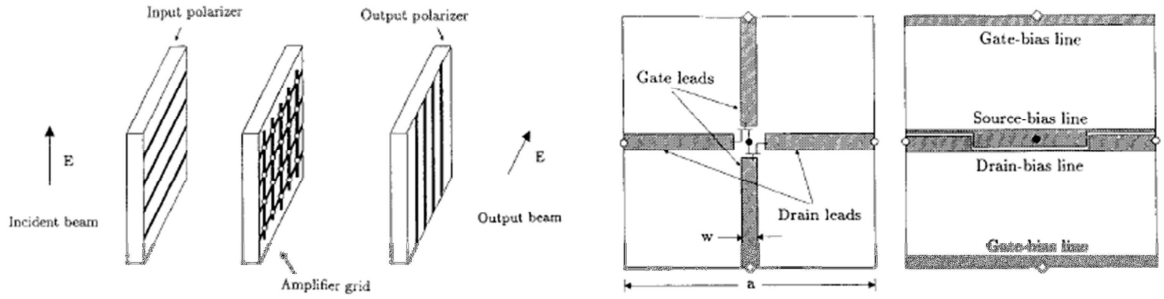

Figure 2.14. Early grid amplifier. Amplifier grid with input and output polarizers, left, Unit cell of a grid amplifier, Front view, centre, and Rear view, right. Symbols indicate the type of connections between front and rear of the grid amplifier. • = 120 Ω source-bias resistor, ◇ = 1 kΩ gate-bias resistor, ○ = drain-bias pin, from [14].

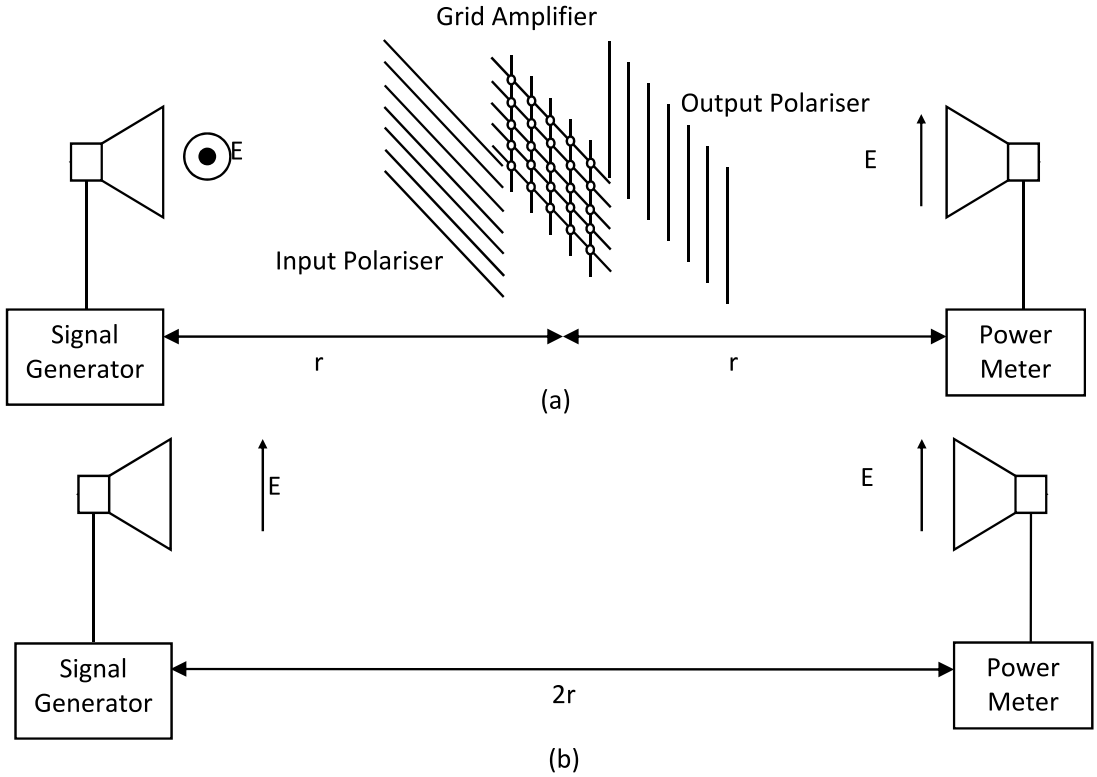

Figure 2.15. Grid amplifier measurement set-up. (a) Measuring the amplifier gain. The gain of each horn is about 10 dB over the frequency range. (b) Calibration measurement with the grid removed and the receiving horn rotated 90° to match the transmitter polarization adapted from [14].

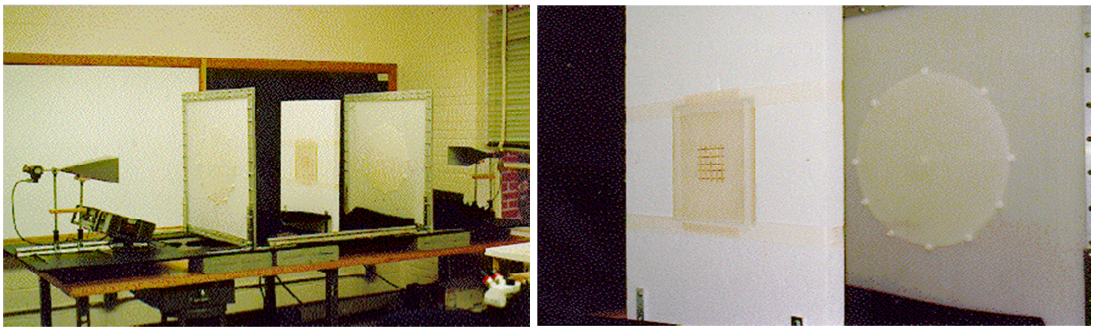

Figure 2.16. Grid amplifier experimental test set-up. (a) Experimental discrete tile test set-up for gain measurement between two horn antennas and (b) close-up of the tile and output polariser, from [17].

stage amplifier on the output side of the tile array via a short section of coaxial transmission line. The input side of the array is illuminated via electro-magnetic radiation from an integrated "hard" horn antenna feed. A "hard" horn feed has dielectric loaded sidewalls in order to obtain a uniform field distribution across the tile / grid amplifier. The radiated signal from the output side of the tile array is collected via a similar hard horn antenna.

One of the issues associated with an array of this size is heat removal. This array uses active devices that consume around 320 W of DC power in total. Several methods have been employed to assist with heat removal including the use of higher thermal conductivity substrates such as Aluminium Nitride (AlN) or Silicon Carbide (SiC) for smaller arrays and diamond for larger arrays but these tend to be more expensive and difficult to process [19]. Here a thicker metal backed substrate has been used, due to lower cost in both material and processing, but this approach is limited by having a requirement to meet QO RF combiner performance which can be limited if the substrate / metal thickness is too large [18]. Liquid cooling has been used in conjunction with thicker metal backed substrates to further improve heat removal but this is a complex solution [19].

Chip Level Tile / Active Array Spatial Combining using Class-E Amplifiers As already mentioned, one of the issues associated with transmission QO amplifiers is thermal management. For a QO transmission amplifier the heat dissipated by all of the active devices needs to be dissipated laterally by conduction, typically through a 2-D heat spreader that has the active tile array mounted to it. As the array size grows, in

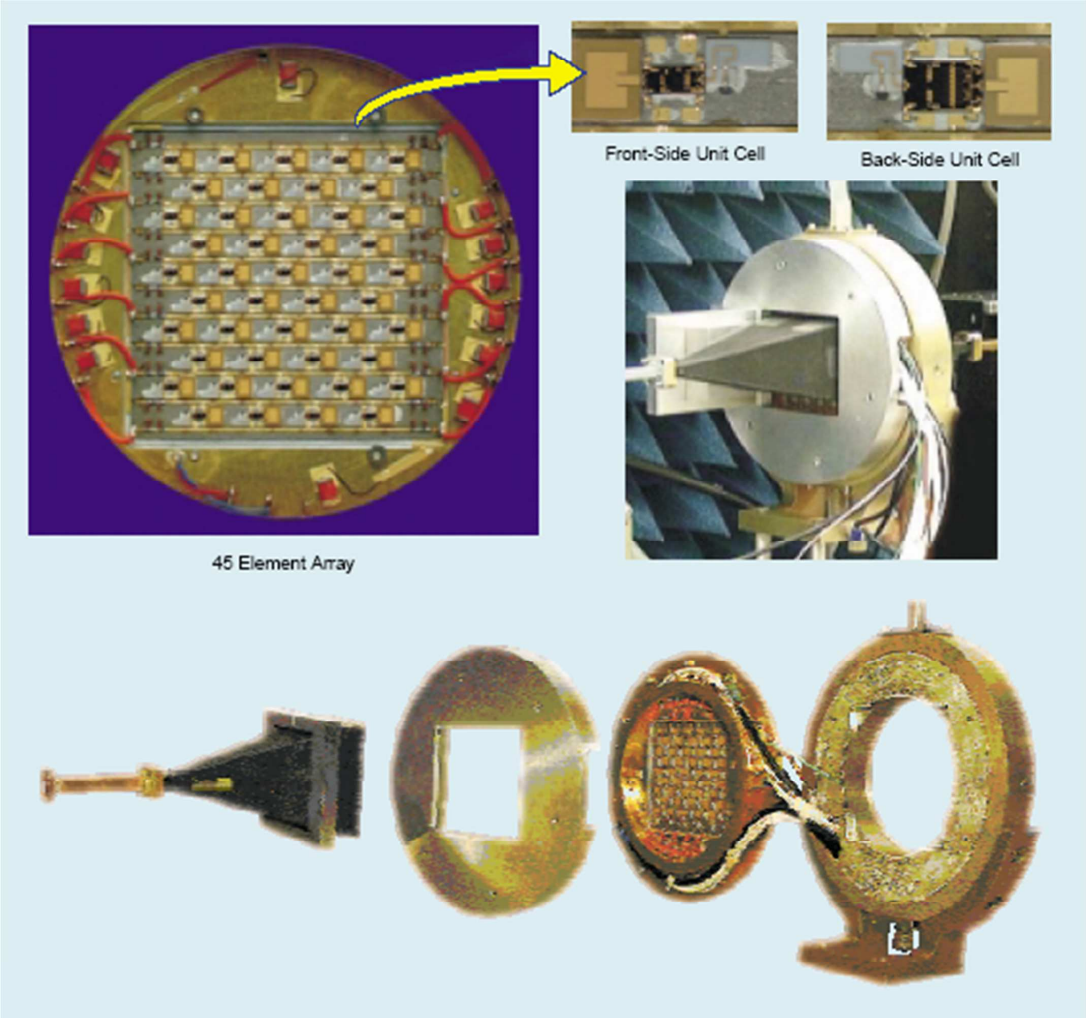

Figure 2.17. Chip level grid amplifier. 45 element Chip level grid amplifier showing frontside and backside views plus assembly arrangements, from [18].

order to increase output power, the heatsinking capability of the heat spreader only increases around its periphery. Thus the centre elements could possibly operate at much higher temperatures than those around the outer edges. This leads to gain and power degradation and if not managed correctly, ultimately leads to system failure. Typically the active devices are operated in Class-A mode with only between 10% to 30% PAE. However a solution to this problem is to operate the active devices in Class-E mode, so that they are operating as switching amplifiers, which have, in theory, an efficiency of 100%, if the complex output load is correctly matched for this mode of operation and frequency and if the output load is also an open circuit at harmonic frequencies. One limitation of this technique is that as a result of the device output capacitance the upper frequency range tends to be low [20]. The maximum frequencies to date are in the upper X-Band range at 10 GHz, Pajic and Popovic [16]. Another requirement

of using Class-E mode amplifiers relates to how the input power must be distributed to the active devices. For amplifiers operating in Class-E mode, having varying input power levels affects both the output signal amplitude and phase (AM/PM conversion) and this significantly degrades the power combining efficiency when operated within a spatial combined amplifier, so the input divider to the amplifiers is via a corporate feed network providing a well known power distribution. This technique has been used previously by Gouker *et al* [21]. Input amplitude variations for spatial combined amplifiers are described in more detail in Sections 2.2.5 and 2.2.5 following.

Monolithic Level Transmission Tile / Grid Spatial Combining To take full advantage of spatial power combining, particularly at millimeter wave frequencies, monolithic level integration of many active devices is required. This has been achieved by several researchers and is now commercially available, Wavestream (now Gilat) [22]. Here, hundreds of active devices are combined in parallel on a single monolithic chip. However with so many active devices in such a small area then appropriate heatsinking is required in order to keep the grid cool. As a result the GaAs substrate is thinned down and mounted on an AlN heat spreader, which is 2 mm thick and has a thermal conductivity of 170 W/m-K, thus providing a good heat transfer path from the chip through to the surrounding housing and heatsink, Kolias and Compton [23]. This chip and heat spreader assembly is then mounted into a frame, and water circulated around the edges to dissipate the heat, Deckman *et al* [24]. Several examples are shown in the Fig.s 2.18 to 2.20.

Monolithic Level Reflection Tile / Grid Amplifier Spatial Combining Also at the monolithic level is the reflection grid amplifier operating in V-Band[3] and fabricated on Indium Phosphide (InP) using TRW's[4] 0.15 micrometre (μ**m**) High Electron Mobility Transistor (HEMT) process., Cheung *et al* [25]. This is a grid amplifier where the incoming signal is amplified by a grid amplifier that is mounted directly to a back short. The cross-polarised amplified output signal is transmitted back towards the input with the output signal being extracted via a cross-polarised horn or orthogonal mode transducer. The benefits of this technique are that the size of the amplifier is reduced, as it is essentially folded back on itself via the reflection of the cross-polarised output signal, and the back short can be used as a heatsink thus providing excellent thermal

[3] 40-75 GHz, Inter-satellite, WiFi and mobile backhaul

[4] Thompson, Ramo, & Wooldridge, now Northrop Grumman

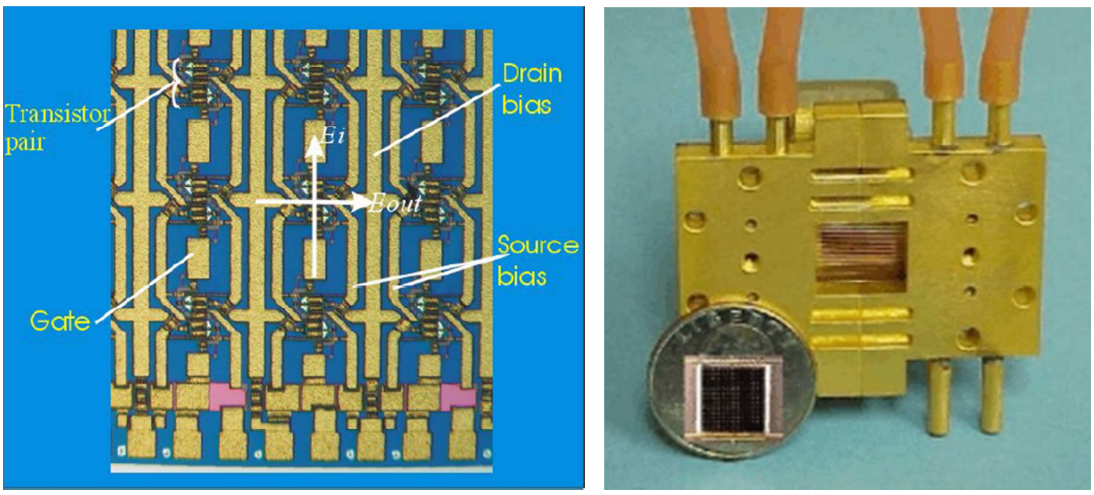

Figure 2.18. Monolithic V-Band grid amplifier. Ei and Eout arrows indicate the input and output polarizations of the field. The unit cell width and height is 400 μm [25] (left) and assembled monolithic transmission grid amplifier showing water-cooling heatsinking, from Caltech [26] (right).

management for the active grid amplifier. A limitation of this technique is that it is difficult to tune the input and output independently and this leads to a reduced operating bandwidth.

Overmoded 3-Dimensional (3-D) Tile / Grid Spatial Combining Bae *et al* [29] has demonstrated a spatially combined power oscillator, but with potential application to a spatially combined amplifier, by the use of an array of fundamental mode waveguides containing Gunn diodes within a closed overmoded waveguide resonator. For this configuration diffraction losses, which are generally seen for small sized arrays using open resonators, are avoided and a mode conversion efficiency of close to 100% can be achieved. A power combining efficiency of 80% is achieved at around 60 GHz. Fig. 2.23 shows the configuration of the overmoded oscillator that consists of an N x M array of fundamental mode Transverse Electric (TE), TE_{10}, waveguides that use pyramidal horns to transition the Gunn diodes to the input and output TE_{N0} overmoded waveguide. The input overmoded waveguide resonator has a cross-sectional area greater than an operating waveguide and also contains a sliding short circuit. The overmoded resonator allows the oscillator to operate in a single mode because the NxM TE_{10} mode array transfers energy to the TE_{N0} overmoded waveguide via the pyramidal horn transitions with 100% conversion efficiency. This is because the electric and magnetic fields at the boundary between the horn array and the overmoded waveguide are exactly the

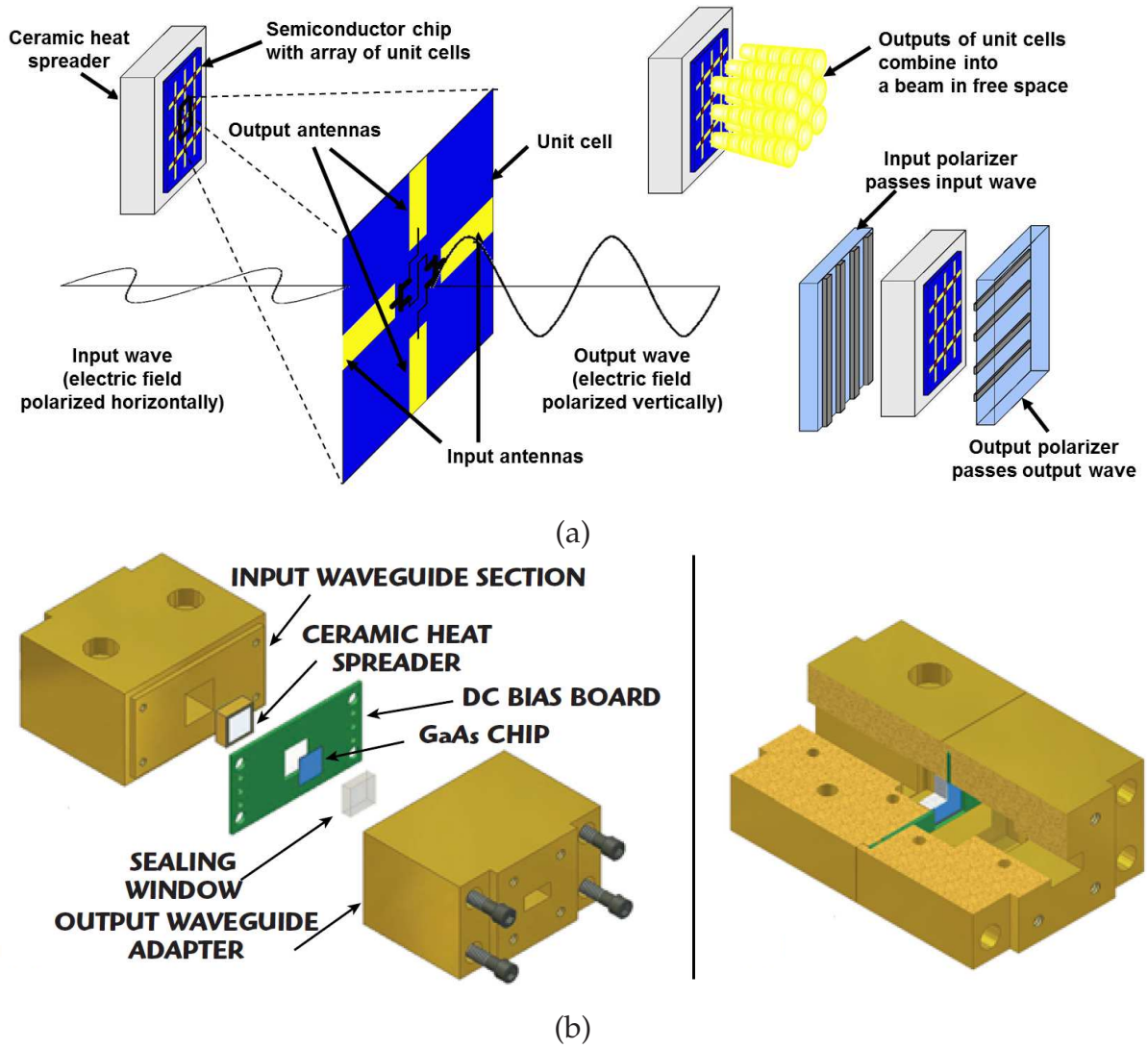

Figure 2.19. Transmission grid amplifier - Wavestream. Construction and assembly, from Rosenberg *et al* [27].

same. The Gunn diodes are mounted in the centre of the TE_{10} mode waveguides with DC bias applied via insulated metal posts. One of the advantages of the solid metal pyramidal horn array is that it provides a large heatsink for the Gunn diodes that have only a 6% DC to RF conversion efficiency. The heatsinking is not optimum as inner array elements cannot directly connect to outer external heatsinks and the horn transitions tend to make the overall assembly longer. For a 3 x 3 array at 61.2 GHz an output power of 1.5 W with a combining efficiency of 83% and an improvement of phase noise from -85.7 to -95.8, dB relative to the carrier (dBc), dBc/Hz over a single diode oscillator has been achieved. It should be noted that an amplifier using this concept has not been demonstrated.

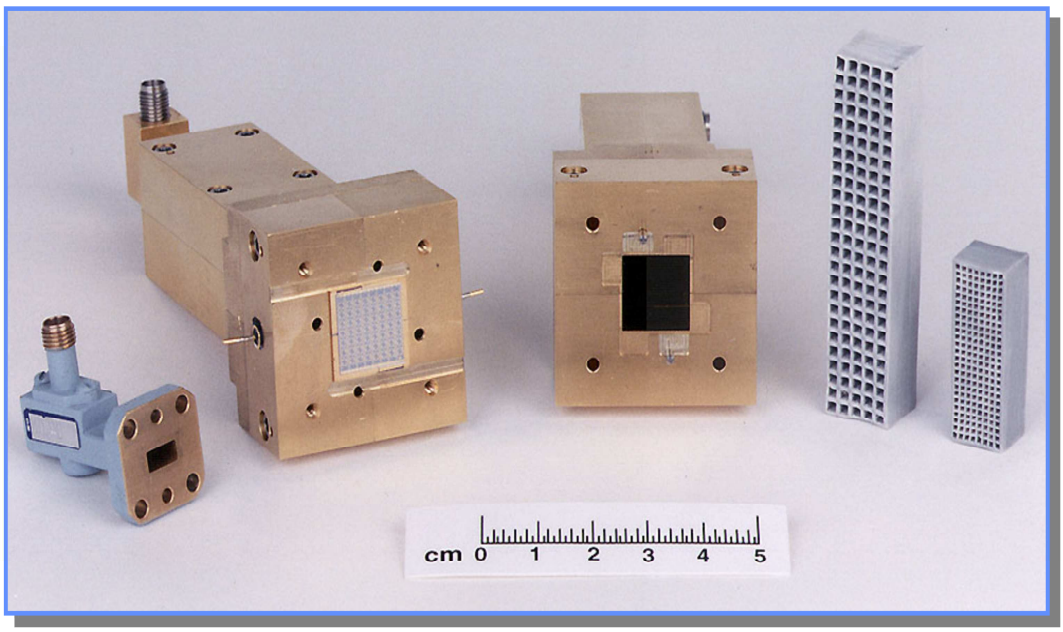

Figure 2.20. Quasi-Optical amplifier - Rockwell . Tapered waveguide structure, from Higgins *et al* [28].

Tray Spatial Combining

Another spatial combining technique uses trays where, in this technique multiple individual MMIC active devices are mounted onto metal carriers that are mounted parallel to the waveguide dominant mode E-field within standard rectangular waveguide. The transition from rectangular waveguide to the MMIC's is accomplished via fin-line to Co-Planar Waveguide (CPW) transitions, as shown in Fig. 2.26. Mounting the MMIC's onto the metal carriers or trays is done in order to improve the heat removal from the active devices [31] and [32]. To further improve the thermal performance an insulating, thermally conductive grease has been used between trays, Cheng *et al* [32], but this has resulted in increased electrical grounding resistance between adjacent trays, which increases the potential for oscillation. This technique has been applied at lower microwave frequencies, X-Band, with RF output powers up to 120 W. Other advantages of tray spatial combining are broad bandwidth and enhanced in / out isolation. There has been no thermal comparison between tray and tile configurations so it is unknown if this configuration provides the best thermal orientation. Also the power handling capability of the fin-line / CPW transitions have not been described so the maximum power output for this configuration is unknown.

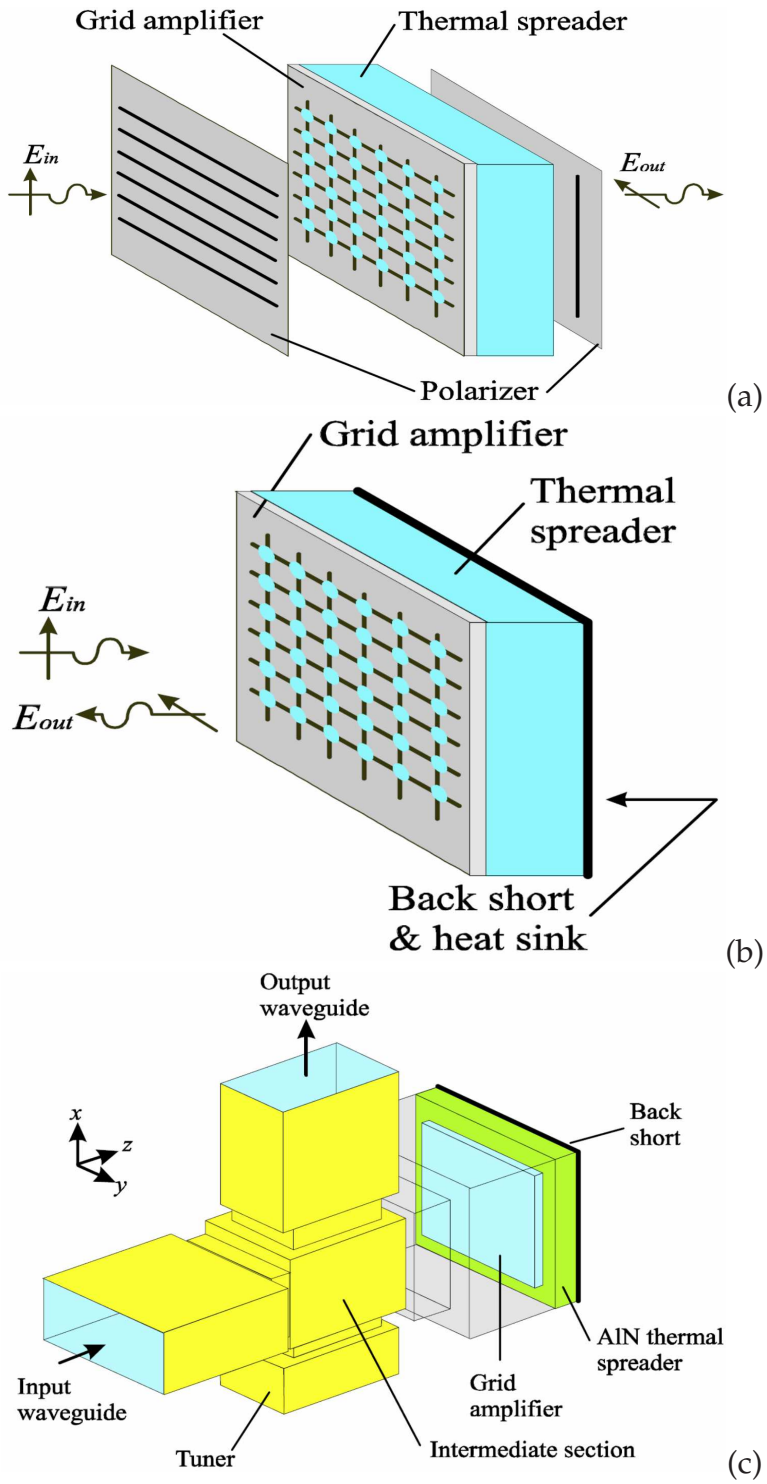

Figure 2.21. Transmission and reflection grid amplifiers. Transmission grid amplifier (a), reflection grid amplifier (b), and layout of the mode-converter for the reflection amplifier (the intermediate section combines the two polarizations before expanding into the over-moded section. The AlN thermal heat spreader and back short transform the grid amplifier impedance by resonating with the inductive component of the chip, (c), from [25].

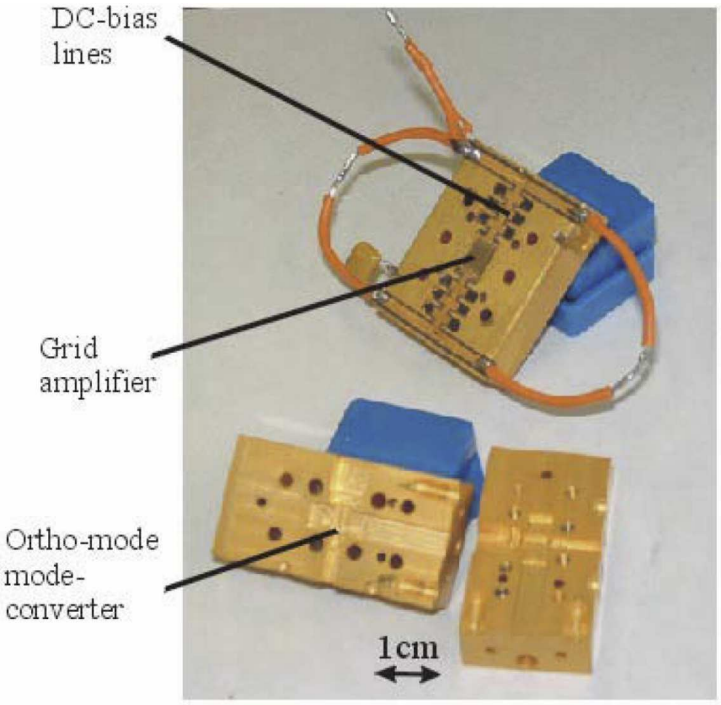

Figure 2.22. Reflection grid amplifier. Fabricated reflection grid amplifier showing ortho-mode mode-converter and DC Bias, from Caltech [26].

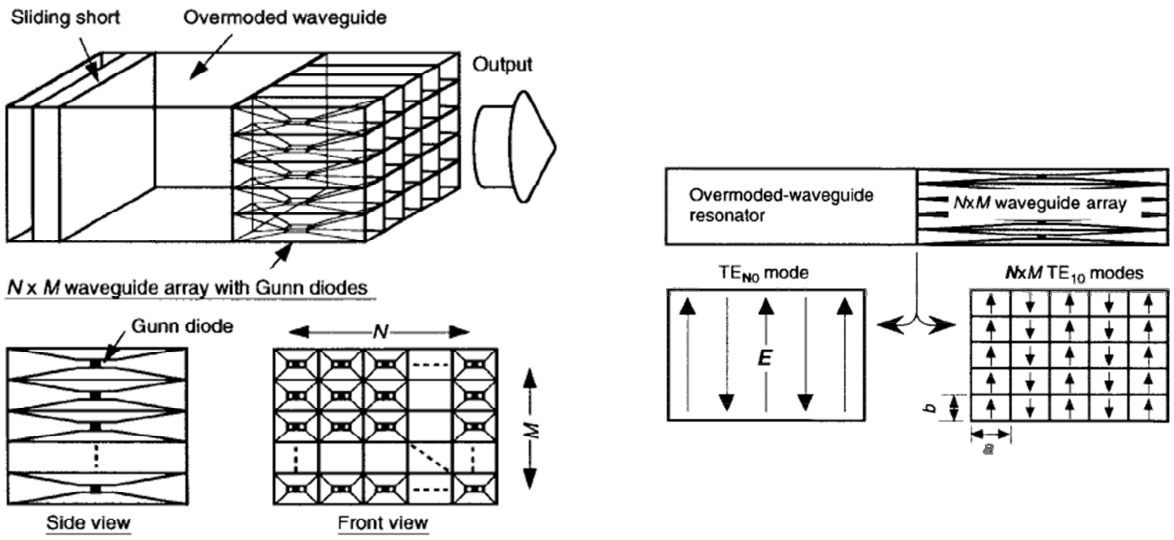

(a) (b)

Figure 2.23. Spatially combined overmoded waveguide oscillator. Configuration of an overmoded waveguide oscillator with Gunn diodes (a), and Mode conversion between the N x M TE_{10} mode array and the TE_{N0} mode in an overmoded waveguide resonator (b), from Bae *et al* [29].

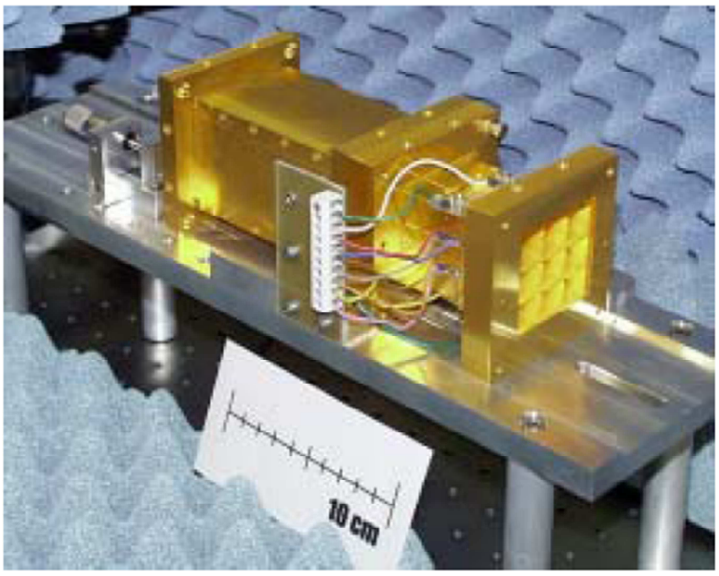

Figure 2.24. Example of a V-Band (60 GHz) overmoded waveguide oscillator. V-Band 3 x 3 diode oscillator, from Bae and Mizuno [30].

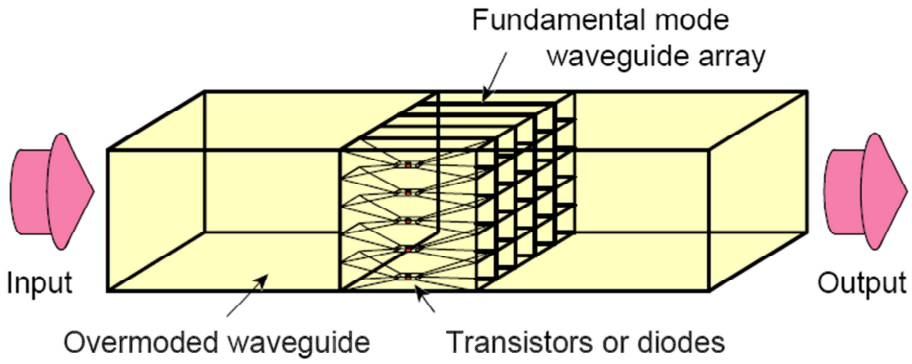

Figure 2.25. Concept for an overmoded waveguide amplifier. From Bae and Mizuno [30].

Waveguide Tray Spatial Combining Tray spatial combining in dominant mode waveguide suffers from the fact that the E-field is not evenly distributed across the waveguide. This means that the trays must be closely packed together around the center of the waveguide so that the E-field variation is minimised or the field incident on the trays must be more evenly distributed to avoid degrading the amplifier efficiency, which can result in soft saturation, Alexanian and York [31] and Jai *et al* [35]. Commercial 14 GHz tray amplifiers are currently available from Wavestream (now Gilat) [36].

There have been no reported studies as to the thermal implications for closely packed trays. Cheng [32] has simulated that for a tray based spatial combiner operating at X-band frequencies, over the range from 8 to 11 GHz, and delivering a power output of

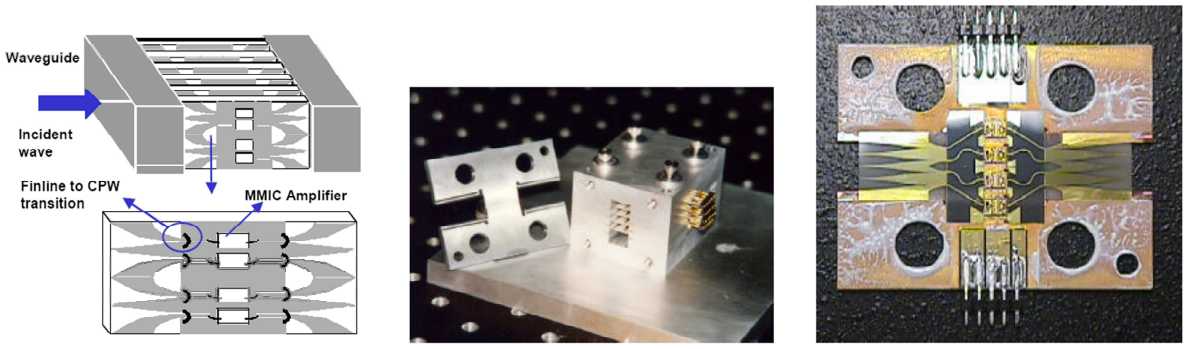

(a) (b) (c)

Figure 2.26. Waveguide spatial combiner. Waveguide based spatial combiner concept (a) York [33], assembled waveguide based spatial combiner (b), and tray containing 4 MMIC's from a waveguide spatial combiner(c), from Cheng and York [34].

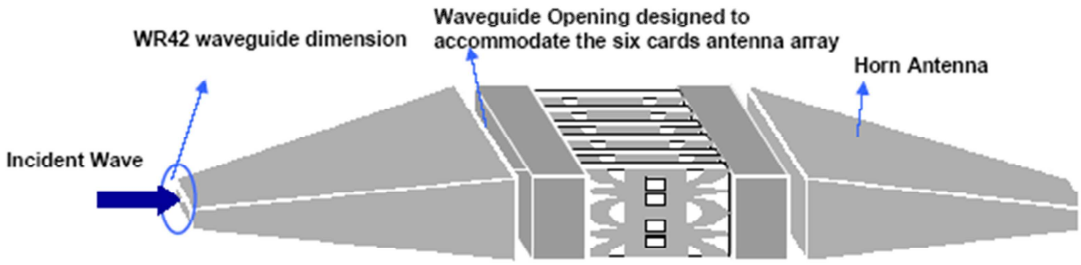

Figure 2.27. Waveguide spatial combiner including input and output tapers. Waveguide based spatial combiner with a taper from standard WR42 size rectangular waveguide, from York [33].

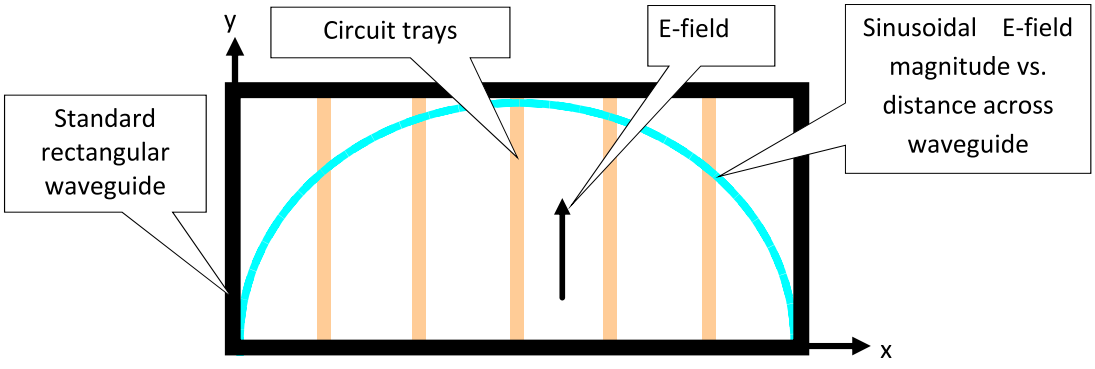

Figure 2.28. Waveguide tray spatial combining - E-field distribution - Equal spacing. Electric field distribution incident on trays placed vertically across a standard rectangular waveguide, adapted from Cheng *et al* [32].

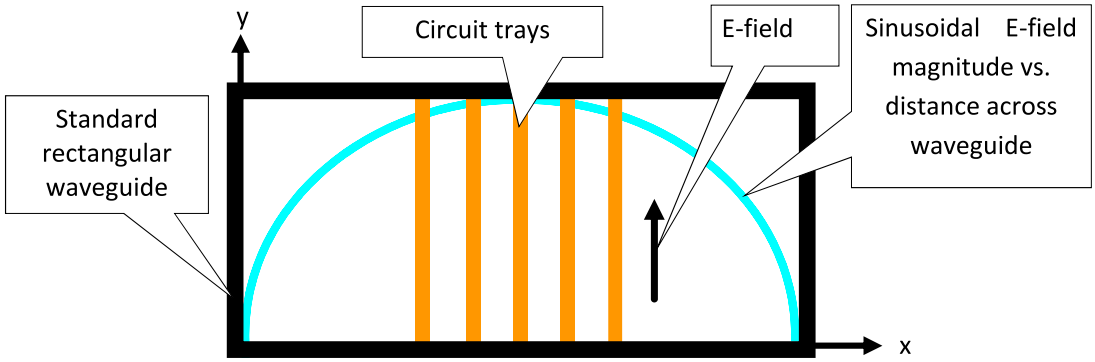

Figure 2.29. Waveguide tray spatial combining - E-field distribution - Close spacing. Electric field distribution incident on closely packed Trays placed vertically across a standard rectangular waveguide, adapted from Cheng *et al* [32].

94.6 W (P1dB) using a total of 4 x 5 W 30% PAE MMIC's mounted to 6 equally spaced trays that the temperature rise at the base of the MMIC's is 52° C above ambient. No data is given for closely spaced trays.

Coaxial Tray Spatial Combining In order to obtain even E-field illumination of trays, another method is to employ them in a radial orientation around the centre conductor of an over-moded Transverse Electro-Magnetic (TEM) coaxial waveguide assembly, however this is also not considered to be the most optimum solution for heat removal, Jai *et al* [35]. The advantages of this technique are increased bandwidth above the standard waveguide tray combiner. The data indicates that for this configuration output power is generally lower compared to rectangular waveguide tray spatial amplifiers, although this is over a wider frequency range, refer to the Spatium data sheet given by CAP Wireless (now Qorvo) [37] and Jai *et al* [38].

Tray Spatial Combining Modifications (Field Modification) As indicated, in Section 2.2.5, the use of trays in standard rectangular waveguide requires that they be more closely packed around the centre of the waveguide. This is where the E-field is greatest and its' magnitude variation is minimised. Minimising the E-field magnitude variation across the trays minimises the output power soft saturation level. Soft saturation is where a number of trays within the amplifier go into saturation before other trays, more specifically the inner trays go into saturation before the outer ones. In order to

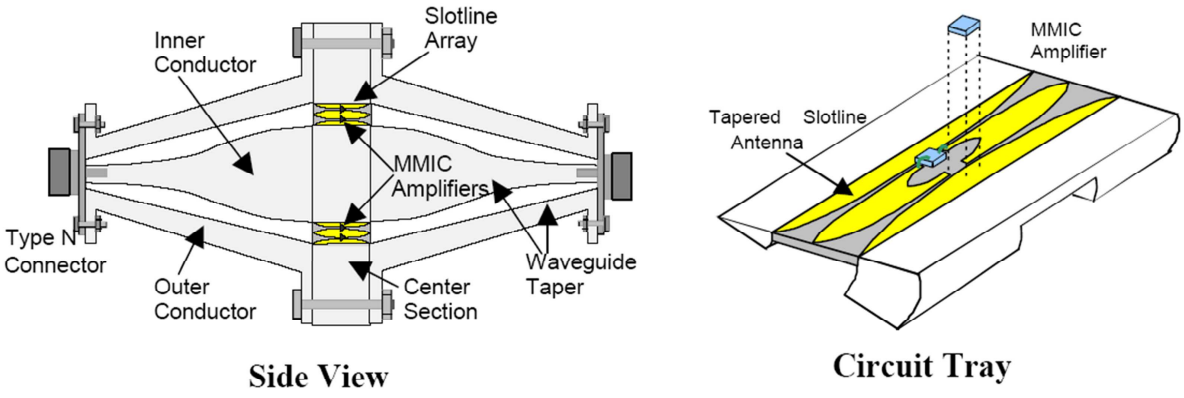

Figure 2.30. Coaxial tray spatial combiner concept. Coaxial tray spatial combiner cross-section and tray, from York *et al* [39].

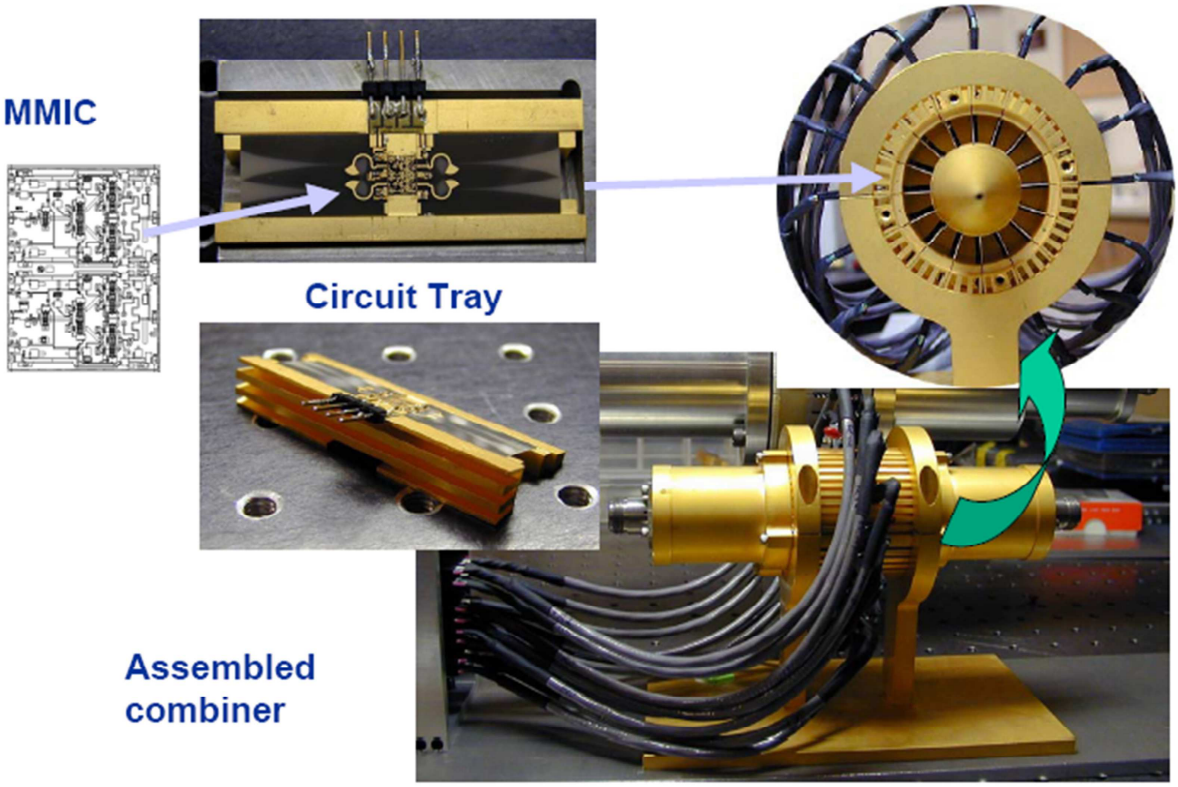

Figure 2.31. Coaxial tray spatial combiner assembly. Coaxial tray spatial combiner assembly, from York *et al* [39].

achieve a more quasi-TEM type mode E-field distribution across the waveguide broad wall dimension, then modification of the field within the waveguide can be achieved by the use of Uni-Planar Electromagnetic Band-Gap Surface or Structure (UC-EBG) modifications to the side walls of the waveguide, Belaid and Wu, Yang *et al*, Karmakar and Mollah [40, 41, 42, 43]. Another technique that can be used to more evenly distribute the E-field within the waveguide is to modify the waveguide walls to provide a hard boundary condition, or uniform field distribution over the waveguide aperture, over a range of frequencies. This Perfect Magnetic Conductor (PMC) evens out the field distribution over that frequency range resulting in even illumination of all the trays within the amplifier. Belaid and Wu [40] have presented results indicating that using waveguide with EBG loaded walls has resulted in P1dB output power improvements of 1.5 dB at 14.75 GHz compared to standard TE_{10} mode waveguide for waveguide based tray spatial amplifiers.

E-field modifications can be achieved by using:

- Dielectric waveguide wall and hard horn loading.
- High impedance electro-magnetic surface waveguide walls (patterns with vias), Sievenpiper *et al* [44].
- electro-magnetic crystal, Higgins *et al* [45].
- Electro-magnetic band gap surfaces UC-EBG (with the possibility of tuning using active varactor diode surfaces) waveguide walls, Belaid and Wu, Yang *et al* [40, 41].
- Use of alternate waveguide modes: Tile, Kamei *et al* [46] and tray (TE_{20}), Belaid *et al* [47]. More detailed background relating to Photonic Band Gap Structure (PBGS) and hard horns is given in Section 2.3.5.

2.2.6 Alternative Mode Tile and Tray Spatial Combining

Alternative Mode Tile Spatial Combining

As an alternative to using hard horn feeds or EBGS waveguide walls to provide uniform TEM field distributions for the input and outputs of grid style QO amplifiers, Kamei *et al* [46] has proposed transitioning from standard TE_{10} mode waveguide to

a larger square aperture overmoded waveguide cross-section. Both the E-plane and Magnetic field vector plane (H-plane) dimensions are increased. The first transition is in the E-plane and the energy from a standard TE_{10} mode waveguide is coupled through a series of irises and essentially split into four TE_{10} mode waveguides. The field distribution in these waveguides is equal in phase and magnitude at their outputs. These waveguides are combined to form the height transition by terminating adjacent waveguide walls a quarter of a wavelength away from the iris coupling holes. The field distribution is uniform in the E-plane and sinusoidal in the H-plane. The H-plane transition consists of two sections of waveguide that increase the guide width from standard to 1.5 (λ_g) in two steps. The size and placement of the H-plane steps is critical to obtaining uniform power and phase distributions. The overall length of the H-plane transition is $0.75\lambda_g$. The field distribution across the $1.5\lambda_g$ aperture is within 3 dB for 75% and within 6 dB for 85% of its width. A mechanical diagram and simulated E and H-plane E-field cuts are shown in Fig. 2.32.

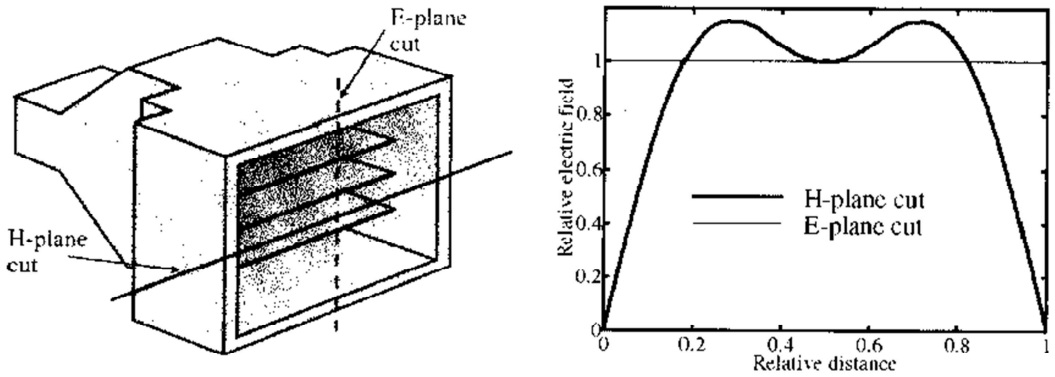

Figure 2.32. Over-moded waveguide transition. Transition to over-moded waveguide and simulated electric field, from Kamei *et al* [46].

Alternative Waveguide Mode Tray Spatial Combining

As indicated in Section 2.2.5, see also Figs. 2.28 and 2.29 , the use of trays in standard rectangular waveguide suffer from the electric field within the waveguide, for the dominant TE_{10} mode, not being evenly distributed across the waveguide, hence leading to reduced combining efficiencies and a lower soft saturation level for the amplifier. Another means of improving on the field distribution is to transform the dominant TE_{10} mode to an alternate waveguide mode being the TE_{20} mode as demonstrated by, Belaid *et al* [47]. Here the TE_{10} mode is transformed into the TE_{20} mode via a fin-line array mode converter or transformer. The fin-line array converters require that

there is a phase difference of 180° between the two fin-lines and that the waveguide can support both the TE_{10} and TE_{20} modes.

The example given by Kamei *et al* [46] showed a modal conversion efficiency of 76% and a TE_{10} mode suppression of 22 dB. Following application of the TE_{20} signal onto four tray amplifiers the outputs of two of the trays are shifted by 180° and the outputs are then spatially combined in the TE_{10} mode at the waveguide output. The combining efficiency using this method for the entire amplifier ranges between 80 to 90% compared with 70 to 80% for TE_{10} mode only spatially combined amplifier. However the structure is complex and the power handling of the TE_{10} to TE_{20} mode converter for the output is not presented. The mode suppression at 22 dB is also low.

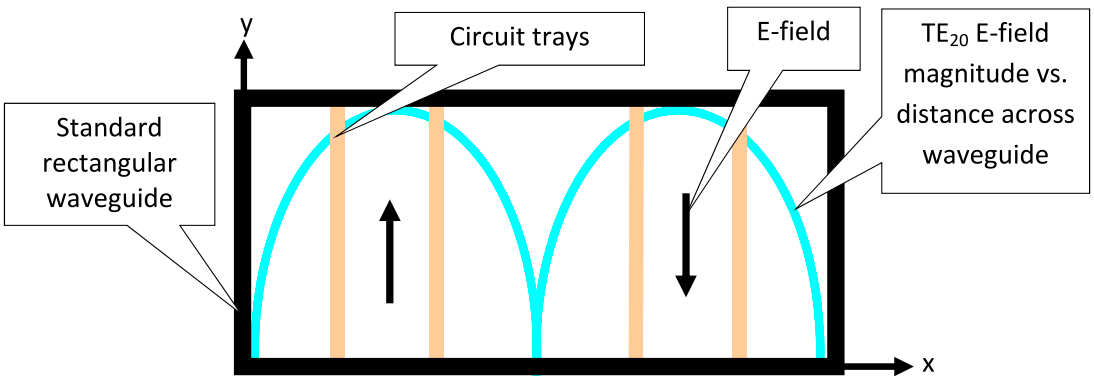

Figure 2.33. TE_{20} mode waveguide - Electric field distribution. Alternate mode waveguide tray combining concept.

2.2.7 Planar Combining

Planar Spatial Combining

The majority of the discussion to date relating to spatial or QO power combining takes place in three-dimensional free space. An alternative, originally proposed by Mink and Schwering [48], to 3-D spatial combining uses a dielectric slab to effectively confine the propagating signal to two dimensions within the dielectric material as a result of total reflection at the dielectric surface, York and Popovic [20] pp. 277-292. The use of a dielectric slab allows for more conventional planar MMIC fabrication, as metallic walls are not required to guide the signals, and improved heat removal as the active devices can be located below the slab in direct contact with heatsink assemblies. Other

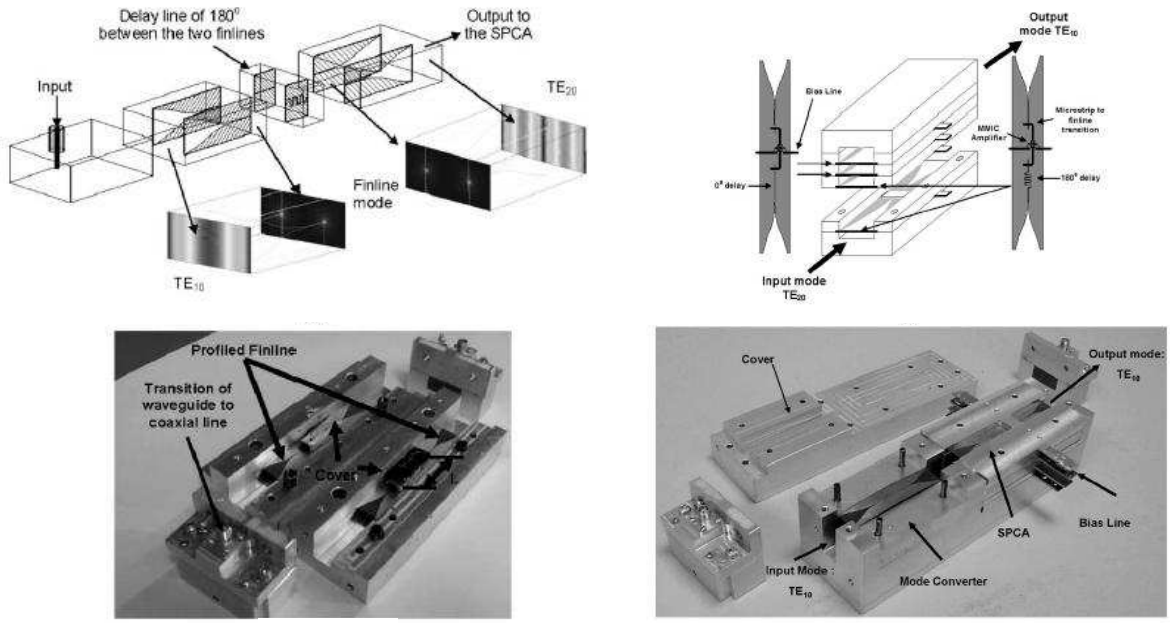

(a) (b)

Figure 2.34. TE_{20} mode waveguide spatial combiner. (a) Alternate mode transformer concept and prototype and (b) alternative mode spatially combined amplifier concept and prototype, from Belaid *et al* [47].

benefits of this technique are reduced size and weight. This structure supports surface modes, which are contained by the dielectric in the vertical dimension, and the transverse dimension supports a QO mode with an essentially Gaussian profile, as shown in shown in Fig. 2.35. Lenses are periodically required to refocus the propagating electro-magnetic signals. These structures are referred to as Dielectric Slab Beam Waveguides (DSBW). Both TE and Transverse Magnetic (TM) modes are supported in DSBW structures with the TE mode preferred. In the TE mode the E-field is parallel to the ground plane and is compatible with slotline microwave integrated circuit technology.

Open DSBW Hwang *et al* [49], as shown in Fig. 2.36, used 12.7 mm thick Rexolite (ϵ_r = 2.57) for the dielectric slab and Macor (ϵ_r = 5.9) for the lenses. The convex lenses have radii of 304.8 mm with focal lengths of 285.4 mm. The distance from the input horn antenna to the first lens was 285.4 mm, the distance from the first to second lenses was 570.8 mm and from the second lens to output horn was 285.4 mm. The overall slab width was 279.4 mm and length 1141.6 mm. The aperture width of both horn antennas

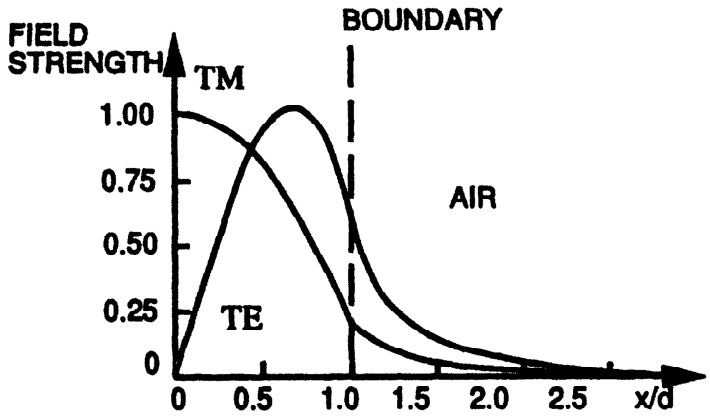

Figure 2.35. Dielectric slab beam waveguide mode field strengths. TE and TM surface mode field strengths for a DSBW system, from York and Popovic [20].

was 90 mm. The propagating TE Gaussian beam-mode signal passes through the slab from the input horn aperture and is focused by the first lens to a width in the centre of the slab between the two lenses that is about the same beam width as the input radiator. At this point, there is an array of four MESFET amplifiers that are formed by using one MESFET (Hewlett-Packard ATF-10235) with an input and output Vivaldi antennas. This array of amplifiers is placed on top of the slab. Adjustment of the individual amplifiers within the array allows the overall gain to be adjusted and optimised. The propagating signal then passes through the second lens to be refocused into the aperture of the output horn antenna. A power gain of 10 dB at 7.4 GHz was achieved. The technique used here is essentially a demonstration of the concept of DSBW and as a result no output P1dB is given and there is no reference to the maximum power handling capacity using DSBW technology. The DC power consumption of 4 off ATF-10235 devices is 0.2 W with each device operated at 2 V and 25 milliAmps (mA).

In a further extension, Hwang *et al* [50] used a similar DSBW as discussed above, but with the amplifiers mounted underneath the dielectric slab and achieved a power gain of 10.5 dB at 7.384 GHz. Mounting the amplifiers beneath the dielectric slab reduces scattering losses associated with the input and output antenna transitions to the MESFETs, however the losses associated with the amplifiers mounted beneath the dielectric slab are still around 5 dB. Locating the amplifiers below the dielectric slab reduces the field perturbations and results in better control of the phase distribution within the array. This is due to the scattering of the field because it is not strongly guided. A metallic cover was also used to increase the output power level by 2 dB. The output P1dB is $<$ -5 dBm. There is no reference to the maximum power handling capacity

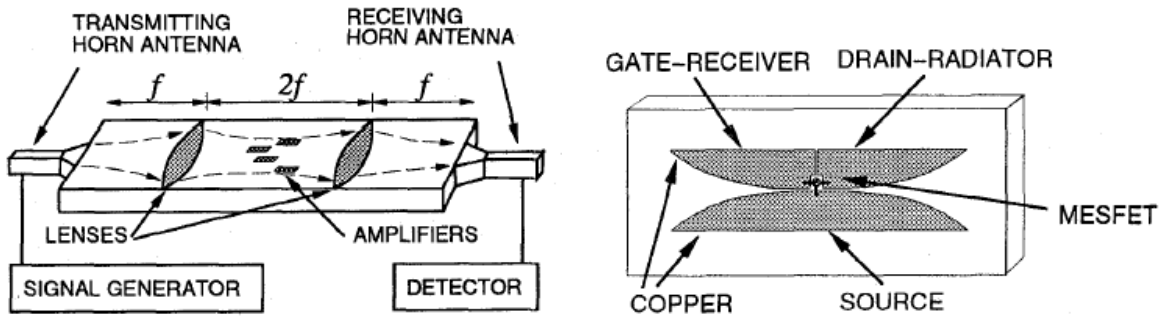

(a) (b)

Figure 2.36. Open Dielectric slab beam waveguide combiner - top mounting. DSBW system using MESFET amplifiers (a) and a single planar MESFET amplifier with Vivaldi input and output antennas as transitions (b), from Hwang *et al* [49].

using DSBW technology. The overall PAE is 5.2% for an input power = +5 dBm with output power = +4 dBm which is low.

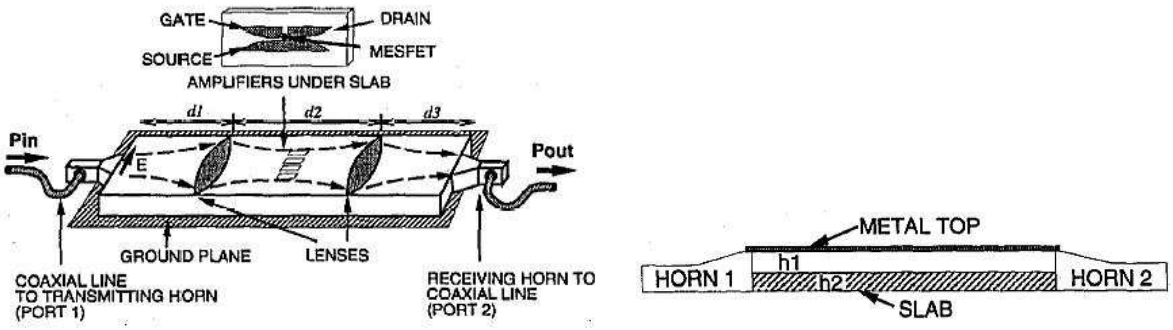

(a) (b)

Figure 2.37. Open Dielectric slab beam waveguides - bottom mounting. DSBW system using MESFET amplifiers (a) and side view of the system with a metallic top (b), from Hwang *et al* [50].

Hwang *et al* [51] again improved on previous DSBW approaches by using concave lenses that reduced scattering and is more appropriate for the design of a power-combining system using MMIC's. Also using higher dielectric substrates, ϵ_r = 10.5, to build the amplifier structures reduced the discontinuities between the amplifier substrate and the ground plane, resulting in reducing the insertion losses from about 5 dB to 1.5 dB. Tapered horns are also used to launch and receive more energy into and from the slab as shown in Fig. 2.39 (a).

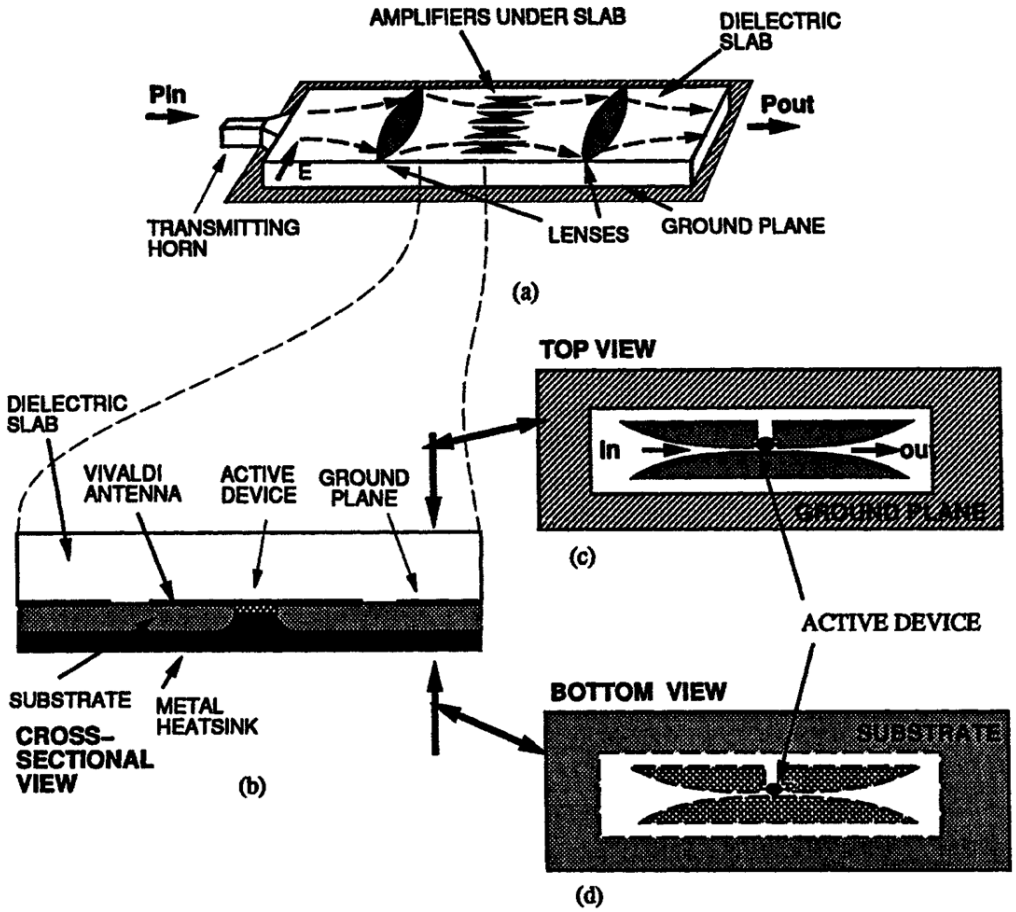

Figure 2.38. Open Dielectric slab beam waveguides - MMIC based. DSBW system using MMIC amplifiers (a) and side, top and bottom views (b), (c), and (d) of the system showing how active MMIC devices can be connected directly to a heatsink, from [20].

For this DSBW the highest amplifier gain of 19.5 dB was achieved at 7.228 GHz with an insertion loss of 3.5 dB. By using concave lenses, the system gain at 7.24 GHz is about 5 dB with a P1dB of 9 dBm. The maximum output power is 5 dBm but this is 25 dB into saturation. There has been no commercialised use of DSBW to date, however technology advancements in other areas have progressed, for example the transition from microstrip to dielectric filled rectangular waveguide, Deslandes and Wu [52], termed Substrate Integrated Waveguide (SIW), has progressed as shown in Fig. 2.39 (b) . Another example is shown in Fig. 2.40 following, Farrall and Young [53]. These will enable DSBW systems to advance towards a more commercialised outcome.

Closed DSBW Closed DSBW spatial combining has been proposed by Hicks *et al* [54] as a means to overcome some of the issues associated with open DSBW systems described in Section 2.2.7. A closed DSBW consists of a dielectric between a top and

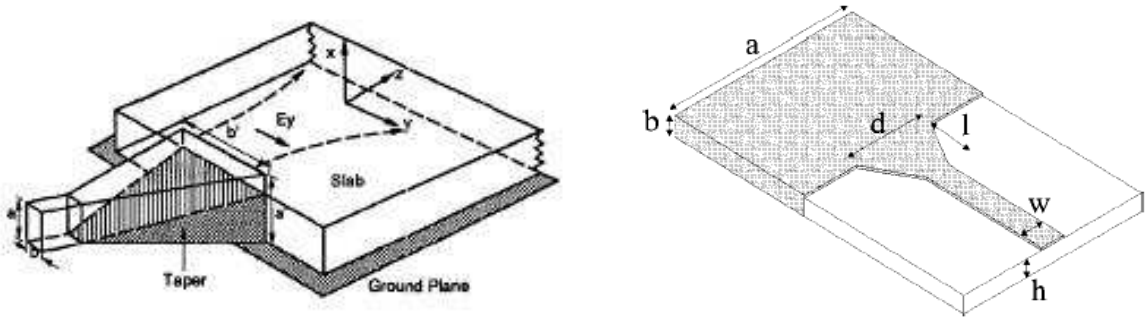

(a) (b)

Figure 2.39. Dielectric slab beam waveguides - transition methods. Improved energy transfer from a launching horn antenna into a DSBW structure (a) Hwang *et al* [51] and a proposed TM mode transition from microstrip to rectangular waveguide on the same substrate (b), from Deslandes and Wu [52].

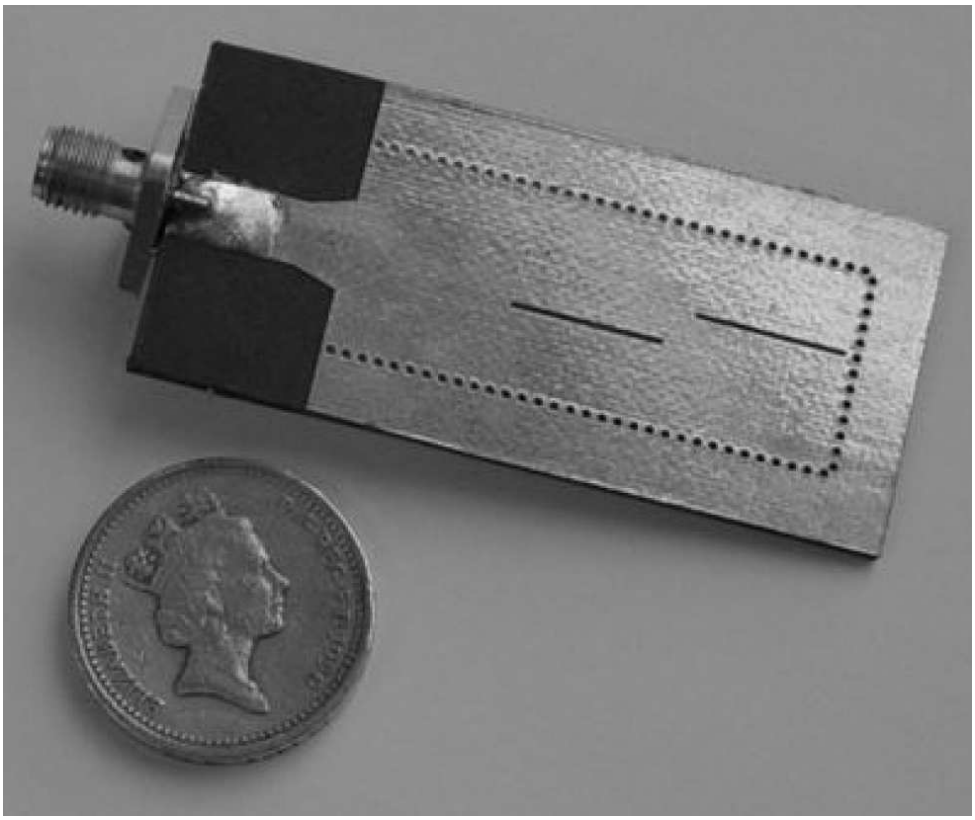

Figure 2.40. Dual slot antenna & microstrip / waveguide transition. Photograph of a dual slot antenna showing implementation of the integrated microstrip to rectangular waveguide transition on the same substrate. Note that the waveguide sidewalls are formed using vias, from Farrall and Young [53].

bottom ground planes. Some of the issues associated with an open DSBW structure related to; (i) excessive scattering losses, if the amplifier array is placed on top of the dielectric, (ii) scattering losses associated with the Vivaldi antennas, (iii) radiation losses from the dielectric top and sidewalls and (iv) beam confinement to within the dielectric slab. Hence open system losses can be minimised by placing the amplifier array in the bottom ground plane beneath the slab, using a top ground plane above the slab and changing from Vivaldi to slot antennas. Having top and bottom ground planes creates a parallel plate waveguide which confines the TM wave beam within the dielectric maximizing the coupling to the amplifier array in the bottom ground plane. This mode of propagation of the electro-magnetic signal is different to the open DSBW, which uses a surface-wave mode of a grounded dielectric slab.

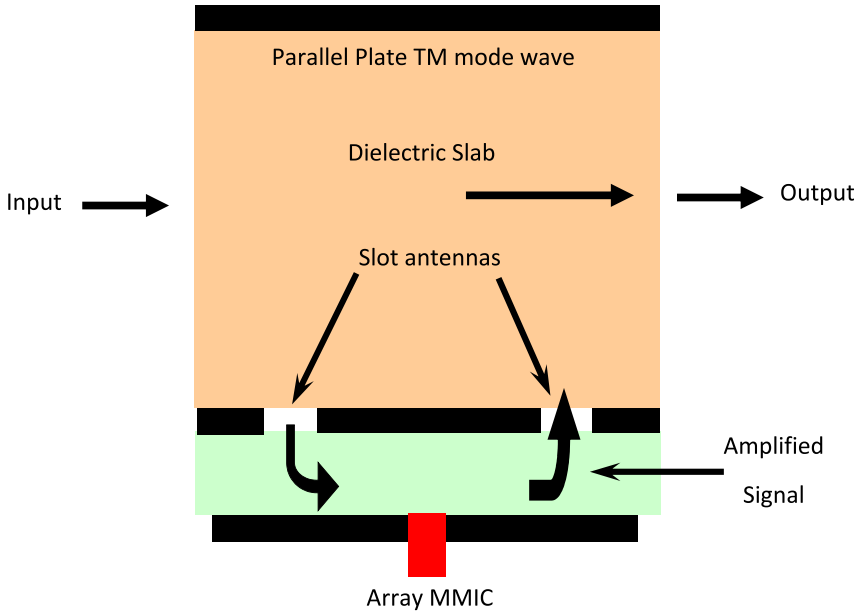

Figure 2.41. Closed Dielectric slab beam waveguides. Concept of a closed DSBW, adapted from Hicks *et al* [54].

Slot antennas are used instead of Vivaldi antennas because the slot antennas present a reduced metal area to the applied signal, thus reducing scattering losses. The slot antennas also provide improved isolation, as they are not located on the same plane like the Vivaldi antenna approach. A disadvantage of the slot antennas is that they offer reduced bandwidth compared to the Vivaldi antennas. Bandwidth is also reduced because of the limited bandwidth of the phase match between the path that the signal takes in propagating through the dielectric slab and the path through the amplifiers. Again the benefits of having the active devices mounted below the dielectric material, as shown in Fig. 2.38, are that heatsinking of the active devices is improved.

Talbot Effect Combiner Another potential "Planar" combiner that could be used for MMICs at millimeter wave frequencies is the Talbot effect combiner, Tayag *et al* [55]. This combiner uses the Talbot effect, of lens-less optical self-imaging, at microwave frequencies as an equal N way divider / combiner. At microwave frequencies the Talbot effect within a planar guided-wave structure is described as Multi-Mode Interference (MMI).

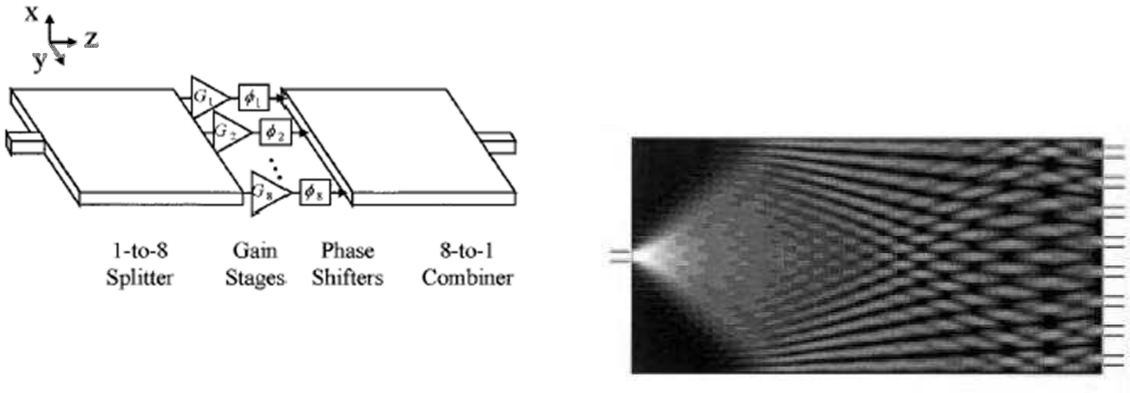

(a) (b)

Figure 2.42. Talbot effect spatial combing. Talbot effect spatially combined amplifier configuration (a) and simulated electric field distribution of a 1:8 power splitter (b), from Tayag *et al* [55].

Consider the 1:8 splitter of Fig. 2.42 (a). Here the input rectangular, TE mode only, waveguide feeds the centre of the much wider rectangular waveguide, which supports multiple lateral TE modes but only a single transverse mode. At the junction of the two waveguides, the single input mode decomposes into ν lateral modes that are supported in the wider waveguide MMI region. As each of the lateral modes propagates through the MMI region with a different phase velocity, the phase difference between the modes accumulates. At the plane where the accumulated phase differences reach an integer multiple of 2 (π), an image, the self-image of the input field distribution is formed. For a compact 1:N way splitter, if an MMI region is centre fed from the input, then only even symmetric modes will be excited. The MMI length is given by

$$z = 1/N(nW^2/\lambda_0), \tag{2.1}$$

where n is the effective refractive index of the transverse waveguide mode, λ_0 is the free space wavelength and W is the lateral width of the MMI region. The splitter can be

operated as a combiner using the same MMI splitter dimensions but the relative phase inputs, from the amplifiers to be combined, must be $\pi/2$, -$3\pi/4$, -$\pi/4$, 0, 0, -$\pi/4$, -$3\pi/4$, $\pi/2$. This input phase requirement ensures that the MMI modes constructively interfere to efficiently combine into the single output waveguide. A prototype of the MMI operating at microwave frequencies, 8.231 GHz, has been demonstrated and a spatial power amplifier has been demonstrated by Keller *et al* [56] at millimeter wave frequencies.

Planar Dielectric-Slab Quasi-Optical (PDQ) power combiner Open DSBW structures propagating the TE mode use E-fields that are parallel to ground planes that are at the base of the dielectric slabs but it is difficult to cleanly excite the TE mode with no perturbation or scattering losses. Yagi-Uda slot antenna arrays (with one reflector and one director), fed by microstrip lines are used to efficiently excite the dominant DSBW mode with the E-field normal to the slab ground plane. Microstrip delay lines are used to focus the guided waves onto the active elements. The delay line length is similar to dielectric lens thickness. Perkons *et al* [57] have used the TM mode and termed this a PDQ that uses Rogers RT 6010 dielectric material for both the microstrip substrate and as the dielectric slab with the microstrip substrate thickness being 0.51 mm thick and the dielectric slab being 5.1 mm thick. A peak gain of 11 dB, with a 3 dB bandwidth of 0.65 GHz, at 8.25 GHz has been achieved using twenty, Hewlett-Packard MGA-64135, GaAs FET MMICs that are cascaded to form ten gain block stages. Output P1dB was 16 dBm at 8.25 GHz.

Similarly to the effects of TE mode E-field variation for tray amplifiers in a rectangular waveguide, amplitude taper on the Yagi-Uda slot array causes reduced output power (soft saturation) with the centre elements delivering more output power compared to the edge elements.

Planar Aperture-Coupled Waveguide Spatial Combining

Hicks *et al* [54, 58, 59] proposed using a stripline array of amplifiers that are coupled to input and output waveguides by waveguide to stripline slot transitions, see Figs. 2.45 (a) and (b). The benefits of this multilayer approach are that the waveguide to stripline slot antennas reduce scattering and improve isolation, but with reduced bandwidth. At this stage there are limited practical results and no commercial outcomes. A gain of 10 dB at 10 GHz for one TM strip-slot cell versus 20 dB for a cascaded Vivaldi antenna

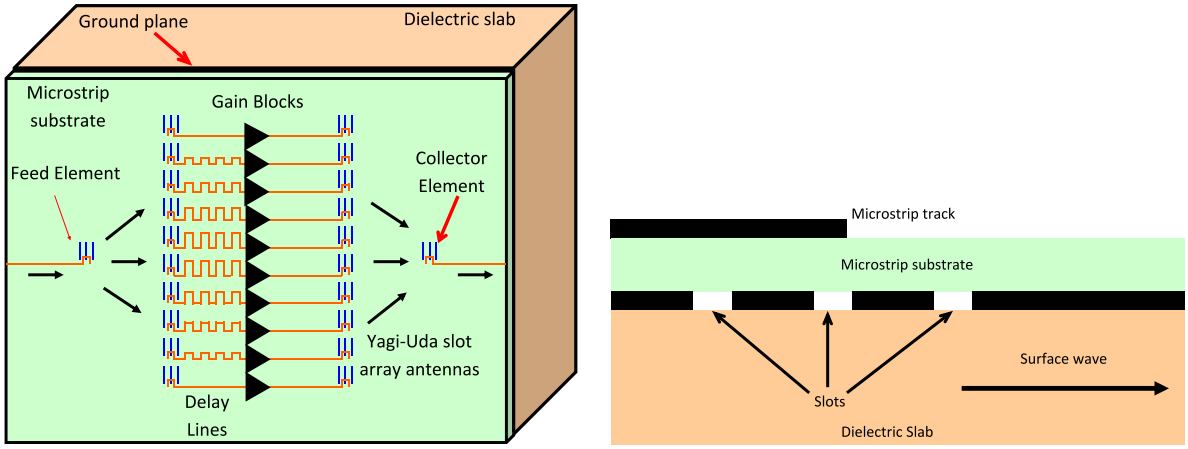

Figure 2.43. Planar dielectric-slab Quasi-Optical (PDQ) combiner concept. Concept of a ten-element PDQ power combiner using Yagi-Uda slot-array antennas (a) and cross-section of the PDQ assembly (b), adapted from Perkons *et al* [57].

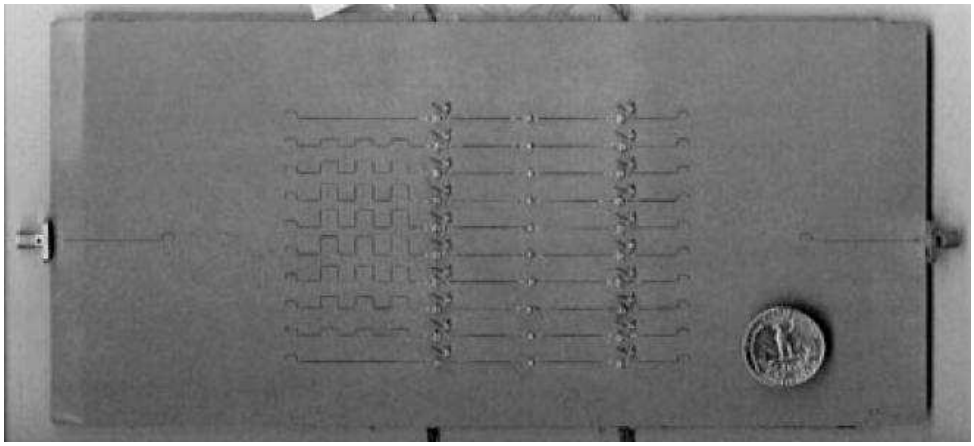

Figure 2.44. Planar dielectric-slab Quasi-Optical (PDQ) combiner implementation. Photograph of the topside of the PDQ combiner prototype, from Perkons *et al* [57].

cell has been achieved so far. Thermal performance of this concept has not been determined and it is unknown if it might be worse as a result of having the active devices sandwiched between the two waveguides.

An alternative combining technique that has been employed using a microstrip resonant slotted waveguide approach, Bashirullah and Mortazawi [60]. Here resonant waveguide to microstrip slots are used to couple and divide energy from an input waveguide into eight IMFETs and then these amplified signals are then combined via output resonant microstrip to waveguides slots into an output waveguide, is shown in Figs. 2.46 and 2.47. For an eight-element combiner the coupling per stage is 9 dB.

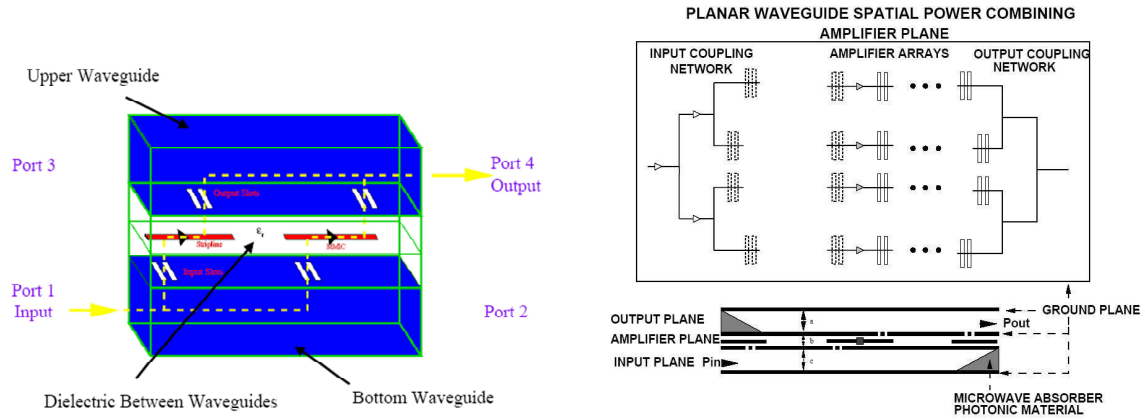

(a) (b)

Figure 2.45. Planar aperture-coupled waveguide spatial combining. A single unit aperture coupled stripline to waveguide transition, from Hicks *et al* [58] (a) and Aperture coupled planar waveguide amplifier array, from Hicks [59].

A combining efficiency of 88% has been achieved with a 3 dB bandwidth of 500 MHz at 10 GHz with a P1dB exceeding 14 W. This technique has the benefits of excellent heatsinking and ease of fabrication but it is large and has low output power at its frequency of operation compared to what is available from current internally matched GaAs MESFET devices, Toshiba [7].

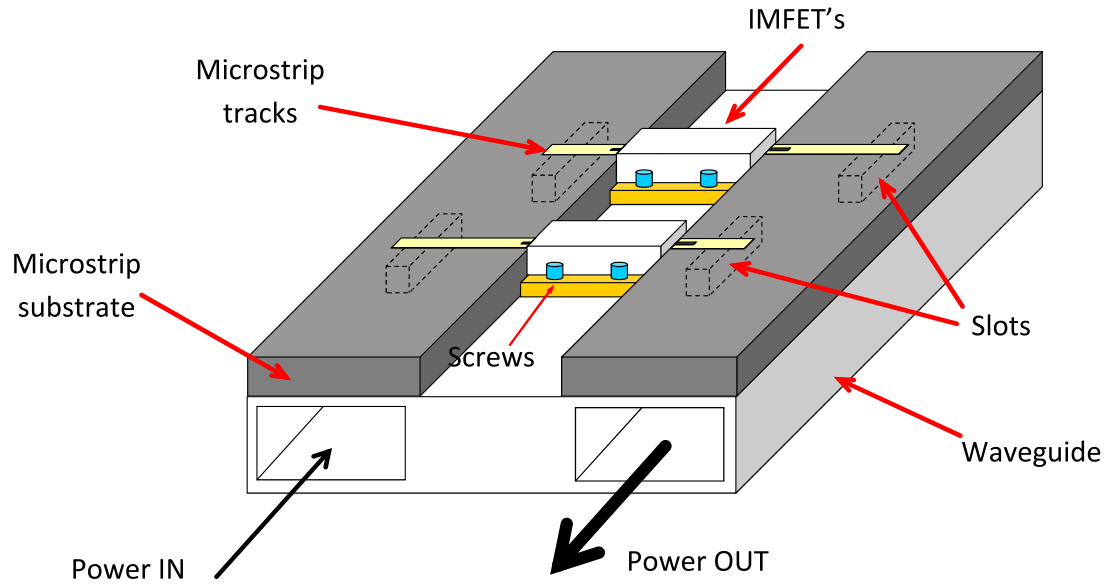

Figure 2.46. Slotted waveguide power divider / combiner topology. Adapted from Bashirullah and Mortazawi [60].

Another example, Eswarappa *et al* [61] of this type of combining, for operation at 28 GHz, is shown in Fig. 2.48.

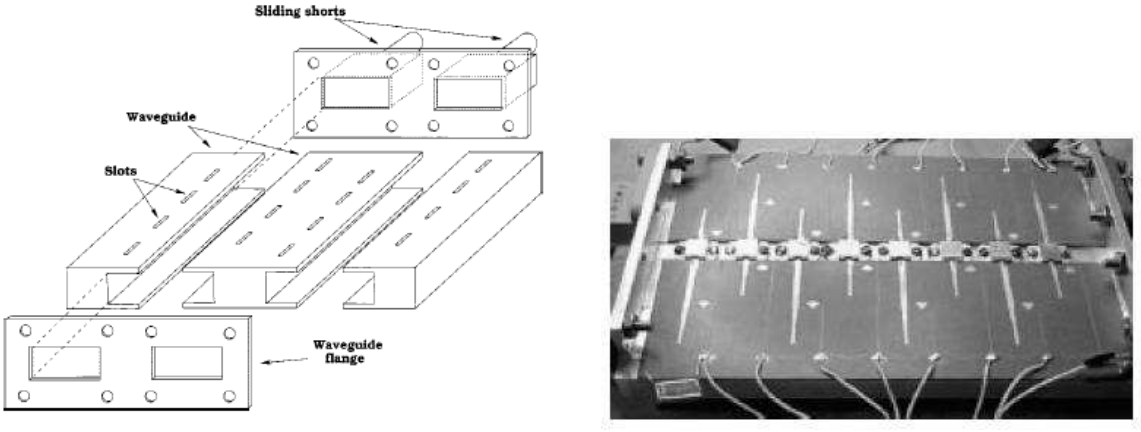

(a) (b)

Figure 2.47. Slotted waveguide power divider / combiner topology assembly and prototype. Slotted waveguide power divider / combiner mechanical assembly (a) and an X-Band waveguide power amplifier prototype using eight internally matched MESFETs, from Bashirullah and Mortazawi [60].

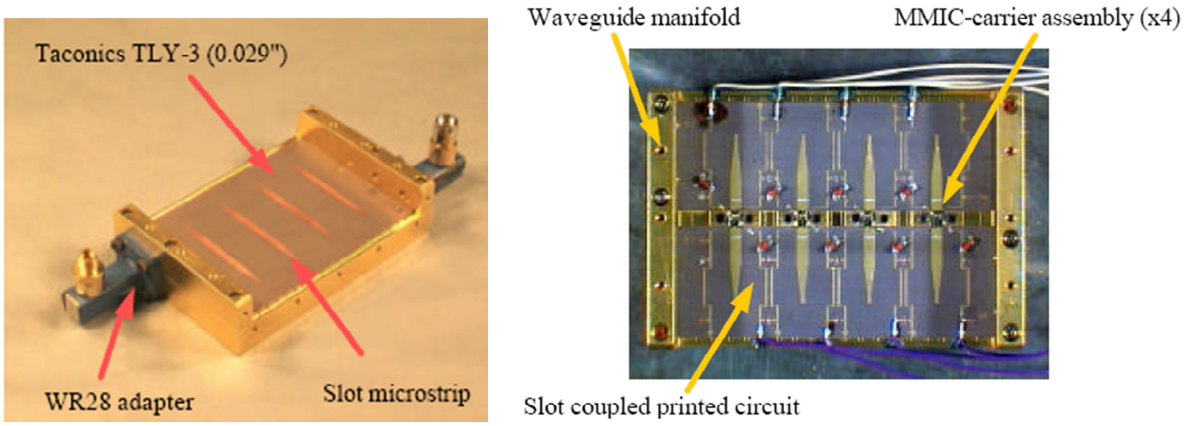

(a) (b)

Figure 2.48. 28 GHz slotted waveguide array and amplifier. (a) Passive slotted waveguide 4-array 28 GHz divider/combiner and (b) 28 GHz slotted waveguide array power amplifier assembly, from Eswarappa *et al* [61].

Planar Serial / Chain Combining

The slotted waveguide traveling wave combiner is also considered, Jiang *et al* [62], because it provides a wider bandwidth as the structure is non-resonant. In this case various levels of power coupling between slotted waveguide/microstrip, obtained by using waveguide inductive posts, are utilised to achieve a traveling-wave multiport divider/combiner, as shown in Fig. 2.49. This circuit achieves high power combining efficiency over a wide bandwidth at Ka-Band[5] while still being relatively simple to fabricate and also providing for excellent thermal management of the active devices. An eight-device traveling wave amplifier, targeted for 30 to 35 GHz operation, has achieved 19.4 dB gain at 34 GHz with a P1dB of 33 dBm at 32.2 GHz with a combining efficiency of 88%. The 3 dB bandwidth was 3.2 GHz. No waveguide/microstrip transition power handling was reported. The passive eight-way power dividing/combining circuit had an insertion loss of 1.8 dB minimum at 32.5 GHz and a maximum insertion loss of just over 4 dB at 30 GHz. The mechanical assembly is the same as shown in Fig. 2.47 (a).

Planar Cavity Combining

The planar cavity combiner, Lee *et al* [63], and shown in Fig. 2.50, offers another potential low cost combining technique in that the top of the standard waveguide cavity is formed by the microstrip to waveguide slot transitions for each of the devices to be combined. The benefit of this technique, beyond the low cost construction, is that the combining efficiency is 95% (by simulation), however the transition losses, due to the low cost construction, limit the performance. It has also not been demonstrated with power levels above 20 dBm (100 milliwatts).

2.2.8 Radial Combining Conical Waveguide

Conical waveguide combining has been used by Quine *et al* [64] and Harp and Russell [65] as reported in Chang and Sun [2]. In this approach the signal is combined in phase and reflected back to a circulator. The combining has been applied to GaAs IMPact ionisation Avalanche Transit-Time (IMPATT) diodes. The benefits of this approach are that the diodes can be mounted for optimum heatsinking but the assembly

[5] 26.5-40 GHz; Downlink 17.7-19.7 GHz, Uplink 27.5-29.5 GHz

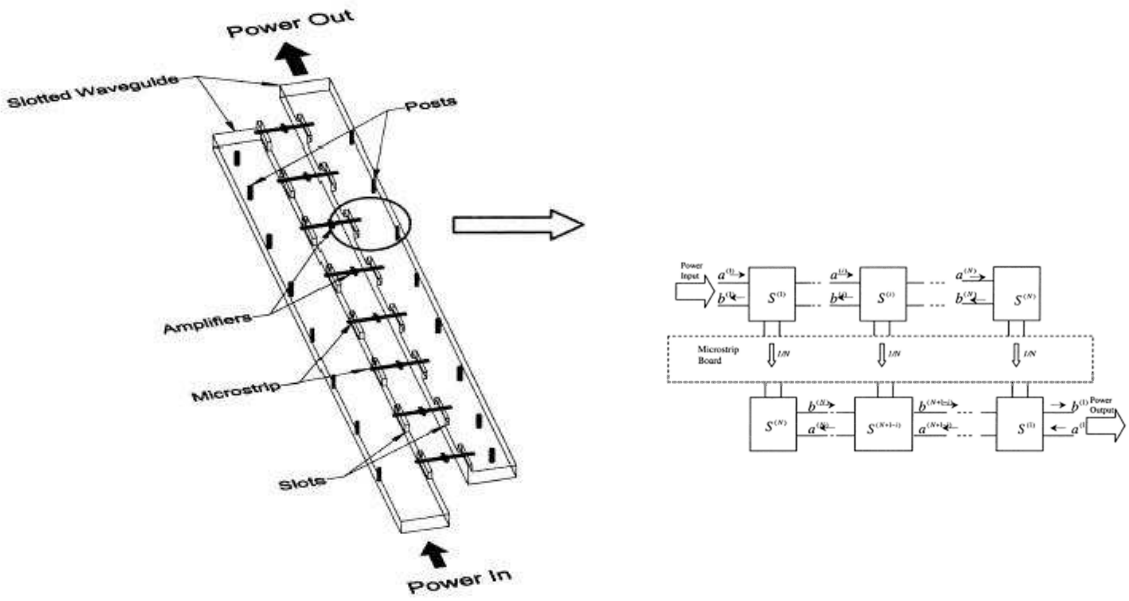

(a) (b)

Figure 2.49. Slotted waveguide traveling wave power amplifier. Illustration of a Ka-Band eight-device slotted-waveguide power amplifier showing the power dividing / combining circuit assembled with MMIC amplifiers (a) and schematic of the N = 3-port network blocks for each stage of the traveling wave N-Way power divider / combiner (b), from Jiang *et al* [62].

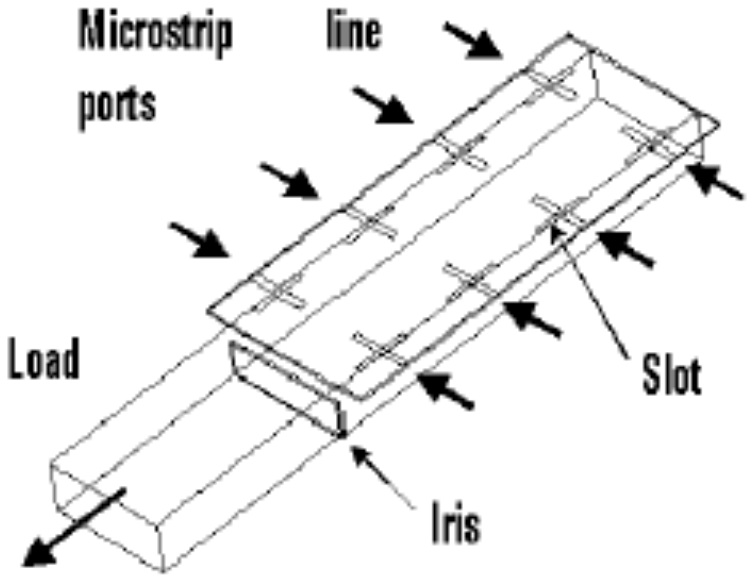

Figure 2.50. Planar cavity combiner. Waveguide cavity power combining structure with planar circuit outside the cavity, from Lee *et al* [63].

is complex and the generation of unwanted modes occurs requiring mode suppression filters and absorbers.

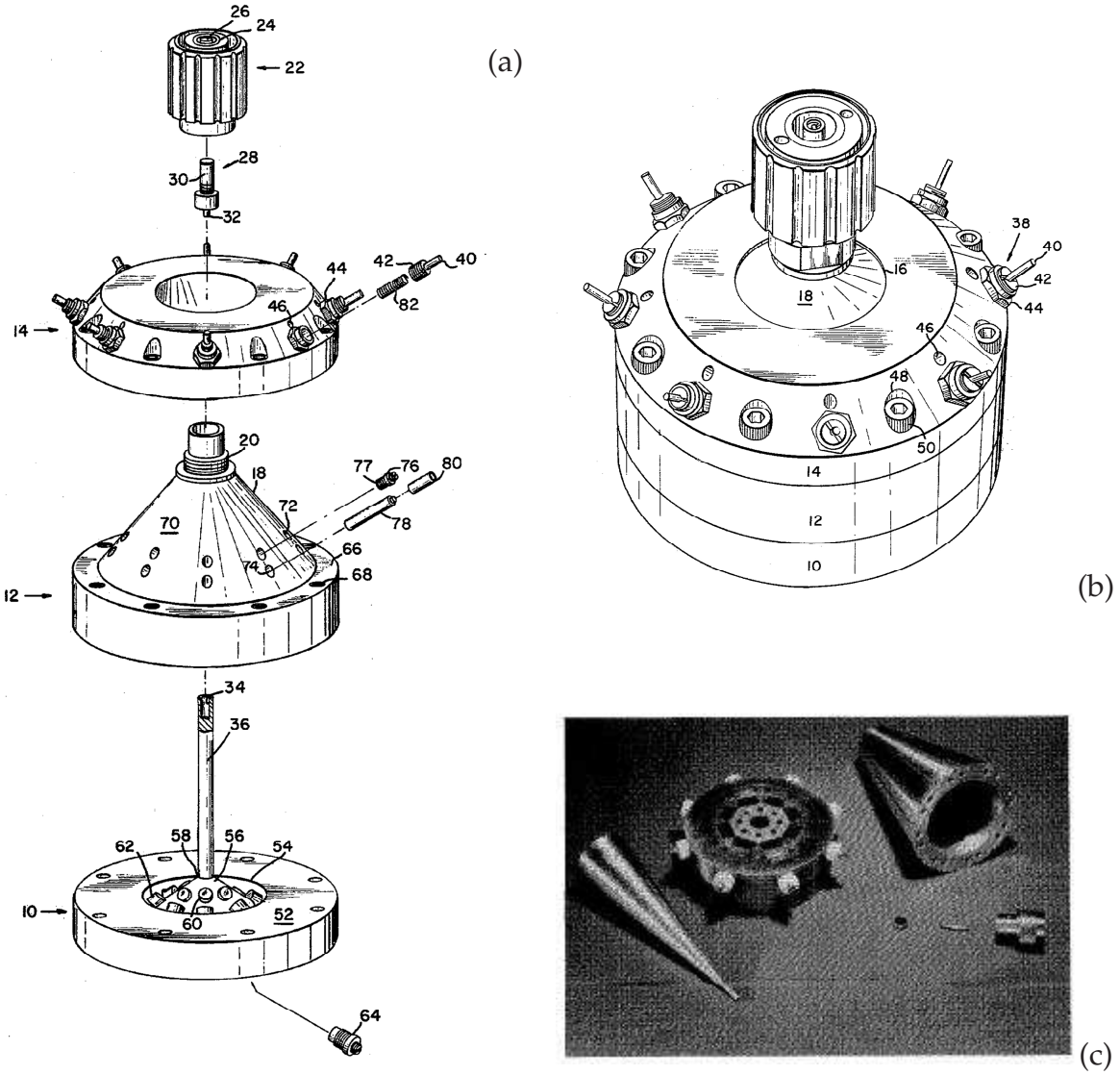

Figure 2.51. Radial combined conical waveguide. Eight IMPATT diode (reflection amplifier) conical waveguide power combiner (a) and (b) from Harp and Russell [65] and (c) from Quine *et al* [64].

2.3 Electric Field Modification Techniques

2.3.1 Photonic / Electro-magnetic Band Gap Structures and their Application to Spatial Power Combining

In order to discuss some of the more advanced field modification techniques that are being used with spatially combined amplifiers then a brief background relating to the PBGS[6] is required. The discussion will be related to EBGS with PBGS being referred to interchangeably. The various types of EBGS to be discussed and their application to spatial combining are shown in Fig. 2.52. Dielectric material is used extensively for microwave circuit applications because of its relatively low cost and processing ease. Dielectric material is used to manufacture microwave PCBs thus creating microwave integrated circuits. In this application the dielectric material is used to load the walls of waveguiding structures thus altering the boundary conditions at the waveguide walls and this adjusts the field distribution within the waveguide. Other means of modifying the field distribution within waveguiding structures is to use corrugations and by utilising EBGS. This adds an additional variant to the plain dielectric loading of waveguide structures. These different techniques will be described and discussed further in the following sections.

2.3.2 Bumpy Surfaces

Bumpy surfaces will be used as the starting point to describe other surfaces that are used as EBGS. In the past, surface waves propagating over a finite frequency range, have been suppressed on metal surfaces by the use of a lattice of small bumps applied to the surface of a metal sheet. The bumps cause the surface waves to scatter and the resulting interference prevents the surface waves from propagating, thus producing a two-dimensional electro-magnetic Bandgap. For wavelengths that are much longer than the period of the lattice then the surface waves are unaffected but when the surface waves are at shorter wavelengths then the bumps affect the surface wave. When one-half wavelength fits between rows of bumps then standing waves on the surface exist having either peaks centered on the bumps or troughs centered between the bumps as shown in Fig. 2.53. These two modes have slightly different frequencies between which surface waves cannot propagate.

[6] A PBGS is a structure that operates at or near the visible region of the electro-magnetic spectrum and that exhibits either a 2-D or 3-D "band gap" where the transmitted wave, over a particular range of frequencies, is greatly reduced. An EBGS is the microwave frequency PBGS.

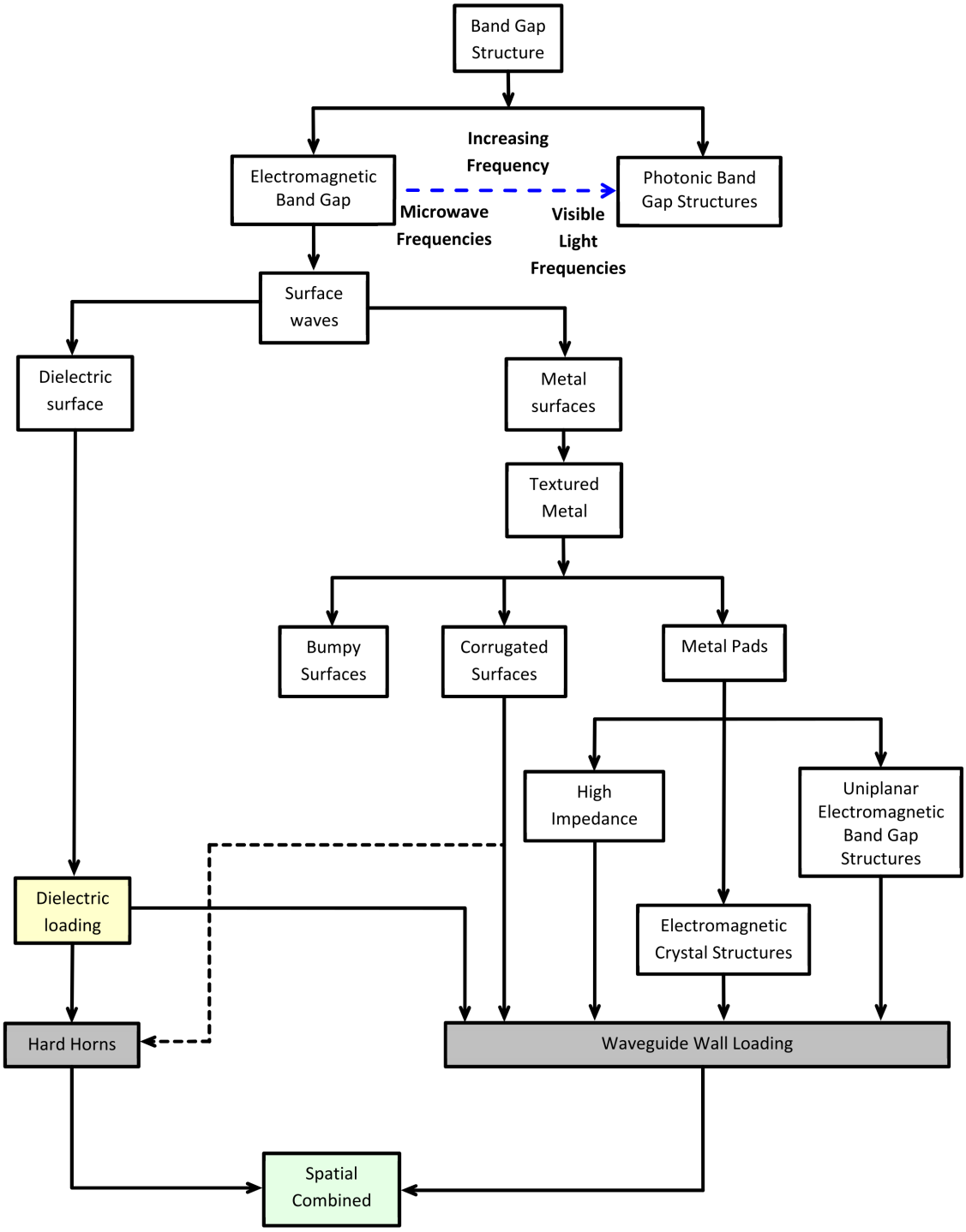

Figure 2.52. Band gap structures for spatially combined amplifiers. Band gap structures and the development and application to spatial combiner amplifiers.

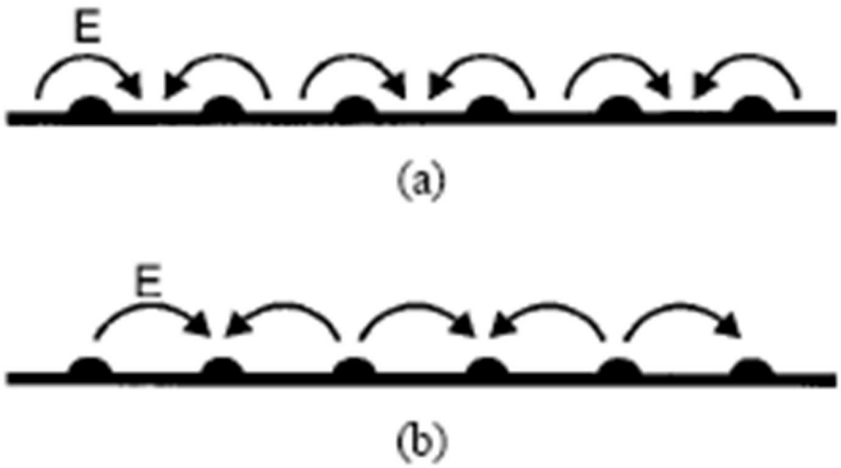

Figure 2.53. Bumpy metal surfaces. (a) mode at the upper edge of the Bandgap, where the electric field wraps around the bumps and (b) mode at the lower edge of the Bandgap where the electric field extends across the bumps, from Sievenpiper *et al* [44].

2.3.3 Corrugated Surfaces

Following on from the bumpy metal surface, a corrugated surface consists of a metal slab where a series of vertical slots have been formed. The slot width is small so that many of them fit within one wavelength across the metal slab. Each slot can be considered to be a parallel plate transmission line that runs from the top of the metal slab to the bottom of the slab. If the slots are one quarter of a wavelength deep then the short circuit at the bottom of the slots is transformed into an open circuit at the top of the slots. Therefore the impedance on the surface, at the top of the slots, is high. With many slots per wavelength the corrugated structure will have an effective surface impedance that is the impedance of the slots. The overall behavior of this structure is considered to have a surface boundary condition that is determined by the corrugations. If the slot depths are greater than one quarter-wavelength then the surface impedance is capacitive and TM surface waves are forbidden. An incident plane wave, having its E-field perpendicular to the corrugations, will appear to be reflected with no phase reversal as the effective reflection plane is at the bottom of the slots, one quarter-wavelength away.

2.3.4 Metal Pads

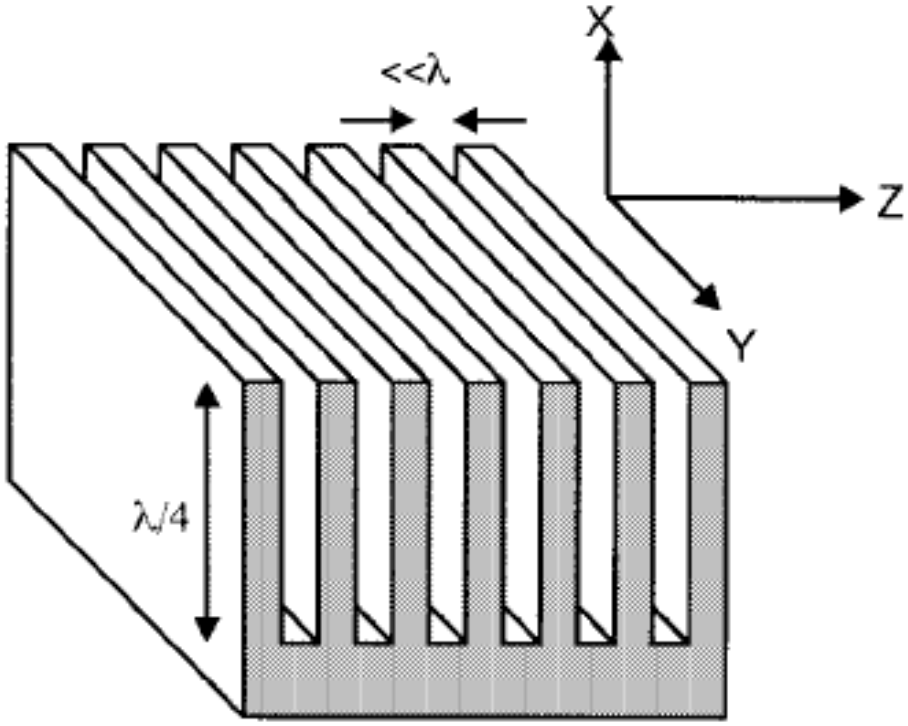

Figure 2.54. Corrugated metal surfaces. From Sievenpiper *et al* [44].

High Impedance Electro-magnetic Surfaces

High Impedance Electromagnetic Surfaces (HIES) [44], can be considered to be an extension / modification to a corrugated surface where the corrugations have been folded out to form lumped elements and are distributed in a two-dimensional lattice. Typically these surfaces are formed by standard PCB fabrication techniques where copper patterns are formed on the surface of a dielectric sheet by chemical etching. These patterns are connected to a bottom ground plane by plated through-hole vias. The surface impedance can be modeled as a parallel resonant circuit that can be tuned to provide a high impedance surface over a particular frequency range. Periodic structures, formed by two or three-dimensional metal, dielectric or metal-dielectric structures that prohibit the propagation of electro-magnetic waves are known as photonic crystals. The HIES can be considered to be a 2-D photonic crystal that prevents the propagation of RF surface currents within a particular frequency range. The surface is inductive at low frequencies and capacitive at high frequencies. The Bandgap has been lowered in frequency by using capacitive loading of the top hexagonal PCB patterns.

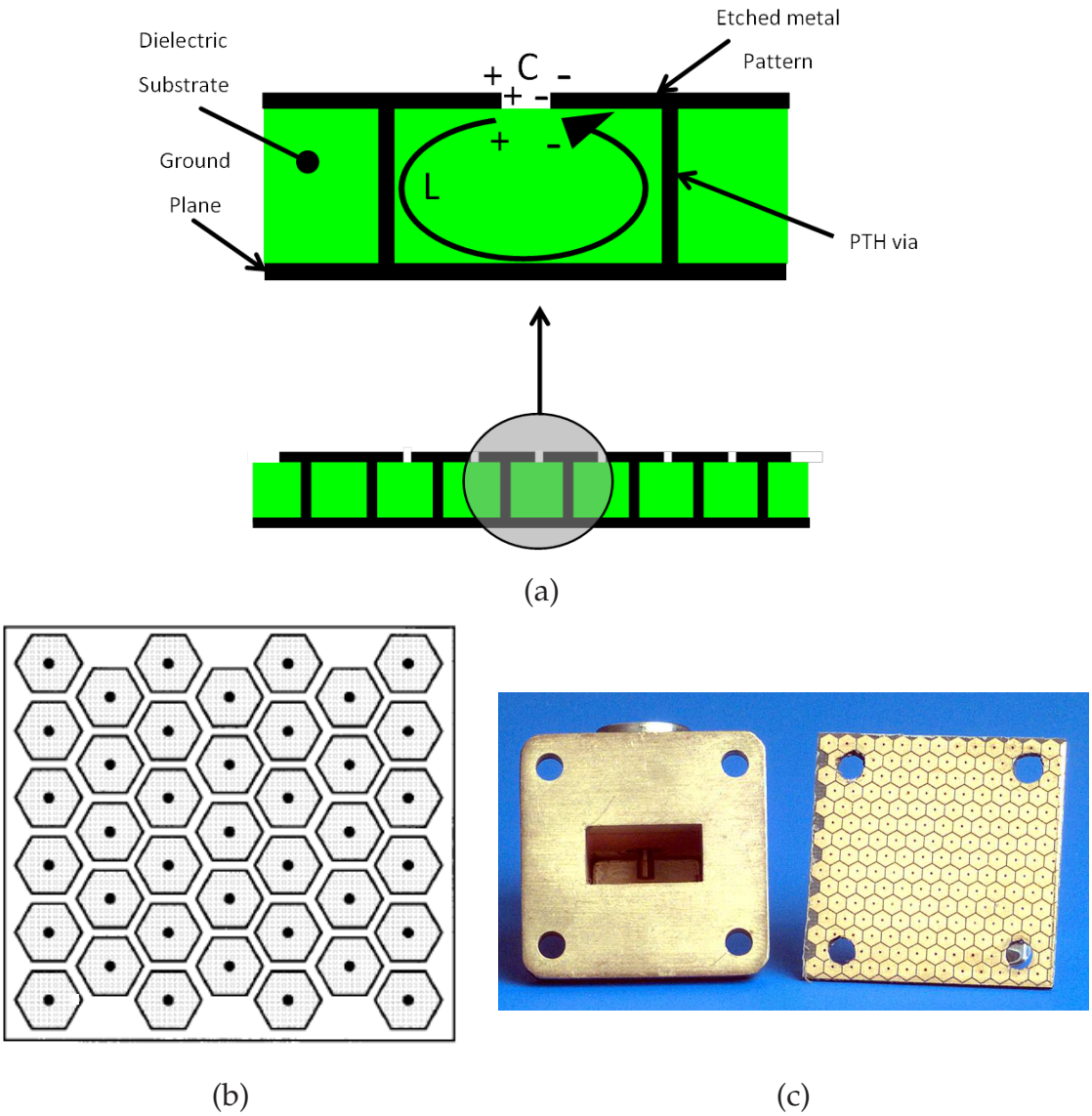

Figure 2.55. High-impedance PCB surface. (a) Cross section of a high-impedance surface fabricated as a printed circuit board. The structure consists of a lattice of metal plates connected to a solid ground plane by vertical conducting via, (b) Top view of the high-impedance surface, showing a lattice of hexagonal metal plates, from Sievenpiper *et al* [44] and (c) high impedance electro-magnetic surface fabricated on PCB material next to a WR75 waveguide to coaxial adaptor, from Higgins *et al* [28].

Fig. 2.56 shows the surface TE and TM transmission and reflection properties from the HIES shown in Fig. 2.55. For this structure the period was 2.54 mm, the gap between the hexagonal patches was 0.15 mm, the PCB thickness was 1.55 mm and the dielectric constant was ϵ_r = 2.2. Fig. 2.56 (a) shows the transmission performance for a TE surface wave via a pair of coaxial surface probes oriented parallel to the HIES. The transmission is weak at low frequencies but jumps up about 30 dB at 17 GHz and then continues relatively flat at higher frequencies. In contrast the TM transmission of Fig. 2.56 (b), measured via monopole probes oriented vertically at the sheet edges, indicates transmission at lower frequencies followed by a sharp drop of 30 dB at 11 GHz that gradually increases slightly with increasing frequency. The frequencies where the signals drop sharply define the TE and TM Bandgap edges respectively, i.e. the TM Bandgap edge is at 11 GHz and the TE Bandgap edge is at 17 GHz.

The reflection phase properties of the HIES is measured using 2 broadband microwave horns placed next to each other facing the HIES within a microwave frequency absorbing chamber with one horn transmitting and the other receiving. Referring to Fig. 2.56 (c), the reflection phase indicates a 180° reflection at low frequencies, as per a metal surface, with the phase sloping downward and reducing to zero at the resonance frequency of the HIES. The phase continues to slope downward with increasing frequency eventually reaching -180° at the highest frequency. Between the frequencies where the reflection phase is 90° to -90°, plane waves are reflected in phase, rather than out of phase. The region between these two frequencies corresponds to the TE / TM transmission Bandgap region.

Electro-Magnetic Crystal Structures

Another variant on the HIES has been termed the Electro-Magnetic Crystal Structure (EMXT) [45]. The EMXT consists of a dielectric substrate that has one side of continuous metal ground plane and the other side has a pattern of metal strips etched into the surface and through hole vias every wavelength connecting the strips through the dielectric substrate to the ground plane. The through hole vias are used to suppress undesirable surface modes. The major difference between the HIES and the EMXT surfaces is that the EMXT surface is sensitive to the polarization of the incident wave. The Bandgap frequency is determined by the substrate height, h, strip width, w, and strip gap, g. The gap provides the capacitance while the strip width and substrate height provides the inductance of an equivalent resonant circuit. An incident EM wave with an E-field across the strips will be coupled across the parallel resonant circuit and the

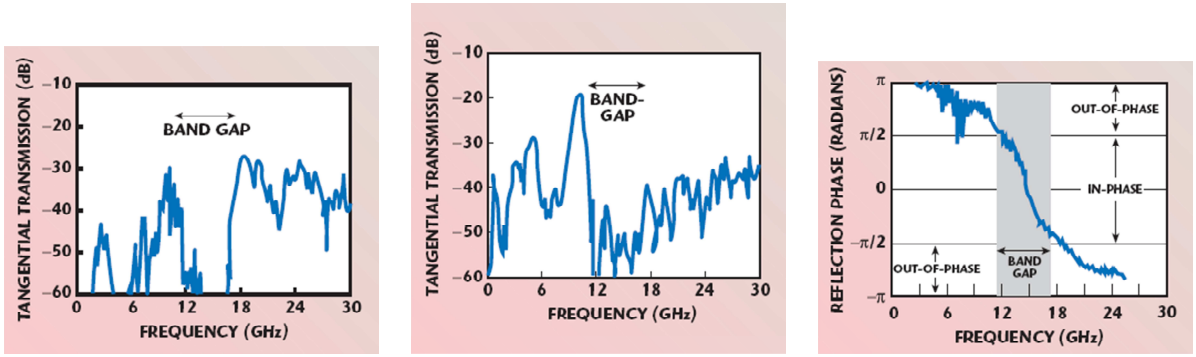

(a) (b) (c)

Figure 2.56. TE and TM surface wave transmission and reflection over high-impedance surfaces. TE Surface wave transmission across a 2-layer high-impedance surface where the surface waves are suppressed within the Bandgap (a), TM surface wave transmission across a high-impedance surface (b) and reflection phase versus frequency for a 2 layer high impedance surface (c), from Karmakar and Mollah [43].

incoming wave is reflected with a $+1.0 \angle 0°$ coefficient. On the other hand an orthogonal incident EM wave will have its' E-field oriented along the strips and is reflected with a $+1.0 \angle 180°$ coefficient. This structure is considered to be better suited to spatially combined amplifiers in waveguide because the high impedance is only required in one direction.

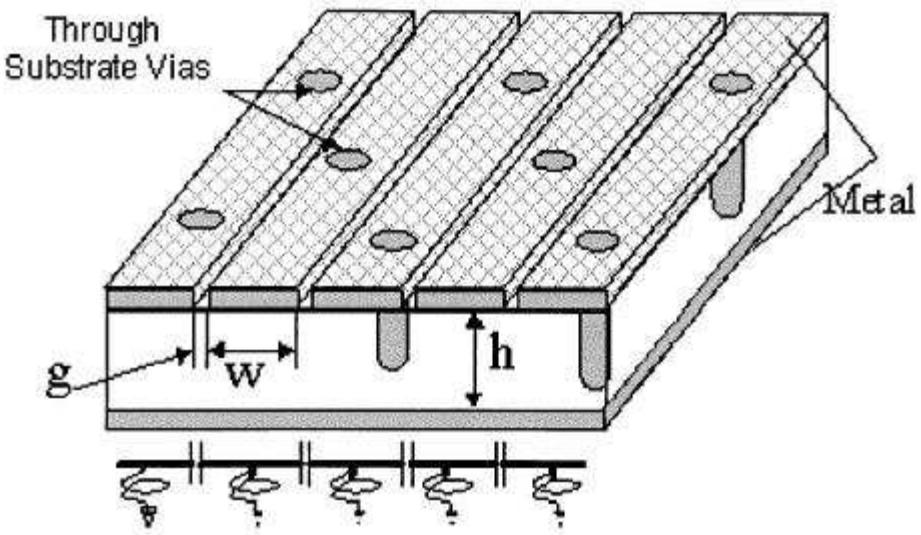

Figure 2.57. Electro-magnetic crystal structures. Physical structure of an electro-magnetic crystal structure, from Higgins *et al* [45].

Uni-planar Compact PBG Surfaces

Yang *et al* [66] has further developed the metal pad concept to form a Uni-Planar Compact PBG Surface or Structure (UC-PBGS). This consists of a dielectric substrate with metal pads that are etched into either the surface or the ground plane and that are connected together by narrow metal tracks / lines without the need for plated through via holes or multilayer substrates forming a distributed Inductor Capacitor (LC) network. This type of surface has a distinctive stopband, is relatively small in size and is low loss. Without the need for through hole plated vias it presents a low cost, easily manufacturable option for constructing TEM waveguides, see Section 2.3.6, however details relating to the power handling capacity of these structures have not currently been described.

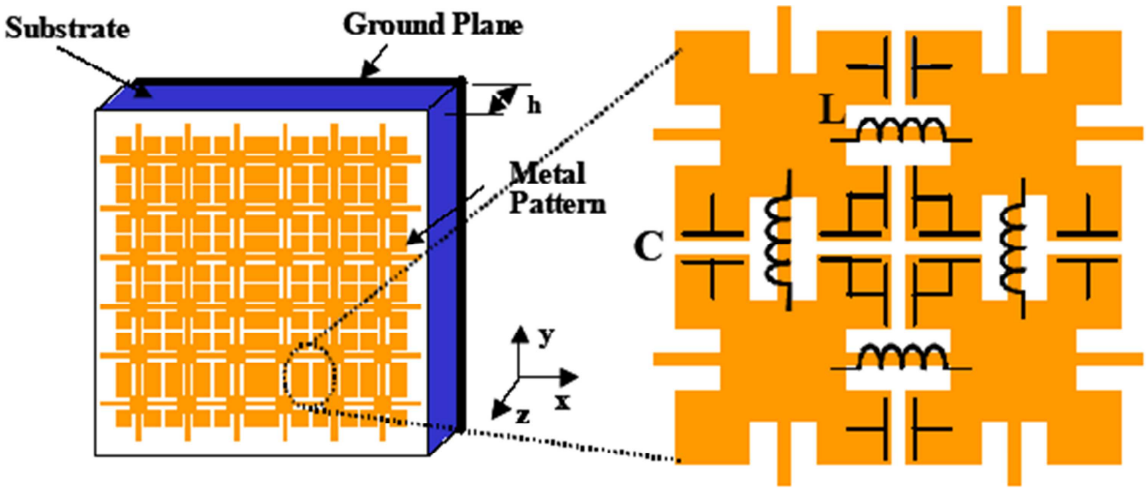

Figure 2.58. Uni-planar compact photonic band gap (UC-PBG) structure. From Beregana [67].

2.3.5 Hard Horns

As the size of a spatially combined amplifier can be large, then to transition from standard waveguide to the spatially combined amplifier aperture size requires a transition that can take the form of a pyramidal horn antenna. In order to provide a uniform field distribution over the aperture of the horn feed, to evenly illuminate the spatially combined amplifier ensuring efficient power combining and also allowing all of the active devices of the spatial amplifier to simultaneously saturate, then the horn walls are modified so as to provide a "Hard" boundary condition, Kildal [68], i.e. a soft horn

has zero E-field intensity at the waveguide walls whereas a hard horn has uniform E-field distribution over the horn aperture. Both dielectric loaded and corrugated hard horns will be discussed in Section 2.3.5 and Section 2.3.5 respectively.

Dielectric Loaded

As indicated above in order to transition from standard waveguide to the aperture of a spatially combined amplifier and achieve efficient power combining and ensure simultaneous active device saturation then a hard boundary transition is required and this can be achieved by loading the walls of a suitable pyramidal horn feed with dielectric material as discussed by Ali *et al* [69]. Fig. 2.59 (a) shows the overall multilayer QO amplifier system with Fig. 2.59 (b) and (c) showing the dielectric loaded pyramidal horn antenna with the dielectric material placed on each sidewall parallel to the E-field.

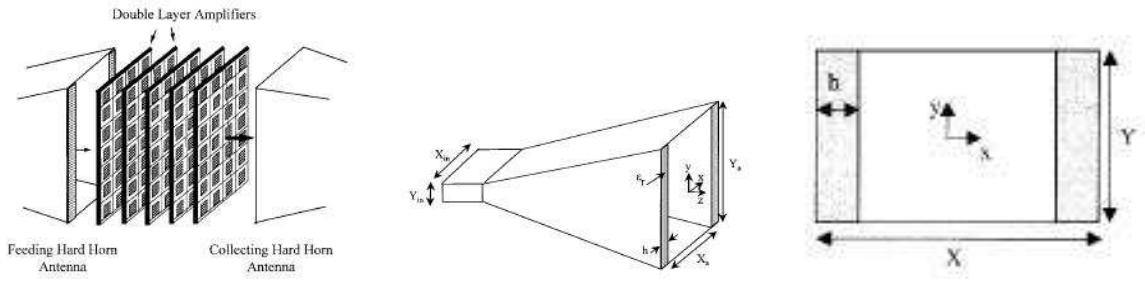

(a) (b) (c)

Figure 2.59. Closed system quasi-optical amplifier using hard horns. Closed system QO amplifier (a), dielectric loading for a pyramidal hard horn feed (b), and cross-section of a hard horn, from Ali *et al* [69].

A suitable analysis using mode-matching techniques can be applied Ali *et al* [69] allowing for the optimisation of the dielectric material's dielectric constant (permittivity) and thickness, h, in order to obtain field distribution uniformity and efficiency as well as bandwidth. There is however no indication of power handling capability of this technique. Some of the factors that must be considered in order to optimise the horn's performance are:

- Dielectric constant versus bandwidth. A higher dielectric constant gives a better power distribution efficiency but reduces the horn bandwidth.
- Power uniformity versus dielectric thickness. A thinner dielectric gives a higher frequency of operation.

- There is an optimum dielectric thickness for fixed dielectric constant and frequency that gives a $\pm$ 1 dB E-field variation across the aperture.
- Horn aperture size also effects bandwidth and efficiency.
- At 30 GHz a 4 dB improvement in P1dB with an optimised hard horn versus a standard horn antenna.
- Thinner dielectric means that there is a reduced signal level in the dielectric giving lower losses and better efficiency.
- Lower reflections at the QO amplifier array means that there is less chance for over-moding to occur.

Corrugated - Dielectric Filled

In a corrugated "hard" horn, as shown in Fig. 2.60 from Pickens *et al* [70], the dielectric only loaded sidewalls of a pyramidal horn antenna are replaced with longitudinal corrugations that are filled with dielectric material and the wall profiles have a cosine taper. The advantages of the dielectric filled corrugations are considered to be lower loss performance, thus improving combining efficiency, and the cosine taper improves the overall return loss performance of the hard horn. Consideration needs to be given to the transition from standard waveguide to the tapered corrugated waveguide in order to minimise the excitation of higher-order waveguide modes. For the example cited the frequency range of operation is from 31.8 to 32.3 GHz. No power handling data is presented.

2.3.6 Waveguide with EBG Wall Loading

Power combining in waveguide is attractive because low diffraction loss and broad bandwidth can be achieved [41]. Dielectric loading or using oversized waveguides are often used to provide a uniform field distribution. For smaller dielectric loaded waveguides there are no advantages over standard empty waveguide. Performance can be improved by the use of higher dielectric constant materials or corrugations but the bandwidth is reduced. UC-PBGSs offer the possibility of constructing TEM waveguides with uniform field distributions. UC-PBGSs act as a reflector at the stopband frequency where periodic loading changes the surface impedance to an open circuit.

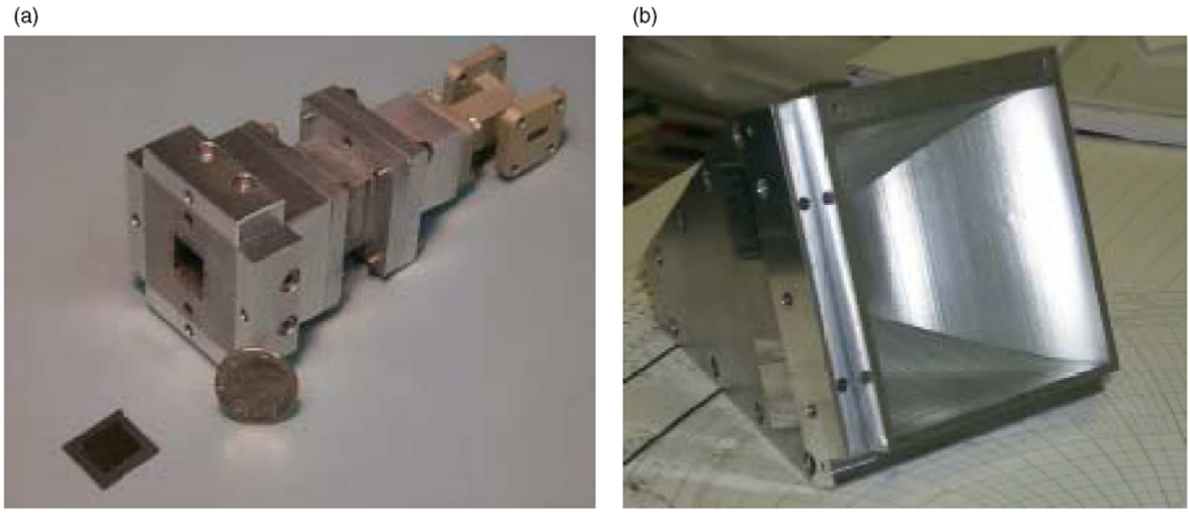

Figure 2.60. Corrugated "hard" horns. for (a) dual-linear and (b) single-linear polarization, from Pickens *et al* [70].

This concept can be applied to build a uniform field TEM waveguide. Replacing the two sidewalls of a standard waveguide with a UC-PBG wall, shown in Fig. 2.61 where the structure of the waveguide is formed by Perfect Electric Conductor (PEC) material, will result in a parallel plate mode being established as a result of the magnetic boundary conditions, thus providing a uniform field distribution. An example of the E-field as a result of being loaded with PBG material is shown in Fig. 2.62. This can then be used to feed a QO power-combining array. Standard etching of thin substrate materials can be used, providing easier to manufacture feeds compared to high dielectric constant loaded hard horns or corrugations. There are no presentations as to the power handling capacity of waveguides loaded with UC-PBG structures.

2.3.7 Comparison of electric field modification structures

A comparison of the various types of electric field modification structures and their advantages and disadvantages is provided in Table 2.1.

2.4 Conclusion

This chapter has presented an initial comparison of SSPA combining technologies. The work forms part of an initial study into available SSPA combining technologies and can be used in determining the best SSPA combining technology outcome. As a result

2.4 Conclusion

Table 2.1. Comparison of electric field modification structures.

Type	Description	Characteristics	Advantages	Disadvantages
Corrugated metal surface [44]	Vertical slots in a metal slab, slot depth $\lambda/4$, slot width $<<\lambda$. By machining or etching.	Surface impedance high & characteristic impedance of the slots	Power handling capability	expensive to manufacture
Metal pads				
HIES [44]	Etched Hexagonal pads, distributed in a 2D lattice, on top of PCB dielectric material with vias to the ground plane at hexagonal pads centres.	Prevents propagation of RF surface currents over a particular frequency range.	PCB fabrication, low cost & accurate. Surface impedance modelled as a parallel resonant circuit tuned for high impedance over a frequency range.	Plated through hole vias add cost.
EMXT [45]	HIES variant. Metal strips etched on PCB top surface with plated through hole vias connecting strips to ground plane every λ.	Surface sensitive to polarization of incident wave. Bandgap frequency range dependent on substrate height, strip width & gaps.	Better suited to spatial combining.	
UC-PBGS [66]	PCB with etched metal pads connected with narrow metal tracks, without plated through hole vias connecting to the ground plane.	Creates TEM mode waveguide used to provide evenly distributed E-fields for spatial combining.	PCB fabrication, no plated through hole vias, reducing processing and costs.	Power handling capability.
Hard Horns				
Dielectric loaded [69]	Dielectric lined walls of horns transitioning from rectangular waveguide to spatial tile arrays, providing even E-Field to spatial tile array, minimising soft saturation.	Straight pyramidal taper only.		
Dielectric loaded corrugations [70]	Dielectric loaded corrugated horn walls transitioning from rectangular waveguide to spatial tile arrays, providing even E-Field to spatial tile array, minimising soft saturation.	Cosine taper.	Improved insertion & return loss.	Complex manufacturing & higher cost. Power handling capability.
EBG waveguide				
Through narrow walls [40]	TEM mode evenly distributed E-field waveguide for tray spatial combining.		Spatially combined amplifier, P_{out} increase 1.5 dB over 1 GHz B/W from 14.5-16.5 GHz	Custom waveguide applications.
Inside narrow walls [43]	TEM mode evenly distributed E-field waveguide for tray spatial combining.		Easily fitted to narrow walls of rectangular waveguide	

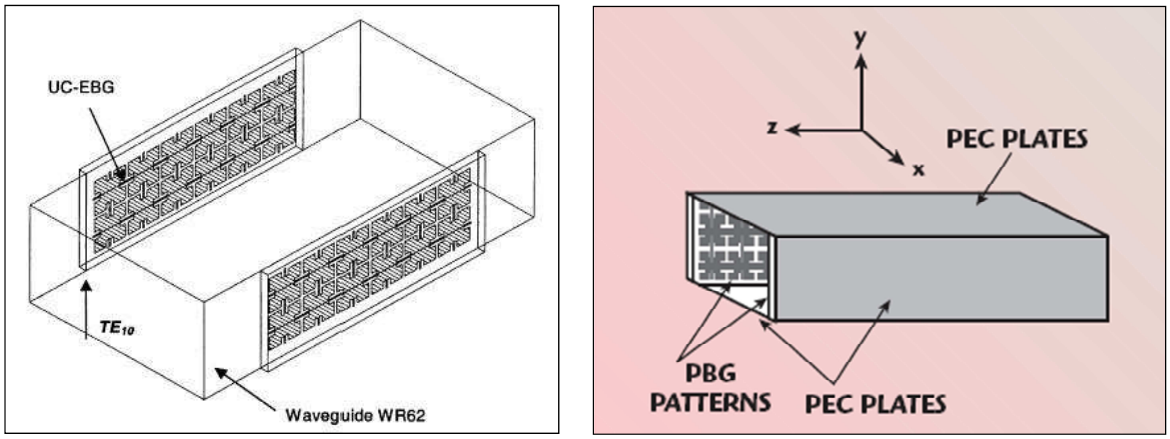

(a) (b)

Figure 2.61. TEM waveguide structures. TEM waveguide, (a) through the waveguide side walls, from Belaid and Wu [40] and (b) on the inside of the waveguide side walls, from Karmakar and Mollah [43].

of this review further research is proposed to facilitate the selection of the most appropriate power combining technology selection and design methodology, for a particular service requirement with a given set of initial requirements and specifications and this method is presented in the following chapter.

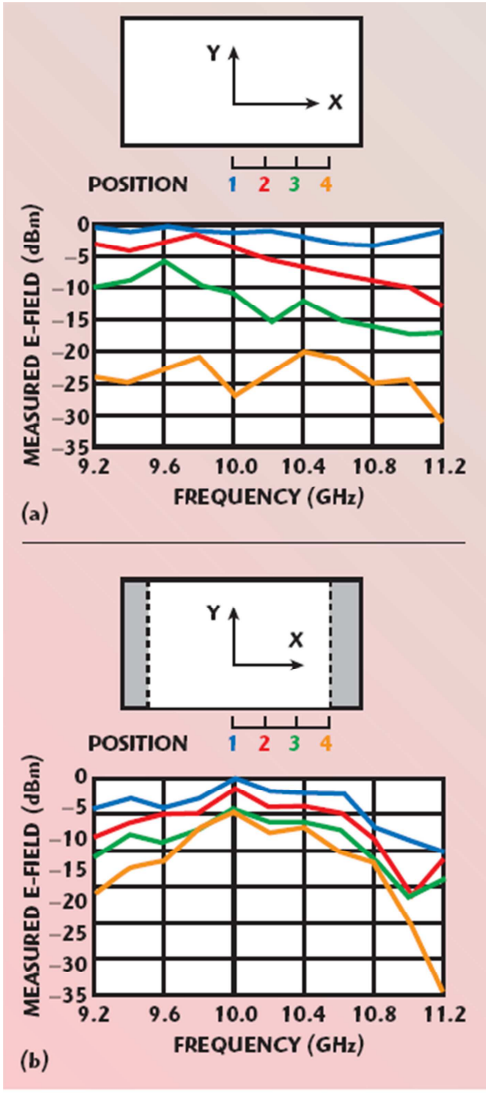

Figure 2.62. TEM waveguide E-field profiles. Measured E-field profiles at different positions across the waveguide broad wall dimension; (a) standard metallic waveguide and (b) PBG loaded waveguide, from Karmakar and Mollah [43].

Chapter 3

Figure Of Merit Design Methodology Applied to Power Amplifier Combining Technologies

WITHIN the design methodology umbrella, specific research into higher power handling, lower loss waveguide and transition structures that offer enhanced SSPA output power and combining efficiencies will also be proposed. As a further part of the design methodology research, a thermal versus electro-magnetic optimisation of the waveguiding structures will need to be undertaken.

A comparative analysis between well established and more recent SSPA combining techniques is also presented. Based on this analysis, a new FOM methodology is presented that can form part of a process to optimise SSPA design within the constraints of service, technology and performance requirements. Also, this formalises the process of determining the most appropriate SSPA design path, from the earliest stages, based on the above constraints as well as providing a detailed technology comparison to allow optimum technology selection.

3.1 Introduction

Chapter 2 reviewed the available literature and it can be seen that there has been significant research in the areas of microwave and millimeter wave SSPAs, that make use of a wide range of power combining techniques in order to obtain higher output powers over a range of frequencies. From this review there are several areas where further new contributions can be made. These have been grouped into the following main areas:

Overall design methodology: This area includes development of a general amplifier design methodology, for power combining and power amplifier design, which provides optimum thermal, electrical and electro-magnetic performance for a given set of specifications, with optimisation of the most appropriate technology and design solutions being an integral part of the methodology. This methodology will be multilayered in that it will provide for the selection of the most appropriate technology, by formalising less tangible (more fuzzy) parameters, as well as a methodology for the detailed design and optimisation of an amplifier within the selected technology. Part of the technology selection and design methodology will consider manufacturability as an essential selection and design parameter.

Technology approach: This area includes research into what specific technology improvements in the areas of field modification, transitions and power handling capacities can be made, and

Technology implementation: This direction covers research into how the methodology and technology approaches can be implemented practically so that there are usable outcomes suitable for industry.

These research areas are all linked and the target is to expand on some of these areas for designing and manufacturing for SSPAs. A new approach is also proposed that allows for the selection of an appropriate technology through, incorporating advanced waveguide structures, resulting in an improvement in the thermal performance, allowing for higher output powers with reduced cost, within the constraints of volume and improved manufacturability for a given environment and set of specifications.

3.2 Design Methodology

Following on from Chapter 2, it can be seen that although there are many technologies and techniques for designing higher power SSPAs, there is no unified design methodology that allows for selecting a technology and design approach to deliver the most appropriate and optimum SSPA outcome based on a set of requirements.

The significant contribution of determining the most appropriate technology and defining an appropriate design methodology to this area is that it provides a way of minimising risk for performance, cost, delivery time, manufacturability and reliability, to an overall process while also delivering the most optimum outcome. The proposed design methodology will be used to

1. determine the most appropriate technology for the particular service and then
2. determine the most appropriate design within that technology area to meet the required service specifications.

Research to determine the most appropriate and optimum design methodology, will allow the selection of the most appropriate power combining and amplifier outcome based on a given set of specifications, will initially be based on a combiner and amplifier technology comparison summarised in Fig. 3.1 (Part 1) and Fig. 3.2 (Part 2). These figures use the research data from the technologies and techniques presented in the previous chapter as starting point specifications, and FOMs, if available, in order to provide a more comprehensive range and means of being able to compare the different spatial combining technologies and techniques as an initial means of making a technology selection for an initial input set of requirements for an SSPA design. The varying horizontal shadings group the various technology types together as also shown in Table 3.1. The magenta shadings are for specifications that are not currently described in the literature or available. The brighter yellow shadings are estimates of the technology specifications. The sky blue column headings are for Specification Parameters (SPs), with weightings applied following QFD, FMEA and service reliability weightings. The darker red column headings are for FOMs. An initial comparison has been made and discussed below.

From the initial power combiner / amplifier technology comparisons of Fig. 3.1 (Part 1) and Fig. 3.2 (Part 2) it can be seen that a monolithic level corporate [9] combining

1	2	3	4	5	6	7	8	9	10	11	12	13	14	15	16	17	18	19	20	21	22	23	24	25	26	27	28	29	30	31	32
COMBINER TYPE ↓	Reference ↓	Active device ↓	Centre Frequency	Highest Frequency	B / W	P_{out} (P_{1dB}) RF		P1dB Frequency	S.S. Gain (Min.)	Gain Slope	Gain Ripple	IMD (P_{1dB} - 6dB / tone)	OIP3	OIP3 (Calc.)	Return Loss Input	Return Loss Output	AM/PM @P_{1dB}-2dB	G.D.	Noise Figure	SFDR	Residual ϕ_{noise}	Spurs (inc. Harms) @ P1dB	Modes TEM/QTEM	DC			DE (%) @ P1dB =P_{outRF} /P_{inDC}	Number of Elements	Combiner loss Corporate = loss/stage, Spatial = I/P & O/P loss	Combiner Efficiency	Graceful Degradation
			GHz	GHz	GHz	W	dBm	GHz	dB	dB	dB p-p	dBc	dBm	dBm	dB	dB	▽dB	ns	dB	dB	dBc/Hz	dBc	TE/TM	V	A	W	%	N	dB	η %	y/n
Service:Land fixed Small Satellite Earth Terminal Parameter Weighting level→				19	29	29		29	39	49	49	39	39	39	49	39	39	59	49	39	49	49				59	59				39
WEIGHTING →				5.26	3.45	3.45		3.45	2.56	2.04	2.04	2.56	0.00	2.56	-2.04	-2.56	2.56	1.69	2.04	2.56	2.04	-2.04				1.69	1.69				2.56
WEIGHTING COMMENTS →	Land fixed Satellite Earth Terminal																			1.38E-23											y= log(N*2.56*100), n>-1
Corporate Monolithic Level 1	[9]	TGA4022-EPU	20.5	23.00	5.00	1.80	32.55	21.50	26.00	2.00	3.00	-25.00	39.05	39.05	-15.00	-20.00	3.00	10.00	10.00	57.94			QTEM	7	1	5.88	31.00	8	0.15	90	y
Weighted score →				121.05	17.24	6.21		74.14	66.67	1.02	0.68	64.10	0.00	100.14	30.61	51.28	0.85	0.17	0.20	148.55		0.00				28.83	52.54				231
Corporate Chip Level	[7]	TIM5964-60SL	6.15	6.40	0.50	50.10	47.00	6.40	8.50	0.80	1.60	-26.00	54.00	54.00	-15.00	-20.00	3.00	10.00	10.00	77.21			QTEM	10	13	132.00	38.00	4	0.15	80	y
Weighted score →				33.68	1.72	172.76		22.07	21.79	2.55	1.28	66.67	0.00	138.46	30.61	51.28	0.85	0.17	0.20	197.97		0.00				1.28	64.41				154
Corporate hybrid waveguide	[5]	TIM1414-18L	14.25	14.50	0.50	40.00	46.02	14.50	30.00	1.00	1.00	-25.00	52.52	52.52	-15.00	-15.00	2.00	10.00	8.00	64.13		-30.00	TE10	10	36	360.00	12.00	4	0.15	96	y
Weighted score →				76.32	1.72	137.93		50.00	76.92	2.04	2.04	64.10	0.00	134.67	30.61	38.46	1.28	0.17	0.26	164.43		61.22				0.47	20.34				154
Tile Discrete Level Spatial Combiner	[71]	FSC10LG	3.3	3.35	0.09	0.003777	5.77	3.30	11.00	3.00	3.00	-10.00	4.77	4.77	-10.00	-10.00	3.00	10.00	10.00	73.48			TE10	4	3	12.00	1.00	50	2.00	50	y
Weighted score →				17.61	0.31	0.01		11.38	28.21	0.68	0.68	25.64	0.00	12.23	20.41	25.64	0.85	0.17	0.20	188.41		0.00				14.12	1.69				435
Tile Chip Level Spatial Combiner	[19]	Northrop Grumman 1/2 Driver & 1W PA	34	34.40	0.80	19.95	43.00	34.00	13.00	3.00	5.00	-32.00	53.00	53.00	-10.00	-10.00	3.00	10.00	10.00	72.79			TE/TEM	5	64	317.50	7.00	45	1.40	73	y
Weighted score →				181.05	2.76	68.79		117.24	33.33	0.68	0.41	82.05	0.00	135.90	20.41	25.64	0.85	0.17	0.20	186.65		0.00				0.53	11.86				423
Tile Monolithic Level Spatial Combiner TX GA	[24]	GaAs pHEMT	37.2	37.85	1.30	2.30	33.62	37.20	8.00	4.00	3.00	-32.00	43.60	43.62	-10.00	-10.00	2.00	10.00	10.00	74.16		-55.00	TE10			30.00	8.00	512	2.00	63	y
Transmission Grid Amplifier Weighted score →				199.21	4.48	7.93		128.28	20.51	0.51	0.68	82.05	0.00	111.84	20.41	25.64	1.28	0.17	0.20	190.14		112.24				5.65	13.56				694
Tile Monolithic Level Spatial Combiner RX LA	[72]	TRW InP HEMT	58	58.29	0.58	2.0000	33.01	58.00	2.50	1.00	3.00	-32.00	10.00	43.01	-13.00	-17.00	3.00	10.00	10.00	80.12			TEM/QTEM	1	9	10.80	19.00	200	2.00	85	y
Reflection Grid Amplifier Weighted score →				306.79	2.00	6.90		200.00	6.41	2.04	0.68	82.05	0.00	110.28	26.53	43.59	0.85	0.17	0.20	205.43		0.00				15.69	32.20				590
Tile Discrete Level Spatial Combiner CLASS-E	[16]	AFM04P2-000	10	11.00	2.00	1.80	32.55	10.20	10.00	2.00	3.00	-22.00	37.50	37.55	-13.00	-17.00	3.00	10.00	10.00	71.14		-45.00	TE10/01	4	0	1.34	134.00	16	1.40	79	y
Class-E Amplifiers Weighted score →				57.89	6.90	6.21		35.17	25.64	1.02	0.68	56.41	0.00	96.29	26.53	43.59	0.85	0.17	0.20	182.42		91.84				126.11	227.12				308
Tray Waveguide Spatial Combiner 1	[36]	MBA-KUS025	14.125	14.50	0.75	20.00	43.01	14.50	70.00	3.00	3.00	-25.00	50.00	49.51	-19.00	-19.00	2.00	1.00	8.00	36.12		-55.00	TE10			275.00	8.00	8	2.00	89	y
Weighted score →				76.32	2.59	68.97		50.00	179.49	0.68	0.68	64.10	0.00	126.95	38.78	48.72	1.28	1.69	0.26	92.60		112.24				0.62	13.56				231
Tray Hard Boundary WG (UC-PBG)	[40]	GaAstek ITT3502D	15.5	17.00	3.00	0.18	22.50	14.75	9.50	0.50	0.25	-32.00	32.50	32.50	-10.00	-10.00	3.00	10.00	2.50	74.88			TE/TEM	5	1	3.60	5.00	12	0.65	86	y
Weighted score →				89.47	10.34	0.61		50.86	24.36	4.08	8.16	82.05	0.00	83.34	20.41	25.64	0.85	0.17	0.82	192.01		0.00				47.08	8.47				276
Tray Coax Spatial Combiner 1	[73, 38]	CHPA0618-2	12.00	18.00	12.00	40.00	46.02	18.00	21.00	4.00	3.00	-32.00	56.00	56.02	-9.00	-7.00	2.00	1.00	5.50	62.78		-30.00	TEM	10	40	400.00	10.00	16	1.00	90	y
Weighted score →				94.74	41.38	137.93		62.07	53.85	0.51	0.68	82.05	0.00	143.64	18.37	17.95	1.28	1.69	0.37	160.97		61.22				0.42	16.95				308
Tray Alternate Mode WG (TE20)	[47]	MAAPGM0040	14.5	15.00	1.00	1.00	30.00	14.08	10.50	1.00	0.50	-32.00	40.00	40.00	-15.00	-15.00	3.00	10.00	10.00	73.00			TE20	8	1	9.00	13.00	4	1.00	80	y
Weighted score →				78.95	3.45	3.45		48.53	26.92	2.04	4.08	82.05	0.00	102.56	30.61	38.46	0.85	0.17	0.20	197.18		0.00				21.19	22.03				154
2D Planar TE HDSBW	[54]	MESFETS	7.75	8.50	1.50	0.000126	-9.00	7.40	4.50	2.00	1.00	-32.00	1.00	1.00	-10.00	-10.00	3.00	10.00	10.00	65.15			TE	2	0	0.20	1.00	4	1.00	85	y
Weighted score →				44.74	5.17	0.00		25.52	11.54	1.02	2.04	82.05	0.00	2.57	20.41	25.64	0.85	0.17	0.20	187.06		0.00				647.46	1.69				154
2D Planar TM PDQ	[57]	MGA-64 135	8.25	8.58	0.65	0.039810	16.00	8.25	11.00	3.00	3.00	-32.00	32.00	26.00	-10.00	-10.00	3.00	10.00	10.00	72.67			TM	10	1	5.00	1.00	10	1.00	80	y
Weighted score →				45.13	2.24	0.14		28.45	28.21	0.68	0.68	82.05	0.00	66.67	20.41	25.64	0.85	0.17	0.20	186.32		0.00				33.90	1.69				256
3D Planar Chain Slotted Waveguide 2	[62]	TGA1073A-SCC	34	35.60	3.20	2.00	33.01	32.20	19.40	6.00	3.00	-32.00	43.00	43.01	-10.00	-10.00	3.00	10.00	10.00	63.91			TE10	6	2	10.56	19.00	8	1.00	80	y
Weighted score →				187.37	11.03	6.90		111.03	49.74	0.34	0.68	82.05	0.00	110.28	20.41	25.64	0.85	0.17	0.20	163.87		0.00				16.05	32.20				231
Conical Waveguide	[64, 74]	Raytheon M2-928-A / MS-50372 diodes	14.5	15.00	1.00	3.08	34.89	34.89	3.50	10.00	10.00	-32.00	44.89	44.89	-16.54	-16.54	3.00	10.00	10.00	78.00			TE/TEM	38	0	10.99	29.00	8	0.50	64	y
Weighted score →				78.95	3.45	10.62		120.31	8.97	0.20	0.20	82.05	0.00	115.09	33.76	42.41	0.85	0.17	0.20	200.00		0.00				15.42	49.15				231
= INTERMEDIATE STEP		= NO RESULT					= ESTIMATE						SPs								FOMs						SPs & FOMs			

Figure 3.1. Combiner and amplifier technology comparison. Part 1

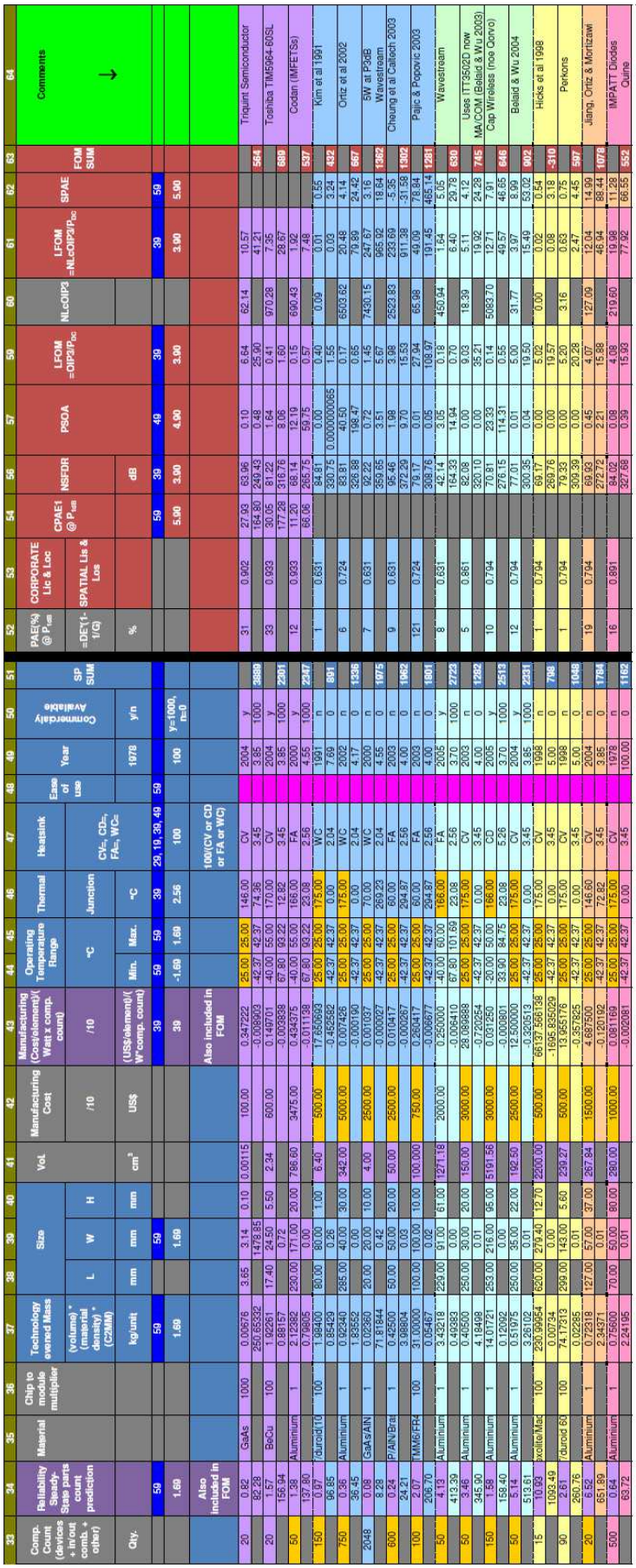

33	34	35	36	37	38	39	40	41	42	43	44	45	46	47	48	49	50	51	52	53	54	56	57	59	60	61	62	63	64
Comp. Count (devices + in/out comb. + other)	Reliability Steady-State parts count prediction	Material	Chip to module multiplier	Technology owned Mass	Size			Vol.	Manufacturing Cost	Manufacturing (Cost/element)/(W*comp. count)	Operating Temperature Range		Thermal	Heatsink	Ease of use	Year	Commercially Available	SP SUM	PAE(%) @ P_{sat}	CORPORATE Lic & Loc	CPAE1 @ P_{sat}	NSFDR	P5OA	LFOM =OIP3/P_{DC}	NLcOIP3	LFOM =NLcOIP3/P_{DC}	SPAE	FOM SUM	Comments
				(volume) * (material density) * (2/3Mg)	L	W	H		/10	/10	Min.	Max.	°C	CV_{Si}, CD_{Si}, FA_{Si}, WC_{Si}					=DET(1-1/G)	SPATIAL Lis & Los		dB						
Qty.				kg/unit	mm	mm	mm	cm^3	US$	(US$/element)/(W*comp. count)	°C		°C					%											
	59			59		59				39	59	59	39	29, 19, 39, 49	59						59	39	49	39		39	59		
	1.69			1.69		1.69				39	-1.69	1.69	2.56	100		100	y=1000, n=0				5.00	3.00	4.00	3.00		3.00	5.00		
	Also included in FOM									Also included in FOM				100/(CV or CD or FA or WC)															
20	0.82	GaAs	1000	0.00676	3.65	3.14	0.10	0.00115	100.00	0.347222	25.00	25.00	146.00	CV		2004	y	3889	31	0.902	27.93	63.96	0.10	6.64	62.14	10.57			564	Triquint Semiconductor
	92.28			250.65332		1478.95				-0.008903	-42.37	42.37	74.36	3.45	3.85	1000					164.80	249.43	0.48	25.90		41.21			
20	1.57	BeCu	100	1.92261	17.40	24.50	5.50	2.34	600.00	0.149701	-40.00	55.00	170.00	CV		2004	y	2501	33	0.933	30.05	81.22	1.64	0.41	970.28	28.57			689	Toshiba TIM5964-60SL
	156.94			0.88157		0.72				-0.003838	67.80	93.22	12.82	3.45	3.85	1000					177.28	316.76	8.06	1.60		7.35			
50	1.38	Aluminium	1	2.12382	220.00	171.00	20.00	786.60	3475.00	0.434375	-40.00	55.00	166.00	FA		2000	y	2247	12	0.933	11.20	68.14	12.19	0.15	690.43	1.92			537	Codan IMFETSs)
	137.80			0.79805		0.00				-0.011138	67.80	93.22	23.08	2.56	4.55	1000					66.06	265.75	59.75	0.57		7.48			
150	0.97	duroid10	100	1.98400	80.00	80.00	1.00	6.40	500.00	17.656693	25.00	25.00	175.00	WC		1991	n	891	1	0.631		84.91	0.00	0.40	0.09	0.01	0.55		Kim et al 1991
	96.85			0.85429		0.26				-0.452582	-42.37	42.37	0.00	2.04	7.69	0						330.75	0.000000085	1.55		0.03	3.24	432	
750	0.36	Aluminium	1	0.92340	285.00	40.00	30.00	342.00	5000.00	0.007426	25.00	25.00	175.00	WC		2002	n	1536	6	0.724		83.81	40.50	0.17	6503.62	20.48	4.14		Ortiz et al 2002
	36.45			1.82652		0.00				-0.000190	-42.37	42.37	0.00	2.04	4.17	0						326.88	198.47	0.65		79.89	24.42	667	
2048	0.08	GaAsAlN	1	0.02360	20.00	20.00	10.00	4.00	2500.00	0.001037	25.00	25.00	70.00	WC		2000	n	1975	7	0.631		92.22	0.72	1.45	7430.15	247.67	3.16		SW at P3dB Wavestream
	8.28			71.81844		0.42				-0.000027	-42.37	42.37	269.23	2.04	4.55	0						359.65	3.51	5.67		965.92	18.64	1362	
600	0.24	P/AlN/Bra	1	0.42500	50.00	50.00	20.00	50.00	2500.00	0.010417	25.00	25.00	60.00	FA		2003	n	1962	9	0.631		95.46	1.98	3.98	2523.83	233.69	-5.35		Cheung et al Caltech 2003
	24.21			3.99804		0.03				-0.000267	-42.37	42.37	204.87	2.56	4.00	0						372.29	9.70	15.53		911.38	-31.58	1302	
100	2.07	TMM6/FR4	100	31.00000	100.00	100.00	10.00	100.000	750.00	0.260417	25.00	25.00	60.00	FA		2003	n	1801	121	0.724		79.17	0.01	27.94	65.98	49.09	78.84	1201	Pajic & Popovic 2003
	206.70			0.05467		0.02				-0.006677	-42.37	42.37	204.87	2.56	4.00	0						308.76	0.05	108.97		191.45	465.14		
50	4.13	Aluminium	1	3.43218	229.00	91.00	61.00	1271.18	2000.00	0.250000	-40.00	60.00	168.00	FA		2005	y	2725	8	0.631		42.14	3.05	0.18	450.94	1.64	5.05		Wavestream
	413.39			0.49383		0.00				-0.006410	67.80	101.69	23.08	2.56	3.70	1000						164.33	14.94	0.70		6.40	29.78	630	
50	3.46	Aluminium	1	0.40500	250.00	30.00	20.00	150.00	3000.00	28.089888	25.00	25.00	175.00	CV		2003	n	1282	5	0.861		82.08	0.00	9.03	18.39	5.11	4.12	745	Uses ITT35I02D now MA/COM (Bellaid & Wu 2003)
	345.90			4.18498		0.01				-0.720254	-42.37	42.37	0.00	3.45	4.00	0						320.10	0.00	35.21		19.92	24.28		
150	1.58	Aluminium	1	14.01721	253.00	216.00	95.00	5191.56	3000.00	0.031250	-20.00	50.00	68.00	CD		2005	y	2513	10	0.794		70.81	23.33	0.14	5083.70	12.71	7.91	646	Cap Wireless (now Convo)
	158.40			0.12092		0.00				-0.000801	33.90	84.75	23.08	5.26	3.70	1000						276.15	114.31	0.55		49.57	46.65		
50	5.14	Aluminium	1	0.51975	250.00	35.00	22.00	192.50	2500.00	12.500000	25.00	25.00	175.00	CV		2004	y	2231	12	0.794		77.01	0.01	5.00	31.77	3.97	8.99	902	Bolaid & Wu 2004
	513.61			3.28102		0.01				-0.320513	-42.37	42.37	0.00	3.45	3.85	1000						300.35	0.04	19.50		15.49	53.02		
15	10.93	xolite/Mac	100	230.99854	620.00	279.40	12.70	2200.00	500.00	66137.566138	25.00	25.00	175.00	CV		1998	n	798	1	0.794		69.17	0.00	5.02	0.00	0.02	0.54		Hicks et al 1998
	1093.49			0.00734		0.00				-1695.835029	-42.37	42.37	0.00	3.45	5.00	0						269.76	0.00	19.57		0.08	3.18	-310	
90	2.61	duroid 60	100	74.17913	299.00	143.00	5.60	239.27	500.00	13.955176	25.00	25.00	175.00	CV		1998	n	1048	1	0.794		79.33	0.00	5.20	3.16	0.63	0.75	597	Perkons
	260.76			0.02285		0.01				-0.357825	-42.37	42.37	0.00	3.45	5.00	0						309.39	0.00	20.28		2.47	4.45		
20	6.52	Aluminium	1	0.72318	127.00	57.00	37.00	267.84	1500.00	4.687500	25.00	25.00	146.60	CV		2004	n	1704	19	0.794		69.93	0.45	4.07	127.09	12.04	14.99	1078	Jiang, Ortiz & Mortizawi
	651.89			2.34371		0.01				-0.120192	-42.37	42.37	72.82	3.45	3.85	0						272.72	2.21	15.88		46.94	88.44		
500	0.64	Aluminium	1	0.75600	70.00	50.00	80.00	280.00	1000.00	0.081169	25.00	25.00	175.00	CV		1978	n	1162	16	0.891		84.02	0.08	4.08	219.60	19.98	11.28		IMPATT Diodes Qume
	63.72			2.24195		0.01				-0.002081	-42.37	42.37	0.00	3.45	100.00	0						327.68	0.59	15.93		77.92	66.55	552	

Figure 3.2. Combiner and amplifier technology comparison. Part 2

technology approach currently provides the best overall technology option for a high power SSPA used in a small satellite earth terminal, the results for this assessment are given in Fig. 3.3 which provides a raw summation of normalised weighted SP requirements obtained from Fig. 3.1 (Part 1) and Fig. 3.2 (Part 2). Other techniques that show potential are Tray Waveguide (TE_{10}) Spatial combining followed by Tray Coaxial (TEM) Spatial combining, with more discussion on this given later in this section. Normalising the results will allow a comparison between normalised SPs and FOM, presented later in this chapter. The method used for normalising a range between 0 and 1 is

$$X_{norm.} = \frac{X - X_{min.}}{X_{max.} - X_{min.}}, \tag{3.1}$$

where $X_{norm.}$ = the normalised value for a particular technology, X = the SP or FOM sum for a particular technology, $X_{max.}$ = the maximum SP or FOM value for the range of technologies and $X_{min.}$ = the minimum SP or FOM value for the range of technologies.

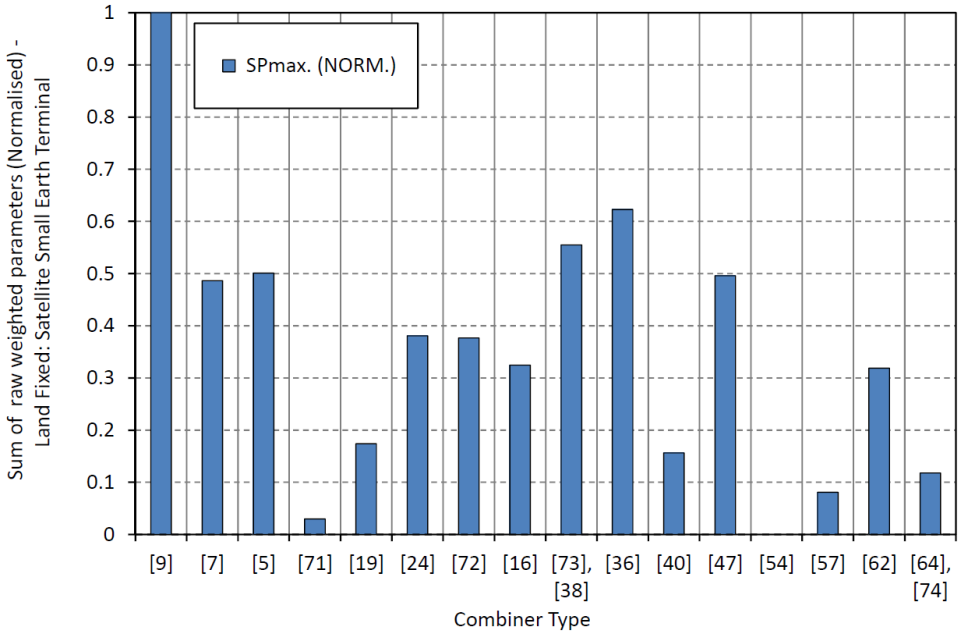

Figure 3.3. Initial combining technology specification parameter comparison. Land fixed service for a small satellite earth terminal. Refer to Table 3.1 to match combining technology with references. Note that the zero value for reference [54] is as a result of the normalising process.

The comparative study includes the technologies that have been reviewed in Section 2.2 and compares them based on specific design parameters as well as establishing an

Table 3.1. Combining technologies.

Combining Technology	Class	Reference
Corporate Monolithic	Corporate	[9]
Corporate Chip		[7]
Corporate Hybrid Waveguide		[5]
Tile Discrete Spatial	Tile	[71]
Tile Chip Spatial		[19]
Tile Monolithic Spatial (Transmission)		[24]
Tile Monolithic Spatial (Reflection)		[72]
Tile Discrete Spatial Class-E		[16]
Tray Coaxial Spatial	Tray	[73, 38]
Tray Waveguide Spatial (TE_{10})		[36]
Tray Hard Boundary Waveguide		[40]
Tray Alternate Mode Waveguide (TE_{20})		[47]
2-D Planar TE Mode	2-D Planar	[54]
2-D Planar TM Mode		[57]
3-D Planar Chain Slotted Waveguide	3-D Planar	[62]
Conical Waveguide	Conical	[64, 74]

overall and scalable FOM comparison, that has been considerably expanded, in terms of specific design parameters and range and types of spatial combining technologies, from that given by Gouker in Mortazawi *et al* [75] pp. 174, as a means of selecting a particular appropriate technology and design strategy. In this research it is proposed to provide a relatively simple to use and quick, more encompassing comparative FOM, having \$/W/kg/°C/mm^3/hr units, similar to the power density FOM quantity as given in Navarro and Chang [3] and York and Popovic [20] pp 15.

As part of the proposed comparison careful consideration had to be given to how parameters between alternative technologies can be compared and how scalable, with respect to frequency, an optimum design methodology can be. Part of the comparison also considers the thermal performance of each technology and details, regarding the thermal research aspects, are given in Section 3.4.5.

Other outcomes, forming part of the design methodology, are models that can be used to compare various technologies, for example similar to the comparison between the number of active elements used for corporate, chain and spatial combining versus combining efficiencies as shown in Fig. 3.4, enabling selections relating to the best methodology to be easily made, by showing where the break points, in terms of trade-offs for

each of the potential methods are located. These models may be used to set particular specifications, for particular services, which will assist in narrowing the technology choices, see for example Khan *et al* [76] Fig. 11.

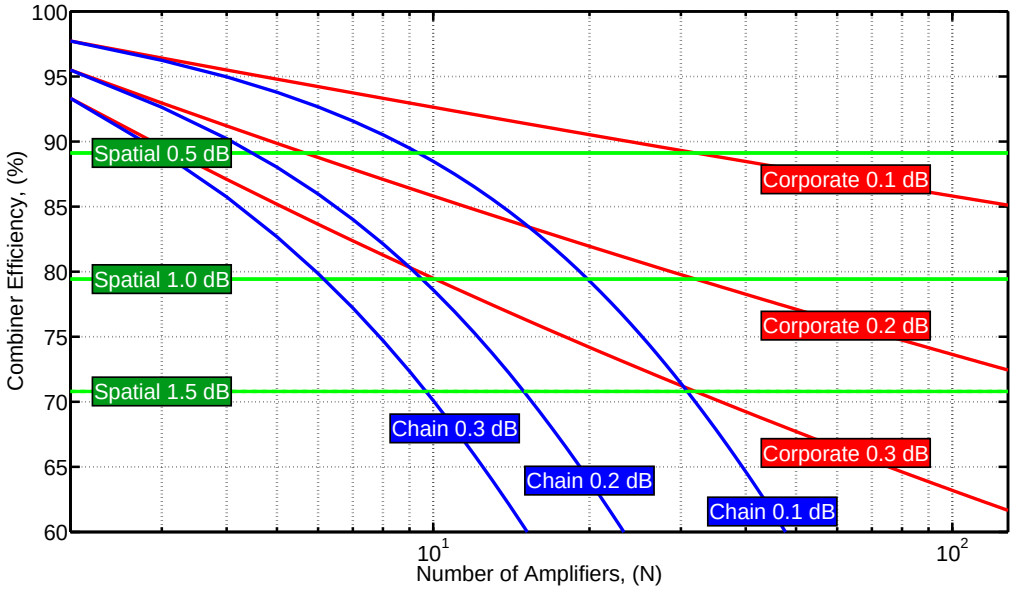

Figure 3.4. Corporate, spatial and chain combiner efficiency comparison. Combiner efficiency comparison between corporate, spatial and chain combiners versus number of elements with various combiner type losses indicated.

Another aspect that has been investigated as part of the design methodology, is the conflict between the spatial combining benefits of using a larger number of efficient low power active devices, Mink [13] Figs. 3 to 5, compared to using a smaller number of higher power active devices. Currently obtaining high linearity, efficient lower power devices is a limitation, as generally to obtain good linearity less efficient Class-A active devices are required. For a large number of these less efficient devices then thermal dissipation becomes a problem. Therefore recommendations relating to the minimum number of usable devices with respect to thermal management requirements will need to be taken into consideration.

To help with the decision process a number of decision analysis techniques, Meehan and Purviance [77], are utilised. These techniques cover; risk, yield (Monte Carlo), sensitivity, optimisation, design centering, Quality Function Deployment (QFD) and Design For Six Sigma (DFSS). The sensitivity analysis will help to determine which parameters can be optimised. In addition, the technique proposed by Antonsson [78]

was considered. This technique is used to allow sets of designs, rather than a single design, to be evaluated. This technique is termed the method of imprecision and uses the mathematics of fuzzy sets, as shown in Fig. 3.5, to represent imprecision as preferences between both the functional requirements and the design preferences of a design. An example fuzzy inference control surface for the selection between a corporate and spatial combiner, based on frequency and output power requirements, is shown in Fig. 3.6.

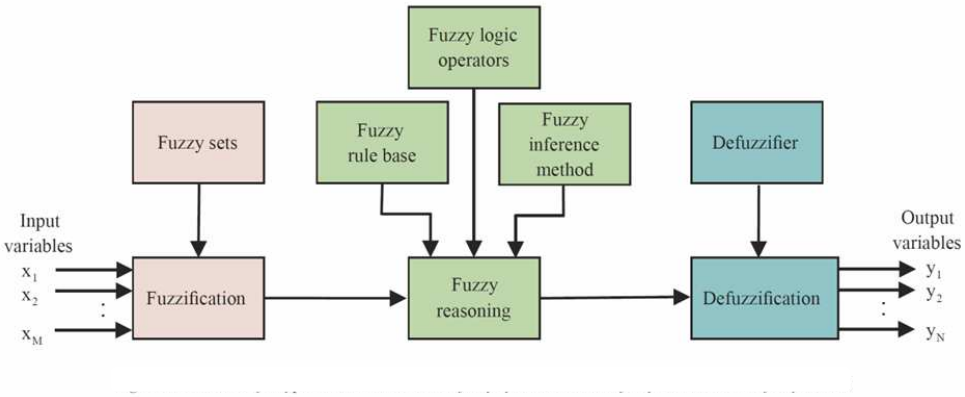

Figure 3.5. Typical rule based fuzzy system.

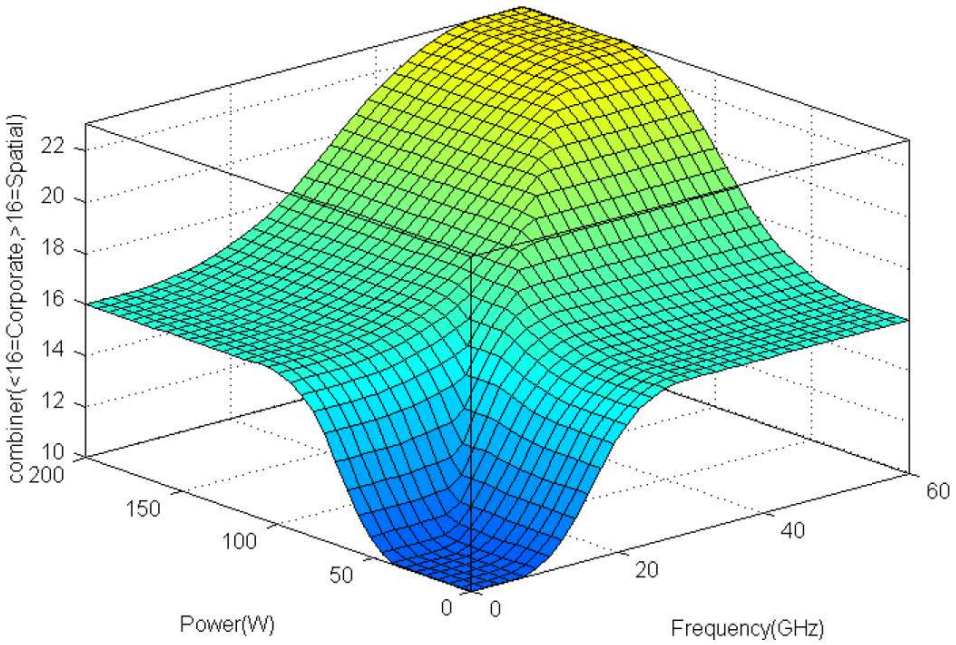

Figure 3.6. Fuzzy inference system control surface. Combiner type (by number of elements) versus power and frequency. Less than $\approx$ 16 elements $\equiv$ corporate combiner and greater than $\approx$ 16 elements $\equiv$ spatial combiner.

Parameter requirement weightings can also be determined by the combination of a QFD, Akao *et al* [79] analysis as shown in Fig. 3.7, reflecting customer expectations and Failure Mode Effects Analysis (FMEA) AIAG [80] from the manufacturing perspective as well as particular service requirements that can be derived from reliability prediction methods, Telcordia [81].

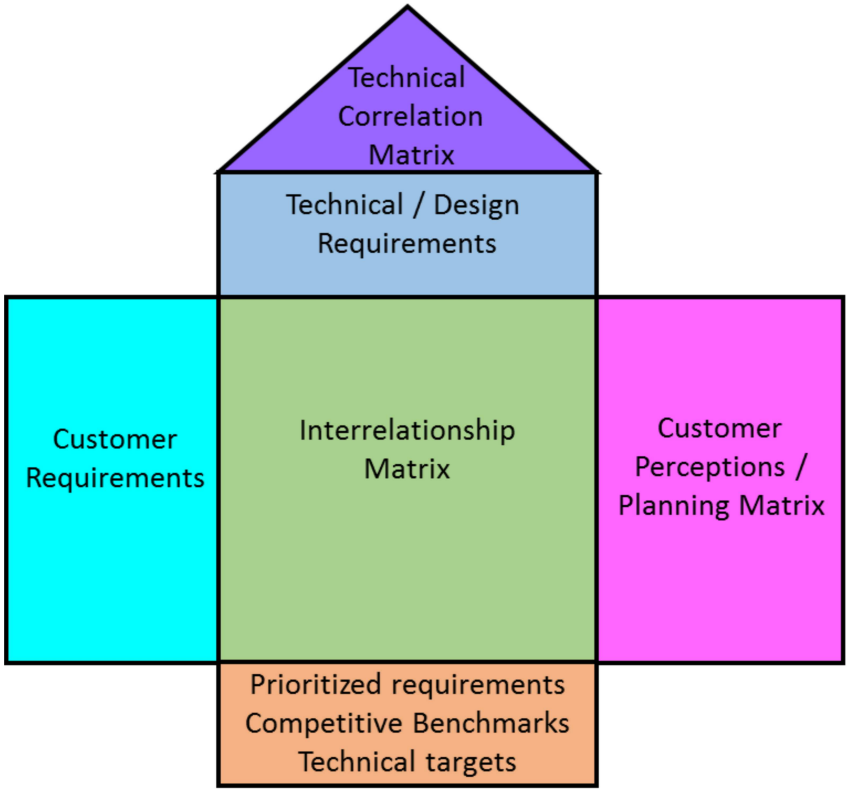

Figure 3.7. Quality function deployment.

These techniques were incorporated within the design methodology as they allow for consideration of other less tangible factors beyond hard specifications. For example, other less tangible factors affecting the design methodology are requirements such as the geographic region where the amplifier will used, company design philosophy, for example deliver first to market then re-design with cost-down loops versus best parameter/manufacturability design that is delivered later to market without cost-down loops. Other factors include, market, application or regulatory specific requirements and customer relationships. The methodology based on service requirements and performance parameters illustrated through a flowchart as given in Fig. 3.8. The different coloured blocks shown within the flowchart are; (i) the yellow block where the detailed design takes place but it is subject to varying inputs that are combined via the circular

block, (ii) the cyan block which impacts both the detailed design and the decision process leading to the technology selection prior to the detailed design. This continues to occur throughout the detailed design process and (iii) the green end block where the detailed design process concludes following successful meeting of all specification that also include the less tangible specification and the technology selection.

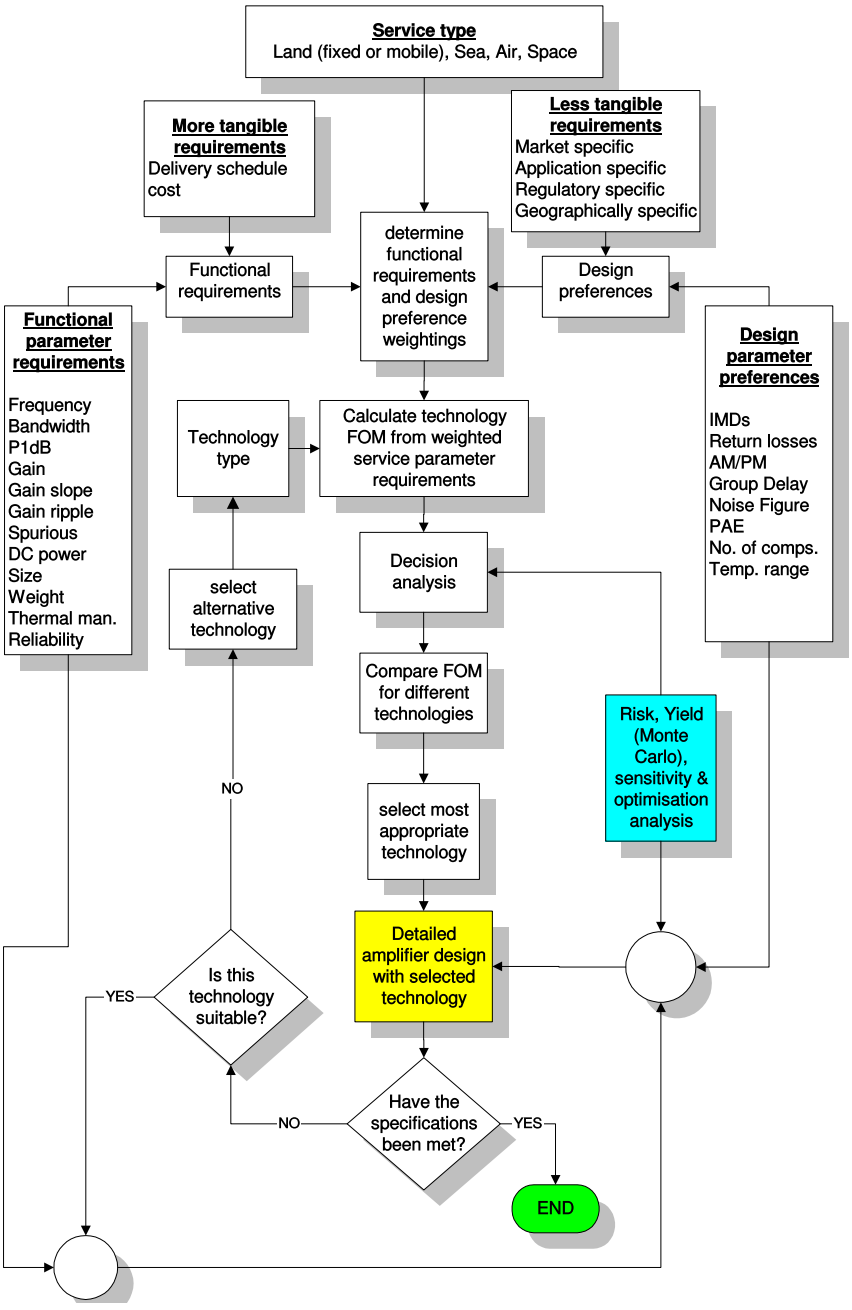

Figure 3.8. Design methodology flowchart. Proposed design methodology flowchart.

An example SSPA is proposed in the Section 3.3 as a means of testing the proposed design methodology approach. The proposed SSPA considers a range of different techniques, with the potential for a higher power output outcome, whose combination have not been previously seen in the literature.

3.3 New Concepts

The objectives for the proposed design methodology validation are to provide the following outcomes:

1. Use higher power Class-A MESFET IMFETS, implying good spectral purity but reduced PAE. This would suggest that low loss waveguide be used as the spatial combining structure with the benefits of being able to handle higher output power and also providing a suitable thermal management and mechanical mounting platform.

2. Determine if the waveguide / electro-magnetic configuration is suitable for spatial combining and able to achieve the output power requirement at the operating frequency,

3. Determine if the electro-magnetic configuration can be managed and optimised thermally,

4. Optimise the mechanical configuration for best electro-magnetic / thermal / DC electrical performance (biasing),

5. Develop high RF power handling, low loss transitions from waveguide to the active devices used in the new waveguide spatial combining configuration,

6. Determine the power handling capability for any EBGS, used within the input and output waveguides to modify the E-field, in order to obtain appropriate field illumination of the transitions / active devices used and

7. Investigating and resolving practical implementation issues such as DC biasing and manufacturability issues for the combining method proposed.

Validation of this research will be by the use of the new design methodology to select the most suitable technology, design process and present results for an example SSPA having the target specifications, as given in Table 3.2, selected from one of the following important satellite communication bands. The example will be consider a C-Band SSPA.

Table 3.2. Proposed research target specifications.

Target Specification	Units	C-Band	Ku-Band
Service type		Fixed earth	Fixed earth
Frequency range	GHz	5.850 6.725	14.0 14.5
Output power	Watts	300+	100+
Gain	dB	8 9	4 5
Size (L x W x H)	mm	150 x 90 x 50	150 x 90 x 50
Cost	US $	<$3,000	<$3,000

Figure 3.9 presents a possible concept for a 6-way hexagonal IMFET combiner, which is similar to a coaxial tray spatial combiner but has the active devices mounted to the outer walls of the waveguide structure to assist with thermal management of the high power IMFETs. Simulations would be required to determine if the TEM mode to the active device transitions would be viable.

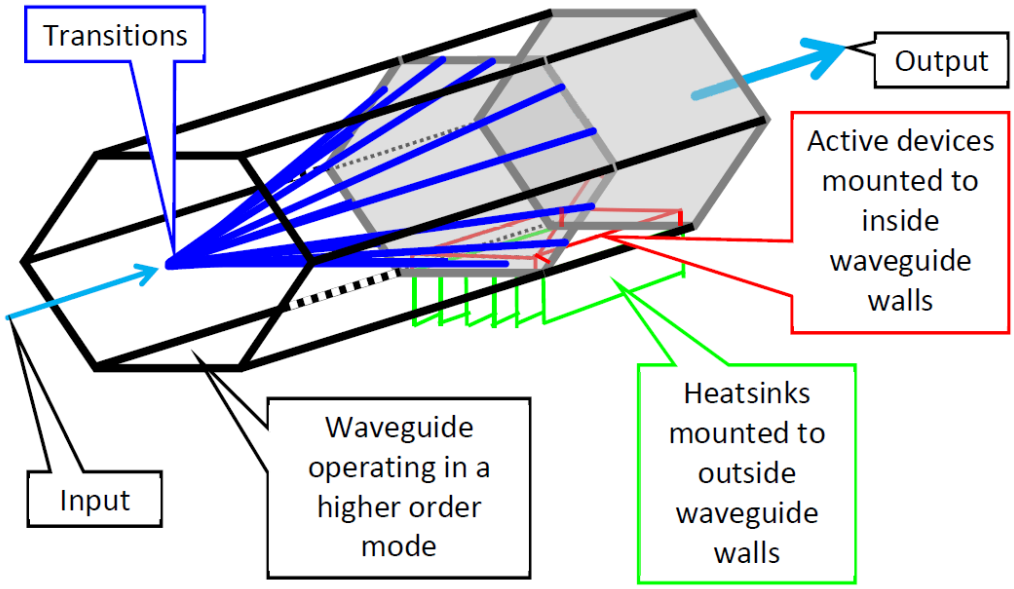

Figure 3.9. Concept for a hexagonal 6-way IMFET combiner.

Another proposed mounting arrangement, shown in Fig. 3.10, has the active devices mounted to the external walls of a more conventional rectangular waveguide structure, thus allowing the devices to be in intimate contact with easily accessible heatsinks. Again simulations would be required to determine if the TE mode to the active device transitions would be viable.

Fig. 3.11 shows some potential combining concepts for transitions from multi-ridge waveguide to standard IMFET's mounted around waveguide walls. The assembly

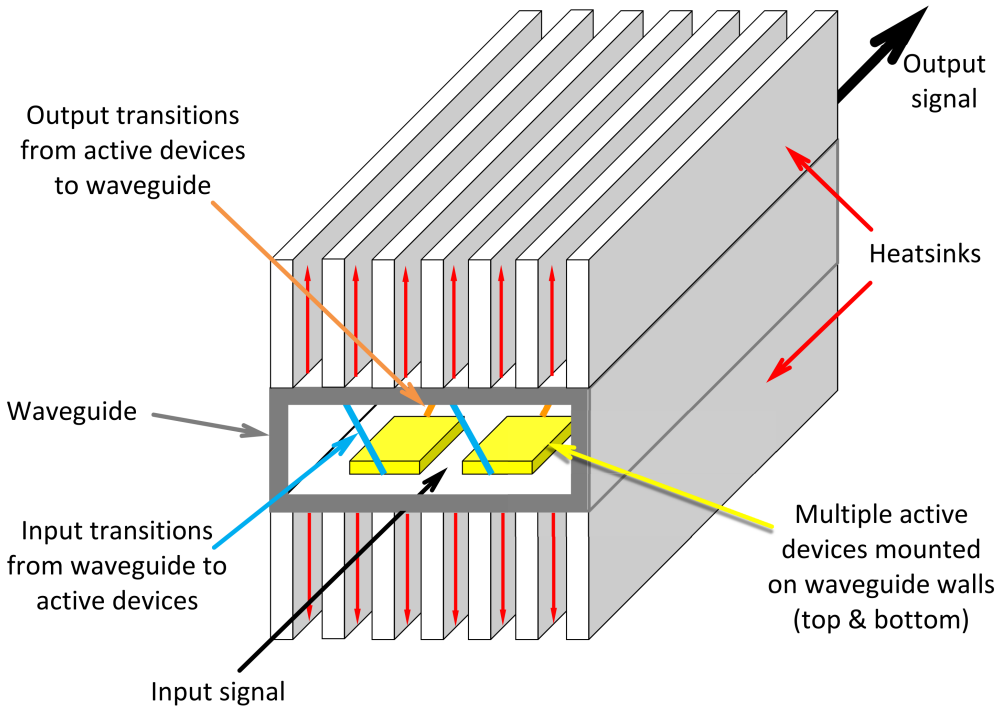

Figure 3.10. Proposed standard waveguide thermal mounting configuration.

shown in Fig. 3.11 (b) shows DC isolated ridge waveguide to microstrip transitions, enabling DC bias to be applied to the gate and drains of the IMFETs. This technique has been employed by Izadian [82, 83] with further investigation required, particularly for high RF power operation.

3.4 Considerations For New Concepts

For the proposed device mounting, the electromagnetic performance of the combining structure will require investigation with the outcome being an optimised electromagnetic solution. A thermal comparison between the various combining technologies also needs to be undertaken to ensure that any new active device mechanical mounting arrangement will improve the thermal management while maintaining the benefits of a spatial combining approach. A global coupled electromagnetic-electrical-thermal simulation and experimental validation has been performed on a spatial combining MMIC

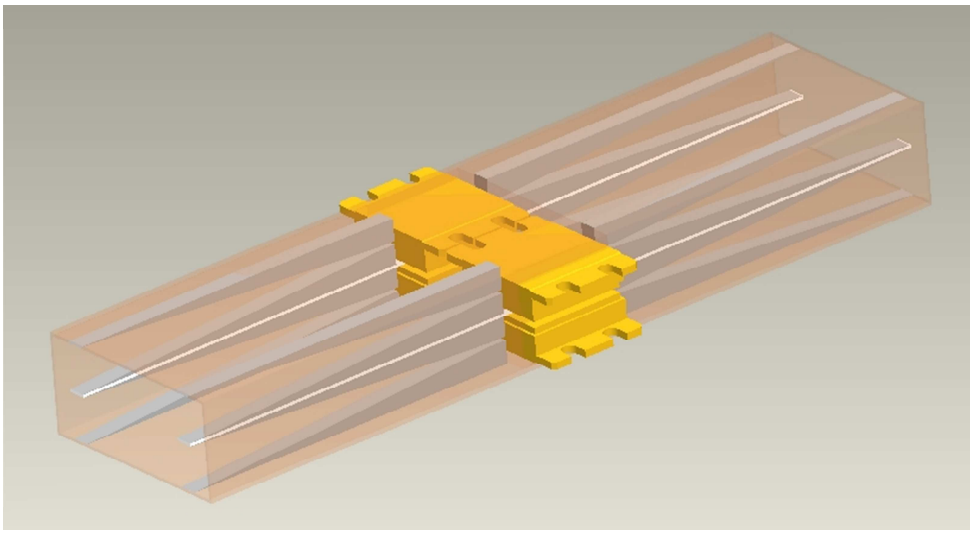

(a)

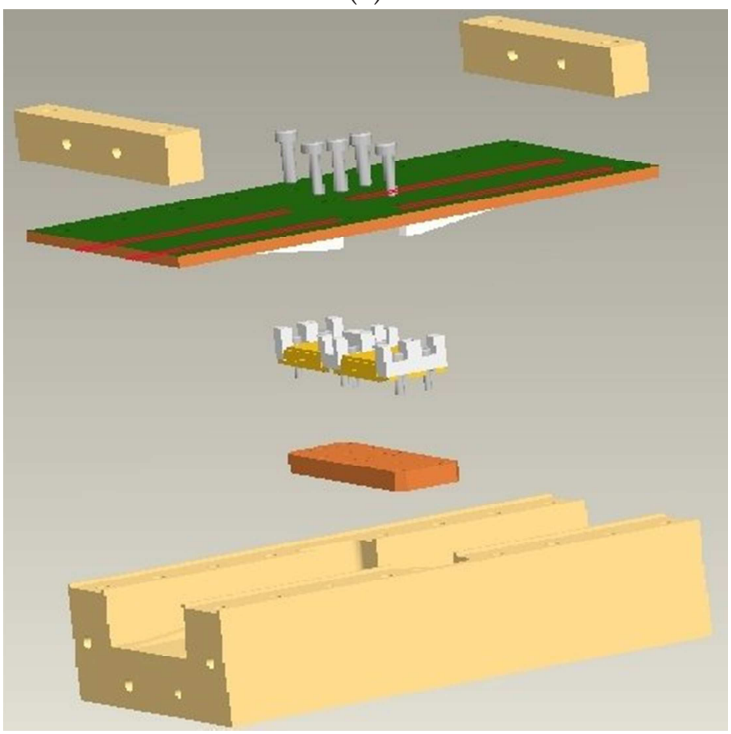

(b)

Figure 3.11. Proposed concept for combining 4 internally matched high power C-Band MESFETs. Concept of combining 4 internally matched high power MESFETs within a standard WR137 C-Band waveguide that is modified with symmetric double ridge transitions (a) and Concept of combining 2 internally matched high power MESFET's within a standard WR137 C-Band waveguide that is modified with symmetric double ridge transitions. Also shown is a means for FET biasing (b).

array by Batty *et al* [84, 85]. Further information about simulating electromagnetic-electrical-thermal performance is provided by Ansoft [86]. Nonetheless, further discussion regarding this part is beyond the scope of the current research.

From the review and technology comparisons, undertaken so far, further research is required to determine which approaches would contribute to improved overall SSPA performance. The newly proposed mechanical / thermal configuration needs to be evaluated to determine if it provides the required electromagnetic performance. If this is the case then this thermal / electromagnetic configuration needs to be optimised.

Other areas of investigation relate to the use of high power IMFET's, to see if they can be used in the manner shown in Fig. 3.10. This will require research in the following areas:

1. Modeling, simulation and optimisation of the electromagnetic performance for the new mechanical / thermal configuration.

2. Determination of the output power that can be achieved using multiple IMFET's.

3. Modelling to determine the best type of transition between the waveguide structure and active devices in order to achieve low insertion loss and highest RF power handling capability thus providing the best combining efficiency at maximum RF output power. Types of transitions to be investigated include multi-ridged waveguide transitions and also evanescent mode transitions with both types of transitions allowing for the provision of DC biasing to the active devices.

4. For multiple active devices and transitions, the need for E-field modification within the waveguide, using either alternative waveguide modes of operation or electromagnetic band-gap structures will need to be investigated and optimised. The most optimum configurations and their RF power handling capacities need to be determined. Some analysis of power handling capacity related to Micro Electro-Mechanical System (MEMS) devices has been conducted by Schoenlinner *et al* [87] and may be relevant here.

Further investigations, beyond GaAs MESFET IMFETs to Wide Band-Gap (WBG) Galliun Nitride (GaN) technology devices, that operate at higher DC voltages, Kameche and Drozdovski [88], and at higher junction temperatures, are required with assessments made to the impact on power supply and thermal management requirements.

3.4.1 Electro-magnetic Considerations - Alternative Waveguide Modes

Following the thermal analysis, on the newly proposed mechanical / thermal configuration that has the active devices mounted to the walls of the waveguide combining structure, alternative waveguide modes might be used to propagate high power RF signals within these waveguide structures and have suitable transitions to and from the active devices. Some of the issues that arise and need to be investigated include:

- Suitable waveguide dimensions contributing to
- Alternative modes excitation or suppression.
- The types of suitable transitions required for input and outputs. They may not necessarily be the same.
- Management of higher losses, and what are they, for alternative modes.
- RF Power handling associated with higher waveguide modes.
- Suitability the structure be easily manufactured and its' cost.

Shown in Fig. 3.12 (a) is the E-Field pattern for square waveguide propagating the TE_{11} mode superimposed with 2 off active devices, mounted to each of the waveguide walls. This may be a suitable mode to use. Also shown in Fig. 3.12 (b) is the loss performance versus waveguide size comparison. From this it can be seen that higher order modes propagate at higher losses so that this needs to be considered in the overall combining efficiency calculations. Note that Fig. 3.12 (b) is for circular waveguide with

$$\overline{\alpha} = \frac{\alpha}{\left[f\frac{R_m}{Z_0}\right]}, \tag{3.2}$$

$$\overline{D} = D/\lambda. \tag{3.3}$$

where $\overline{\alpha}$ is the normalised waveguide attenuation co-efficient with α the waveguie attenuation co-efficient in units of [Np/s], f is frequency, R_m is the waveguide surface resistance, Z_0 is the free space impedance, and $\overline{D}$ is the normalised circular waveguide diameter and λ is the wavelength.

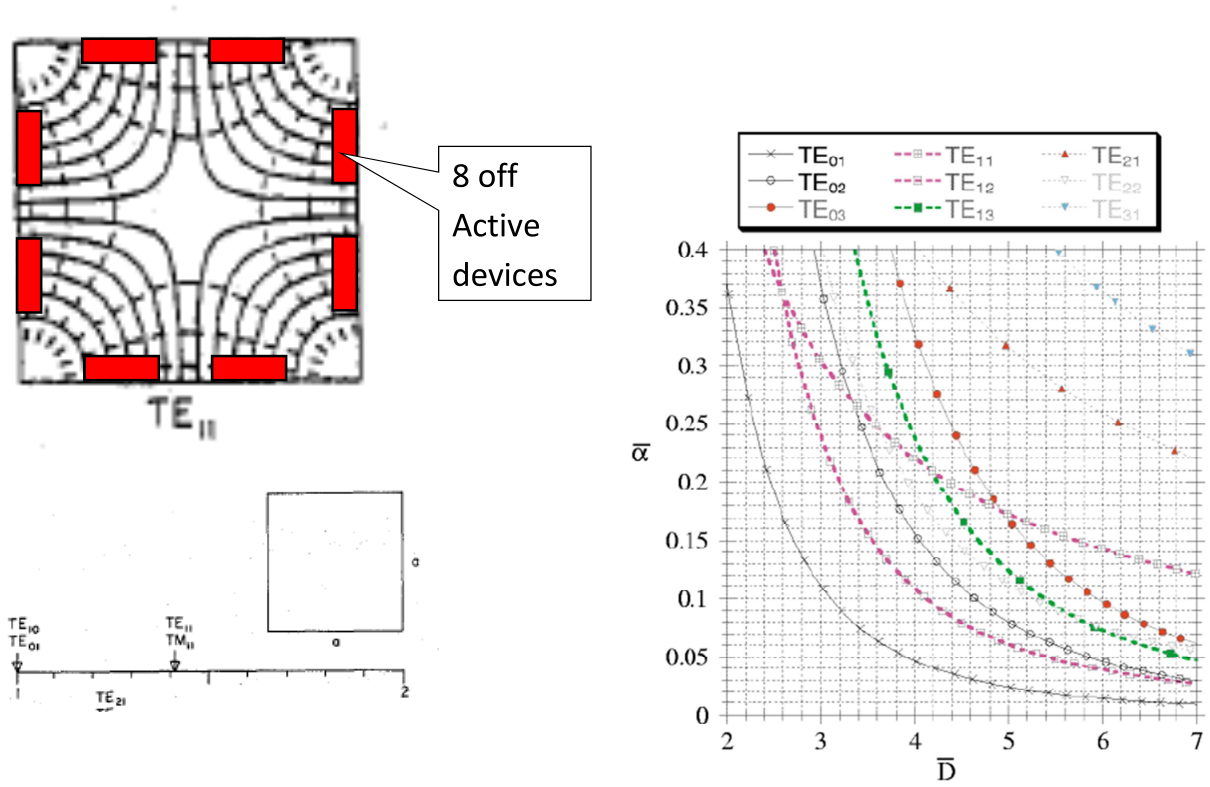

(a) (b)

Figure 3.12. TE_{11} square waveguide. Square waveguide TE_{11} E-field pattern and normalized modal cutoff frequencies, from Lee *et al* [89] (a) and relative attenuation for different TE modes in circular waveguide versus normalised waveguide diameters, from Tantawi *et al* [90] (b).

The majority of high power microwave SSPA's operate using standard TE mode rectangular waveguide so mode converters that convert from and to standard TE mode waveguide may be required. A potential mode converter, from standard mode to alternate mode, is shown in Fig. 3.13. Research will be required to determine the optimum mode to be used and how to design a suitable mode converter.

Corrugated Waveguide "E-guide"

Tall waveguide, where the rectangular waveguide height has been increased, provides lower loss but allows for the propagation of higher order unwanted modes. In order to reduce or eliminate these spurious modes then tall waveguide formed by using corrugations can be employed. This has been termed corrugated "E" waveguide, Dybdal *et al* [92]. Having a more even E-field across the waveguide is beneficial for spatial combining, as detailed in Sections 2.2.5 to 2.2.5 with more details relating to corrugated

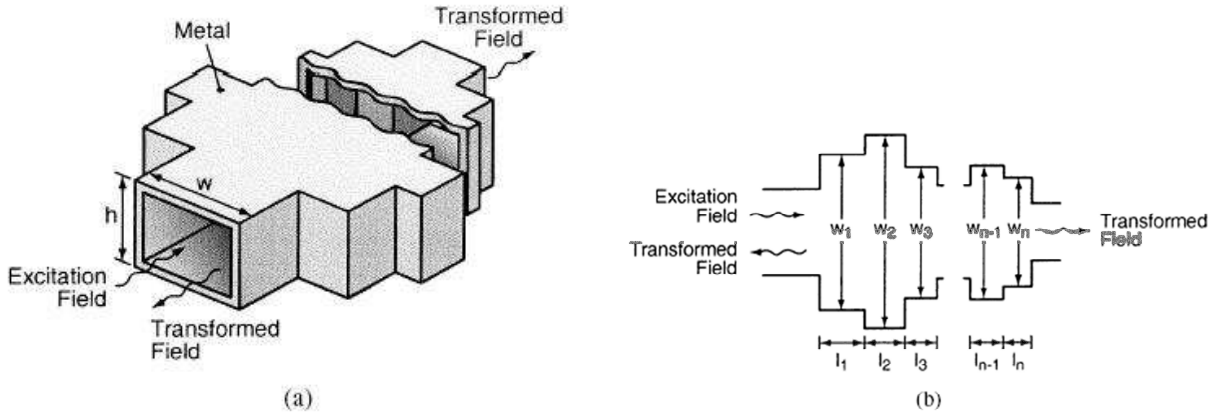

(a) (b)

Figure 3.13. Waveguide structure mode converter. Irregular scattering waveguide structure mode converter (a) and parameters that can be optimised to achieve the complete field transformation (b) from Yang *et al* [91].

waveguide given in Section 2.3.3. The suitability and application of this type of structure to waveguide confined spatial combining / amplifiers needs to be investigated.

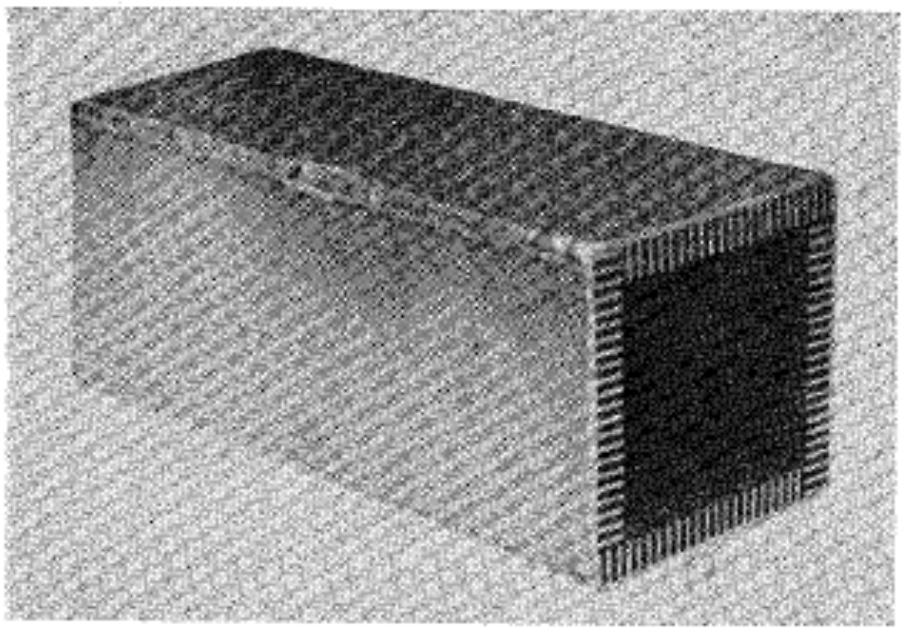

Figure 3.14. Corrugated waveguide "E-guide". Section of "E-Guide", from Dybdal *et al* [92].

3.4.2 Transitions

In order to allow active devices to be mounted within a waveguide structure, to allow for spatial combining, efficient transitions are required that are low loss and can handle high RF powers, thus maximising output powers and improving spatial combining efficiency. Transition design also needs to allow for DC bias to be applied to active devices. Having multiple active devices mounted around the interior walls of the waveguide structure and potentially modifying the E-field within the waveguide to be uniform using corrugations or otherfield modification structures, will provide the maximum benefit from the spatial combining technique. Appropriate transitions for this type of waveguide structure will need to be available. This means that transitions that meet these requirements need to be researched.

Another transition that needs consideration is the evanescent mode transition of Bharj and Mak [93]. This uses evanescent waveguide to transition from microstrip to waveguide and may provide an easy DC biasing option, as the microstrip is DC isolated from the remaining waveguide, however loss and high RF power capability needs to be determined.

3.4.3 Symmetric Ridge and Double Ridge Waveguide

Symmetric double ridge waveguide, Jull *et al* [94], is a potential waveguide structure to transition between standard rectangular waveguide and multiple active devices mounted within the waveguide on the waveguide walls. This type of waveguide is also attractive because in the ridge region the E-field is uniform and for multiple active devices that are spatially combined this means that soft saturation can be avoided. Further research is required to determine the viability of using this waveguide structure for spatial combining. Symmetric double ridge waveguide may be a sub-set of the more general "E-Guide" with a combination of the two being a suitable low loss alternative mode transition combiner.

Other alternatives for providing a uniform E-field within a waveguide structure have been proposed by Chen [95] with ridge waveguide being a simple way to do this in terms of manufacturing. This technique may also be suitable for double symmetric ridge waveguide.

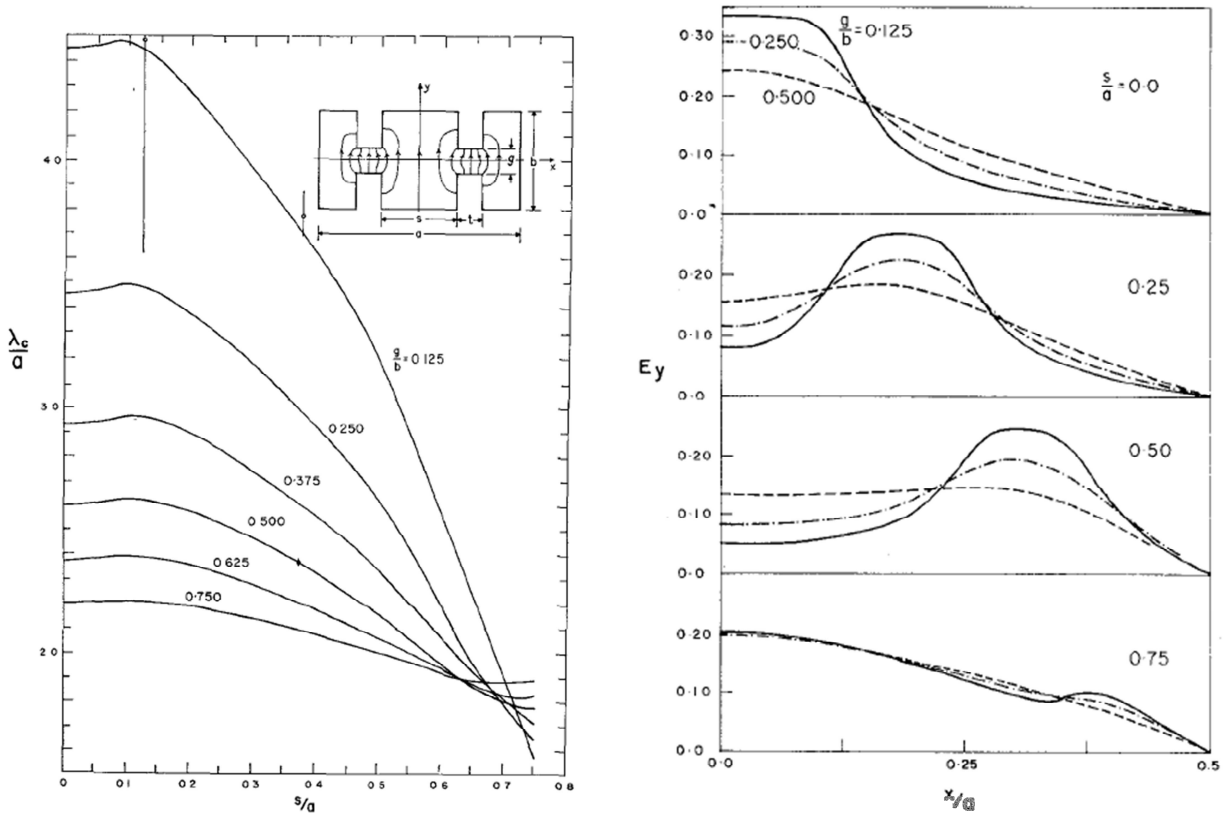

(a) (b)

Figure 3.15. Symmetric double ridge waveguide. (a) Symmetric double ridge waveguide dominant mode cutoff wavelength for b/a=1/2 and t/a=1/8 and (b) relative electric field strength versus ridge position along the $y = 0$ plane for dominant mode propagation with b/a=1/2, t/a=1/8, and h/a=1/32, from Jull *et al* [94].

3.4.4 DC Biasing

In terms of implementation, practical issues will need to be resolved including the provision of DC biasing to active devices within any advanced waveguide structures, particularly at high RF powers, and overall assembly techniques to allow for low cost manufacturing, potentially in high volumes, will need to be addressed. From an electro-magnetic perspective these practical solutions must not generate any unwanted waveguide modes that could reduce overall amplifier performance.

Electro-magnetic Simulations

In order to determine and compare the electro-magnetic performance of the proposed waveguide structures including multi-ridge waveguide, different modes, corrugations,

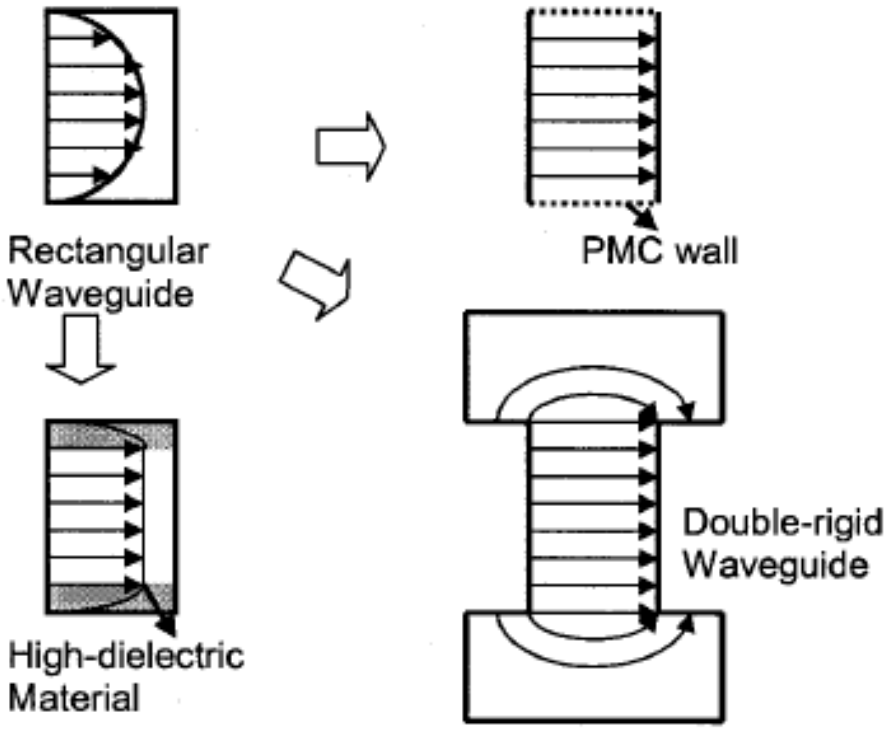

Figure 3.16. Waveguide options for obtaining uniform E-field distributions. Different waveguide options for obtaining uniform E-fields inside a waveguide structure, from Chen [95].

EBG structures and transitions then these will need to be modeled, simulated and optimised. A suitable electro-magnetic software simulation package will be required for this, for example Ansoft High Frequency Structure Simulator (HFSS) and / or Computer Simulation Technology (CST) Microwave Studio.

3.4.5 Thermal Considerations

Although the optimum thermal design and performance of an amplifier can be considered as part of the overall design methodology here it is considered separately. Thermal analyses have been performed on a number of spatial power combining techniques such as: (i) tile array, Kolias and Compton [23], (ii) tile grid Thelander *et al* [96], (ii) rectangular waveguide tray, York [33] and (iv) coaxial tray, York *et al* [39], as shown in Fig. 3.17. No detailed analysis has been presented comparing all types of spatial combining in the literature. So a thermal comparison between all of the types of spatial combining, including the method proposed in this proposal, would be useful. This aspect will be considered when investigating the development of a FOM that allows

the comparison for the different power combining techniques. To determine if the proposed thermal management techniques are viable, various simulations will be needed. They are discussed briefly in the following section.

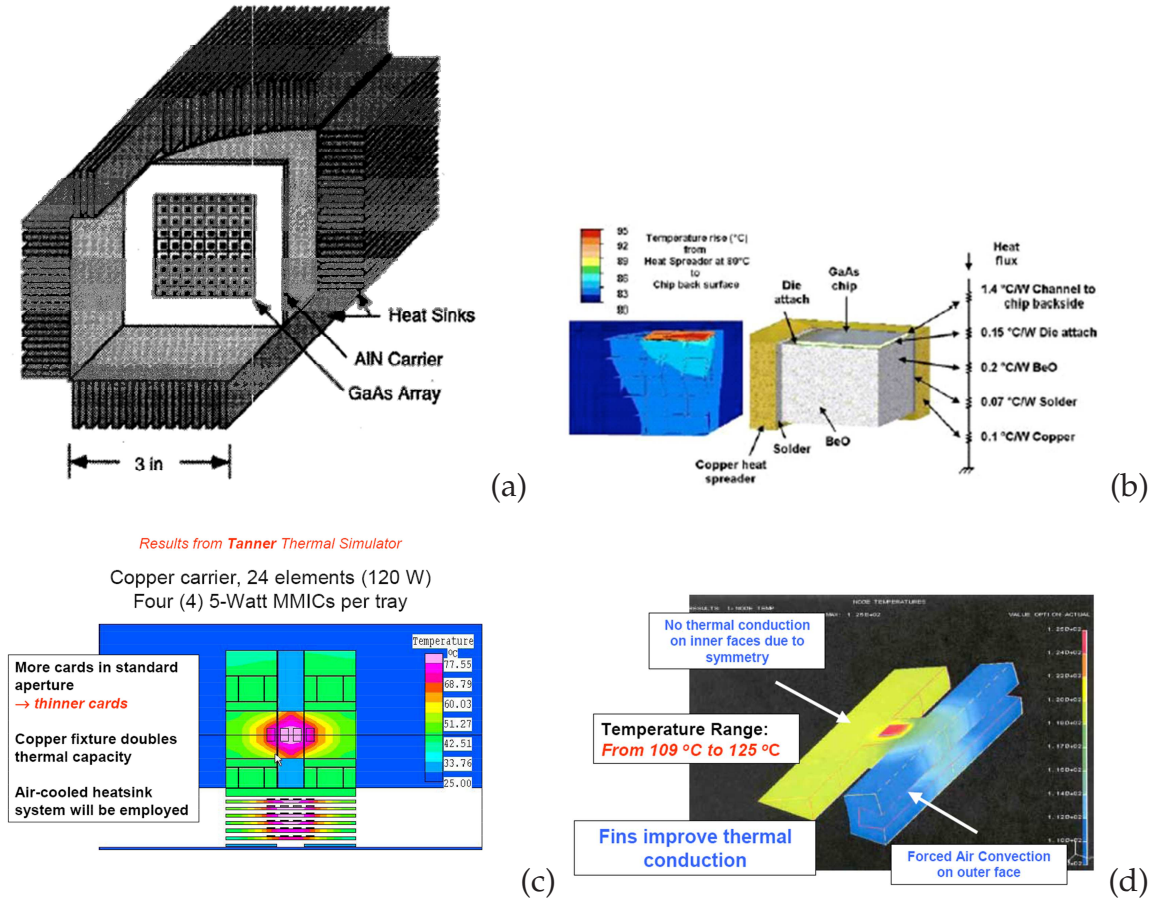

Figure 3.17. Thermal simulation for a Ka-Band tile grid amplifier. Cut-away view of the geometry for simulations of the conduction performance of a tile array mounted on an AlN carrier, from Kolias and Compton [23] (a), 3D finite element thermal model for Ka-Band tile grid amplifier Beta Unit at 10W output, from Thelander *et al* [96] (b), "Tanner" simulation results for standard rectangular waveguide tray amplifier using 24 off copper carriers each with 4 off 5 watt MMICs per tray, from Cheng *et al* [34] (c) and Simulation results from "Ideas" thermal simulator for a copper carrier coaxial tray amplifier with 2 off 10 Watt MMICs per tray, from York *et al* [39] (d).

Thermal Simulations

To thermally compare existing amplifier combining technology performance with the proposed approaches indicated here, appropriate simulation software will be used.

Initial simple comparisons will be made using standard thermal equations, however more complex thermal / electromagnetic comparisons and optimisations will require the use of a thermal / electromagnetic software simulation package, for example Ansoft ePhysics [86], as these packages allow for the simulation of the thermal coupled with the electromagnetic performance.

3.5 New Concept Validation From Recent Research Outcomes

Recently Than *et al* [97, 98] have demonstrated a 600 W C-Band amplifier using spatially combined 45 W IMFETs, Figs. 3.18 and 3.19 . The transitions indicated differ from what has been proposed here. Higher power would be possible by the use of 60 W IMFETs, [7] , or possibly higher using higher power GaN devices, however the transitions and thermal management would need to be carefully considered. Note that the proposed design methodology, technology approaches and implementations will allow for newer higher power GaAs IMFET's as well as high drain voltage and higher temperature GaN and SiC higher power IMFET's.

3.6 Summary

From the review and comparison, and following the subsequent discussions provided in this chapter, there is scope for contributions relating to microwave power amplifier combining techniques in the areas of:

1. Optimum power combining design methodology, including both technology selection and detailed design, for a given type of service with specific parameter requirements,

2. Maintaining or improving on existing performance specifications like power output, frequency, bandwidth, gain, power added efficiency, cost and manufacturability, for the proposed new concept structure while providing suitable thermal management of different types of spatial/power combining technologies,

3. Application of the best thermal management technique for spatial combining and developing new and improved waveguide structures that allow for the use of this optimum thermal management approach while also providing optimum electrical and electro-magnetic performance,

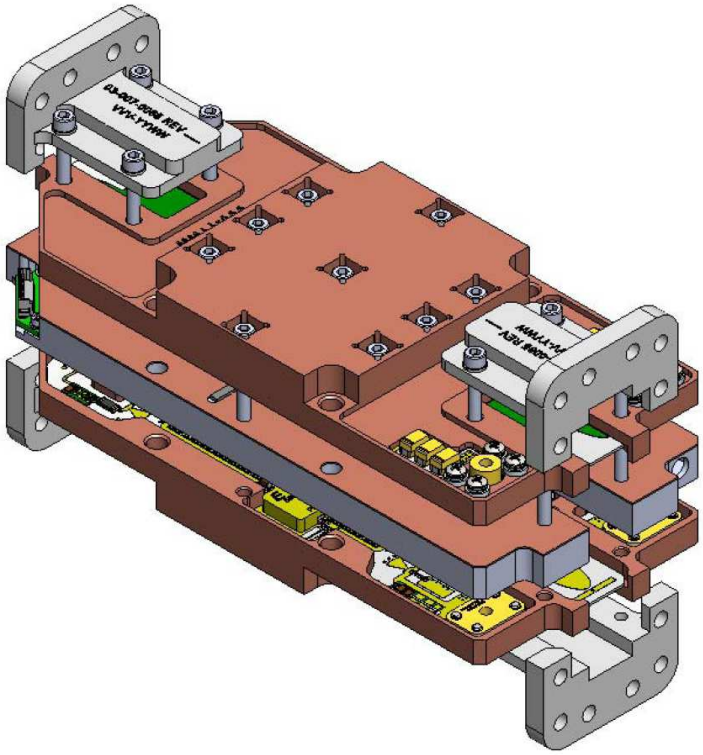

Figure 3.18. Spatially combined C-Band 2 card deck amplifier expanded assembly. From Than *et al* [97].

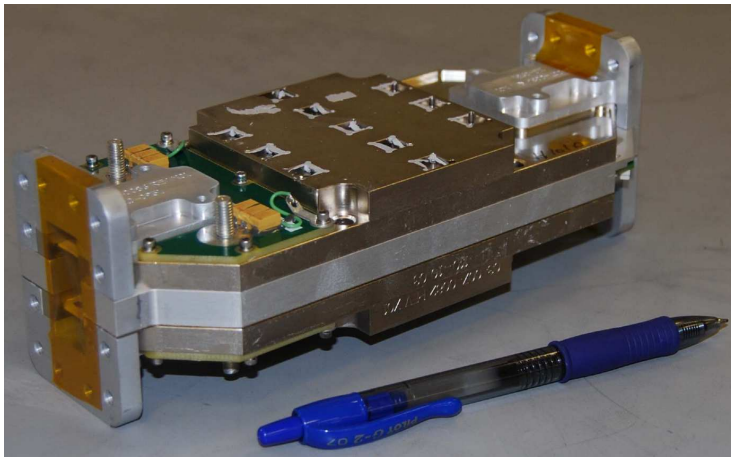

Figure 3.19. Spatially combined C-Band 2 card deck amplifier assembly. From Than *et al* [97].

4. Investigation of waveguide to active device transition structures that allow for higher power handling and low insertion loss thus improving output power capability as well as enhancing combining efficiencies,

5. Use as required of waveguide field distribution, either by using different modes, EBG structures, the use of corrugated waveguide or a combination of these that are also able to handle high RF powers for the benefit of improving spatial combining efficiency and

6. Determining methods that allow for the practical implementation of DC biasing and low cost manufacture of these newly proposed / developed SSPA's.

The approach proposed for this research, in terms of determining an overall design methodology, that uses the comparison of available technologies, along with specific technology approach areas, from proposed overall target specifications, can be justified as an acceptable approach by reference to the methods employed by Kahn *et at* [76] and [99].

In the following section some preliminary research associated with the design methodology, i.e. a comparison of the available technologies, will be presented as well as some background into the proposed design methodology.

3.7 A New Figure of Merit Methodology for Power Amplifier Combining Technologies

3.7.1 Introduction

There is a continuing need, in both the commercial and defense markets, for SSPAs that can deliver high output power and high efficiency while operating at high frequencies with reduced size and area, all at low cost. There is a need to investigate and determine which power combining techniques or architectures can be used to achieve this within a given number of constraints Shellenberg; Bhat *et al* [100, 101].

The goal of this section is to demonstrate how to select an appropriate SSPA technology that can deliver a required outcome based on a customer's service and performance requirements. This forms part of the overall SSPA technology selection and design methodology with the aim of delivering an outcome using the most appropriate

technology by making decisions from both tangible requirements, for example performance specifications, and less tangible requirements such as graceful degradation, time to market or ease of use. The tangible requirement selections will be made by developing and building on available or new FOMs, with technology selections including more recent spatial combining technologies applied to SSPAs. Tangible and less tangible selections will be made using a fuzzy logic approach followed by modern statistical and optimisation design and manufacturing methods, for example Monte Carlo, Simulated Annealing and DFSS, Shina [102], that will then be employed to complete the detailed design. Reliability prediction will be made using the Telcordia method, Telcordia [81].

The structure of this section includes an overview of the different types of services, performance requirements and priority compromises that need to be considered before deciding on a power combining technology, as presented in Section 3.7.2. A range of suitable FOMs is presented in Section 3.7.3, followed by a review of amplifier parameters and weightings to be used as part of the technology selection process in Section 3.7.4. Available SSPA combining technologies are briefly reviewed in Section 3.7.5. This will provide the starting point for the selection of the most appropriate technology for any particular service requirement. Having provided, and analysed a comparison of technologies, then the design methodology will be proposed in Section 3.7.6, that is intended to formalise, from early conceptual requirements, the optimum technology that is appropriate to the SSPA design. Section 3.7.7 provides a combiner technology case study followed by a summary.

3.7.2 Types of Service

SSPAs are required for a wide range of services with varying requirements and priorities for particular performance parameters. This means that particular performance parameters for one type of service can have a different importance placed on it in another service. This change in importance can significantly affect the design outcome. The type of technology that is most appropriate to a particular type of service will benefit from an optimisation process that includes, from the start, both the service requirements and the performance requirements, ITU [103]. Such a process allows a greater range of possibilities when a compromise is required. The types of services that are being considered are: Land Fixed (terrestrial and satellite earth station), Land Mobile (cell phone, vehicular and mobile earth stations terminals), Naval (mobile),

Air (mobile) and Space based (satellites and spacecraft) services. Different services impose different requirements on aspects such as frequency, weight, size, power, environmental factors and reliability. Additional constraints are imposed by regulation, time to market and cost. All of the above require compromises that a more inclusive optimisation can improve. A service level requirements priority analysis is conducted, combined with the parameter weightings assessed for both commercial and defense markets, and is presented in Section 3.7.6.

3.7.3 Figures of Merit

In order to be able to make a more meaningful comparison between power combining technologies, a combination of suitable FOMs is proposed. Several different FOMs, useful for comparing SSPA performance, have been considered from the literature and are presented in Table 3.3, from active device comparisons through to system comparison levels.

The aim of this work is to select the most suitable combining technology by determining the maximum of the sum of the FOMs, after the parameter weightings of Table 3.4 have been applied, compared to a straight sum of weighted specification parameters

$$FOM_{max} = \sum_i W_i \cdot FOM_i, (proposed), \tag{3.15}$$

$$SP_{max} = \sum_j W_j \cdot SP_j, (straight\ sum\ of\ weighted\ SPs), \tag{3.16}$$

where FOM_i = FOM of the ith parameter from Table 3.3, SP_j = jth specification parameter and $W_{i,j}$ = i, jth weightings from Table 3.4, respectively.

3.7.4 Amplifier Parameters and Weightings

The specification parameters listed in Table 3.4, cover the majority of parameters needed to describe an SSPA. These parameters will be used for initial technology comparisons. The specification parameter weightings in Table 3.4 (weighting columns) are determined by the combination of a QFD, Akao *et al* [79] analysis and FMEA AIAG [80] for the particular service requirements of Section 3.7.2. An example of service versus parameter weightings for some selected parameters is given in Table 3.6.

Table 3.3. Combining technology FOMs.

Figure of Merit	Equation	Equ. Ref.	Reference
Power State Of the Art (PSOA)	PSOA $= \frac{(f^3 \cdot P_{out}^2)}{(4 \cdot 10^5)}$ f = frequency (GHz), P_{out} = output power (W)	(3.4)	[104]
PAE	$PAE = \frac{P_{out}-P_{in}}{P_{DC}}$	(3.5)	
PAE - Corporate[7]	CPAE $= PAE\frac{(L_{ic}GL_{oc}-1)}{(L_{ic}(G-1))}$ where: α_{ic} = I/P comb.[8]loss / stage, $L_{ic} = \alpha_{ic}^{\log 2(N_c)}$ = I/P comb. loss, $L_{oc} = \alpha_{oc}^{\log 2(N_c)}$ = O/P comb. loss, α_{oc} = O/P combiner loss / stage G = Gain, N_c = No. of comb. stages	(3.6)	[105]
PAE - Spatial	SPAE $= PAE\frac{(L_{is}GL_{os}-1)}{(L_{is}(G-1))}$ where: G = Gain, L_{is} = I/P combiner loss, L_{os} = O/P combiner loss,	(3.7)	
Device O/P 3rd order-intercept-point	$OIP3_d = P_{out}$/tone+$\frac{3IMD}{2}$ where: $3IMD$ = 3rd-order-intermodulation-distortion	(3.8)	
Linearity - combined	$OIP3_c = N_c \cdot L_c \cdot OIP3_d$ where: L_c = comb. in or out loss	(3.9)	[38]
Linearity - alternative	LFOM $= \frac{OIP3_{d,\ or\ c}}{P_{DC}}$	(3.10)	[106]
Device Spurious Free Dynamic Range (SFDR)	$SFDR_d = \left[\frac{OIP3_d}{(FGk_BT_0\Delta f)}\right]^{2/3}$ where: F = noise factor, G = gain, k_B = Boltzman's constant, T_0 = ambient temperature, Δf = instantaneous bandwidth	(3.11)	[38]
SFDR - combined	$SFDR_c = N_c^{2/3} SFDR_d$	(3.12)	
Cost	($/element)/(Watt∗component count) $= (\$/N)/(W * CC)$	(3.13)	
Reliability - Steady-state (Parts Count failure rate - λ_{PC} - Failures in 10^9 hours (FITs))	$\lambda_{PC} = \pi_E \sum_i^n N_i \lambda_{SS_i}$ where: π_E = unit Environment Factor, N_i = quantity of each type of device, λ_{SS_i} = mean device steady-state failure rate prediction	(3.14)	[81]

[7]Ideal combiner, no amplitude or phase imbalance. [8]comb. = combiner.

Table 3.4. SSPA specification parameters, FOMs and weightings.

Main Specification Parameter[9]	Secondary Specification Parameter	Weightings	
		SP	FOM
Frequency	Highest Frequency	5.26	4.8
(3.4)	Bandwidth	3.45	*
RF Power	P_{1dB} at centre frequency	3.45	4.8
(3.4), (3.5), (3.6),	$P_{saturation}$	*	*
Gain	Small signal	2.56	*
	Slope	2.04	*
	Ripple	2.04	*
Return Loss	Input	2.04	*
	Output	2.56	*
Linearity	AM/PM	2.56	*
(3.8), (3.9), (3.10),	Group Delay	1.69	*
(3.11), (3.12)	Spur / harmonics	2.04	*
	IMDs (OIP3)	2.56	3.9
	Noise Figure	2.04	*
	Spurious Free Dynamic Range	2.56	3.9
	Phase Noise	*	*
Response time	Rise	*	*
	Fall	*	*
	Pulse overshoot	*	*
	Pulse droop	*	*
	Ringing/settling	*	*
Mode	Coaxial	*	*
	Waveguide	*	*
	Planar	*	*
DC power	Power (P_{DC})	1.69	*
	Voltage	*	*
	Current	*	*
Power-Added-	Device	1.69	*
Efficiency (PAE)	Corporate combining	*	5.9
(3.5), (3.6), (3.7)	Spatial combining	*	5.9
	Number of stages	*	*
Conducted and	Emissions	*	*
Radiated	Susceptibility	*	*
Size	Dimensions	1.69	*
	Mass	1.69	*
Reliability	Number of components	1.69	1.69
(3.14)	MTTF (FITs)	1.69	1.69
	Maintenance	*	*
Vibration	Vibration	*	*
and Shock	Shock	*	*
Thermal	Temperature minimum	1.69	*
	Temperature maximum	1.69	*
	Device junction temperature	2.56	*
	Heatsink type (CV, CD, FA, WC)[10]	(3.45, 5.26, 2.56, 2.04)	*
Humidity	Relative (%)	*	*
Altitude	Air $V_{breakdown}$	*	*
Space	Multipaction	*	*
Sealing	Ingress Protection rating	*	*
	Corrosion Resistance	*	*
Cost (3.13)	$	39	*
Commercial	Manufacturability	*	*
	Time to Market	*	*
	Volume	*	*
	Ease of use	*	*
	Graceful degradation	2.56	*

[9] FOM as defined in Table 3.3. [10] CV=convection, CD=conduction, FA=forced air, WC=water cooled. *Not yet considered.

Table 3.5. Combining technologies.

Combining Technology	Class	Reference
Corporate Monolithic	Corporate	[9]
Corporate Chip		[7]
Corporate Hybrid Waveguide		[5],
Tile Discrete Spatial	Tile	[71]
Tile Chip Spatial		[19]
Tile Monolithic Spatial (Transmission)		[24]
Tile Monolithic Spatial (Reflection)		[72]
Tile Discrete Spatial Class-E		[16]
Tray Coaxial Spatial	Tray	[73, 38]
Tray Waveguide Spatial (TE_{10})		[36]
Tray Hard Boundary Waveguide		[40]
Tray Alternate Mode Waveguide (TE_{20})		[47]
2-D Planar TE Mode	2-D Planar	[54]
2-D Planar TM Mode		[57]
3-D Planar Chain Slotted Waveguide	3-D Planar	[62]
Conical Waveguide	Conical	[64, 74]

3.7.5 Combining Technologies

The combining technologies to be compared have been drawn from the available literature, Triquint, Toshiba, Codan, Kim *et al*, Ortiz *et al*, Deckman *et al*, Cheung *et al*, Pajic and Popovic, Courtney *et al*, Wavestream, Belaid and Wu, Belaid *et al*, Hicks *et al*, Perkons *et al*, Jiang *et al*, Quine *et al*, and Beyers and de Villiers [9, 7, 5, 71, 19, 24, 72, 16, 73, 36, 40, 47, 54, 57, 62, 64, 74], and cover more established combining technologies, e.g. corporate and serial combining, as well as more recent techniques and technologies like spatial tile and tray combining and various hybrids of both. Recent applications for spatial combining are at much higher frequencies using monolithic chips, although enhancements of other methods continue as applications arise. The combining technologies that will be compared are listed in Table 3.5. In the following comparison some demonstration technologies are also included as reference points. If a particular parameter from Table 3.5 is not available for a particular technology, then a typical worst case weighting value is assigned based on parameters from Walker [107].

3.7.6 Proposed Selection Methodology

The proposed design methodology is shown in Fig. 3.20, with fuzzy sets, Passino and Yurkovich [108], used to formalise the early service level requirements and when these

are used with appropriate FOMs from Section 3.7.3, the fuzzy set outcomes will determine the technology parameters that will be most suited to optimisation. Table 3.6 shows the importance of various service parameter requirements following a QFD analysis, based on a commercial customer case study.

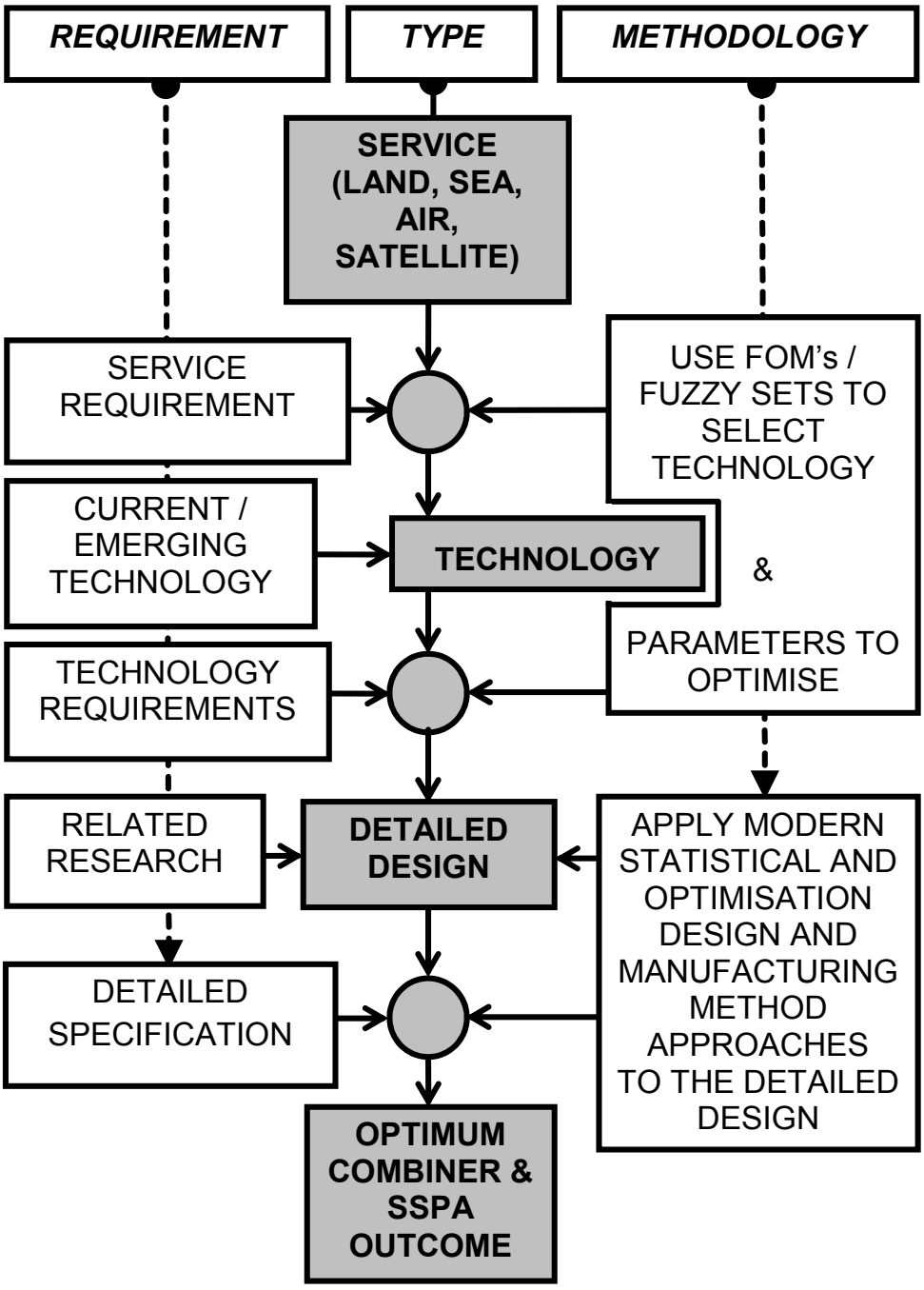

Figure 3.20. Proposed design methodology flowchart.

Table 3.6. Service versus parameter requirement examples.

Service type	Parameter[11]				
	MTTF	$/W	PAE	Mass	Corrosion Resistance
Land Fixed	7	7	6	1	2
Land mobile	3	9	8	8	3
Naval (mobile)	7	3	2	1	8
Air (mobile)	9	2	6	8	1
Space	9	1	7	9	1

[11] 1 = least important, 9 = most important.

Modern statistical and optimisation design and manufacturing methods, for example Monte Carlo, Simulated Annealing and DFSS, will then be used as part of the detailed design, followed by reliability predictions using the Telcordia method, [81].

3.7.7 Combiner Technology Case Study

Having identified technologies and appropriate SSPA performance parameters, shown in Figs. 3.1 (Part 1) and 3.2 (Part 2), an initial technology comparison is performed with the results presented in Fig. 3.21. The blue columns of Fig. 3.21 show the sum of normalised weighted SPs, with both SPs and SP weightings given in the SP weightings column of Table 3.4, being weightings that are appropriate for a small satellite earth terminal SSPA. This shows that for these initial SPs, a Monolithic Level Corporate [9] combining approach would provide the best outcome for a small satellite earth terminal design. A FOM based comparison is now performed using the FOMs approach of Section 3.7.3. For the FOM based approach the red columns of Fig. 3.21 show the comparison for the sum of normalised weighted FOMs, with FOMs from Table 3.3 using equations (3.4), (3.6), (3.10 incorporating 3.8), (3.10 incorporating 3.9), (3.12), and (3.14) and with FOM weightings from Table 3.4 (FOM weightings column). This alternative comparison now suggests that a Tile Monolithic Spatial (Transmission) combining approach [24] would be a more suitable approach. To be able to validate these outcomes a detailed design followed by a prototype build and test for each type of solution would be the ultimate, however tracking research, as indicated in Section 3.5, or market trends may be a less costly but longer approach.

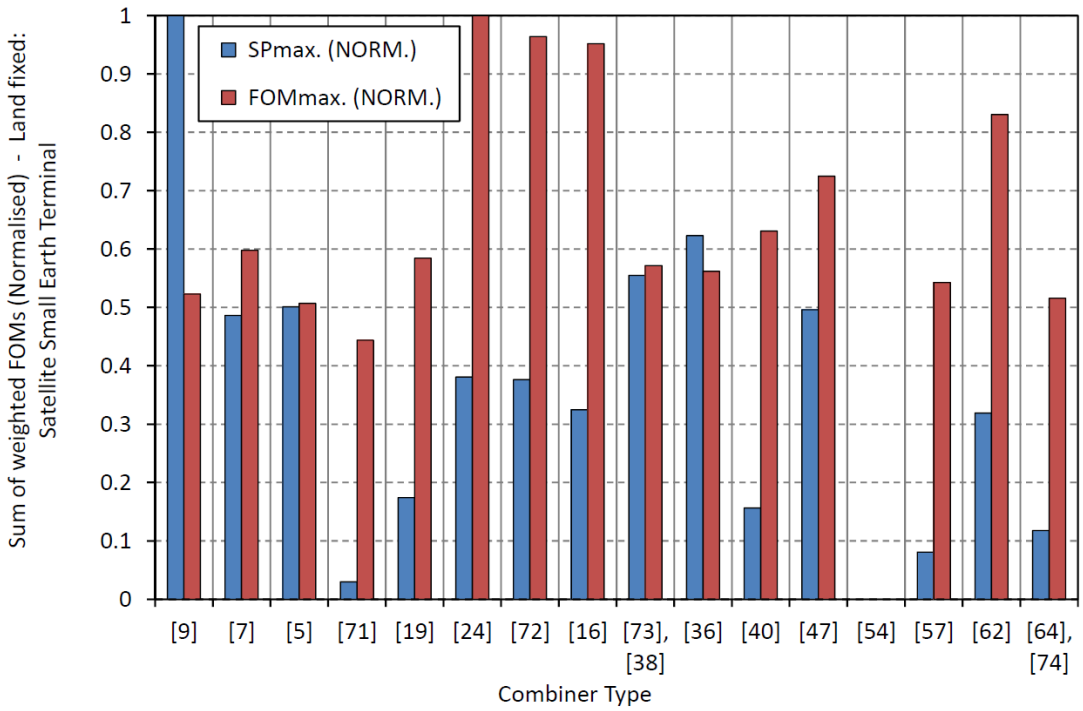

Figure 3.21. Comparison of combiner type versus SP_{max} and FOM_{max}. Comparison of combiner type versus SP_{max}, (3.16), and FOM_{max}, (3.15), for a small satellite earth station SSPA. The y-axis represents the normalised SP or FOM. Refer to Table 3.5 to match combining technology with references. Note that the zero value for reference [54] is as a result of the normalising process.

FOMs need to be carefully chosen, so the development of meaningful FOMs is a major proportion of the current work and future work will determine the most suitable combination of FOMs to be used as part of the design methodology approach for selecting the most appropriate technology suited to a particular service requirement. Comparisons at this stage cover separate monolithic, chip and module level designs but a combination of these approaches may also provide the best solution for an overall design.

3.7.8 Summary

This section has presented an initial comparison of SSPA combining technologies based on already developed and well accepted FOMs. In addition, it has proposed a design methodology that considers the balance of service requirements and performance parameters. Based on this method, as demonstrated, an appropriate technology to meet these requirements can be selected. The work forms part of an initial study into an SSPA design methodology with future directions to consider aspects such as thermal

and Electro-Magnetic Compatibility (EMC) performance, further assisting in determining the best SSPA combining technology outcome.

3.8 Conclusion

This chapter has presented concepts for research into an SSPA that uses spatial power combining, existing high power IMFET devices, field modification techniques for waveguide and waveguide mode matching with associated transitions that allow for active device DC biasing at high RF power levels. Simulation will be required to determine the electro-magnetic and thermal trade-off for this to occur. Also presented is a design methodology that considers both hard design specifications an also less tangible specifications with the aim of being able to select an appropriate design technology. As part of this design methodology an example case study is presented.

In the following chapter behavioral modelling of RF PA devices is introduced and starts with existing memoryless and quasi-memoryless models and reviews and improves on them to allow for fast RF PA device selection.

Chapter 4

Behavioural Modelling of SSPAs

SEVERAL well-known simple behavioural models for SSPA devices are reviewed and compared. This chapter proposes an improvement to White *et al's* AM/AM model and discusses its use of Rapp's AM/AM model. Furthermore AM/PM device modelling is discussed, with an improvement to Honkanen and Haggman's phase shift addition to Rapp's AM/AM model proposed, thus allowing phase shifts greater than zero degrees to be considered. Finally a review of several model's performances beyond available data and into the saturation region is presented. These simple model improvements and additions, combined with the extension of the modelling into the saturation region, thus allow for faster and more accurate system level evaluation, and enable better, crucial output device selections to be made.

This chapter also provides a method for obtaining a time domain behavioural model of a power amplifier from component manufacturer's data, enabling fast system level comparisons of various power amplifier designs. The method uses a physics based approach for determining the model's memory effects with respect to input and output matching networks, bias networks and temperature dependent memory effects. Extensions to allow increased accuracy via further component testing are also considered.

4.1 Accuracy Improvements for SSPA Device Behavioural Modelling

4.1.1 Introduction

In order to quickly compare the suitability of different RF power amplifier (RF PA) devices, a system level evaluation needs to be performed. Typically RF PA devices are the primary source of nonlinearities in multicarrier systems, so selecting the right device is crucial. To quickly compare RF PA devices within a system, accurate and simple behavioural models are needed. Obtaining an RF PA device behavioural model requires either custom testing, which can be very time consuming, or by extraction of data from manufacturer's datasheets. However, information from datasheets may not always provide enough information or data for applications where an RF PA device will be used, for example when an RF PA device is used deep into saturation, associated with modern digital modulation schemes, the Peak to Average Power Ratio (PAPR) can range from 3 to 10 dB. Therefore a model that accurately predicts the performance of an RF PA device, over its full range of operating conditions, using parameters extracted from manufacturer's limited data, is highly desirable. Several behavioural models commonly adopted in the literature are reviewed in Section 4.1.2. In Section 4.1.3 a comparison between these models is provided, showing their applicability as suitable system behavioural models, when parameters are extracted from manufacturer's limited data is presented. Device modelling in the saturation region is presented in Section 4.1.4, followed by an AM/AM and AM/PM modelling discussion in Section 4.1.5. These are then followed by a summary and discussion in Section 4.1.6.

4.1.2 Review of Existing Behavioural Models

Saleh [109] presented a Traveling Wave Tube Amplifier (TWTA) model that does not model SSPAs well. Ghorbani and Sheikhan [110] proposed an SSPA model with both Saleh and Ghorbani & Sheikhan models including AM/AM and AM/PM terms. Rapp [111] proposed another SSPA model providing a better saturation performance but only for AM/AM. This model assumes AM/PM conversion is small enough to be neglected. Honkanen and Haggman [112] provided an AM/PM expression for the Rapp model. White *et al* [113] presented an improved accuracy model when compared to Saleh [109],

Ghorbani [110], and Rapp [111]. An improved accuracy model for an Laterally Diffused Metal Oxide Semiconductor (LDMOS) based SSPA was proposed by O'Droma *et al* [114, 115]. A summary of these models is given in Table 4.1.

4.1.3 Existing Model Improvements

White *et al's* [113] original AM/AM equation is presented in Table 4.1, with $A_{White}(r)$ being the output amplitude and r the normalised input amplitude. Coefficients a and b determine the saturation level and small signal gain respectively while parameters c and d adjust the shape in the SSPA operating region.

Attempts at reproducing White *et al's* [113] results, using this equation gives the results shown in Fig. 4.1.

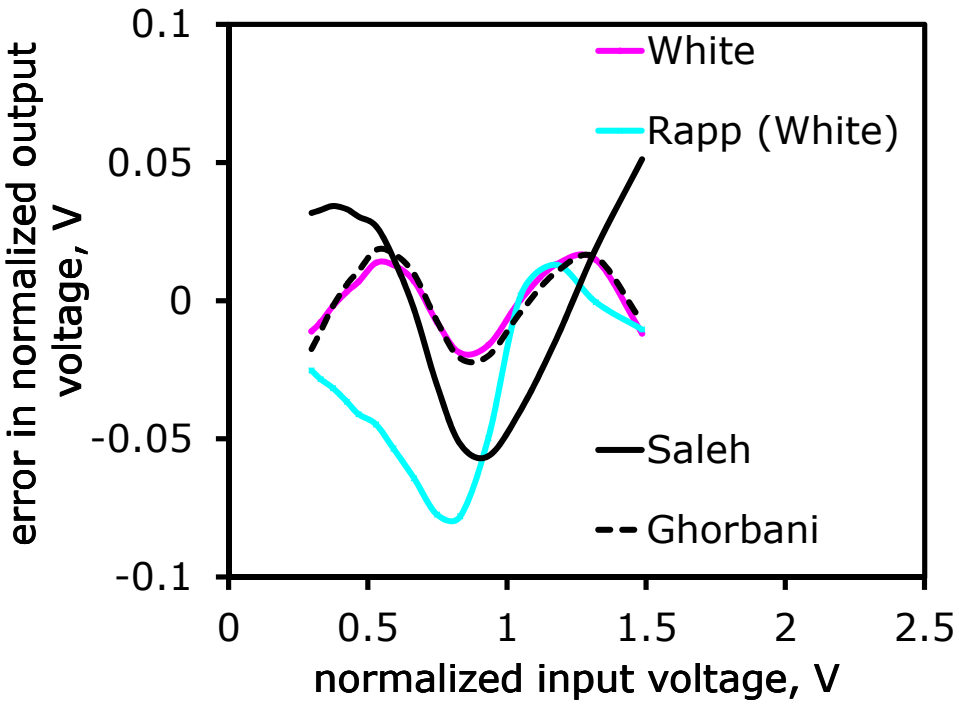

Figure 4.1. White et al versus Rapp, Saleh and Ghorbani and Sheikhan's AM/AM models. Reploting of White *et al's* Fig 1b using $A_{White}(r)$ as given in that paper. Curve fit of models showing the AM/AM normalised output voltage errors in comparison with measured data dynamic range only.

Table 4.1. Simple behavioural models for RF power amplifiers.

Model	AM/AM	AM/PM
	r = input voltage, $A(r)$ = output voltage	$\phi(r)$ = output phase
Saleh, 1981, [109]	$A_{\text{Saleh}}(r) = \frac{\alpha_a r^{\eta_a}}{(1+\beta_a r^{\gamma_a})^{\nu_a}} - \epsilon_a = \frac{\alpha_a r}{1+\beta_a r^2}$ α_a is an Amplitude Fitting Parameter (AFP), β_a is an AFP, $\eta_a = 1$, $\gamma_a = 2$, $\nu_a = 1$, $\epsilon_a = 0$	$\phi_{\text{Saleh}}(r) = \frac{\alpha_\phi r^{\eta_\phi}}{(1+\beta_\phi r^{\gamma_\phi})^{\nu_\phi}} - \epsilon_\phi = \frac{\alpha_\phi r}{1+\beta_\phi r^2}$ α_ϕ is a Phase Fitting Parameter (PFP), β_ϕ is a PFP, $\eta_\phi = 1$, $\gamma_\phi = 2$, $\nu_\phi = 1$, $\epsilon_\phi = 0$
Ghorbani and Sheikan [110]	$A_{\text{Ghorbani}}(r) = \frac{x_1 r^{x_2}}{1+x_3 r^{x_2}} + x_4 r$ x_1, x_2, x_3, x_4 are AFPs	$A_{\text{Ghorbani}}(r) = \frac{y_1 r^{y_2}}{1+y_3 r^{y_2}} + y_4 r$ y_1, y_2, y_3, y_4 are PFPs
Rapp [111], AM/AM, with Honkanen and Haggman [112], AM/PM	$A_{\text{Rapp}}(r) = \frac{gr}{\left[1+\left(\frac{gr}{L}\right)^{2s}\right]^{1/2s}}$ L is the Saturation Limit Level (SLL), g is the Small Signal Gain (SSG), s is the sharpness parameter	$\phi_{\text{HH}}(r) = \frac{b_{\phi HH}}{1+e^{-c_{\phi HH}(r-a_{\phi HH})}} \cdot \frac{1}{p_1 r+p_2}$ $a_{\phi HH}$ is the input turn-on voltage for a BJT, $b_{\phi HH}$ is the turn-on |phase|, $c_{\phi HH}$ is the step change steepness, p_1 & p_2 are downward slope adj. parameters
White *et al*, 2003, [113]	$A_{\text{White}}(r) = a_w\left(1-e^{-b_w r}\right) + c_w r e^{-d_w r^2}$ a_w is the SLL, b_w is the SSG, c_w & d_w are AFPs	$\phi_{\text{White}}(r) = f_w\left(1-e^{-g_w(r-h_w)}\right),\ r \geq h_w$ $\phi_{\text{White}}(r) = 0,\ r < h_w$ f_w is the magnification factor, g_w is the curve slope, h_w is the r-axis range shift
O'Droma *et al*, 2009, [114]	$A_{\text{O'Droma}}(r) = \frac{\alpha_a r^{\eta_a}}{(1+\beta_a r^{\gamma_a})^{\nu_a}} - \epsilon_a$ $\alpha_a, \beta_a, \eta_a, \gamma_a, \nu_a, \epsilon_a$ are AFPs	$\phi_{\text{O'Droma}}(r) = \frac{\alpha_\phi r^{\eta_\phi}}{(1+\beta_\phi r^{\gamma_\phi})^{\nu_\phi}} - \epsilon_\phi$ $\alpha_\phi, \beta_\phi, \eta_\phi, \gamma_\phi, \nu_\phi, \epsilon_\phi$ are PFPs

These results do not match the published results of White *et al's* [113] Fig. 1b. It has been found that to reproduce the correct results, as proposed by White *et al's* [113] Fig. 1b, then the AM/AM model, $A_W(r)$ should be written as:

$$A_{WC}(r) = a[(1 - e^{(-br)}) + cre^{(-dr^2)}], \tag{4.1}$$

and not

$$A_{WC}(r) = a(1 - e^{(-br)}) + cre^{(-dr^2)}. \tag{4.2}$$

Using the corrected equation, (4.1), the error curve as shown in Fig. 4.2, now matches White *et al's* original Fig. 1b curve.

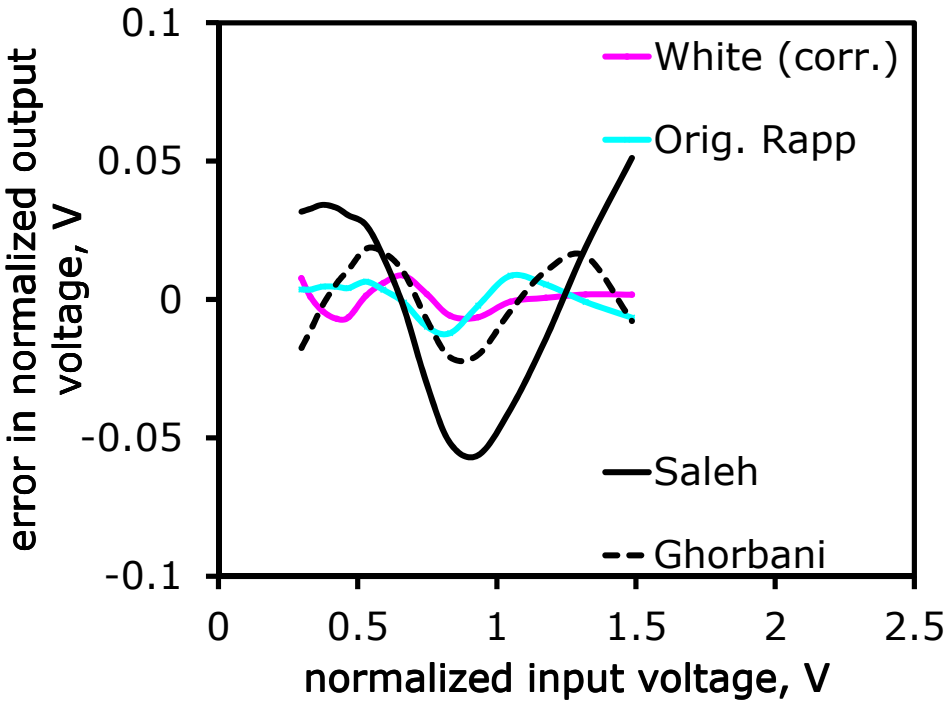

Figure 4.2. Corrected White et al versus original Rapp, Saleh and Ghorbani and Sheikhan's AM/AM models. Corrected White *et al* equation (4.1) and original Rapp equation, Table 4.1.

Also within White *et al's* paper, Rapp's equation is given as:

Table 4.2. Behavioural model versus NMSE comparison.

Model	AM/AM NMSE (dB)
Saleh, [109]	-27.13
Ghorbani and Sheikan, [110]	-35.44
Rapp, [111]	-42.33
Rapp from White *et al*, [111]	-24.97
White *et al*, [113]	-36.95
This work, White *et al* corrected	-44.00
O'Droma *et al* [114], (Modified saleh)	-48.54

$$A_{RW}(r) = \frac{r}{\left[1 + \left(\frac{|r|}{\alpha}\right)^{2\beta}\right]^{1/2\beta}}, \tag{4.3}$$

However if Rapp's original AM/AM equation, as per Table 4.1, is used, including the small signal gain parameter g, then the error results are as shown in Fig. 4.2 and the AM/AM curve fit is shown in Fig. 4.4, indicating that Rapp's equation now has similar error performance compared to White *et al's* equation. An AM/AM NMSE, as defined in Schreurs *et al* [116], FOM comparison is given in Table 4.2 indicating that the original Rapp model compares well with White *et al*'s corrected model.

4.1.4 Modelling into the Saturation Region

In order to compare the original Rapp, White *et al* (corrected) and O'Droma *et al* models, beyond the available data, a new method is used to extend the data into the saturation region. This method is to observe that the maximum end point output poweroutput power (P_{out}), of the PAE versus P_{out} curve(s), typically provided for RF PA devices, is the final saturated output power saturated output power (P_{sat}), as shown in Fig. 4.3.

The existing data can then be extended into the saturation region. Extending the modelling beyond the measured data and into the saturation region, the AM/AM curves of Figs. 4.4 and 4.5 show how the models perform beyond the available data. It can be seen that the original White *et al* equation "rolls over" similar to the Ghorbani and

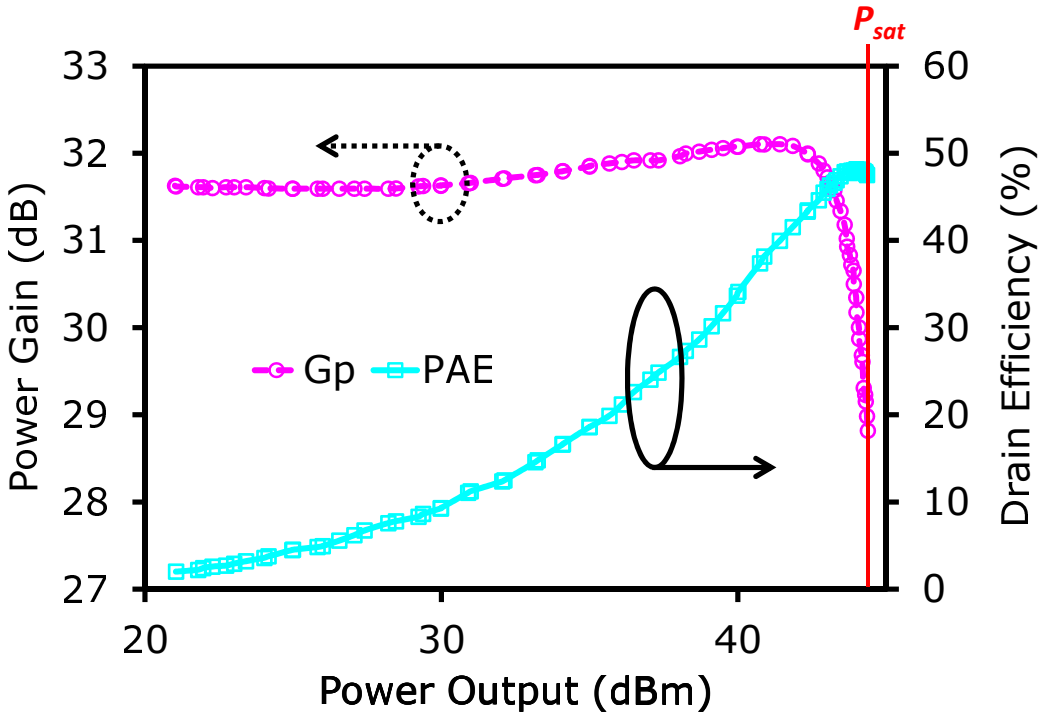

Figure 4.3. Saturation power level for the BLM7G1822S. Power gain and drain efficiency for the BLM7G1822S [117] providing the saturated output power.

Sheikhan [110] model. If the corrected White *et al* equation (4.1) is used, then it performs as would be expected for an LDMOS based SSPA.

The presented results indicate that the Rapp model performs best into the saturation region when only the available data is used to curve fit the models, even compared to the O'Droma *et al* [114]model as shown in Fig. 4.5.

When the extended data is used to curve fit the model then both the Rapp and O'Droma *et al* models are comparable to the corrected White *et al* model, as indicated in Fig. 4.6.

4.1.5 AM/PM

The Honkanen and Haggman phase shift [112] addition to the original Rapp equation, $\phi_{HH}(r)$, as shown in Table 4.1, is noted to have a descending phase with increasing input level but with a maximum of zero degrees phase shift. In order to accommodate devices that do not have a maximum of zero degrees phase shift, an additional offset parameter is proposed, d_{FA}, to the Honkanen and Haggman phase shift model. Hence the updated phase shift model $\phi_{HHO}(r)$ is given as;

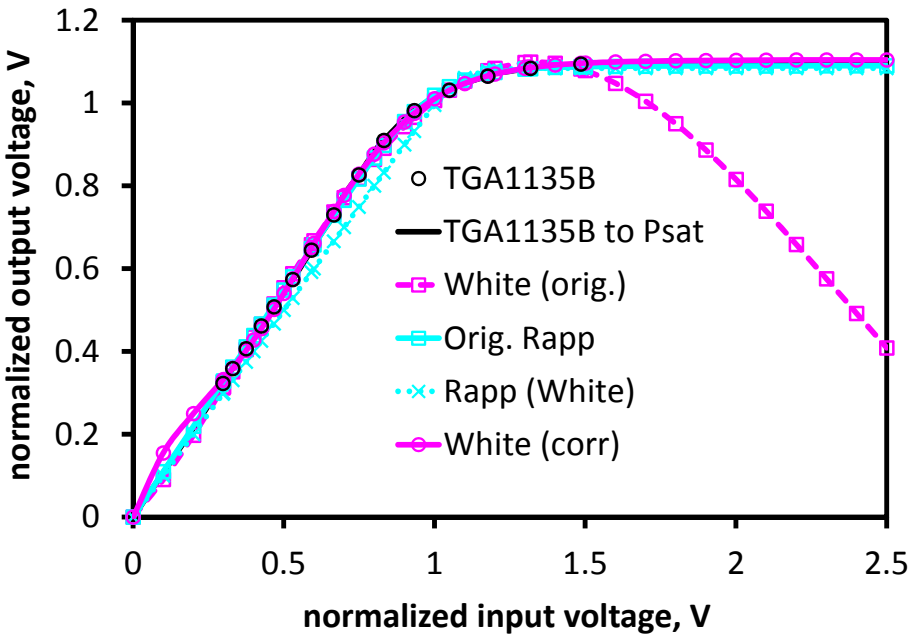

Figure 4.4. AM/AM normalised output versus normalised input voltage measured data versus curve fit plots. Measured AM/AM data and curve fit of normalised output voltage versus normalised input voltage into the saturation region for White *et al's* original and corrected equation comparisons. Also shown is Rapp's original equation and Rapp's equation (4.3) as per White *et al*.

$$\phi_{HHO}(r) = \frac{b}{(1+e^{(-c(r-a))})} \cdot \frac{1}{(p_1 r + p_2)} - d_{FA}, \tag{4.4}$$

Where a is the cut-off input voltage at which the transistor begins to conduct, b is the step amount that the phase changes, in degrees, at switch-on, c determines the steepness of the step-wise change, and p_1 and p_2 are parameters for adjusting the descending slope. The offset parameter d_{FA} allows for positive phase shift. An example of the application is shown in Fig. 4.7 for the LDMOS 2-stage BLM7G1822S-20 power amplifier [117].

Even though the Honkanen and Haggman phase addition has coefficients that are related to bipolar transistor parameters; this model still performs well for LDMOS devices when the correct mapping of these parameters is performed.

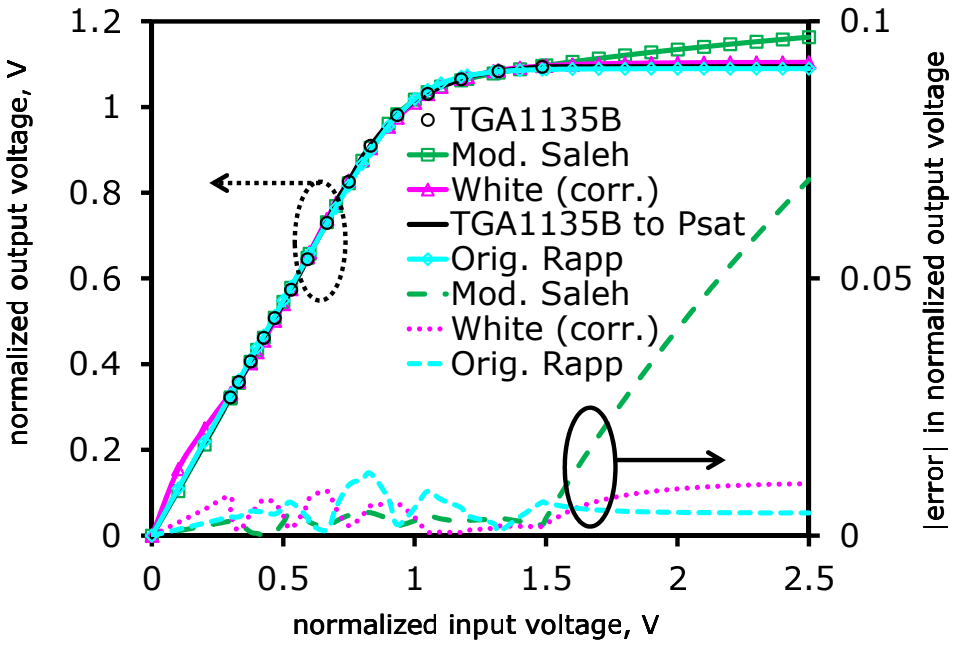

Figure 4.5. Curve fit comparisons into the extended saturation region (a). Rapp, White *et al* (corrected) and O'Droma *et al's*; model comparison of AM/AM curve fit showing normalised output vs input voltage and absolute normalised output voltage errors for existing data and data extended into the saturation region.

4.1.6 Summary

This section has demonstrated the need for fast system level comparisons to aid in the selection of critical RF PA output devices. For SSPA devices, having only below saturation data available, then the original Rapp [111] model, including the Honkanen and Haggman phase shift addition [112] plus the addition introduced in this section, provides the best simple AM/AM and AM/PM model. If the available data extends into the saturation region then the O'Droma *et al* [114, 115] model provides the best behavioural model in that region. This section has also shown improvements for the use of two existing models plus provided an additional parameter, as well as providing a method for determining the saturation power from manufacturer's data. It has also compared the performance of these models when used beyond the provided manufacturer's data information, where typical modern digital modulation signals extend, thus resulting in further improvements and accuracies. These simple model improvements and additions, combined with the extension of the modelling into the saturation region, thus allow for faster and more accurate system level analysis enabling better crucial output device selections to be made.

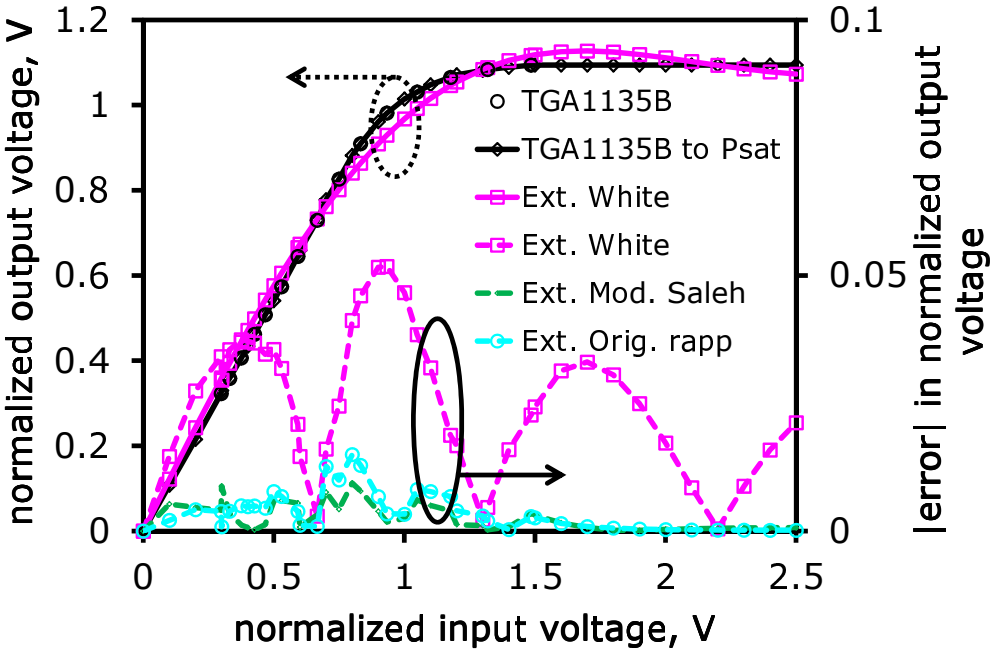

Figure 4.6. Curve fit comparisons into the extended saturation region (b). Corrected White *et al* AM/AM model Curve fit of extended data into the P_{sat} region showing that it performs worse than the original Rapp and O'Droma *et al* models.

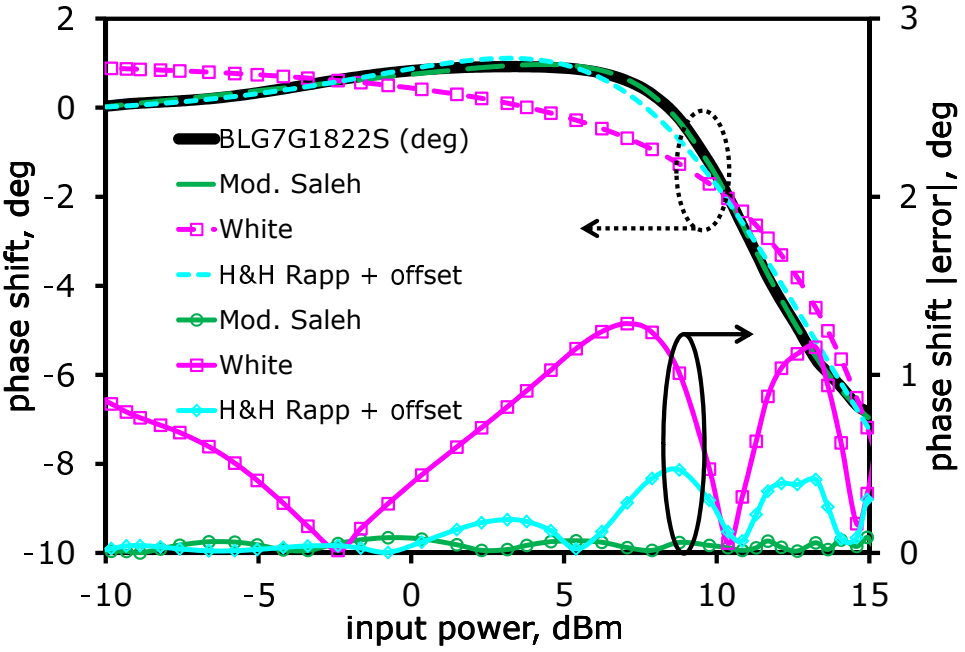

Figure 4.7. Comparison of AM/PM curve fits versus BLM7G1822S data. AM/PM curve fit of BLM7G1822S comparisons of O'Droma *et al*, White *et al* and Honkanen and Haggman AM/PM expression, with additional offset, as well as absolute phase error comparisons.

4.2 Model Extraction of RF PA Devices from Manufacturer's Data

4.2.1 Introduction

The requirements for greater data download capacity from mobile communication systems continue the push for improved wideband performance. A key element in these mobile communication systems is the Power Amplifier (PA). In order to obtain high data rates the PA must exhibit both DC power and RF spectral efficiency while delivering an appropriate RF output power over an increasingly wider bandwidth. Manufactures of PA devices often provide devices for testing, and datasheets based on various measured parameters, without providing simulation models or data for the application required. For a design to commence, initial system level comparisons are required in order to determine if the required output power, efficiency and spectral purity can be achieved over the required bandwidth. To be able to perform these comparisons quickly, suitable system level models are required. Normally, system level models are derived from measurements which is time consuming and costly. However, for quick analysis and comparison, the amount of time and cost involved cannot be justified. In this section a method for extracting system level non-linear behavioural models from a given manufacturers datasheet is provided so that the needed comparisons can be undertaken quickly. So there is a need to have a methodology for building device models based on existing available device datasheets.

This section starts by reviewing current RF PA models proposed in the literature, as discussed in Section 4.2.2, and then investigates the memory effect in RF PAs and how that impacts the amplifier linearity in Section 4.2.3. The proposed modelling methodology is presented in Section 4.2.4, which includes parameter extraction from datasheets and simulation modelling based on extracted parameters and experimental verification is given. In Section 4.2.5, a comparison between simulation results and manufacturer's data as presented in the datasheet are given.

4.2.2 RF Power Amplifier Behavioural Models

Typical early behavioural models for power amplifiers have been based around models for TWTAs. These models are based on the measured amplifier or device performance.

These are relatively straightforward models based around single carrier AM/AM and AM/PM requirements.

For SSPA modelling, and in particular for LDMOS FETs, this model can lead to issues related to AM/PM characteristics, so a Modified Generalised form of the Saleh model (MGS) is more appropriate as given by O'Droma [114], as shown in Table 4.1.

For a given set of values (η, ν, γ and ϵ), optimum values for (α, β) can be extracted from a measurement dataset, being the manufacturers datasheet parameters for either AM/AM or AM/PM characteristics.

Whilst the above models are sufficient for single carrier situations, they are insufficient for current requirements. Current requirements for PA circuits or devices now require other considerations beyond AM/AM, AM/PM and harmonic responses to now include Inter-Modulation Distortion (IMD), spectral regrowth, Adjacent Channel Power Ratio (ACPR), Noise Power Ratio (NPR), sweet spot evolution, thermal dependence and self-heating and bias effects [118].

In order to operate power amplifiers more efficiently, devices must be operated closer to their maximum output power, however this increases IMD. To operate at higher output powers, linearisers are used to reduce IMD effects. For wide bandwidth signals, memory effects associated with power amplifier devices can have significant effects on efficiency and Adjacent Channel Interference (ACI). These effects, if not considered, can also degrade the linearisers's performance. With these increased requirements, memory effects can become significant in determining the PA performance.

4.2.3 Memory Effects

Memory effects in an RF PA mean that the output at a given time relates not only to the input at that time but also to the input at previous times. The sources of memory effects in an RF PA are dependent on the device itself and the networks surrounding the RF PA, such as the matching and biasing networks as shown in Fig. 4.8 [119]. Memory effects originate from the frequency filtering behaviour of the matching and bias networks as well as the thermal and trapping effects of the RF PA device itself. Trapping effects occur inside the semiconductor bulk as a result of the energy levels within the semiconductor bandgaps causing transconductance and output conductance dispersion, resulting in the capture and release of free charges and the time constants associated with this action.

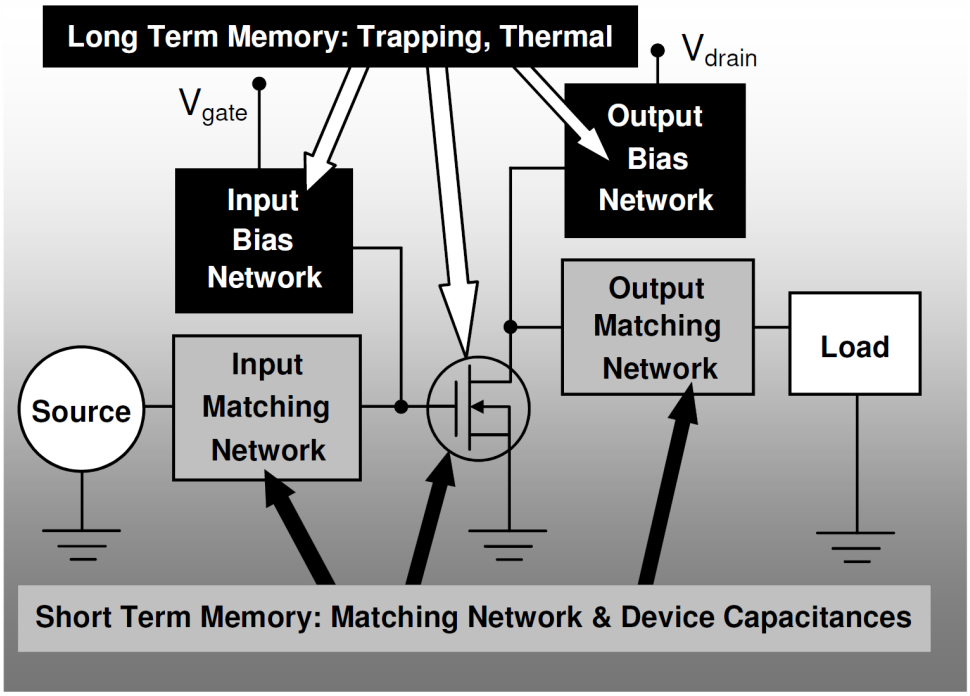

Figure 4.8. Memory effects associated with an RF power amplifier device. Physical PA layout showing physical matching, bias and thermal networks that contribute to memory effects.

Memory effects cause asymmetric IMD sidebands that are a function of carrier spacing. The proposed model of the memory effects is shown in Fig. 4.9, derived from Kenney and Fedorenko [120].

Short-term memory effects are associated with the input and output matching networks whereas long-term memory effects are associated with the device thermal response and the bias networks. Memory effect time constants can range from 1 nanosecond (ns) or less for short term memory effects to around 1 microsecond (μs) and into the lower millisecond (ms) range for long term memory effects, Parker and Rathmell [121].

4.2.4 Modelling Methodology

The behavioural model, including memory effects, is physics based as derived from Kenney and Fedorenko [120], see Fig. 4.9 and the model is given in the frequency domain and consists of three essential sections: (i) the memoryless non-linear section, that is determined by curve fits of input power (P_{in}) versus P_{out} and AM/PM data to the MGS model as described in Section 4.2.2, (ii) thermal memory effect, and (iii) the bias

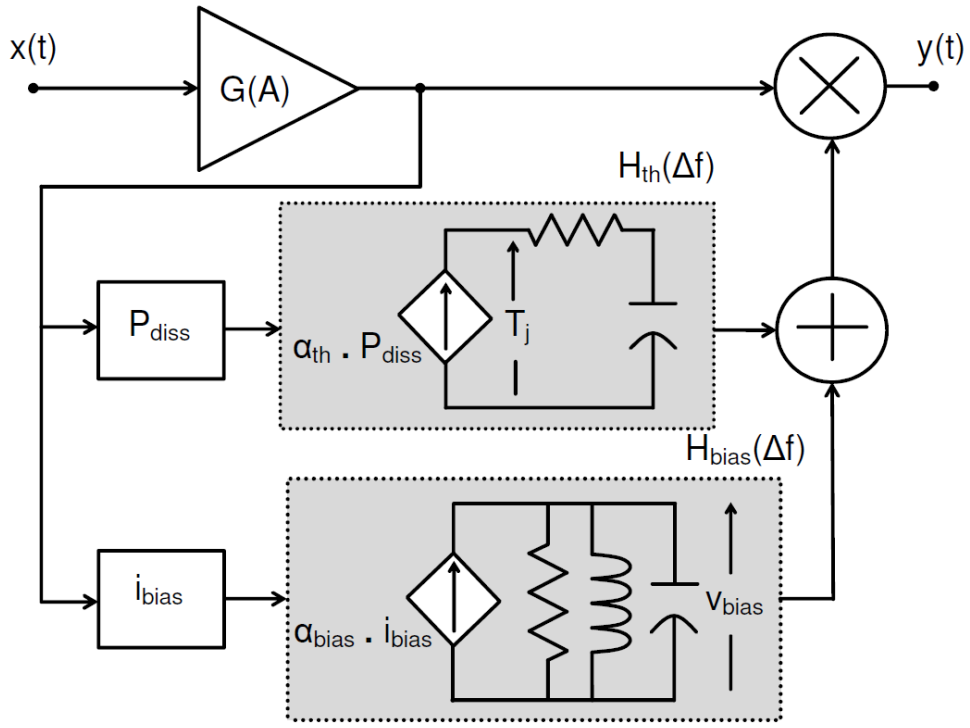

Figure 4.9. Physically based simple frequency domain behavioural model for an RF PA. Derived from [120]

memory effect. The implementation of these separate thermal and bias memory models is undertaken in Simulink but now in the time domain. Modelling of the thermal memory effect in the time domain follows the technique as described by Parker and Rathmell [121] and the bias memory effect time domain modelling follows standard Parallel Resistor-Inductor-Capacitor (PRLC) resonant circuit theory as given by Hayt and Kemmerly [122].

The implementation of the modified memoryless MGS model in Simulink is shown in Fig. 4.10 and the implementation of memory effects with the MGS model is shown in Fig. 4.11.

The overall modelling methodology is shown by the flowchart of Fig. 4.12. The P_{in} versus P_{out} data, from Fig. 13 of the MW7IC18100NBR1 device datasheet [123], is used, along with representative AM/PM data, to determine the modified Saleh model coefficients via a least squares curve fitting routine implemented in Matlab. This is then validated against the P_{in} versus P_{out} datasheet data, Fig. 4.13, and forms the non-linear portion of the model.

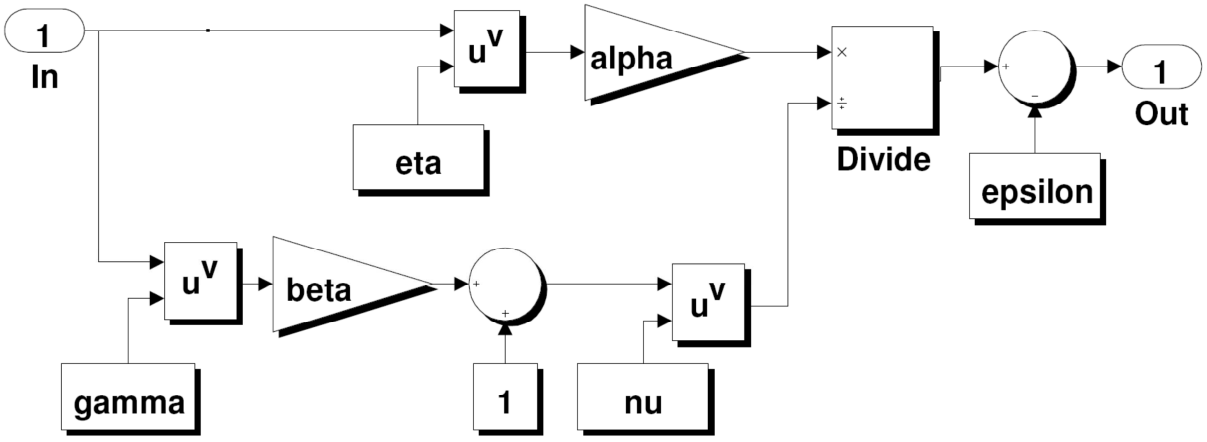

Figure 4.10. Implementation of the MGS model in Simulink.

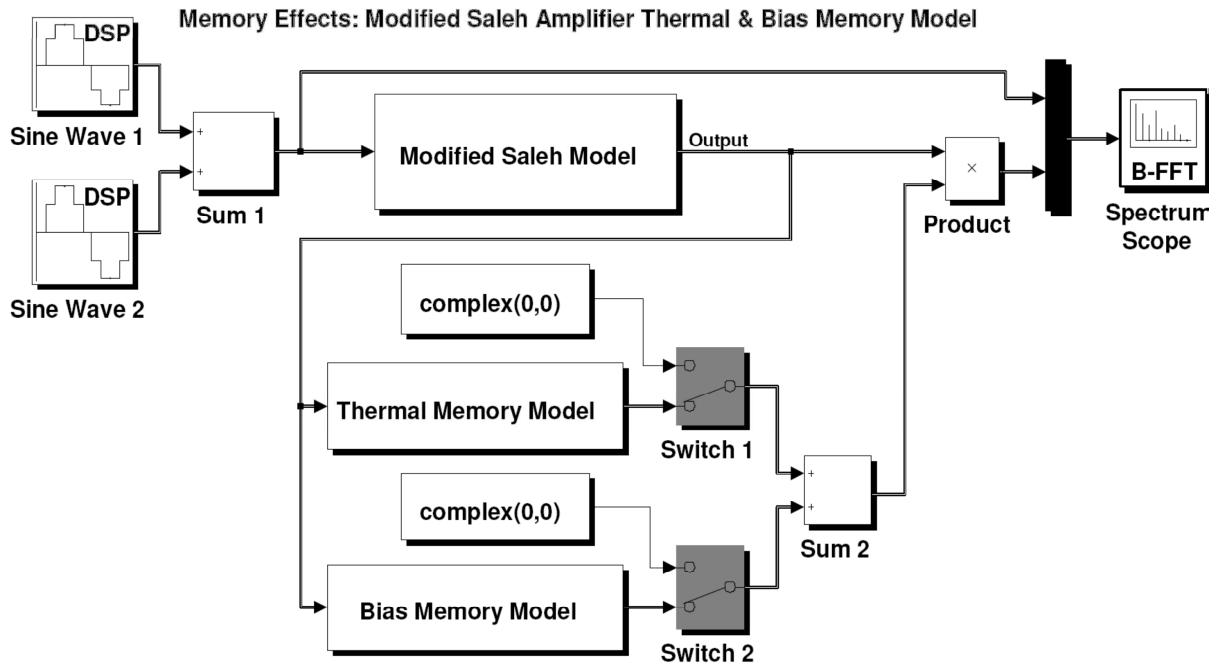

Figure 4.11. Simulink implementation of memory effects with the MGS model.

Further device data, as shown in Fig. 4.12, is then used for the thermal and bias memory effects parameter extraction. This data is extracted directly from the device datasheet.

With extracted non-linear and memory effect parameters, the model outputs, as per Fig. 4.11, can be compared with the device IMD results.

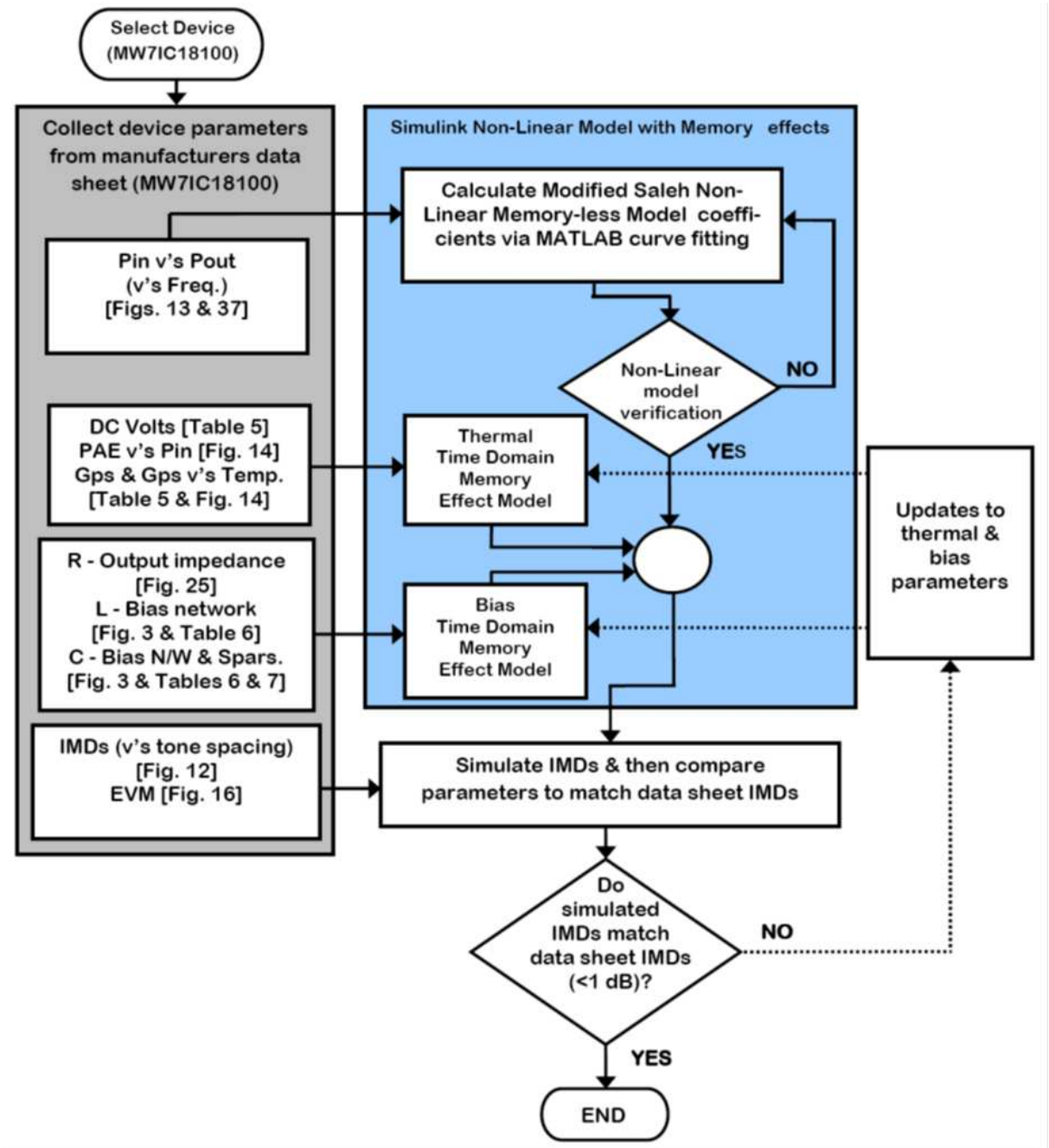

Figure 4.12. Flowchart of amplifier modelling with memory effects.

Datasheet Parameters

For the Freescale (now NXP) MW7IC18100NBR1 [123], fundamental P_{in}/P_{out} data, Fig. 4.13, as well as 3rd, 5th, and 7th order IMD parameters at fixed, Fig. 4.14, and varying tone spacings are given.

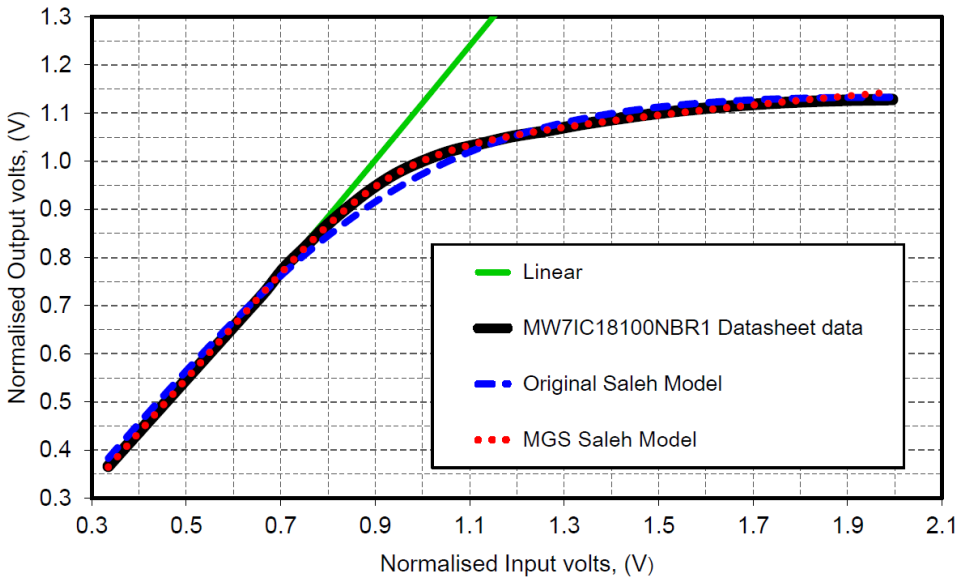

Figure 4.13. Comparison between MW7IC18100NBR1 datasheet data versus Saleh and Modified Saleh models. Reference [123], Figure 13, P_{in} versus P_{out} data including a comparison of the Original Saleh and MGS models versus MW7IC18100NBR1 datasheet data.

From Fig. 4.14 it can be seen that this device does exhibit memory effects as characterised by the IMD asymmetries.

For other devices only P_{in} versus P_{out} data may be given so extra measurements can be conducted using available manufacturer's test jigs [123] as shown in Fig. 4.16.

Detailed matching and bias networks are given in the datasheet. The data required for the model extraction is shown in the left hand side box of the flowchart shown in Fig. 4.12.

Simulation and Parameter Extraction

For the given P_{in} versus P_{out} data set, Fig. 4.13, and the measured AM/PM data, MGS model coefficients have been determined to be, for AM/AM, 1.107, 2.2835, 1.0154, 0.084998, 10.191 and 0 and for AM/PM 2000, 0.061921, -0.00073489, -0.0098204, 1.2912 and 1981.7 corresponding to $\alpha, \beta, \eta, \nu, \gamma$, and ϵ, respectively.

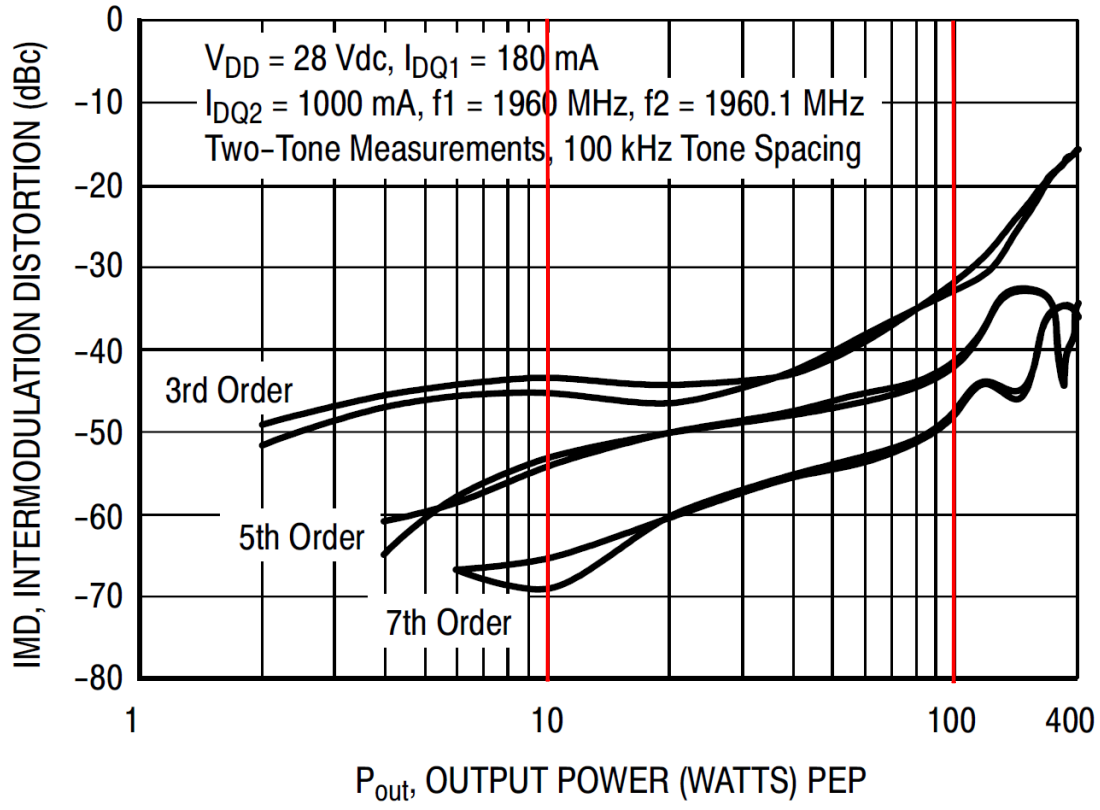

Figure 4.14. Two tone IMD data for MW7IC18100NBR1 10 W to 100 W. MW7IC18100NBR1 [123], Figure 11, two tone intermodulation distortion versus output power at fixed 100 kHz tone spacing, showing IMD asymmetries.

The original Saleh modelling is compared to the MGS modelling in Fig. 4.13 and also in Fig. 4.17. In Fig. 4.17 the difference between the MW7IC18100NBR1 data, the original Saleh model and the MGS model is given, showing reduced errors for the MGS model.

Simulations have been performed and the relevant memory parameters have been adjusted to match the IMDs, as given in the device datasheet, over a range of tone spacing's. These are; thermal resistance (R_{th}) = 10 K/W, thermal capacitance (C_{th}) = 20 nanojoule (nJ)/K for the thermal memory, Boumaiza and Ghannouchi [124], and Resistance (R) = 2 Ω , L = 1 nanohenry (nH) and C = 1 nanofarad (nF) for the bias memory parameters. Results of the simulation are shown in Fig. 4.18

A sample of the simulated IMD performance for a 200 kilohertz (kHz) carrier spacing is given in Fig. 4.19.

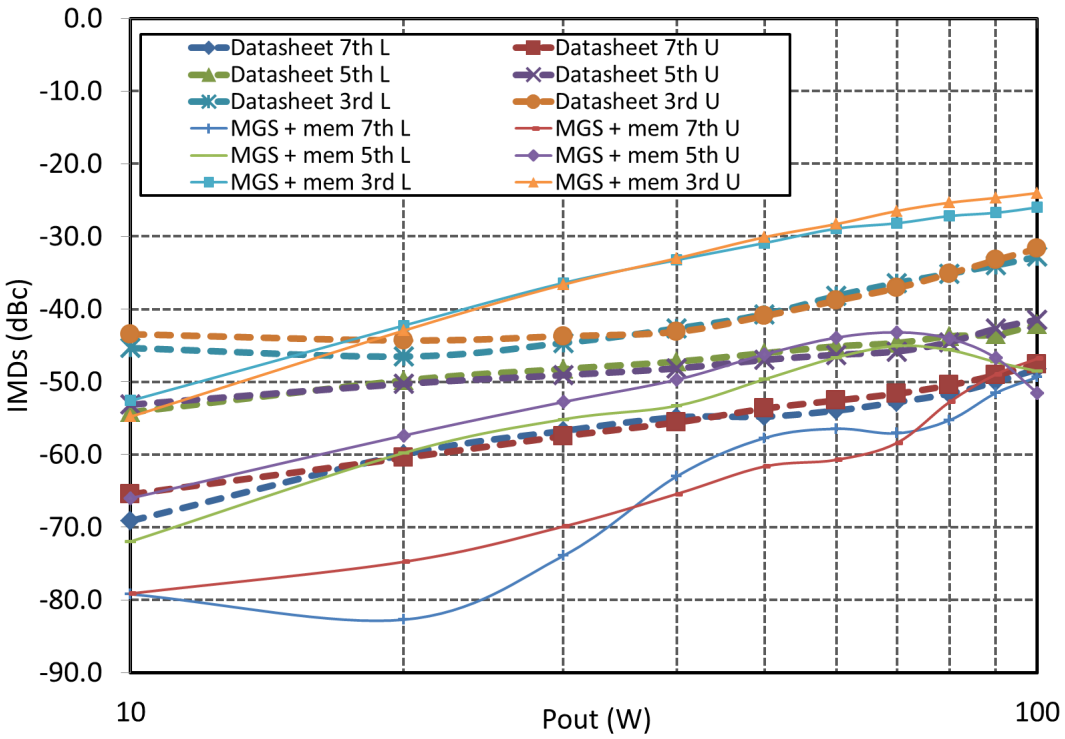

Figure 4.15. Two tone IMD data for MW7IC18100NBR1 10 W to 100 W versus simulation results. MW7IC18100NBR1 [123], Figure 11, two tone intermodulation distortion fixed 100 kHz tone spacing from 10 to 100W compared to simulation results.

4.2.5 Comparisons

The simulated versus datasheet IMD performance is compared in Table 4.3 for output powers over the range from 10 to 100 W Peak Envelope Power (PEP). Note that in Table 4.3 the shaded rows are datasheet values and the un-shaded rows are simulated data from the proposed model. The simulated results show good agreement between datasheet powers over the range from 10 to 100 W for 3rd order IMDs. It is noted that the presented simulation data deviates more from the datasheet values for 5th and 7th order IMDs. This indicates that the proposed model is limited in predicting higher order IMDs and more non-linear dynamics need to be introduced. It is also expected that these deviations are, in part, due to the limited range of P_{in} versus P_{out} data available from the datasheet, Fig. 4.13, used to generate the MGS model.

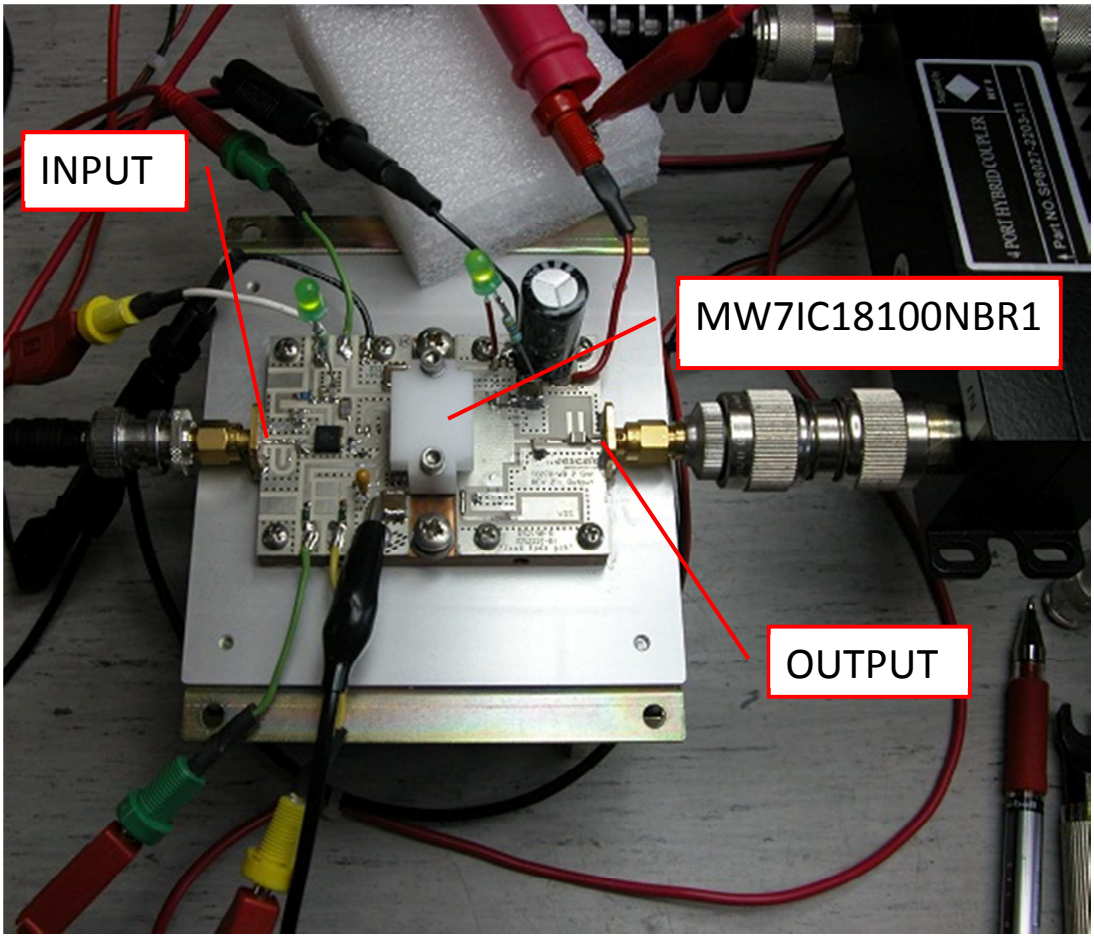

Figure 4.16. Freescale MW7IC18100 test jig. Freescale MW7IC18100 test jig [123] for extended measurements.

Table 4.3. Comparison of datasheet versus simulated IMDs versus output power.

Datasheet / Model	P_{out} (W, PEP)	3rd IMDs (dBc)		5th IMDs (dBc)		7th IMDs (dBc)	
		Lower	Upper	Lower	Upper	Lower	Upper
Datasheet	10	-45.3	-43.4	-54.2	-53.1	-69.1	-65.5
Model	10	-44.2	-45.6	-53.9	-55.0	-59.3	-62.9
Datasheet	50	-45.3	-43.4	-54.2	-53.1	-69.1	-65.5
Model	50	-44.2	-45.6	-53.9	-55.0	-59.3	-62.9
Datasheet	100	-45.3	-43.4	-54.2	-53.1	-69.1	-65.5
Model	100	-44.2	-45.6	-53.9	-55.0	-59.3	-62.9

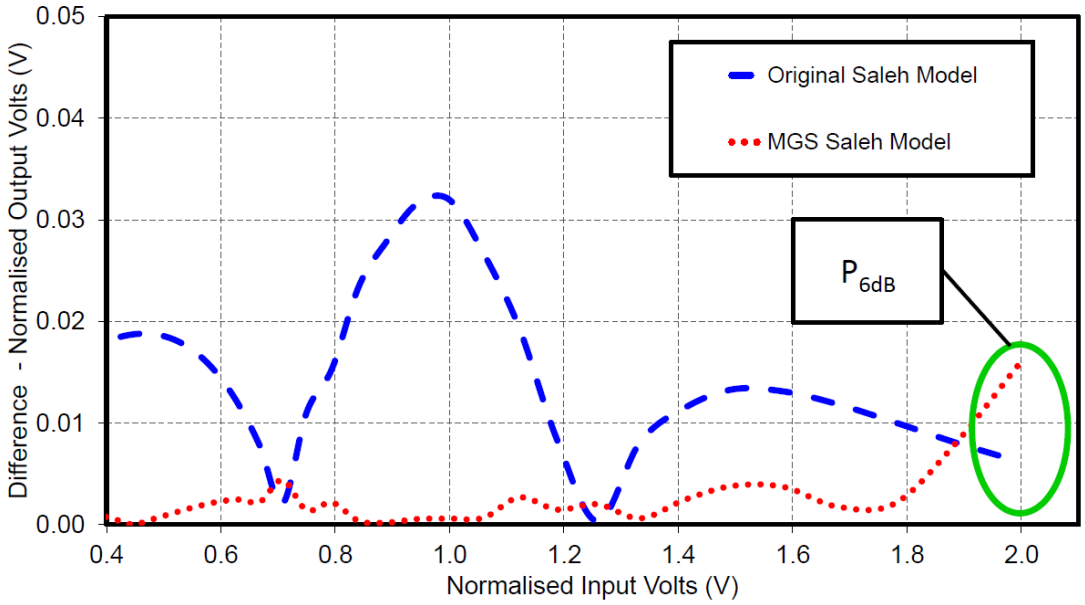

Figure 4.17. Normalised output voltage difference comparison. Comparison of the normalised output voltage difference between the MW7IC18100NBR1 datasheet data and the Original Saleh and MGS models.

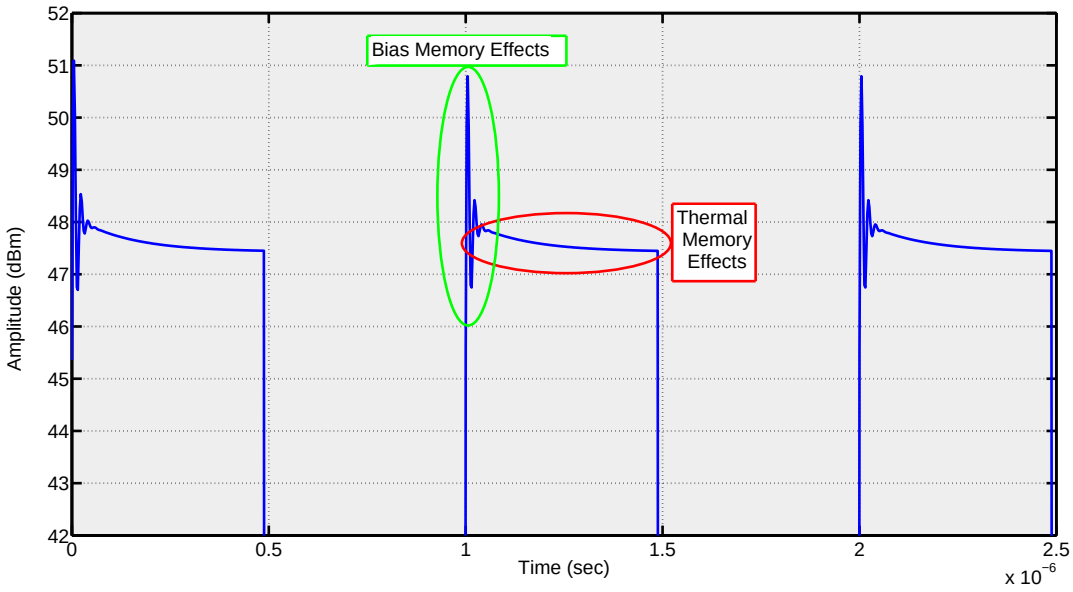

Figure 4.18. Thermal memory effects - time domain response. Time domain response of pulsed RF showing bias and thermal effects.

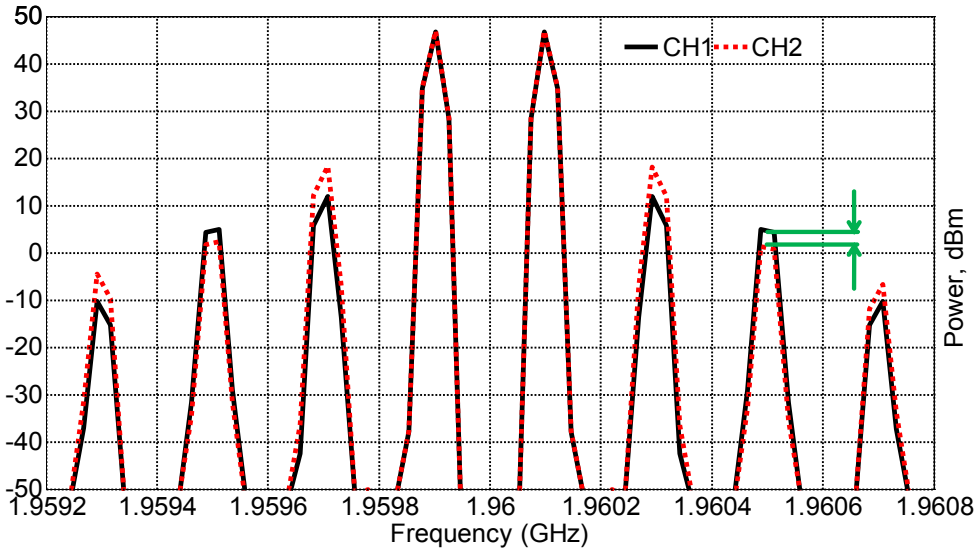

Figure 4.19. Simulink output of the proposed model for 2-Tones with 200 kHz tone spacing. The dotted line shows MGS model simulation when including thermal and bias memory effects, while the solid line shows the simulation results when the memory effects are not included. Note the asymmetry for the 3^{rd}, 5^{th}, and 7^{th} order IMDs between these simulations.

4.2.6 Summary

This section has presented a modelling methodology for extraction of non-linear model parameters, including memory effects, from manufacturer's amplifier datasheets. The results presented in Table 4.3 show good agreement between simulation and the manufacturer's datasheet, validating the methodology. This methodology can be used to provide timely early system level comparisons prior to device selection, testing and detailed design, resulting in a significant time and cost saving when surveying devices for product development.

4.3 Conclusion

This chapter has identified the need for fast system level comparisons to aid in the selection of critical RF PA output devices. For SSPA devices, having only below saturation data available, the original Rapp AM/AM model including the Honkanen and Haggman phase shift model plus the addition introduced in this section, provides the best simple AM/AM and AM/PM model. If the available data extends into the saturation region then the O'Droma MGS model provides the best behavioural model into

that region. This chapter has also demonstrated improvements in two existing models as well as providing a method for determining the saturation power from manufacturer's data. Performance of these models has been compared when used beyond the provided manufacturer's data, where typical modern digital modulation signals extend, thus resulting in further improvements and accuracies. These simple model improvements and additions, combined with the extension of the modelling into the saturation region, thus allow for faster and more accurate system level analysis enabling better crucial output device selections to be made.

This chapter has also presented a modelling methodology for the extraction of nonlinear model parameters, including memory effects, from manufacturer's SSPA device datasheets. The results presented show good agreement between simulation and manufacturer's data, validating the methodology. This methodology can be used to provide timely early system level comparisons prior to device selection, testing and detailed design, resulting in a significant time and cost saving when surveying devices for product development.

In the following chapter further more recent simple and accurate models are investigated with new models developed to leverage off these improved accuracy models for application over a range of current wireless technologies. These more recent models also use semi-physical parameters allowing fast modelling from readily determined semi-physical starting points. Also developed are segmentation techniques that allow for further accuracy enhancement. These new models and techniques are validated over a range of technologies and measurement conditions.

Chapter 5

Generalised Quasi-Memoryless and Memoryless Behavioural Models

THIS chapter presents an optimised segmented modeling approach using a new QM (AM/AM & AM/PM) BM allowing for RF PA modelling over a wide range of SSPA technologies. The new QM model combines an existing semi-physical AM/AM memoryless BM, recently proposed by Cann [125], that correctly predicts small signal region Third Order IMD (3^{rd} IMD), with the newly proposed AM/PM model derived from this existing AM/AM model. Using segmentation and optimisation methods, performance comparisons of the new model are presented showing NMSE AM/PM improvements up to 20 dB, as well as over 5 dB improvement in 3^{rd} IMD performance. Also presented is a technique to improve the accuracy of a simple semi-physical memoryless (AM/AM only) BM, also suitable over a wide range of SSPA technologies, demonstrating between 5 dB to 20 dB NMSE AM/AM improvement. Comparisons against other well known QM and memoryless BMs are conducted using measured data and with data presented in the literature. Effects of these improvements on lineariser performance are also evaluated. The models significantly improve system level modelling by allowing designers to accurately predict system performance using various RF PA devices over a range of technologies, based available manufacturers' data or simple tests. Segmentation discontinuity issues are also discussed.

5.1 An Optimised Segmented Quasi-Memoryless (AM/AM & AM/PM) Nonlinear Behavioral Modeling Approach for RF Power Amplifiers

5.1.1 Introduction

There are increasing requirements for modern wireless communications systems to provide improved data throughput as well as improved spectral distortion performance and increased power efficiencies. As PA devices have a very significant impact on achieving these demanding requirements then improved behavioural modelling of PA devices at the system level is essential. Having a BM, with an aim to provide PA designers with a simple means of modelling PA devices quickly over a range of technologies would be most advantageous.

Another need for improved AM/AM and AM/PM models is associated with RF analog predistortion (RF APD) systems, which are commonly used as an alternative to produce simple and low cost solutions for Small Cell repeaters [126], in contrast to advanced Digital PreDistoration (DPD) systems where simplicity and cost are traded for increased performance. Improved accuracy models operating over a wider dynamic range also have benefits for use in envelope-predistortion linearisers that operate over larger dynamic ranges [127].

Recently Glock *et al.* [128] described a new QM BM for AM/PM modelling to address certain phase responses in GaAs and Complementary Metal Oxide Semiconductor (CMOS) technologies. Glock's justification for using a QM BM is based on the proposition that simple static models are both less complex and less computationally intensive and that well designed RF PAs exhibit low memory effects, as indicated by the careful application of device biasing networks and techniques to reduce memory effects, as noted by Lee *et al.* [129], with the levels of errors associated with static BMs being acceptable for mobile handset applications.

Glock's proposed new model is a semi-physical AM/PM model, derived from Rapp's AM/AM model [111], providing the benefit of a simple QM BM, where model parameters are based on measured device performance. The model's semi-physical parameters can also be reused from the AM/AM model, making it attractive to RF PA designers. This is very powerful for PA designers as it provides immediate initial starting

points for curve fitting of semi-physical parameters for the AM/AM model which are also used in the AM/PM modelling.

The recent application of standard CMOS processing technology, being applied to the manufacture of low cost wireless RF PAs, used for mobile handsets Aoki *et al.* [130], will be a useful advance, however not all CMOS devices have AM/PM responses similar to those discussed by Glock. CMOS phase responses similar to Glock have been reported by Afsahi *et al.* [131] but phase responses similar to LDMOS devices in CMOS are shown by Fuhrmann [132] and Oßmann [133]. Considering the need for miniaturization and the need for system level modelling before moving to an integrated solution, there is also a need for simple QM BMs that cover a range of device technologies and varying phase responses.

In this chapter, Section 5.1.2 presents the need for simple BMs, including a brief review of other modelling approaches and technology modelling capability. A discussion on the benefits of BM accuracy improvements to lineariser performance is given in Section 5.1.3. Section 5.1.4 presents a new AM/PM model that is based on a recent AM/AM model which is capable of producing the correct 3rd IMD response in the small signal region. This new AM/PM model also has a semi-physical basis providing an accurate, usable and relevant BM for PA designers. In Section 5.1.5 a segmentation and optimisation method are proposed and discussed to further improve the overall accuracy of the AM/PM model, allowing the model to be used over a range of different technologies. Verification of the model and methods proposed in this section are demonstrated through comparison with measured data as well as with data presented in the literature. Consideration of the proposed model and accuracy improvement method is presented, with respect to 3rd IMD performance and impact on linearisation improvement, in section 5.1.6. Followed by a discussion and summary.

The primary contribution presented in this section is an optimised segmented modelling approach using a new AM/PM model based on a simple AM/AM model that provides more accurate small signal 3rd IMD performance. This approach provides up to 20 dB NMSE improvement when modelling the AM/PM characteristics of an amplifier and further results in lineariser 3rd IMD predication improvements of over 5 dB, as discussed in Section 5.1.6. Segment boundary discontinuities are also considered and it is demonstrated that worst case discontinuities have no noticeable effect on the modeled amplifier spectrum when using digitally modulated signals. Further to this the model is semi-physical and is shown to be suitable over a range of technologies.

5.1.2 SSPA Behavioural Models

The Need for Simple Models

As non-linearities of RF PAs are the major contributors to the performance degradation of a wireless system, a system level simulation is used to evaluate the RF PA's impact on the overall system performance. The use of time domain or frequency domain techniques requires a full knowledge of all of the relevant circuit elements and accurate nonlinear models of the RF PA, which for an initial system level evaluation may not be easily available or might require too much effort for an initial evaluation. In addition, such modelling is computationally demanding and requires very long simulation times. A more suitable method for system level modelling is to use simple bandpass QM BMs of an RF PA, resulting in fast, but still accurate, simulations that can be used to assess the RF PA's impact on system performance and allow for rapid RF PA device comparisons and selections. In such amplifiers the complex input to output envelope voltage relationship is given by

$$v_{out}(t) = \mathrm{Re}\left[G(v(t))e^{j(\phi(t)+\varphi(v(t))+\omega_c t)}\right], \tag{5.1}$$

where $G(v(t))$ and $\varphi(v(t))$ describe the instantaneous input to output envelope voltage gain and phase and these represent the RF PA's AM/AM and AM/PM responses, respectively. The RF carrier frequency is given by ω_c. The envelope model described by (5.1) thus describes the RF PA's nonlinearities in terms of its AM/AM and AM/PM responses. These can be readily determined from either device manufacturer's datasheets or through further measurements and testing. Thus there is a need for an accurate and simple RF PA BM for use in system level simulations that can allow for device evaluation and selection. Here a memoryless BM is an AM/AM only model and a quasi-memoryless BM is an AM/AM plus AM/PM model as defined by Bösch and Gatti [134] in their Fig. 1.

The very significant benefit of semi-physical device BMs is that they provide the best starting point for any Least Squared Curve Fitting (LSCF) that will typically be required in order to extract these parameters plus any non-physical model parameters. This is particularly important and powerful for practical PA designers as it provides them with a fast way of assessing suitable PA device alternatives, using parameters that are readily available in device datasheets, without the need for further complex

testing and measurements. This can be used for both the AM/AM and AM/PM response estimations. Glock used Rapp's AM/AM model for the AM/AM component and also to extract the AM/PM model. In that model only the sharpness parameter, s, and linear slope d parameters are non-physical. This section defines a semi-physical model as one where most model parameters are determined by the physical nature of the device performance, for example Cann's 2012 AM/AM model uses small signal gain and saturation levels as parameter values. For the sharpness parameter this is readily determined by an initial estimate that when evaluated can quickly be adjusted to provide a value that matches device performance.

A further significant benefit for PA designers would be to have one model that is suitable for both AM/AM and AM/PM modelling with the added advantage in being; applicable to a range of current technologies, simple, computationally efficient, physical or semi-physical in nature, accurate and fast.

The O'Droma model [114], can provide an excellent fit to a range of AM/AM and AM/PM curve shapes but the parameters for this model do not have a physical origin. As a result, determining the starting point values for this and other non-physically based model parameters for LSCF can be difficult and may require more sophisticated methods to determine these starting point values. So an appropriate selection of the starting points is needed to ensure a final optimum outcome. With semi-physical based models, the majority of parameter starting points are taken from available data, thus avoiding possible guessing or further measurements. For the non-physical parameters of the Rapp and Cann 2012 AM/AM models, several plots of the AM/AM responses can be made for a particular device, for different s values. By comparing these plots with measured data, an estimate of the starting value for s can be found. Having semi-physical starting points is also a very useful means of self checking the LSCF parameter results, as the final values for LSCF parameter results should be very close to the starting values.

Review of Simple PA Behavioural Models

This section recognises the heritage of several BMs from TWTA backgrounds, as this has been an early starting point for several PA BMs. Although TWTAs are still relevant and in use nowadays, the focus of this section is solid state PA technologies, such as GaAs, CMOS and LDMOS.

There are several existing well established QM BMs that offer PA designers a simple and fast means of providing system analyses to assist them in selecting a suitable device for their RF PA requirements. In 1980 Cann [135], introduced a simple AM/AM semi-physical memoryless model for an over driven or soft-limiting solid state amplifier that used bipolar technology, allowing the knee sharpness to be adjusted while maintaining small signal linearity. Then in 1981 Saleh [109] introduced a simple model for a TWTA that required only 2 parameters for both AM/AM and AM/PM modelling.

In 1991 Ghorbani and Sheikhan [110] proposed an SSPA specific model, for both AM/AM and AM/PM of the same form, having only 4 parameters to address inaccuracies of using TWTA based models for SSPAs. Rapp [111] in 1991, presented a memoryless AM/AM only model for GaAs FET SSPAs that also included semi-physical parameters. Honkanen and Haggman [112] in 1997, applied Rapp's model as part of a Bipolar Junction Transistor (BJT) AM/AM model while introducing a new AM/PM model defined with a maximum of zero degrees phase shift. White *et al.* [113] in 2003, introduced new models for AM/AM and AM/PM to better model Ka-Band SSPAs, when compared to the Saleh, Ghorbani and Sheikhan, and Rapp models.

In 2009 Saleh's model was further developed by O'Droma *et al.* [114], with respect to LDMOS, addressing the discontinuity seen in the application of Saleh's original AM/PM model when applied to typical LDMOS AM/PM characteristics.

In 2012 Cann [125] updated his 1980 model to eliminate issues found with the original model when calculating small signal 3^{rd} IMD products, with the model again based on semi-physical parameters.

Later, in 2013, O'Droma and Yiming [136] proposed a modified Bessel-Fourier model that provided improved accuracy with performance extending into the saturation region beyond available data. The model can be used with a low number of fitting parameters and accuracy can be improved by increasing the number of fitting parameters. It is suitable for memoryless modelling including both AM/AM and AM/PM characteristics of nonlinear PAs. Although accurate, it is not physically based.

Part of this research in 2015, [137], proposed an extension to Honkanen and Haggman's AM/PM model, allowing it to model phase shifts greater than zero degrees and also provided a correction to White *et al's* AM/AM model. Also in 2015 Glock [128] presented an approach based on Rapp's AM/AM model but introduced a new AM/PM model determined from the first derivative of the Rapp AM/AM model plus additional terms.

In this section these simple models, along with the definitions of their respective parameters, are summarized in Table 5.1.

Other models that have also been considered in the literature are as follows. Cunha *et al.* [138], proposed a Rational Function-based model that includes memory effects, while Rawat *et al.* [139], proposed Generalized Rational Functions for reduced complexity behavioural models but was targeted at inverse modelling, including memory effects, for DPD applications. Harguem *et al.* [140], proposed using Gegenbauer polynomials and Jebali *et al.* [141], proposed using Zernike polynomials. Both of these approaches target improved numerical stability with minimal computational cost, when compared to Volterra series approaches, but the models are more mathematically complex compared to the simple memoryless models proposed in this chapter. Safari *et al.* [142], proposed using cubic splines. While these models are alternatives to the simple BMs presented in Table 5.1, they tend to also be more complex mathematically and depart from the simple semi-physical BM approach.

Table 5.1: Simple behavioural models for RF power amplifiers, comparisons & technologies

Model, Year	**AM/AM**	**AM/PM**	**Technology Modeled**
	r = input voltage, $A(r)$ = output voltage	$\phi(r)$ = output phase	
Cann, 1980, [135], Loyka, 1982, [143]	$A_{\text{Cann'80}}(r) = \frac{gr}{\left[1+\left(\frac{g\lvert r\rvert}{L}\right)^s\right]^{1/s}}$, [135] $= \frac{Lsgn(r)}{\left[1+\left(\frac{L}{g\lvert r\rvert}\right)^s\right]^{1/s}}$, [143] L = SLL, g = SSG, s = sharpness parameter	———	Over-driven soft limiting amplifier, AM/AM only
Saleh, 1981, [109]	$A_{\text{Saleh}}(r) = \frac{\alpha_a r^{\eta_a}}{(1+\beta_a r^{\gamma_a})^{\nu_a}} - \epsilon_a = \frac{\alpha_a r}{1+\beta_a r^2}$ α_a = AFP, β_a = AFP, $\eta_a = 1$, $\gamma_a = 2$, $\nu_a = 1$, $\epsilon_a = 0$	$\phi_{\text{Saleh}}(r) = \frac{\alpha_\phi r^{\eta_\phi}}{(1+\beta_\phi r^{\gamma_\phi})^{\nu_\phi}} - \epsilon_\phi = \frac{\alpha_\phi r}{1+\beta_\phi r^2}$ α_ϕ = PFP, β_ϕ = PFP, $\eta_\phi = 1$, $\gamma_\phi = 2$, $\nu_\phi = 1$, $\epsilon_\phi = 0$	TWTA

Continued on next page

Table 5.1 – continued from previous page

Model, Year	AM/AM	AM/PM	Technology Modeled
Ghorbani and Sheikan, 1991, [110]	$A_{\text{Ghorbani}}(r) = \frac{x_1 r^{x_2}}{1+x_3 r^{x_2}} + x_4 r$ x_1, x_2, x_3, x_4 = AFPs	$A_{\text{Ghorbani}}(r) = \frac{y_1 r^{y_2}}{1+y_3 r^{y_2}} + y_4 r$ y_1, y_2, y_3, y_4 = PFPs	SSPA
Rapp, 1991, [111]	$A_{\text{Rapp}}(r) = \frac{gr}{\left[1+\left(\frac{gr}{L}\right)^{2s}\right]^{1/2s}}$ L = SLL, g = SSG, s = sharpness parameter	————	SSPA, AM/AM only
Honkanen and Haggman, 1997, [112]	$A_{\text{Honkanen}}(r) = \frac{V_o'(r)}{\left[1+\left(\frac{V_o'(r)}{L}\right)^{2s}\right]^{1/2s}}$, [111] $V_o'(r) = \left(e^{kr}-1\right), r+V_b \leq r_{tr}$ & $V_o'(r) = \nu(r+V_b) + b_{aHH} - e^{kr} + 1, r+V_b > r_{tr}$ $V_b = r = 0$ adj. point, r_{tr} = exp. to lin. response transition point, k = exp. curve steepness, ν = exp. curve, lin. portion, nom. gain, $b_{aHH} = e^{kr} - 1 - \nu r_{tr}$	$\phi_{\text{HH}}(r) = \frac{b_{\phi HH}}{1+e^{-c_{\phi HH}(r-a_{\phi HH})}} \cdot \frac{1}{p_1 r+p_2}$ $a_{\phi HH}$ = is the input turn-on voltage for a BJT, $b_{\phi HH}$ = turn-on |phase|, $c_{\phi HH}$ = step change steepness, p_1, p_2 = downward slope adj. parameters	BJT AM/AM adaption of [111], AM/PM to zero degrees only
White *et al*, AM/AM, [113], Fisher and Al-Sarawi, AM/AM correction, [137]	$A_{\text{White}}(r) = a_w\left(1-e^{-b_w r}\right) + c_w r e^{-d_w r^2}$, $A_{\text{FACorr.}}(r) = a_w\left[\left(1-e^{-b_w r}\right) + c_w r e^{-d_w r^2}\right]$	$\phi_{\text{White}}(r) = f_w\left(1-e^{-g_w(r-h_w)}\right), r \geq h_w$ $\phi_{\text{White}}(r) = 0, r < h_w$	Ka Band SSPAs
White *et al*, AM/PM [113]	a_w = SLL, b_w = SSG, c_w, d_w = AFPs	f_w = mag., g_w = curve slope, h_w = r range shift	
Cann, [125]	a_w = SLL, c_w = SSG, b_w, d_w = AFPs		Cann's view on White's parameters
O'Droma *et al*, 2009, [114]	$A_{\text{O'Droma'09}}(r) = \frac{\alpha_a r^{\eta_a}}{(1+\beta_a r^{\gamma_a})^{\nu_a}} - \epsilon_a$ $\alpha_a, \beta_a, \eta_a, \gamma_a, \nu_a, \epsilon_a$ = AFPs	$\phi_{\text{O'Droma'09}}(r) = \frac{\alpha_\phi r^{\eta_\phi}}{(1+\beta_\phi r^{\gamma_\phi})^{\nu_\phi}} - \epsilon_\phi$ $\alpha_\phi, \beta_\phi, \eta_\phi, \gamma_\phi, \nu_\phi, \epsilon_\phi$ = PFPs	LDMOS SSPA

Continued on next page

Table 5.1 – continued from previous page

Model, Year	AM/AM	AM/PM	Technology Modeled
Cann, 2012, [125]	$A_{\text{Cann'12}}(r) = \frac{L}{s}\ln\left[\frac{1+e^{s(\frac{gr}{L}+1)}}{1+e^{s(\frac{gr}{L}-1)}}\right] - L$ L = SLL, g = SSG, s = sharpness parameter	————	Over-driven soft limiting amplifier, AM/AM only
O'Droma *et al*, 2013, [136]	$A_{\text{O'Droma'13}}(r) = \sum_{k=1}^{M} b_{(2k-1)a} J_1\left(\frac{2\pi}{\gamma_a D}(2k-1)r\right)$ D = Input Amplitude Dynamic Range, γ_a = period ratio of FS to IVTCs, $b_{(2k-1)a}$ = AFPs, J_1 = Bessel fn. of 1st kind, M = no. of AFPs	$\phi_{\text{O'Droma'13}}(r) = \sum_{k=1}^{M} b_{(2k-1)\phi} J_1\left(\frac{2\pi}{\gamma_\phi D}(2k-1)r\right)$ D = Input Amplitude Dynamic Range, γ_ϕ = period ratio of FS to IVTCs, $b_{(2k-1)\phi}$ = PFPs, J_1 = Bessel fn. of 1st kind, M = no. of PFPs	LDMOS SSPA Fourier series (FS), instantaneous voltage transfer characteristics (IVTCs)
Glock *et al*, 2015, [128]	Use Rapp 1991 AM/AM model [111] L = SLL, g = SSG, s = sharpness parameter	$\phi_{\text{Glock}}(r) = \frac{(a_{Gl}-b_{Gl})r+c_{Gl}-d_{Gl}}{\left(1+\left(\frac{gr}{L}\right)^{2s}\right)^{1/2s+1}} + b_{Gl}r + d_{Gl}$ a_{Gl} = linear region slope, b_{Gl} = sat. region slope, c_{Gl} = phase at r = 0, d_{Gl} = sat. region lin. approx. of phase delta	65 nm GaAs & 28 nm CMOS PAs
Fisher and Al-Sarawi, 2015, [137]	Use Rapp 1991 AM/AM model [111] L = SLL, g = SSG, s = sharpness parameter	$\phi_{\text{FA}}(r) = \frac{b_{HH}}{1+e^{-c_{HH}(r-a_{HH})}} \cdot \frac{1}{p_1 r+p_2} + d_{FA}$ $a = a_{\phi_{HH}}$, $b = b_{\phi_{HH}}$, $c = c_{\phi_{HH}}$, $p_1 = p_1$, $p_2 = p_2$, d_{FA} = phase offset	AM/PM $\geq$ zero degrees applied to LDMOS
This work	Use Cann 2012 AM/AM model [125] L = SLL, g = SSG, s = sharpness parameter	$\phi(r) = [(a-b)r + c - d]\frac{A'(r)}{g} + br + d$, $\frac{A'(r)}{g} = \left[\frac{\left(e^{s(\frac{gr}{L}+1)} - e^{s(\frac{gr}{L}-1)}\right)}{\left[1+e^{s(\frac{gr}{L}+1)}\right]\left[1+e^{s(\frac{gr}{L}-1)}\right]}\right]$ $a = a_{Gl}, b = b_{Gl}, c = c_{Gl}, d = d_{Gl}$	LDMOS, HFET, E-pHEMT, InGaP, HBT, Si CMOS FETs, GaN, SiC

Comparing PA Behavioural Models - AM/AM & AM/PM

In order to compare these BMs, NMSE, using (5.2) below, as well as frequency domain comparisons, made via Simulink with a Wide-band Code Division Multiple Access (WCDMA) digitally modulated baseband envelope signal applied to the RF PA model's input and with its' output presented in the frequency domain via the Simulink Fast Fourier Transform (FFT) based spectrum analyser element. These comparisons are presented for the various AM/PM and AM/AM models described in this paper.

NMSE is used to provide a measure of the error between the estimate from the model and measured data, for both the AM/AM and AM/PM models, and is defined in dB, as [144]

$$\mathrm{NMSE}_{\mathrm{dB}} = 10\log_{10}\left(\frac{\sum_{n=0}^{N}|y_{\mathrm{meas.}}(n)-y_{\mathrm{model}}(n)|^2}{\sum_{n=0}^{N}|y_{\mathrm{meas.}}(n)|^2}\right), \tag{5.2}$$

where N is the number of samples, $y_{\mathrm{meas.}}$ is the complex baseband envelope of the measured PA output and y_{model} is the complex baseband envelope of the model output.

Another comparison for SSPA behavioural models is computational speed and parameter count. In terms of computational speed this has not been included as for several models, fits could not be obtained from initial starting points, except for semi-physical models, where the starting points were readily available from the measured or manufacturer's data, a significant advantage.

In terms of parameter count Table 5.2 below shows the number of parameters required for each model listed in Table 5.1.

Technology Comparisons

To investigate the suitability of the various models as presented in Table 5.1, including the new model of this chapter, testing was performed, via the simple test set-up shown in Fig. 5.1, on devices from a range of technologies, such as an LDMOS FET, GaAs Heterojunction FET (HFET), GaAs Enhancement-mode pseudomorphic High-Electron-Mobility-Transistor (E-pHEMT), Indium Gallium Phosphide (InGaP) Heterojunction-Bipolar-Transistor (HBT), Silicon (Si) CMOS FETs, and a GaN on SiC HEMT.

Table 5.2. Behavioural model versus number of parameters comparison.

Model	Number of Parameters	
	AM/AM	AM/PM
Cann 1980, [135]	3	–
Saleh, [109]	2	2
Ghorbani and Shiekan, [110]	4	4
Rapp, [111]	3	–
Honkanen and Haggman, [112]	5	5
White *et al*, [113]	4	4
O'Droma *et al* 2009, [114]	5	6
Cann 2012, [125]	4	–
O'Droma *et al* 2013, [136] Modified Bessel Fourier coeff. no. = M (odd number) and γ.	M+1	M+1
Glock *et al*, [128]	3$\star$	3$\star$+4
Fisher and Al-Sarawi, [137]	PM only	6
This work	3$\star$	3$\star$+4
This work, Segmented Method	3$\star$	3$\star$+4+4+4

$\star$ = AM/AM parameters re-used in AM/PM model.

The modelling results for these devices and other devices from the literature, are shown below in terms of AM/AM and AM/PM NMSE in Figs. 5.3 (a) and (b), respectively and also in Table 5.3. Plots for all of the AM/AM and AM/PM results are provided in Appendix A. These show the curve fit performances used to generate Figs. 5.3 (a) and (b) and also Table 5.3. These results show that the O'Droma models, both the Modified Saleh and Modified Bessel Fourier (M = 7) models, perform very well for AM/AM followed by the Rapp and Cann 2012 models. In terms of AM/AM modelling it can be seen from Fig. 5.3 (a) that most models perform reasonably well over a range of technologies. This would be expected based on similar AM/AM curve shapes for typical AM/AM responses.

In terms of AM/PM performance, the results are quite different. For some devices the NMSE values for these results seem to be acceptable however examination of actual curve fit data reveals a different outcome. Marginal fits and failures have been identified within Table 5.3 and are now discussed. Some models are unable to fit the

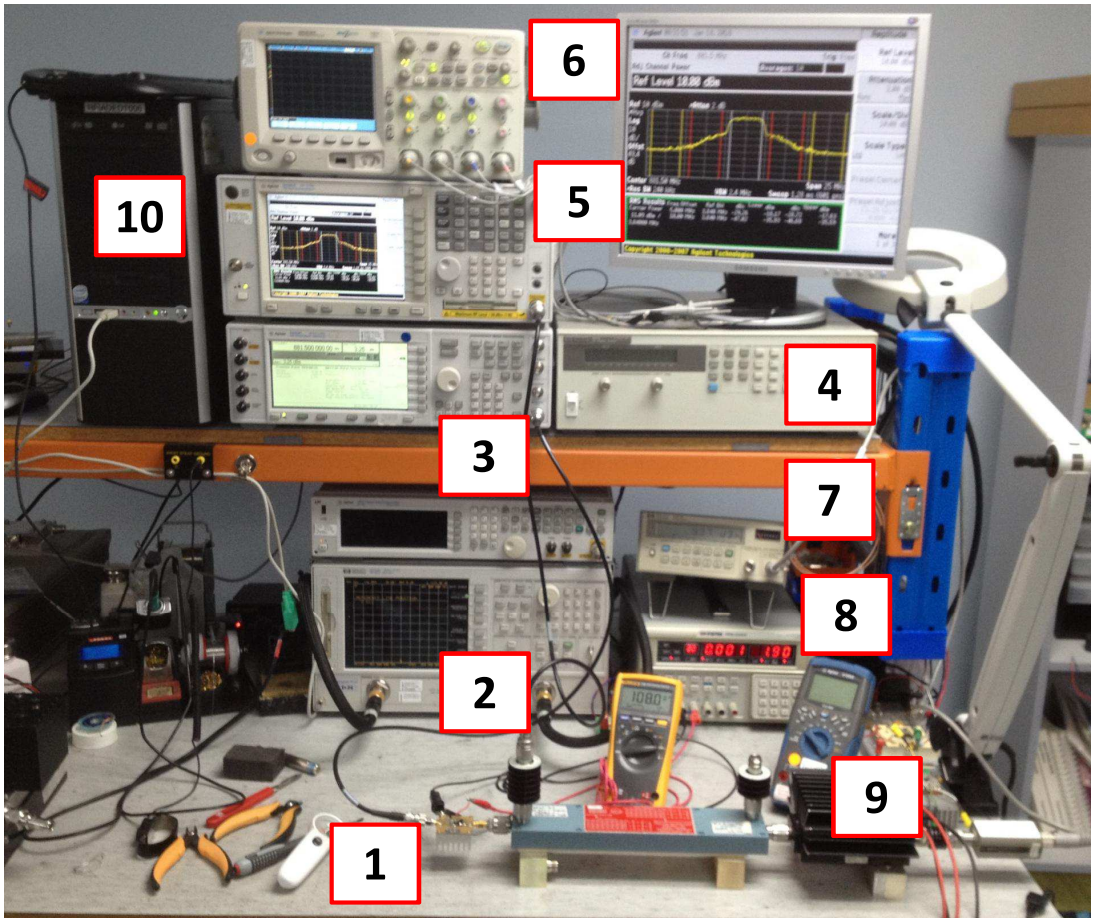

Figure 5.1. Test setup for measuring the SHF-0189 HFET. 1) DUT, 2) Vector Network Analyser, 3) Signal Generator, 4) Power Supply 1, 5) Spectrum Analyser, 6) Digital Storage Oscilloscope, 7) Power meter, 8) Power Supply 2, 9) Multimeter, & 10) Computer.

data while others perform better for some technologies. Again the O'Droma (Modified Saleh) model performs very well over the range of technologies followed by the Glock model and the model presented in this work, based on Cann's 2012 AM/AM model. The O'Droma Modified Bessel Fourier model requires from 3 to 15 parameters to fit the range of technologies however for Glock's Fig. 11 in [128] 2.2V curve data, although it provides a general shape fit for M = 13 it has a superimposed rippled response. The benefit of the AM/PM model presented here is that it fits all technologies, is semi-physical, is accurate in terms of predicting 3rd IMDs with a moderate number fitting parameters $N = 7$. For the models that do not perform well or fail, no analysis, similar to that given by O'Droma [114], is presented as this is beyond the scope of this chapter.

The results presented in this chapter are based on either measured data generated from this research, data from device manufacturer's datasheets or data presented in the literature. Device data measured by the authors uses a single tone Continuous Wave (CW) signal for modeling and uses a WCDMA modulated signal for frequency comparison. Also data from manufacturer's datasheets is for a single tone CW signal. For data used from within the literature this is identified, where provided. The frequencies and signal types for this data are identified in the header of Table 5.3. Literature and device manufacturer's data within figures includes the literature or device manufacturer's references.

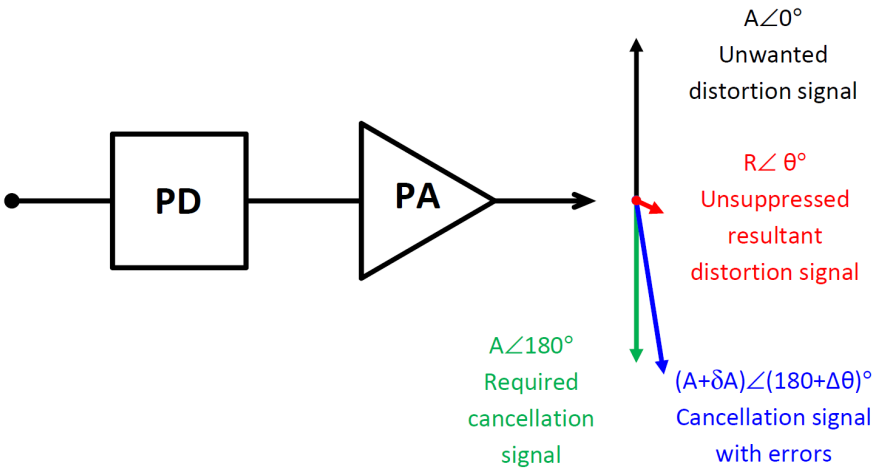

Figure 5.2. Predistorter / Power Amplifier combination. Showing the vector cancellation process for 3rd IMDs.

5.1.3 Lineariser Benefits From AM/PM Accuracy Improvements

For simple low cost RF predistortion linearisers to compete with other more sophisticated linearisers, for example DPD linearisers that are complex and require expensive hardware having higher power consumption, then their accuracy must also also be comparable [126]. Thus a means to quantify the benefits of AM/AM and AM/PM modelling accuracy improvement, when applied to a low cost lineariser, is required.

Nojima and Konno presented an analysis [150] for a combined predistorter (PD) and PA that uses a 3rd order approximation for the PA, as shown in Fig. 5.2, provides an equation for calculating the achievable 3rd IMD reduction, S_{IMD}. In this equation, the difference in the PD amplitude error (δ in dB) and phase error ($\Delta\theta$ in degrees) from the complete cancellation conditions of equal amplitude and opposite phase, between the PD and PA and is given by

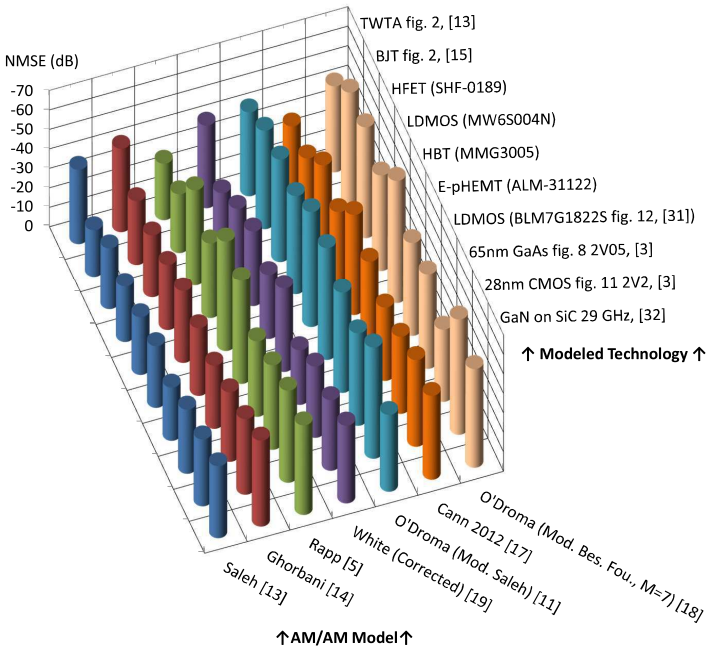

(a)

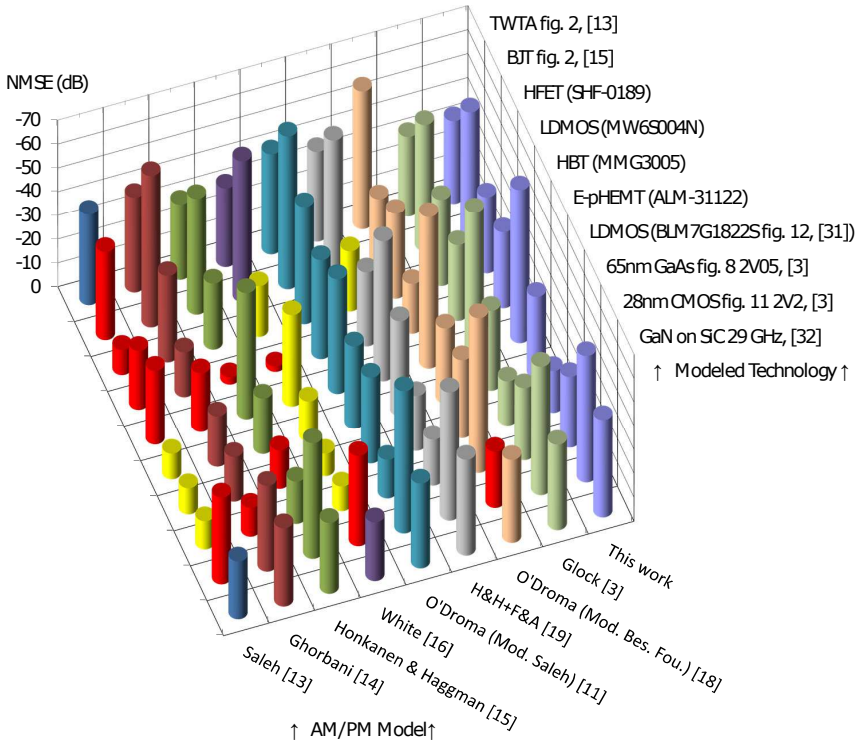

(b)

Figure 5.3. Comparison of models NMSE versus technologies. (a) AM/AM and (b) AM/PM with red columns indicating an LSC fit fail and yellow columns indicating an LSC marginal fit.

Table 5.3. AM/AM and AM/PM NMSE results comparison of models versus technologies.

Model	TWTA Fig. 2 [109]	BJT Fig. 2 [112]	HFET SHF-0189 [145]	LDMOS MW6S004N [146]	HBT MMG3005 [147]	E-pHEMT ALM-31122 [148]	LDMOS BLM7G1822S◇ [117]	GaAs Fig.8 [128]	CMOS Fig.11 [128]	GaN/SiC APN180 [149]
AM/AM NMSE (dB)										
Saleh [109]	-38.20	-24.08	-31.68	-28.69	-29.68	-31.74	-27.38	-33.00	-34.64	-37.75
Ghorbani [110]	-42.82	-32.86	-32.18	-33.94	-37.13	-34.79	-32.50	-35.74	-38.92	-44.76
Rapp [111]	-29.03	-30.24	-49.22	-38.83	-56.70	-53.26	-38.81	-43.44	-47.33	-46.44
White [137] (Cor.)	-42.41	-24.65	-33.52	-38.79	-33.31	-43.01	-28.10	-36.63	-36.30	-40.18
O'Droma [114]	-40.08	-50.57	-52.67	-50.85	-59.54	-57.95	-51.60	-47.55	-57.20	-39.48
Cann 2012 [125]	-29.70	-30.16	-43.53	-36.43	-51.88	-44.77	-37.70	-39.61	-44.56	-43.11
O'Droma [136], N=7	-44.10	-57.83	-56.95	-49.10	-63.22	-48.26	-49.00	-37.09	-59.20	-50.73
AM/PM NMSE (dB)										
Saleh [109]	-38.05	-36.90†	-10.59†	-0.32†	-31.08†	-10.73‡	-10.93‡	-11.79‡	-36.31†	-24.25
Ghorbani [110]	-39.83	-63.63	-36.14	-18.82	-24.70†	-21.23	-18.72	-12.07	-35.86†	-32.81
Honkanen [112]	-31.63	-48.64	-27.65	-3.08†	-52.92	-23.38	-16.09	-17.68	-48.37	-29.72
White[113]	-33.13	-59.14	-21.25‡	-2.28†	-38.39‡	-16.82‡	-9.43‡	-10.27‡	-37.76†	-24.62
O'Droma [114]	-42.14	**-64.24**	-49.18	-40.03	-48.09	-34.59	**-36.16**	-16.17	-59.71	-35.45
Fisher [137]	-37.82	-57.21	-25.19‡	-29.01	-58.67	-39.81	-23.10	-19.27	-53.87	-40.13
Glock [128]	-33.44	-53.08	-36.25	-30.41	-60.16	-33.48	-18.61	-30.37	-54.00	-35.77
O'Droma [136], N=	**-57.78** 7	-27.22‡ 15	-35.77 15	-20.84 15	-63.60 15	-31.41 7	-32.81 7	**-223.54**⋆ 13	**-23.54**† 13	-34.72 3
This work	-34.74	-53.03	-31.98	-30.48	-64.24	-34.02	-17.65	-29.77	-53.14	-40.92
This work (Seg.)	-42.81	-56.56	**-48.36**	**-46.72**	**-75.58**	**-45.78**	-33.71	-52.72	**-75.81**	**-44.79**

† = unable to fit AM/PM response, ‡ = marginal fit, ◇ = AM/PM normalised to zero degrees, ⋆ = capped at -65 dB in Fig. 5.3 (b).

Note: Only first named author listed in the Model column. Blue text indicates best performance across AM/PM models.

$$S_{IMD} = -10\log_{10}\left[1 + 10^{\delta/10} - 2\cdot 10^{\delta/20}\cos(\Delta\theta)\right], \tag{5.3}$$

For this combination, the distortion reduction achievable is a function of the amplitude and phase errors between the combined PD and PA. Normally the PD is adjusted to provide an equal amplitude and opposite phase for the 3rd IMD component at the output of the PA. Using Faulkner *et al's* [151] approach, the PD is configured to be an ideal PD for the measured PA AM/AM and AM/PM responses. By replacing the measured PA results with the AM/AM and AM/PM model, the IMD distortion can be attributed to the PA BM performance. An assessment of further AM/AM and AM/PM modelling improvement on IMDs and linearisation performance can thus be determined and for the model and segmentation method presented here. This assessment is given in Section 5.1.6.

5.1.4 New AM/PM Model Generation

AM/AM Accuracy Improvement

Rapp's AM/AM model [111] has the same equation form as the model first proposed by Cann in 1980 but without the modulus function. Cann's 1980 AM/AM model equation is given as

$$A(r) = \frac{L\,\mathrm{sgn}(r)}{\left[1 + \left(\frac{L}{g|r|}\right)^s\right]^{1/s}} = \frac{gr}{\left[1 + \left(\frac{g|r|}{L}\right)^s\right]^{1/s}}, \tag{5.4}$$

where g, r, L and s are the small signal gain, input amplitude, output limit level, and sharpness parameters, respectively.

In 1996 Litva and Lo [152] identified that Cann's 1980 AM/AM model had issues in generating correct small signal 3rd IMD responses. This was confirmed and the reason for this issue was determined by Loyka [143] in 2000. Cann's new memoryless AM/AM model, presented in 2012, is given as [125]

$$A(r) = \frac{L}{s}\ln\left[\frac{1 + e^{s(\frac{gr}{L}+1)}}{1 + e^{s(\frac{gr}{L}-1)}}\right] - L, \tag{5.5}$$

with the parameters as described in Table 5.1. It should be noted that the issues in the old model are related to modelling two discrete tones used to generate IMD products, however for a typical digital modulation scheme no issues were observed. This more accurate AM/AM model will form the basis for the new AM/PM model discussed below.

Glock's approach of taking the derivative of the AM/AM model, to create an AM/PM model, has been applied to Cann's 2012 AM/AM model.

Following Glock's derivative technique, Cann's 2012 improved AM/AM model can similarly be fully described by its derivatives in the linear and saturation regions, hence the first derivative of the improved 2012 Cann AM/AM model can serve as the basis for a new AM/PM model. This new AM/PM model, derived from Cann's 2012 AM/AM model, is termed the Cann 2012 AM/AM based AM/PM model and hereafter will be referred to as Cann 12B. With reference to (5.5), the small signal gain normalized first derivative of the improved Cann AM/AM equation is given by, with the derivation shown in Appendix B,

$$\frac{A'(r)}{g} = \left[\frac{\left(e^{s(\frac{gr}{L}+1)} - e^{s(\frac{gr}{L}-1)} \right)}{\left[1 + e^{s(\frac{gr}{L}+1)}\right] \left[1 + e^{s(\frac{gr}{L}-1)}\right]} \right], \tag{5.6}$$

with the parameters as described in Table I. Similar to Glock's derivation, the resulting AM/PM model is determined as

$$\phi(r) \quad = [(a-b)r + c - d]\frac{A'(r)}{g} + br + d, \tag{5.7}$$

where a and b are the gradients in the linear and saturation regions respectively, c defines the phase difference when the input amplitude is zero and d in combination with b are a linear approximation of the phase difference in the saturation region. These parameters are also given in Table 5.1.

This alternative AM/PM model gives very similar results to Glock's AM/PM model, i.e. it is within 1 dB of AM/PM NMSE for Glock's Fig. 11 in [128] , 2.2V curve, shown as part of Glock's Fig. 11 in [128] test data, reproduced here in Fig. 5.4 (a).

For the figures shown in Fig. 5.4; (a) Comparison of curve fit for Glock's Fig. 11 in [128], 2V2 curve, data (black solid curve), Glock's AM/PM model (green dotted curve) & new Cann 12B AM/PM model derived using Glock's method, this work, (magenta

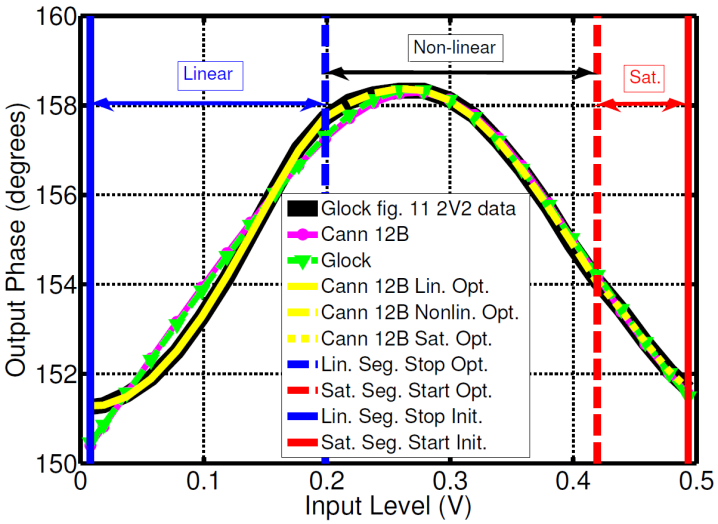

(a)

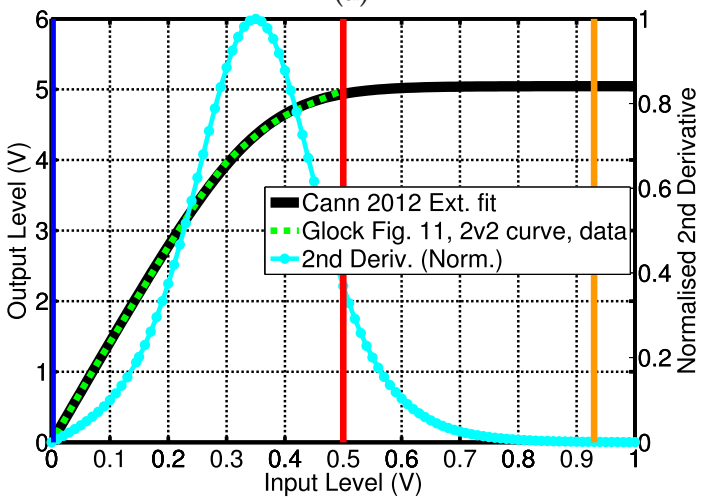

(b)

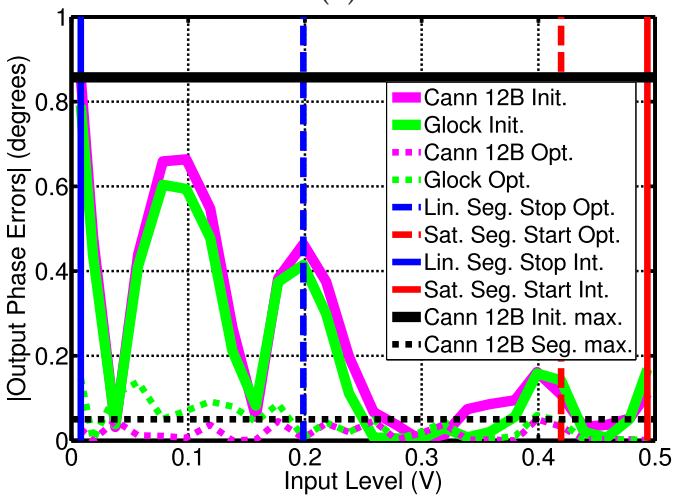

(c)

Figure 5.4. Comparison of curve fits for Glock's Fig. 11.

solid circle trace), (b) Glock's Fig. 11 in [128], 2V2 curve, AM/AM data (green dotted curve), extended AM/AM data (solid black curve), using [137] & normalised (to the maximum value) numerical 2nd derivative of extended AM/AM data (cyan solid circle curve) using Matlab. The solid blue vertical line is the initial end of the linear region, the solid orange vertical line is start of saturation region by the 2nd derivative calculation. The solid red vertical line is the end of the available AM/PM data, effectively the end of the saturation region for the available data, (c) Comparison of absolute Output Phase errors versus input voltage from Glock's Fig. 11 in [128], 2V2 curve, data, showing before and after segmentation optimisation. Also shown are the maximum Cann 12B AM/PM model absolute output phase errors for both the initial (black solid line) & segmented (black dotted line) approach being 0.86 and 0.05 degrees respectively.

5.1.5 Method to Improve New AM/PM Model Accuracy

Segmented Curve Fitting - AM/PM

Glock's technique, for determining the linear, non-linear and saturation regions from the AM/AM characteristic response can also be utilised for further AM/PM modelling improvements. This technique can be used to determine the linear, non-linear or saturation region segments of AM/PM responses so that curve fits of these segments can be applied in a similar approach to that used by Zhu *et al*, [127], for piecewise curve fitting of non-linear segments of AM/AM and AM/PM envelope tracking amplifiers and more recently by Magesacher *et al*, [153], presenting an optimal segmentation approach but with an increased number of segments. In this case the benefits of segmented curve fitting are a more accurate model results, thus assisting with the comparisons for device selection after system analysis, and also for defining potential improvements in linearisation margin for a particular device.

By applying the new Cann 12B AM/PM model for each segmented region and by optimising the end of the linear region segment and start of the saturation region segment, an overall improvement of around 20 dB can be achieved in AM/PM NMSE at the expense of further simple processing steps for each segment. This technique can be applied to both the Glock and Cann models across a range of technologies. Similar to Glock's AM/PM model, the Cann 12B AM/PM model has the ability to provide starting values for LSC fitting for each of the segments.

In order to use these models for an improved AM/PM accuracy estimation, the second derivative of the AM/AM response is used to determine the linear and saturation regions. From Glock's AM/AM data it can be seen that more data points into the saturation region are required. Previously we have developed an approach [137], see also Chapter 4, Section 4.1.4, based on Rapp's AM/AM model that extrapolates the AM/AM performance into the saturation region, which has been demonstrated through testing of an LDMOS device. As Glock's paper uses the Rapp AM/AM model then this data can be extended into the saturation region. Similarly for Cann's 2012 AM/AM model, data can be extended into the saturation region. Using the extended AM/AM data, the transition from the linear to saturation regions can be precisely determined as a function of input level when the 2^{nd} derivative of the AM/AM data equals zero, see Fig. 5.4 (b). As can be seen from this plot, the linear region stop point (vertical blue solid line) occurs when the input level is 0 V and the saturation region start point (vertical orange solid line) occurs well beyond the available data, by the 2^{nd} derivative calculation. This means that the practical LSCF data starting range extends from when the input level = 0 V to where it is at the full extent of the available data (vertical red solid line), in this case where the input level = 0.5 V. The region between the solid blue and red lines is practically the full AM/PM model region for initial LSCF and these points being the starting points for the AM/PM segmentation method optimisation.

Initial AM/PM curve fits for both the Glock and Cann 12B AM/PM models have been performed over the entire available data for Glock's Fig. 11 in [128], 2V2 curve data, with the results from both the Glock (green down triangle curve) and the Cann 12B AM/PM (magenta circle curve) models shown in Fig. 5.4 (a). These are single segment fits between the linear region stop and saturation region start points. This is the same as using the AM/PM model over the entire data range. Although the device phase range is small for some devices, around 6° to 8°, this is still significant in terms of linearisers being able to reduce IMDs, particularly for analog predistorters, as indicated by Cripps [154]. Further improvements as a result of increased accuracy will be beneficial in this area.

The following section will discuss how to improve the modelling accuracy by identifying and then optimising the linear and saturation regions.

Table 5.4. Comparison of AM/AM and AM/PM NMSE for Glock's Fig. 11. 2V2 curve, data [128].

AM/AM - NMSE (dB)		AM/PM - NMSE (dB)		
Model	Full	Model	Full (Initial)	Segmented Optimimised
Rapp	-48.91	Glock	-54.00	-68.00
Cann 2012	-46.04	This work	-53.14	-75.90

Optimised Segmented Curve Fitting - AM/PM

To further improve the accuracy of the AM/PM model an optimisation routine was developed to identify the optimum linear stop and saturation start region points to provide an enhanced data fit in terms of NMSE performance. A comparison between the initial fit and the optimised fit for each of the segments is shown in Fig. 5.4 (a) (yellow curves). This is only shown for the new Cann 12B AM/PM model.

A comparison between the Glock and Cann 12B absolute phase errors, for both initial and optimised segmentation versus input voltage for Glock's Fig. 11 in [128], 2V2 curve, data are shown in Fig. 5.4 (c). The inital results are shown as solid curves with the optimised segmented results shown as dotted curves. An NMSE AM/PM comparison between these models and the corresponding improvements using the segmentation technique are given in Table 5.4. It can be seen that for an initial full data range fit, both models have an NMSE AM/PM within 1 dB of each other, however after the segmentation optimisation the new Cann 12B AM/PM model has better than 20 dB improvement compared to a 14 dB improvement for the Glock AM/PM model.

An optimising segmented curve fitting algorithm, shown in the Algorithm 1, was developed to further improve NMSE. The algorithm starting points for the second derivatives cannot be zero due to their numerical nature, so there is a requirement to have 2^{nd} derivative zero limits, in this research the selected value should be below 0.001, to suit the numerical data. During the minimisation process there are some segment ranges where the resultant discontinuities are higher than the given data, resulting in poorer segment fits. This is due to using parameter starting values for the full range of data in those segments. This can be corrected by determining suitable starting points for each segment but this has not been implemented within this algorithm. Even with

Table 5.5. Comparison of AM/AM and AM/PM NMSE for BLM7G1822S Fig. 12. BLM7G1822S device manufacturer's measured data extracted from datasheet Fig. 12 [117].

AM/AM - NMSE (dB)		AM/PM - NMSE (dB)		
Model	Full	Model	Full (Initial)	Segmented Optimised
Rapp	-38.81	Glock	-17.41	-38.07
Cann 2012	-37.68	This work	-16.61	-41.97

such improvement in the starting point, the overall curve fit performance is still worse than the segmented approach.

Application to LDMOS Devices

Applying the new Cann 12B AM/PM model to devices having LDMOS type phase responses shows that this model can also be used to fit data from such devices. Glock's AM/PM model also fits LDMOS phase data, refer to Fig. 5.5 (a).

Applying the Optimised segmentation approach to the new Cann 12B AM/PM model for LDMOS phase responses results in vastly improved results and NMSE improvements making the new Cann 12B AM/PM model suitable for use as an AM/PM model for LDMOS devices. Fig. 5.5 (a) shows the results of the Optimised segmentation approach as applied to a BLM7G1822S device [117]. A comparison of the initial fit versus optimised segmentation fit approach for absolute phase errors for the BLM7G1822S device is shown in Fig. 5.5 (b), with NMSE results shown in Table 5.5.

Frequency Domain Comparisons & Discontinuity Effects at Segment Boundaries - AM/PM

A comparison using Glock and Cann 2012 models over the full input range, without segmentation and optimisation, against measured data for the SHF-0189 HFET [145] is given in Fig. 5.6. The test set up is shown in Fig. 5.1. These plots show that the new model provides a better fit to the measured data compared to Glock's model and that the Optimised segmented method provides further modelling improvement.

Investigations into the effects of discontinuities at segment boundaries have revealed that although the new Cann 12B AM/PM model does not have continuous derivatives

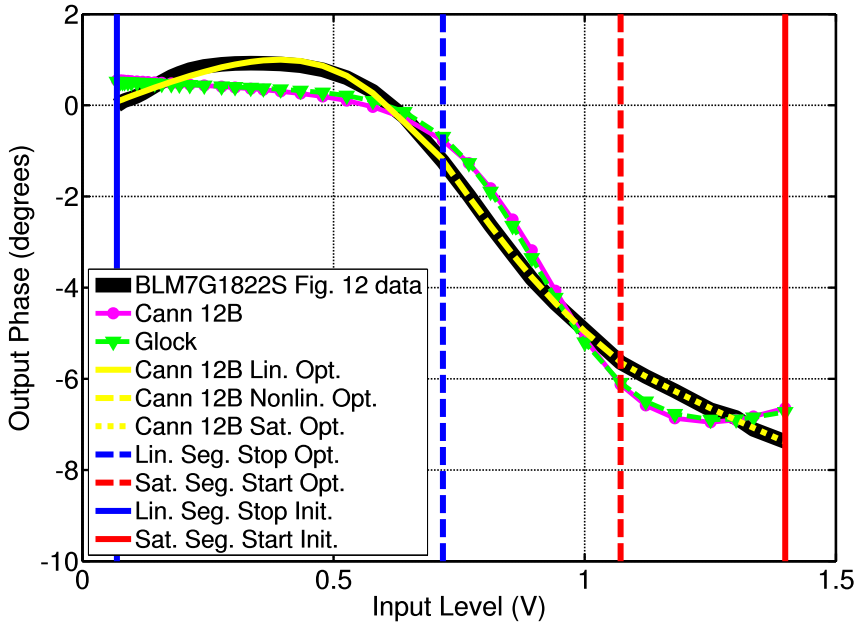

(a)

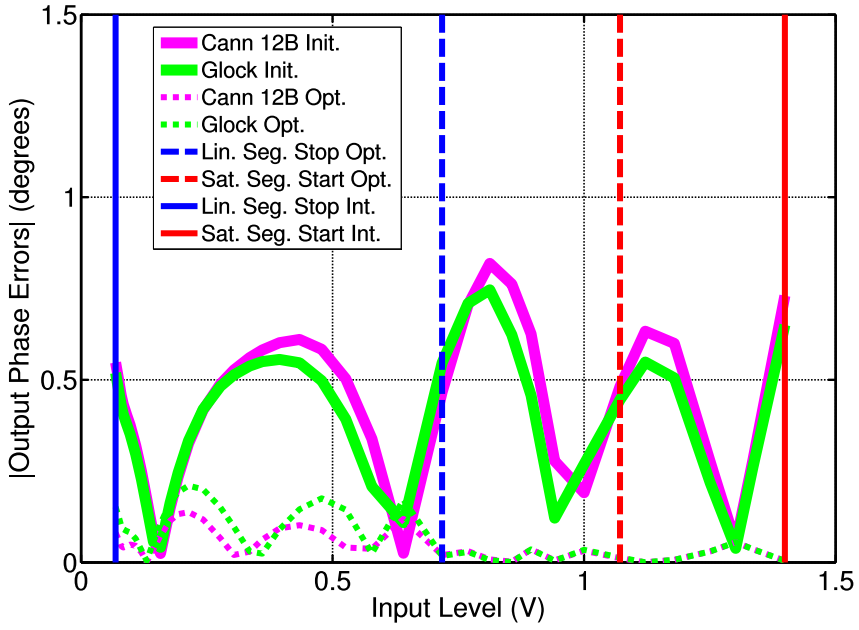

(b)

Figure 5.5. Comparison of curve fits for BLM7G1822S. (a) Comparison of curve fits between the Cann 12B and Glock AM/PM models for the BLM7G1822S device manufacturer's measured data from datasheet Fig. 12 [117] & Cann 12B AM/PM model all segments after optimisation, for the BLM7G1822S device manufacturer's measured data from datasheet Fig. 12 [117] and (b) Comparison of |Output Phase errors| versus input voltage from the BLM7G1822S device manufacturer's measured data from datasheet Fig. 12[117], showing the before and new segmented approach after optimisation.

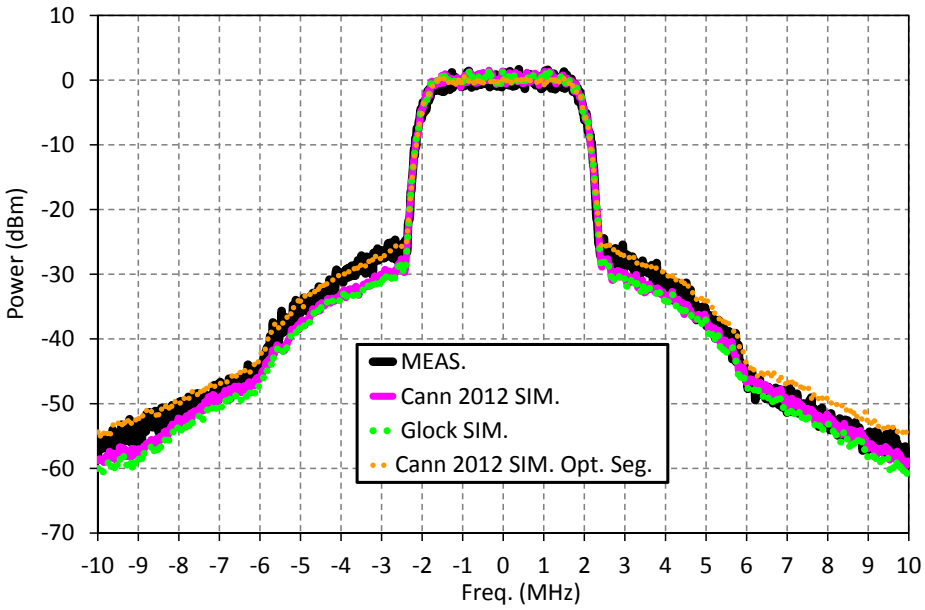

Figure 5.6. SHF-0189 measured versus Simulink simulations for WCDMA. Comparison of measured versus Simulink simulations for WCDMA, comparing Glock versus Cann 2012 full & Optimised segmented models for measured SHF-0189, [145], device data. Resolution bandwidth (RBW) for both measured & simulation data is 30 kHz.

over the segment boundaries, the phase shift errors between the segment boundaries, after optimisation, are very small and have a negligible effect on the Adjacent Channel Leakage Ratio (ACLR) response. This has been investigated for a WCDMA digitally modulated signal with the same power spectral density level as used in Glock's Fig. 9 in [128]. The worst case discontinuity error, of 0.0333 degrees, for either of the linear-nonlinear or nonlinear-saturation segment boundaries was increased, above the optimised value, until the second ACLR level increased by 1 dB and this occurred at 100 times the worst case discontinuity error with no noticeable increase found for the first ACLR, concluding that the Optimised segmented new Cann 12B AM/PM model has negligible discontinuity effects, even when considering worst case discontinuities at the segment boundaries. Comparisons between the Optimised segmentation discontinuity error result and 100 times this error are shown in Fig. 5.7. The Resolution Bandwidth (RBW) for both Figs. 5.6 and 5.7 is 30 kHz.

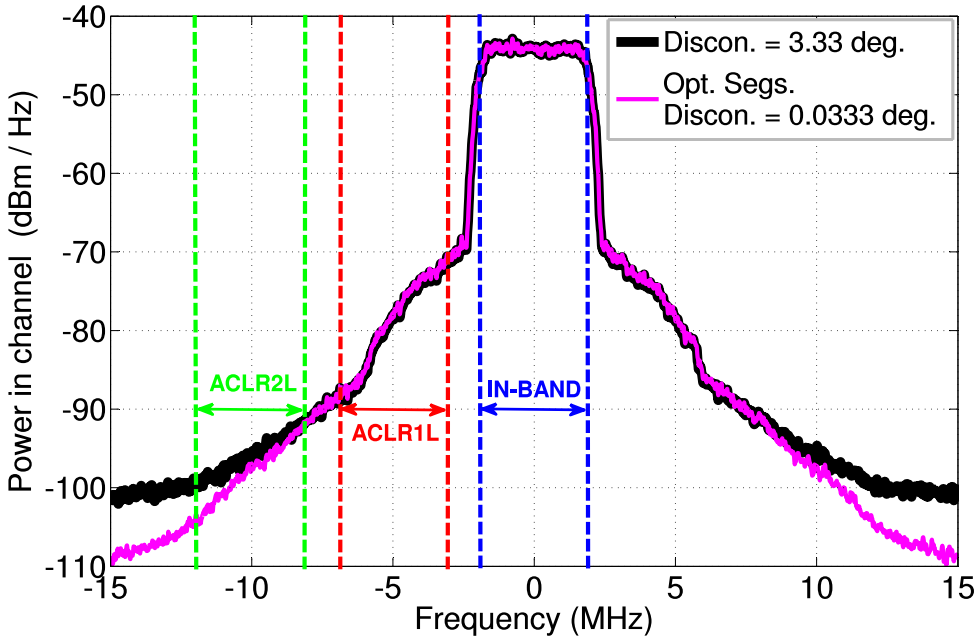

Figure 5.7. Discontinuity effects on a WCDMA modulated signal. Discontinuity effects on a WCDMA modulated signal, simulated using Simulink, for Optimised segmented Cann's 2012 AM/AM & AM/PM model of Glock's Fig.11 in [128], 2V2 curve, data. With no discontinuity ACLR1L/2L = -31.8/-52.1 dBc. With 3.33 deg. discontinuity ACLR1L/2L = -32.0/-51.1 dBc. The In-band wanted signal is between the dashed blue vertical lines with ACLR1 between the dashed red vertical lines and ACLR2 between the dashed green vertical lines (only lower ACLR bands are shown) all with 3.84 MHz integration bandwidths. The integrated power over the in-band wanted signal is 21.5 dBm. Resolution bandwidth (RBW) is 30 kHz.

5.1.6 Impact on IMDs & Linearisation Improvement

An assessment of how the simple models perform in predicting 3rd IMD performance of RF PAs over a wide dynamic range has been made by simulating the 3rd IMDs using Simulink and comparing the simulations against manufacturer's measured IMD data, SHF-0189 device [155] page 5. Plots of the 3rd IMD comparisons are shown in Fig. 5.8. Comparisons of the absolute 3rd IMD errors are shown in Fig. 5.9. The 3rd IMD results of the combined Cann 2012 AM/AM and new AM/PM model perform better than other models, even though the O'Droma (Modified Saleh) model shows very good curve fitting results, in terms of AM/AM and AM/PM absolute measured minus modeled amplitude and phase errors, compared to the Rapp / Glock model or Cann 2012 AM/AM and new AM/PM model presented here. Figure 5.8 also shows a

plot of the manufacturer's measured 5th IMDs indicating that 3rd IMDs are the dominant IMDs. Based on this and the results of the comparison of the measured versus simulated results for a WCDMA signal shown in Fig. 5.6, where effects of higher order IMD products are included, the simple model presented here is considered to be suitable, particularly for an analog predistorter.

The Cann 2012 AM/AM & new AM/PM model have ≈ 2 dB improvement in Average Error (AE) compared to the O'Droma model and over 5 dB AE improvement compared to the Glock model. The Optimised segmented Cann12B model method improves the AE by a further ≈ 1 dB. The model presented here does not account for "sweet spots" that may be seen in some devices. This is beyond the scope of this section and simple model.

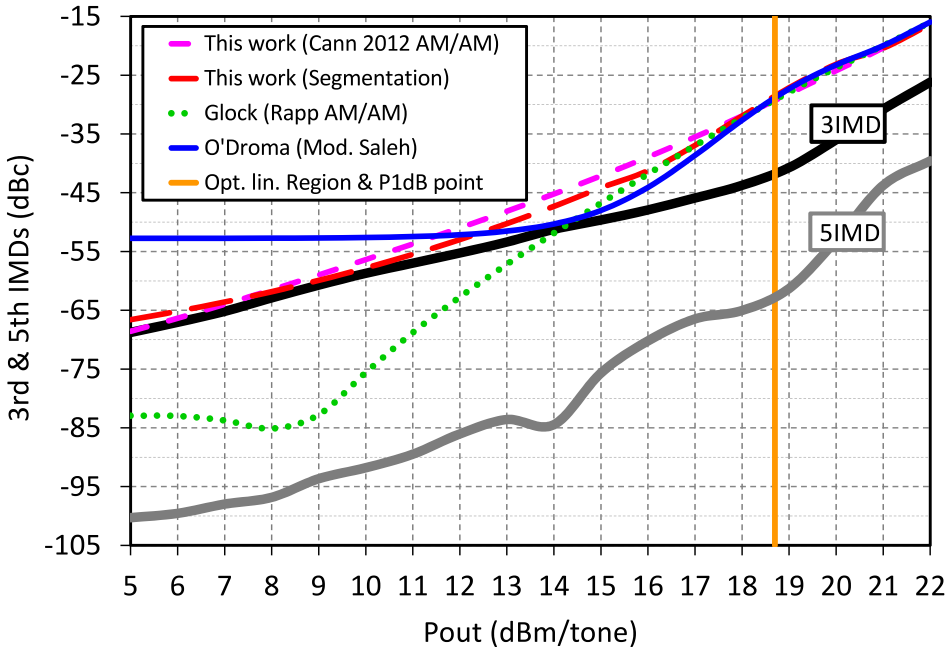

Figure 5.8. SHF0189 measured versus Simulink comparison of 3rd & 5th IMDs. 3rd & 5th IMD manufacturer's measured data for the SHF-0189 device from [155] page 5 versus Simulink simulated comparison of the O'Droma (Modified Saleh), Glock & Cann 2012 models, all including both AM/AM & AM/PM components. For the segmented model of this work the Optimised linear segment point & P1dB point are shown as the solid orange vertical line. The optimised saturation region point is at 24 dBm per carrier but that is beyond the available data. The 5th IMD trace shows that the 3rd IMDs dominate IMD performance.

In terms of the new model and method's 3rd IMD linearisation improvement, as discussed in Section 5.1.3, the maximum absolute amplitude error for the Cann 2012

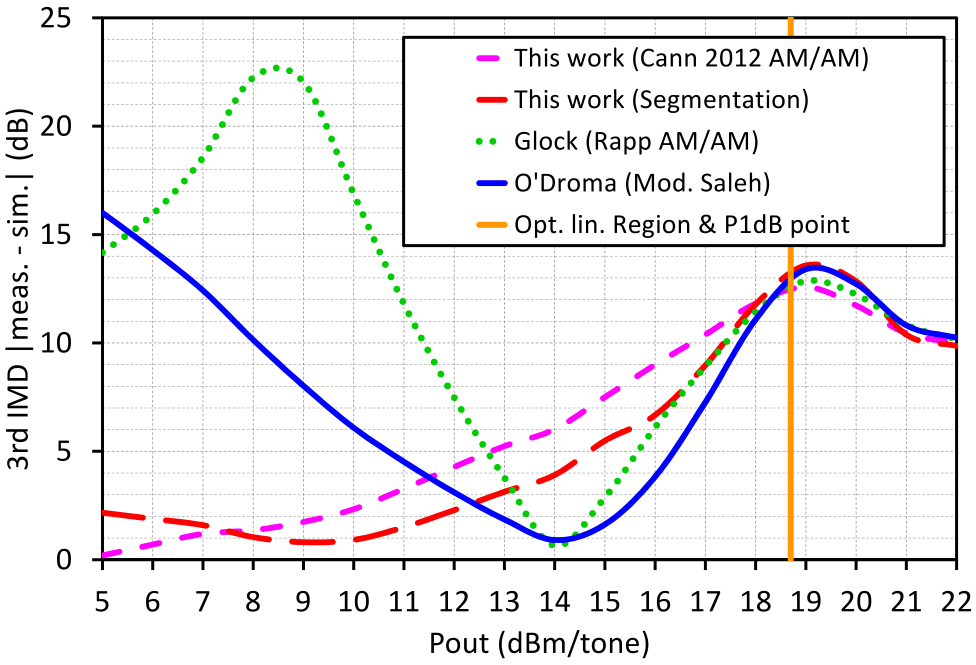

Figure 5.9. SHF0189 measured versus Simulink error comparison of 3rd IMDs. 3rd IMD |measured minus Simulink simulated| error for the O'Droma (Modified Saleh), Glock, Cann 2012 & Optimised segmented Cann 2012 models, all including both AM/AM & AM/PM components. The AE for Cann 2012 AM/AM & AM/PM is ≈ 6 dB compared to ≈ 8 & 11 dB for the O'Droma and Glock models respectively. The Optimised segmented Cann 2012 model AE improves 3rd IMD over the Cann 2012 model by a further ≈ 1 dB. For the segmented model of this work the Optimised linear segment point & P1dB point are shown as the solid orange vertical line. The optimised saturation region point is at 24 dBm per carrier but that is beyond the available data.

AM/AM model LSC fit, between the measured data and modeled results is 0.14 dB, with the absolute amplitude error defined as the maximum absolute difference between the model and data values in dB. The full and Optimised segmented Cann 12B AM/PM absolute output phase errors are 0.86 and 0.05 degrees respectively, shown as the solid and dotted horizontal lines in Fig. 5.4(c). The output phase error is defined as the difference between the measured and modeled output phase. Figure 5.10 shows a plot of (5.3), where the intermodulation distortion reduction is plotted against phase error for various amplitude errors. For the 0.14 dB Cann 2012 AM/AM amplitude error curve, the full and segmentation phase errors are at 0.86 and 0.05 degrees, respectively, as indicated by the solid red arrowed lines. The 2.7 dB difference between these two points is the improvement in the linearisation performance that can be achieved due to the proposed improved accuracy Cann 12B AM/PM model. For each of the various

technologies, TWTA, BJT, HFET, LDMOS, HBT, E-pHEMT, GaAs, CMOS, GaN/SiC and including Glock's device data, the AM/PM NMSEs were determined for both the full and segmented methods. The NMSE improvements between the full and segmentation methods are shown in comparison to the linearisation 3rd IMD improvements for each technology type in Table 5.6.

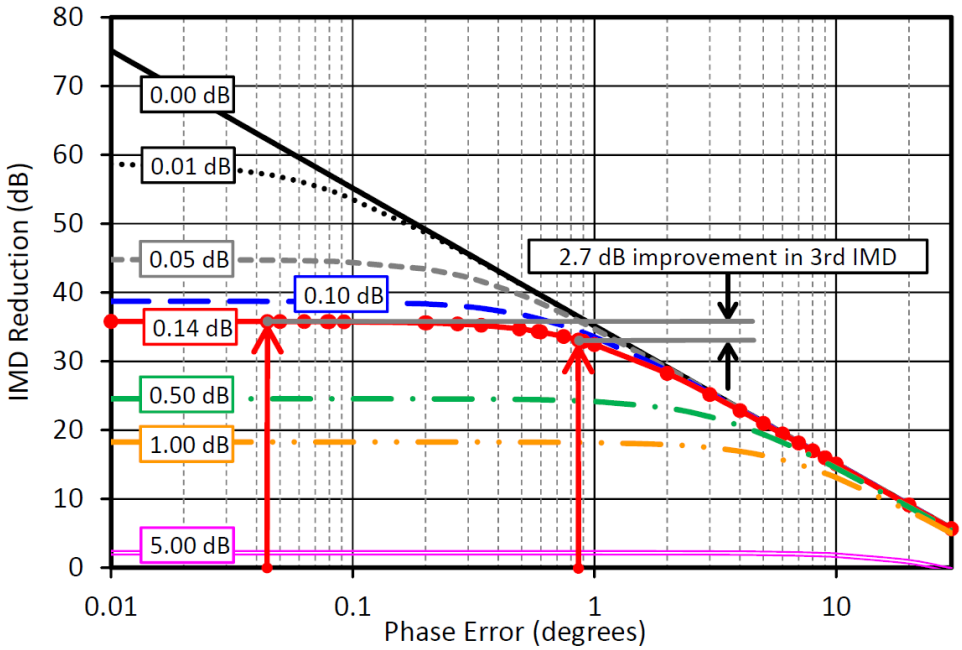

Figure 5.10. Lineariser 3rd IMD reduction versus phase errors for a range of amplitude errors. Improvement in 3rd IMDs as a result of the new model segmentation method when applied to Glock's Fig.11 in [128], 2V2 curve, data.

5.1.7 Summary

In this section we have presented and described a new semi-physical AM/PM model, derived from a simple more accurate AM/AM model, showing its suitability over a range of RF PA device technologies. The combination of the new AM/PM model and more accurate AM/AM model accurately predict 3rd IMD and ACPR performance against measured device data.

A segmented curve-fitting approach, using the new AM/PM model, has also been presented showing up to 20 dB NMSE improvement when modelling amplifier AM/PM characteristics, also resulting in lineariser 3rd IMD improvements of over 5 dB. Simulations of segment boundary discontinuities have shown that worst case discontinuities have no effect on the modeled amplifier spectrum for digitally modulated signals.

Table 5.6. Technology NMSE & linearization improvement comparison.

Device	Cann 12B AM/PM NMSE (dB)		NMSE Improvement (dB)	Seg. IMD Improvement (dB)
	Full	Opt. Seg.		
TWTA [109]	-34.74	-42.81	8.07	0.102
BJT [112]	-53.03	-56.56	3.53	0.002
HFET [145]	-31.98	-48.36	16.38	6.428
LDMOS1 [146]	-31.90	-48.14	16.24	0.046
HBT [147]	-64.24	-75.58	11.34	0.299
E-pHEMT [148]	-34.02	-45.78	11.74	1.018
LDMOS2 [117]	-17.65	-33.71	16.06	0.270
GaAs [128]	-29.77	-52.72	22.95	0.001
CMOS [128]	-53.14	-75.81	22.67	2.700
GaN/SiC [149]	-40.92	-44.79	3.87	0.017

Throughout this section, data from within the literature, manufacturer's datasheets or our testing have been used.

5.2 Memoryless (AM/AM only) Behavioral Model for RF Power Amplifiers

5.2.1 Introduction

With the ever pressing demands for modern wireless communications systems to provide increased data capacity, as well as reduced spectral emissions and increased power efficiencies, RF PA devices play a crucial role in being able to achieve these demanding goals. As such improved behavioural modelling of PA devices at the system level is essential. Having a simple, fast and efficient BM that can be used over a range of device technologies, for RF PA devices, would be most advantageous in allowing the RF PA designer the ability to select this RF PA device quickly and accurately from a range of different devices and technologies. Solid State device AM/AM responses are of the same generic shape, hence having a semi-physical model, enabling the estimation of AM/AM response performance with improved accuracy, for these devices over a large dynamic range and technologies would provide a significant advantage to RF PA

Algorithm 1 Minimize AM/PM NMSE in dB.

Require: Combined AM/PM NMSE (dB) is minimum.

Ensure: V_{in}, V_{out} & ϕ_{out} are real & > 0.

INPUT V_{out} vs. V_{in} & ϕ_{out} vs. V_{in} dataset for the device under test (DUT).
Determine d^2V_{out}/dV_{in}^2 (2^{nd} Deriv.)
if $d^2V_{out}/dV_{in}^2 \neq 0$ after the first occurrence when $d^2V_{out}/dV_{in}^2 = 0$ **then**
    V_{out} vs. V_{in} data does not extend far enough into the Saturation region so extend the V_{out} vs. V_{in} data using [137], refer to Fig. 5.4 (b).
end if
if $d^2V_{out}/dV_{in}^2 = 0$, on the first occurrence. **then**
    $V_{in_{Lin}}$ is the Linear region *stop* point.
else if $d^2V_{out}/dV_{in}^2 = 0$, on the second occurrence. **then**
    $V_{in_{Sat}}$ is the Saturation region *start* point.
end if
Note: ϕ_{out} vs. V_{in} data between $V_{in_{Lin}}$ & $V_{in_{Sat}}$ is the Nonlinear region data.
for $V_{in} = 0$ to $V_{in_{Lin}}$ **do**
    Least Squares Curve Fit (LSCF) ϕ_{out} vs. $V_{in_{Lin}}$ using $\phi(r)$, Eqn. (5.7),
end for
for $V_{in} = V_{in_{Lin}}$ to $V_{in_{Sat}}$ **do**
    LSCF ϕ_{out} using $\phi(r)$, Eqn. (5.7), for the Nonlinear region.
end for
for $V_{in} = V_{in_{Sat}}$ to $V_{in_{max}}$ **do**
    LSCF ϕ_{out} vs. $V_{in_{Sat}}$ using $\phi(r)$, Eqn. (5.7), for the Saturation region data.
end for
for $V_{in} = 0$ to $V_{in_{max}}$ **do**
    Calculate AM/PM NMSE A (dB), using (5.2), for the combined Linear, Nonlinear & Saturation region segments.
    Adjust $V_{in_{Lin}}$ & $V_{in_{Sat}}$ to give $V_{in_{Lin1}}$ & $V_{in_{Sat1}}$
end for
repeat
    Steps 12: to 24: using $V_{in_{Lin1}}$ & $V_{in_{Sat1}}$ calculate AM/PM NMSE B (dB), using Eqn. (5.2), for the *combined* Linear, Nonlinear & Saturation region segments.
until NMSE B (dB) $<$ NMSE A (dB)
Note: It may occur that NMSE A (dB) $<$ NMSE B (dB), i.e. the initial segmentation is optimum.
Output all calculated curve fit coefficients. **END**

designers. Such a model would allow system level modelling and performance evaluation without the need for complex and in depth device models or further complex testing.

This section only focuses on AM/AM modelling, and does not cover AM/PM modelling as covered in Section 5.1, in investigating how simple modelling can be used to quickly asses RF PA device performance for solid state devices, as AM/PM performance can be considered to be small enough to be neglected [111], in some cases. This will also reduce the complexity and computation times thus aiding in a faster device selection process. Improving the AM/AM modelling accuracy will also benefit the RF PA device selection process. Section 5.2.2 presents the need for simple BMs, including a brief review of other modelling approaches and technology modelling capabilities. Benefits of BM accuracy improvements to linearisers performance are discussed in Section 5.2.3. Section 5.2.2 presents a new method that is based on a recent AM/AM model which is capable of producing the correct 3rd IMD response in the small signal region. A segmentation and optimisation method is proposed and discussed that further improves the overall accuracy of the AM/AM model and demonstrates its applicability over a range of different technologies. Consideration of the proposed model and accuracy improvement method, with respect to 3rd IMD performance and impact on linearisation improvement are discussed in Section 5.2.5, followed by a summary.

A summary of the contributions presented in this section are: (i) an Optimised segmented AM/AM curve-fitting approach, using a recent improved accuracy AM/AM model, providing up to 20 dB NMSE improvement, (ii) demonstration of up to 17 dB in linearisers 3rd IMD reduction predication improvement, (iii) an accurate AM/AM model that is applicable for a wide range of solid state power amplifier technologies, (iv) a model parameter fitting approach that uses a simple algorithm and simulation that takes into account segment boundary discontinuities, and (v) demonstration that worst case discontinuities have no noticeable effect on the modeled amplifier spectrum when using digitally modulated signals.

5.2.2 SSPA Behavioural Models - AM/AM

Section 5.1.2 and Section 5.1.2 have discussed the need for simple models and also provided a review of these simple BMs with a summary comparison of these models, along with the definitions of their respective parameters, provided in Table 5.1.

Comparing PA Behavioural Models - AM/AM

To facilitate comparing these BMs, the NMSE in dB can be used. The definition that will be used throughout this section is given by the definition given in [144], as provided in Section 5.1.2 and (5.2).

To evaluate these BMs and the new method presented here, in the frequency domain, comparisons are made using Simulink, where a WCDMA baseband envelope digitally modulated signal is applied to the RF PA model and the output is presented in the frequency domain via the Simulink FFT based spectrum analyzer element, for the AM/AM models described in this section.

AM/AM Model Selection

For the reasons provided in Section 5.1.4, Cann's new memoryless AM/AM model, presented recently [125], will again be used and is given as

$$A(r) = \frac{L}{s} \ln \left[\frac{1 + e^{s(\frac{gr}{L}+1)}}{1 + e^{s(\frac{gr}{L}-1)}} \right] - L, \tag{5.8}$$

where g, r, L and s are the small signal gain, input amplitude, output limit level, and sharpness parameters, respectively. It should be noted that the issues in the old model are related to modelling two discrete tones used to generate IMD products, however for a typical digital modulation scheme no issues were observed. This improved AM/AM model will be used as the basis for this AM/AM modelling method.

5.2.3 Lineariser Benefits From AM/AM Accuracy Improvements

Similar to the discussion of Section 5.1.3 related to the need for low cost RF predistortion linearisers being comparable to DPD linearisers, in terms of accuracy while reducing cost and complexity, Nojima and Konno's analysis is again used to quantify the benefits of this trade-off. Equation (5.3) is used to determine the 3rd IMD reduction benefits, achievable as a result of a PA's AM/AM modelling accuracy improvements, for the combination of a PA and PD when the PD amplitude and phase errors are considered to be fixed. The impact of AM/AM modelling improvement on the 3rd IMDs and linearisation performance, due to the AM/AM accuracy improvement method presented here, is discussed further in Section 5.2.5.

5.2.4 Segmented Curve Fitting Method to Improve AM/AM Model Accuracy

Glock *et al.* [128] recently described a new QM BM for AM/PM. The rationale for the development of this model was that simple static models are both less complex and less computationally intensive. Glock utilized techniques to determine the linear, non-linear and saturation regions from the AM/AM characteristic response and these techniques can also be utilized to determine the linear, non-linear or saturation region segments of AM/AM responses of Cann's 2012 AM/AM model. Furthermore, the curve fits of these segments can be applied in a similar approach to that used by Zhu *et al*, [127], for piecewise curve fitting of non-linear segments of AM/AM and AM/PM envelope-tracking amplifiers. As a result, the segmented curve fitting provides more accurate model results and assists with comparing devices for system analysis purposes, as well as defining potential improvements in linearisation margin for a particular device.

By applying the recent Cann AM/AM model for each segmented region across a range of technologies and by optimising the end of the linear region segment and start of the saturation region segment, an overall improvement of between 5 dB to 20 dB can be achieved in AM/AM NMSE at the expense of further simple processing steps for each segment, depending on RF PA device technology. The recent Cann AM/AM model also has the ability to provide starting values for LSC fitting for each of the segments.

To improve the AM/AM accuracy estimation of this model, the second derivative of the AM/AM response is used to determine both the linear and saturation regions. Using AM/AM data from Glock's Fig. 11 2V2 curve, it can be seen that more data points are required when penetrating further into the saturation region, so the approach developed by [137], based on Rapp's AM/AM model, to extrapolate the AM/AM performance into the saturation region can be used. As Glock's paper uses the Rapp AM/AM model then this AM/AM data can be extended into the saturation region. Similarly for Cann's recent AM/AM model, data can be extended into the saturation region. Using the extended AM/AM data, the transition from the linear to saturation regions can be determined as a function of input level when the 2^{nd} derivative of the AM/AM data equals zero, see Fig. 5.11. As can be seen from this plot, the linear region stop point (vertical blue solid line) occurs when the input level = 0 V and the saturation region start point (vertical orange solid line) occurs well beyond the available data, by the 2^{nd} derivative calculation. This means that the practical LSCF data starting range extends

from when the input level = 0 V to where the input level is at the full extent of the available data (vertical red solid line), in this case when the input level = 0.5 V. The region between the solid blue and red lines is practically the full AM/AM model region for initial LSCF with these points being the starting points for the AM/AM segmentation method optimisation.

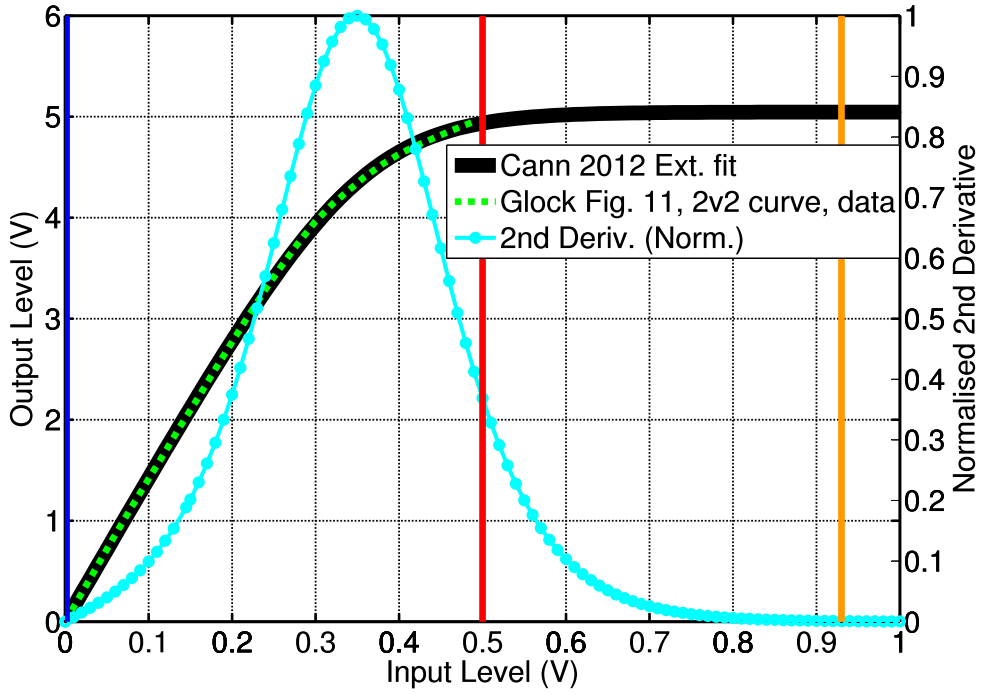

Figure 5.11. Glock's Fig. 11, 2V2 curve. Saturation extension and second derivative response. Glock's Fig. 11, 2V2 curve, [128] AM/AM data (green dotted curve), extended AM/AM data (solid black curve), using [137] & normalised (to the maximum value) numerical 2nd derivative of extended AM/AM data (cyan solid circle curve) using Matlab. The solid blue vertical line is the initial end of the linear region, the solid orange vertical line is start of saturation region by the 2nd derivative calculation. The solid red vertical line is the end of the available AM/AM data, effectively the end of the saturation region for the available data.

Initial AM/AM curve fits for both the recent Cann and Glock (Rapp) AM/AM models have been performed over the entire available data for Glock's Fig. 11, 2V2 curve data, with the results from both the Glock (Rapp) (green down triangle curve) and the recent Cann AM/AM (magenta circle curve) models shown in Fig. 5.12. These are single segment fits between the linear region stop and saturation region start points. This is the same as using the AM/AM model over the entire available data range.

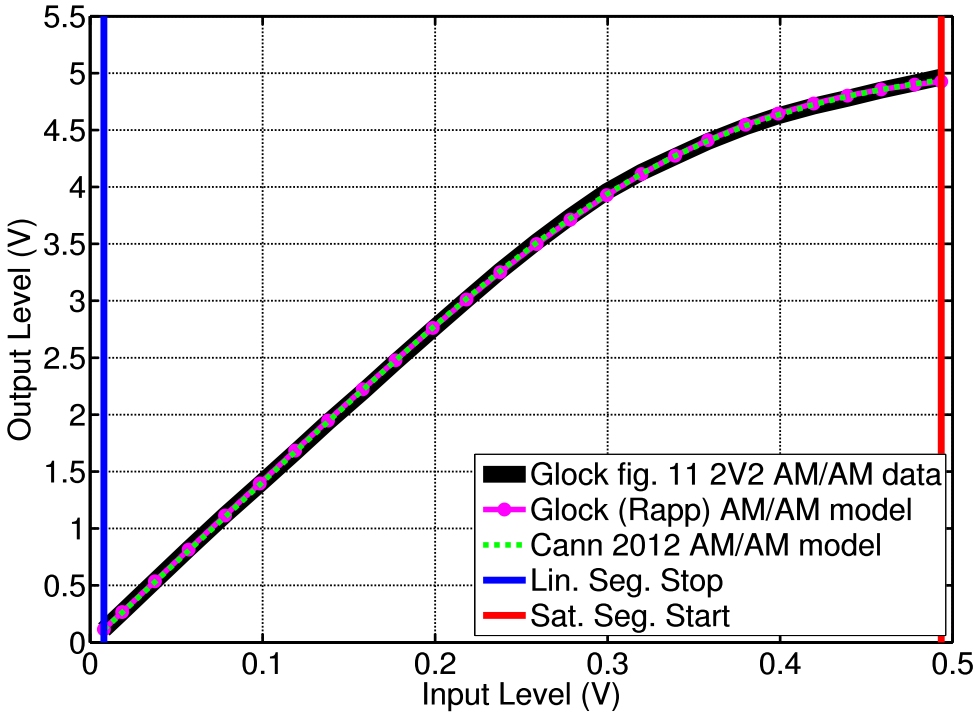

Figure 5.12. Glock Fig. 11, 2V2 curve. AM/AM curve fit comparisons. Comparison of curve fit for Glock Fig. 11, 2V2 curve, data [128] (black solid curve), Glock's (Rapp) AM/AM model (green dotted curve) & recent Cann AM/AM model (magenta solid circle trace).

Optimised Segmented Curve Fitting - AM/AM

To further improve the accuracy of the AM/AM model an optimisation routine was developed to identify the optimum linear stop and saturation start region points to provide an enhanced data fit in terms of NMSE performance. A comparison between the initial fit and the optimised fit for each of the segments is shown in Fig. 5.13 (yellow curves). This is only shown for the recent Cann AM/AM model.

When comparing the LSC fit over the full range of data, Fig. 5.12, compared to the segmented linear, non-linear and saturation region data, Fig. 5.13, it is difficult to see any difference. However a comparison between the Glock (Rapp) and recent Cann absolute AM/AM errors (in dB), for both initial and optimised segmentation versus input voltage for Glock's Fig. 11, 2V2 curve, data are shown in Fig. 5.14, reveals the improvements in absolute error obtained by using the segmentation method. The initial results are shown as solid curves with the optimised segmented results shown as dotted curves. An NMSE AM/AM comparison between these models and the corresponding improvements using the segmentation technique show that, following segmentation

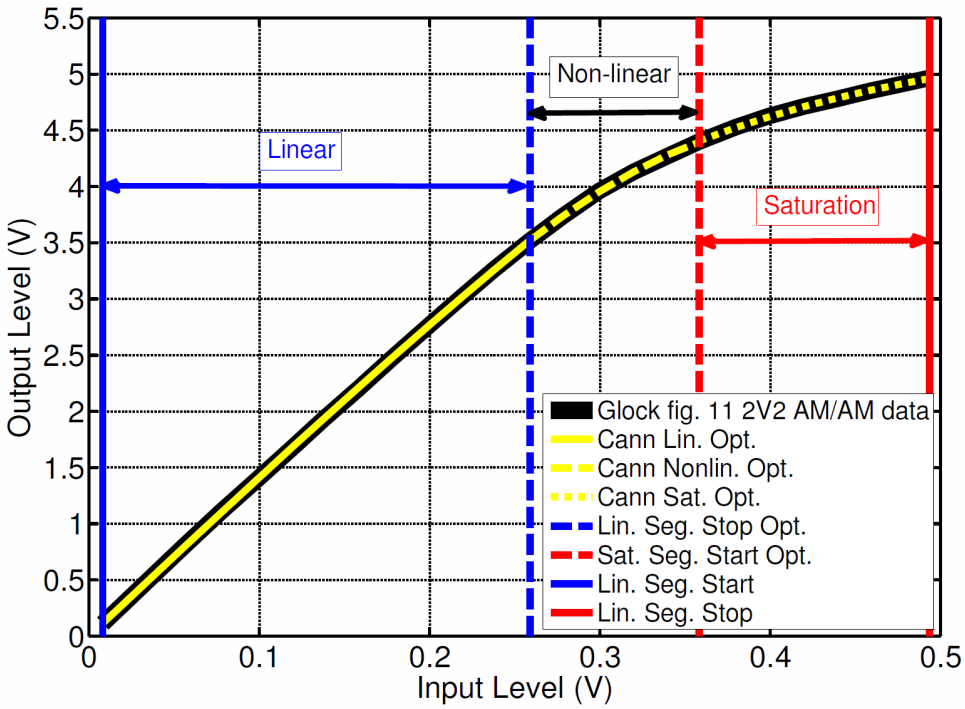

Figure 5.13. Glock Fig. 11, 2V2 curve. AM/AM segmented curve fit comparisons. Comparison of curve fit for Glock Fig. 11, 2V2 curve, data [128] (black solid curve) and the optimised segmented curve fits for the recent Cann AM/AM model (yellow curves). The optimised linear segment is between the input voltage range of 0 V to 0.26 V, with the optimised non-linear segment between 0.26 V and 0.36 V and the remaining saturation segment is between 0.36 V and 0.5 V.

optimisation, the recent Cann AM/AM model has better than 10 dB improvement. In Section 5.2.5, Table 5.7 shows the improvements in NMSE by using the segmentation method over a range of technologies.

An algorithm for optimising segmented curve fitting was prepared to further improve NMSE and is presented as Algorithm 2. The algorithm starting points for the second derivatives cannot be zero due to their numerical nature, so there is a requirement to have 2^{nd} derivative zero limits, in our case we have selected this value to be below 0.001, to suit the numerical data. During the minimisation process there are some segment ranges where the discontinuities at segment boundaries are higher than the given data resulting in poorer segment fits. This is due to using parameter starting values for the full range of data in those segments. This can be corrected by determining suitable starting points for each segment but this has not been implemented within this algorithm. Even with such improvement in the starting point, the overall curve fit performance is still worse than the segmented approach.

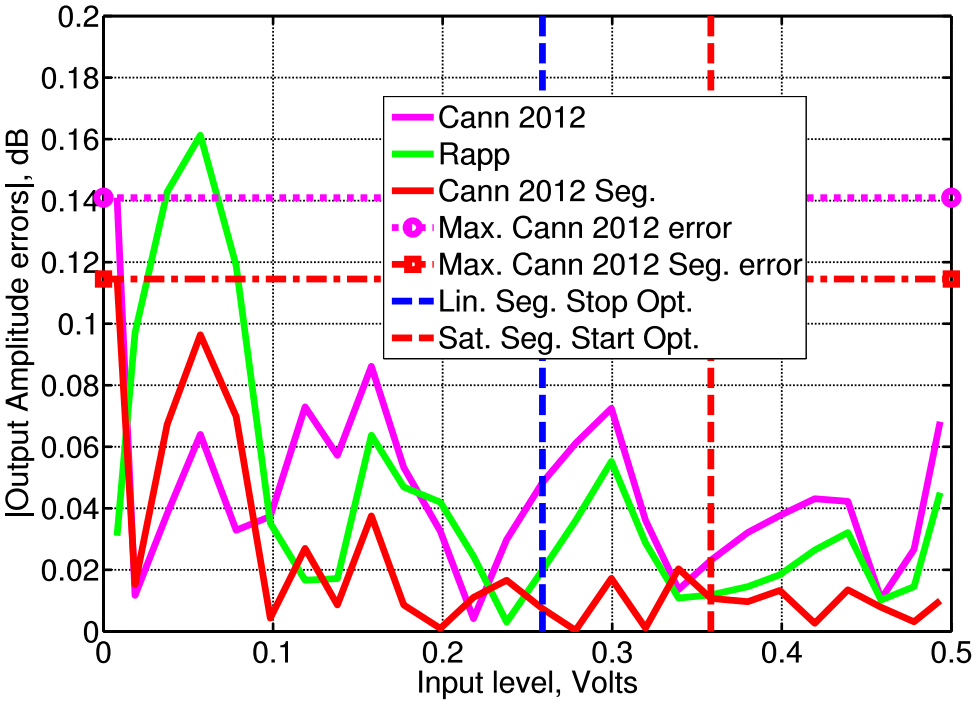

Figure 5.14. Glock Fig. 11, 2V2 curve. AM/AM output amplitude error comparisons. Comparison of |Output Amplitude errors| versus input voltage from Glock's Fig. 11, 2V2 curve, data [128], showing before and after segmented approach optimisation. Also shown are the maximum for Cann's recent AM/AM model amplitude errors for both the initial (magenta solid line) & segmented (red solid line) approach being 0.14 and 0.115 dB respectively.

Frequency Domain Comparisons & Discontinuity Effects at Segment Boundaries - AM/AM

A comparison of the recent Cann model, with and without optimised segmentation, against measured data with a WCDMA signal applied, for the SHF-0189 HFET [145], are given in Fig. 5.15. These plots show that the optimised segmentation method provides a better fit to the measured data compared to the non segmented model.

To determine the effects of discontinuities, due to not having continuous derivatives over the segment boundaries, further investigation of Cann's AM/AM model showed that after optimisation, the voltage errors between the segment boundaries are very small and have a negligible effects on the ALCR response. This has been investigated using a digitally modulated WCDMA signal with the same power spectral density level as used in Glock's Fig. 9. The worst case discontinuity error, of 0.0111 volts, for either of the linear-to-nonlinear or nonlinear-to-saturation segment boundaries was increased, above the optimised value, until the second ACLR level increased by ≈ 1

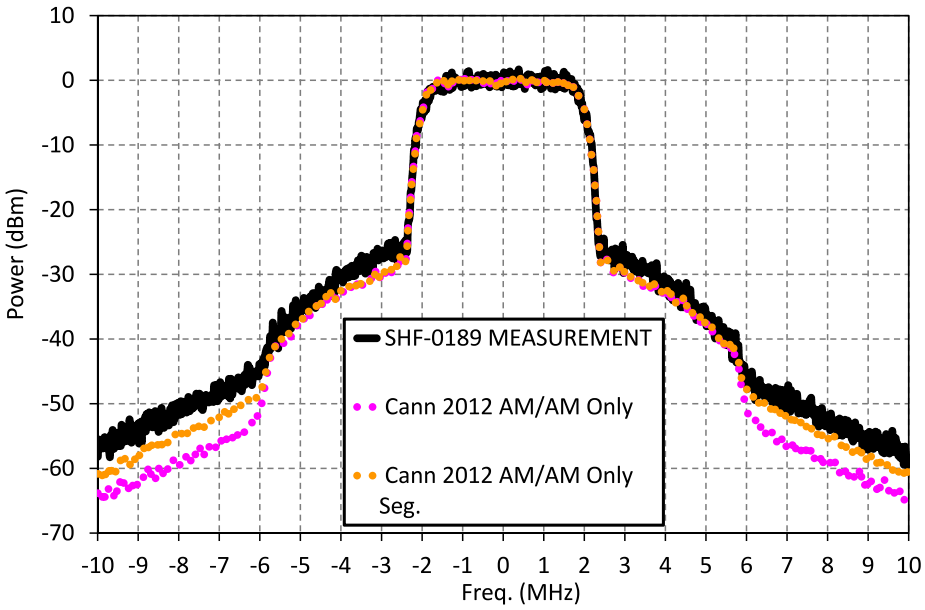

Figure 5.15. Comparison of measured versus Simulink simulations for WCDMA, AM only. Comparing Glock versus recent Cann full & Optimised segmented models for the SHF-0189, [145], data. Resolution bandwidth for both measured & simulation data is 30 kHz. Measured center frequency is 881.5 MHz.

dB and this occurred at 10 times the worst case discontinuity error. So it is clear that the Optimised segmented recent Cann AM/AM model has negligible discontinuity effects, even when considering worst case discontinuities at the segment boundaries. Comparisons between the Optimised segmentation discontinuity error result and 10 times this error are shown in Fig. 5.16.

5.2.5 Impact on IMDs & Linearisation Improvement - AM/AM

Cann's recent AM/AM model and the optimised segmentation method have been assessed to determine how they perform in predicting 3rd IMD performance for RF PAs over a wide dynamic range by simulating the 3rd IMDs using Simulink and comparing the simulations against manufacturer's measured IMD data, SHF-0189 device [155] page 5. Plots of the 3rd IMD comparisons are shown in Fig. 5.17 with comparisons of the absolute 3rd IMD errors shown in Fig. 5.18. The results indicate that the recent Cann AM/AM model performs better than the Rapp or O'Droma AM/AM (Modified Saleh) models, even though the O'Droma (Modified Saleh) model shows very good curve fitting results. The recent Cann AM/AM model has $\approx$ 2.6 dB improvement in

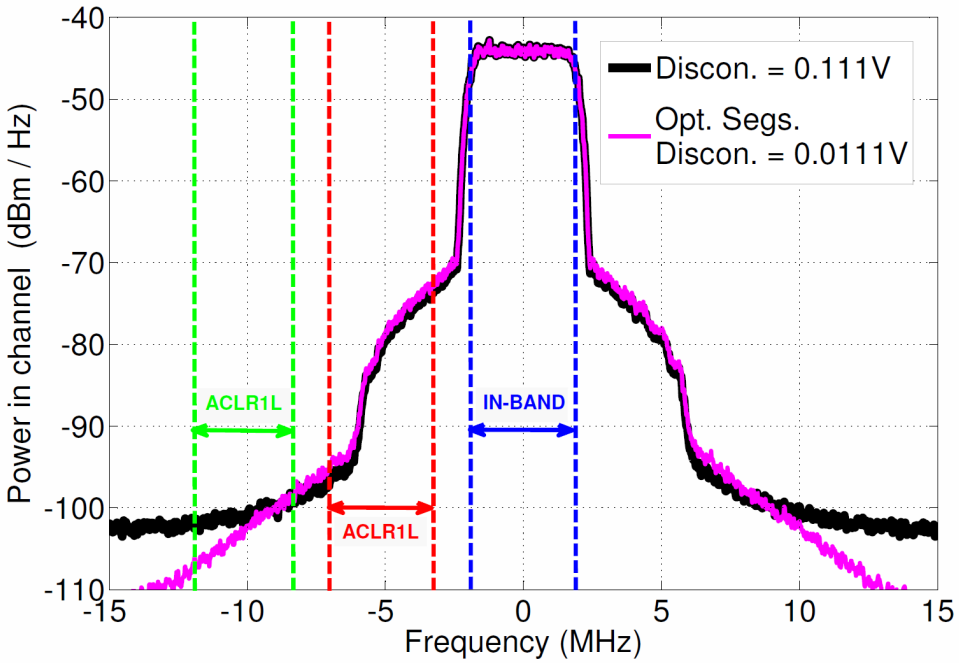

Figure 5.16. Discontinuity effects on a WCDMA modulated signal, simulated using Simulink, AM/AM only. Cann's recent Optimised segmented AM/AM model of Glock's Fig.11, 2V2 curve, data [128] data. With no discontinuity ACLR1L/2L = -33.75/-56.2 dBc. With 0.111 volt discontinuity ACLR1L/2L = -33.0/-57.3 dBc. In-band wanted between dashed blue vertical lines, ACLR1 between dashed red vertical lines and ACLR2 between dashed green vertical lines (lower bands only shown) with 3.84 MHz integration bandwidth. The integrated power over the wanted 3.84 MHz BW is 21.6 dBm. RBW is 30 kHz.

AE compared to the O'Droma model and over 10 dB AE improvement compared to the Glock (Rapp) model. The optimised segmented method, using the recent Cann AM/AM model, improves the AE by a further $\approx$ 0.7 dB.

The maximum absolute amplitude error, of the full and optimised segmented method, using the recent Cann AM/AM model, of Glock's Fig. 11 AM/AM device data, from LSC fitting, are 0.141 dB and 0.115 dB respectively. These are shown on a plot of (5.3), Fig. 5.19, where the intermodulation distortion improvement is plotted against phase error for various amplitude errors. The difference between the full and optimised segmented method equates to a 3rd IMD improvement of 1.79 dB at 0.1° phase error.

Table 5.7 shows the NMSE for each of the various technologies, BJT, HFET, LDMOS FET, HBT, E-pHEMT, GaAs (Glock's Fig. 8 device data), CMOS (Glock's Fig. 11 device data) and GaN on SiC HEMT. The AM/AM NMSEs were determined for both the full and segmented methods. Table 5.7 also shows the 3rd IMD linearisation improvement

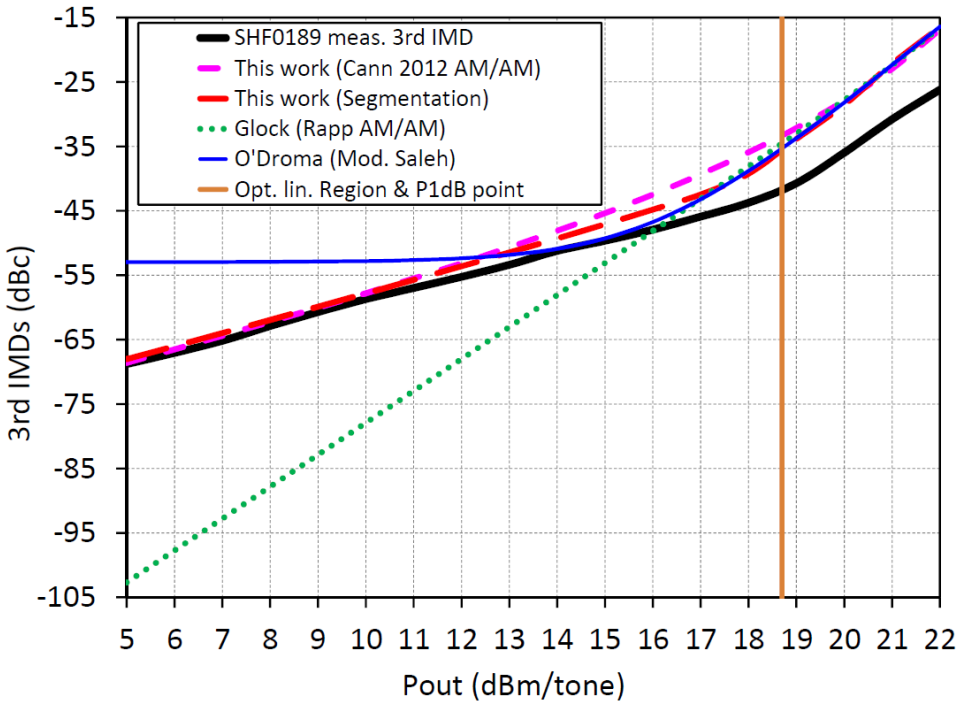

Figure 5.17. SHF-0189 measured device 3rd IMD data versus Simulink simulation comparison, AM only. [155] page 5, comparing O'Droma (Modified Saleh), Glock & recent Cann models, all including both AM/AM components. Two tone measurements at 900 MHz, 1 MHz tone spacing.

across device technology as a result of the optimised segmentation method AM/AM improvements.

5.2.6 Summary

In this section we have presented and demonstrated the use of a more accurate simple AM/AM model that is suitable for use over a range of RF PA device technologies.

A segmented curve-fitting approach, using the proposed recent AM/AM model, has also been presented that provides up to 20 dB NMSE improvement when modelling the AM/AM characteristics of the amplifier, further resulting in lineariser 3rd IMD improvements of up to 17 dB.

A model parameter fitting approach using a simple algorithm has been indicated along with simulations accounting for segment boundary discontinuities, demonstrating that such worst case discontinuities have no effect on the modeled amplifier spectrum when using digitally modulated signals.

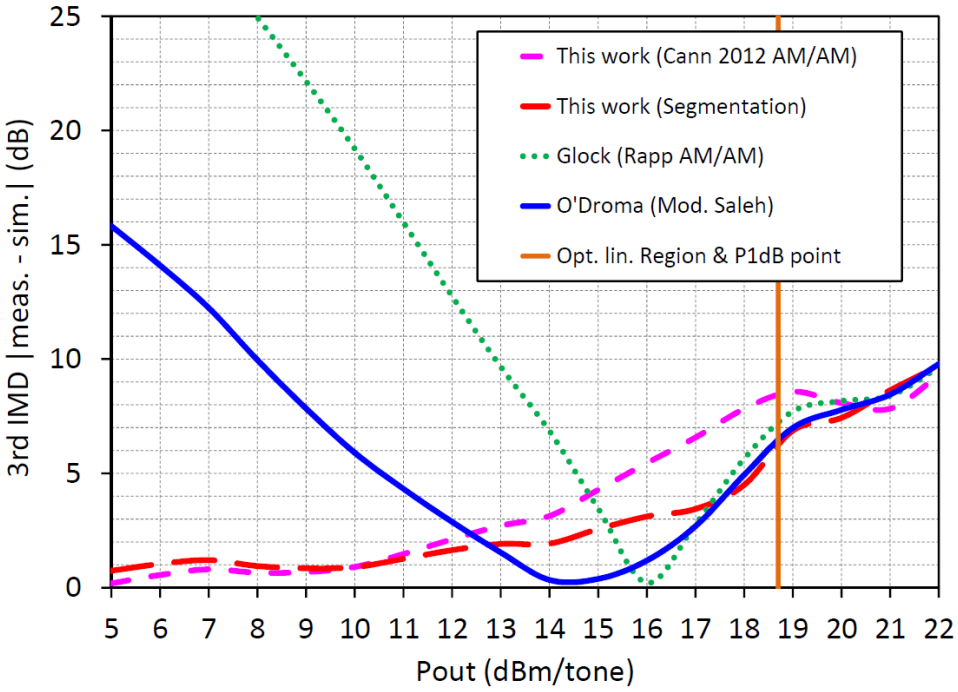

Figure 5.18. SHF-0189 measured device 3rd IMD data versus Simulink simulation error comparison, AM only. 3rd IMD |measured minus Simulink simulated| error for the O'Droma (Modified Saleh), Glock (Rapp), recent Cann & Optimised segmented recent Cann models for AM/AM only. The AE for Cann's recent AM/AM model is $\approx$ 4dB compared to $\approx$ 6.5 & 13.9 dB for the O'Droma and Glock (Rapp) models respectively. The Optimised segmented recent Cann model AE further improves 3rd IMD over the recent Cann model by $\approx$ 0.7 dB.

Table 5.7. Technology NMSE & linearisation improvement comparison AM/AM only.

Device	Cann 12B AM/AM NMSE (dB)		NMSE Improvement (dB)	IMD Improvement (dB)
	Full	Segmented		
BJT [112]	-30.16	-35.28	5.12	3.02
HFET [145]	-43.53	-62.84	19.31	13.51
HBT [147]	-58.88	-64.86	5.98	6.43
E-pHEMT [148]	-44.77	-63.41	18.64	13.90
LDMOS [117]	-37.68	-42.40	4.72	1.39
GaAs [128]	-39.61	-58.20	18.59	0.75
CMOS [128]	-46.04	-56.07	10.03	1.79
GaN/SiC [149]	-43.10	-48.40	5.30	17.62

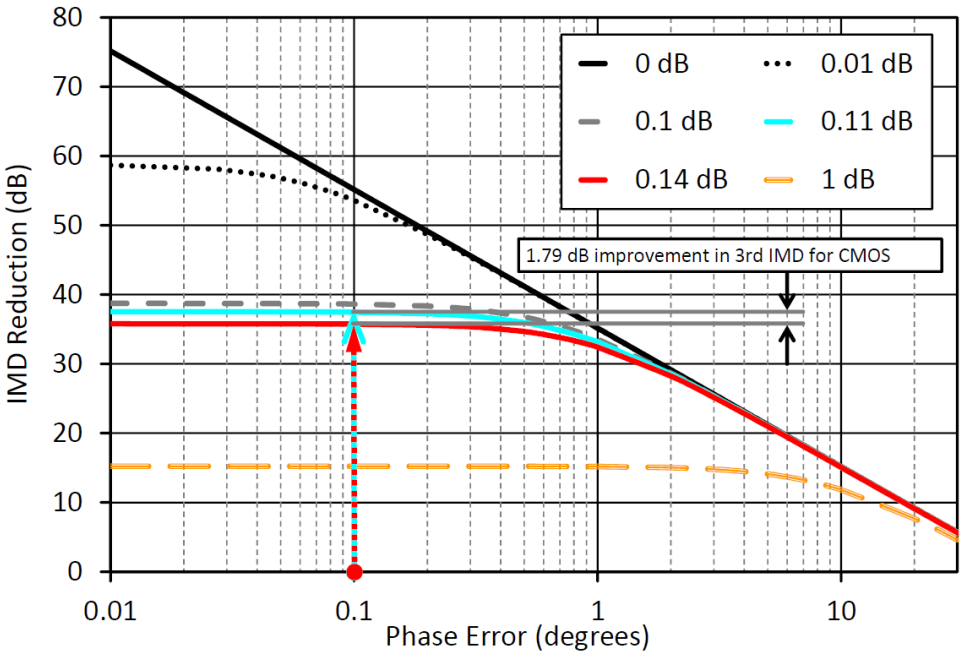

Figure 5.19. Lineariser 3rd IMD reduction versus phase errors for a range of amplitude errors, AM only. The cyan vertical arrow shows the 3rd IMD improvement in linearisation for the optimised segemnted approach compared to the full recent Cann AM/AM model, red dotted vertical arrow, both at 0.1° phase error.

5.3 Conclusion

This chapter has presented and demonstrated a new semi-physical AM/PM model, derived from a simple more accurate AM/AM model, showing its suitability over a range of RF PA device technologies. The combination of the new AM/PM model and more accurate AM/AM model accurately predict 3rd IMD and ACPR performance against measured device data.

A segmented curve-fitting approach, using the new AM/PM model, has also been presented showing up to 20 dB NMSE improvement when modelling amplifier AM/PM characteristics, also resulting in lineariser 3rd IMD improvements of over 5 dB. Simulations of segment boundary discontinuities have shown that worst case discontinuities have no effect on the modeled amplifier spectrum for digitally modulated signals.

Throughout this chapter, data from within the literature, manufacturer's datasheets or testing has been used. For any device selection it is recommend that appropriate testing on one or more devices be performed in order to validate any device performance against requirements.

5.3 Conclusion

This chapter has also presented and demonstrated the use of a more accurate simple AM/AM model that is suitable for use over a range of RF PA device technologies.

A segmented curve-fitting approach, using the proposed recent AM/AM model, has also been presented that provides up to 20 dB NMSE improvement when modelling the AM/AM characteristics of the amplifier, further resulting in lineariser 3^{rd} IMD improvements of up to 17 dB over the range of technologies shown in Table 5.7.

A model parameter fitting approach using a simple algorithm has been indicated along with simulations accounting for segment boundary discontinuities, demonstrating that such worst case discontinuities have no effect on the modeled amplifier spectrum when using digitally modulated signals.

In the next chapter the use of some of these simple behavioural models has been applied to simple low cost analog pre-distorter linearisers in line with less complex, low cost approaches more suited to small cell cellular repeaters compared to more expensive and complex, power hungry DPD approaches.

Algorithm 2 Minimize AM/AM NMSE in dB.

Require: Combined AM/AM NMSE (dB) is minimum.

Ensure: V_{in} & V_{out} are real & > 0.

1: **INPUT** V_{out} vs. V_{in} data-set for the amplifier.
2: Determine d^2V_{out}/dV_{in}^2 (2^{nd} Derivative)
3: **if** $d^2V_{out}/dV_{in}^2 \neq 0$ after the first occurrence when $d^2V_{out}/dV_{in}^2 = 0$ **then**
4: V_{out} vs. V_{in} data does not extend far enough into the saturation region so extend the V_{out} vs. V_{in} data using [137], refer to Fig.5.11.
5: **end if**
6: **if** $d^2V_{out}/dV_{in}^2 = 0$, on the first occurrence. **then**
7: $V_{in_{Lin}}$ is the linear region *stop* point.
8: **else if** $d^2V_{out}/dV_{in}^2 = 0$, on the second occurrence. **then**
9: $V_{in_{Sat}}$ is the saturation region *start* point.
10: **end if**
11: Note: V_{out} vs. V_{in} data between $V_{in_{Lin}}$ & $V_{in_{Sat}}$ is the non-linear region data.
12: **for** $V_{in} = 0$ to $V_{in_{Lin}}$ **do**
13: Least Squares Curve Fit (LSCF) V_{out} vs. $V_{in_{Lin}}$ using (5.8)
14: **end for**
15: **for** $V_{in} = V_{in_{Lin}}$ to $V_{in_{Sat}}$ **do**
16: LSCF V_{out} using (5.8), for the non-linear region.
17: **end for**
18: **for** $V_{in} = V_{in_{Sat}}$ to $V_{in_{max}}$ **do**
19: LSCF V_{out} vs. $V_{in_{Sat}}$ using (5.8), for the saturation region data.
20: **end for**
21: **for** $V_{in} = 0$ to $V_{in_{max}}$ **do**
22: Calculate AM/AM NMSE A (dB), using (5.2), for the combined linear, non-linear & saturation region segments.
23: Adjust $V_{in_{Lin}}$ & $V_{in_{Sat}}$ to give $V_{in_{Lin1}}$ & $V_{in_{Sat1}}$
24: **end for**
25: **repeat**
26: Steps 12: to 24: using $V_{in_{Lin1}}$ & $V_{in_{Sat1}}$ calculate AM/AM NMSE B (dB), using (5.2), for the *combined* linear, non-linear & saturation region segments.
27: **until** NMSE B (dB) $<$ NMSE A (dB)
28: Note: It may occur that NMSE A (dB) $<$ NMSE B (dB), i.e. the initial segmentation is optimum.
29: Output all calculated curve fit coefficients. **END**

Chapter 6

RF PA Linearisation Techniques

THIS chapter describes an envelope predistortion lineariser scheme that uses integrated analog components for the low cost implementation of IMD reduction in RF PAs. Integrated logarithmic amplifiers and phase detectors are used to sample the input and output signals before and after the RF PA to measure the complex gain and phase information, which is used to control an integrated predistorter IC that contains adjustable gain and phase components within a single IC package. Comparisons of a range of well-known and developed RF PA behavioural models are evaluated to determine the most suitable behavioural model for this linearisation scheme, including the RF PA driver and memory effects. All component models are based on parameters extracted from readily available device datasheets for the driver and RF PA, thus minimizing the need for extra measurements.

6.1 Analog RF Predistorter Simulation using Well-Known Behavioural Models - Introduction

There is a continual need for improved spectrally efficient communication schemes at ever reducing costs. The RF PA is a major component within a communication system thus having a significant impact on both the spectral purity and system cost. It is therefore important to consider the performance of the RF PA to achieve these system requirements. To achieve maximum system efficiency then an RF PA needs to be operated at or near its maximum output power. With today's digital modulation, such a need impacts on spectral regrowth and other users, so linearisation schemes must be employed to overcome this shortcoming. The type of linearisation scheme will also have an impact on both the output spectrum and overall system cost. This chapter investigates a simple low cost lineariser implementation using readily available analog components. The use of these simple components offers moderate linearisation improvements at low cost compared to more complex; in size, implementation cost and power consumption, digital pre-distortion or other linearisation schemes such as Cartesian loop or feed forward, or envelope restoration, Kennington [156]. This chapter demonstrates that gain and phase detection offer the benefit of reducing lineariser complexity by eliminating any down / up conversions, also reducing potential spurious issues and system complexity and costs are also reduced by combining the lineariser elements within a single IC. An estimate of the PCB area needed for this lineariser is 25 mm x 25 mm. In addition, this chapter evaluates a number of behavioural models and demonstrates their linearisation performance when included in this proposed linearisation approach.

6.2 Proposed linearisation Scheme

The envelope pre-distortion scheme to be used is shown in Fig. 6.1 based on Woo [157]. This scheme uses simple low cost readily available analog ICs. The original paper [157] uses individual discrete Voltage Variable Attenuators (VVAs) and Voltage Variable Phase Shifters (VVPSs), whereas this chapter proposes the use of an all-in-one adjustable gain and phase shifter linearisation IC from Maxim, the MAX2010 [158] shown in Fig. 6.2.

The MAX2010 offers a range of gain and phase breakpoints that are adjustable thus suitable for a range of RF PA gain and phase expansion points. Coarse and fine gain

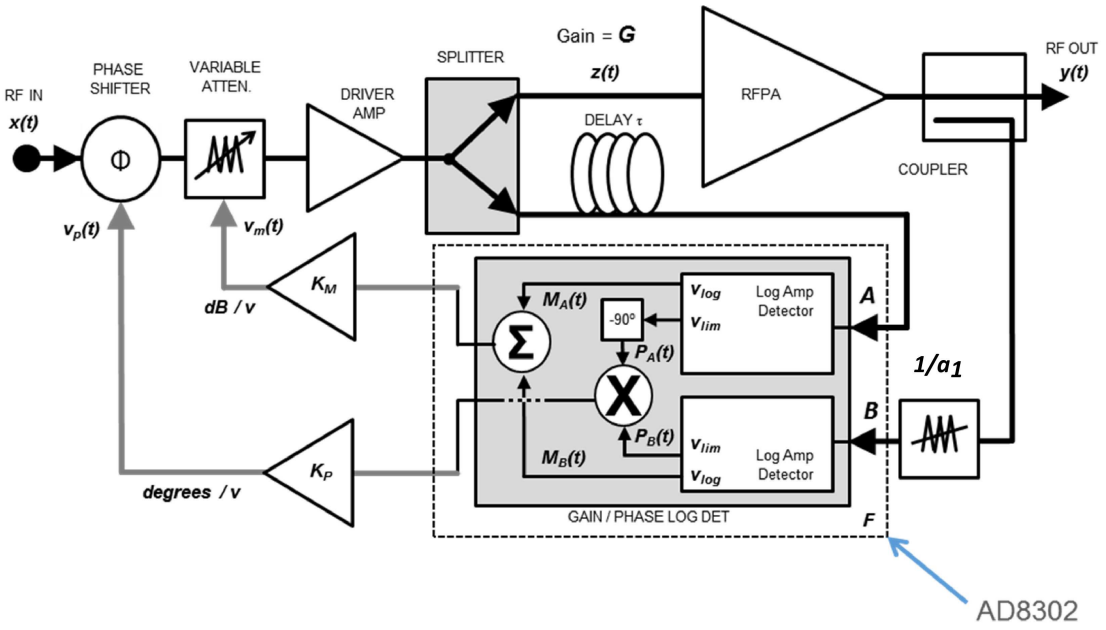

Figure 6.1. Analog envelope pre-distortion lineariser. Analog envelope pre-distortion lineariser from Woo [157] including driver amplifier and splitter.

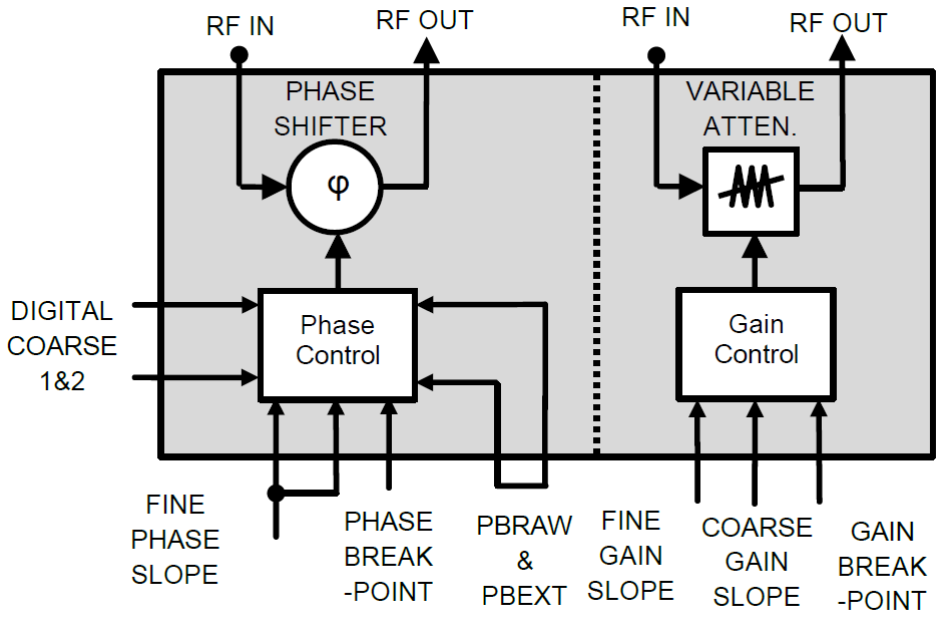

Figure 6.2. Maxim MAX2010, gain and phase lineariser IC. [158].

and phase slope adjustments are also available for wide range of RF PAs. The MAX2010 device data is sufficient to enable the extraction of the needed phase and gain parameters for the behavioural models. Parameters K_M and K_P are formed via operational amplifiers and these can be optimally adjusted for magnitude and phase gains plus

offsets to cater for the 30 mV/dB and 10 mV/° slopes of the Analog Devices gain / phase logarithmic detector, AD8302 IC [159].

6.2.1 Lineariser Theory

The theory of this lineariser is as follows. An example lineariser structure is as shown in Fig. 6.3

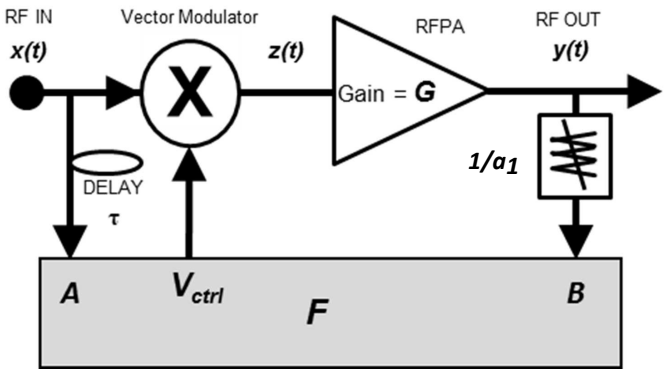

Figure 6.3. Existing predistortion model.

where $x(t)$ = input signal, $z(t)$ = predistorted input signal to the RF PA, $G\{\bullet\}$ = complex gain function of the RF PA and $F\{\bullet\}$ = pre-distortion function. Conventional predistorters use $x(t)$ to calculate the predistortion function $F\{\bullet\}$.

$$\begin{aligned} y(t) &= z(t) \cdot G(|z(t)|) && (6.1)\\ &= [x(t) \cdot F(|x(t)|)] \cdot G(|z(t)|), && (6.2)\\ &= [x(t) \cdot F(|x(t)|)] \cdot G(|x(t) \cdot F)|x(t)|)|). && (6.3) \end{aligned}$$

$$G(|z(t)|) \cong \sum_{k=1}^{n} a_k \cdot |z^{(k-1)}(t)|. \quad (6.4)$$

where a_k are complex coefficients of kth order and $F(|x(t)|)$ = Polynomial pre-inverse of $G(|x(t) \cdot F(|x(t)|)|)$. However determining the inverse of $G(\bullet)$ is complex and not straightforward for an analog implementation. For analog implementation the lineariser can be configured as shown in Fig. 6.4

Using $z(t)$ as the reference signal,

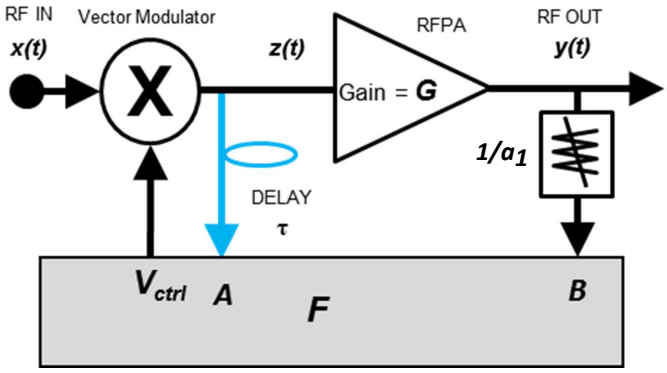

Figure 6.4. New predistortion model. New predistortion model.

$$y(t) = z(t) \cdot G(|z(t)|), \tag{6.5}$$

$$= [x(t) \cdot F(|z(t)|)] \cdot G(|z(t)|). \tag{6.6}$$

$$F(|x(t)|) = a_1 \cdot G^{-1}(|z(t)|). \tag{6.7}$$

where $F(\bullet)$ = the inverse of $G(\bullet)$, a_1 sets the overall system gain and τ, shown in Fig. 6.4, equalises the delay between $z(t)$ and $y(t)$ and this can be implemented using analog components, as shown in more detail in Fig. 6.1.

6.2.2 Logarithmic Detector Theory

Referring to Fig. 6.1 the controlling inputs to the vector modulator's voltage variable attenuator and phase shifter, from the gain / phase detector's outputs are given by

$$V_{MAG}(t) = V_{SLP} \cdot \log\left[\frac{M_A(t)}{M_B(t)}\right], \tag{6.8}$$

$$V_{PHS}(t) = V_{\phi} \cdot [\angle P_A - \angle P_B - 90^{\circ}]. \tag{6.9}$$

where parameters V_{SLP} and V_{ϕ} are the voltage slope in V/dB and phase slope in $^{\circ}$/dB respectively. M_A and M_B are the magnitudes of the AD8302's inputs and P_A and P_B are the phases of the AD8302's inputs. For the logarithmic detector, AD8302 [159], this device can be modeled by the following equations

$$V_{out}(t) = K_{SLP} \cdot \log\left[\frac{V_{in}(t)}{V_L}\right] + \epsilon. \tag{6.10}$$

where K_{SLP} = detector log slope, V_L = minimum input voltage and ϵ = deviation from ideal,

$$V_{in}(t) = Re[(v_{Iin}(t) + jv_{Qin}(t))e^{j\omega_c t}], \tag{6.11}$$

$$A(t) = \sqrt{v_{Iin}^2(t) + v_{Qin}^2(t)}. \tag{6.12}$$

where $A(t)$ is the envelope of the input signal,

$$P_A = 10\log\left[\frac{A^2(t)}{2R_{in}}\right] + 30. \tag{6.13}$$

where P_A is the power of the envelope in dBm,

$$\epsilon = SE\sin\left[2\pi\left(\frac{P_A - P_{Min}}{E_c}\right)\right]. \tag{6.14}$$

where S = sensitivity (V/dB), E = peak log error (dB), E_c = log cycle error (dB) and P_{Min}= minimum input power in dBm.

$$V_L = \sqrt{2}\left[R_{in}10^{\left(\frac{P_{Min}-30}{10}\right)}\right]^{0.5}. \tag{6.15}$$

where V_L is the voltage level corresponding to P_{Min},

$$M(t) = 20S\log\left[\frac{A(t)}{V_L}\right] + \epsilon \quad ,if A(t) < V_L \tag{6.16}$$

$$= 0 \quad ,otherwise. \tag{6.17}$$

Then

$$V_{out} = \left[\frac{M(t)}{A(t)}\right] v_{in}(t). \tag{6.18}$$

These equations are used for the Simulink modeling discussed in Section 6.4.

6.2.3 Vector Modulator Elements

The vector modulator consists of the VVA and VVPS elements. Details relating to the amplitude and phase variations for these elements are given in Section 6.2.3 and 6.2.3 that follow.

Voltage Variable Attenuator

The VVA's gain and phase vary with applied voltage with the phase change being minimal as shown in Fig. 6.5. This element is modeled using a 5^{th} order polynomial with co-efficients as given in Table 6.1.

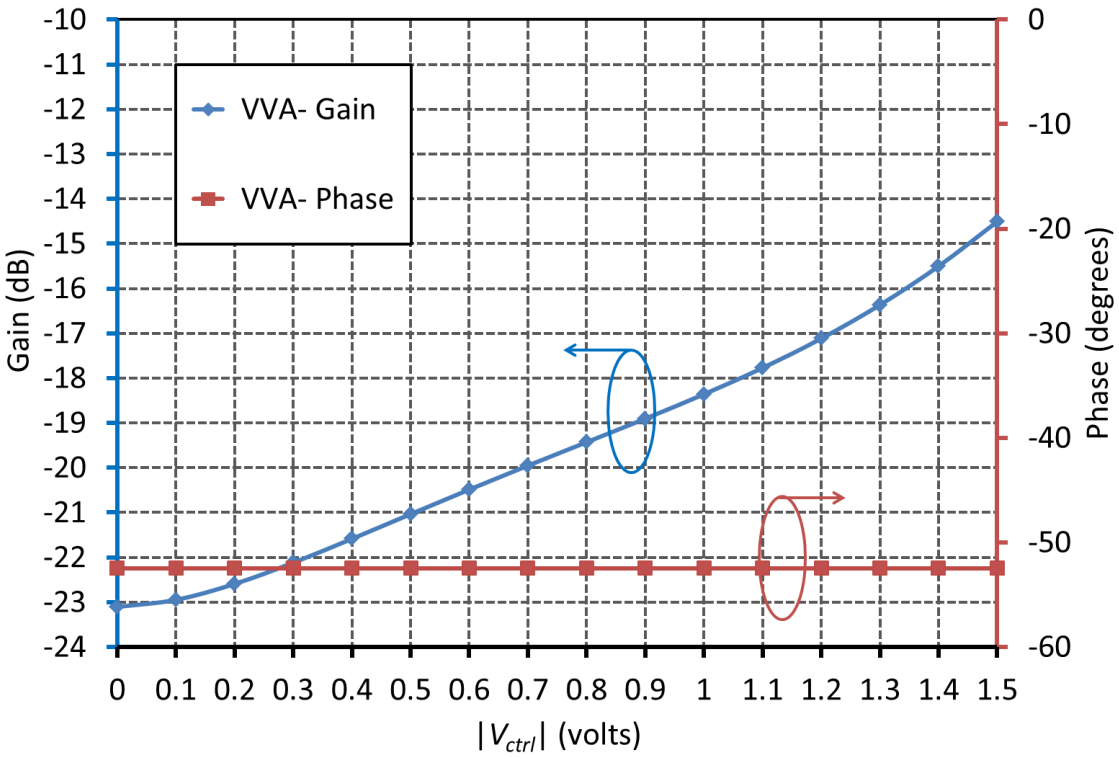

Figure 6.5. Voltage variable attenuator response. VVA Gain and phase response versus $|V_{ctrl}|$.

Voltage Variable Phase Shifter

Similar to the VVA the VVPS's gain and phase vary with applied voltage with this time the gain change being minimal as shown in Fig. 6.6. This element is also modeled using a 5^{th} order polynomial and the co-efficients are given in Table 6.2.

Table 6.1. VVA 5th order polynomial coefficients.

Coefficient	Gain (dB)	Phase (°)
x_0	-23.10	-52.48 (constant)
x_1	0.25	-52.48
x_2	15.06	-52.48
x_3	-19.53	-52.48
x_4	11.01	-52.48
x_5	-2.04	-52.48

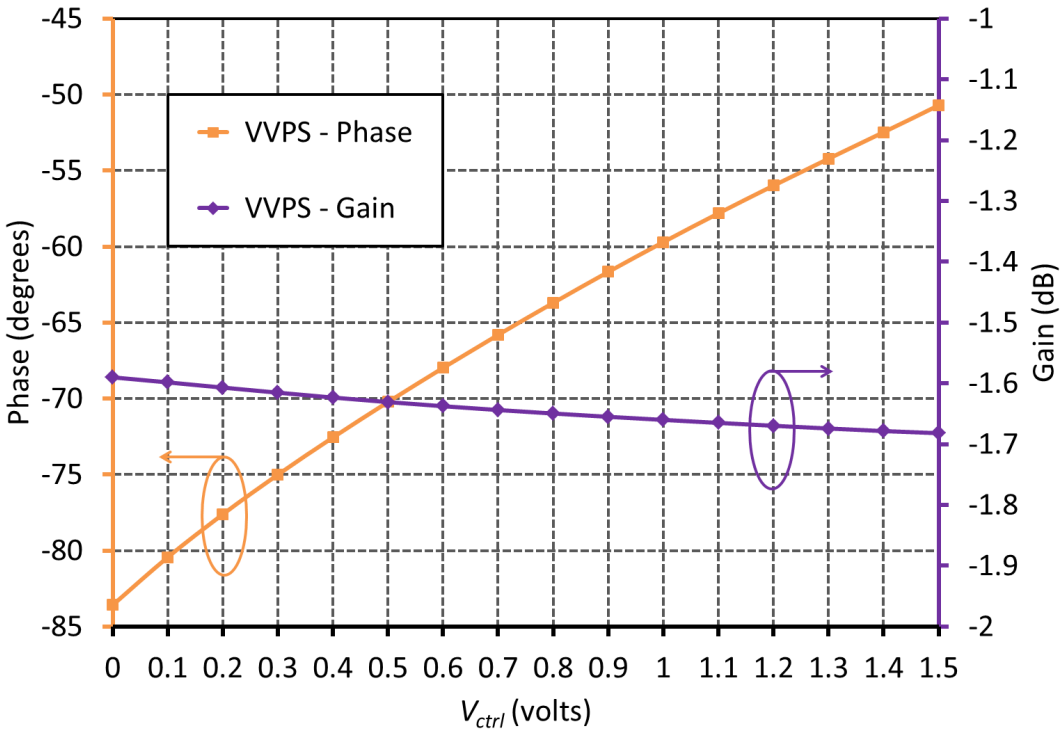

Figure 6.6. Voltage variable phase shifter response. VVPS Phase and gain response versus V_{ctrl}.

6.2.4 RF Power Amplifier

The RF PA device used is the same as the one used in [157]. This amplifier is a 0.5 W, GaAs HFET PA, Sirenza SHF-0189, operated at 881.5 MHz. The AM/AM and AM/PM characteristics versus Pin are shown in Fig. 6.7. For modeling this RF PA, the original Rapp model [111] is used for the amplitude response, while the phase model used is based on the updated version of the Honkanen and Haggman phase model [112] as given in Table 6.3.

Table 6.2. VVPS 5th order polynomial coefficients.

Coefficient	Gain (dB)	Phase (°)
x_0	-0.02	3.22
x_1	-0.08	-13.63
x_2	0.11	22.52
x_3	-0.04	-21.64
x_4	-0.08	33.41
x_5	-1.59	-83.58

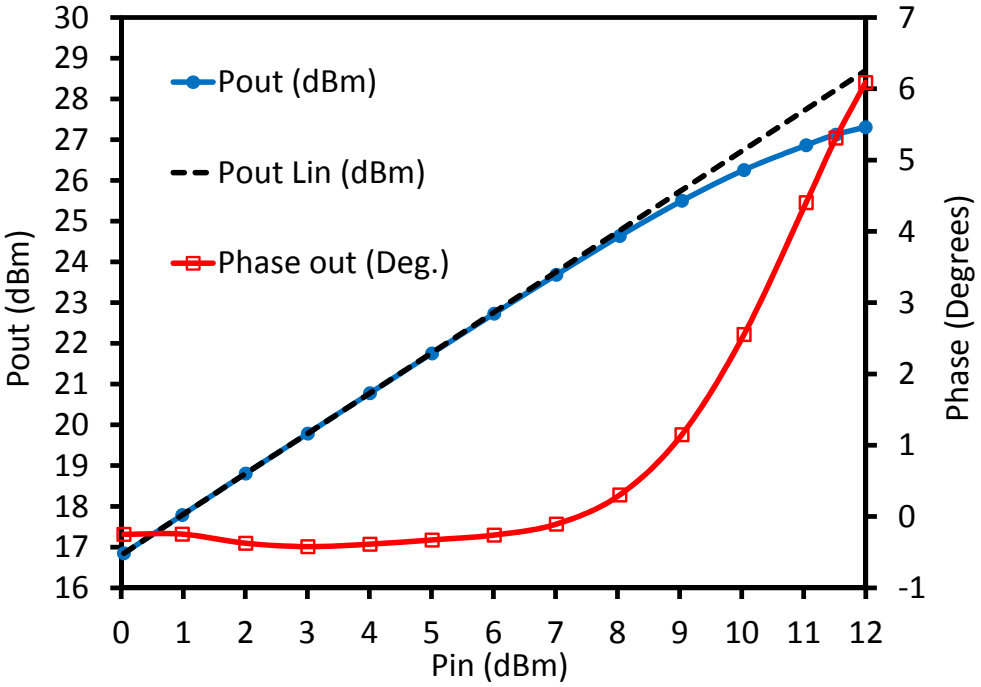

Figure 6.7. Sirenza SHF-0189 Pin versus Pout and phase data. Derived from Woo [157].

For this study, several other well-known models, with some recent additions as detailed in Table 6.3 [112, 109, 110, 113, 114, 137], were also used to model the RF PA device data and a comparison has been made to evaluate their applicability for this type of linearisation scheme.

Table 6.3. Improved simple behavioural models for RF power amplifiers.

Model	AM/AM	AM/PM
	r = input voltage,	
	$A(r)$ = output voltage	$\phi(r)$ = output phase
Saleh [109]	$A_{\text{Saleh}}(r) = \frac{\alpha_a r^{\eta_a}}{(1+\beta_a r^{\gamma_a})^{\nu_a}} - \epsilon_a = \frac{\alpha_a r}{1+\beta_a r^2}$ α_a = AFP, β_a = AFP, $\eta_a = 1$, $\gamma_a = 2$, $\nu_a = 1$, $\epsilon_a = 0$	$\phi_{\text{Saleh}}(r) = \frac{\alpha_\phi r^{\eta_\phi}}{(1+\beta_\phi r^{\gamma_\phi})^{\nu_\phi}} - \epsilon_\phi = \frac{\alpha_\phi r}{1+\beta_\phi r^2}$ α_ϕ = PFP, β_ϕ = PFP, $\eta_\phi = 1$, $\gamma_\phi = 2$, $\nu_\phi = 1$, $\epsilon_\phi = 0$
Ghorbani and Sheikan [110]	$A_{\text{Ghorbani}}(r) = \frac{x_1 r^{x_2}}{1+x_3 r^{x_2}} + x_4 r$ x_1, x_2, x_3, x_4 = AFPs	$A_{\text{Ghorbani}}(r) = \frac{y_1 r^{y_2}}{1+y_3 r^{y_2}} + y_4 r$ y_1, y_2, y_3, y_4 = PFPs
Rapp [111] AM/AM, Honkanen and Haggman AM/PM inc. Fisher and Al-Sarawi [137] phase offset addition[1]	$A_{\text{Rapp}}(r) = \frac{gr}{\left[1+\left(\frac{gr}{L}\right)^{2s}\right]^{1/2s}}$ L = SLL, g = SSG, s = sharpness param.	$\phi_{\text{HH}}(r) = \frac{b_{\phi_{HH}}}{1+e^{-c_{\phi_{HH}}(r-a_{\phi_{HH}})}} \cdot \frac{1}{p_1 r+p_2} - d_{FA}$ $a_{\phi_{HH}}$ = input (BJT) turn-on voltage, $b_{\phi_{HH}}$ = turn-on |phase|, $c_{\phi_{HH}}$ = step change steepness, p_1, p_2 = downward slope adj. params., d_{FA} = phase offset
White *et al* [113], AM/AM corrected[2] by Fisher and Al-Sarawi [137]	$A_{\text{White}}(r) = a_w[(1-e^{-b_w r}) + c_w r e^{-d_w r^2}]$ a_w = SLL, b_w = SSG, c_w, d_w = AFPs	$\phi_{\text{White}}(r) = f_w\left(1-e^{-g_w(r-h_w)}\right),\ r \geq h_w$ $\phi_{\text{White}}(r) = 0,\ r < h_w$ f_w = magnification factor, g_w = curve slope, h_w = r-axis range shift
O'Droma *et al* [114]	$A_{\text{O'Droma}}(r) = \frac{\alpha_a r^{\eta_a}}{(1+\beta_a r^{\gamma_a})^{\nu_a}} - \epsilon_a$ $\alpha_a, \beta_a, \eta_a, \gamma_a, \nu_a, \epsilon_a$ = AFPs	$\phi_{\text{O'Droma}}(r) = \frac{\alpha_\phi r^{\eta_\phi}}{(1+\beta_\phi r^{\gamma_\phi})^{\nu_\phi}} - \epsilon_\phi$ $\alpha_\phi, \beta_\phi, \eta_\phi, \gamma_\phi, \nu_\phi, \epsilon_\phi$ = PFPs

[1] Fisher and Al-Sarawi phase offset addition, d_{FA}, allows positive phase shifts.

[2] Fisher and Al-Sarawi correction of White *et al's* AM/AM model, square brackets [] addition, provides a correct match to White *et al's* results [113].

6.2.5 Group Delay

The MAX2010 has a maximum given group delay of 2.4 ns and the group delay of the Sirenza SHF-0189 is 1.4 ns from [157]. To accommodate this delay in a physical implementation, a small footprint, low cost, Surface Mount Technology (SMT), Low Temperature Co-fired Ceramic (LTCC) component(s) are used. These devices are available from Elmec Technology [160] and operate over the frequency range of interest and cover delays from ps up to 3 ns. The total group delay of 3.8 ns can be obtained by the series combination of two of these LTCC SMT components. These group delays are utilised in the following simulations.

6.3 Amplitude and Phase Error Impacts on Predistorter Intermodulation Reduction

Variations of the gain and phase logarithmic amplifier detector IC and the variable gain and pre-distortion lineariser IC have an effect on the overall ability of the lineariser to improve the output IMD performance. The equation describing the combined effects of these variations on the amount of IMD improvement is given by (6.19), [150].

$$S_{IMD} = -10\log_{10}\left[1 + 10^{\delta/10} - 2\cdot 10^{\delta/20}\cos(\Delta\theta)\right]. \tag{6.19}$$

where S_{IMD} is the intermodulation improvement in dB, δ is the amplitude variation in dB and $\Delta\theta$ is the phase variation in degrees. This equation is plotted in Fig. 6.8 and indicates that to maintain a 20 dB IMD improvement, the gain variation must be less than ± 1 dB and the phase variation must be less than 6 degrees.

Errors for the gain-phase detector IC and gain-phase linearisation IC, taken from the datasheets, are provided in Table 6.4.

Considering all of the errors listed in Table 6.4 and following an Root Sum Squared (RSS) analysis, then an IMD improvement of greater than 15 dB should be expected.

6.4 Modelling and Simulation

The behavioural modeling of the RF PA was developed using the least squares curve fitting technique for the equations given in Table 6.3. The input and output voltages

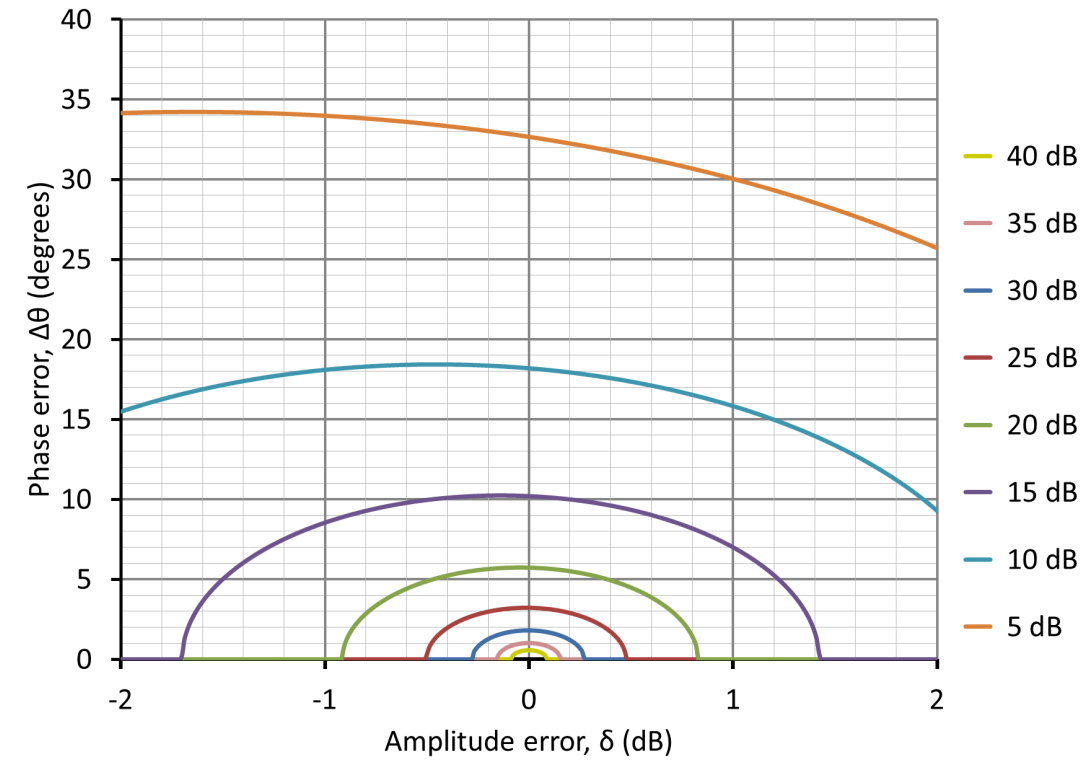

Figure 6.8. Pre-distorter 3rd IMD reduction versus gain and phase errors.

are normalized to the 1 dB compression point (P1dB) of the Sirenza SHF-0189 being at Pin = 11.5 dBm and Pout = 27.12 dBm. Details of all extracted parameters for each of the models are given in Table 6.5. The lineariser, shown in Fig. 6.1, and vector modulator, shown in Fig. 6.2, are modeled using Simulink with the simulated before and after lineariser 3rd and 5th order IMDs are shown in Fig. 6.10, using the original Rapp AM/AM model and the Honkanen and Haggman AM/PM model [112] with the phase update, d, provided in [137].

6.4.1 3rd and 5th Order Intermodulation Simulation Results

To validate this method and the RF PA models used, a Simulink model was created as shown in Fig. 6.9.

The simulation results from the Simulink model are shown in Fig. 6.10 and show a third order intermodulation performance (3IMD) improvement of between 3.5 dB to 10.8 dB for the original Rapp model including the Honkanen and Haggman phase model plus the addition from these authors [137]. All models showed linearisation improvement except the O'Droma model, as shown in Table 6.6, which shows both the

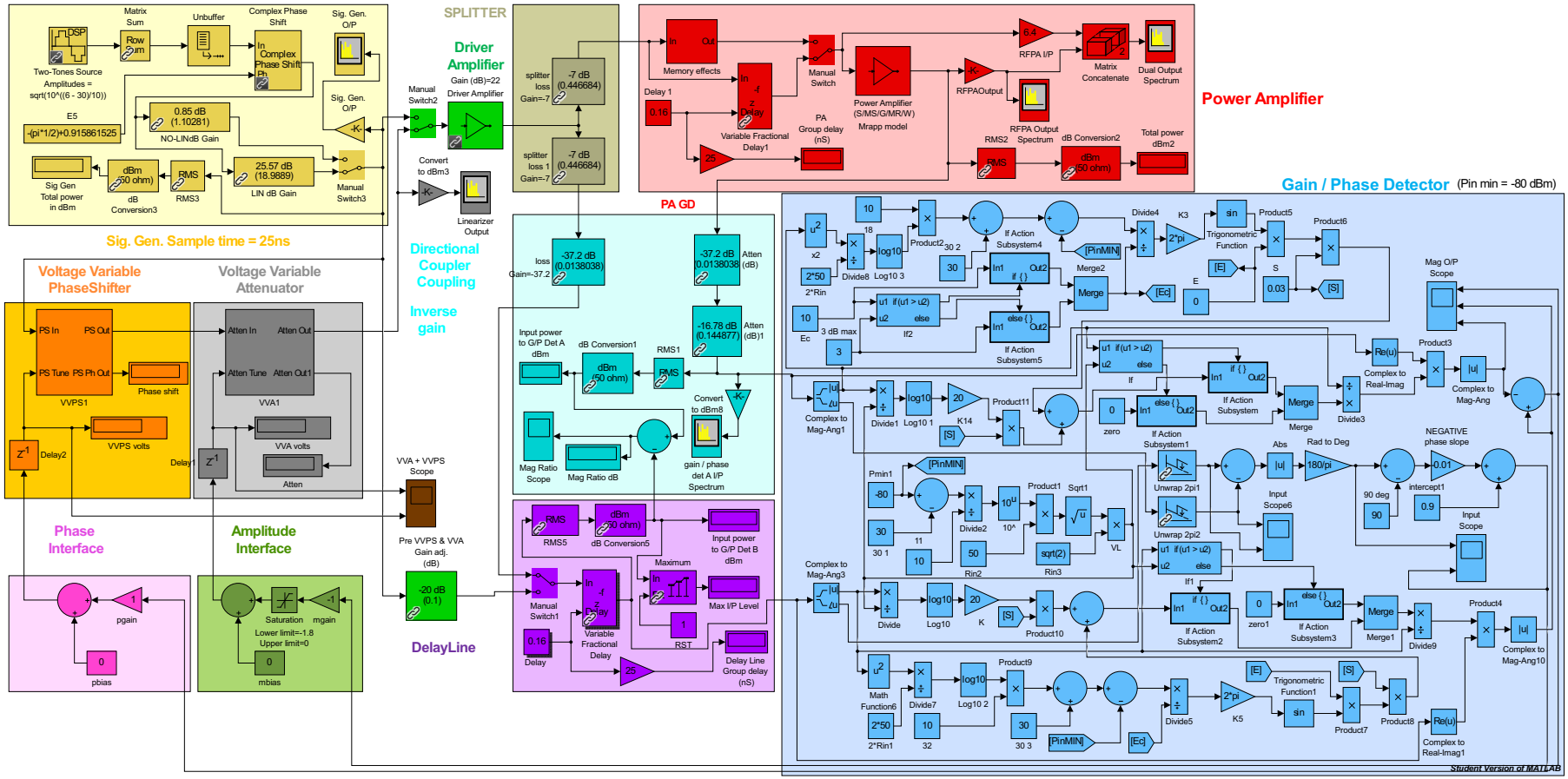

Figure 6.9. Simulink model. Simulink model.

Table 6.4. Gain / Phase detector and linearisation IC errors.

Parameter	Specification
Attenuator / Phase shift IC	
Phase Breakpoint vs Temperature	±1.5 dB
Phase slope vs Temperature	0.05 °/dB
Phase Parasitic Gain expansion	+0.4 dB
Gain Breakpoint vs Temperature	-0.5 dB
Gain slope vs Temperature	-0.01 dB/dB
Gain Parasitic Gain expansion	+3°
Detector IC	
Magnitude Dynamic Range (900 MHz)	±1 dB per 58 dB
Magnitude Slope	28.7 mV/dB/dB
Gain Deviation vs Temperature	0.25 dB
Gain Measurement Balance	0.20 dB
Phase Dynamic Range (900 MHz)	±1 dB per 143°
Phase slope	10.1 mV/°
Phase Deviation vs Temperature	0.75°
Phase Measurement Balance	0.8°

worst case and best case for both the 3rd and 5th order IMD products. Surprisingly the O'Droma [114] model did not show a 3rd order IMD product improvement as per all of the other models considering NMSE as a FOM performance, as defined by [116] and listed for all models in Table 6.7.

No further optimization of the input path delay or optimization of the K_m and K_p parameters provided further improved IMD suppression performance. Over a power input range from +13 to +21 dBm per carrier, the amount of linearisation improvement varied with each model for both the 3rd and 5th order IMD products. The 3rd and 5th order IMD performance and simulated results for the SHF-0189 device are shown in Fig. 6.11. There was also a degree of asymmetry seen with some models more than others. The asymmetry may be caused by variations in the variable attenuator or phase shifter models.

Table 6.5. Extracted behavioural model parameters. Normalized to P1dB.

Model	AM/AM	AM/PM
Saleh [109]	α_a=1.2015	α_ϕ=0.0288
	β_a=0.1974	β_ϕ=-0.6472
Ghorbani and Sheikan [110]	x_1=273.044	y_1=0.2769
	x_2=1.0013	y_2=6.7083
	x_3=0.0029	y_3=1.5281
	x_4=-271.264	y_4=-0.0172
Rapp [111] AM/AM & Honkanen and Haggman [112] AM/PM with Fisher and Al-Sarawi [137] addition	A=1.1449	a=0.9174
		b=2.1904
	α=1.1151	c=9.9697
		p_1=7.2366
	β=2.8142	p_2=7.8934
		d=0.0072
White *et al* [113] with Fisher and Al-Sarawi [137] AM/AM correction	a=-0.0798	f=273.3693
	b=-0.5017	g=4.677e-8
	c=-14.4528	h=0.9496
	d=0.1925	
O'Droma *et al* [114]	α_a=1.1344	α_ϕ=-0.1426
	β_a=1.3359	β_ϕ=0.0484
	η_a=0.9902	η_ϕ=0.3467
	γ_a=6.2165	γ_ϕ=6.3138
	ν_a=0.1504	ν_ϕ=4.5738
	ϵ_a=0	ϵ_ϕ=-0.1293

Table 6.6. Intermodulation improvement versus model type at +24 dBm total output level.

Model	linearisor OFF (dBc)		linearisor ON (dBc)		Improvement (dB)			
	3rd	5th	3rd	5th	3rd		5th	
					Worst	Best	Worst	Best
Saleh [109]	27.5	49.6	32.6	42.7	5.0	6.6	-6.9	-0.06
Ghorbani and Sheikan [110]	27.3	38.1	30.8	38.6	3.5	10.8	0.4	6.0
Rapp [111] AM/AM & Honkanen and Haggman [112] AM/PM with Fisher and Al-Sarawi [137] addition	27.8	39.5	31.2	38.8	3.4	10.4	-0.7	7.9
White *et al* [113] with Fisher and Al-Sarawi [137] AM/AM correction	28.3	57.8	28.8	60.3	0.6	0.65	2.4	3.0
O'Droma *et al* [114]	28.9	41.5	27.2	46.1	-1.7	-1.1	4.7	6.5

Table 6.7. Improved behavioural models versus NMSE comparison.

Model	AM/AM NMSE (dB)
Saleh, [109]	-36.5
Ghorbani and Sheikan, [110]	-42.5
Rapp [111] AM/AM & Honkanen and Haggman [112] AM/PM with Fisher and Al-Sarawi [137] addition	-58.7
White *et al* [113] with Fisher and Al-Sarawi [137] AM/AM correction	-37.1
O'Droma *et al* [114], (Modified Saleh)	-61.8

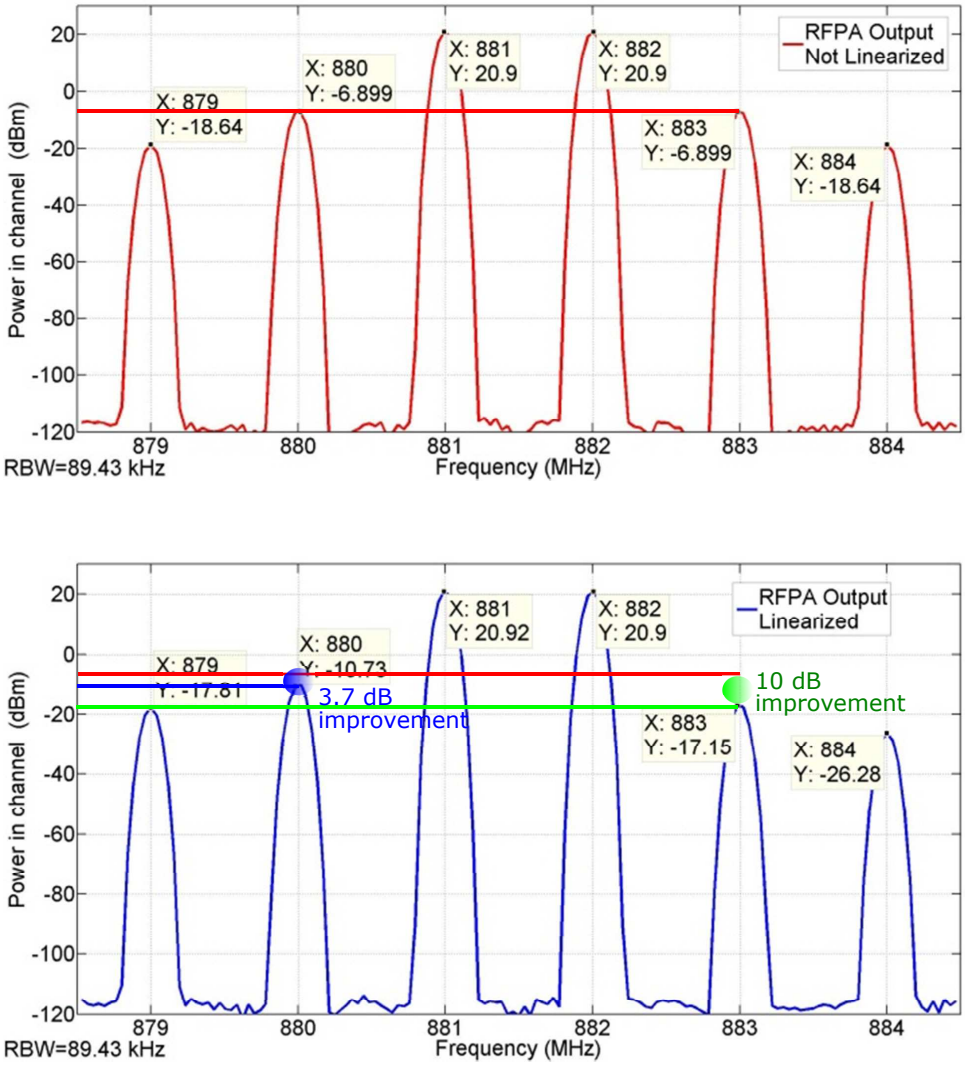

Figure 6.10. RF PA IMD Simulink simulations. Simulink simulation result of the RF PA before (top) and after (bottom) linearisation. Tone spacing is 1 MHz with an output level of +21 dBm per tone.

6.4.2 WCDMA Simulation Results

Results for a WCDMA input signal are shown in Fig. 6.12, with the linearisation improvement occurring more in the first adjacent channels compared to the next adjacent channels further from the center frequency. This is predictable when the 5^{th} order linearisation performance is examined with this not being as significant as the 3^{rd} order improvements.

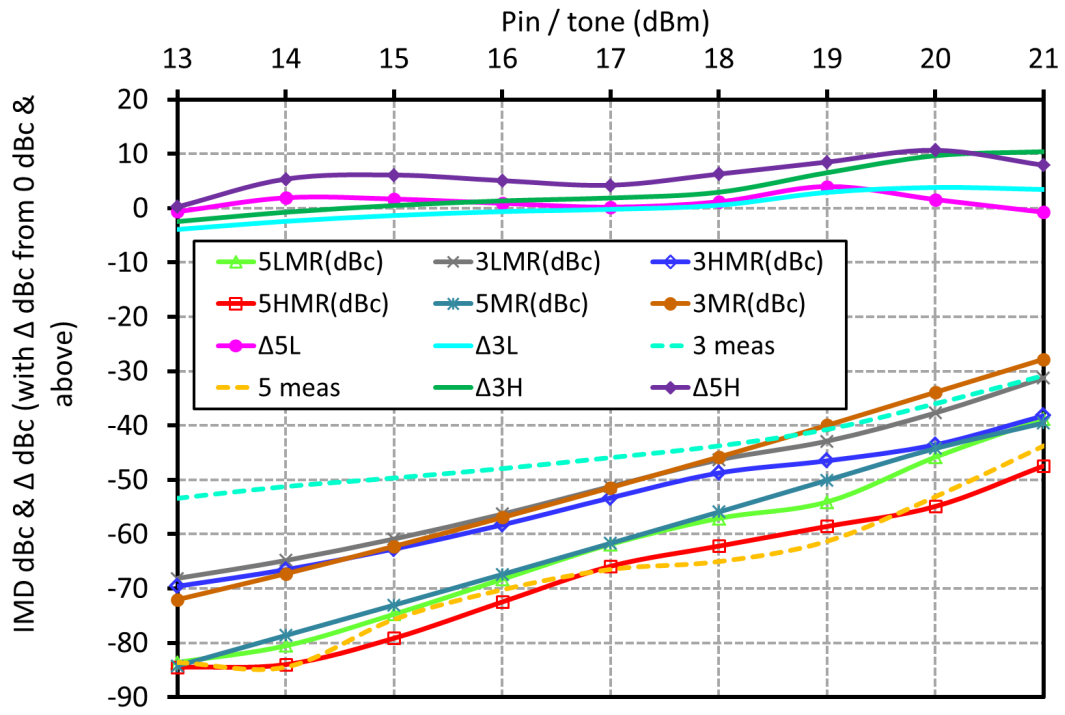

Figure 6.11. SHF-0189 measured versus simulated IMD performance. SHF-0189 measured IMD performance, from [155], plus simulated pre-distorter (using original Rapp model plus update Honkanen and Haggman phase model) IMD performance vs input level per carrier (dBm).

6.5 Conclusion

An envelope predistortion lineariser, using small, targeting low cost analog components, has been simulated using several well-known existing and improved behavioural models, with the results indicating that the combination of a simple analog lineariser with an improved simple behavioural model can provide lineariser performance improvements to a maximum of 10 dB over a limited input power range of 3 to 4 dB from the device P1dB point.

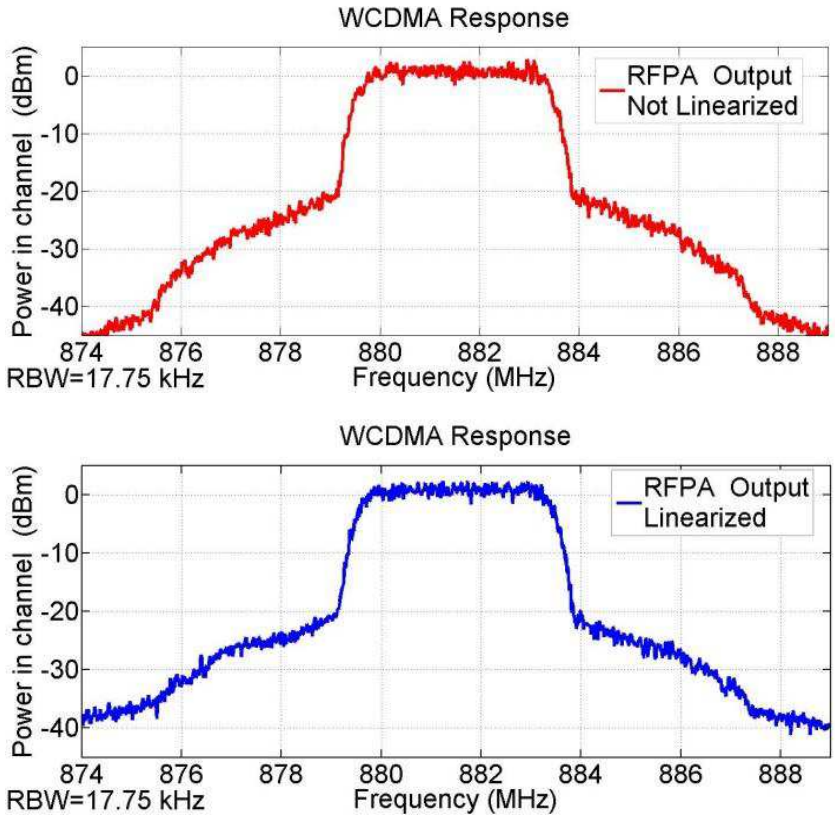

Figure 6.12. RF PA WCDMA Simulink simulations. Simulink simulation results of the RF PA before (top) and after (bottom) linearisation. WCDMA input signal, Pout=24 dBm.

Chapter 7

Conclusion and Future Research

THIS thesis has presented and investigated concepts for obtaining higher power amplifiers based on combining technologies as well as proposing a technology selection and design methodology method. It has also presented improvements, new models and techniques for behavioural modelling associated with RF PAs for the purpose of fast RF PA output device comparison and selection while preserving modelling accuracy in system analysis. Low cost RF linearisation methods have also been investigated to cater for low cost, low power, low complexity applications. This chapter provides conclusions from this research including a look at possible future research areas.

7.1 Introduction

The research work presented in this thesis covers three areas. The first part investigates combining technologies and techniques and developes a design methodology to be able to select the most appropriate solution for a range of parameters. Part two investigates and presents new memoryless and quasi-memoryless behavioural models and techniques for RF PA device comparison and selection. The final part looks at low cost analog lineariser simulation using a range of memoryless and quasi-memoryless behavioural models.

7.2 Power Combining Technologies and a FOM Design Methodology

7.2.1 Power Amplifier Combining Technologies: Chapter 2

Background: Chapter 2 highlighted a need for power combining techniques that can meet the emerging requirements for high power output stages. In the literature a wide range of techniques and technologies are presented, however a comprehensive overview of these different techniques and technologies seems to be lacking, so there is need to provide an overview of the different approaches to power combining techniques and technologies.

Contribution: This thesis provides a comprehensive and updated review of available power combining technologies for solid state power amplifiers. These technologies cover a broad range of frequencies and methods. It also investigates and reviews other techniques that can further enhance the outcomes associated with spatial combining technologies. It also considers the use of established combining technologies, like corporate combining in the form of IMFETs, in concert with spatial combining techniques.

7.2.2 FOM Design Methodology for Power Amplifier Combining: Chapter 3

Background: After considering the different power combining techniques, a number of Figure's of Merit exist that are commonly used to highlight specific power combining parameters suited to application requirements. Nonetheless, a Figure of Merit

approach for evaluating a suitable technology for a range of requirements, including specifications as well as less well defined parameters, appears to be missing from the literature. Hence the need for a design methodology, over a broader range of parameters, that allows for such a comparison.

Contribution: From the review in Chapter 2 a need emerged for a way of being able to select the most appropriate combining technologies and technique in order to meet a range of requirements that go beyond only hard requirements and also considered other factors that are less tangible, for example amplifier graceful degradation or servicing requirements. The method developed is based around FOMs already published in the literature and also modern decision making techniques. This has been demonstrated through a case study and commercially validated and described in the literature by other research groups.

7.3 Quasi-Memoryless and Memoryless Behavioural Modelling of SSPAs

7.3.1 Behavioural Modelling of SSPAs: Chapter 4

Background: Much of the RF PA modelling in the literature is memoryless or quasi-memoryless behavioural modelling with limited accuracy and is technology specific, so the need exists for improved accuracy models that can be applied to a range of devices and characteristics. Such a requirement is to develop a generic model that allows behavioural modelling of different amplifier technologies without compromising either the speed and accuracy of these models. In addition it would be preferred to have models that are physics-based, reflect currently available devices, with operation well into saturation, and that include memory effects.

Contribution: This chapter investigated improvements to existing memoryless and quasi-memoryless behavioral models and also extended them so that they could be used beyond the limitation of zero degrees phase shift that can occur for LDMOS devices. A technique was also introduced that extended AM/AM device data into the saturation region and the models were compared into this region. Simulation results indicated that for models extracted from existing data that when extended into the saturation region the Rapp model showed the best performance being relevant to

currently used LDMOS devices. Also provided is a physics based model that incorporates memory effects to enable designers to quickly model devices from manufacturer's datasheet, thus enabling them to make fast device selections.

7.3.2 Generalised Quasi-memoryless and Memoryless Behavioural Models: Chapter 5

Background: Recent more accurate AM/AM and AM/PM models and techniques are used to generate a more accurate quasi-memoryless model that is semi-physically based. The accuracy is further enhanced by using an optimised segmentation technique based on derivatives of a devices' AM/AM data. Performance is validated for both two tone and WCDMA signals. Discontinuity effects at segmentation boundaries are also considered and are shown to have no impact on modelling or accuracy.

Contribution: This chapter provides a comprehensive review of memoryless and quasi-memoryless behavioural models over the last 40 years and identifies more suitable models for the PA designer. The development of a new AM/PM model, based on a more accurate AM/AM model, is provided as well as a straightforward segmentation method that provides even further modelling accuracy improvements. The benefits of accuracy enhancements are quantitatively shown to improve linearisation performance for both two tone and WCDMA signals.

7.4 RF PA Linearisation Techniques

Background: With the current need for enhanced data access, cellular systems are trending towards Small Cell repeaters. These are typically smaller and need to be low cost and less complex, as a result, and also more efficient. This means that more complex power hungry DPD type linearisers are less favourable options from a commercial perspective. For these low cost linearisers to be viable they need to approach the operating performance of DPD type linearisers.

Contribution: This chapter investigates and simulates, using Simulink, an analog based, low cost lineariser. The simulation also uses and compares a range of memoryless and quasi-memoryless behavioural models. In this work digital WCDMA signals, as well as two tone signals, are used to evaluate the analog lineariser performance by monitoring ACLR and 3rd IMDs.

7.5 Future Research Directions

Like many theses, along the way, many questions arise, suggesting other areas for possible research, and some other areas that are not fully explored. Also like many theses time does not permit further research time to be spent in answering these questions or in fully exploring some areas. These questions and open research areas are gathered here and discussed as possible further research areas.

Power Amplifier Combining Technologies: Chapter 2 Further review the use of GaN devices, that are now starting to establish themselves and compete against GaAs MESFETs and LDMOS devices in the market place, by providing more power in the same area as well as operating at higher temperatures and power supply voltages. The impacts of both higher operating temperatures and power supply voltages require further review from a thermal management perspective as well as impact related to power supply design. Also associated with higher RF power densities is the need for further investigations on the impact of RF power handling on transition methods and field modification techniques.

FOM Design Methodology for Power Amplifier Combining: Chapter 3 expanded design and technology selection methodologies. Further research and investigations into alternative mechanical, thermal, field modification, electro-magnetic and optimisation techniques for low cost design of higher power SSPAs would also be beneficial. A number of parameters and a majority of FOMs in Table 3.4 are not listed so future work would be to fully specify these parameters and FOMs so that more accurate selections can be made.

Behavioural Modelling of SSPAs: Chapter 4 Investigate the application of the technique developed by Schmidt [161], with subsequent software [162], for the use in determining equations based on measured data. This could be used to model AM/AM and AM/PM from measured data.

Generalised Quasi-memoryless and Memoryless Behavioural Models: Chapter 5 Combine both the new segmented AM/AM model and AM/PM model. Investigations would be required to see if this further improves modelling accuracy. Also consider developing an optimisation routine, for the combined AM/AM and AM/PM models using the segmentation technique, for further additional accuracy improvements.

For any device selection it is recommend that appropriate testing on one or more devices be performed in order to validate any device performance against requirements.

Investigate if the memoryless and quasi-memoryless models can be expanded to include both 5^{th} order IMDs and "Sweet spot" as both of these can be useful in further improving lineariser performance.

Investigate the performance of the newly developed AM/PM model when it is operated deep into saturation.

RF PA Linearisation Techniques: Chapter 6 Investigate "Direct Sideband RF PD linearisers" where a sample of the ACLR is measured directly at the PA output, with no down conversion via mixing using local oscillators, and is filtered and fed back via the analog gain / phase logarithmic detector to control a vector modulator for the purpose of low cost linearisation.

Appendix A

THIS appendix contains the AM/AM & AM/PM plots used for generating the NMSE data shown in Figs. 5.3 (a) and (b) and in Table 5.3.

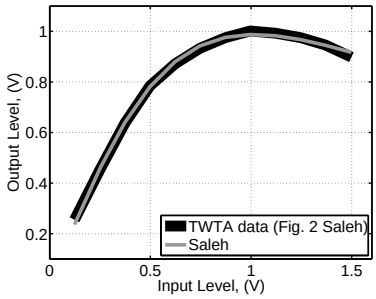

(a) NMSE = -38.20 dB

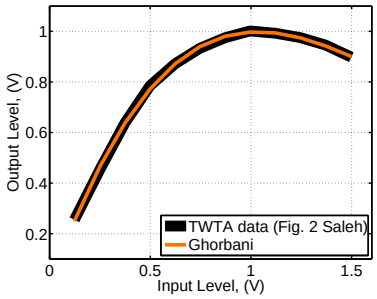

(b) NMSE = -42.82 dB

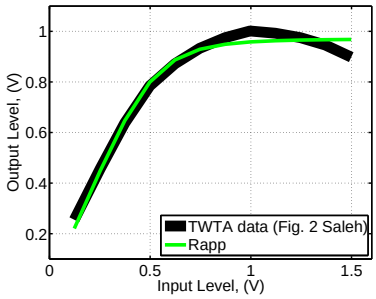

(c) NMSE = -29.03 dB

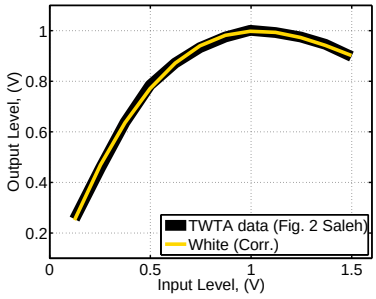

(d) NMSE = -42.14 dB

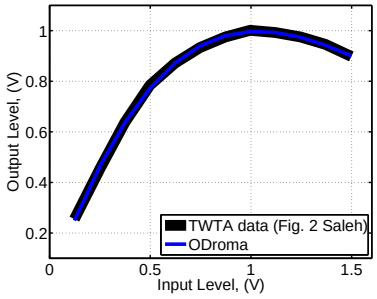

(e) NMSE = -40.08 dB

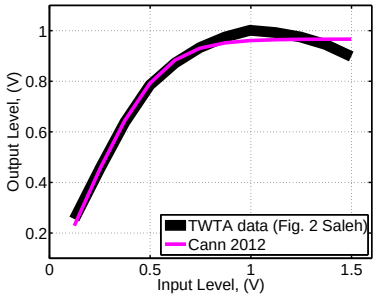

(f) NMSE = -29.70 dB

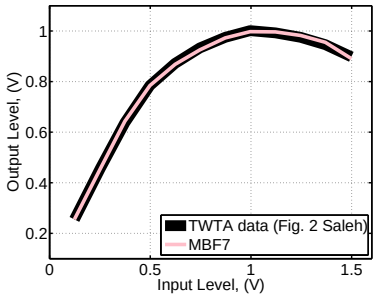

(g) NMSE = -44.10 dB

Figure A.1. TWTA (Fig. 2 Saleh) AM/AM plots. (a) = Saleh [109], (b) = Ghorbani [110], (c) = Rapp [111], (d) = White (corrected) [137], (e) = O'Droma (Modified Saleh) [114], (f) = Cann 2012 [125], & (g) = O'Droma (Modified Bessel Fourier) [136] $M = 7$.

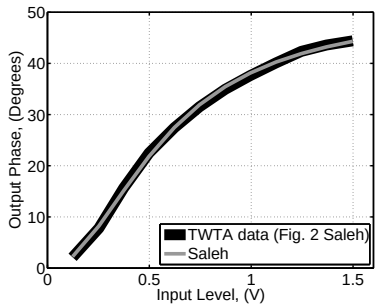

(i) NMSE = -38.05 dB

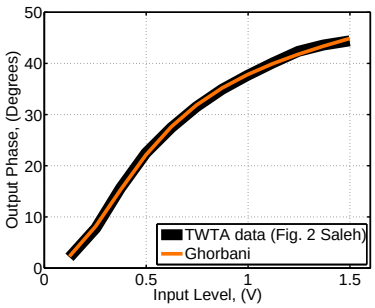

(ii) NMSE = -39.83 dB

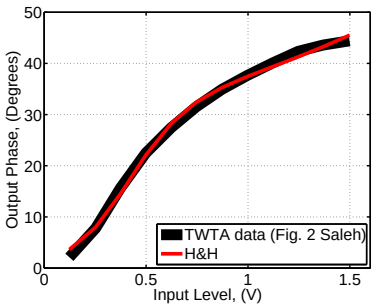

(iii) NMSE = -31.63 dB

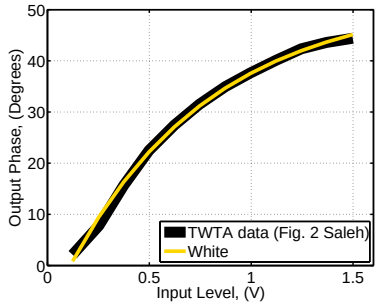

(iv) NMSE = -33.13 dB

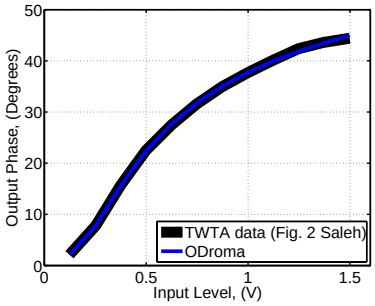

(v) NMSE = -42.14 dB

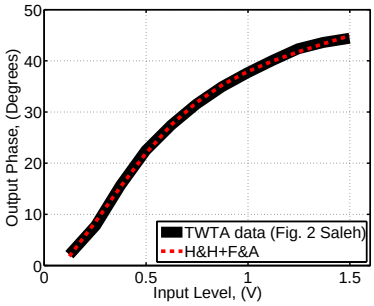

(vi) NMSE = -37.82 dB

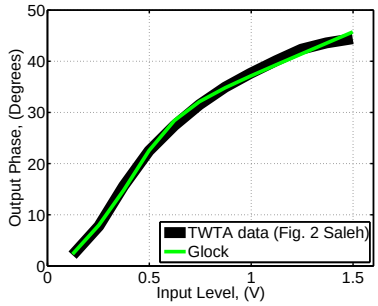

(vii) NMSE = -33.44 dB

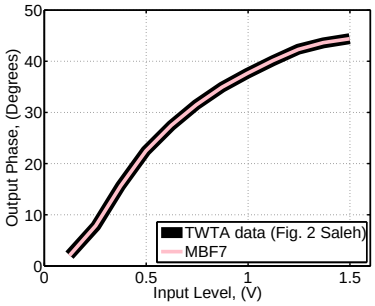

(viii) NMSE = -57.78 dB

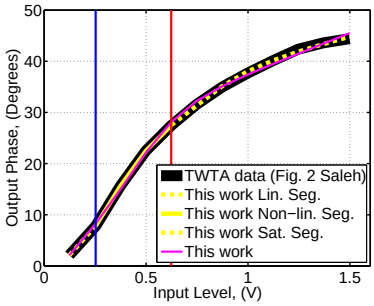

(ix) NMSE = -34.74 dB & -42.81 dB (Seg.)

Figure A.2. TWTA (Fig. 2 Saleh) AM/PM plots. (i) = Saleh [109], (ii) = Ghorbani [110], (iii) = Honkanen & Haggman [112], (iv) = White [113], (v) = O'Droma (Modified Saleh) [114], (vi) = Fisher [137], (vii) = Glock [128], (viii) = O'Droma (Modified Bessel Fourier) [136] $M = 7$, & (ix) = This work including segmentation.

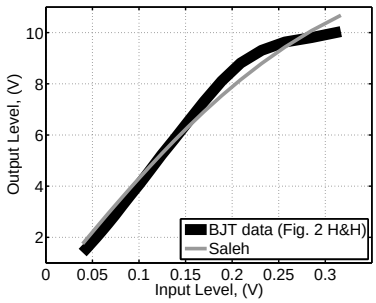

(a) NMSE = -24.08 dB

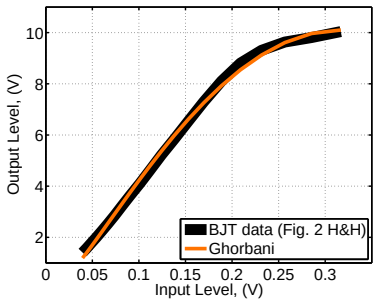

(b) NMSE = -32.86 dB

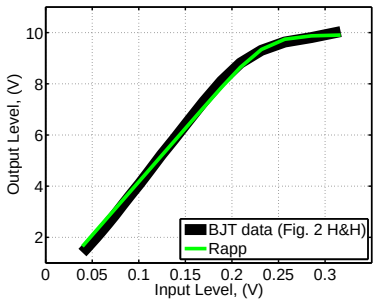

(c) NMSE = -30.24 dB

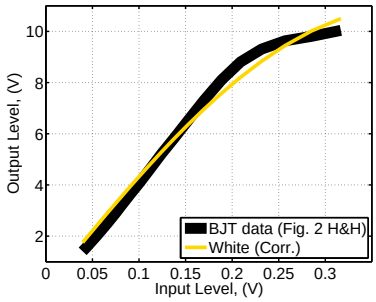

(d) NMSE = -24.65 dB

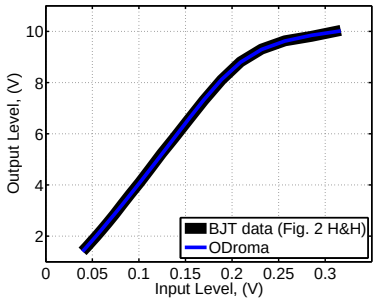

(e) NMSE = -50.57 dB

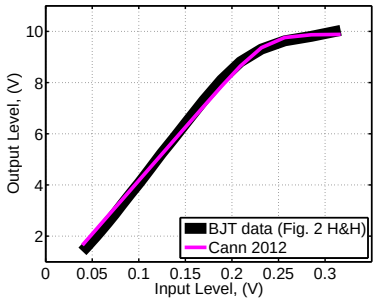

(f) NMSE = -30.16 dB

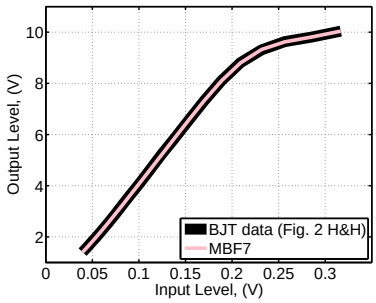

(g) NMSE = -57.83 dB

Figure A.3. BJT (Fig. 2 Honkanen & Haggman) AM/AM plots. (a) = Saleh [109], (b) = Ghorbani [110], (c) = Rapp [111], (d) = White (corrected) [137], (e) = O'Droma (Modified Saleh) [114], (f) = Cann 2012 [125], & (g) = O'Droma (Modified Bessel Fourier) [136] $M = 7$.

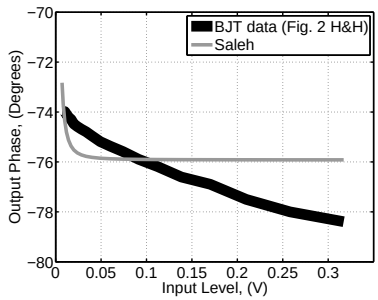

(i) NMSE = -36.90 dB

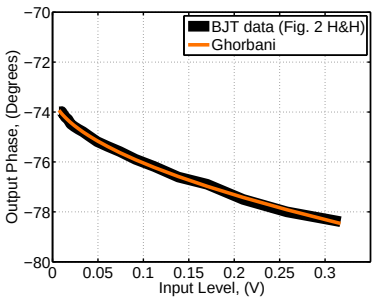

(ii) NMSE = -63.63 dB

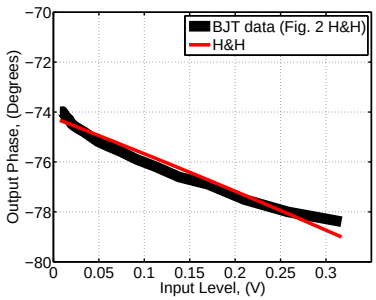

(iii) NMSE = -48.64 dB

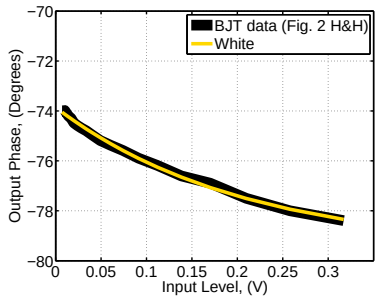

(iv) NMSE = -59.14 dB

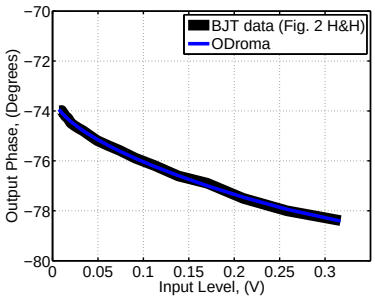

(v) NMSE = -64.24 dB

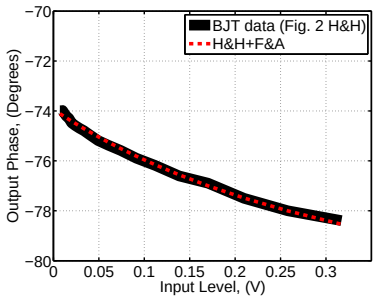

(vi) NMSE = -57.21 dB

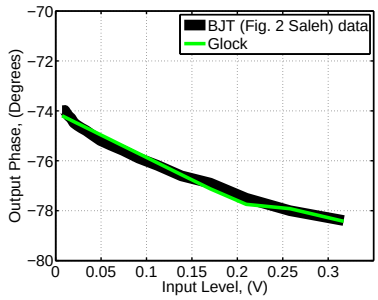

(vii) NMSE = -53.08 dB

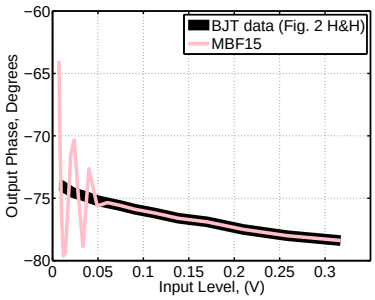

(viii) NMSE = -27.22 dB

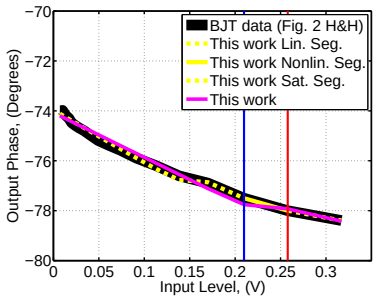

(ix) NMSE = -53.03 dB & -56.56 dB (Seg.)

Figure A.4. BJT (Fig. 2 Honkanen & Haggman) AM/PM plots. (i) = Saleh [109], (ii) = Ghorbani [110], (iii) = Honkanen & Haggman [112], (iv) = White [113], (v) = O'Droma (Modified Saleh) [114], (vi) = Fisher [137], (vii) = Glock [128], (viii) = O'Droma (Modified Bessel Fourier) [136] $M = 15$, & (ix) = This work including segmentation.

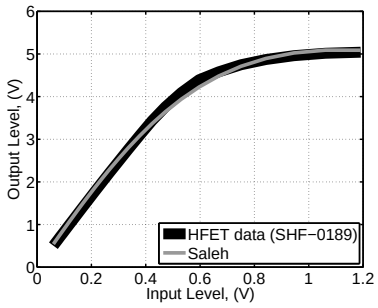

(a) NMSE = -31.68 dB

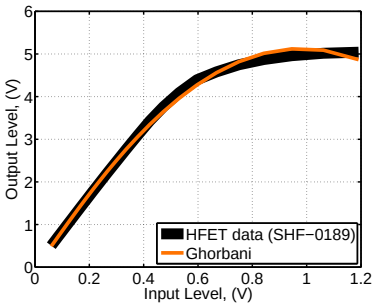

(b) NMSE = -32.18 dB

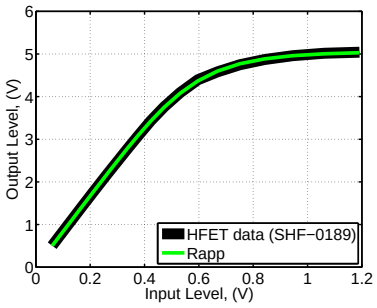

(c) NMSE = -49.22 dB

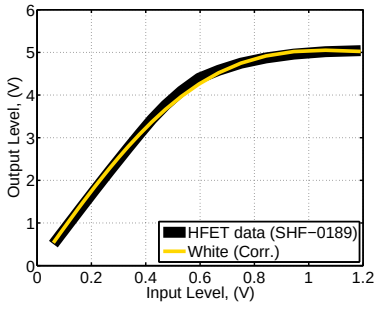

(d) NMSE = -33.52 dB

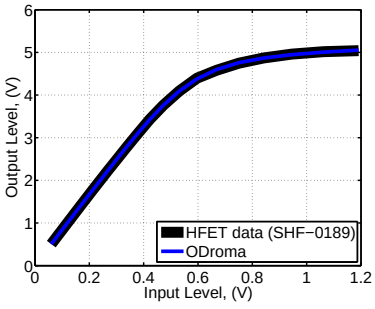

(e) NMSE = -52.67 dB

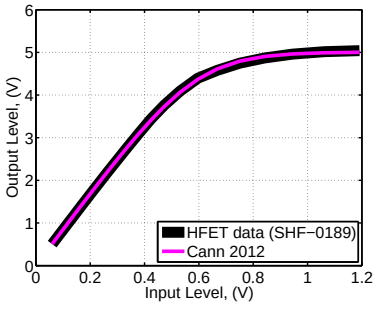

(f) NMSE = -43.53 dB

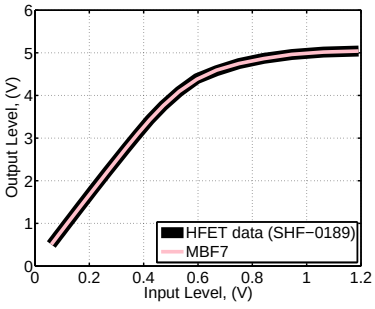

(g) NMSE = -56.95 dB

Figure A.5. HFET (SHF-0189) AM/AM plots. (a) = Saleh [109], (b) = Ghorbani [110], (c) = Rapp [111], (d) = White (corrected) [137], (e) = O'Droma (Modified Saleh) [114], (f) = Cann 2012 [125], & (g) = O'Droma (Modified Bessel Fourier) [136] $M = 7$.

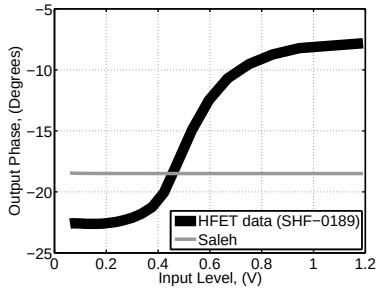

(i) NMSE = -10.59 dB

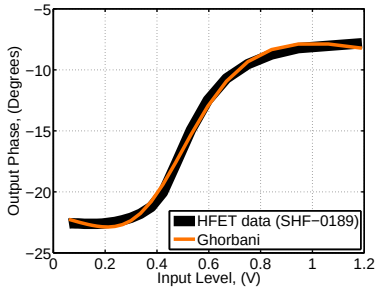

(ii) NMSE = -36.14 dB

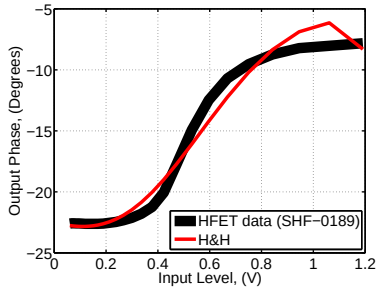

(iii) NMSE = -27.65 dB

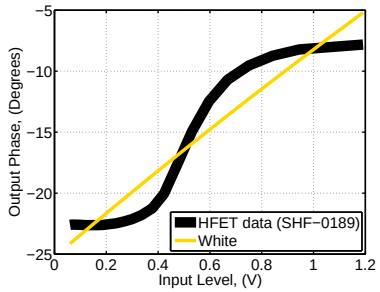

(iv) NMSE = -21.25 dB

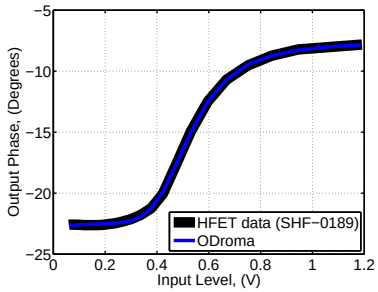

(v) NMSE = -49.18 dB

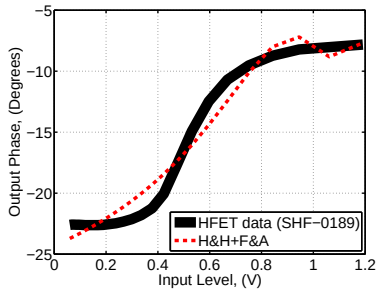

(vi) NMSE = -25.19 dB

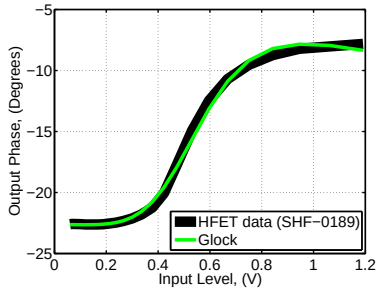

(vii) NMSE = -36.25 dB

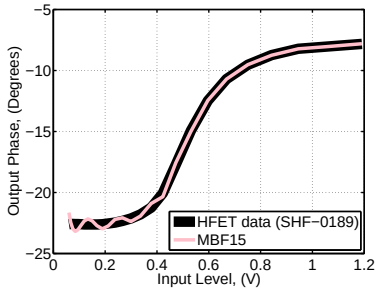

(viii) NMSE = -35.77 dB

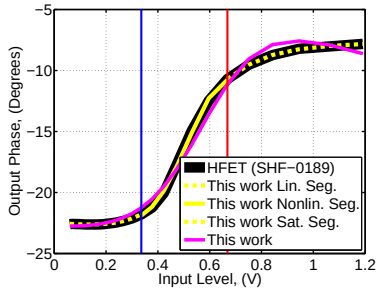

(ix) NMSE = -31.98 dB & -48.36 dB (Seg.)

Figure A.6. HFET (SHF-0189) AM/PM plots. (i) = Saleh [109], (ii) = Ghorbani [110], (iii) = Honkanen & Haggman [112], (iv) = White [113], (v) = O'Droma (Modified Saleh) [114], (vi) = Fisher [137], (vii) = Glock [128], (viii) = O'Droma (Modified Bessel Fourier) [136] $M = 15$, & (ix) = This work including segmentation.

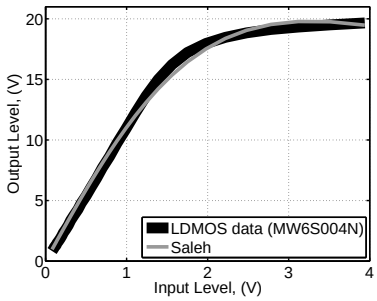

(a) NMSE = -28.69 dB

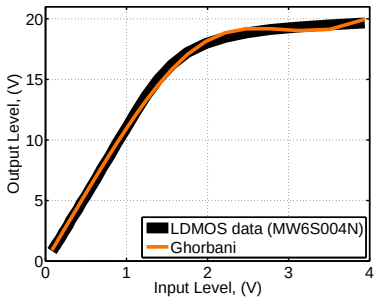

(b) NMSE = -33.94 dB

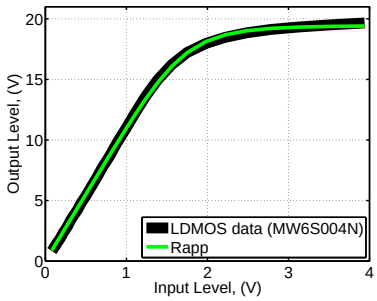

(c) NMSE = -38.83 dB

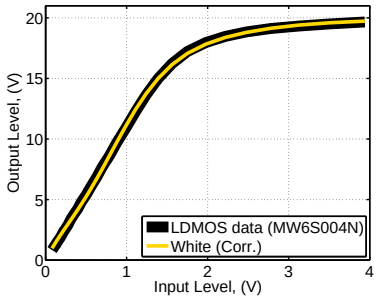

(d) NMSE = -38.79 dB

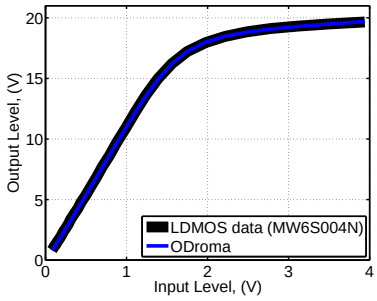

(e) NMSE = -50.85 dB

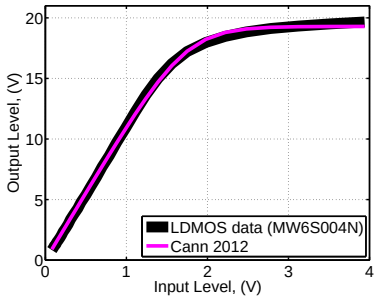

(f) NMSE = -36.43 dB

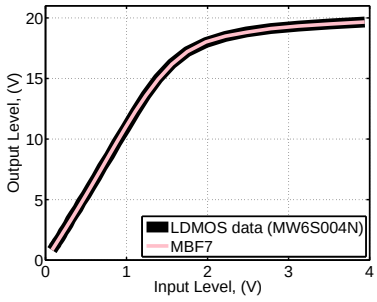

(g) NMSE = -49.10 dB

Figure A.7. LDMOS (MW6S004N) AM/AM plots. (a) = Saleh [109], (b) = Ghorbani [110], (c) = Rapp [111], (d) = White (corrected) [137], (e) = O'Droma (Modified Saleh) [114], (f) = Cann 2012 [125], & (g) = O'Droma (Modified Bessel Fourier) [136] $M = 7$.

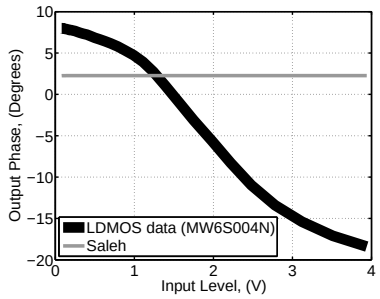

(i) NMSE = -0.32 dB

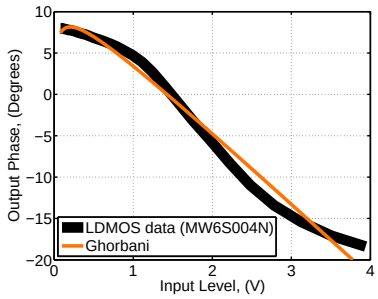

(ii) NMSE = -18.82 dB

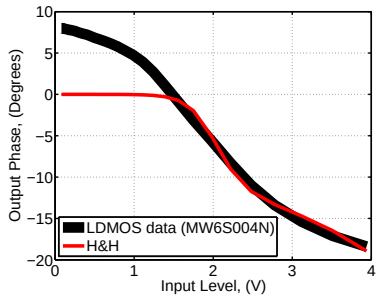

(iii) NMSE = -3.08 dB

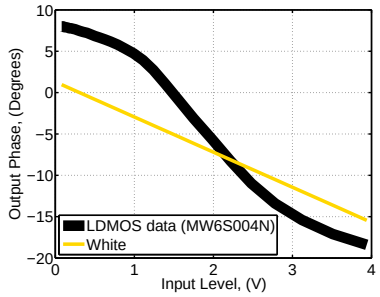

(iv) NMSE = -2.28 dB

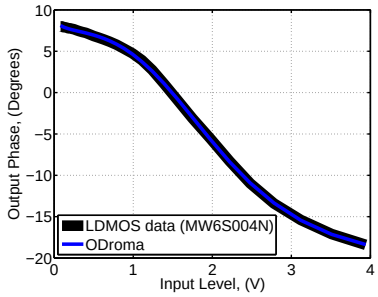

(v) NMSE = -40.03 dB

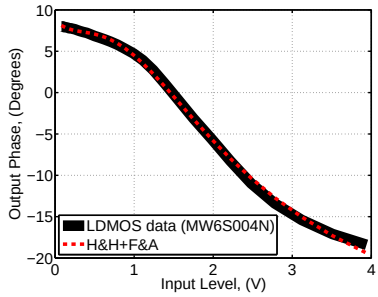

(vi) NMSE = -29.01 dB

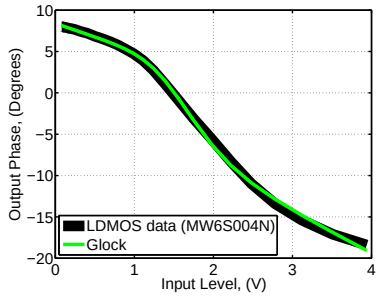

(vii) NMSE = -30.41 dB

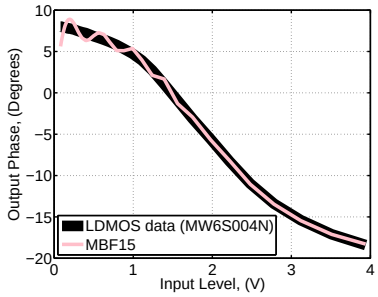

(viii) NMSE = -20.84 dB

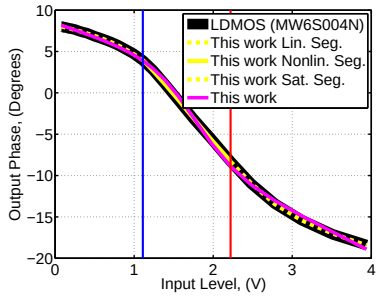

(ix) NMSE = -30.48 dB & -46.72 dB (Seg.)

Figure A.8. LDMOS (MW6S004N) AM/PM plots. (i) = Saleh [109], (ii) = Ghorbani [110], (iii) = Honkanen & Haggman [112], (iv) = White [113], (v) = O'Droma (Modified Saleh) [114], (vi) = Fisher [137], (vii) = Glock [128], (viii) = O'Droma (Modified Bessel Fourier) [136] $M = 15$, & (ix) = This work including segmentation.

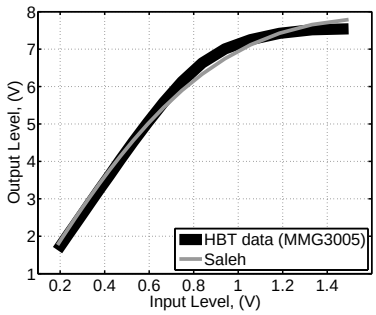

(a) NMSE = -29.68 dB

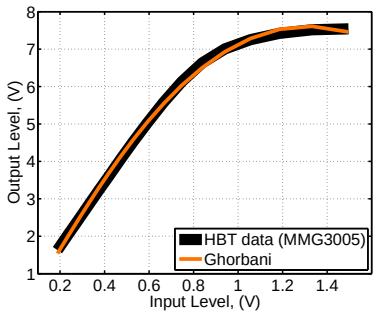

(b) NMSE = -37.13 dB

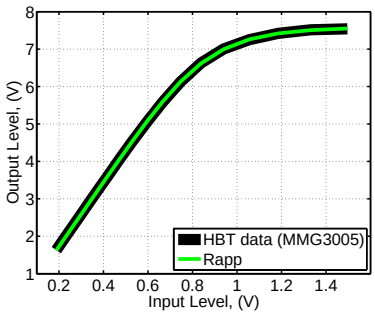

(c) NMSE = -56.70 dB

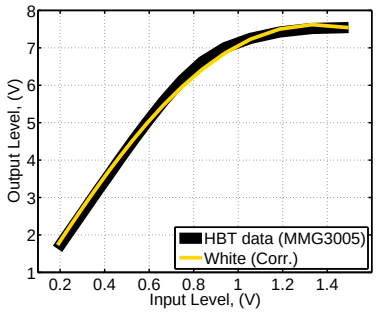

(d) NMSE = -33.31 dB

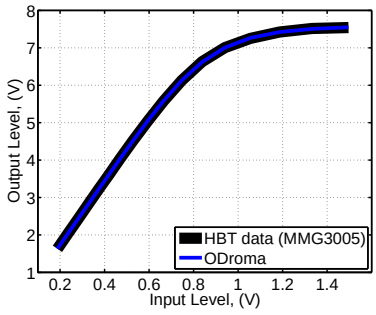

(e) NMSE = -59.54 dB

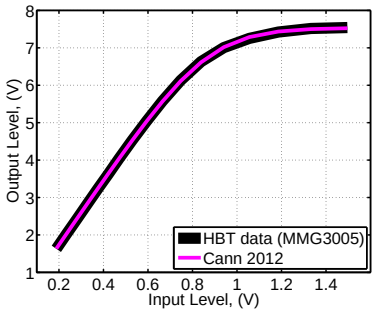

(f) NMSE = -51.88 dB

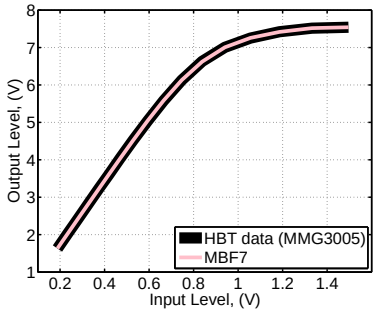

(g) NMSE = -63.22 dB

Figure A.9. HBT (MMG3005) AM/AM plots. (a) = Saleh [109], (b) = Ghorbani [110], (c) = Rapp [111], (d) = White (corrected) [137], (e) = O'Droma (Modified Saleh) [114], (f) = Cann 2012 [125], & (g) = O'Droma (Modified Bessel Fourier) [136] $M = 7$.

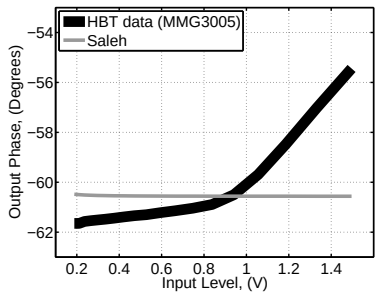

(i) NMSE = -31.08 dB

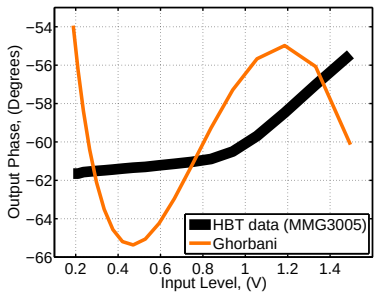

(ii) NMSE = -24.70 dB

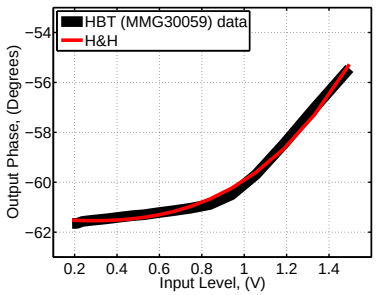

(iii) NMSE = -52.92 dB

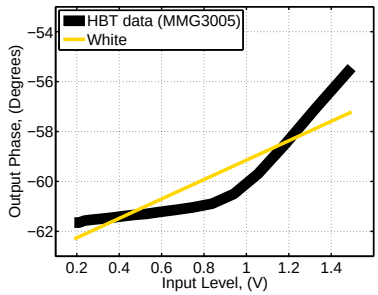

(iv) NMSE = -38.39 dB

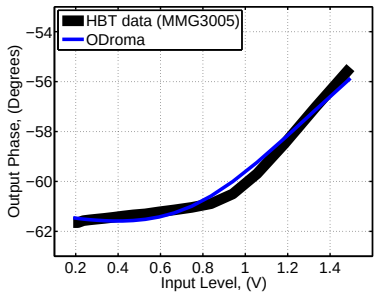

(v) NMSE = -48.09 dB

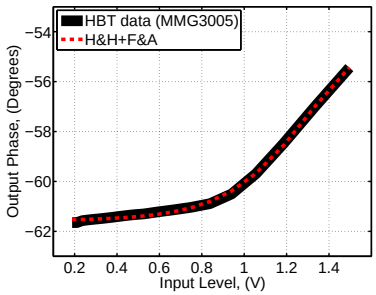

(vi) NMSE = -58.67 dB

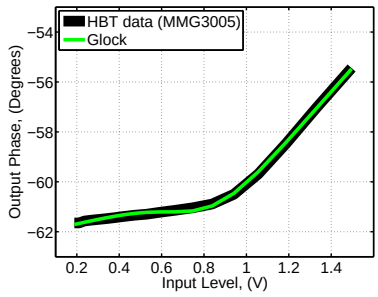

(vii) NMSE = -60.16 dB

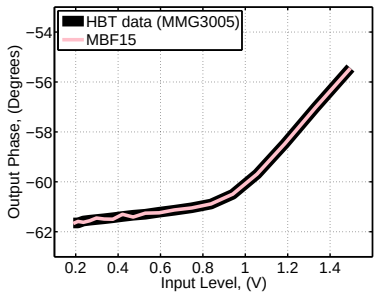

(viii) NMSE = -63.60 dB

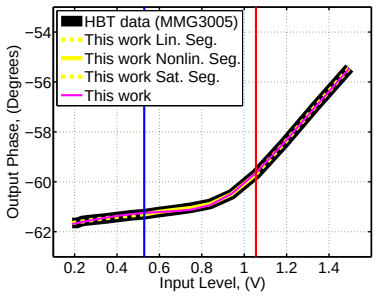

(ix) NMSE = -64.24 dB & -75.58 dB (Seg.)

Figure A.10. HBT (MMG3005) AM/PM plots. (i) = Saleh [109], (ii) = Ghorbani [110], (iii) = Honkanen & Haggman [112], (iv) = White [113], (v) = O'Droma (Modified Saleh) [114], (vi) = Fisher [137], (vii) = Glock [128], (viii) = O'Droma (Modified Bessel Fourier) [136] $M = 15$, & (ix) = This work including segmentation.

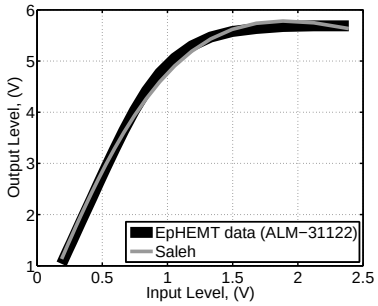

(a) NMSE = -31.74 dB

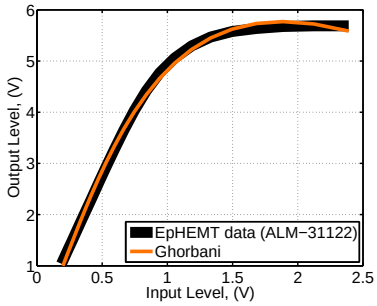

(b) NMSE = -34.79 dB

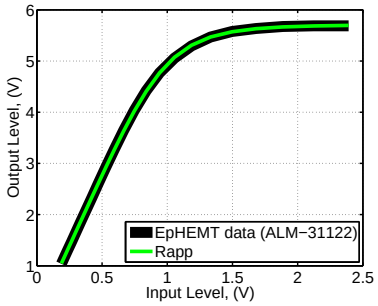

(c) NMSE = -53.26 dB

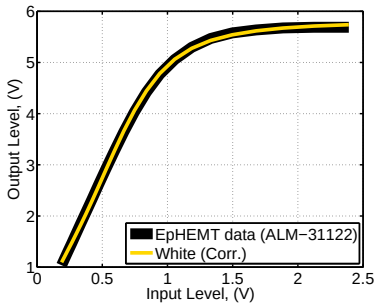

(d) NMSE = -43.01 dB

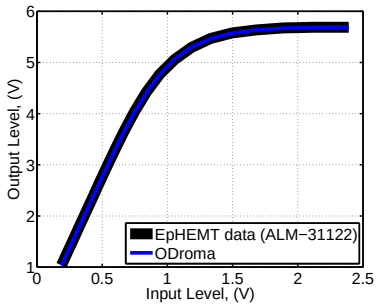

(e) NMSE = -57.95 dB

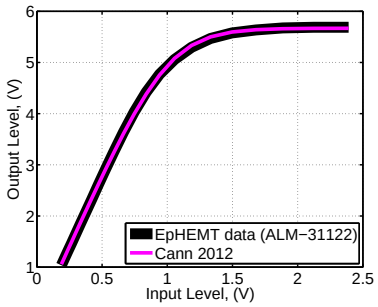

(f) NMSE = -44.77 dB

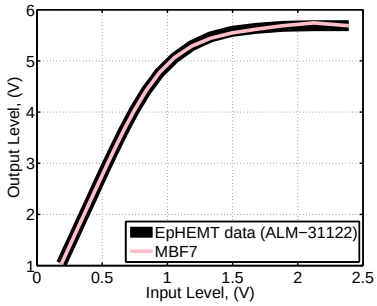

(g) NMSE = -48.26 dB

Figure A.11. E-pHEMT (ALM-31122) AM/AM plots. (a) = Saleh [109], (b) = Ghorbani [110], (c) = Rapp [111], (d) = White (corrected) [137], (e) = O'Droma (Modified Saleh) [114], (f) = Cann 2012 [125], & (g) = O'Droma (Modified Bessel Fourier) [136] $M = 7$.

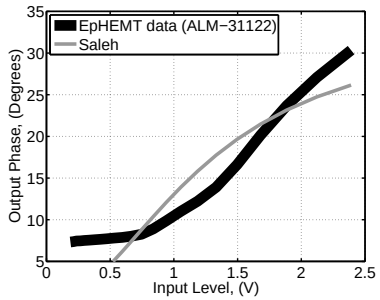

(i) NMSE = -10.73 dB

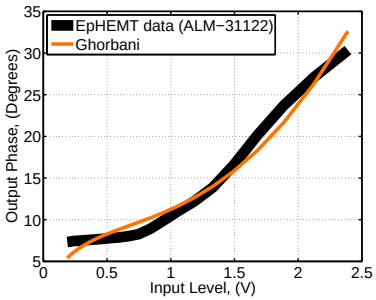

(ii) NMSE = -21.23 dB

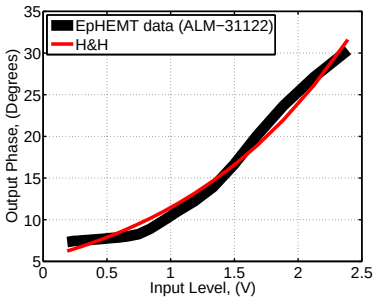

(iii) NMSE = -23.38 dB

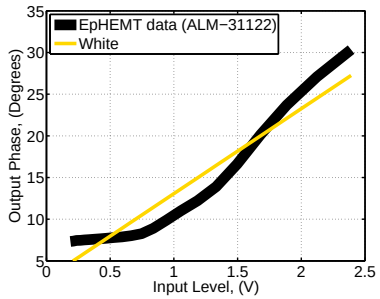

(iv) NMSE = -16.82 dB

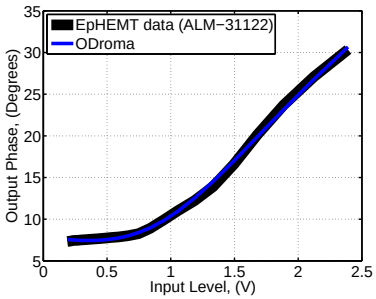

(v) NMSE = -34.59 dB

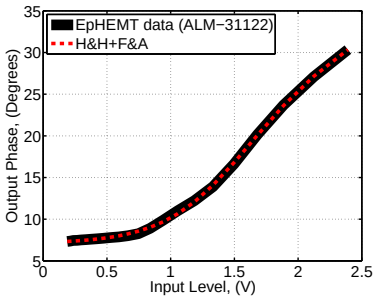

(vi) NMSE = -39.81 dB

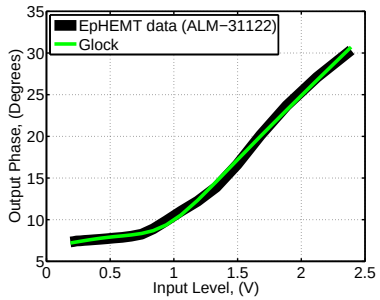

(vii) NMSE = -33.48 dB

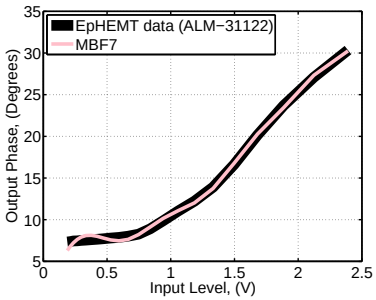

(viii) NMSE = -31.41 dB

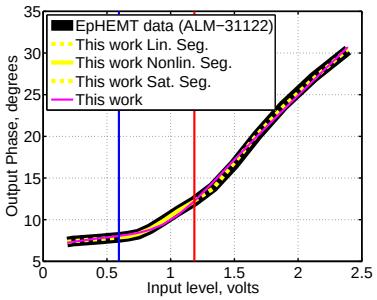

(ix) NMSE = -34.02 dB & -45.78 dB (Seg.)

Figure A.12. E-pHEMT (ALM-31122) AM/PM plots. (i) = Saleh [109], (ii) = Ghorbani [110], (iii) = Honkanen & Haggman [112], (iv) = White [113], (v) = O'Droma (Modified Saleh) [114], (vi) = Fisher [137], (vii) = Glock [128], (viii) = O'Droma (Modified Bessel Fourier) [136] $M = 7$, & (ix) = This work including segmentation.

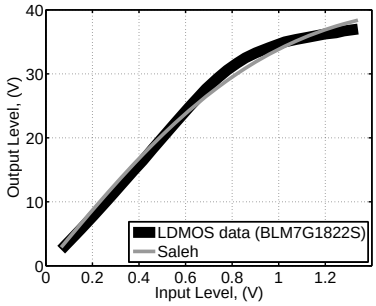

(a) NMSE = -27.38 dB

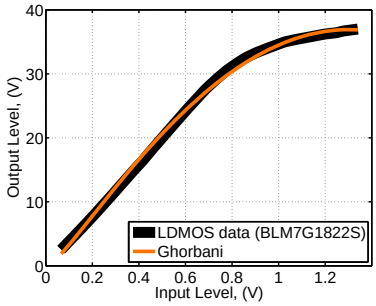

(b) NMSE = -32.50 dB

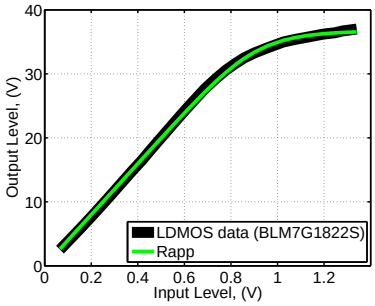

(c) NMSE = -38.81 dB

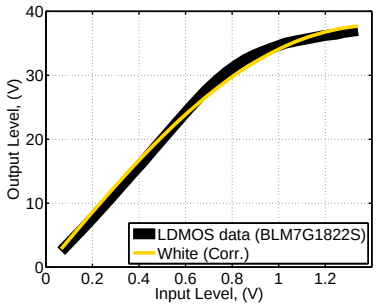

(d) NMSE = -28.10 dB

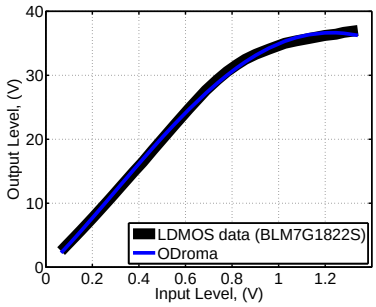

(e) NMSE = -51.60 dB

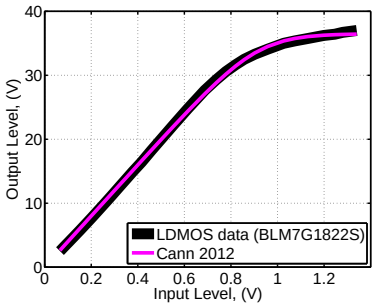

(f) NMSE = -37.70 dB

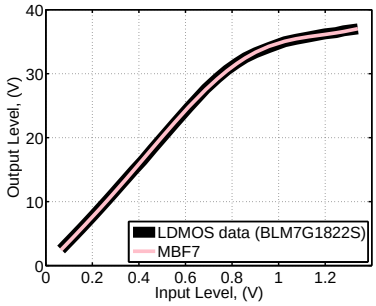

(g) NMSE = -49.00 dB

Figure A.13. LDMOS (BLM7G1822S) AM/AM plots. (a) = Saleh [109], (b) = Ghorbani [110], (c) = Rapp [111], (d) = White (corrected) [137], (e) = O'Droma (Modified Saleh) [114], (f) = Cann 2012 [125], & (g) = O'Droma (Modified Bessel Fourier) [136] $M = 7$.

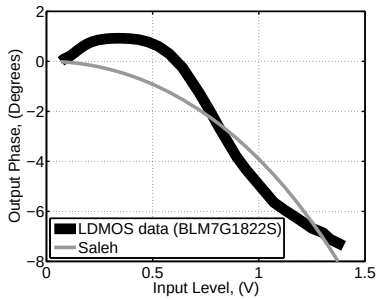

(i) NMSE = -10.93 dB

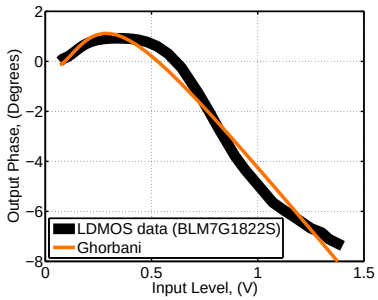

(ii) NMSE = -18.72 dB

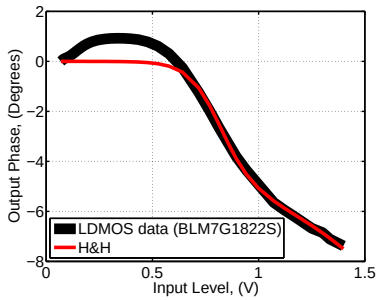

(iii) NMSE = -16.09 dB

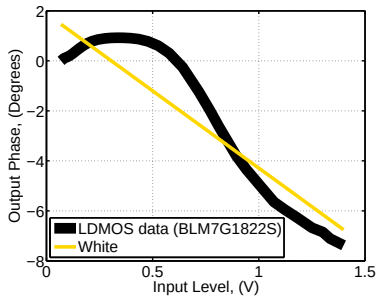

(iv) NMSE = -9.43 dB

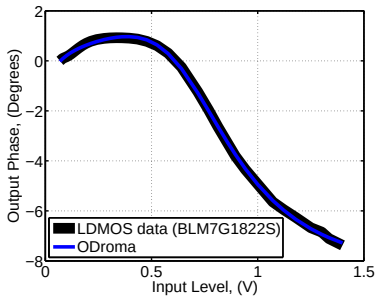

(v) NMSE = -36.16 dB

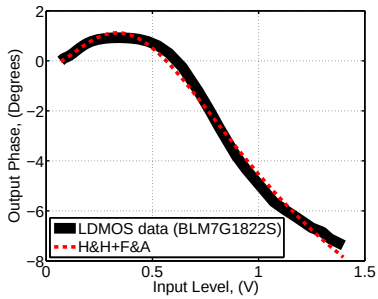

(vi) NMSE = -23.10 dB

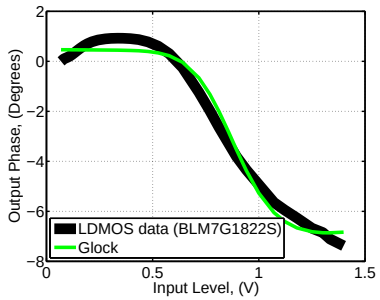

(vii) NMSE = -18.61 dB

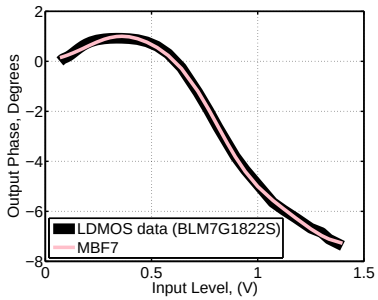

(viii) NMSE = -32.81 dB

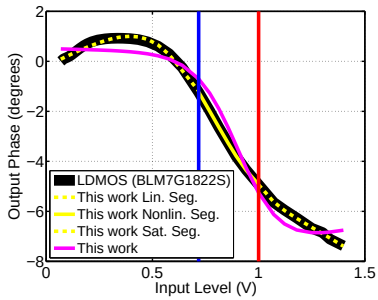

(ix) NMSE = -17.65 dB & -33.71 dB (Seg.)

Figure A.14. LDMOS (BLM7G1822S) AM/PM plots. (i) = Saleh [109], (ii) = Ghorbani [110], (iii) = Honkanen & Haggman [112], (iv) = White [113], (v) = O'Droma (Modified Saleh) [114], (vi) = Fisher [137], (vii) = Glock [128], (viii) = O'Droma (Modified Bessel Fourier) [136] $M = 7$, & (ix) = This work including segmentation.

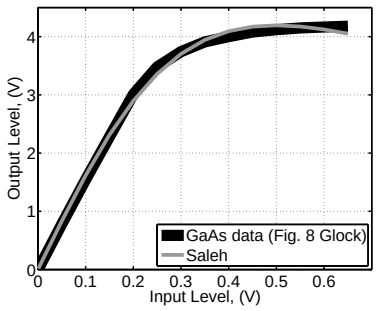

(a) NMSE = -33.00 dB

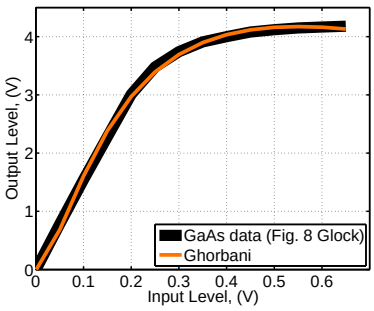

(b) NMSE = -35.74 dB

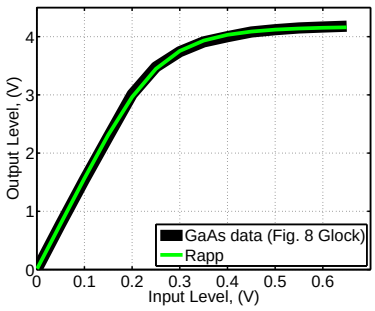

(c) NMSE = -43.44 dB

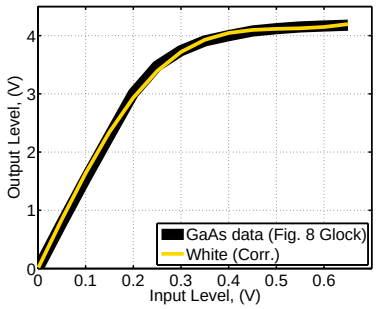

(d) NMSE = -36.63 dB

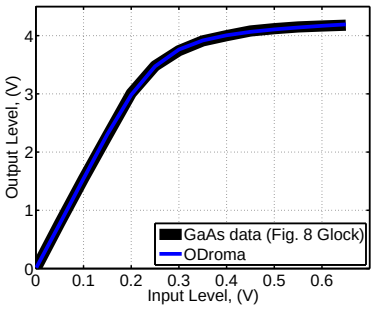

(e) NMSE = -47.55 dB

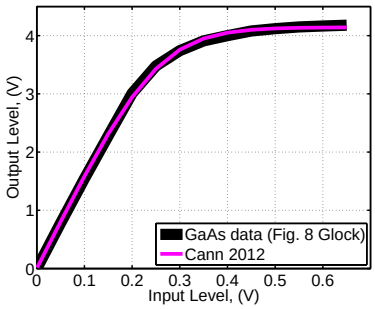

(f) NMSE = -39.61 dB

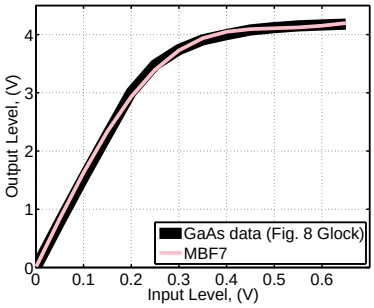

(g) NMSE = -37.09 dB

Figure A.15. GaAs (Fig. 8 Glock) AM/AM plots. (a) = Saleh [109], (b) = Ghorbani [110], (c) = Rapp [111], (d) = White (corrected) [137], (e) = O'Droma (Modified Saleh) [114], (f) = Cann 2012 [125], & (g) = O'Droma (Modified Bessel Fourier) [136] $M = 7$.

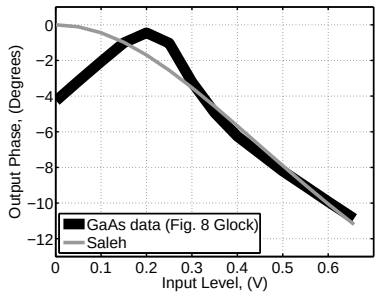

(i) NMSE = -11.79 dB

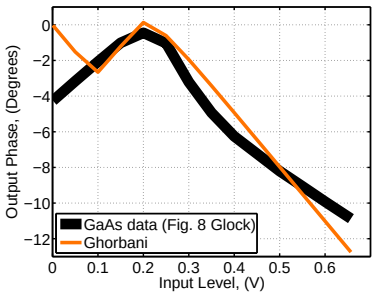

(ii) NMSE = -12.07 dB

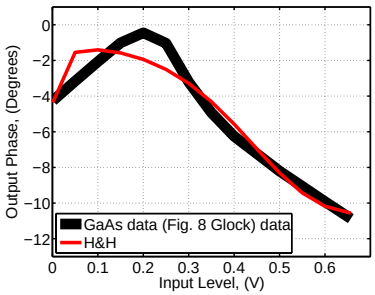

(iii) NMSE = -17.68 dB

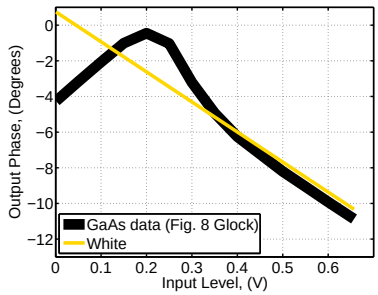

(iv) NMSE = -10.27 dB

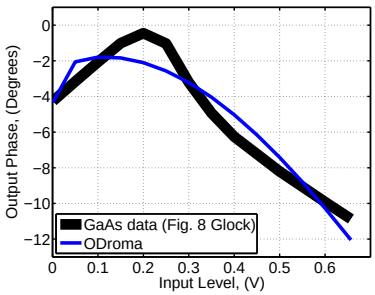

(v) NMSE = -16.17 dB

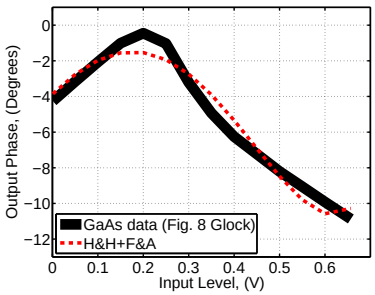

(vi) NMSE = -19.27 dB

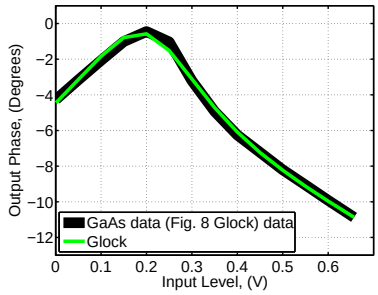

(vii) NMSE = -30.37 dB

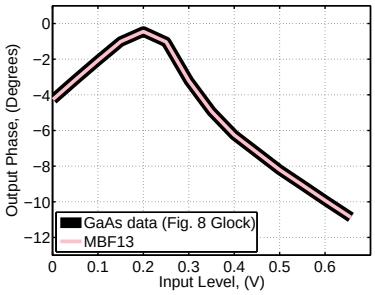

(viii) NMSE = -223.54 dB

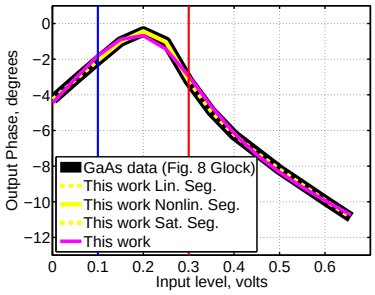

(ix) NMSE = -29.77 dB & -52.72 dB (Seg.)

Figure A.16. GaAs (Fig. 8 Glock) AM/PM plots. (i) = Saleh [109], (ii) = Ghorbani [110], (iii) = Honkanen & Haggman [112], (iv) = White [113], (v) = O'Droma (Modified Saleh) [114], (vi) = Fisher [137], (vii) = Glock [128], (viii) = O'Droma (Modified Bessel Fourier) [136] $M = 13$, & (ix) = This work including segmentation.

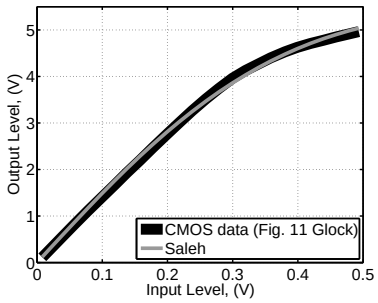

(a) NMSE = -34.64 dB

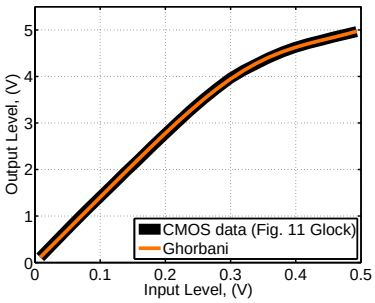

(b) NMSE = -38.92 dB

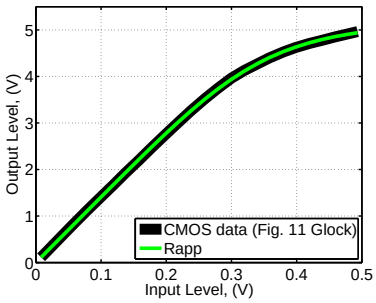

(c) NMSE = -47.33 dB

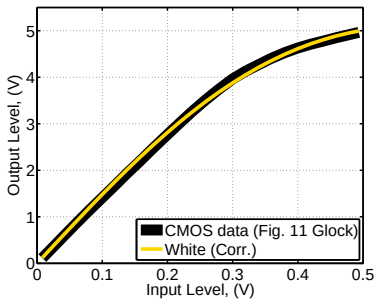

(d) NMSE = -36.30 dB

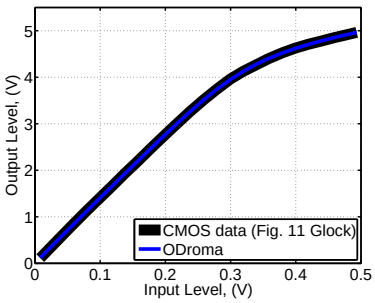

(e) NMSE = -57.20 dB

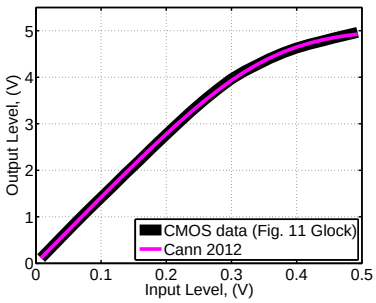

(f) NMSE = -44.56 dB

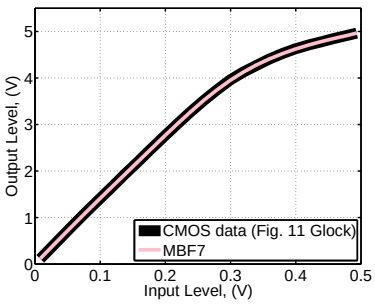

(g) NMSE = -59.20 dB

Figure A.17. CMOS (Fig. 11 Glock) AM/AM plots. (a) = Saleh [109], (b) = Ghorbani [110], (c) = Rapp [111], (d) = White (corrected) [137], (e) = O'Droma (Modified Saleh) [114], (f) = Cann 2012 [125], & (g) = O'Droma (Modified Bessel Fourier) [136] $M = 7$.

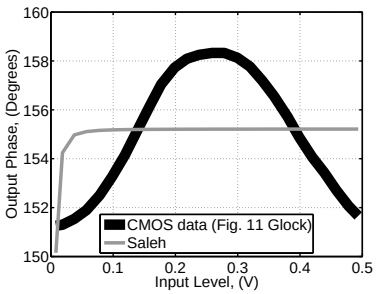

(i) NMSE = -36.31 dB

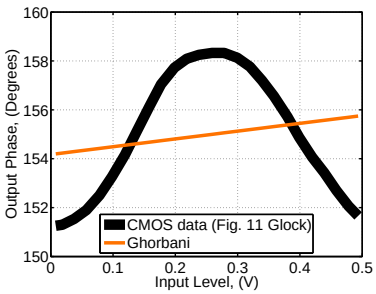

(ii) NMSE = -35.86 dB

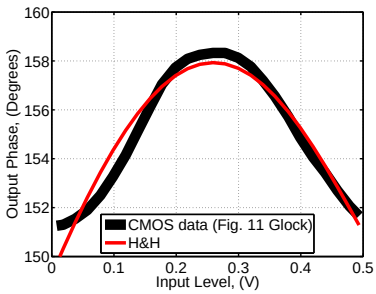

(iii) NMSE = -48.37 dB

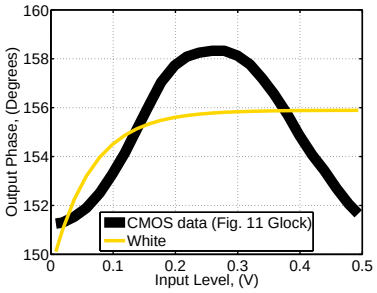

(iv) NMSE = -37.76 dB

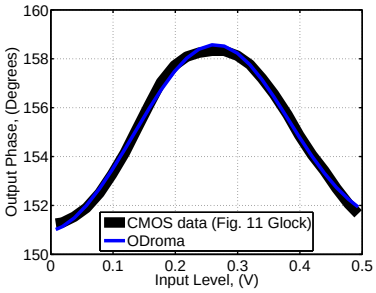

(v) NMSE = -59.71 dB

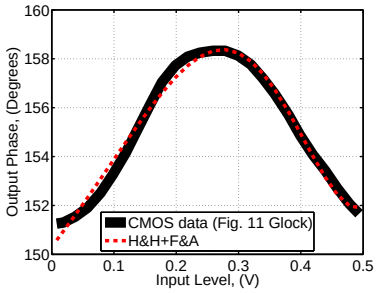

(vi) NMSE = -53.87 dB

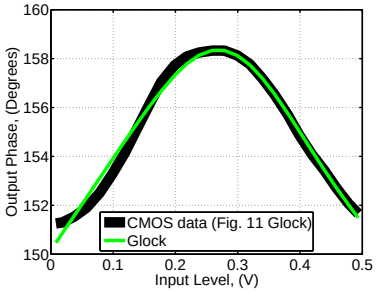

(vii) NMSE = -54.00 dB

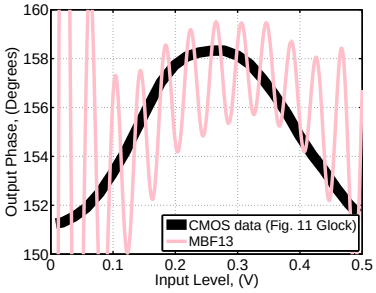

(viii) NMSE = -23.54 dB

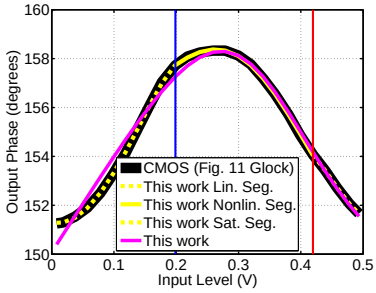

(ix) NMSE = -53.14 dB & -75.81 dB (Seg.)

Figure A.18. CMOS (Fig. 11 Glock) AM/PM plots. (i) = Saleh [109], (ii) = Ghorbani [110], (iii) = Honkanen & Haggman [112], (iv) = White [113], (v) = O'Droma (Modified Saleh) [114], (vi) = Fisher [137], (vii) = Glock [128], (viii) = O'Droma (Modified Bessel Fourier) [136] $M = 13$, & (ix) = This work including segmentation.

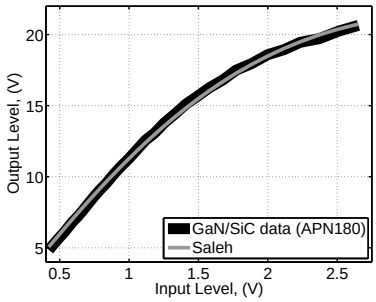

(a) NMSE = -35.75 dB

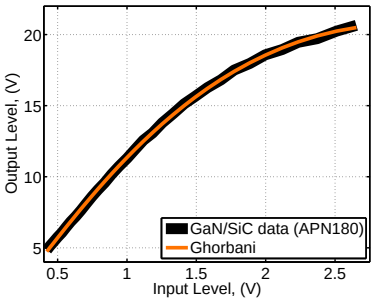

(b) NMSE = -44.76 dB

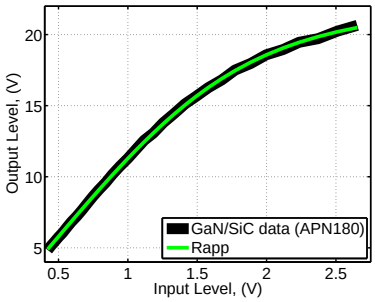

(c) NMSE = -46.44 dB

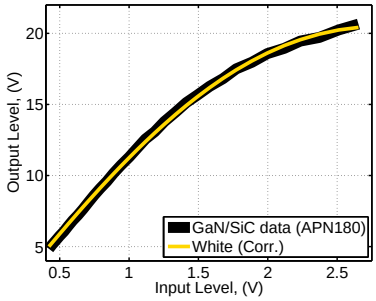

(d) NMSE = -40.18 dB

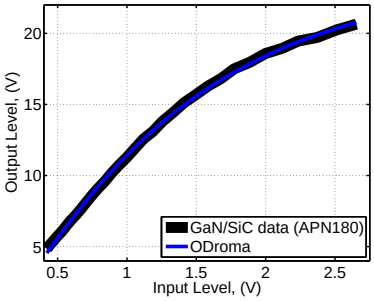

(e) NMSE = -39.48 dB

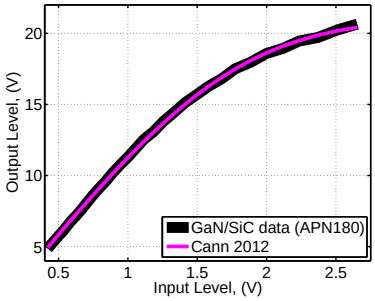

(f) NMSE = -43.11 dB

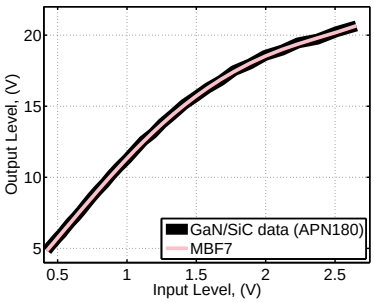

(g) NMSE = -50.73 dB

Figure A.19. GaN/SiC (APN180) AM/AM plots. (a) = Saleh [109], (b) = Ghorbani [110], (c) = Rapp [111], (d) = White (corrected) [137], (e) = O'Droma (Modified Saleh) [114], (f) = Cann 2012 [125], & (g) = O'Droma (Modified Bessel Fourier) [136] $M = 7$.

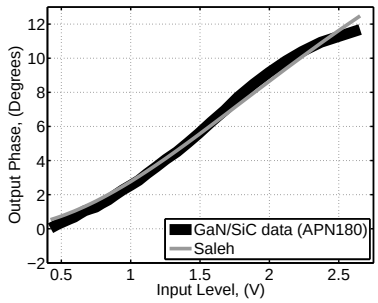

(i) NMSE = -24.25 dB

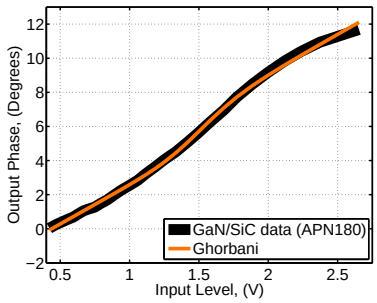

(ii) NMSE = -32.81 dB

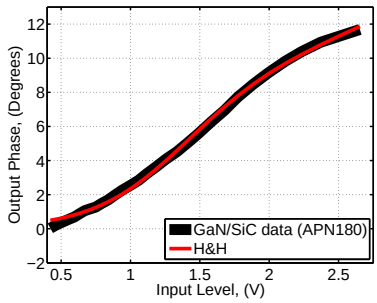

(iii) NMSE = -29.72 dB

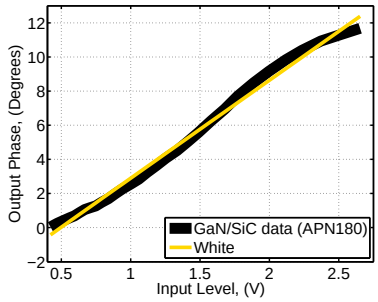

(iv) NMSE = -24.62 dB

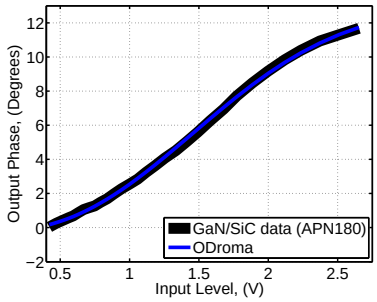

(v) NMSE = -35.45 dB

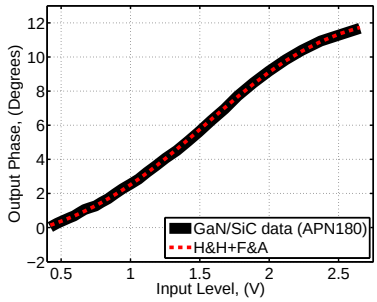

(vi) NMSE = -40.13 dB

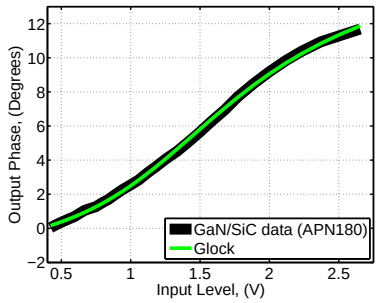

(vii) NMSE = -35.77 dB

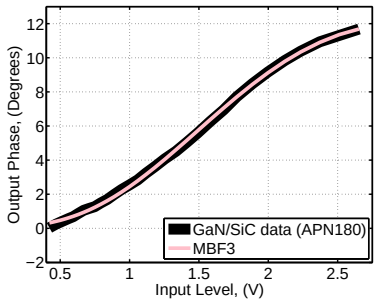

(viii) NMSE = -34.72 dB

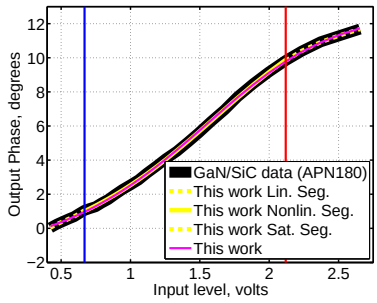

(ix) NMSE = -40.92 dB & -44.79 dB (Seg.)

Figure A.20. GaN/SiC (APN180) AM/PM plots. (i) = Saleh [109], (ii) = Ghorbani [110], (iii) = Honkanen & Haggman [112], (iv) = White [113], (v) = O'Droma (Modified Saleh) [114], (vi) = Fisher [137], (vii) = Glock [128], (viii) = O'Droma (Modified Bessel Fourier) [136] $M = 3$, & (ix) = This work including segmentation.

Appendix B

Derivative Calculation of Cann's 2012 AM/AM Model

THIS appendix shows the derivative calculation of Cann's 2012 AM/AM model for use in determining a new AM/PM model.

Step 1

$$\frac{\mathrm{d}}{\mathrm{d}x}\left[\frac{l\ln\left(\frac{\mathrm{e}^{s\left(\frac{gx}{l}+1\right)}+1}{\mathrm{e}^{s\left(\frac{gx}{l}-1\right)}+1}\right)}{s}-l\right] \tag{B.1}$$

Step 2

$$=\frac{l}{s}\cdot\frac{\mathrm{d}}{\mathrm{d}x}\left[\ln\left(\frac{\mathrm{e}^{s\left(\frac{gx}{l}+1\right)}+1}{\mathrm{e}^{s\left(\frac{gx}{l}-1\right)}+1}\right)\right]+\frac{\mathrm{d}}{\mathrm{d}x}\left[-l\right] \tag{B.2}$$

Step 3

$$=\frac{\frac{\mathrm{e}^{s\left(\frac{gx}{l}-1\right)}+1}{\mathrm{e}^{s\left(\frac{gx}{l}+1\right)}+1}\cdot\frac{\mathrm{d}}{\mathrm{d}x}\left[\frac{\mathrm{e}^{s\left(\frac{gx}{l}+1\right)}+1}{\mathrm{e}^{s\left(\frac{gx}{l}-1\right)}+1}\right]\cdot l}{s}+0 \tag{B.3}$$

Step 4

$$=\frac{\frac{\left(\mathrm{e}^{s\left(\frac{gx}{l}-1\right)}+1\right)\cdot\frac{\mathrm{d}}{\mathrm{d}x}\left[\mathrm{e}^{s\left(\frac{gx}{l}+1\right)}+1\right]-\frac{\mathrm{d}}{\mathrm{d}x}\left[\mathrm{e}^{s\left(\frac{gx}{l}-1\right)}+1\right]\cdot\left(\mathrm{e}^{s\left(\frac{gx}{l}+1\right)}+1\right)}{\left(\mathrm{e}^{s\left(\frac{gx}{l}-1\right)}+1\right)^{2}}l\left(\mathrm{e}^{s\left(\frac{gx}{l}-1\right)}+1\right)}{s\left(\mathrm{e}^{s\left(\frac{gx}{l}+1\right)}+1\right)} \tag{B.4}$$

Step 5

$$=\frac{l\left[\left(\frac{\mathrm{d}}{\mathrm{d}x}\left[\mathrm{e}^{s\left(\frac{gx}{l}+1\right)}\right]+\frac{\mathrm{d}}{\mathrm{d}x}\left[1\right]\right)\left(\mathrm{e}^{s\left(\frac{gx}{l}-1\right)}+1\right)-\left(\frac{\mathrm{d}}{\mathrm{d}x}\left[\mathrm{e}^{s\left(\frac{gx}{l}-1\right)}\right]+\frac{\mathrm{d}}{\mathrm{d}x}\left[1\right]\right)\left(\mathrm{e}^{s\left(\frac{gx}{l}+1\right)}+1\right)\right]}{s\left(\mathrm{e}^{s\left(\frac{gx}{l}-1\right)}+1\right)\left(\mathrm{e}^{s\left(\frac{gx}{l}+1\right)}+1\right)} \tag{B.5}$$

Step 6

$$= \frac{l\left[\left(e^{s\left(\frac{gx}{l}+1\right)} \cdot \frac{d}{dx}\left[s\left(\frac{gx}{l}+1\right)\right]+0\right)\left(e^{s\left(\frac{gx}{l}-1\right)}+1\right) - \left(e^{s\left(\frac{gx}{l}-1\right)} \cdot \frac{d}{dx}\left[s\left(\frac{gx}{l}-1\right)\right]+0\right)\left(e^{s\left(\frac{gx}{l}+1\right)}+1\right)\right]}{s\left(e^{s\left(\frac{gx}{l}-1\right)}+1\right)\left(e^{s\left(\frac{gx}{l}+1\right)}+1\right)} \tag{B.6}$$

Step 7

$$= \frac{l\left[s\left(\frac{g}{l} \cdot \frac{d}{dx}[x]+\frac{d}{dx}[1]\right) \cdot \left(e^{s\left(\frac{gx}{l}-1\right)}+1\right)e^{s\left(\frac{gx}{l}+1\right)} - s\left(\frac{g}{l} \cdot \frac{d}{dx}[x]+\frac{d}{dx}[-1]\right) \cdot e^{s\left(\frac{gx}{l}-1\right)}\left(e^{s\left(\frac{gx}{l}+1\right)}+1\right)\right]}{s\left(e^{s\left(\frac{gx}{l}-1\right)}+1\right)\left(e^{s\left(\frac{gx}{l}+1\right)}+1\right)} \tag{B.7}$$

Step 8

$$= \frac{l\left[\left(\frac{1g}{l}+0\right)s\left(e^{s\left(\frac{gx}{l}-1\right)}+1\right)e^{s\left(\frac{gx}{l}+1\right)} - \left(\frac{1g}{l}+0\right)se^{s\left(\frac{gx}{l}-1\right)}\left(e^{s\left(\frac{gx}{l}+1\right)}+1\right)\right]}{s\left(e^{s\left(\frac{gx}{l}-1\right)}+1\right)\left(e^{s\left(\frac{gx}{l}+1\right)}+1\right)} \tag{B.8}$$

Step 9 - Final result

$$= \frac{l\left(\frac{gs\left(e^{s\left(\frac{gx}{l}-1\right)}+1\right)e^{s\left(\frac{gx}{l}+1\right)}}{l} - \frac{gse^{s\left(\frac{gx}{l}-1\right)}\left(e^{s\left(\frac{gx}{l}+1\right)}+1\right)}{l}\right)}{s\left(e^{s\left(\frac{gx}{l}-1\right)}+1\right)\left(e^{s\left(\frac{gx}{l}+1\right)}+1\right)} \tag{B.9}$$

Step 10 - Alternative result

$$= \frac{l\left(e^{s\left(\frac{gx}{l}-1\right)}+1\right)\left(\frac{gse^{s\left(\frac{gx}{l}+1\right)}}{l\left(e^{s\left(\frac{gx}{l}-1\right)}+1\right)} - \frac{gse^{s\left(\frac{gx}{l}-1\right)}\left(e^{s\left(\frac{gx}{l}+1\right)}+1\right)}{l\left(e^{s\left(\frac{gx}{l}-1\right)}+1\right)^2}\right)}{s\left(e^{s\left(\frac{gx}{l}+1\right)}+1\right)} \tag{B.10}$$

Simplified - this is the result shown in (5.6)

$$\frac{\mathrm{d}}{\mathrm{d}x}\left[\frac{l\ln\left(\frac{\mathrm{e}^{s\left(\frac{gx}{l}+1\right)}+1}{\mathrm{e}^{s\left(\frac{gx}{l}-1\right)}+1}\right)}{s}-l\right]=\frac{g\left(\mathrm{e}^{s\left(\frac{gx}{l}+1\right)}-\mathrm{e}^{s\left(\frac{gx}{l}-1\right)}\right)}{\left(\mathrm{e}^{s\left(\frac{gx}{l}-1\right)}+1\right)\left(\mathrm{e}^{s\left(\frac{gx}{l}+1\right)}+1\right)} \tag{B.11}$$

Appendix C

THIS appendix shows the published papers as a result of this research.

An Optimized Segmented Quasi-Memoryless Nonlinear Behavioral Modeling Approach for RF Power Amplifiers

Paul O. Fisher, *Member, IEEE*, and Said F. Al-Sarawi, *Member, IEEE*

***Abstract*— This paper presents an optimized segmented modeling approach using a new quasi-memoryless (QM) behavioral model (BM) that allows for RF power amplifier (RF PA) modeling over a range of different solid state PA technologies. The presented model is a combination of an existing semiphysical amplitude-modulation-to-amplitude-modulation (AM/AM) memoryless BM, which correctly predicts third-order intermodulation distortion (3rd IMD) response in the small signal region, with the newly proposed amplitude-modulation-to-phase-modulation (AM/PM) model derived from the existing AM/AM model. Using the segmentation and optimization methods, performance comparisons with this new model are presented, showing normalized mean squared error AM/PM improvements up to 20 dB, as well as over 5-dB improvement in predicting the 3rd IMD using the proposed model. Comparisons against other well-known QM BMs are conducted using measured data as well as with data presented in the literature. The effects of these improvements on linearizer performance are also evaluated. The model significantly improves system-level modeling by allowing designers to accurately predict system performance using various RF PA devices over a range of technologies, based on data available through manufacturers' data or simple tests.**

***Index Terms*— Behavioral models (BMs), linearization techniques, power amplifier (PA) technologies, quasi-memoryless (QM) modeling, RF power amplifiers (RF PAs).**

I. Introduction

THERE are increasing requirements for modern wireless communications systems to provide improved data throughput as well as improved spectral distortion performance and increased power efficiencies. As PA devices have a very significant impact on achieving these demanding requirements, improved behavioral modeling of PA devices at the system level is essential. Having a behavioral model (BM), with an aim to provide PA designers with a simple means of modeling PA devices quickly over a range of technologies would be most advantageous.

Manuscript received February 27, 2017; revised May 24, 2017; accepted June 21, 2017. *(Corresponding author: Paul O. Fisher.)*

P. O. Fisher is with the School of Electrical and Electronic Engineering, University of Adelaide, Adelaide, SA 5005, Australia, and also with RF Industries, Adelaide, SA 5009, Australia (e-mail: paul.fisher@adelaide.edu.au; paul.fisher@rfi.com.au).

S. F. Al-Sarawi is with the School of Electrical and Electronic Engineering, University of Adelaide, Adelaide, SA 5005, Australia (e-mail: said.alsarawi@adelaide.edu.au).

Color versions of one or more of the figures in this paper are available online at http://ieeexplore.ieee.org.

Digital Object Identifier 10.1109/TMTT.2017.2723010

Another need for improved amplitude-modulation-to-amplitude-modulation (AM/AM) and AM-to-phase-modulation (AM/PM) models is associated with RF analog predistortion systems, which are commonly used as an alternative to produce simple and low-cost solutions for small cell repeaters [1], in contrast to advanced digital predistortion (DPD) systems where simplicity and cost are traded for increased performance. Improved accuracy models operating over a wider dynamic range also have benefits for use in envelope-predistortion linearizers that operate over larger dynamic ranges [2]. Recently, Glock *et al.* [3] described a new QM BM for AM/PM modeling to address certain phase responses in gallium arsenide (GaAs) and complementary metal oxide semiconductor (CMOS) technologies. Glock's justification for using a QM BM is based on the proposition that simple static models are both less complex and less computationally intensive and that well-designed RF PAs exhibit low memory effects, as indicated by the careful application of device biasing networks and techniques to reduce memory effects, as noted in [4], with the levels of errors associated with static BMs being acceptable for mobile handset applications.

Glock's proposed new model is a semiphysical AM/PM model, derived from Rapp's AM/AM model [5], providing the benefit of a simple QM BM, where model parameters are based on measured device performance. The model's semiphysical parameters can also be reused from the AM/AM model, making it attractive to RF PA designers. This is very powerful for PA designers as it provides immediate initial starting points for curve fitting of semiphysical parameters for the AM/AM model that are also used in the AM/PM modeling.

The recent application of standard CMOS processing technology, being applied to the manufacture of low-cost wireless RF PAs, used for mobile handsets [6], will be a useful advance; however, not all CMOS devices have AM/PM responses similar to those discussed in [3]. CMOS phase responses similar to [3] have been reported in [7], but phase responses similar to laterally diffused metal oxide semiconductor (LDMOS) devices in CMOS are shown in [8] and [9]. Considering the need for miniaturization and the need for system-level modeling before moving to an integrated solution, there is also a need for simple QM BMs that cover a range of device technologies and varying phase responses.

In this paper, Section II presents the need for simple BMs, including a brief review of other modeling approaches and

Figure C.1. Journal article 2017, Page 1.

technology modeling capability. A discussion on the benefits of BM accuracy improvements to linearizer performance is given in Section III. Section IV presents a new AM/PM model that is based on a recent AM/AM model that is capable of producing the correct third-order intermodulation distortion (3rd IMD) response in the small signal region. This new AM/PM model also has a semiphysical basis providing an accurate, usable, and relevant BM for PA designers. In Section V, segmentation and optimization methods are proposed and discussed to further improve the overall accuracy of the AM/PM model, allowing the model to be used over a range of different technologies. Verification of the model and methods proposed in this paper are demonstrated through comparison with measured data as well as with data presented in the literature. Consideration of the proposed model and accuracy improvement method is presented, with respect to 3rd IMD performance and impact on linearization improvement, in Section VI, followed by the conclusion and the acknowledgment. For the benefit of the reader, this paper is best viewed in color.

The primary contribution presented in this paper is an optimized segmented modeling approach using a new AM/PM model based on a simple AM/AM model that provides more accurate small signal 3rd IMD performance. This approach gives up to 20-dB normalized mean squared error (NMSE) improvement when modeling the AM/PM characteristics of an amplifier and further results in linearizer 3rd IMD predication improvements of over 5 dB, as discussed in Section VI. Segment boundary discontinuities are also considered, and it is demonstrated that worst-case discontinuities have no noticeable effect on the modeled amplifier spectrum when using digitally modulated signals. Further to this, the model is semiphysical and is shown to be suitable over a range of technologies.

II. SSPA Behavioral Models

A. Need for Simple Models

As nonlinearities of RF PAs are the major contributors to the performance degradation of a wireless system, a system-level simulation is used to evaluate the impact of RF PA on the overall system performance. The use of time domain or frequency domain techniques requires a full knowledge of all of the relevant circuit elements and accurate nonlinear models of the RF PA, which for an initial system-level evaluation may not be easily available or might require too much effort for an initial evaluation. In addition, such modeling is computationally demanding and requires a very long simulation times. A more suitable method for system-level modeling is to use simple bandpass QM BMs of an RF PA, resulting in fast, but still accurate, simulations that can be used to assess the impact of RF PA on system performance and allow for rapid RF PA device comparisons and selections. In such amplifiers, the complex input to output envelope voltage relationship is given by

$$v_{\text{out}}(t) = \text{Re}[G(v(t))e^{j(\phi(t)+\varphi(v(t))+\omega_c t)}] \quad (1)$$

where $G(v(t))$ and $\varphi(v(t))$ describe the instantaneous input to output envelope voltage gain and phase and these represent the AM/AM and AM/PM responses of RF PA, respectively. The RF carrier frequency is given by ω_c. The envelope model described by (1) thus describes the nonlinearities of RF PA in terms of its AM/AM and AM/PM responses. These can be readily determined either from device manufacturer datasheets or through further measurements and testing. Thus, there is a need for an accurate and simple RF PA BM for use in system-level simulations that can allow for device evaluation and selection. Here, a memoryless BM is an AM/AM only model and a quasi-memoryless (QM) BM is an AM/AM plus AM/PM model as defined in [10, Fig. 1].

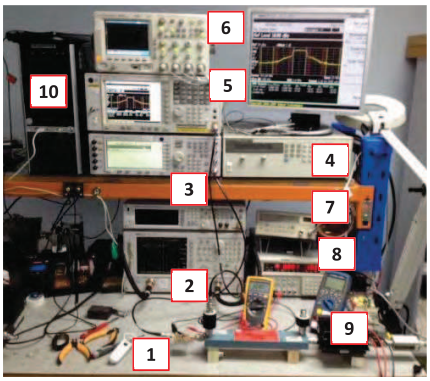

Fig. 1. Test setup for measuring the SHF-0189 HFET. 1) Device under test. 2) Vector network analyzer. 3) Signal generator. 4) Power supply 1. 5) Spectrum analyzer. 6) Digital storage oscilloscope. 7) Power meter. 8) Power supply 2. 9) Multimeter. 10) Computer.

The very significant benefit of semiphysical device BMs is that they provide the best starting point for any least squared curve fitting (LSCF) that will typically be required in order to extract these parameters plus any nonphysical model parameters. This is particularly important and powerful for practical PA designers as it provides them with a fast way of assessing suitable PA device alternatives, using parameters that are readily available in device datasheets, without the need for further complex testing and measurements. This can be used for both the AM/AM and AM/PM response estimations. Glock *et al.* [3] used Rapp's AM/AM model for the AM/AM component and also to extract the AM/PM model. In that model, only the smoothness parameter s and linear slope d parameters are nonphysical. This paper defines a semiphysical model as one where most model parameters are determined by the physical nature of the device performance, for example, Cann's 2012 AM/AM model [12] uses small signal gain and saturation levels as parameter values. For the sharpness parameter, this is readily determined by an initial estimate that when evaluated can quickly be adjusted to provide a value that matches device performance.

A further significant benefit for PA designers would be to have one model that is suitable for both AM/AM and AM/PM modeling and that: spans a range of current technologies and is simple, computationally efficient, physical or semiphysical in nature, accurate, and fast.

Figure C.2. Journal article 2017, Page 2.

The O'Droma model [11] can provide an excellent fit to a range of AM/AM and AM/PM curve shapes but the parameters for this model do not have a physical origin. As a result, determining the starting point values for this and other nonphysically-based model parameters for LSCF can be difficult and may require more sophisticated methods to determine these starting point values. So an appropriate selection of the starting points is needed to ensure a final optimum outcome. With semiphysical-based models, the majority of parameter starting points are taken from available data, thus avoiding possible guessing or further measurements. For the nonphysical parameters of the Rapp and Cann 2012 AM/AM models several plots of the AM/AM responses can be made for a particular device, for different s values. By comparing these plots with measured data, an estimate of the starting value for s can be found. Having semiphysical starting points is also a very useful means of self-checking the LSCF parameter results, as the final values for LSCF parameter results should be very close to the starting values.

B. Review of Simple PA Behavioral Models

This paper recognizes the heritage of several BMs from traveling wave tube amplifier (TWTA) backgrounds, as this has been an early starting point for several PA BMs. Although TWTAs are still relevant and in use nowadays, the focus of this paper is on solid state PA (SSPA) technologies, such as GaAs, CMOS, and LDMOS.

There are several existing well-established QM BMs that offer PA designers a simple and fast means of providing system analyses to assist them in selecting a suitable device for their RF PA requirements. Cann [12] introduced a simple AM/AM semiphysical memoryless model for an overdriven or soft-limiting solid state amplifier that used bipolar technology, allowing the knee sharpness to be adjusted while maintaining small signal linearity. Then, Saleh [13] introduced a simple model for a TWTA that required only two parameters for both AM/AM and AM/PM modeling.

Ghorbani and Sheikhan [14] proposed an SSPA specific model, for both AM/AM and AM/PM of the same form, having only four parameters to address inaccuracies of using TWTA-based models for SSPAs. Rapp [5] presented a memoryless AM/AM only model for GaAs FET SSPAs that also included semiphysical parameters. Honkanen and Haggman [15] applied Rapp's model as part of a bipolar junction transistor (BJT) AM/AM model while introducing a new AM/PM model defined with a maximum of 0° phase shift. White *et al.* [16] introduced new models for AM/AM and AM/PM to better model Ka-Band SSPAs, when compared with the Saleh, Ghorbani, and Rapp models.

Saleh's model was further developed in [11], with respect to LDMOS, addressing the discontinuity seen in the application of Saleh's original AM/PM model when applied to typical LDMOS AM/PM characteristics.

Cann [17] updated his 1980 model to eliminate issues found with the original model when calculating small signal 3rd IMD products, with the model again based on semiphysical parameters.

Later, O'Droma and Yiming [18] proposed a modified Bessel–Fourier model that provided improved accuracy with performance extending into the saturation region beyond available data. The model can be used with a low number of fitting parameters, and accuracy can be improved by increasing the number of fitting parameters. It is suitable for memoryless modeling including both AM/AM and AM/PM characteristics of nonlinear PAs. Although accurate, it is not physically based.

We proposed [19], an extension to Honkanen and Haggman's AM/PM model, allowing it to model phase shifts greater than 0° and also provided a correction to White's AM/AM model. Also, Glock *et al.* [3] presented an approach based on Rapp's AM/AM model but introduced a new AM/PM model determined from the first derivative of the Rapp AM/AM model plus additional terms.

In this paper, these simple models, along with the definitions of their respective parameters, are summarized in Table I.

Other models that have also been considered in the literature are as follows. Cunha *et al.* [20] proposed a rational function-based model that includes memory effects, while Rawat *et al.* [21] proposed generalized rational functions for reduced complexity BMs but was targeted at inverse modeling, including memory effects, for DPD applications. Harguem *et al.* [22] proposed using Gegenbauer polynomials and Jebali *et al.* [23] proposed using Zernike polynomials. Both of these approaches target improved numerical stability with minimal computational cost, when compared to Volterra series approaches, but the models are more mathematically complex compared with the simple memoryless models of this paper. Safari *et al.* [24] proposed using cubic splines. While these models are alternatives to the simple BMs presented in Table I, they also tend to be more complex mathematically and depart from the simple semiphysical BM approach.

C. Comparing PA Behavioral Models

In order to compare these BMs, NMSE, using (2) below, as well as frequency domain comparisons, made via SIMULINK with a wide-band code division multiple access (WCDMA) digitally modulated baseband envelope signal applied to the RF PA model's input and with its output presented in the frequency domain via the SIMULINK fast-Fourier-transform (FFT)-based spectrum analyzer element. These comparisons are presented for the various AM/PM and AM/AM models described in this paper.

NMSE is used to provide a measure of the error between the estimate from the model and measured data, for both the AM/AM and AM/PM models, and is defined in dB, as [26]

$$\mathrm{NMSE_{dB}} = 10\log_{10}\left(\frac{\sum_{n=0}^{N}|y_{\mathrm{meas.}}(n) - y_{\mathrm{model}}(n)|^2}{\sum_{n=0}^{N}|y_{\mathrm{meas.}}(n)|^2}\right) \tag{2}$$

where N is the number of samples, $y_{\mathrm{meas.}}$ is the complex baseband envelope of the measured PA output, and y_{model} is the complex baseband envelope of the model output.

Another comparison for SSPA BMs is computational speed and parameter count. In terms of computational speed this has not been included as for several models, fits could not

Figure C.3. Journal article 2017, Page 3.

This article has been accepted for inclusion in a future issue of this journal. Content is final as presented, with the exception of pagination.

TABLE I
SIMPLE BMS FOR RF PAS, COMPARISONS AND TECHNOLOGIES

Model, Year	AM/AM	AM/PM	Technology Modeled
	r = input voltage, $A(r)$ = output voltage	r = input voltage, $\phi(r)$ = output phase	
Cann, 1980, [12], Loyka, 1982, [25]	$A_{\text{Cann'80}}(r) = \frac{Lsgn(r)}{\left[1+\left(\frac{L}{g\lvert r\rvert}\right)^{s}\right]^{1/s}}$, [25] $= \frac{gr}{\left[1+\left(\frac{g\lvert r\rvert}{L}\right)^{s}\right]^{1/s}}$, [12] L = saturation limit level (SLL), g = small signal gain (SSG), s = sharpness parameter	——— ———	Over-driven soft limiting amplifier, AM/AM only
Saleh, 1981, [13]	$A_{\text{Saleh}}(r) = \frac{\alpha_a r^{\eta_a}}{(1+\beta_a r^{\gamma_a})^{\nu_a}} - \epsilon_a = \frac{\alpha_a r}{1+\beta_a r^2}$ α_a = amplitude fitting parameter (AFP), β_a = AFP, η_a = 1, γ_a = 2, ν_a = 1, ϵ_a = 0	$\phi_{\text{Saleh}}(r) = \frac{\alpha_\phi r^{\eta_\phi}}{(1+\beta_\phi r^{\gamma_\phi})^{\nu_\phi}} - \epsilon_\phi = \frac{\alpha_\phi r}{1+\beta_\phi r^2}$ α_ϕ = phase fitting parameter (PFP), β_ϕ = PFP, η_ϕ = 1, γ_ϕ = 2, ν_ϕ = 1, ϵ_ϕ = 0	TWTA
Ghorbani, 1991, [14]	$A_{\text{Ghorbani}}(r) = \frac{x_1 r^{x_2}}{1+x_3 r^{x_2}} + x_4 r$ x_1, x_2, x_3, x_4 = AFPs	$A_{\text{Ghorbani}}(r) = \frac{y_1 r^{y_2}}{1+y_3 r^{y_2}} + y_4 r$ y_1, y_2, y_3, y_4 = PFPs	SSPA
Rapp, 1991, [5]	$A_{\text{Rapp}}(r) = \frac{gr}{\left[1+\left(\frac{gr}{L}\right)^{2s}\right]^{1/2s}}$ L = SLL, g = SSG, s = sharpness parameter	——— ———	SSPA, AM/AM only
Honkanen, 1997, [15]	$A_{\text{Honkanen}}(r) = \frac{V_o'(r)}{\left[1+\left(\frac{V_o'(r)}{L}\right)^{2s}\right]^{1/2s}}$, [5] $V_o'(r) = \left(e^{kr}-1\right), r+V_b \le r_{tr}$ & $V_o'(r) = \nu\left(r+V_b\right) + b_{aHH} - e^{kr} + 1, r+V_b > r_{tr}$ $V_b = r$ = 0 adj. point, r_{tr} = exp. to lin. response transition point, k = exp. curve steepness, ν = exp. curve, lin. portion, nom. gain, $b_{aHH} = e^{kr} - 1 - \nu r_{tr}$	$\phi_{HH}(r) = \frac{b_{\phi HH}}{1+e^{-c_{\phi HH}(r-a_{\phi HH})}} \cdot \frac{1}{p_1 r+p_2}$ $a_{\phi HH}$ = input (BJT) turn-on voltage, $b_{\phi HH}$ = turn-on |phase|, $c_{\phi HH}$ = step change steepness, p_1, p_2 = downward slope adj. parameters	BJT AM/AM adaption of [5], AM/PM to zero degrees only
White, 2003, [16], Fisher, 2015, [19] White, [16] Cann, [17]	$A_{\text{White}}(r) = a_w\left(1-e^{-b_w r}\right) + c_w r e^{-d_w r^2}$, $A_{\text{White}}(r) = a_w\left[\left(1-e^{-b_w r}\right) + c_w r e^{-d_w r^2}\right]$ a_w = SLL, b_w = SSG, c_w, d_w = AFPs a_w = SLL, c_w = SSG, b_w, d_w = AFPs	$\phi_{\text{White}}(r) = f_w\left(1-e^{-g_w(r-h_w)}\right), r \ge h_w$ $\phi_{\text{White}}(r) = 0, r < h_w$ f_w = mag., g_w = curve slope, $h_w = r$ range shift	Ka Band SSPAs Cann's view on White's parameters
O'Droma, 2009, [11]	$A_{\text{O'Droma'09}}(r) = \frac{\alpha_a r^{\eta_a}}{(1+\beta_a r^{\gamma_a})^{\nu_a}} - \epsilon_a$ $\alpha_a, \beta_a, \eta_a, \gamma_a, \nu_a, \epsilon_a$ = AFPs	$\phi_{\text{O'Droma'09}}(r) = \frac{\alpha_\phi r^{\eta_\phi}}{(1+\beta_\phi r^{\gamma_\phi})^{\nu_\phi}} - \epsilon_\phi$ $\alpha_\phi, \beta_\phi, \eta_\phi, \gamma_\phi, \nu_\phi, \epsilon_\phi$ = PFPs	LDMOS SSPA
Cann, 2012, [17]	$A_{\text{Cann'12}}(r) = \frac{L}{s}\ln\left[\frac{1+e^{s\left(\frac{gr}{L}+1\right)}}{1+e^{s\left(\frac{gr}{L}-1\right)}}\right] - L$ L = SLL, g = SSG, s = sharpness parameter	——— ———	Over-driven soft limiting amplifier, AM/AM only
O'Droma, 2013, [18]	$A_{\text{O'Droma'13}}(r) = \sum_{k=1}^{M} b_{(2k-1)a} J_1\left(\frac{2\pi}{\gamma_a D}(2k-1)r\right)$ D = Input Amplitude Dynamic Range, γ_a = period ratio of FS to IVTCs, $b_{(2k-1)a}$ = AFPs, J_1 = Bessel fn. of 1st kind, M = no. of AFPs	$\phi_{\text{O'Droma'13}}(r) = \sum_{k=1}^{M} b_{(2k-1)\phi} J_1\left(\frac{2\pi}{\gamma_\phi D}(2k-1)r\right)$ D = Input Amplitude Dynamic Range, γ_ϕ = period ratio of FS to IVTCs, $b_{(2k-1)\phi}$ = PFPs, J_1 = Bessel fn. of 1st kind, M = no. of PFPs	LDMOS SSPA Fourier series (FS), instantaneous voltage transfer characteristics (IVTCs)
Glock, 2015, [3]	Use Rapp 1991 AM/AM model [5] L = SLL, g = SSG, s = sharpness parameter	$\phi_{\text{Glock}}(r) = \frac{(a_{Gl}-b_{Gl})r+c_{Gl}-d_{Gl}}{\left(1+\left(\frac{gr}{L}\right)^{2s}\right)^{1/2s+1}} + b_{Gl} r + d_{Gl}$ a_{Gl} = linear region slope, b_{Gl} = sat. region slope, c_{Gl} = phase at r = 0, d_{Gl} = sat. region lin. approx. of phase delta	65 nm GaAs & 28 nm CMOS PAs
Fisher, 2015, [19]	Use Rapp 1991 AM/AM model [5] L = SLL, g = SSG, s = sharpness parameter	$\phi_{FA}(r) = \frac{b_{HH}}{1+e^{-c_{HH}(r-a_{HH})}} \cdot \frac{1}{p_1 r+p_2} + d_{FA}$ $a = a_{\phi_{HH}}$, $b = b_{\phi_{HH}}$, $c = c_{\phi_{HH}}$, $p_1 = p_1$, $p_2 = p_2$, d_{FA} = phase offset	AM/PM $\ge$ zero degrees applied to LDMOS
This work	Use Cann 2012 AM/AM model [17] L = SLL, g = SSG, s = sharpness parameter	$\phi(r) = [(a-b)r + c - d]\frac{A'(r)}{g} + br + d$, $\frac{A'(r)}{g} = \left[\frac{\left(e^{s\left(\frac{gr}{L}+1\right)} - e^{s\left(\frac{gr}{L}-1\right)}\right)}{\left[1+e^{s\left(\frac{gr}{L}+1\right)}\right]\left[1+e^{s\left(\frac{gr}{L}-1\right)}\right]}\right]$ $a = a_{Gl}, b = b_{Gl}, c = c_{Gl}, d = d_{Gl}$	LDMOS, HFET, E-pHEMT, InGaP, HBT, Si CMOS FETs, GaN, SiC

be obtained from initial starting points, except for semiphysical models, where the starting points were readily available from the measured or manufacturer's data, a significant advantage.

In terms of parameter count, Table II shows the number of parameters required for each model listed in Table I.

D. Technology Comparisons

To investigate the suitability of the various models as presented in Table I, including the new model of this paper, testing was performed, via the simple test setup shown in Fig. 1, on devices from a range of technologies, such as an LDMOS FET, GaAs heterojunction FET (HFET), GaAs enhancement mode

Figure C.4. Journal article 2017, Page 4.

TABLE II
BM VERSUS NUMBER OF PARAMETERS COMPARISON

Model	Number of Parameters	
	AM/AM	AM/PM
Cann 1980, [12]	3	–
Saleh, [13]	2	2
Ghorbani, [14]	4	4
Rapp, [5]	3	–
Honkanen, [15]	5	5
White, [16]	4	4
O'Droma 2009, [11]	5	6
Cann 2012, [17]	4	–
O'Droma 2013, [18] Mod. Bess. Fou. coeff. no. = M (odd number) and γ.	M+1	M+1
Glock, [3]	3*	3*+4
Fisher, [19]	PM only	6
This work	3*	3*+4
This work, Segmented Method	3*	3*+4+4+4

* = AM/AM parameters re-used in AM/PM model.

pseudomorphic high-electronmobility-transistor (E-pHEMT), indium gallium phosphide (InGaP) heterojunction-bipolar-transistor (HBT), silicon (Si) CMOS FETs, and a galliun nitride (GaN) on silicon carbide (SiC) HEMT.

The modeling results for these devices and other devices from the literature are shown below in terms of AM/AM and AM/PM NMSE, in Table III. These results show that the O'Droma's models, both the Mod. Saleh and Mod. Bessel–Fourier ($M = 7$) models perform very well for AM/AM followed by the Rapp and Cann 2012 models. In terms of AM/AM modeling, it can be seen from the AM/AM section of Table III that most models perform reasonably well over a range of technologies. This would be expected based on similar AM/AM curve shapes for typical AM/AM responses.

In terms of AM/PM performance, the results are quite different. For some devices, the NMSE values present as acceptable; however, examination of actual curve fit data reveals a different outcome. For space reasons, plots could not be included so various marginal fits and failures have been identified within Table III and are now discussed. Some models are unable to fit the data, while others perform better for some technologies. Again the O'Droma's (Mod. Saleh) model performs very well over the range of technologies followed by the Glock's model and the model presented in this paper, based on Cann's 2012 AM/AM model. The O'Droma Mod. Bessel–Fourier model requires from 3 to 15 parameters to fit the range of technologies; however when used to model Glock's data [3, Fig. 11, 2V2 curve], although it provides a general shape fit for $M = 13$, it has a superimposed rippled response. The benefit of the AM/PM model presented here is that it fits all technologies, is semiphysical, is accurate in terms of predicting 3rd IMDs with a moderate number of fitting parameters ($M = 7$). For the models that do not perform well or fail, no analysis, similar to that given in [11], is presented as this is beyond the scope of this paper.

The results presented in this paper are based on either measured data by the authors, data from device manufacturer's datasheets, or data presented in the literature. Device data measured by the authors uses a single tone continuous wave (CW) signal for modeling and uses a WCDMA modulated signal for frequency comparison. Data from manufacturer's data sheets is a single tone CW signal. For data used from within the literature, this is identified, where provided. The frequencies and signal types for this data are identified in the header of Table III. Literature and device manufacturer's data within figures include the literature or device manufacturer's references.

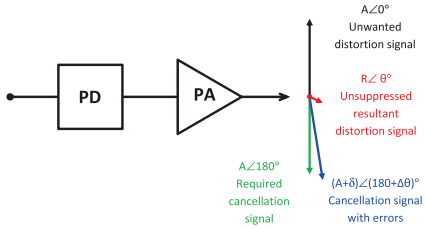

Fig. 2. PD/PA combination showing the vector cancellation process for 3rd IMDs.

III. LINEARIZER BENEFITS FROM ACCURACY IMPROVEMENTS

For simple low cost RF predistortion linearizers to compete with other more sophisticated linearizers, e.g., DPD linearizers that are complex and require expensive hardware having higher power consumption, their accuracy must also be comparable [1]. Thus, a means to quantify the benefits of AM/AM and AM/PM modeling accuracy improvement, when applied to a low-cost linearizer, is required.

Nojima and Konno's [33] analysis, for a combined predistorter (PD) and PA that uses a third-order approximation for the PA, as shown in Fig. 2, provides an equation for calculating the achievable 3rd IMD reduction S_{IMD}. In this equation, the difference in the PD amplitude error (δ in dB) and phase error ($\Delta\theta$ in degrees) from the complete cancellation conditions of equal amplitude and opposite phase, between the PD and the PA and is given by

$$S_{\mathrm{IMD}} = -10\log_{10}\left[1 + 10^{\delta/10} - 2\cdot 10^{\delta/20}\cos(\Delta\theta)\right]. \quad (3)$$

For this combination, the distortion reduction achievable is a function of the amplitude and phase errors between the combined PD and PA as a result of the PD. Normally, the PD is adjusted to provide an equal amplitude and opposite phase for the 3rd IMD component at the output of the PA. Using Faulkner *et al.'s* [34] approach, the PD is configured to be an ideal PD for the measured PA AM/AM and AM/PM responses. By replacing the measured PA results with the AM/AM and AM/PM models, the IMD distortion can be attributed to the PA BM performance. An assessment of further AM/AM and AM/PM modeling improvement on IMDs and linearization performance can thus be determined for the model and segmentation method presented here. This assessment is given in Section VI.

TABLE III
AM/AM AND AM/PM NMSE RESULTS COMPARISON OF MODELS VERSUS TECHNOLOGIES

Model	Technology									
	TWTA [13] Fig. 2	**BJT** [15] Fig. 2	**HFET** [27] SHF-0189	**LDMOS** [28] MW6S004N	**HBT** [29] MMG3005	**E-pHEMT** [30] ALM-31122	**LDMOS** [31] BLM7G1822S◇	**GaAs** [3] Fig.8	**CMOS** [3] Fig.11	**GaN/SiC** [32] APN180
	Signal Type & Frequency									
	CW 4.1GHz.	-	CW & WCDMA 881.5MHz. Two Tones at 900MHz, spacing 1MHz.	CW 881.5MHz.	CW 881.5MHz.	CW 881.5MHz.	CW 2140MHz.	-	-	CW 29GHz.
AM/AM NMSE (dB)										
Saleh [13]	-38.20	-24.08	-31.68	-28.69	-29.68	-31.74	-27.38	-33.00	-34.64	-37.75
Ghorbani [14]	-42.82	-32.86	-32.18	-33.94	-37.13	-34.79	-32.50	-35.74	-38.92	-44.76
Rapp [5]	-29.03	-30.24	-49.22	-38.83	-56.70	-53.26	-38.81	-43.44	-47.33	-46.44
White [19] (Cor.)	-42.41	-24.65	-33.52	-38.79	-33.31	-43.01	-28.10	-36.63	-36.30	-40.18
O'Droma [11]	-40.08	-50.57	-52.67	-50.85	-59.54	-57.95	-51.60	-47.55	-57.20	-39.48
Cann 2012 [17]	-29.70	-30.16	-43.53	-36.43	-51.88	-44.77	-37.70	-39.61	-44.56	-43.11
O'Droma [18] Parameters = 7	-44.10	-57.83	-56.95	-49.10	-63.22	-48.26	-49.00	-37.09	-59.20	-50.73
AM/PM NMSE (dB)										
Saleh [13]	-38.05	-36.90†	-10.59†	-0.32†	-31.08†	-10.73⋆	-10.93⋆	-11.79⋆	-36.31†	-24.25
Ghorbani [14]	-39.83	-63.63	-36.14	-18.82	-24.70†	-21.23	-18.72	-12.07	-35.86†	-32.81
Honkanen [15]	-31.63	-48.64	-27.65	-3.08†	-52.92	-23.38	-16.09	-17.68	-48.37	-29.72
White [16]	-33.13	-59.14	-21.25⋆	-2.28†	-38.39⋆	-16.82⋆	-9.43⋆	-10.27⋆	-37.76†	-24.62
O'Droma [11]	-42.14	-64.24	-49.18	-40.03	-48.09	-34.59	-36.16	-16.17	-59.71	-35.45
Fisher [19]	-37.82	-57.21	-25.19⋆	-29.01	-58.67	-39.81	-23.10	-19.27	-53.87	-40.13
Glock [3]	-33.44	-53.08	-36.25	-30.41	-60.16	-33.48	-18.61	-30.37	-54.00	-35.77
O'Droma [18] Parameters = ( )	-57.78 (7)	-27.22 (15)	-35.77 (15)	-20.84 (15)	-63.60 (15)	-31.41 (7)	-32.81 (7)	-223.54 (13)	-23.54† (13)	-34.72 (3)
This work	-34.74	-53.03	-31.98	-31.90	-64.24	-34.02	-17.65	-29.77	-53.14	-40.92
This work (Seg.)	-42.81	-56.56	-48.36	-48.14	-75.58	-45.78	-33.71	-52.72	-75.81	-44.79

† = unable to fit AM/PM response, ⋆ = marginal fit, ◇ = AM/PM normalised to zero degrees.

IV. NEW AM/PM MODEL GENERATION

A. AM/AM Accuracy Improvement

Rapp's AM/AM model [5] has the same equation form as the model first proposed in [12] but without the modulus function. Cann's 1980 AM/AM model equation is given as

$$A(r) = \frac{L\mathrm{sgn}(r)}{\left[1+\left(\frac{L}{g|r|}\right)^s\right]^{1/s}} = \frac{gr}{\left[1+\left(\frac{g|r|}{L}\right)^s\right]^{1/s}} \tag{4}$$

where g, r, L, and s are the small signal gain (SSG), input amplitude, output limit level, and sharpness parameters, respectively.

Litva and Lo [35] identified that Cann's 1980 AM/AM model had issues in generating correct small signal 3rd IMD responses. This was confirmed and the reason for this issue was determined in [25]. Cann's new memoryless AM/AM model, presented in 2012, is given as [17]

$$A(r) = \frac{L}{s}\ln\left[\frac{1+e^{s\left(\frac{gr}{L}+1\right)}}{1+e^{s\left(\frac{gr}{L}-1\right)}}\right] - L \tag{5}$$

with the parameters as described in Table I. It should be noted that the issues in the old model are related to modeling two discrete tones used to generate IMD products; however, for a typical digital modulation scheme, no issues were observed. This more accurate AM/AM model will form the basis for the new AM/PM model discussed below.

Glock's approach of taking the derivative of the AM/AM model, to create an AM/PM model, has been applied to Cann's 2012 AM/AM model.

Following Glock's derivative technique, Cann's 2012 improved AM/AM model can similarly be fully described by its derivatives in the linear and saturation regions, hence the first derivative of the improved Cann's 2012 AM/AM model can serve as the basis for a new AM/PM model. This new AM/PM model, derived from Cann's 2012 AM/AM model, is termed the Cann's 2012 AM/AM-based AM/PM model and hereafter will be referred to as Cann 12B. With reference to (5), the SSG normalized first derivative of the improved Cann AM/AM equation is given by

$$\frac{A'(r)}{g} = \left[\frac{\left(e^{s\left(\frac{gr}{L}+1\right)} - e^{s\left(\frac{gr}{L}-1\right)}\right)}{\left[1+e^{s\left(\frac{gr}{L}+1\right)}\right]\left[1+e^{s\left(\frac{gr}{L}-1\right)}\right]}\right] \tag{6}$$

with the parameters as described in Table I. Similar to Glock's derivation, the resulting AM/PM model is

Figure C.6. Journal article 2017, Page 6.

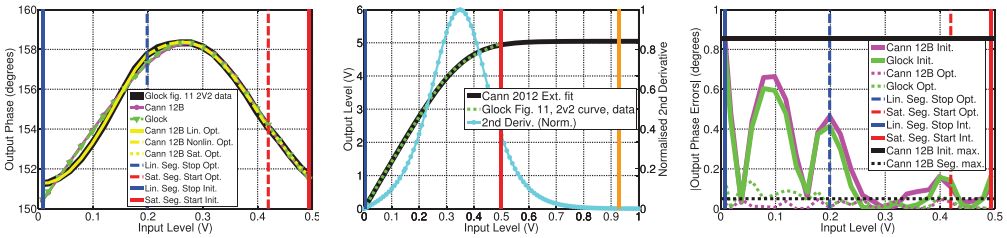

Fig. 3. (a) Comparison of [3, Fig. 11, 2V2 curve], data (solid black curve), Glock's AM/PM model (dotted green curve) and new Cann 12B AM/PM model derived using Glock's method, from this paper (solid magenta circle trace). (b) Glock's model in [3, Fig. 11, 2V2 curve], AM/AM data (dotted green curve), extended AM/AM data (solid black curve), using [19] and normalized (to the maximum value) numerical second derivative of extended AM/AM data (solid cyan circle curve) using MATLAB. The solid blue vertical line is the initial end of the linear region, the solid orange vertical line is start of saturation region by the second derivative calculation. The solid red vertical line is the end of the available AM/PM data, effectively the end of the saturation region for the available data. (c) Comparison of |Output Phase errors| versus input voltage in [3, Fig. 11, 2V2 curve], data, showing before and after segmented approach optimization. Also, shown are the maximum Cann 12B AM/PM model absolute output phase errors for both the initial (solid black line) and segmented (dotted black line) approach being 0.86° and 0.05°, respectively.

determined as

$$\phi(r) = [(a-b)r + c - d]\frac{A'(r)}{g} + br + d \tag{7}$$

where a and b are the gradients in the linear and saturation regions, respectively, c defines the phase difference when the input amplitude is zero, and d in combination with b are a linear approximation of the phase difference in the saturation region. These parameters are also given in Table I.

This alternative AM/PM model gives very similar results to Glock's AM/PM model, i.e., it is within 1 dB of AM/PM NMSE in [3, Fig. 11, 2V2 curve], shown as part of Glock's model in [3, Fig. 11] test data, reproduced here in Fig. 3(a).

V. Method to Improve New AM/PM Model Accuracy

A. Segmented Curve Fitting

Glock's technique, for determining the linear, nonlinear, and saturation regions from the AM/AM characteristic response can also be utilized for further AM/PM modeling improvements. This technique can be used to determine the linear, nonlinear, or saturation region segments of AM/PM responses so that curve fits of these segments can be applied in a similar approach to that used in [2], for piecewise curve fitting of nonlinear segments of AM/AM and AM/PM envelop tracking amplifiers and more recently in [36], presenting an optimal segmentation approach but with an increased number of segments. In this case, the benefits of segmented curve fitting are that a more accurate model results, thus assisting with the comparisons for device selection after system analysis, and also for defining potential improvements in linearization margin for a particular device.

By applying the new Cann 12B AM/PM model for each segmented region and by optimizing the end of the linear region segment and start of the saturation region segment, an overall improvement of around 20 dB can be achieved in AM/PM NMSE at the expense of further simple processing steps for each segment. This technique can be applied to both the models of Glock and Cann across a range of technologies. Similar to Glock's AM/PM model, the Cann's 12B AM/PM model has the ability to provide starting values for LSCF for each of the segments.

In order to use these models for an improved AM/PM accuracy estimation, the second derivative of the AM/AM response is used to determine the linear and saturation regions. From Glock's AM/AM data, it can be seen that more data points into the saturation region are required. Previously, we have developed an approach [19] based on Rapp's AM/AM model that extrapolates the AM/AM performance into the saturation region, which has been demonstrated through testing of an LDMOS device. As Glock's paper uses the Rapp AM/AM model, this data can be extended into the saturation region. Similarly for Cann's 2012 AM/AM model, data can be extended into the saturation region. Using the extended AM/AM data, the transition from the linear to saturation regions can be precisely determined as a function of v_{in} when the second derivative of the AM/AM data equals zero [see Fig. 3(b)]. As can be seen from this plot, the linear region stop point (vertical solid blue line) is at $v_{\text{in}} = 0$ V and saturation region start point (vertical orange solid line) is well beyond the available data, by the second derivative calculation. This means that the practical LSCF data starting range extends from $v_{\text{in}} = 0$ V to where v_{in} is at the full extent of the available data (vertical red solid line), in this case where $v_{\text{in}} = 0.5$ V. The region between the solid blue and red lines is practically the full AM/PM model region for initial LSCF and these points being the starting points for the AM/PM segmentation method optimization.

Initial AM/PM curve fits for both the Glock and Cann 12B AM/PM models have been performed over the entire available data in [3, Fig. 11, 2V2 curve] data, with the results from both the Glock (green down triangle curve) and the Cann 12B AM/PM (magenta circle curve) models shown in Fig. 3(a). These are single segment fits between the linear region stop and saturation region start points. This is the same as using the AM/PM model over the entire data range. Although the

This article has been accepted for inclusion in a future issue of this journal. Content is final as presented, with the exception of pagination.

TABLE IV
GLOCK'S MEASURED DEVICE DATA FROM [3, FIG. 11, 2V2 CURVE], AM/AM AND AM/PM NMSE COMPARISON

AM/AM - NMSE (dB)		AM/PM - NMSE (dB)		
Model	**Full**	**Model**	**Full (Initial)**	**Seg. Optim.**
Rapp	-48.91	Glock	-54.00	-68.00
Cann 2012	-46.04	This work	-53.14	-75.90

device phase range is small for some devices, around 6° to 8°, this is still significant in terms of linearizers being able to reduce IMDs, particularly for analog PDs, as indicated in [37]. Further improvements as a result of increased accuracy will be beneficial in this area.

The following section will discuss how to improve the modeling accuracy by identifying and then optimizing the linear and saturation regions.

B. Optimized Segmented Curve Fitting

To further improve the accuracy of the AM/PM model, an optimization routine was developed to identify the optimum linear stop and saturation start region points to provide an enhanced data fit in terms of NMSE performance. A comparison between the initial fit and the optimized fit for each of the segments is shown in Fig. 3(a) (yellow curves). This is only shown for the new Cann 12B AM/PM model.

A comparison between the Glock and Cann 12B absolute phase errors, for both initial and optimized segmentation versus input voltage for [3, Fig. 11, 2V2 curve], data are shown in Fig. 3(c). The inital results are shown as solid curves with the optimized segmented results shown as dotted curves. An NMSE AM/PM comparison between these models and the corresponding improvements using the segmentation technique are given in Table IV. It can be seen that for an initial full data range fit, both models have an NMSE AM/PM within 1 dB of each other; however, after the segmentation optimization, the new Cann 12B AM/PM model has better than 20-dB improvement compared with a 14-dB improvement for the Glock's AM/PM model.

An optimizing segmented curve-fitting algorithm, shown in the Appendix, was prepared to further improve NMSE. The algorithm starting points for the second derivatives cannot be zero due to their numerical nature, so there is a requirement to have second derivative zero limits, in our case we have selected this value to be below 0.001, to suit the numerical data. During the minimization process, there are some segment ranges where the discontinuities are higher than the given data resulting in poorer segment fits. This is due to using parameter starting values for the full range of data in those segments. This can be corrected by determining suitable starting points for each segment but this has not been implemented within this algorithm. Even with such improvement in the starting point, the overall curve fit performance is still worse than the segmented approach.

C. Application to LDMOS Devices

Applying the new Cann 12B AM/PM model to devices having LDMOS type phase responses shows that this model can also be used to fit data from such devices. Glock's AM/PM model also fits LDMOS phase data [see Fig. 4(a)].

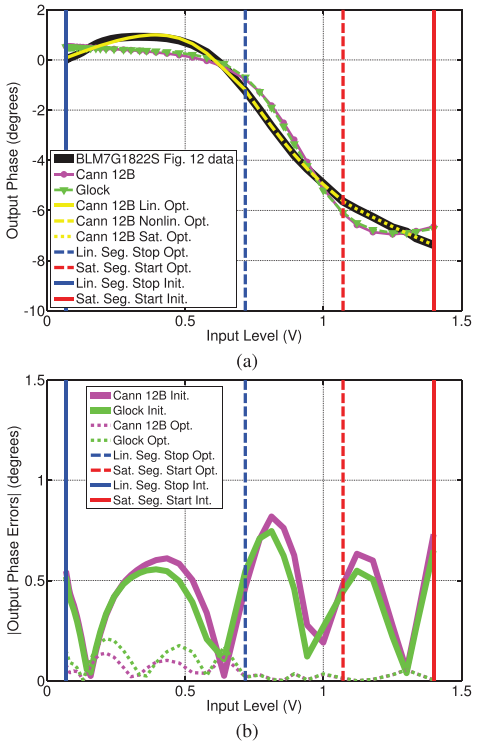

Fig. 4. (a) Comparison of curve fits between the Cann 12B and Glock AM/PM models for the BLM7G1822S device manufacturer's measured data from datasheet [31, Fig. 12] and Cann 12B AM/PM model all segments after optimization, for the BLM7G1822S device manufacturer's measured data from datasheet [31, Fig. 12]. (b) Comparison of |Output Phase errors| versus input voltage from the BLM7G1822S device manufacturer's measured data from datasheet [31, Fig. 12], showing the before and new segmented approach after optimization.

Applying the optimized segmentation approach to the new Cann 12B AM/PM model for LDMOS phase responses results in vastly improved results and NMSE improvements making the new Cann 12B AM/PM model suitable for use as an AM/PM model for LDMOS devices. Fig. 4(a) shows the results of the optimized segmentation approach as applied to a BLM7G1822S device [31]. A comparison of the initial fit versus optimized segmentation fit approach for absolute phase errors for the BLM7G1822S device is shown in Fig. 4(b), with NMSE results shown in Table V.

D. Frequency Domain Comparisons and Discontinuity Effects at Segment Boundaries

A comparison using Glock and Cann 2012 models over the full input range, without segmentation and optimization,

Figure C.8. Journal article 2017, Page 8.

TABLE V
BLM7G1822S DEVICE MANUFACTURER'S MEASURED DATA FROM DATASHEET [31, FIG. 12], AM/AM AND AM/PM NMSE COMPARISON

AM/AM - NMSE (dB)		AM/PM - NMSE (dB)		
Model	Full	Model	Full (Initial)	Seg. Optim.
Rapp	-38.81	Glock	-17.41	-38.07
Cann 2012	-37.68	This work	-16.61	-41.97

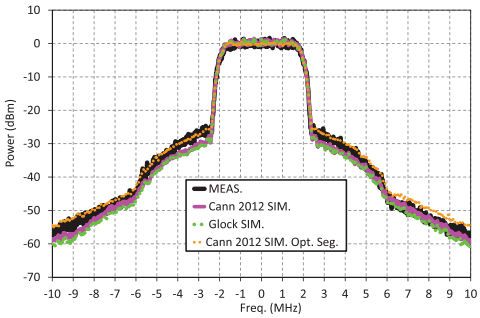

Fig. 5. Comparison of measured versus SIMULINK simulations for WCDMA, comparing Glock versus Cann 2012 full and optimized segmented models for measured SHF-0189 device data [27]. Resolution bandwidth (RBW) for both measured and simulation data is 30 kHz.

against measured data for the SHF-0189 HFET [27] is given in Fig. 5. The test setup is shown in Fig. 1. These plots show that the new model provides a better fit to the measured data compared with Glock's model and that the optimized segmented method provides further modeling improvement.

Investigations into the effects of discontinuities at segment boundaries have revealed that although the new Cann 12B AM/PM model does not have continuous derivatives over the segment boundaries, the phase shift errors between the segment boundaries, after optimization, are very small and have a negligible effect on the adjacent channel leakage ratio (ACLR) response. This has been investigated for a WCDMA digitally modulated signal with the same power spectral density level as used in [3, Fig. 9]. The worst case discontinuity error, of 0.0333°, for either of the linear-nonlinear or nonlinear-saturation segment boundaries was increased, above the optimized value, until the second ACLR level increased by 1 dB and this occurred at 100 times the worst case discontinuity error with no noticeable increase found for the first ACLR, concluding that the optimized segmented new Cann 12B AM/PM model has negligible discontinuity effects, even when considering worst case discontinuities at the segment boundaries. Comparisons between the optimized segmentation discontinuity error result and 100 times this error are shown in Fig. 6.

VI. IMPACT ON IMDS AND LINEARIZATION IMPROVEMENT

An assessment of how the simple models perform in predicting the 3rd IMD performance of RF PAs over a wide dynamic range has been made by simulating the 3rd IMDs

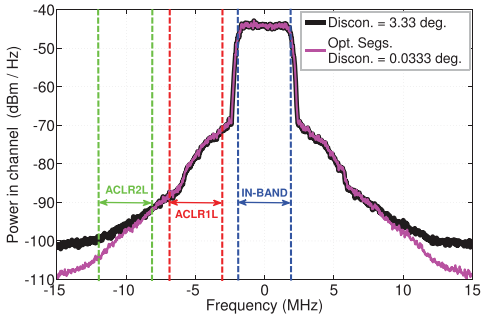

Fig. 6. Discontinuity effects on a WCDMA modulated signal, simulated using SIMULINK, for optimized segmented Cann's 2012 AM/AM and AM/PM model in [3, Fig. 11, 2V2 curve], data. With no discontinuity ACLR1L/2L = −31.8/−52.1 dBc. With 3.33° discontinuity ACLR1L/2L = −32.0/−51.1 dBc. The in-band wanted signal is between the dashed blue vertical lines with ACLR1 between the dashed red vertical lines and ACLR2 between the dashed green vertical lines (only lower ACLR bands are shown) all with 3.84-MHz integration BWs. The integrated power over the in-band wanted signal is 21.5 dBm. RBW is 30 kHz.

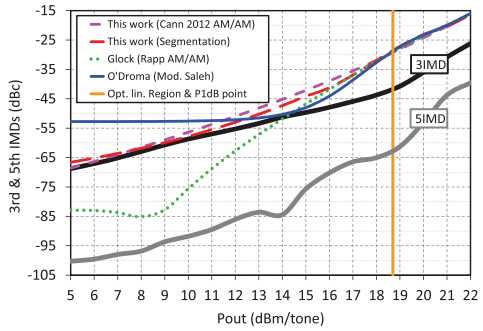

Fig. 7. Third and fifth IMD manufacturer's measured data for the SHF-0189 device from [38, p. 5] versus SIMULINK simulated comparison of the models of O'Droma (Mod. Saleh), Glock, and Cann, all including both AM/AM and AM/PM components. For the segmented model of this paper, the optimized linear segment point and P1dB point are shown as the solid orange vertical line. The optimized saturation region point is at 24 dBm per carrier but that is beyond the available data.

using SIMULINK and comparing the simulations against manufacturer's measured IMD data, SHF-0189 device [38, p. 5]. Plots of the 3rd IMD comparisons are shown in Fig. 7. Comparisons of the absolute 3rd IMD errors are shown in Fig. 8. The 3rd IMD results of the combined 2012 Cann's AM/AM and new AM/PM model perform better than other models, even though the O'Droma's (Mod. Saleh) model shows very good curve-fitting results, in terms of AM/AM and AM/PM absolute measured minus modeled amplitude and phase errors, compared with the Rapp/Glock or 2012 Cann's AM/AM and new AM/PM models presented here. Fig. 7 also shows a plot of the manufacturer's measured 5th IMDs indicating that 3rd IMDs are the dominant IMDs. Based on this and the results of the comparison of the measured versus simulated results for a

This article has been accepted for inclusion in a future issue of this journal. Content is final as presented, with the exception of pagination.

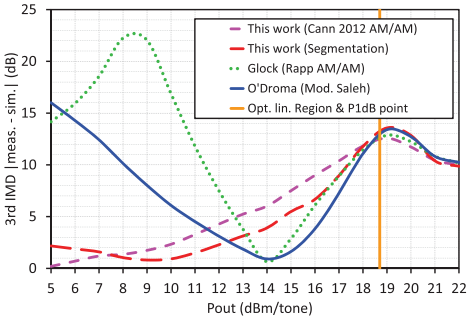

Fig. 8. Third IMD |measured minus SIMULINK simulated| error for the O'Droma (Mod. Saleh), Glock, Cann, and optimized segmented Cann 2012 models, all including both AM/AM and AM/PM components. The AE for Cann 2012 AM/AM and AM/PM is ≈ 6 dB compared with ≈ 8 and 11 dB for the models of O'Droma and Glock, respectively. The optimized segmented Cann 2012 model AE improves 3rd IMD over the Cann's 2012 model by a further ≈ 1 dB. For the segmented model of this paper the optimized linear segment point and P1dB point are shown as the solid orange vertical line. The optimized saturation region point is at 24 dBm per carrier but that is beyond the available data.

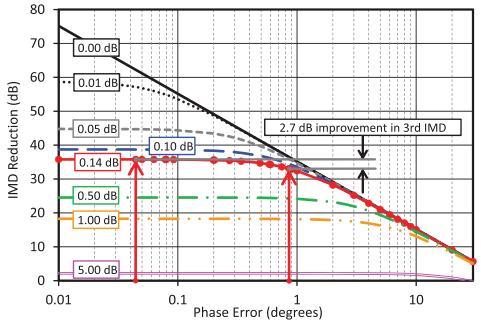

Fig. 9. Third IMD reduction versus phase errors for a range of amplitude errors. Improvement in 3rd IMDs as a result of the new model segmentation method when applied to [3, Fig.11], 2V2 curve, data.

WCDMA signal shown in Fig. 5, where effects of higher order IMD products are included, the simple model presented here is considered to be suitable, particularly for an analog PD.

The Cann's 2012 AM/AM and new AM/PM models have ≈ 2-dB improvement in average error (AE) compared with the O'Droma's model and over 5-dB AE improvement compared with the Glock's model. The optimized segmented Cann12B model method improves the AE by a further ≈ 1 dB. The model presented here does not account for "sweet spots" that may be seen in some devices. This is beyond the scope of this paper and simple model.

In terms of the new model and method's 3rd IMD linearization improvement, as discussed in Section III, the maximum absolute amplitude error, for the Cann's 2012 AM/AM model LSC fit, between the measured data and modeled results, is 0.14 dB, with the absolute amplitude error defined as the maximum absolute difference between the model and data values in dB. The full and optimized segmented Cann 12B AM/PM absolute output phase errors are 0.86° and 0.05°, respectively, shown as the solid and dotted horizontal lines in Fig. 3(c). The output phase error is defined as the difference between the measured and modeled output phases. Fig. 9 shows a plot of (3), where the IMD reduction is plotted against phase error for various amplitude errors. For the 0.14 dB Cann 2012 AM/AM amplitude error curve, the full and segmented phase errors are at 0.86° and 0.05°, respectively, as indicated by the solid red arrowed lines. The 2.7-dB difference between these two points is the improvement in the linearization performance that can be achieved due to the proposed improved accuracy Cann's 12B AM/PM model. For each of the various technologies, TWTA, BJT, HFET, LDMOS, HBT, E-pHEMT, GaAs, CMOS, GaN/SiC, and including Glock's device data, the AM/PM NMSEs were determined for both the full and segmented methods. The NMSE improvements between the full and segmented methods are shown in comparison with the linearization 3rd IMD improvements for each technology type in Table VI.

TABLE VI
TECHNOLOGY NMSE AND LINEARIZATION IMPROVEMENT COMPARISON

Device	Cann 12B AM/PM NMSE (dB)		NMSE Improvement (dB)	Seg. IMD Improvement (dB)
	Full	Opt. Seg.		
TWTA [13]	-34.74	-42.81	8.07	0.102
BJT [15]	-53.03	-56.56	3.53	0.002
HFET [27]	-31.98	-48.36	16.38	6.428
LDMOS1 [28]	-31.90	-48.14	16.24	0.046
HBT [29]	-64.24	-75.58	11.34	0.299
E-pHEMT [30]	-34.02	-45.78	11.74	1.018
LDMOS2 [31]	-17.65	-33.71	16.06	0.270
GaAs [3]	-29.77	-52.72	22.95	0.001
CMOS [3]	-53.14	-75.81	22.67	2.700
GaN/SiC [32]	-40.92	-44.79	3.87	0.017

VII. CONCLUSION

In this paper, we have presented and demonstrated a new semiphysical AM/PM model, derived from a simple more accurate AM/AM model, showing its suitability over a range of RF PA device technologies. The combination of the new AM/PM model and more accurate AM/AM model accurately predict 3rd IMD and ACLR performance against measured device data.

A segmented curve-fitting approach, using the new AM/PM model, has also been presented showing up to 20-dB NMSE improvement when modeling amplifier AM/PM characteristics, also resulting in linearizer 3rd IMD improvements of over 5 dB. Simulations of segment boundary discontinuities have shown that worst case discontinuities have no effect on the modeled amplifier spectrum for digitally modulated signals.

Throughout this paper, data from within the literature, manufacturer's data sheets, or our testing have been used. For any device selection, it is recommended that appropriate testing on one or more devices be performed in order to validate any device performance against requirements.

Figure C.10. Journal article 2017, Page 10.

APPENDIX
SEGMENTATION OPTIMIZATION ALGORITHM

Algorithm 1 Minimize AM/PM NMSE in dB

Require: Combined AM/PM NMSE (dB) is minimum.
Ensure: V_{in}, V_{out} & ϕ_{out} are real & > 0.
1: **INPUT** V_{out} vs. V_{in} & ϕ_{out} vs. V_{in} data set for the device under test (DUT).
2: Determine $d''V_{out}/dV_{in}$ (2nd Deriv.)
3: **if** $d''V_{out}/dV_{in} \neq 0$ after the first occurrence when $d''V_{out}/dV_{in} = 0$ **then**
4: V_{out} vs. V_{in} data does not extend far enough into the Saturation region so extend the V_{out} vs. V_{in} data using [19], refer to Fig. 3(b).
5: **end if**
6: **if** $d''V_{out}/dV_{in} = 0$, on the first occurrence. **then**
7: $V_{in_{Lin}}$ is the Linear region *stop* point.
8: **else if** $d''V_{out}/dV_{in} = 0$, on the second occurrence. **then**
9: $V_{in_{Sat}}$ is the Saturation region *start* point.
10: **end if**
11: Note: ϕ_{out} vs. V_{in} data between $V_{in_{Lin}}$ & $V_{in_{Sat}}$ is the Nonlinear region data.
12: **for** $V_{in} = 0$ to $V_{in_{Lin}}$ **do**
13: Least Squares Curve Fit (LSCF) ϕ_{out} vs. $V_{in_{Lin}}$ using $\phi(r)$, Eqn. (7),
14: **end for**
15: **for** $V_{in} = V_{in_{Lin}}$ to $V_{in_{Sat}}$ **do**
16: LSCF ϕ_{out} using $\phi(r)$, Eqn. (7), for the Nonlinear region.
17: **end for**
18: **for** $V_{in} = V_{in_{Sat}}$ to $V_{in_{max}}$ **do**
19: LSCF ϕ_{out} vs. $V_{in_{Sat}}$ using $\phi(r)$, Eqn. (7), for the Saturation region data.
20: **end for**
21: **for** $V_{in} = 0$ to $V_{in_{max}}$ **do**
22: Calculate AM/PM NMSE A (dB), using (2), for the combined Linear, Nonlinear & Saturation region segments.
23: Adjust $V_{in_{Lin}}$ & $V_{in_{Sat}}$ to give $V_{in_{Lin1}}$ & $V_{in_{Sat1}}$
24: **end for**
25: **repeat**
26: Steps 12: to 24: using $V_{in_{Lin1}}$ & $V_{in_{Sat1}}$ calculate AM/PM NMSE B (dB), using Eqn. (2), for the *combined* Linear, Nonlinear & Saturation region segments.
27: **until** NMSE B (dB) < NMSE A (dB)
28: Note: It may occur that NMSE A (dB) < NMSE B (dB), i.e., the initial segmentation is optimum.
29: Output all calculated curve fit coefficients. **END**

ACKNOWLEDGMENT

The authors would like to thank the assistance and support of RF Industries Private Ltd. for providing the resources and time for the first author to work on this research.

REFERENCES

[1] J. Xia, A. Islam, H. Huang, and S. Boumaiza, "Envelope memory polynomial reformulation for hardware optimization of analog-RF predistortion," *IEEE Microw. Wireless Compon. Lett.*, vol. 25, no. 6, pp. 415–417, Jun. 2015.
[2] A. Zhu, P. J. Draxler, C. Hsia, T. J. Brazil, D. F. Kimball, and P. M. Asbeck, "Digital predistortion for envelope-tracking power amplifiers using decomposed piecewise volterra series," *IEEE Trans. Microw. Theory Techn.*, vol. 56, no. 10, pp. 2237–2247, Oct. 2008.
[3] S. Glock, J. Rascher, B. Sogl, T. Ussmueller, J.-E. Mueller, and R. Weigel, "A memoryless semi-physical power amplifier behavioral model based on the correlation between AM–AM and AM–PM distortions," *IEEE Trans. Microw. Theory Techn.*, vol. 63, no. 6, pp. 1826–1835, Jun. 2015.
[4] Y.-S. Lee, M.-W. Lee, S.-H. Kam, and Y.-H. Jeong, "A high-linearity wideband power amplifier with cascaded third-order analog predistorters," *IEEE Microw. Wireless Compon. Lett.*, vol. 20, no. 2, pp. 112–114, Feb. 2010.
[5] C. Rapp, "Effects of HPA-nonlinearity on a 4-DPSK/OFDM-signal for a digital sound broadcasting signal," in *Proc. 2nd Eur. Conf. Satellite Commun. (ESA SP-332)*, Liège, Belgium, Oct. 1991, pp. 179–184.
[6] I. Aoki *et al.*, "A fully-integrated quad-band GSM/GPRS CMOS power amplifier," *IEEE J. Solid-State Circuits*, vol. 43, no. 12, pp. 2747–2758, Dec. 2008.
[7] A. Afsahi, A. Behzad, V. Magoon, and L. E. Larson, "Linearized dual-band power amplifiers with integrated baluns in 65 nm CMOS for a 2×2 802.11n MIMO WLAN SoC," *IEEE J. Solid-State Circuits*, vol. 45, no. 5, pp. 955–966, May 2010.
[8] J. Fuhrmann, P. Oßmann, K. Dufrêne, H. Pretl, and R. Weigel, "A 28 nm standard CMOS watt-level power amplifier for LTE applications," in *Proc. IEEE Topical Conf. Power Amplif. Wireless Radio Appl. (PAWR)*, Jan. 2015, pp. 1–3.
[9] P. Oßmann *et al.*, "Design of a fully integrated two-stage watt-level power amplifier using 28-nm CMOS technology," *IEEE Trans. Microw. Theory Techn.*, vol. 64, no. 1, pp. 188–199, Jan. 2016.
[10] W. Bösch and G. Gatti, "Measurement and simulation of memory effects in predistortion linearizers," *IEEE Trans. Microw. Theory Techn.*, vol. 37, no. 12, pp. 1885–1890, Dec. 1989.
[11] M. O'Droma, S. Meza, and Y. Lei, "New modified Saleh models for memoryless nonlinear power amplifier behavioural modelling," *IEEE Commun. Lett.*, vol. 13, no. 6, pp. 399–401, Jun. 2009.
[12] A. Cann, "Nonlinearity model with variable knee sharpness," *IEEE Trans. Aerosp. Electron. Syst.*, vol. AES-16, no. 6, pp. 874–877, Nov. 1980.
[13] A. A. A. Saleh, "Frequency-independent and frequency-dependent nonlinear models of TWT amplifiers," *IEEE Trans. Commun.*, vol. 29, no. 11, pp. 1715–1720, Nov. 1981.
[14] A. Ghorbani and M. Sheikhan, "The effect of solid state power amplifiers (SSPAs) nonlinearities on MPSK and M-QAM signal transmission," in *Proc. 6th Int. Conf. Digit. Process. Signals Commun.*, Sep. 1991, pp. 193–197.
[15] M. Honkanen and S.-G. Haggman, "New aspects on nonlinear power amplifier modeling in radio communication system simulations," in *Proc. IEEE Int. Symp. Pers., Indoor Mobile Radio Commun. (PIMRC)*, vol. 3. Sep. 1997, pp. 844–848.
[16] G. P. White, A. G. Burr, and T. Javornik, "Modelling of nonlinear distortion in broadband fixed wireless access systems," *Electron. Lett.*, vol. 39, no. 8, pp. 686–687, Apr. 2003.
[17] A. J. Cann, "Improved nonlinearity model with variable knee sharpness," *IEEE Trans. Aerosp. Electron. Syst.*, vol. 48, no. 4, pp. 3637–3646, Oct. 2012.
[18] M. O'Droma and L. Yiming, "A new Bessel-Fourier memoryless nonlinear power amplifier behavioral model," *IEEE Microw. Wireless Compon. Lett.*, vol. 23, no. 1, pp. 25–27, Jan. 2013.
[19] P. O. Fisher and S. F. Al-Sarawi, "Improving the accuracy of SSPA device behavioral modeling," in *Proc. Int. Conf. Inf. Commun. Technol. Res. (ICTRC)*, May 2015, pp. 278–281.
[20] T. R. Cunha, P. M. Lavrador, E. G. Lima, and J. C. Pedro, "Rational function-based model with memory for power amplifier behavioral modeling," in *Proc. Workshop Integr. Nonlinear Microw. Millim.-Wave Circuits (INMMIC)*, Apr. 2011, pp. 1–4.
[21] M. Rawat, K. Rawat, F. M. Ghannouchi, S. Bhattacharjee, and H. Leung, "Generalized rational functions for reduced-complexity behavioral modeling and digital predistortion of broadband wireless transmitters," *IEEE Trans. Instrum. Meas.*, vol. 63, no. 2, pp. 485–498, Feb. 2014.
[22] A. Harguem, N. Boulejfen, F. M. Ghannouchi, and A. Gharsallah, "Robust behavioral modeling of dynamic nonlinearities using Gegenbauer polynomials with application to RF power amplifiers," *Int. J. RF Microw. Comput.-Aided Eng.*, vol. 24, no. 2, pp. 268–279, 2014.

Figure C.11. Journal article 2017, Page 11.

[23] C. Jebali, N. Boulejfen, M. Rawat, A. Gharsallah, and F. Ghannouchi, "Modeling of wideband radio frequency power amplifiers using Zernike polynomials," *Int. J. RF Microw. Computer-Aided Eng.*, vol. 22, no. 3, pp. 289–296, 2012.
[24] N. Safari, P. Fedorenko, J. S. Kenney, and T. Roste, "Spline-based model for digital predistortion of wide-band signals for high power amplifier linearization," in *IEEE MTT-S Int. Microw. Symp. Dig.*, Jun. 2007, pp. 1441–1444.
[25] S. L. Loyka, "On the use of Cann's model for nonlinear behavioral-level simulation," *IEEE Trans. Veh. Technol.*, vol. 49, no. 5, pp. 1982–1985, Sep. 2000.
[26] M. Isaksson, D. Wisell, and D. Ronnow, "A comparative analysis of behavioral models for RF power amplifiers," *IEEE Trans. Microw. Theory Techn.*, vol. 54, no. 1, pp. 348–359, Jan. 2006.
[27] Sirenza Microdevices. *(EDS-101240 Rev E) SHF-0189, 0.05–6 GHz, 0.5 Watt GaAs HFET*, accessed on Sep. 18, 2016. [Online]. Available: http://datasheet.octopart.com/SHF-0189-Sirenza-datasheet-129519.pdf
[28] NXP. (Jun. 2009). *MW6S004NT1, Up to 2000 MHz, LDMOS RF Power Field Effect Transistor, Revision: 4*, accessed on Sep. 18, 2016. [Online]. Available: http://www.nxp.com/
[29] NXP. (Oct. 2014). *MMG3005NT1, 800–2000 MHz, Heterojunction Bipolar Transistor, Revision: 9*, accessed on Sep. 18, 2016. [Online]. Available: http://nxp.com/
[30] Avago Technologies. (Feb. 10, 2014). *ALM-31122, 700 MHz–1 GHz E-pHEMT, 1 Watt High Linearity Amplifier*, accessed on Sep. 18, 2016. [Online]. Available: http://www.avagotech.com/
[31] Ampleon. (Sep. 2015). *BLM7G1822S-20, 1805 MHz to 2170 MHz, LDMOS 2-Stage Power MMIC, Revision: 4-1*, accessed on Sep. 18, 2016. [Online]. Available: http://www.ampleon.com/
[32] Northrop Grumman. (May 2014) *APN180, 27-31 GHz GaN Power Amplifier*, accessed on Sep. 18, 2016. [Online]. Available: http://www.northropgrumman.com/
[33] T. Nojima and T. Konno, "Cuber predistortion linearizer for relay equipment in 800 MHz band land mobile telephone system," *IEEE Trans. Veh. Technol.*, vol. VT-34, no. 4, pp. 169–177, Nov. 1985.
[34] M. Faulkner, M. Johansson, and W. Yates, "Error sensitivity of power amplifiers using pre-distortion," in *Proc. 41st IEEE Veh. Technol. Conf.*, May 1991, pp. 451–456.
[35] J. Litva and T. K.-Y. Lo, Eds., *Digital Beamforming in Wireless Communications*, 1st ed. Norwood, MA, USA: Artech House, 1996, ch. 4, sec. 4.4.1, pp. 79–81.
[36] T. Magesacher, P. Singerl, and M. Mataln, "Optimal segmentation for piecewise RF power amplifier models," *IEEE Microw. Wireless Compon. Lett.*, vol. 26, no. 11, pp. 909–911, Nov. 2016.
[37] S. C. Cripps, Ed., *RF Power Amplifiers for Wireless Communications*, 2nd ed. Norwood, MA, USA: Artech House, 2006, ch. 14, sec. 14.1, p. 400.
[38] Sirenza Microdevices. *(EAN-101798 Rev A) SHF-0189, Amplifier Application Circuits, DESIGN APPLICATION NOTE—AN-031*, accessed on Sep. 18, 2016. [Online]. Available: http://application-notes.digchip.com/147/147-47818.pdf

Paul O. Fisher (S'79–M'81) received the B.Eng. degree (with distinction) in communications engineering from the Royal Melbourne Institute of Technology, Melbourne, VIC, Australia, in 1981, and the M.Eng. degree in radio frequency engineering from the University of Adelaide, Adelaide, SA, Australia, in 2003, where he is currently pursuing the Ph.D. degree in electrical and electronic engineering.

He was with the British Aerospace Dynamics Group, Space Communications Division, Stevenage, U.K., with Codan Pty. Ltd., Satellite Communications Group, Adelaide, and with NEC Australia, Space Communications Sub-Division, Radio Group, Melbourne, where he has been involved in a range of engineering design, development and manufacturing projects covering both space and terrestrial segment products related to antennas and electronic modules over L- to Ku-band frequency ranges. He is currently the Engineering Manager with RF Industries, Adelaide, where he is involved in the design and development of radio communications products for the cellular and land mobile radio markets.

Said F. Al-Sarawi (S'92–M'96) received the General Certificate in marine radio communication and B.Eng. degree (first class hons.) in marine electronics and communication from the Arab Academy for Science and Technology, Alexandria, Egypt, in 1987 and 1990, respectively, and the Ph.D. degree in mixed analog and digital circuit design techniques for smart wireless systems with special commendation in electrical and electronic engineering and the Graduate Certificate in education (Higher Education) from the University of Adelaide, Adelaide, SA, Australia, in 2003 and 2006, respectively.

He is currently the Director with the Center for Biomedical Engineering and a Founding Member of the Education Research Group of Adelaide, University of Adelaide. His current educational research is focused on innovative teaching techniques for engineering education, research skill development, and factors affecting students' evaluations of courses in different disciplines. His current research interests include design techniques for mixed signal systems in CMOS and optoelectronic technologies for high-performance radio transceivers, low-power and low-voltage radio-frequency identification systems, data converters, mixed-signal design, and microelectromechanical systems for biomedical applications.

Dr. Al-Sarawi was a recipient of the University of Adelaide Alumni Postgraduate Medal (formerly Culross) for outstanding academic merit at the postgraduate level and the Commonwealth Postgraduate Research Award (Industry).

Figure C.12. Journal article 2017, Page 12.

A New Figure of Merit Methodology for Power Amplifier Combining Technologies

Paul O. Fisher[1,2] and Said F. Al-Sarawi[1]
[1]School of Electrical and Electronic Engineering, The University of Adelaide, SA 5005, Australia
Email: (paul.fisher@adelaide.edu.au; said.alsarawi@adelaide.edu.au)
[2]RF Industries, (RFI), Allenby Gardens, SA, 5009, Australia
Email: (paul.fisher@rfi.com.au)

***Abstract*— A comparative analysis between well established and more recent solid state power amplifier (SSPA) combining techniques is presented. Based on this analysis, a new Figure of Merit (FOM) methodology is presented that can form part of a process to optimise SSPA design within the constraints of service, technology and performance requirements. Also, this formalises the process of determining the most appropriate SSPA design path, from the earliest stages, based on the above constraints as well as providing a detailed technology comparison to allow optimum technology selection.**

***Index Terms*—Solid State Power Amplifiers, Power-combining networks, Design methodology.**

I. Introduction

THERE is a continuing need, in both the commercial and defense markets, for SSPAs that can deliver high output power and high efficiency while operating at high frequencies with reduced size and area, all at low cost. So there is a need to investigate and determine which power combining techniques or architectures can be used to achieve this within a given number of constrains [1], [2].

The goal of this paper is to demonstrate how to select an appropriate SSPA technology that can deliver a required outcome based on a customer's service and performance requirements. This forms part of the overall SSPA technology selection and design methodology with the aim of delivering an outcome using the most appropriate technology by making decisions from both tangible requirements, for example performance specifications, and less tangible requirements such as graceful degradation, time to market or ease of use. The tangible requirement selections will be made by developing and building on available or new FOMs, with technology selections including more recent spatial combining technologies applied to SSPAs. Tangible and less tangible selections will be made using a fuzzy logic approach followed by modern statistical and optimisation design and manufacturing methods, e.g. Monte Carlo, Simulated Annealing and Design For Six Sigma (DFSS) [3], that will then be employed to complete the detailed design. Reliability prediction will be made using the Telcordia method [4].

The structure of this paper includes an overview of the different types of services, performance requirements and priority compromises that need to be considered before deciding on a power combining technology, as presented in Section II. A range of suitable FOMs is presented in Section III followed by a review of amplifier parameters and weightings to be used as part of the technology selection process in Section IV. Available SSPA combining technologies are briefly reviewed in Section V. This will provide the starting point for the selection of the most appropriate technology for any particular service requirement. Having provided, and analysed a comparison of technologies, then the design methodology will be proposed in Section VI, that is intended to formalise, from early conceptual requirements, the optimum technology that is appropriate to the SSPA design. Section VII provides a combiner technology case study followed by a conclusion and acknowledgment.

II. Types of Service

SSPAs are required for a wide range of services with varying requirements and priorities for particular performance parameters. This means that particular performance parameters for one type of service can have a different importance placed on it in another service. This change in importance can significantly affect the design outcome. The type of technology that is most appropriate to a particular type of service will benefit from an optimisation process that includes, from the start, both the service requirements and the performance requirements [5]. Such a process allows a greater range of possibilities when a compromise is required. The types of services that are being considered are: Land Fixed (terrestrial and satellite earth station), Land Mobile (cell phone, vehicular and mobile earth stations terminals), Naval (mobile), Air (mobile) and Space based (satellites and spacecraft) services. Different services impose different requirements on aspects such as frequency, weight, size, power, environmental factors and reliability. Additional constraints are imposed by regulation, time to market and cost. All of the above require compromises that a more inclusive optimisation can improve. A service level requirements priority analysis is conducted, combined with the parameter weightings assessed for both commercial and defense markets and presented in Section VI.

III. Figures of Merit

In order to be able to make a more meaningful comparison between power combining technologies, a combination of suitable FOMs is proposed. Several different FOMs, useful

978-1-5090-5306-3/16/$31.00

Figure C.13. Conference paper 2016-2, Page 1.

for comparing SSPA performance, have been considered from the literature and are presented in Table I, from active device comparisons through to system comparison levels.

TABLE I: Combining Technology FOMs

Figure of Merit	Equation	Ref.
Power State Of the Art (PSOA)	PSOA = $\frac{(f^3 \cdot P_{out}^2)}{(4 \cdot 10^5)}$, (1) f = frequency (GHz), P_{out} = output power (watts)	[6]
PAE	$PAE = \frac{P_{out}-P_{in}}{P_{DC}}$, (2)	
PAE - Corporate[1]	CPAE = $PAE\frac{(L_{ic}GL_{oc}-1)}{(L_{ic}(G-1))}$, (3) where: α_{ic} = I/P comb.[2]loss / stage, $L_{ic} = \alpha_{ic}^{\log 2(N_c)}$ = I/P comb. loss, $L_{oc} = \alpha_{oc}^{\log 2(N_c)}$ = O/P comb. loss, α_{oc} = O/P combiner loss / stage G = Gain, N_c = No. of comb. stages	[7]
PAE - Spatial	SPAE = $PAE\frac{(L_{is}GL_{os}-1)}{(L_{is}(G-1))}$, (4) where: G = Gain, L_{is} = I/P combiner loss, L_{os} = O/P combiner loss,	
Device O/P 3rd order-intercept-point	$OIP3_d = P_{out}/tone + \frac{3IMD}{2}$, (5) where: $3IMD$ = 3rd-order-intermodulation-distortion	
Linearity - combined	$OIP3_c = N_c \cdot L_c \cdot OIP3_d$, (6) where: L_c = comb. in or out loss	[8]
Linearity - alternative	LFOM = $\frac{OIP3_{d,\ or\ c}}{P_{DC}}$, (7)	[9]
Device Spurious Free Dynamic Range (SFDR)	$SFDR_d = \left[\frac{OIP3_d}{(FGk_BT_0\Delta f)}\right]^{2/3}$, (8) where: F = noise factor, G = gain, k_B = Boltzman's constant, T_0 = ambient temperature, Δf = instantaneous bandwidth	[8]
SFDR - combined	$SFDR_c = {N_c}^{2/3} SFDR_d$, (9)	
Cost	dollars/watt = $\$/W$, (10)	
Reliability	$R = e^{-(t/MTTF)}$, (11) where: t = time, $MTTF = \sum_i t_i/U$, t_i = time to failure in hours, for the ith element & U = No. of units	[4]

[1]Ideal combiner, no amplitude or phase imbalance. [2]comb. = combiner.

The aim of this work is to select the most suitable combining technology by determining the maximum of the sum of the FOMs, after the parameter weightings of Table II have been applied, compared to a straight sum of specification parameters (SP)

$$FOM_{max} = \sum W_i \cdot FOM_i, \tag{12}$$

$$SP_{max} = \sum_j^i W_j \cdot SP_j, \tag{13}$$

where FOM_i = FOM of the ith parameter from Table I, SP_j = jth specification parameter and $W_{i,j}$ = i, jth weightings from Table II, respectively.

IV. Amplifier Parameters

The parameters listed in Table II, cover the majority of parameters needed to describe an SSPA. These parameters will be used for initial technology comparisons. The parameter weightings in Table II are determined by the combination of a Quality Function Deployment (QFD) [10] analysis and Failure Mode Effects Analysis (FMEA) [11] for the particular service requirements of Section II.

TABLE II: SSPA Parameters and Weightings

Main Specification Parameter[3]	Secondary Specification Parameter	Weightings SP	Weightings FOM
Frequency (1)	Center Frequency	5.26	4.8
	Bandwidth	3.45	*
RF Power (1), (2), (3),	P_{1dB} at centre frequency	3.45	4.8
	$P_{saturation}$	3.45	*
Gain	Small signal	2.56	*
	Slope	2.04	*
	Ripple	2.04	*
Return Loss	Input	2.04	*
	Output	2.56	*
Linearity (5), (6), (7), (8), (9)	AM/PM	2.56	*
	Group Delay	1.69	*
	Spur / harmonics	2.04	*
	IMDs (OIP3)	2.56	3.9
	Noise Figure	2.04	*
	Spurious Free Dynamic Range	2.56	3.9
	Phase Noise	*	*
Response time	Rise	*	*
	Fall	*	*
	Pulse overshoot	*	*
	Pulse droop	*	*
	Ringing/settling	*	*
Mode	Coaxial	2.56	*
	Waveguide	2.56	*
	Planar	2.56	*
DC power	Power (P_{DC})	1.69	*
	Voltage	1.69	*
	Current	1.69	*
Power-Added-Efficiency (PAE) (2), (3), (4)	Device	1.69	*
	Corporate combining	1.69	5.9
	Spatial combining	1.69	5.9
	Number of stages	1.69	5.9
Conducted & Radiated	Emissions	*	*
	Susceptibility	*	*
Size	Dimensions	1.0	*
	Mass	1.0	*
Reliability (11)	Number of components	1.69	1.69
	MTTF	1.69	1.69
	Maintenance	*	*
Vibration & Shock	Vibration	*	*
	Shock	*	*
Thermal	Temperature above ambient	1.69	*
	Operating temperature range	1.69	*
	Device junction temperature	2.56	*
	Heatsink type	1.0	*
Humidity		*	*
Altitude Space	Air $V_{breakdown}$	*	*
	Multipaction	*	*
Sealing	Ingress Protection rating	*	*
	Corrosion Resistance	*	*
Cost (10)	\$/W	*	*
Commercial	Manufacturability	*	*
	Time to Market	*	*
	Volume	*	*
	Ease of use	*	*
	Graceful degradation	2.56	*

[3]Related FOM as defined in Table I. *Not considered at this stage.

Figure C.14. Conference paper 2016-2, Page 2.

V. Combining Technologies

The combining technologies to be compared have been drawn from the available literature, [12]–[28], and cover more established combining technologies, e.g. corporate and serial combining, as well as more recent techniques and technologies like spatial tile and tray combining and various hybrids of both. Recent applications for spatial combining are at much higher frequencies using monolithic chips, although enhancements of other methods continue as applications arise. The combining technologies that will be compared are listed in Table III. In the following comparison some demonstration technologies are also included as reference points. If a particular parameter from Table III is not available for a particular technology, then a typical worst case weighting value is assigned based on parameters from [29].

TABLE III: Combining Technologies

Combining Technology	Class	Reference
Corporate Monolithic	Corporate	[12]
Corporate Chip		[13]
Corporate Hybrid Waveguide		[14],
Tile Discrete Spatial	Tile	[15]
Tile Chip Spatial		[16]
Tile Monolithic Spatial (Transmission)		[17]
Tile Monolithic Spatial (Reflection)		[18]
Tile Discrete Spatial Class-E		[19]
Tray Coaxial Spatial	Tray	[8], [20]
Tray Waveguide Spatial (TE_{10})		[21]
Tray Hard Boundary Waveguide		[22]
Tray Alternate Mode Waveguide (TE_{20})		[23]
2D Planar TE Mode	2D Planar	[24]
2D Planar TM Mode		[25]
3D Planar Chain Slotted Waveguide	3D Planar	[26]
Conical Waveguide	Conical	[27], [28]

VI. Proposed Selection Methodology

The proposed design methodology is shown in Fig. 1, with fuzzy sets [30] used to formalise the early service level requirements and when these are used with appropriate FOMs from Section III, the fuzzy set outcomes will determine the technology parameters that will be most suited to optimisation. Table IV shows the importance of various service parameter requirements following a QFD analysis, based on a commercial customer case study.

TABLE IV: Service vs parameter requirement examples

Service type	Parameter[4]				
	MTTF	$/W	PAE	Mass	Corrosion Resistance
Land Fixed	7	7	6	1	2
Land mobile	3	9	8	8	3
Naval (mobile)	7	3	2	1	8
Air (mobile)	9	2	6	8	1
Space	9	1	7	9	1

[4] 1 = least important, 9 = most important.

Modern statistical and optimisation design and manufacturing methods, e.g. Monte Carlo, Simulated Annealing and DFSS, will then be used as part of the detailed design, followed by reliability predictions using the Telcordia method [4].

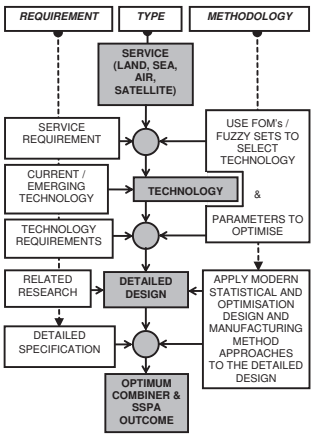

Fig. 1: Proposed design methodology flowchart.

VII. Combiner Technology Case Study

Having identified the technologies and appropriate SSPA performance parameters, the FOMs shown in Section III have been used to achieve an initial technology comparison. The blue columns of Fig. 2 show the sum of weighted SPs, with both SPs and SP weightings from Table II and weightings appropriate for a small satellite earth station SSPA. This shows that for initial SPs, a tile monolithic (Reflection) spatial combiner would provide the best outcome for SSPA design. The red columns of Fig. 2 show the comparison for the sum of weighted FOMs, with FOMs from Table II and weightings from Table I. This alternative comparison now suggests that a 2D planar TE mode spatial combining approach would be a more suitable approach. To be able to validate these outcomes a detailed design followed by a prototype build and test of each type solution would be the ultimate, however tracking research or market trends may be a less costly but longer approach. A design and validation will be provided at a future time.

FOMs need to be carefully chosen, so the development of meaningful FOMs is a major proportion of the current work and future work will determine the most suitable combination of FOMs to be used as part of the design methodology approach for selecting the most appropriate technology suited to a particular service requirement. Comparisons at this stage cover separate monolithic, chip and module level designs but a combination of these approaches may also provide the best solution for an overall design.

VIII. Conclusion

This paper has presented an initial comparison of SSPA combining technologies based on already developed and well

Figure C.15. Conference paper 2016-2, Page 3.

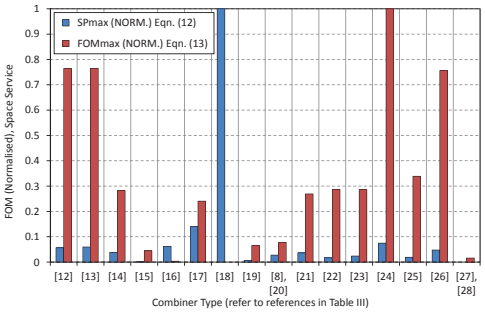

Fig. 2: Comparison of combiner type vs SP_{max}, (12) & FOM_{max}, (13) for a small satellite earth station SSPA. The y-axis represents the normalised SP or FOM.

accepted FOMs. In addition, it has proposed a design methodology that considers the balance of service requirements and performance parameters. Based on this method, as demonstrated, an appropriate technology to meet these requirements can be selected. The work forms part of an initial study into a SSPA design methodology with future work to consider aspects such as thermal and electro-magnetic compatibility (EMC) performance, further assisting in determining the best SSPA combining technology outcome.

ACKNOWLEDGMENT

The authors wish to acknowledge the assistance and support of RF Industries (RFI) Pty. Ltd. for providing time for the first author to work on this research and also acknowledge the supervisory input and initial manuscript feedback provided by Associate Professor Chris Coleman and Professor Andrew Parfitt.

REFERENCES

[1] J. Schellenberg, "The evolution of power combining techniques: From the 60s to today," in *2015 IEEE MTT-S International Microwave Symposium*, May 2015, pp. 1–4.

[2] R. Bhat, A. Chakrabarti, and H. Krishnaswamy, "Large-scale power combining and mixed-signal linearizing architectures for watt-class mmwave CMOS power amplifiers," *IEEE Transactions on Microwave Theory and Techniques*, vol. 63, no. 2, pp. 703–718, Feb 2015.

[3] S. G. Shina, *Six Sigma Electronics Design and Manufacturing*, 1st ed. McGraw-Hill, 2002.

[4] Telcordia. (2005) Telcordia Reliability Prediction Procedure, SR-332, Issue 4. [Online]. Available: http://telecom-info.telcordia.com/

[5] *Handbook on Satellite Communications (HSC)*, 3rd ed. ITU, March 2002, ch. 1, Sec. 1.5, pp. 30-39.

[6] D. Miller and M. Drinkwine. (2003) High voltage microwave devices: An overview. [Online]. Available: http://www.gaasmantech.org/Digests/2003/2003PDF/7-1.pdf

[7] R. A. York, "Some considerations for optimal efficiency and low noise in large power combiners," *IEEE Transactions on Microwave Theory and Techniques*, vol. 49, no. 8, pp. 1477–1482, August 2001.

[8] P. Jia, L.-Y. Chen, A. Alexanian, and R. A. York, "Broad-band high-power amplifier using spatial power-combining technique," *IEEE Transactions on Microwave Theory and Techniques*, vol. 51, no. 12, pp. 2469–2475, Dec 2003.

[9] K. W. Kobayashi, M. Nishimoto, L. T. Tran, H. Wang, J. C. Cowles, T. R. Block, J. H. Elliott, B. R. Allen, A. K. Oki, and D. C. Streit, "A 44-GHz high IP3 InP-HBT amplifier with practical current reuse biasing," *IEEE Transactions on Microwave Theory and Techniques*, vol. 46, no. 12, pp. 2541–2552, Dec 1998.

[10] Y. Akao, S. Mizuno, and K. Ishihara, *The Customer-Driven Approach to Quality Planning and Deployment*, 1st ed., Y. Akao and S. Mizuno, Eds. Asian Productivity Organization, January 1994.

[11] AIAG. (Fourth Edition (2008)) Potential Failure Mode and Effects Analysis (FMEA). Reference Manual. [Online]. Available: http://www.aiag.org/

[12] Triquint Semiconductor inc. (April 23, 2004) TGA4022, 18 - 23 GHz, 32.5 dBm Nominal P1dB, K-Band High Power Amplifier. [Online]. Available: http://www.triquint.com/

[13] TOSHIBA. (13-02-2015) TIM5964-60SL-422, 5.9GHz to 6.4GHz P1dB=48.0dBm Internally Matched Microwave Power GaAs FET. [Online]. Available: https://www.toshiba.co.jp/

[14] Codan Pty Ltd. (August, 2005) Codan 5940 High Power SSPA. [Online]. Available: http://www.codan.com.au/

[15] M. Kim, J. Rosenberg, R. Smith, R. Weilke, J. B. Hacker, M. P. DeLisio, and D. Rutledge, "A grid amplifier," *IEEE Microwave and Guided Wave Letters*, vol. 1, no. 11, pp. 322–324, November 1991.

[16] S. C. Ortiz, J. Hubert, L. Mirth, E. Schlecht, and A. Mortazawi, "A high-power Ka-band quasi-optical amplifier array," *IEEE Transactions on Microwave Theory and Techniques*, vol. 50, no. 2, pp. 487–494, Feb 2002.

[17] B. Deckman, D. S. Deakin, E. Sovero, and D. Rutledge, "A 5-watt, 37-GHz monolithic grid amplifier," in *Microwave Symposium Digest. 2000 IEEE MTT-S International*, vol. 2, June 2000, pp. 805–808 vol.2.

[18] C.-T. Cheung, R. Tsai, R. Kagiwada, and D. B. Rutledge, "V-band transmission and reflection grid amplifier packaged in waveguide," in *Microwave Symposium Digest, 2003 IEEE MTT-S International*, vol. 3, June 2003, pp. 1863–1866 vol.3.

[19] S. Pajic and Z. B. Popovic, "An efficient X-band 16-element spatial combiner of switched-mode power amplifiers," *IEEE Transactions on Microwave Theory and Techniques*, vol. 51, no. 7, pp. 1863–1870, July 2003.

[20] P. G. Courtney, J. Zeng, T. Tran, H. Trinh, and S. Behan, "120W Ka band power amplifier utilizing GaN MMICs and coaxial waveguide spatial power combining," in *IEEE Compound Semiconductor Integrated Circuit Symposium (CSICS)*, Oct 2015, pp. 1–4.

[21] Wavestream. (Rev B 0602-2014) MBA-KUS040, 40W Ku-Band matchbox power amplifier. [Online]. Available: http://www.wavestream.com/uploads/products/25w-40w-mba-ku-matchbox-power-amplifier.pdf

[22] M. Belaid and K. Wu, "Spatial power amplifier using a passive and active tem waveguide concept," *IEEE Transactions on Microwave Theory and Techniques*, vol. 51, no. 3, pp. 684–689, Mar 2003.

[23] M. Belaid, R. Martinez, and K. Wu, "A mode transformer using fin-line array for spatial power-combiner applications," *IEEE Transactions on Microwave Theory and Techniques*, vol. 52, no. 4, pp. 1191–1198, April 2004.

[24] C. W. Hicks, H.-S. Hwang, M. B. Steer, J. W. Mink, and J. F. Harvey, "Spatial power combining for two-dimensional structures," *IEEE Transactions on Microwave Theory and Techniques*, vol. 46, no. 6, pp. 784–791, Jun 1998.

[25] A. F. Perkons, Y. Qian, and T. Itoh, "Tm surface-wave power combining by a planar active-lens amplifier," *IEEE Transactions on Microwave Theory and Techniques*, vol. 46, no. 6, pp. 775–783, Jun 1998.

[26] X. Jiang, S. C. Ortiz, and A. Mortazawi, "A Ka-band power amplifier based on the traveling-wave power-dividing/combining slotted-waveguide circuit," *IEEE Transactions on Microwave Theory and Techniques*, vol. 52, no. 2, pp. 633–639, Feb 2004.

[27] J. P. Quine, J. G. McMullen, and D. D. Khandelwal, "Ku-band IMPATT amplifiers and power combiners," in *Microwave Symposium Digest, 1978 IEEE-MTT-S International*, June 1978, pp. 346–348.

[28] R. D. Beyers and D. I. L. de Villiers, "Compact conical-line power combiner design using circuit models," *IEEE Transactions on Microwave Theory and Techniques*, vol. 62, no. 11, pp. 2650–2658, Nov 2014.

[29] J. L. B. Walker, Ed., *Handbook of RF and Microwave Power Amplifiers*, 1st ed., ser. The Cambridge RF and Microwave Engineering Series. Section 6.3.2 pp. 236-241: Cambridge University Press, 2012.

[30] K. M. Passino and S. Yurkovich, *Fuzzy Control*, 1st ed. Section 3.6 pp. 161-168: Addison-Wesley, 1998.

Figure C.16. Conference paper 2016-2, Page 4.

2016 3rd Asia-Pacific World Congress on Computer Science and Engineering

Memoryless AM/AM Behavioral Model for RF Power Amplifiers

Paul O. Fisher[1,2] and Said F. Al-Sarawi[1]
[1]School of Electrical and Electronic Engineering, The University of Adelaide, SA 5005, Australia
Email: (paul.fisher@adelaide.edu.au; said.alsarawi@adelaide.edu.au)
[2]RF Industries, (RFI), Allenby Gardens, SA, 5009, Australia
Email: (paul.fisher@rfi.com.au)

***Abstract*— This paper presents a technique that allows a simple semi-physical amplitude-modulation-to-amplitude-modulation (AM/AM) model for RF power amplifier modeling, over a wide range of solid state technologies, with improved accuracy. The proposed technique builds on a recent memoryless behavioral model (BM), recently proposed by Cann, and demonstrates between 5 dB to 20 dB normalized mean squared error (NMSE) improvement, compared to the existing memoryless BM model, in AM/AM modeling over a range of RF power amplifier (RF PA) technologies, through comparison with our and other measured data from the literature. In addition, it provides an accurate prediction of third order intermodulation distortion (3rd IMD) linearization improvement of up to 17 dB. The proposed model can be used for system modeling or RF PA linearization applications. Issues related to segmentation discontinuities are also discussed.**

***Index Terms*—Memoryless Behavioral Models, Simulation, Linearizer, Low Cost, RF Power Amplifiers, Analog Predistortion, Adjacent Channel.**

I. Introduction

With the ever pressing demands for modern wireless communications systems to provide increased data capacity, as well as reduced spectral emissions and increased power efficiencies, RF PA devices play a crucial role in being able to achieve these demanding goals. As such improved behavioral modeling of PA devices at the system level is essential. Having a simple, fast and efficient BM that can be used over a range of device technologies, for RF PA devices, would be most advantageous in allowing the RF PA designer the ability to select this RF PA device quickly and accurately from a range of different devices and technologies.

Recent approaches for providing linear communication systems are to utilize advanced digital processing techniques which can be complex, expensive and less power efficient. However, in applications where the emphasis is more on simple, low cost and efficient solutions rather high performance, e.g. Small Cell repeaters [1], there is a need to develop techniques that allow for improved modeling accuracy while considering device operation over a wider dynamic range. This can have added benefits for use with envelope-tracking, predistortion linearizers that operate over larger dynamic ranges [2].

A new quasi memoryless (QM) BM for amplitude-modulation-to-phase-modulation (AM/PM) was recently described by Glock *et al.* [3]. The rationale for the development of this model is that simple static models are both less complex and less computationally intensive. Their work emphasized that memory effects are less prominent in well designed RF PAs and thus can be reduced to an acceptable level for mobile handset applications by careful amplifier biasing [4]. Their model addresses certain phase responses in semiconductor technologies such as gallium arsenide (GaAs) and Complementary Metal Oxide Semiconductor (CMOS).

Solid State device AM/AM responses are of the same generic shape, hence having a semi-physical model to estimate the AM/AM response of these devices with improved accuracy over a large dynamic range and range of technologies would be beneficial. Such models are of significant advantage to RF PA designers as they allow system modeling and performance evaluation without the need for complex and in depth device models.

This paper only focuses on AM/AM modeling, and does not cover AM/PM modeling in investigating how simple modeling can be used to quickly asses RF PA device performance for solid state devices, as AM/PM performance can be considered to be small enough to be neglected [5]. This will also reduce the complexity and computation times thus aiding in a faster device selection process. Improving the AM/AM modeling accuracy will also benefit the RF PA device selection process. Section II presents the need for simple BMs, including a brief review of other modeling approaches and technology modeling capabilities. Section II-D presents a new method that is based on a recent AM/AM model which is capable of producing the correct 3rd IMD response in the small signal region. Benefits of BM accuracy improvements to linearizer performance are discussed in Section III. A segmentation and optimization method is proposed and discussed in Section IV further improving the overall accuracy of the AM/AM model and demonstrating its applicability over a range of different technologies. Consideration of the proposed model and accuracy improvement method, with respect to 3rd IMD performance and impact on linearization improvement are discussed in Section V. Followed by a conclusion and acknowledgment.

A summary of the contributions presented in this paper are: (i) an optimized segmented curve-fitting approach, using a recent improved accuracy AM/AM model, providing up to 20 dB NMSE improvement, (ii) demonstrated improvement of up to 17 dB in linearizer 3rd IMD predication, (iii) an accurate AM/AM model that is applicable for a wide range of solid

978-1-5090-5753-5/16 $31.00 © 2016 IEEE
DOI 10.1109/APWC.on.CSE.2016.29

Figure C.17. Conference paper 2016-1, Page 1.

state power amplifier technologies, (iv) a model parameter fitting approach that uses a simple algorithm and simulation that takes into account segment boundary discontinuities, and (v) demonstrating that worst case discontinuities have no noticeable effect on the modeled amplifier spectrum when using digitally modulated signals.

II. SSPA Behavioral Models

A. The Need for Simple Models

One of the major factors contributing to the performance degradation of a wireless system are the non-linearities contributed by RF PAs, so for a system level evaluation the impact of this amplifier on the system's performance needs to be investigated. This can be achieved using detailed RF PA device parameters and accurate nonlinear models. However for an initial system level evaluation such information may not be available or may require too much effort to obtain. In addition, such modeling is computationally intensive and requires very long simulation times. In contrast, a system level modeling that use simple bandpass BMs of an RF PA can result in fast, but still accurate, simulations that can be used to assess the RF PA technologies and their impact on system performance. Hence allowing for rapid RF PA device comparisons, evaluations and selections.

The envelope model describing an RF PAs non-linearities, in terms of its AM/AM and AM/PM responses, can be derived from the complex input to output envelope voltage relationship as given by

$$v_{out}(t) = \mathrm{Re}\left[G(v(t))e^{j(\phi(t)+\varphi(v(t))+\omega_c t)}\right], \quad (1)$$

where ω_c is the RF carrier frequency, $G(v(t))$ and $\varphi(v(t))$ describe the instantaneous input to output envelope voltage gain and phase and these represent the RF PA's AM/AM and AM/PM responses, respectively. Some of these can be obtained from the manufacturer's datasheet or through further measurements and testing.

As part of performing a rapid and accurate system analysis, and selecting the RF PA device, then having a semi-physical based device BM provides the very significant benefit of the best starting point for least squared curve fitting (LSCF) that will typically be required in order to extract these model's parameters, plus any non-physical model parameters. This is extremely important and powerful for practical PA designers as it provides them with a fast way of assessing suitable PA device alternatives, using parameters that are readily available in device datasheets, without the need for further complex testing and measurements. Only the smoothness parameter, s, is non-physical. By having a unified physical or semi-physical AM/AM model that spans a range of solid state power amplifier technologies, is simple and computationally efficient, then this will greatly facilitate system level modeling.

B. Review of Simple PA Behavioral Models

In the literature several well established memoryless BMs offer PA designers with both a simple and fast means to conduct system level modeling, hence allowing them to be used for selecting a suitable device to meet system level requirements. Of these BMs, Cann 1980 [6] introduced a semi-physical AM/AM memoryless model. The model can be used for an over driven or soft-limiting bipolar based solid state amplifier by allowing the knee sharpness to be adjusted. Then Saleh [7] introduced a simple behavioral model that requires only 2 parameters for both AM/AM and AM/PM modeling, however this model was focused around Traveling Wave Tube Amplifiers (TWTAs). Another model that specifically targeted modeling the AM/AM and AM/PM of SSPAs was proposed by Ghorbani and Sheikhan [8]. Both the AM/AM and AM/PM models have the same form, and use only 4 parameters, while addressing inaccuracies associated with using TWTA based models for SSPAs. It is worth mentioning that the parameters for these models were not physically based.

At the same time Rapp [5], presented another memoryless AM/AM model for GaAs FET SSPAs that did included semi-physical parameters. Later on Honkanen and Haggman [9] applied Rapp's model as part of a bipolar junction transistor (BJT) AM/AM model. They also provided a new AM/PM model however it has the limitation of a maximum zero degrees phase shift. Then new models for AM/AM and AM/PM where introduced by White *et al.* [10] to better model Ka Band SSPAs. The proposed model for Ka band SSPAs provided improved accuracy when compared to the Saleh, Ghorbani and Rapp models.

Saleh's model was further developed by O'Droma *et al.* [11], with respect to Laterally Diffused Metal Oxide Semiconductor (LDMOS) field-effect-transistors (FETs), addressing the discontinuity seen in the application of Saleh's original AM/PM model when applied to typical LDMOS AM/PM characteristics, thus making Saleh's TWTA model suitable for use with solid state devices, however the parameters are still not physically based.

Cann 2012 [12] updated his earlier model to eliminate issues found with the original model when calculating small signal 3rd order IMD products, with the model again based on semi-physical parameters.

Recently Glock [3] presented an approach based around Rapp's AM/AM model but introduced a new AM/PM model determined from the first derivative of the Rapp AM/AM model plus additional terms.

The O'Droma model [11], can provide an excellent fit to a range of AM/AM and AM/PM curve shapes but the parameters for this model do not have a physical origin. As a result, determining the starting point values for this and other non-physically based model parameters for LSCF can be difficult and may require more sophisticated methods to determine these starting point values. So an appropriate selection of the starting points is needed to ensure an optimum outcome. With semi-physical based models, the majority of parameter starting points are taken from available data, thus avoiding possible guessing or further measurements.

For the non-physical parameters of the Rapp and recent Cann 2012 AM/AM only models, several plots of the AM/AM

Figure C.18. Conference paper 2016-1, Page 2.

responses can be made for a particular device, for different s values. By comparing these plots with measured data, an estimate of the starting value for s can be found. Having semi-physical starting points is also a very useful means of self checking the LSCF parameter results, as the final values for LSCF parameter results should be very close to the starting values.

C. Comparing PA Behavioral Models

To facilitate comparing these BMs, the NMSE in dB can be used. The definition that will be used through out this paper is given by [13]

$$\text{NMSE}_{\text{dB}} = 10\log_{10}\left(\frac{\sum_{n=0}^{N}|y_{MOD}[n]-y[n]|^2}{\sum_{n=0}^{N}|y[n]|^2}\right), \quad (2)$$

where N is the number of samples, $y[n]$ is the complex baseband envelope of the measured PA output and $y_{MOD}[n]$ is the complex baseband envelope of the model output.

To evaluate these BMs and new method in the frequency domain, comparisons are made using Simulink, where a wide-band code division multiple access (WCDMA) baseband envelope digitally modulated signal is applied to the RF PA model and the output is presented in the frequency domain via the Simulink Fast Fourier Transform (FFT) based spectrum analyzer element, for the AM/AM models described in this paper.

D. AM/AM Model Selection

Rapp's AM/AM model [5], used by Glock, has the same equation form as the model originally proposed by Cann but without the modulus function. Cann's original 1980 AM/AM model equation is given as

$$A(r) = \frac{L\text{sgn}(r)}{\left[1+\left(\frac{L}{g|r|}\right)^s\right]^{1/s}} = \frac{gr}{\left[1+\left(\frac{g|r|}{L}\right)^s\right]^{1/s}}, \quad (3)$$

where g, r, L and s are the small signal gain, input amplitude, output limit level, and sharpness parameters, respectively.

Litva and Lo [14] identified that Cann's original 1980 AM/AM model had issues related to correctly generating 3rd IMD responses in the small signal region. This was confirmed and the reason for this issue was determined by Loyka [15]. Cann's new memoryless 2012 AM/AM model, presented recently, is given as [12]

$$A(r) = \frac{L}{s}\ln\left[\frac{1+e^{s(\frac{gr}{L}+1)}}{1+e^{s(\frac{gr}{L}-1)}}\right] - L, \quad (4)$$

where g, r, L and s are the small signal gain, input amplitude, output limit level, and sharpness parameters, respectively. It should be noted that the issues in the old model are related to modeling two discrete tones used to generate IMD products, however for a typical digital modulation scheme no issues were observed. This improved AM/AM model will be used as the basis for our modeling method.

III. Linearizer Benefits From Accuracy Improvements

For simple low cost RF predistortion linearizers to be able to compete with more sophisticated linearizers, like DPD linearizers having complex and expensive hardware with higher power consumption, then the accuracy of low cost RF predistortion linearizers must be comparable to DPD linearizers [1]. To quantify the benefits of AM/AM modeling accuracy improvement, when applied to a low cost RF predistortion linearizer, a means of quantifying this benefit is required. Based on an analysis by Nojima and Konno [16], an equation for calculating the amount of 3rd IMD reduction, S_{IMD}, achievable from a predistorter (PD) and power amplifier as function of the AM/AM and AM/PM errors, is given by

$$S_{IMD} = -10\log_{10}\left[1+10^{\delta A/10}-2\cdot 10^{\delta A/20}\cos(\delta\theta)\right], \quad (5)$$

where δA and $\delta\theta$ are the amplitude error in dB and the phase error in degrees respectively. For this combination, the amount of distortion reduction achievable is a function of the amplitude and phase errors as contributed by the PD. If the PD errors are considered to be fixed, then any degradation in the intermodulation distortion reduction can be attributed to BM amplitude inaccuracies for a fixed phase. The impact of AM/AM modeling improvement on the IMDs and linearization performance, due to this model is discussed further in Section V.

IV. Segmented Curve Fitting Method to Improve AM/AM Model Accuracy

Similar to the techniques utilized by Glock to determine the linear, non-linear and saturation regions from the AM/AM characteristic response, this technique can also be utilized to determine the linear, non-linear or saturation region segments of the AM/AM responses of Cann's 2012 AM/AM model. Furthermore, the curve fits of these segments can be applied in a similar approach to that used by Zhu *et al*, [2], for piecewise curve fitting of non-linear segments of AM/AM and AM/PM envelop-tracking amplifiers. As a result, the segmented curve fitting provides more accurate model results and assists with comparing devices for system analysis purposes, as well as defining potential improvements in linearization margin for a particular device.

By applying the recent Cann 2012 AM/AM model for each segmented region across a range of technologies and by optimizing the end of the linear region segment and start of the saturation region segment, an overall improvement of between 5 dB to 20 dB can be achieved in AM/AM NMSE at the expense of further simple processing steps for each segment, depending on RF PA device technology. The recent Cann 2012 AM/AM model also has the ability to provide starting values for LSC fitting for each of the segments.

To improve the AM/AM accuracy estimation of this model, the second derivative of the AM/AM response is used to determine both the linear and saturation regions. Using AM/AM data from Glock's Fig. 11 2V2 curve, it can be seen that

Figure C.19. Conference paper 2016-1, Page 3.

more data points are required when penetrating further into the saturation region, so the approach developed by [17], based on Rapp's AM/AM model, to extrapolate the AM/AM performance into the saturation region can be used. As Glock's paper uses the Rapp AM/AM model then this AM/AM data can be extended into the saturation region. Similarly for Cann's recent 2012 AM/AM model, data can be extended into the saturation region. Using the extended AM/AM data, the transition from the linear to saturation regions can be determined as a function of v_{in} when the 2nd derivative of the AM/AM data equals zero, see Fig. 1. As can be seen from this plot, the linear region stop point (vertical blue solid line) is at v_{in} = 0 V and saturation region start point (vertical orange solid line) is well beyond the available data, by the 2nd derivative calculation. This means that the practical LSCF data starting range extends from v_{in} = 0 V to where v_{in} is at the full extent of the available data (vertical red solid line), in this case where v_{in} = 0.5 V. The region between the solid blue and red lines is practically the full AM/AM model region for initial LSCF with these points being the starting points for the AM/AM segmentation method optimization.

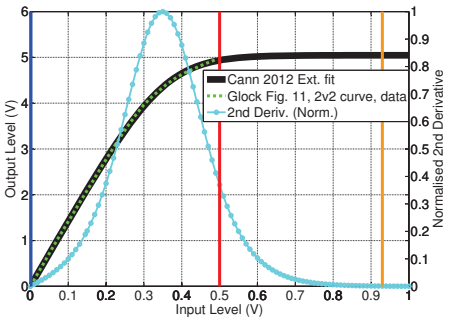

Fig. 1. Glock's Fig. 11, 2V2 curve, [3] AM/AM data (green dotted curve), extended AM/AM data (solid black curve), using [17] & normalised (to the maximum value) numerical 2nd derivative of extended AM/AM data (cyan solid circle curve) using Matlab. The solid blue vertical line is the initial end of the linear region, the solid orange vertical line is start of saturation region by the 2nd derivative calculation. The solid red vertical line is the end of the available AM/AM data, effectively the end of the saturation region for the available data.

Initial AM/AM curve fits for both the recent Cann 2012 and Glock (using Rapp's AM/AM model) AM/AM models have been performed over the entire available data for Glock's Fig. 11, 2V2 curve data, with the results from both the Glock (using Rapp's AM/AM model) (green down triangle curve) and the recent Cann 2012 AM/AM (magenta circle curve) models shown in Fig. 2. These are single segment fits between the linear region stop and saturation region start points. This is the same as using the AM/AM model over the entire available data range.

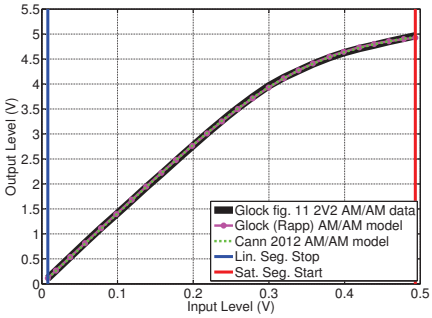

Fig. 2. Comparison of curve fit for Glock's Fig. 11, 2V2 curve, data [3] (black solid curve), Glock's (using Rapp's AM/AM model) AM/AM model (green dotted curve) & recent Cann 2012 AM/AM model (magenta solid circle trace).

A. *Optimized Segmented Curve Fitting*

To further improve the accuracy of the AM/AM model an optimization routine was developed to identify the optimum linear stop and saturation start region points to provide an enhanced data fit in terms of NMSE performance. A comparison between the initial fit and the optimised fit for each of the segments is shown in Fig. 3 (yellow curves). This is only shown for the recent Cann 2012 AM/AM model.

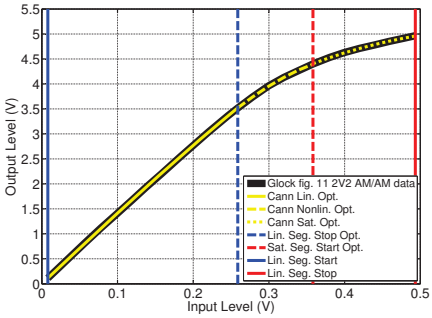

Fig. 3. Comparison of curve fit for Glock's Fig. 11, 2V2 curve, data [3] (black solid curve) and the optimised segmented curve fits for the recent Cann 2012 AM/AM model (yellow curves). The optimised linear segment is between the input voltage range of 0 V to 0.26 V, with the optimised non-linear segment between 0.26 V and 0.36 V and the remaining saturation segment is between 0.36 V and 0.5 V.

When comparing the LSC fit over the full range of data, Fig. 2, compared to the segmented linear, non-linear and saturation region data, Fig. 3, it is difficult to see any difference. However a comparison between the Glock (using Rapp's AM/AM model) and recent Cann 2012 absolute AM/AM errors (in dB), for both initial and optimised segmentation versus input voltage for Glock's Fig. 11, 2V2 curve, data are shown in

Figure C.20. Conference paper 2016-1, Page 4.

Fig. 4, reveals the improvements in absolute error obtained by using the segmentation method. The improvements can be seen between the Cann 2012 (solid magenta) and segmented Cann 2012 (solid red) curves. The initial maximum error result is shown as the horizontal dotted magenta line with the optimised segmented result shown as the horizontal red dash - dot line. An NMSE AM/AM comparison between these models and the corresponding improvements using the segmentation technique show, following segmentation optimization, that the recent Cann 2012 AM/AM model has better than 10 dB improvement. In Section V, Table I shows the improvements in NMSE by using the segmentation method over a range of technologies.

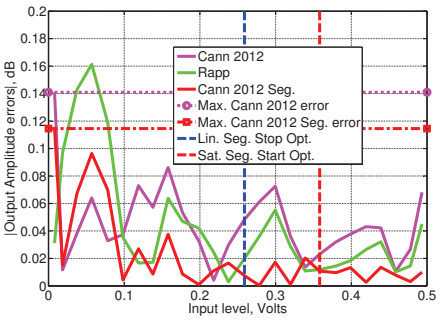

Fig. 4. Comparison of |Output Amplitude errors| versus input voltage from Glock's Fig. 11, 2V2 curve, data [3], showing before and after segmented approach optimization. Also shown are the maximum for Cann's recent 2012 AM/AM model amplitude errors for both the initial (magenta solid line) & segmented (red solid line) approach being 0.14 and 0.115 dB respectively.

An algorithm for optimising segmented curve fitting was prepared to further improve NMSE and is presented as Algorithm 1. The algorithm starting points for the second derivatives cannot be zero due to their numerical nature, so there is a requirement to have 2nd derivative zero limits, in our case we have selected this value to be below 0.001, to suit the numerical data. During the minimisation process there are some segment ranges where the discontinuities are higher than the given data resulting in poorer segment fits. This is due to using parameter starting values for the full range of data in those segments. This can be corrected by determining suitable starting points for each segment but this has not been implemented within this algorithm. Even with such improvement in the starting point, the overall curve fit performance is still worse than the segmented approach.

B. Frequency Domain Comparisons & Discontinuity Effects at Segment Boundaries

A comparison of the recent Cann 2012 model, with and without optimised segmentation, against measured data with a WCDMA signal applied, for the SHF-0189 HFET [18] are given in Fig. 5. These plots show that the optimized segmented

Algorithm 1 Minimize AM/AM NMSE in dB

Require: Combined AM/AM NMSE (dB) linear, non-linear & saturation region segments are minimum.
Ensure: V_{in} & V_{out} are real & > 0.
1: **INPUT** V_{out} vs. V_{in} data-set for the amplifier.
2: Determine $d''V_{out}/dV_{in}$ (2nd Derivative)
3: **if** $d''V_{out}/dV_{in} \neq 0$ after the first occurrence when $d''V_{out}/dV_{in} = 0$ **then**
4: V_{out} vs. V_{in} data does not extend far enough into the saturation region so extend the V_{out} vs. V_{in} data using [17], refer to Fig.1.
5: **end if**
6: **if** $d''V_{out}/dV_{in} = 0$, on the first occurrence. **then**
7: $V_{in_{Lin}}$ is the linear region *stop* point.
8: **else if** $d''V_{out}/dV_{in} = 0$, on the second occurrence. **then**
9: $V_{in_{Sat}}$ is the saturation region *start* point.
10: **end if**
11: Note: V_{out} vs. V_{in} data between $V_{in_{Lin}}$ & $V_{in_{Sat}}$ is the non-linear region data.
12: **for** $V_{in} = 0$ to $V_{in_{Lin}}$ **do**
13: Least Squares Curve Fit (LSCF) V_{out} vs. $V_{in_{Lin}}$ using (4)
14: **end for**
15: **for** $V_{in} = V_{in_{Lin}}$ to $V_{in_{Sat}}$ **do**
16: LSCF V_{out} using (4), for the non-linear region.
17: **end for**
18: **for** $V_{in} = V_{in_{Sat}}$ to $V_{in_{max}}$ **do**
19: LSCF V_{out} vs. $V_{in_{Sat}}$ using (4), for the saturation region data.
20: **end for**
21: **for** $V_{in} = 0$ to $V_{in_{max}}$ **do**
22: Calculate AM/AM NMSE A (dB), using (2), for the combined linear, non-linear & saturation region segments.
23: Adjust $V_{in_{Lin}}$ & $V_{in_{Sat}}$ to give $V_{in_{Lin1}}$ & $V_{in_{Sat1}}$
24: **end for**
25: **repeat**
26: Steps 12: to 24: using $V_{in_{Lin1}}$ & $V_{in_{Sat1}}$ calculate AM/AM NMSE B (dB), using (2), for the *combined* linear, non-linear & saturation region segments.
27: **until** NMSE B (dB) $<$ NMSE A (dB)
28: Note: It may occur that NMSE A (dB) $<$ NMSE B (dB), i.e. the initial segmentation is optimum.
29: Output all calculated curve fit coefficients. **END**

method provides a better fit to the measured data compared to the non segmented model.

To determine the effects of discontinuities at segment boundaries, investigations have revealed that although the recent Cann 2012 AM/AM model, using the optimised segmentation method does not have continuous derivatives over the segment boundaries, the voltage errors between the segment boundaries, after optimization, are very small and have a negligible effect on the adjacent channel leakage ratio (ALCR) response. This has been investigated for a WCDMA digitally

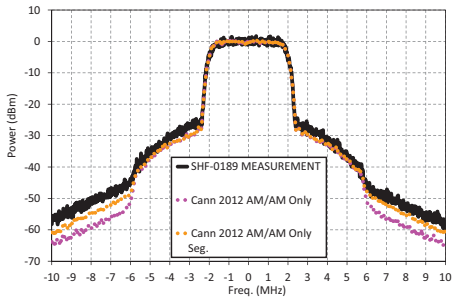

Fig. 5. Comparison of measured versus Simulink simulations for WCDMA, comparing Glock versus recent Cann 2012 full & optimized segmented models for the SHF-0189, [18], data. Resolution bandwidth (RBW) for both measured & simulation data is 30 kHz. Measured center frequency is 881.5 MHz.

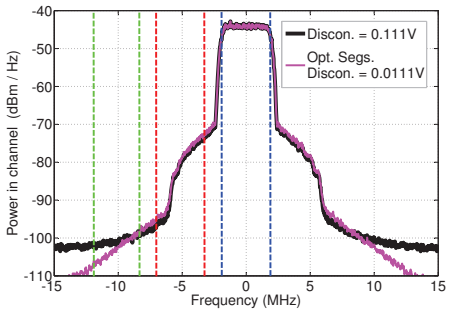

Fig. 6. Discontinuity effects on a WCDMA modulated signal, simulated using Simulink, for Cann's recent 2012 optimized segmented AM/AM model of Glock's Fig.11, 2V2 curve, data [3] data. With 0.0111 volt discontinuity ACLR1L/2L = -33.2/-57.3 dBc. With 0.111 volt discontinuity ACLR1L/2L = -33.7/-56.2 dBc. In-band wanted between dashed blue vertical lines, ACLR1 between dashed red vertical lines and ACLR2 between dashed green vertical lines (lower bands only shown) with 3.84 MHz integration bandwidth (BW). The integrated power over the wanted 3.84 MHz BW is 21.6 dBm. RBW is 30 kHz.

modulated signal with the same power spectral density level as used in Glock's Fig. 9. The worst case discontinuity error, of 0.0111 volts, for either of the linear to nonlinear or nonlinear to saturation segment boundaries was increased, above the optimised value, until the second ACLR level increased by $\approx$ 1 dB and this occurred at 10 times the worst case discontinuity error with no noticeable increase found for the first ACLR, concluding that the optimized segmented recent Cann 2012 AM/AM model has negligible discontinuity effects, even when considering worst case discontinuities at the segment boundaries. Comparisons between the optimized segmentation discontinuity error result and 10 times this error are shown in Fig. 6.

V. Impact on IMDs & Linearization Improvement

Cann's recent 2012 AM/AM model and the optimised segmentation method have been assessed to determine how they perform in predicting 3rd IMD performance for RF PAs over a wide dynamic range by simulating the 3rd IMDs using Simulink and comparing the simulations against manufacturer's measured IMD data, SHF-0189 device [19] page 5. Plots of the 3rd IMD comparisons are shown in Fig. 7 with comparisons of the absolute 3rd IMD errors shown in Fig. 8. The results indicate that the recent Cann 2012 AM/AM model performs better than the Rapp or O'Droma (Modified Saleh) AM/AM models, even though the O'Droma (Modified Saleh) model shows very good curve fitting results. The recent Cann 2012 AM/AM model has $\approx$ 2.6 dB improvement in average error (AE) compared to the O'Droma model and over 10 dB AE improvement compared to the Glock (using Rapp's AM/AM model) model. The optimized segmented recent Cann model method improves the AE by a further $\approx$ 0.7 dB.

The maximum absolute amplitude error, of the full and optimised segmented recent Cann 2012 AM/AM model of Glock's Fig. 11 AM/AM device data from LSC fitting, are 0.141 dB and 0.115 dB respectively. These are shown on a plot of (5),

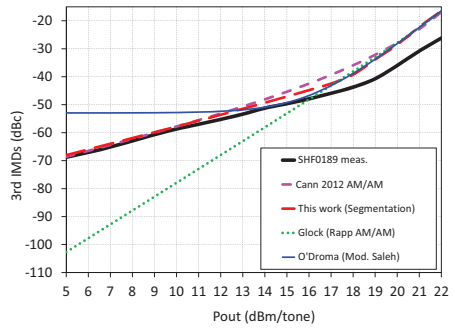

Fig. 7. 3rd IMD measured device data SHF-0189 [19] page 5 versus Simulink simulated comparison of the O'Droma (Mod. Saleh), Glock & recent Cann 2012 models, all including both AM/AM components. Two tone measurements at 900 MHz, 1 MHz tone spacing.

Fig. 9, where the intermodulation distortion improvement is plotted against phase error for various amplitude errors. The difference between the full and optimised segmented method equates to a 3rd IMD improvement of 1.79 dB at 0.1° phase error.

Table I shows the NMSE for each of the various technologies, BJT, heterojunction FET (HFET), LDMOS FET, heterojunction-bipolar-transistor (HBT), enhancement mode pseudomorphic high-electronmobility-transistor (E-pHEMT), GaAs (Glock's Fig. 8 device data), CMOS (Glock's Fig. 11 device data) and galliun nitride (GaN) on silicon carbide

Figure C.22. Conference paper 2016-1, Page 6.

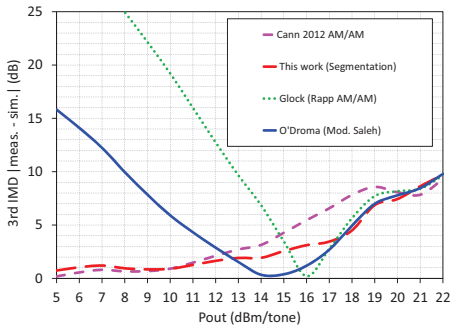

Fig. 8. 3rd IMD |measured minus Simulink simulated| error for the O'Droma (Mod. Saleh), Glock (using Rapp's AM/AM model), recent Cann 2012 & optimized segmented recent Cann 2012 models for AM/AM only. The AE for Cann's recent 2012 AM/AM model is $\approx$ 4dB compared to $\approx$ 6.5 & 13.9 dB for the O'Droma and Glock (using Rapp's AM/AM model) models respectively. The optimized segmented recent Cann 2012 model AE further improves 3rd IMD over the recent Cann 2012 model by $\approx$ 0.7 dB.

(GaN/SiC) HEMT. The AM/AM NMSEs were determined for both the full and segmented methods. Table I also shows the 3rd IMD linearization improvement across device technology as a result of the optimised segmentation method AM/AM improvements.

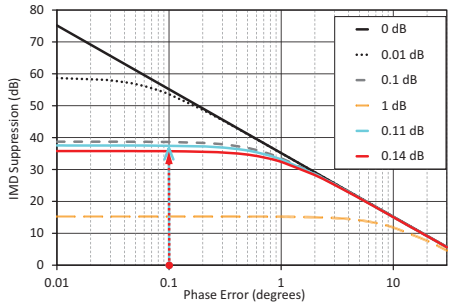

Fig. 9. IMD suppression versus phase errors for a range of amplitude errors. The cyan vertical arrow shows the 3rd IMD improvement in linearization for the optimised segemnted approach compared to the full recent Cann 2012 AM/AM model, red dotted vertical arrow, both at 0.1° phase error.

VI. Conclusion

In this paper we have presented and demonstrated the use of a more accurate simple AM/AM model that is suitable for use over a range of RF PA device technologies.

A segmented curve-fitting approach, using the proposed recent AM/AM model, has also been presented that provides up to 20 dB Normalized Mean Squared Error (NMSE) improvement when modeling the AM/AM characteristics of the amplifier, further resulting in linearizer 3rd IMD improvements of up to 17 dB.

A model parameter fitting approach using a simple algorithm has been indicated along with simulations accounting for segment boundary discontinuities, demonstrating that such worst case discontinuities have no effect on the modeled amplifier spectrum when using digitally modulated signals.

Future work will be to investigate improving AM/PM modeling accuracy and to combine that work with this current work on AM/AM modeling to determine how the combined AM/AM and AM/PM accuracy improvements will increase linearizer 3rd IMD performance.

TABLE I
Technology NMSE & Linearization Improvement Comparison

Device [Ref.]	Cann 12B AM/AM NMSE (dB)		NMSE Imp. (dB)	IMD Imp. (dB)
	Full	Seg.		
BJT [9]	-30.16	-35.28	5.12	3.02
HFET [18]	-43.53	-62.84	19.31	13.51
HBT [20]	-58.88	-64.86	5.98	6.43
E-pHEMT [21]	-44.77	-63.41	18.64	13.90
LDMOS [22]	-37.68	-42.40	4.72	1.39
GaAs [3]	-39.61	-58.20	18.59	0.75
CMOS [3]	-46.04	-56.07	10.03	1.79
GaN/SiC [23]	-43.10	-48.40	5.30	17.62

Acknowledgment

The authors wish to acknowledge the assistance and support of RF Industries (RFI) Pty. Ltd. for providing resources and time for the first author to work on this research.

References

[1] J. Xia, A. Islam, H. Huang, and S. Boumaiza, "Envelope memory polynomial reformulation for hardware optimization of analog-RF predistortion," *IEEE Microwave and Wireless Components Letters*, vol. 25, no. 6, pp. 415–417, June 2015.

[2] A. Zhu, P. J. Draxler, C. Hsia, T. J. Brazil, D. F. Kimball, and P. M. Asbeck, "Digital predistortion for envelope-tracking power amplifiers using decomposed piecewise Volterra series," *IEEE Transactions on Microwave Theory and Techniques*, vol. 56, no. 10, pp. 2237–2247, Oct 2008.

[3] S. Glock, J. Rascher, B. Sogl, T. Ussmueller, J.-E. Mueller, and R. Weigel, "A memoryless semi-physical power amplifier behavioral model based on the correlation between AM-AM and AM-PM distortions," *IEEE Transactions on Microwave Theory and Techniques*, vol. 63, no. 6, pp. 1826–1835, June 2015.

[4] Y. S. Lee, M. W. Lee, S. H. Kam, and Y. H. Jeong, "A high-linearity wideband power amplifier with cascaded third-order analog predistorters," *IEEE Microwave and Wireless Components Letters*, vol. 20, no. 2, pp. 112–114, Feb 2010.

[5] C. Rapp, "Effects of HPA-nonlinearity on a 4-DPSK/OFDM-signal for a digital sound broadcasting signal," in *Proceedings Second European Conf. on Sat. Comm. (ESA SP-332), Liege, Belgium*, oct 1991, pp. 179–184.

[6] A. Cann, "Nonlinearity model with variable knee sharpness," *IEEE Transactions on Aerospace and Electronic Systems*, vol. AES-16, no. 6, pp. 874–877, 1980.

[7] A. Saleh, "Frequency-independent and frequency-dependent nonlinear models of TWT amplifiers," *IEEE Transactions on Communications*, vol. 29, no. 11, pp. 1715–1720, 1981.

Figure C.23. Conference paper 2016-1, Page 7.

[8] A. Ghorbani and M. Sheikhan, "The effect of solid state power amplifiers (SSPAs) nonlinearities on MPSK and M-QAM signal transmission," in *Sixth International Conference on Digital Processing of Signals in Communications*, Sep 1991, pp. 193–197.
[9] M. Honkanen and S.-G. Haggman, "New aspects on nonlinear power amplifier modeling in radio communication system simulations," in *IEEE International Symposium on Personal, Indoor and Mobile Radio Communications, PIMRC*, vol. 3, 1997, pp. 844–848.
[10] G. White, A. Burr, and T. Javornik, "Modelling of nonlinear distortion in broadband fixed wireless access systems," *Electronics Letters*, vol. 39, no. 8, pp. 686–687, 2003.
[11] M. O'Droma, S. Meza, and Y. Lei, "New modified Saleh models for memoryless nonlinear power amplifier behavioural modelling," *IEEE Communications Letters*, vol. 13, no. 6, pp. 399–401, 2009.
[12] A. Cann, "Improved nonlinearity model with variable knee sharpness," *IEEE Transactions on Aerospace and Electronic Systems*, vol. 48, no. 4, pp. 3637–3646, 2012.
[13] M. Isaksson, D. Wisell, and D. Ronnow, "A comparative analysis of behavioral models for RF power amplifiers," *IEEE Transactions on Microwave Theory and Techniques*, vol. 54, no. 1, pp. 348–359, 2006.
[14] J. Litva and T. K.-Y. Lo, Eds., *Digital Beamforming in Wireless Communications*, 1st ed. Norwood, MA, USA: Artech House, Inc., 1996, ch. 4, sec. 4.4.1, pp. 79-81.
[15] S. Loyka, "On the use of Cann's model for nonlinear behavioral-level simulation," *IEEE Transactions on Vehicular Technology*, vol. 49, no. 5, pp. 1982–1985, 2000.
[16] T. Nojima and T. Konno, "Cuber predistortion linearizer for relay equipment in 800 MHz band land mobile telephone system," *IEEE Transactions on Vehicular Technology*, vol. 34, no. 4, pp. 169–177, Nov 1985.
[17] P. Fisher and S. Al-Sarawi, "Improving the accuracy of SSPA device behavioral modeling," in *International Conference on Information and Communication Technology Research, ICTRC*, 2015, pp. 278–281.
[18] Sirenza Microdevices. (EDS-101240 Rev E) SHF-0189, 0.05 - 6 GHz, 0.5 Watt GaAs HFET. [Online]. Available: http://datasheet.octopart.com/SHF-0189-Sirenza-datasheet-129519.pdf
[19] ——. (EAN-101798 Rev A) SHF-0189, Amplifier Application Circuits, DESIGN APPLICATION NOTE — AN-031. [Online]. Available: http://application-notes.digchip.com/147/147-47818.pdf
[20] NXP. (Revision: 9, October, 2014) MMG3005NT1, 800 - 2000 MHz, Heterojunction Bipolar Transistor. [Online]. Available: http://nxp.com/
[21] Avago Technologies. (February 10, 2014) ALM-31122, 700 MHz - 1 GHz E-pHEMT, 1 Watt High Linearity Amplifier. [Online]. Available: http://www.avagotech.com/
[22] Ampleon. (Revision: 4 - 1 September, 2015) BLM7G1822S-20, 1805 MHz to 2170 MHz, LDMOS 2-stage power MMIC. [Online]. Available: http://www.ampleon.com/
[23] Northrop Grumman. (Revision: May, 2014) APN180, 27-31 GHz GaN Power Amplifier. [Online]. Available: http://www.northropgrumman.com/

Figure C.24. Conference paper 2016-1, Page 8.

Analog RF Predistorter Simulation using Well-Known Behavioral Models

Paul O. Fisher[1,2] and Said F. Al-Sarawi[1]

[1]School of Electrical & Electronic Engineering, The University of Adelaide, Adelaide, SA, 5005, Australia

[2]RF Industries (RFI), Allenby Gardens, SA, 5009, Australia

Email: {paul.fisher,said.alsarawi}@adelaide.edu.au

***Abstract* — This paper describes an envelope pre-distortion linearizer scheme that uses integrated analog components for the low cost implementation of intermodulation distortion product (IMDs) reduction in RF power amplifiers (RFPAs). Integrated logarithmic amplifiers & phase detectors are used to sample the input and output signals before and after the RFPA to measure the complex gain & phase information, which is used to control an integrated pre-distorter integrated circuit (IC) that contains adjustable gain & phase components within a single IC package. Comparisons of a range of well-known and updated RFPA behavioral models are evaluated to determine the most suitable behavioral model for this linearization scheme. The simulation model also allows for the addition of RFPA memory effects and driver & RFPA noise figures to be included and compared. All component models are based on parameters extracted from device data sheets for the driver & RFPA, thus minimizing the need for special measurements.**

***Index Terms* — Linearizer, RF power amplifiers, pre-distorter, integrated circuits, simulation, linearization loop.**

I. Introduction

There is a continual need for improved spectrally efficient communication schemes at ever reducing costs. The RFPA is a major component within a communication system thus having a significant impact on both the spectral purity and system cost. It is therefore important to consider the performance of the RFPA to achieve these system requirements. To achieve maximum system efficiency then an RFPA needs to be operated at or near its' maximum output power. With today's digital modulation, such a need impacts on spectral regrowth and other users, so linearization schemes must be employed to overcome this shortcoming. The type of linearization scheme will also have an impact on both the output spectrum and overall system cost.

This paper investigates a simple low cost linearizer implementation using readily available analog components. The use of these simple components offer moderate linearization improvements at low cost compared to more complex; in size, implementation cost & power consumption, digital pre-distortion or other linearization schemes, for example Cartesian loop or feed forward, or envelope restoration. [1].

In this paper we demonstrate that gain and phase detection offer the benefit of reducing linearizer complexity by eliminating any down / up conversions, also reducing potential spurious issues and system complexity and cost is also reduced by combining the linearizer elements within a single IC. An estimate of the PCB area needed for this linearizer is 25mm x 25mm. In addition, this paper evaluates a number of behavioral models and demonstrates their linearization performance when included in this proposed linearization approach.

II. Proposed Linearization Scheme

The envelope pre-distortion scheme to be used is shown in Fig. 1 [2].

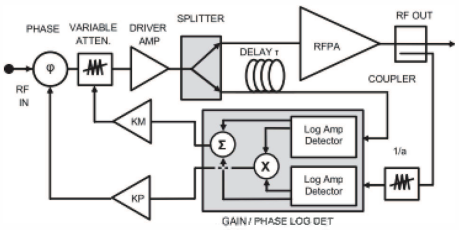

Fig. 1. Analog envelope pre-distortion linearizer from Woo [2] including driver amplifier and splitter.

This scheme uses simple low cost readily available analog integrated circuits (ICs). The original paper [1] uses individual discrete voltage variable attenuators (VVAs) and voltage variable phase shifters (VVP's), whereas this paper proposes the use of an all in one adjustable gain and phase shifter linearization IC from Maxim, the MAX2010 [3] shown in Fig. 2.

978-1-4799-8389-6/15/$31.00 ©2015 IEEE

Figure C.25. Conference paper 2015-2, Page 1.

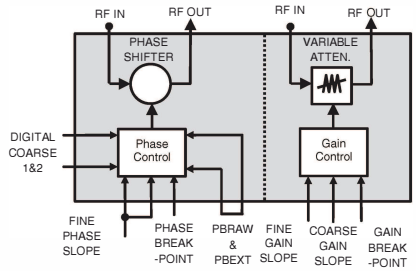

Fig. 2. Maxim MAX2010, gain and phase linearizer IC [3].

This IC offers a range of gain & phase breakpoints that are adjustable thus suitable for a range of RFPA gain and phase expansion points. Coarse and fine gain and phase slope adjustments are also available suiting a range of RFPAs. The data provided for the MAX2010 device is sufficient to enable the extraction of the needed phase and gain parameters for the behavioral models.

The K_m and K_p parameters are formed via operational amplifiers and these can be optimally adjusted for magnitude and phase gains plus offsets to cater for the 30 mV/dB and 10 mV/° slopes of the Analog Devices gain / phase logarithmic detector, AD8302 IC [4].

A. RF Power Amplifier

For this paper the RFPA device used is the same as the one used in [2]. This amplifier is a 0.5W, GaAs HFET PA

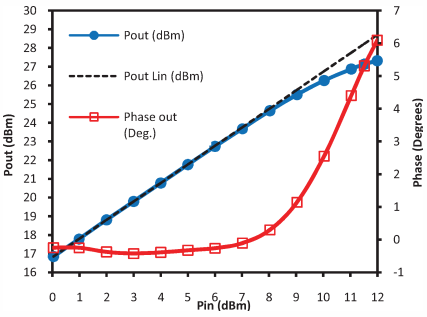

Fig. 3. Sirenza SHF-0189 P_{in} vs P_{out} and phase data derived from Woo [2].

(Sirenza SHF-0189) operated at 881.5 MHz, Fig. 3. For modeling this RFPA, the original Rapp model [5] is used for the amplitude response, while the phase model used is based on the updated version of the Honkanen & Haggman phase model [6] as given in Table 1.

TABLE 1
SIMPLE BEHAVIORAL MODELS FOR RF POWER AMPLIFIERS

Model	AM/AM	AM/PM
Saleh [7]	$A_s(r) = \frac{\alpha_a r}{1+\beta_a r^2}$	$\emptyset_s(r) = \frac{\alpha_\emptyset r^2}{1+\beta_\emptyset r^2}$
Ghorbani & Sheikan [8]	$A_G(r) = \frac{x_1 r^{x_2}}{1+x_3 r^{x_2}} + x_4 r$	$\emptyset_G(r) = \frac{y_1 r^{y_2}}{1+y_3 r^{y_2}} + y_4 r$
Rapp [5] (with updated Honkanen & Haggman [6] Phase)[a]	$A_R(r) = \frac{A \times r}{(1+(A \times r/\alpha)^{2\beta})^{1/2\beta}}$	$\emptyset_{HH}(r) = \frac{b}{1+e^{-c(r-a)}} \cdot \frac{1}{p_1 r + p_2} - d$
Corrected[b] White et al [9]	$A_W(r) = a[(1 - e^{-br}) + cre^{-dr^2}]$	$\emptyset_W(r) = f(1 - e^{-g(r-h)}),\ r \geq h$ $\emptyset_W(r) = 0, r < h$
O'Dorma et al [10]	$A_{MS}(r) = \frac{\alpha_a r^\eta}{(1+\beta_a r^\gamma)^\nu} - \varepsilon$	$\emptyset_{MS}(r) = \frac{\alpha_\emptyset r^\eta}{(1+\beta_\emptyset r^\gamma)^\nu} - \varepsilon$

[a]Rapp model includes the Honkanen & Haggman phase addition, $\emptyset_{HH}(r)$ plus the additional parameter d by these authors [11], allowing for positive phase shifts.
[b]Addition of square brackets, [ ], around White et al's AM/AM model, $A_W(r)$ to provide a correct match to White et al's results [11].

For this study, several other well-known models, with some recent additions as detailed in Table 1, were also used to model the RFPA device data and a comparison has been made to evaluate their applicability for this type of linearization scheme.

B. Group Delay

The MAX2010 has a maximum given group delay of 2.4 ns and the group delay of the Sirenza SHF-0189 is 1.4 ns from [2]. To accommodate this delay in a physical implementation, small footprint, low cost, surface mount technology (SMT) and low temperature co-fired ceramic (LTCC) components will be used. These are available for this frequency range covering ps up to 3 ns [12]. The total group delay of 3.8 ns can be obtained by the series combination of two SMT LTCC components. These group delays will be allowed for in the following simulations.

III. AMPLITUDE AND PHASE ERRORS

Variations of the gain and phase logarithmic amplifier detector IC and the variable gain and pre-distortion linearizer IC have an effect on the overall ability of the linearizer to improve the output IMD performance. The equation describing the combined effects of these

Figure C.26. Conference paper 2015-2, Page 2.

variations on the amount of IMD improvement is given by equation (1), [13].

$$U = -10\log\left(1 + 10^{\delta/10} - 2 \cdot 10^{\delta/20} \cdot \cos(\Delta\theta)\right) \quad (1)$$

Where U is the intermodulation improvement in dB, δ is the amplitude variation in dB and $\Delta\theta$ is the phase variation in degrees. This equation is plotted in Fig. 4 and indicates that to maintain a 20 dB IMD improvement then the gain variation must be less than ±1 dB and the phase variation must be less than 6 degrees.

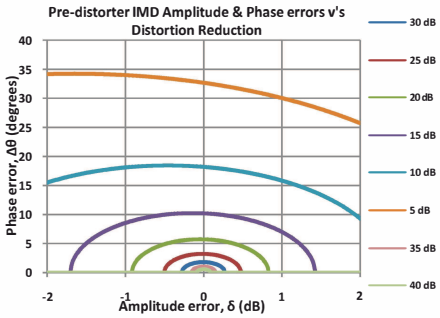

Fig. 4. Pre-distorter IMD reduction v's gain and phase errors.

Errors for the gain-phase detector IC and gain-phase linearization IC, taken from the data sheets, are provided in Table 2.

TABLE 2
GAIN /PHASE DETECTOR & LINEARIZATION IC ERRORS

Parameter	Specification
Linearizer IC	
Phase Breakpoint vs Temp.	±1.5 dB
Phase slope vs Temperature	0.05 °/dB
Phase Parasitic gain expansion	+0.4 dB
Gain Breakpoint vs Temp.	-0.5 dB
Gain slope vs Temperature	-0.01 dB/dB
Gain Parasitic Phase expansion	+3°
Detector IC	
Magnitude dynamic range (900 MHz)	±1 dB per 58 dB
Magnitude slope	28.7mV/dB
Gain Deviation vs Temperature	0.25 dB
Gain measurement balance	0.20 dB
Phase dynamic range (900 MHz)	±1 dB per 143°
Phase slope	10.1mV/°
Phase Deviation vs Temperature	0.75°
Phase measurement balance	0.8°

Considering all of the errors listed in Table 2 and following an RSS analysis then an IMD improvement of greater than 15 dB should be expected.

IV. MODELING AND SIMULATION

The behavioral modeling of the RFPA was developed using the least squares curve fitting technique for the equations given in Table 1. The input and output voltages are normalized to the 1 dB compression point (P1dB) of the Sirenza SHF-0189 being at P_{in} = 11.5 dBm & P_{out} = 27.12 dBm. Details of all extracted parameters for each of the models are given in Table 3. The linearizer, shown in Fig. 1, and vector modulator, shown in Fig. 2. are modeled using Simulink with the simulated before and after linearizer 3rd & 5th order IMDs are shown in Fig. 5, using the original Rapp AM/AM model and the Honkanen & Haggman AM/PM model [6] with the phase update, d, provided in [11].

TABLE 3
EXTRACTED BEHAVIORAL MODEL PARAMETERS
(NORMALIZED TO P_{1DB})

Model	AM/AM	AM/PM
Saleh [5]	α_a = 1.2015	α_Φ = 0.0288
	β_a = 0.1974	β_Φ = -0.6472
Ghorbani & Sheikan [9]	$x1$ = 273.044	$y1$ = 0.2769
	$x2$ = 1.0013	$y2$ = 6.7083
	$x3$ = 0.0029	$y3$ = 1.5281
	$x4$ = -271.264	$y4$ = -0.0172
Rapp [11] (with updated Honkanen & Haggman [8] Phase)	A = 1.1449	a = 0.9174
		b =2 .1904
	α =1.1151	c = 9.9697
		p_1 = 7.2366
	β = 2.8142	p_2 = 7.8934
		d = 0.0072
Corrected White et al [6]	a = -0.0798	f = 273.3693
	b = -0.5017	g = 4.677e-08
	c = -14.4528	h = 0.9496
	d = 0.1925	
O'Dorma et al [7]	α_a = 1.1344	α_Φ = -0.1426
	β_a = 1.3359	β_Φ = 0.0484
	η_a = 0.9902	η_Φ = 0.3467
	γ_a = 6.2165	γ_Φ = 6.3138
	ν_a = 0.1504	ν_Φ = 4.5738
	ε_a = 0	ε_Φ = -0.1293

A. 3rd and 5th Order Intermodulation Simulation Results

The simulation results, Fig. 5, show a third order intermodulation performance (3IMD) improvement of between 3.5 dB to 10 .8 dB for the original Rapp model including the Honkanen & Haggman phase model plus the addition from these authors [11]. All models showed linearization improvement except the O'Dorma model, as shown in Table 4. Table 4 shows both the worst case and

Figure C.27. Conference paper 2015-2, Page 3.

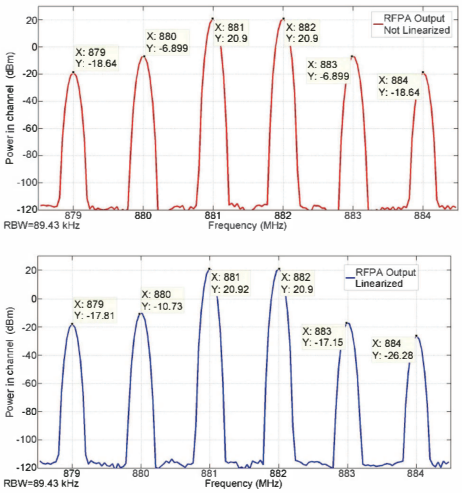

Fig. 5. Simulink simulations result of the RFPA before (top) and after (bottom) linearization. Tone spacing is 1 MHz with an output level of +21 dBm per tone.

TABLE 4
INTERMODULATION IMPROVEMENT V'S MODEL TYPE AT +24 DBM TOTAL OUTPUT LEVEL

Model	Linearizer OFF (dBc)		Linearizer ON (dBc)		Improvement (dBc)	
	3rd	5th	3rd	5th	3rd	5th
Saleh [5]	27.5	49.6	32.6	42.7	5.0 {6.3}	-6.9 {-.06}
Ghorbani & Sheikan [9]	27.3	38.1	30.8	38.6	3.5 {10.8}	0.4 {6.0}
Rapp [10] (with updated Honkanen & Haggman Phase)	27.8	39.5	31.2	38.8	3.4 {10.4}	-0.7 {7.9}
Corrected White et al [6]	28.3	57.8	28.8	60.3	0.6 {0.65}	2.4 {3.0}
O'Dorma et al [7]	28.9	41.5	27.2	46.1	-1.7 {-1.1}	4.7 {6.5}

1. Worst case improvement shown with best case in brackets {}.

best case, best case results shown in brackets {}, for both the 3rd and 5th order IMD products.

Surprisingly the O'Dorma [10] model did not show a 3rd order IMD product improvement as per all of the other models considering the normalized mean squared error (NMSE), figure of merit (FOM) performance, as defined by [14] and listed for all models in Table 5.

TABLE 5
NMSE V'S MODEL TYPE

Model	AM-AM NMSE (dB)
Saleh [7]	-36.5
Ghorbani & Sheikan [8]	-42.5
Rapp [5] (with updated Honkanen & Haggman Phase [6])	-58.7
Corrected White et al [9]	-37.1
O'Dorma et al [10]	-61.8

1. Rapp model includes the Honkanen & Haggman phase addition, $\emptyset_{HH}(r)$ plus the additional parameter d by these authors [11], allowing for positive phase shifts.

No further optimization of the input path delay or optimization of the K_m and K_p parameters provided further improved IMD suppression performance.

Over a power input range from +13 to +21 dBm per carrier, the amount of linearization improvement varied with each model for both the 3rd and 5th order IMD products. The 3rd and 5th order IMD performance and simulated results for the SHF-0189 device are shown in Fig. 6. There was also a degree of asymmetry seen with some models more than others. The asymmetry may be caused by variations in the variable attenuator or phase shifter models.

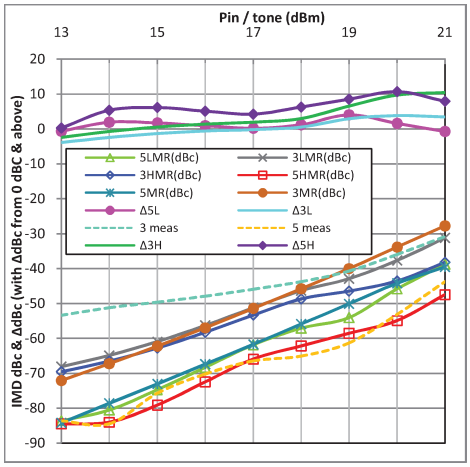

Fig. 6. SHF-0189 measured IMD performance, from [15], plus simulated pre-distorter (using original Rapp model plus update Honkanen & Haggman phase model) IMD performance v's input level per carrier (dBm).

Figure C.28. Conference paper 2015-2, Page 4.

B. W-CDMA Simulation Results

Results for a wideband code division multiple access (W-CDMA) input signal are shown in Fig. 7, with the linearization improvement occurring more in the first adjacent channels compared to the next adjacent channels further from the center frequency. This is predictable when the 5th order linearization performance is examined with this not being as significant as the 3rd order improvements.

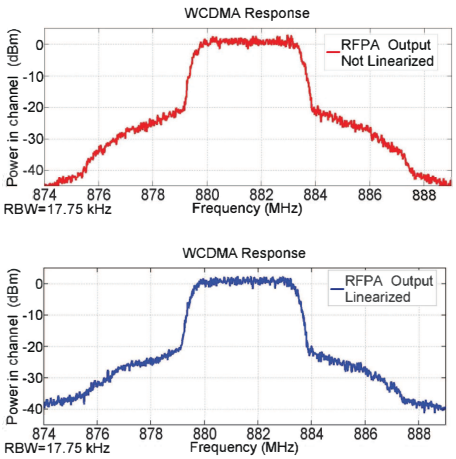

Fig. 7. Simulink simulations result of the RFPA before (top) and after (bottom) linearization. WCDMA input signal, Pout=24 dBm.

V. Conclusion

An envelope pre-distortion linearizer, using small, low cost analog components, has been simulated using several well-known existing and improved behavioral models, with the results indicating that the combination of a simple analog linearizer with an improved simple behavioral model can provide linearizer performance improvements to a maximum of 10 dB over a limited input power range of 3 to 4 dB from the device P1dB point.

Acknowledgement

The authors wish to acknowledge the assistance and support of the RFI for providing resources and time for the first author to work on this research.

References

[1] P. B. Kennington, "High-Linearity RF Power Amplifier Design", Artech House, Boston, 2000, ISBN-13:978-1580531436

[2] W. Woo and J. S. Kenney, "A New Envelope Predistortion Linearization Architecture for Handset Power Amplifiers," *Proc. Of IEEE Radio and Wireless Conference,* pp. 174 – 178, Sept. 2004.

[3] http://datasheets.maximintegrated.com/en/ds/MAX2010.pdf : Accessed November 2014.

[4] http://www.analog.com/media/cn/technical-documentation/data-sheets/AD8302.pdf:Accessed November 2014.

[5] C. Rapp, "Effects of HPA-nonlinearity on a 4-DPSK/OFDM-signal for a digital sound broadcasting system", *Proc. of 2nd European Conf. on Satellite Communications*, Liege, Belgium, October 1991, pp. 179 - 184.

[6] M. Honkanen and S-G Haggman, "New Aspects on Nonlinear Power Amplifier Modeling in Radio Communication System Simulations," *Proc. Of IEEE Int. SYM. On Personal, Indoor and Mobile Radio Communications,* vol. 3, pp. 844 – 848, Sept. 1997.

[7] A. A. M. Saleh, "Frequency-Independent and Frequency-Dependent Nonlinear Models of TWT Amplifiers," *IEEE Trans on Communications*, vol. 29, no. 11, pp. 1715 - 1720, Nov. 1981.

[8] A. Ghorbani and M. Sheikhan, *"The Effect of Solid State Power Amplifiers (SSPAs) Nonlinearities on MPSK and M-QAM Signal Transmission". Proc. Of 6th Int. Conf. on Digital Processing of Signals in Communications*, pp. 193 – 197, Sept. 1991.

[9] G. P. White, A. G. Burr and T. Javornik, "Modelling of nonlinear distortion in broadband fixed wireless access systems," *IEE Electronic Letters*, vol. 39, no. 8, pp. 686 - 687, 2003.

[10] M. O'Dorma, S. Meza, and Y. Lei, "New Modified Saleh Models for Memoryless Nonlinear Power Amplifier Behavioural Modelling," *IEEE Communications Letters*, vol. 13, no. 6, pp. 399 - 401, June 2009.

[11] P. O. Fisher and S. F. Al-Sarawi, "Improving the Accuracy of SSPA Device Behavioral Modeling," To be presented at ICTRC2015, Abu Dhabi, May 2015.

[12] http://www.elmetech.com/images/webE PDF/CDMwn124009j.pdf: Accessed November 2014.

[13] T. Nojima and T. Konno, "Cuber Predistortion Linearizer for Relay Equipment in 800 MHz Band Land Mobile Telephone System," *IEEE Trans. Vehicular Tech.*, vol. VT-34, no. 4, pp. 169-177, Nov. 1985.

[14] D. Schreurs, M., O'Dorma, A. A., Goacher, and M. Gadringer, "RF Power Amplifier Behavioral Modeling" (The Cambridge RF and Microwave Engineering series, Cambridge University Press, 2009, 1st edition), Ch. 3, Sec. 3.3, pp. 98 - 99.

[15] Sirenza Microdevices, "Design Application Note AN-031 – SHF-0189 Amplifier Application Circuits", EAN-101798 Rev. A, page 5.

Figure C.29. Conference paper 2015-2, Page 5.

2015 International Conference on Information and Communication Technology Research (ICTRC2015)

Improving the Accuracy of SSPA Device Behavioral Modeling

Paul O. Fisher[1, 2] and Said F. Al-Sarawi[1]

[1]School of Electrical & Electronic Engineering, The University of Adelaide, Adelaide, SA, 5005, Australia

[2]RF Industries (RFI), Allenby Gardens, SA, 5009, Australia

Email: {paul.fisher,said.alsarawi}@adelaide.edu.au

***Abstract* — Several well-known simple behavioral models for solid state power amplifier (SSPA) devices are reviewed and compared. This paper proposes an improvement to White et al's model and discusses their use of the Rapp model for AM/AM and AM/PM device modeling. Furthermore an improvement to Honkanen & Haggman's phase shift addition to Rapp's model is given thus allowing phase shifts greater than zero degrees to be considered. Finally a review of several models' performances beyond available data and into the saturation region is presented.**

These simple model improvements and additions, combined with the extension of the modeling into the saturation region, thus allow for faster and more accurate system level analysis, enabling better crucial output device selections to be made.

***Index Terms* — Behavioral models, SSPAs, White Model, Rapp Model.**

I. Introduction

In order to quickly compare the suitability of different RF power amplifier (RFPA) devices, a system level analysis needs to be performed. Typically RFPA devices are the primary source of nonlinearities in multicarrier systems, so selecting the right device is crucial. To quickly compare RFPA devices within a system, accurate and simple behavioral models are needed.

Obtaining a RFPA device behavioral model requires either custom testing, which can be very time consuming, or manufacturer's datasheets can be used. Datasheets however, may not always provide information or data for applications where an RFPA device will be used, for example when an RFPA device is used deep into saturation, associated with modern digital modulation schemes, the peak to average power ratios (PARPs) can range from 3 to 10 dB. Therefore a model that accurately predicts the performance of an RFPA device, over its' full range of operating conditions, using parameters extracted from manufacturer's limited data, is highly desirable.

This paper reviews several behavioral models commonly adopted in the literature, Section II. In addition, in Section III, it compares their applicability as system behavioral models when parameters for these models are extracted from manufacturer's limited data. Device modeling in the saturation region is presented in Section IV, followed by an amplitude/amplitude (AM/AM) and amplitude/phase modulation (AM/PM) modeling discussion in Section V. These are then followed by a conclusion in Section VI and an acknowledgment.

II. Review Of Existing Behavioral Models

Saleh [1] presented a Traveling Wave Tube Amplifier (TWTA) model that does not model SSPAs well. Ghorbani & Sheikhan [2] proposed an SSPA model with both the Saleh and Ghorbani & Sheikhan models including AM/AM and AM/PM terms. Rapp [3] proposed another SSPA model providing a better saturation performance but only for AM/AM, as Rapp suggested that AM/PM conversion is small enough to be neglected. Honkanen & Haggman [4] provided an AM/PM expression for the Rapp model. White et al [5] indicated an improved accuracy model compared to [1], [2], and [3]. An improved accuracy model for a laterally diffused metal oxide semiconductor (LDMOS) based SSPA was proposed by O'Dorma et al [6]. A summary of these models is given in Table1.

Table 1
Simple behavioral models for RF power amplifiers.

Model	AM/AM	AM/PM
Saleh [1]	$A_S(r) = \frac{\alpha_a r}{1+\beta_a r^2}$	$\emptyset_s(r) = \frac{\alpha_\emptyset r^2}{1+\beta_\emptyset r^2}$
Ghorbani & Sheikan [2]	$A_G(r) = \frac{x_1 r^{x_2}}{1+x_3 r^{x_2}} + x_4 r$	$\emptyset_G(r) = \frac{y_1 r^{y_2}}{1+y_3 r^{y_2}} + y_4 r$
Rapp [3] (with Honkanen & Haggman [4] Phase)	$A_R(r) = \frac{A \times r}{(1+(A \times r/\alpha)^{2\beta})^{1/2\beta}}$	$\emptyset_{HH}(r) = \frac{b}{1+e^{-c(r-a)}} \cdot \frac{1}{p_1 r + p_2}$
White et al [5]	$A_W(r) = a(1-e^{-br}) + cre^{-dr^2}$	$\emptyset_W(r) = f(1 - e^{-g(r-h)}),\ r \geq h$ $\emptyset_W(r) = 0, r < h$
O'Dorma et al [6]	$A_{MS}(r) = \frac{\alpha_a r^\eta}{(1+\beta_a r^\gamma)^\nu} - \varepsilon$	$\emptyset_{MS}(r) = \frac{\alpha_\emptyset r^\eta}{(1+\beta_\emptyset r^\gamma)^\nu} - \varepsilon$

978-1-4799-8966-9/15/$31.00 ©2015 IEEE

Figure C.30. Conference paper 2015-1, Page 1.

III. Existing Model Improvements

White et al's [5] original AM/AM equation is presented in Table 1, with $A_W(r)$ being the output amplitude and r the normalized input amplitude. Coefficients a and b determine the saturation level and small signal gain respectively while parameters c & d adjust the shape in the SSPA operating region.

Attempts at reproducing White et al's [5] results, using this equation give the results shown in Fig. 1*a*. These results do not match the published results of White et al's Fig. 1 *b* [5]. It has been found that to reproduce the correct results, as proposed by White et al's Fig. 1*b* [5] then the AM/AM model, $A_{WC}(r)$ should be written as;

$$A_{WC}(r) = a[(1 - e^{-br}) + cre^{-dr^2}] \quad (1)$$

Using the corrected equation (1), the error curves, as shown in Fig. 1*b*, now match White's original Fig. 1*b* curve.

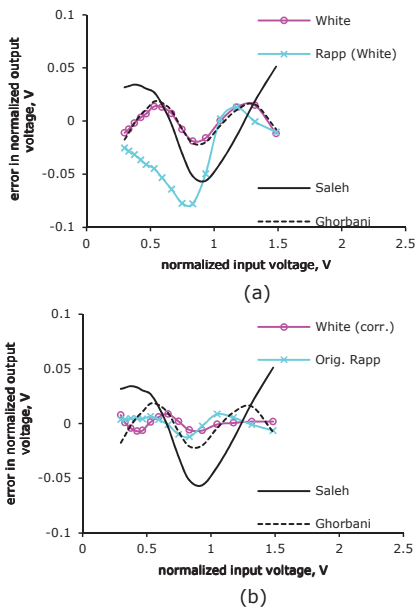

Fig. 1 Curve fit of models showing the AM/AM normalized output voltage errors for the measured data dynamic range only. (a) White et al's Fig 1b using the equation as given in that paper. (b) Corrected White et al equation (1) & original Rapp equation, Table 1.

Also within White et al's paper, Rapp's equation is given as;

$$A_{RW}(r) = r/(1 + (|r|/\alpha)^{2\beta})^{1/2\beta}) \quad (2)$$

However if Rapp's original equation, as per Table 1, is used, including the small signal gain parameter A, then the error results are as shown in Fig. 1*b* and the AM/AM curve fit is shown in Fig. 3, indicating that Rapp's equation now has similar error performance compared to White et al's equation. An AM/AM normalized mean squared error (NMSE) figure-of-merit (FOM) comparison, as defined in [7], is given in Table 2 indicating that the original Rapp model compares well with White et al's corrected model.

Table 2
NMSE FOM results for AM/AM Modelling.

Model	AM/AM NMSE (dB)
Saleh [1]	-27.13
Ghorbani & Sheikhan [2]	-35.44
Rapp [3]	-42.33
Rapp from White et al [5]	-24.97
White et al [5]	-36.95
White et al, corrected (this paper)	-44.00
Modified Saleh, O'Dorma et al [6]	-48.54

IV. Modeling Into The Saturation Region

In order to compare the original Rapp, White et al (corrected) and O'Dorma et al models, beyond the available data, a method is used to extend the data into the saturation region. This method is to observe that the maximum end point output power (P_{out}), of the power added efficiency (PAE) versus P_{out} curve(s), typically provided for RFPA devices, is the final saturated output power, Fig. 2.

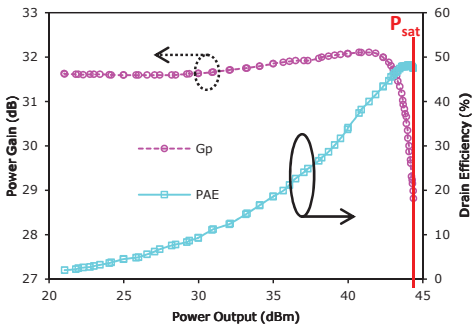

Fig. 2 Power gain & Drain efficiency for the BLM7G1822S [8] providing the saturated output power.

The existing data can then be extended into the saturation region.

Extending the modeling beyond the measured data and into the saturation region, the AM/AM curves of Figs. 3 &

978-1-4799-8966-9/15/$31.00 ©2015 IEEE

Figure C.31. Conference paper 2015-1, Page 2.

2015 International Conference on Information and Communication Technology Research (ICTRC2015)

4 show how the models perform beyond the available data. It can be seen that the original White et al equation 'rolls over' similar to the Ghorbani & Sheikhan model [2]. If the corrected White et al equation (1) is used, then it performs as would be expected for an LDMOS based SSPA.

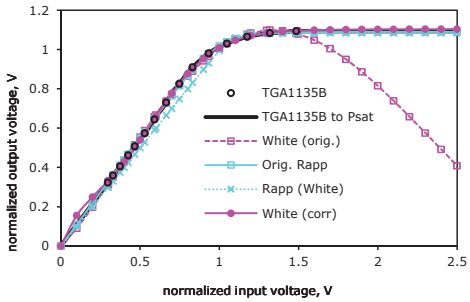

Fig. 3 Measured AM/AM data and curve fit of normalized output voltage versus normalized input voltage into the saturation region for White et al's original and corrected equation comparisons. Also shown is Rapp's original equation and Rapp's equation (2) as per White et al.

Results indicate that the Rapp model performs best into the saturation region when only available data is used to curve fit the models, even compared to the O'Dorma et al model [6] as shown in Fig. 4.

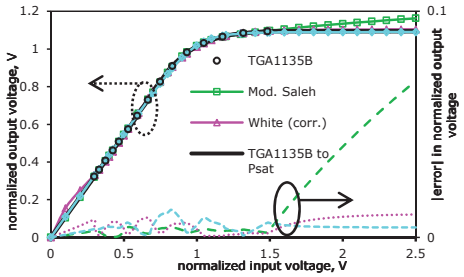

Fig. 4 Rapp, White et al (corrected) & O'Dorma et al model comparison of AM/AM curve fit showing normalized output vs input voltage and absolute normalized output voltage errors for existing data and data extended into the saturation region.

When the extended data is used to curve fit the model then both the Rapp & O'Dorma et al models are comparable to the corrected White et al model, as indicated in Fig. 5.

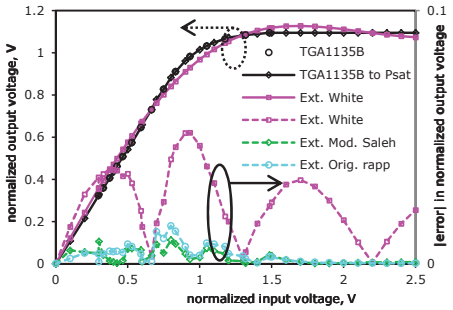

Fig. 5 Corrected White et al AM/AM model Curve fit of extended data into the P_{sat} region showing that it performs worse than the original Rapp or O'Dorma et al models.

V. AM/PM

The Honkanen & Haggman phase shift addition [4] to the original Rapp equation, $\emptyset_{HH}(r)$, as shown in Table 1, is noted to have a descending phase with increasing input level but with a maximum of zero degrees phase shift. In order to accommodate devices that do not have a maximum of zero degrees phase shift, we propose an additional offset parameter, d, to the Honkanen & Haggman phase shift model. Hence the updated phase shift model $\emptyset_{HHO}(r)$ is given as equation (3);

$$\emptyset_{HHO}(r) = \frac{b}{1+e^{-c(r-a)}} \cdot \frac{1}{p_1 r + p_2} - d \tag{3}$$

Where a is the cut-off input voltage at which the transistor begins to conduct, b is the switch-on step magnitude in degrees, c determines the steepness of the step-wise change, and p_1 and p_2 are parameters for adjusting the descending slope. The offset parameter d allows for positive phase shift. An example of the application is shown in Fig. 6 for the LDMOS 2-stage power amplifier [8].

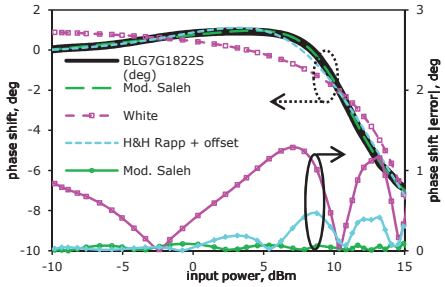

Fig. 6 AM/PM Curve fit of BLM7G1822S comparisons of O'Dorma et al, White et al & Honkanen & Haggman AM/PM

978-1-4799-8966-9/15/$31.00 ©2015 IEEE

Figure C.32. Conference paper 2015-1, Page 3.

expression, with additional offset, as well as absolute phase error comparisons.

Even though the Honkanen & Haggman phase addition has coefficients that are related to bipolar transistor parameters; this model still performs well for LDMOS devices.

VI. Conclusion

This paper has demonstrated the need for fast system level comparisons to aid in the selection of critical RFPA output devices. For SSPA devices, having only below saturation data available, then the Original Rapp model [3], including the Honkanen & Haggman phase shift addition [4] plus the addition introduced in this paper, provides the best simple AM/AM and AM/PM model. If the available data extends into the saturation region then the O'Dorma et al [6] model provides the best behavioral model in that region.

This paper has also shown improvements for the use of two existing models plus provided an additional parameter, as well as providing a method for determining the saturation power from manufacturer's data. It has also compared the performance of these models when used beyond the provided manufacturer's data information, where typical modern digital modulation signals extend, thus resulting in further improvements and accuracies.

These simple model improvements and additions, combined with the extension of the modeling into the saturation region, thus allow for faster and more accurate system level analysis enabling better crucial output device selections to be made.

Acknowledgment

The authors wish to acknowledge RF Industries for their assistance with time to work on this research provide to the first author.

References

[1] A. A. M. Saleh, "Frequency independent and frequency dependent non-linear models of TWT amplifiers", *IEEE Trans. Commun.*, vol. 29, no. 11, pp. 1715 – 1720, Nov. 1981.

[2] A. Ghorbani and M. Sheikhan, "The effects of solid state power amplifier (SSPA) nonlinearities on M-PSK and M-QAM signal transmission", *6th Int. Conf. on Digital Processing of Signals in Communications, Loughborough, UK*, 1991, pp. 193 – 197.

[3] C. Rapp, "Effects of HPA-nonlinearity on a 4-DPSK/OFDM-signal for a digital sound broadcasting system", *Proc. of 2nd European Conf. on Satellite communications, Liege, Belgium*, pp. 179 – 184, October 1991.

[4] M. Honkanen and S-G. Haggman, "New Aspects on nonlinear power amplifier modelling in radio communication system simulations", *IEEE Commun., Lett.,* vol. 13, no. 6, pp. 844 – 848, June 1997.

[5] G. P. White, A. G., Burr, and T., Javornik, "Modelling of nonlinear distortion in broadband fixed wireless access systems", *Electron. Lett.,* 2003, vol. 39, pp. 686 – 687, April 2003.

[6] M. O'Dorma, S., Meza and Y. Lei, "New Modified Saleh Models for Memoryless Nonlinear Power Amplifier Behavioral Modelling", *IEEE Commun. Lett.*, vol. 13, No. 6, pp. 399 - 401, June 2009.

[7] D. Schreurs, M., O'Dorma, A. A., Goacher, and M. Gadringer, "RF Power Amplifier Behavioral Modeling" (The Cambridge RF and Microwave Engineering series, Cambridge University Press, 2009, 1st edition), Ch. 3, Sec. 3.3, pp. 98 - 99.

[8] NXP Semiconductors BLM7G1822S Objective data sheet', http://www.nxp.com/documents/data_sheet/BLM7G1822S-40PB_S-40PBG.pdf , accessed August 2014.

978-1-4799-8966-9/15/$31.00 ©2015 IEEE

Figure C.33. Conference paper 2015-1, Page 4.

Nonlinear Behavioral Model Extraction of RF Power Amplifier Devices from Manufacturer's Data

Paul Fisher[1,2]

[1]School of Electrical and Electronic Engineering
The University of Adelaide
Adelaide, Australia
Paul.fisher@adelaide.edu.au

[2]Radio Frequency Industries Pty. Ltd.
RFI
Adelaide, Australia
Paul.fisher@rfi.com.au

***Abstract*—In this paper a method for obtaining a time domain behavioral model of a power amplifier from component manufacturer's data, enabling fast system level comparisons of various power amplifier designs is presented. The method uses a physics based approach for determining the model's memory effects with respect to input and output matching networks, bias networks and temperature. Additional component testing provides increased accuracy of the model.**

Keywords— Power Amplifiers, Non-Linear Behavioural Models, Model Extraction.

I. Introduction

The requirements for greater data download capacity from mobile communication systems continue the push for improved wideband performance. A key element in these mobile communication systems is the Power Amplifier (PA). In order to obtain high data rates the PA must exhibit both low DC power and RF spectral efficiency while delivering an appropriate RF output power over an increasingly wider bandwidth. Manufactures of PA devices often provide devices for testing, and data sheets based on various measured parameters, without providing simulation models or data for the application required. For a design to commence, initial system level comparisons are conducted in order to determine if the required output power, efficiency and spectral purity can be achieved over the required bandwidth. To be able to perform these comparisons quickly, suitable system level models are required. Ideally, system level models are derived from measurements, which are time consuming and costly. However, for the purpose of quick analysis and comparison, the amount of time and cost involved are unjustifiable. In this paper a method for extracting system level non-linear behavioral models from a given manufacturer's data sheet is provided so that the needed comparisons can be undertaken quickly. So there is a need to have a methodology for building device models based on existing available device data sheets.

This paper starts by reviewing current RF PA models proposed in the literature, as discussed in Section II, and then investigates the memory effect in RF PAs and how that impacts the amplifier linearity in Section III. The proposed modeling methodology is presented in Section IV, which includes parameter extraction from data sheet and simulation modeling based on extracted parameters and experimental verification is given. In Section V, a comparison between simulation results and manufacturer's data as presented in the data sheet are given. This is followed by a conclusion in Section VI and an acknowledgment.

II. RF Power Amplifier Behavioural Models

Typical early behavioral models for power amplifiers have been based around models for Travelling Wave Tube Amplifiers (TWTAs). These models are based on the measured amplifier or device performance. These are relatively straightforward models based around single carrier AM-AM and AM-PM requirements. The basic Saleh model [1] is given by:

$$A(r) = (\alpha_a r) / (1+\beta_a r^2), \quad \text{AM-AM} \tag{1}$$

$$\Phi(r) = (\alpha_p r^2) / (1+\beta_p r^2), \quad \text{AM-PM} \tag{2}$$

Where r is the input signal amplitude and α_a, β_a and α_p, β_p represent amplitude and phase coefficients respectively.

For Solid State Power Amplifier (SSPA) modeling, and in particular for LDMOS FETs, this model can lead to issues related to AM-PM characteristics, so a Modified General form of the Saleh model (MGS) is more appropriate as given by [2]:

$$Z(r) = (\alpha r^{\eta}) / (1 + \beta r^{\gamma})^{\nu} - \varepsilon, \tag{3}$$

Again r is the input signal amplitude but the exponent γ and the phase shift ε have been added. For a given set of values (η, ν, γ and ε), optimum values for (α, β) can be extracted from a measurement data-set, being the manufacturers data sheet parameters for either AM-AM or AM-PM characteristics.

Whilst the above models are sufficient for single carrier situations, they are insufficient for current requirements. Current requirements for PA circuits or devices now require other considerations beyond AM-AM, AM-PM and harmonic responses to now include Inter-Modulation Distortion (IMD), spectral regrowth, Adjacent Channel Power Ratio (ACPR), Noise Power Ratio (NPR), sweet spot evolution, thermal dependence, self- heating and bias effects [3].

In order to operate power amplifiers more efficiently, devices must be operated closer to their maximum output

978-1-4799-2452-3/13/$31.00 ©2013 IEEE

Figure C.34. Conference paper 2013, Page 1.

power, however this increases IMD. To operate at higher output powers, linearizers are used to reduce IMD effects. For wide bandwidth signals, memory effects associated with power amplifier devices can have significant effects on efficiency and Adjacent Channel Interference (ACI). These effects, if not considered, can also degrade the linearizer's performance. With these increased requirements, memory effects can become significant in determining the PA performance.

III. Memory Effects

Memory effects in an RF PA mean that the output at a given time relates not only to the input at that time but also to the input at previous times. The sources of memory effects in an RF PA are dependent on the device itself and the networks surrounding the RF PA such as the matching and biasing networks as shown in Fig. 1.

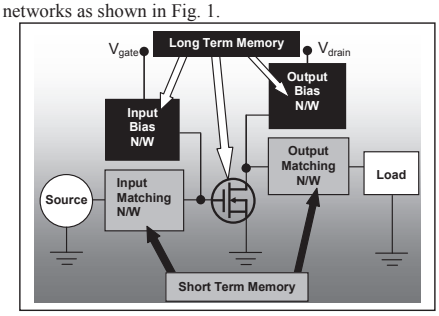

Fig. 1. Physical PA layout showing physical matching, bias and thermal networks (N/Ws) that contribute to memory effects.

Memory effects cause asymmetric IMD sidebands that are a function of carrier spacing. The proposed model of the memory effects is shown in Fig. 2 (Derived from [4]).

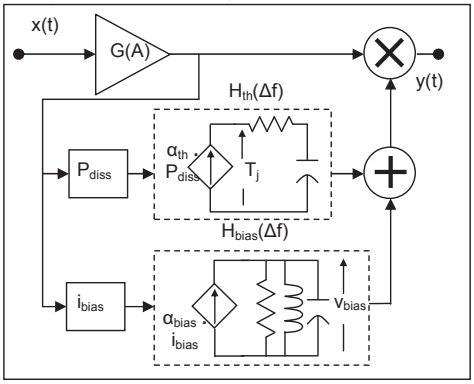

Fig. 2. Frequency domain behavioral model for an RF PA including physically based memory effects from derived from [4].

Short-term memory effects are associated with the input and output matching networks whereas long-term memory effects are associated with the device thermal response and the bias networks. Memory effect time delays can range from 1 ns to 1 ms [4].

IV. Modelling Methodology

The behavioral model, including memory effects, is physics based, as derived from [4], see Fig. 2. The model from [4] is given in the frequency domain and consists of three essential sections: (i) a memory-less non-linear section, that is determined by curve fits of Pin / Pout and AM to PM data to the MGS model as described in section II, (3), (ii) a thermal memory effect, and (iii) a bias memory effect. The implementation of these separate thermal and bias memory models is undertaken in Simulink but now in the time domain. Modeling of the thermal memory effect in the time domain follows the technique as described in [5] and the bias memory effect time domain modeling follows standard RLC resonant circuit theory as given in [6].

The implementation of the memory-less MGS model in Simulink is shown in Fig. 3 and the implementation of memory effects with the MGS model is shown in Fig. 4.

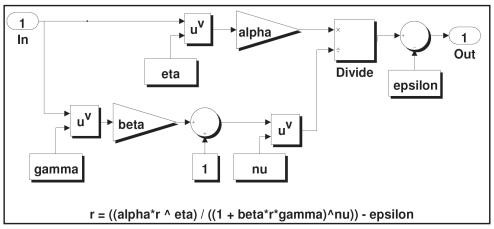

Fig. 3. Implementation of the MGS model in Simulink.

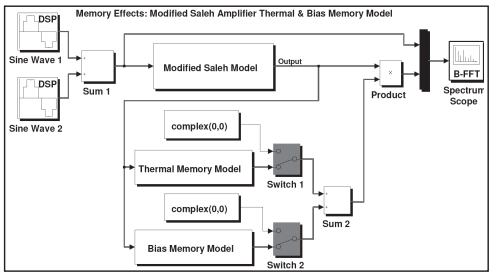

Fig. 4. Simulink implementation of memory effects with the MGS model.

The overall modeling methodology is shown by the flowchart of Fig. 5. The Pin versus Pout data from Fig. 13 of [7] is used, along with measured AM-PM data, to determine the MGS model coefficients via a least squares curve-fitting routine implemented in Matlab. This is then validated against the Pin versus Pout datasheet data, Fig. 6(a), and forms the non-linear portion of the model.

Further device data, as shown in Fig. 5, is then used for the thermal and bias memory effects parameter extraction. This

data is extracted directly from the device data sheet. Future automated extraction is being considered.

With extracted non-linear and memory effect parameters, the model outputs, from Fig. 4, are compared with the device IMD results. This process will be automated in the future.

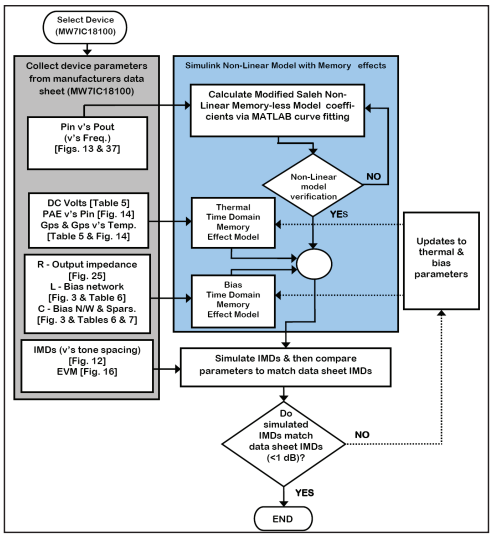

Fig. 5. Flowchart of amplifier modeling with memory effects.

A. Data Sheet Parameters

For the Freescale MW7IC18100NBR1 [7], fundamental Pin/Pout data, Fig. 6(a), as well as 3rd, 5th, and 7th order IMD parameters at fixed, Fig. 6(b), and varying tone spacing's are given.

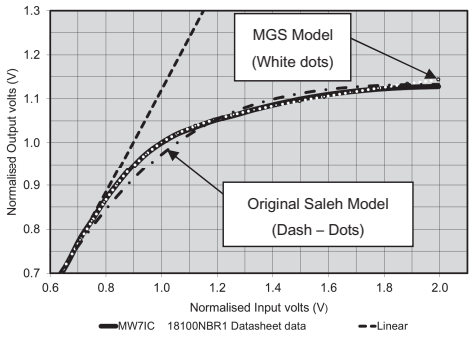

Fig. 6(a). Reference [7], Figure 13, Pin versus Pout data including a comparison of the Original Saleh and MGS models versus MW7IC18100NBR1 datasheet data.

From Fig. 6(b) it can be seen that this device does exhibit memory effects as characterized by the IMD asymmetries.

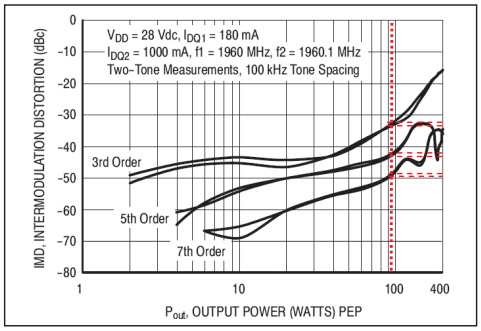

Fig. 6(b). Reference [7], Figure 12, two tone intermodulation distortion vs. output power at fixed 100 kHz tone spacing, showing IMD asymmetries.

For other devices only Pin/Pout data may be given so extra measurements can be conducted using available manufacturer's test jigs [7] as shown in Fig. 7.

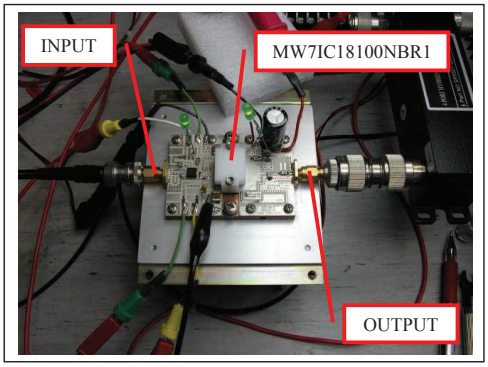

Fig. 7. Freescale [7] MW7IC18100 test jig for extended measurements.

Detailed matching and bias networks for both devices are also given in the data sheets. The data required for the model extraction is shown in the left hand side box of the flowchart shown in Fig. 5.

B. Simulations and Parameter Extraction

For the given Pin versus Pout data-set, Fig. 6(a), and the measured AM-PM data, MGS model coefficients have been determined to be, for AM-AM, 1.107, 2.2835, 1.0154, 0.084998, 10.191 and 0 and for AM-PM 2000, 0.061921, -0.00073489, -0.0098204, 1.2912 and 1981.7 corresponding to α, β, η, ν, γ and ε, respectively.

The original Saleh modeling is compared to the MGS modeling in Fig. 6(a) and also in Fig. 8. In Fig. 8 the difference between the MW7IC18100NBR1 data, the original

Figure C.36. Conference paper 2013, Page 3.

Saleh model and the MGS model is given, showing reduced errors for the MGS model.

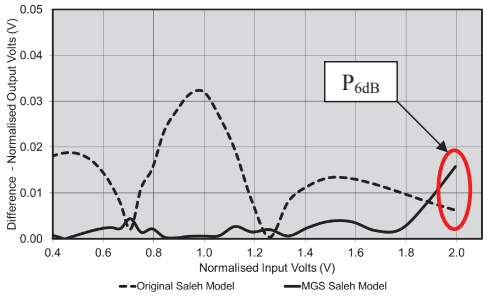

Fig. 8. Comparison of the nornalised output voltage difference between the MW7IC18100NBR1 datasheet data and the Original Saleh and MGS models .

Simulations have been performed and the relevant memory parameters have been adjusted to match the IMDs, as given in the device data sheet, over a range of tone spacing's. These are; R_{th} = 10 k/W, C_{th} = 20 nJ/K for the thermal memory [8] and R = 2 , L = 1 nH and C = 1 nF for the bias memory parameters. A sample of the simulated IMD performance for a 200 kHz carrier spacing is given in Fig. 9.

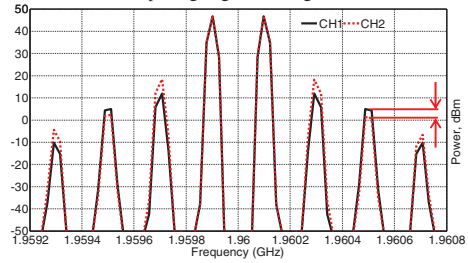

Fig. 9. Simulink output of the proposed model for 2-Tones with 200 kHz tone spacing The dotted line shows MGS model simulation when including thermal and bias memory effects, while the solid line shows the simulation results when the memory effects are not included. Note the asymmetry for the 3rd, 5th, and 7th order IMDs between these simulations.

V. Comparisons

The simulated versus datasheet IMD performance is compared in Table 1 for output powers over the range from 10 to 100W PEP. Note that in Table 1 the shaded rows are datasheet values and the un-shaded rows are simulated data from the proposed model. The simulated results show good agreement between datasheet powers over the range from 10 to 100 W for 3rd order IMDs. It is noted that the presented simulation data deviates more from the datasheet values for 5th and 7th order IMD's. This indicates that the proposed model is limited in predicting higher order IMDs and more non-linear dynamics need to be introduced. It is also expected that these deviations are, in part, due to the limited range of Pin versus Pout data available from the datasheet, Fig. 6(a), used to generate the MGS model.

TABLE 1: Comparison of simulated IMDs vs. Datasheet IMDs (Fig. 6(b)).

Pout	3rd IMD's (dBc)		5th IMD's (dBc)		7th IMD's (dBc)	
(W, PEP)	Lower	Upper	Lower	Upper	Lower	Upper
10	-45.3	-43.4	-54.2	-53.1	-69.1	-65.5
10	-44.2	-45.6	-53.9	-55.0	-59.3	-62.9
50	-40.7	-40.9	-46.0	-47.0	-54.8	-53.7
50	-37.0	-37.7	-52.4	-56.5	-60.9	-60.1
100	-32.8	-31.7	-42.1	-41.4	-48.3	-47.6
100	-27.8	-27.8	-43.1	-43.7	-51.4	-52.5

VI. Conclusion

This paper has presented a modeling methodology for extraction of non-linear model parameters, including memory effects, from manufacturer's amplifier data sheets. The results presented in Table 1 show good agreement between simulation and the manufacturer's data sheet, validating the methodology. This methodology can be used to provide timely early system level comparisons prior to device selection, testing and detailed design, resulting in a significant time and cost saving when surveying devices for product development.

Acknowledgment

The author would like to acknowledge the supervisory and final manuscript feedback inputs of Associate Professor Chris Coleman and Dr Said Al-Sarawi from The School of Electrical and Electronic Engineering and to RFI for allowing the use of their testing facilities.

References

[1] A. A. M. Saleh, "Frequency-Independent and Frequency-Dependent Nonlinear Models of TWT Amplifiers," *IEEE Transactions on Communications*, vol. Com-29, pp. 1715 - 1720, November 1981.

[2] D. Schreurs, M. O'Dorma, A. A. Goacher, & M. Gadringer, *RF Power Amplifier Behavioral Modeling*. 1st Ed. The Cambridge RF and Microwave Engineering series, Cambridge University Press, 2009, Ch. 3, p. 106.

[3] A. Alabadelah, et al. "Nonlinear Models of Microwave Power Devices and Circuits", in *12th GAAS Symposium - Amsterdam*, pp. 191 - 194, Amsterdam, The Netherlands, 2004.

[4] J. S. Kenney and P. Fedorenko. "Identification of RF Power Amplifier Memory Effect Origins using Third-Order Intermodulation Distortion Amplitude and Phase Asymmetry", in *IEEE MTT-S International Microwave Symposium*, San Francisco, CA, pp. 1121 - 1124, 2006.

[5] A. E. Parker and J. G. Rathmell, "Broad-Band Characterization of FET Self-Heating," *IEEE Transactions on Microwave Theory and Techniques*, vol. 53, pp. 2424 - 2429, July 2005.

[6] W. H. Hyat and J. E. Kemmerly, *Engineering Circuit Analysis*. International Student ed. Electrical & Electronic Engineering Series: McGraw-Hill, 1971.

[7] "Freescale MW7IC18100 Data Sheet", Available online at: http://cache.freescale.com/files/rf_if/doc/data_sheet/MW7IC18100N.pdf?pspll=1, Accessed: 31/5/13

[8] S. Boumaiza and F. M. Ghannouchi, "Thermal Memory Effects Modeling and Compensation in RF Power Amplifiers and Predistortion Linearizers," *IEEE Transactions on Microwave Theory and Techniques*, vol. 51, pp. 2427 - 2433, December 2003.

Figure C.37. Conference paper 2013, Page 4.

Bibliography

[1] K. J. Russell, "Microwave power combining techniques," *IEEE Transactions on Microwave Theory and Techniques*, vol. 27, no. 5, pp. 472–478, May 1979.

[2] K. Chang and C. Sun, "Millimeter-wave power-combining techniques," *IEEE Transactions on Microwave Theory and Techniques*, vol. 31, no. 2, pp. 91–107, Feb 1983.

[3] J. Navarro and K. Chang, *Integrated Active Antennas and Spatial Power Combining*, 1st ed., ser. Wiley Series in Microwave and Optical Engineering. New York, U.S.A.: Wiley, 1996, ch. 4, sec. 4.2, pp. 72.

[4] M. P. DeLisio and R. A. York, "Quasi-optical and spatial power combining," *IEEE Transactions on Microwave Theory and Techniques*, vol. 50, no. 3, pp. 929–936, Mar 2002.

[5] Codan Pty Ltd., "Codan 5940 High Power SSPA," http://www.codan.com.au/, 2005, [Online: Accessed 29/4/2010].

[6] J. L. B. Walker, Ed., *High-power GaAs FET Amplifiers*, 1st ed., ser. The Artech House Antennas Microwave Library. Norwood, MA 02062: Artech House, 1993, chapter 2, section 2.7.2 pp. 133-134.

[7] TOSHIBA, "TIM5964-60SL-422, 5.9 GHz to 6.75 GHz P1dB = 48.0 dBm Internally Matched Microwave Power GaAs FET," http://www.toshiba.co.jp/sis/en/des/micro/prod/prodlist/semicon/d-sheet/tim5964-60sl-422_20150213_no1079.pdf, 2015, [Online: Accessed 12/4/2017].

[8] Mimix. (June, 2005) XP1006, 8.5 to 11.0 GHz MMIC Power Amplifier Chip. [Online]. Available: http://www.mimixbroadband.com/PDFfiles/xp1006.pdf

[9] Triquint Semiconductor inc., "TGA4022, 18 - 23 GHz, 32.5 dBm Nominal P1dB, K-Band High Power Amplifier," http://www.qorvo.com/products/p/TGA4022, 2009, [Online: Accessed 12/4/2017].

[10] L. Wang, W. Dou, and H. Meng, "Study of millimeter wave spatial beam synthesis based on quasi-optical technology," in *2016 IEEE 5th Asia-Pacific Conference on Antennas and Propagation (APCAP)*, July 2016, pp. 333–334.

[11] L. H. Huang and W. B. Dou, "Quasi-optical beam power combining at submillimeter wave band," in *2016 IEEE 9th UK-Europe-China Workshop on Millimetre Waves and Terahertz Technologies (UCMMT)*, Sept 2016, pp. 138–140.

[12] D. Staiman, M. Breese, and W. Patton, "New technique for combining solid-state sources," *IEEE Journal of Solid-State Circuits*, vol. 3, no. 3, pp. 238–243, Sept 1968.

[13] J. W. Mink, "Quasi-optical power combining of solid-state millimeter-wave sources," *IEEE Transactions on Microwave Theory and Techniques*, vol. 34, no. 2, pp. 273–279, Feb 1986.

[14] M. Kim, J. J. Rosenberg, R. P. Smith, R. M. W. II., J. B. Hacker, M. P. DeLisio, , and D. B. Rutledge, "A 100-element HBT grid amplifier," *IEEE Microwave & Guided Wave Letters*, vol. 1, no. 11, pp. 322–324, Nov 1991.

[15] M. Kim, E. A. Sovero, J. B. Hacker, M. P. D. Lisio, J.-C. Chiao, S.-J. Li, D. R. Gagnon, J. J. Rosenberg, and D. B. Rutledge, "A 100-element HBT grid amplifier," *IEEE Transactions on Microwave Theory and Techniques*, vol. 41, no. 10, pp. 1762–1771, Oct 1993.

[16] S. Pajic and Z. B. Popovic, "An efficient X-band 16-element spatial combiner of switched-mode power amplifiers," *IEEE Transactions on Microwave Theory and Techniques*, vol. 51, no. 7, pp. 1863–1870, July 2003.

[17] M. B. Steer, L. P. B. Katehi, S. Mohammadi, J. F. Whitaker, and A. B. Yakovlev, "Architectures and prototyping laboratory for the development of space-based microwave power transmission systems," http://www.ursi.org/files/RSBissues/RSB_311_2004_12.pdf, 2004, [Online: Accessed 12/4/2017].

[18] J. Harvey, E. R. Brown, D. B. Rutledge, and R. A. York, "Spatial power combining for high-power transmitters," *IEEE Microwave Magazine*, vol. 1, no. 4, pp. 48–59, Dec 2000.

[19] S. C. Ortiz, J. Hubert, L. Mirth, E. Schlecht, and A. Mortazawi, "A high-power Ka-band quasi-optical amplifier array," *IEEE Transactions on Microwave Theory and Techniques*, vol. 50, no. 2, pp. 487–494, Feb 2002.

[20] R. A. York and Z. B. Popovic, Eds., *Active and Quasi-Optical Arrays for Solid-State Power Combining*, 1st ed., ser. Wiley Series in Microwave and Optical Engineering. New York, U.S.A.: Artech House, 1997, chapter 3, section 3.2 pp. 208-210.

[21] M. A. Gouker, J. T. Delisle, and S. M. Duffy, "A circuit-fed tile-approach configuration for millimeter-wave spatial power combining," *IEEE Transactions on Microwave Theory and Techniques*, vol. 50, no. 1, pp. 17–21, Jan 2002.

[22] Wavestream, "Via satellite's tech focus report spatial power combining," http://www.wavestream.com/pdf/Via_Satellite_Tech_Focus_Article.pdf, 2004, [Online: Accessed 12/4/2017].

[23] N. J. Kolias and R. C. Compton, "Thermal management for high-power active amplifier arrays," *IEEE Transactions on Microwave Theory and Techniques*, vol. 44, no. 6, pp. 963–966, Jun 1996.

[24] B. Deckman, D. S. Deakin, E. Sovero, and D. Rutledge, "A 5-watt, 37-GHz monolithic grid amplifier," in *Microwave Symposium Digest. 2000 IEEE MTT-S International*, vol. 2, June 2000, pp. 805–808.

[25] C.-T. Cheung, R. Tsai, R. Kagiwada, and D. B. Rutledge, "V-Band Transmission and Reflection Grid Amplifier Packaged in Waveguide," http://www.its.caltech.edu/, 2003, [Online: Accessed 7/10/2014].

[26] Caltech, "Quasi-Optical Power Amplifier," http://www.its.caltech.edu/~mmic/reshpubindex/lawrence.html, 2005, [Online: Accessed 7/10/2014].

[27] J. J. Rosenberg, M. P. DeLisio, B. C. Deckman, C.-T. Cheung, D. B. Rutledge, and R. A. York, "The grid amplifier: Enabling high power millimeter-wave systems," *Microwave Journal*, vol. 46, no. 12, pp. 64–78, Dec 2003.

[28] J. A. Higgins, M.Kim, J.Hacker, D. Sievenpiper, and E. Yablonovitch, "Waveguides using PBG developed ground plane as sidewalls (for application in quasi-optic amplifiers)," http://www.ee.ucla.edu/~pbmuri/1998-review/higgins/WECSjan99.PPT, 1999, [Online: Accessed 1/8/2005].

[29] J. Bae, T. Unou, T. Fujii, and K. Mizuno, "Spatial power combining of gunn diodes using an overmoded-waveguide resonator at millimeter wavelengths," *IEEE Transactions on Microwave Theory and Techniques*, vol. 46, no. 12, pp. 2289–2294, Dec 1998.

[30] J. Bae and K. Mizuno, "Coherent power combining of solid-state devices," http://www.kurasc.kyoto-u.ac.jp/jusps/S2-4.pdf, 2003, [Online: Accessed 1/8/2005].

[31] A. Alexanian and R. A. York, "Broadband spatially combined amplifier array using tapered slot transitions in waveguide," *IEEE Microwave and Guided Wave Letters*, vol. 7, no. 2, pp. 42–44, Feb 1997.

[32] N.-S. Cheng, P. Jia, D. B. Rensch, and R. A. York, "A 120-W X-Band spatially combined solid-state amplifier," *IEEE Transactions on Microwave Theory and Techniques*, vol. 47, no. 12, pp. 2557–2561, Dec 1999.

[33] R. A. York, "Broadband microwave power combiners using active arrays in an oversized coaxial waveguide," http://www.ucop.edu/research/micro/97_98/97_217.pdf, 1997-98, [Online: Accessed 1/8/2005].

[34] ——, "N. cheng and v. chen and and b. york," http://my.ece.ucsb.edu/yorklab/Projects/Amplifiers/X-band/MAFET%20PI%20Review%203-99.pdf, 2001, [Online: Accessed 1/8/2005].

[35] P. Jia, L.-Y. Chen, A. Alexanian, and R. A. York, "Multioctave spatial power combining in oversized coaxial waveguide," *IEEE Transactions on Microwave Theory and Techniques*, vol. 50, no. 5, pp. 1355–1360, May 2002.

[36] Wavestream, "MBA-KUS040, 40 W Ku-Band matchbox power amplifier," http://www.wavestream.com/uploads/products/25w-40w-mba-ku-matchbox-power-amplifier.pdf, 2014, [Online: Accessed 17/10/2016].

[37] CAP Wireless, "Spatium Ultra Broadband SSPA," http://www.triquint.com/products/spatium, 2017, [Online: Accessed 12/4/2017].

[38] P. Jia, L.-Y. Chen, A. Alexanian, and R. A. York, "Broad-band high-power amplifier using spatial power-combining technique," *IEEE Transactions on Microwave Theory and Techniques*, vol. 51, no. 12, pp. 2469–2475, Dec 2003.

[39] B. York, H. Xu, and P. Jai, "GaN/BST circuits and power combiners," http://my.ece.ucsb.edu/cane/reviews/nov02/York.pdf, 2002, [Online: Accessed 1/8/2005].

[40] M. Belaid and K. Wu, "Spatial power amplifier using a passive and active tem waveguide concept," *IEEE Transactions on Microwave Theory and Techniques*, vol. 51, no. 3, pp. 684–689, Mar 2003.

[41] F.-R. Yang, K.-P. Ma, Y. Qian, and T. Itoh, "A novel TEM waveguide using uniplanar compact photonic-bandgap (UC-PBG) structure," *IEEE Transactions on Microwave Theory and Techniques*, vol. 47, no. 11, pp. 2092–2098, Nov 1999.

[42] N. C. Karmakar and M. N. Mollah, "Potential applications of PBG engineered structures in microwave engineering: Part i," *Microwave Journal*, vol. 47, no. 7, pp. 22–44, July 2004.

[43] ——, "Potential applications of PBG engineered structures in microwave engineering: Part ii," *Microwave Journal*, vol. 47, no. 9, pp. 122–137, Sept 2004.

[44] D. Sievenpiper, L. Zhang, R. F. J. Broas, N. G. Alexopolous, and E. Yablonovitch, "High-impedance electromagnetic surfaces with a forbidden frequency band," *IEEE Transactions on Microwave Theory and Techniques*, vol. 47, no. 11, pp. 2059–2074, Nov 1999.

[45] J. A. Higgins, H. Xin, A. Sailer, and M. Rosker, "Ka-band waveguide phase shifter using tunable electromagnetic crystal sidewalls," *IEEE Transactions on Microwave Theory and Techniques*, vol. 51, no. 4, pp. 1281–1288, Apr 2003.

[46] T. Kamei, C.-T. Cheung, J. J. Rosenberg, and D. B. Rutledge, "Design and simulation of a mode converter for the excitation of quasi-optical amplifiers," in *IEEE International Symposium on Antennas and Propagation, Fukuoka, Japan*, August 2000, pp. 1–3, http://www.its.caltech.edu/ mmic/reshpubindex/papers/kamei.pdf.

[47] M. Belaid, R. Martinez, and K. Wu, "A mode transformer using fin-line array for spatial power-combiner applications," *IEEE Transactions on Microwave Theory and Techniques*, vol. 52, no. 4, pp. 1191–1198, April 2004.

[48] J. W. Mink and F. K. Schwering, "A hybrid dielectric slab-beam waveguide for the sub-millimeter wave region," *IEEE Transactions on Microwave Theory and Techniques*, vol. 41, no. 10, pp. 1720–1729, Oct 1993.

[49] H. Hwang, G. P. Monahan, M. B. Steer, J. W. Mink, J. Harvey, A. Paollea, and F. K. Schwering, "A dielectric slab waveguide with four planar power amplifiers," in

Microwave Symposium Digest, 1995., IEEE MTT-S International, May 1995, pp. 921–924.

[50] H. Hwang, T. W. Nuteson, M. B. Steer, J. W. Mink, J. Harvey, and A. Paolella, "A quasi-optical dielectric slab power combiner," *IEEE Microwave and Guided Wave Letters*, vol. 6, no. 2, pp. 73–75, Feb 1996.

[51] H. S. Hwang, T. W. Nuteson, M. B. Steer, J. W. Mink, J. Harvey, and A. Paolella, "Two-dimensional quasi-optical power combining system: performance and component design," in *Microwave Symposium Digest, 1996., IEEE MTT-S International*, vol. 2, June 1996, pp. 927–930.

[52] D. Deslandes and K. Wu, "Integrated microstrip and rectangular waveguide in planar form," *IEEE Microwave and Wireless Components Letters*, vol. 11, no. 2, pp. 68–70, Feb 2001.

[53] A. J. Farrall and P. R. Young, "Integrated waveguide slot antennas," *Electronics Letters*, vol. 40, no. 16, pp. 974–975, Aug 2004.

[54] C. W. Hicks, H.-S. Hwang, M. B. Steer, J. W. Mink, and J. F. Harvey, "Spatial power combining for two-dimensional structures," *IEEE Transactions on Microwave Theory and Techniques*, vol. 46, no. 6, pp. 784–791, Jun 1998.

[55] T. J. Tayag, M. B. Steer, J. F. Harvey, A. B. Yakovlev, and J. Davis, "Spatial power splitting and combining based on the talbot effect," *IEEE Microwave and Wireless Components Letters*, vol. 12, no. 1, pp. 9–11, Jan 2002.

[56] M. G. keller, J. Shaker, and Y. M. M. Antar, "Millimeter-wave talbot effect spatial power amplifier," in *2006 12th International Symposium on Antenna Technology and Applied Electromagnetics and Canadian Radio Sciences Conference*, July 2006, pp. 1–4.

[57] A. F. Perkons, Y. Qian, and T. Itoh, "TM surface-wave power combining by a planar active-lens amplifier," *IEEE Transactions on Microwave Theory and Techniques*, vol. 46, no. 6, pp. 775–783, Jun 1998.

[58] C. W. Hicks, A. B. Yakovlev, and M. B. Steer, "Aperture-coupled stripline-to-waveguide transitions for spatial power combining," *The Applied Computational Electromagnetics Society Journal*, vol. 18, no. 4, pp. 33–40, Nov 2003.

[59] C. W. Hicks, "Experimental and electromagnetic modeling of waveguide-based spatial power combining systems," 2002.

[60] R. Bashirullah and A. Mortazawi, "A slotted-waveguide power amplifier for spatial power-combining applications," *IEEE Transactions on Microwave Theory and Techniques*, vol. 48, no. 7, pp. 1142–1147, Jul 2000.

[61] C. Eswarappa, T. Hongsmatip, N. Kinayman, R. Anderson, and B. Ziegner, "A compact millimeter-wave slotted-waveguide spatial array power combiner," in *Microwave Symposium Digest, 2003 IEEE MTT-S International*, vol. 2, June 2003, pp. 1439–1442.

[62] X. Jiang, S. C. Ortiz, and A. Mortazawi, "A Ka-band power amplifier based on the traveling-wave power-dividing/combining slotted-waveguide circuit," *IEEE Transactions on Microwave Theory and Techniques*, vol. 52, no. 2, pp. 633–639, Feb 2004.

[63] J. Lee, Y.-T. Lee, and S. Nam., "A new cavity power combining technique for planar circuit sources," http://ael.snu.ac.kr/paper_file/APMC%202003_11_Jaechun%20Lee.pdf, 2003, [Online: Accessed 12/4/2017].

[64] J. P. Quine, J. G. McMullen, and D. D. Khandelwal, "Ku-band IMPATT amplifiers and power combiners," in *Microwave Symposium Digest, 1978 IEEE-MTT-S International*, June 1978, pp. 346–348.

[65] R. S. Harp and K. J. Russell, "Conical power combiner," Patent US 4,188,590, 02 12, 1980, Acessed: 12/4/2017. [Online]. Available: http://pdfpiw.uspto.gov/.piw?Docid=4188590&idkey=NONE&homeurl=http%3A%252F%252Fpatft.uspto.gov%252Fnetahtml%252FPTO%252Fpatimg.htm

[66] F.-R. Yang, K.-P. Ma, Y. Qian, and T. Itoh, "A uniplanar compact photonic-bandgap (uc-pbg) structure and its applications for microwave circuit," *IEEE Transactions on Microwave Theory and Techniques*, vol. 47, no. 8, pp. 1509–1514, Aug 1999.

[67] J. M. L. Beregana, "Photonic bandgap structures in microstrip technology: Study using the coupled mode formalism and applications," 2002.

[68] P. S. Kildal, "Definition of artificially soft and hard surfaces for electromagnetic waves," *Electronics Letters*, vol. 24, no. 3, pp. 168–170, Feb 1988.

[69] M. A. Ali, S. C. Ortiz, T. Ivanov, and A. Mortazawi, "Analysis and measurement of hard-horn feeds for the excitation of quasi-optical amplifiers," *IEEE Transactions on Microwave Theory and Techniques*, vol. 47, no. 4, pp. 479–487, Apr 1999.

[70] W. S. Pickens, L. W. Epp, and D. J. Hoppe, "Hard horn design for quasi-optical power combining using solid-state power amplifiers," http://ipnpr.jpl.nasa.gov/progress_report/42-156/156E.pdf, 1999, [Online: Accessed 12/4/2017].

[71] M. Kim, J. Rosenberg, R. Smith, R. Weilke, J. B. Hacker, M. P. DeLisio, and D. Rutledge, "A grid amplifier," *IEEE Microwave and Guided Wave Letters*, vol. 1, no. 11, pp. 322–324, November 1991.

[72] C.-T. Cheung, R. Tsai, R. Kagiwada, and D. B. Rutledge, "V-band transmission and reflection grid amplifier packaged in waveguide," in *Microwave Symposium Digest, 2003 IEEE MTT-S International*, vol. 3, June 2003, pp. 1863–1866.

[73] P. G. Courtney, J. Zeng, T. Tran, H. Trinh, and S. Behan, "120 W Ka band power amplifier utilizing GaN MMICs and coaxial waveguide spatial power combining," in *IEEE Compound Semiconductor Integrated Circuit Symposium (CSICS)*, Oct 2015, pp. 1–4.

[74] R. D. Beyers and D. I. L. de Villiers, "Compact conical-line power combiner design using circuit models," *IEEE Transactions on Microwave Theory and Techniques*, vol. 62, no. 11, pp. 2650–2658, Nov 2014.

[75] A. Mortazawi, T. Itoh, and J. Harvey, Eds., *Active antennas and quasi-optical arrays*. Wiley-IEEE Press, 1999, ch. 4, pp. 174–177.

[76] P. Kahn, L. Epp, and A. Silva, "A Ka-Band wideband-gap solid-state power amplifier: General architecture considerations," http://ipnpr.jpl.nasa.gov/progress_report/42-162/162F.pdf, 2005, [Online: Accessed 7/3/2017].

[77] M. Meehan and J. Purviance, *Yield and Reliability in Microwave Circuit and System Design*, ser. Artech House Antennas and Propagation Library. Artech House, 1993.

[78] E. K. Antonsson, *Imprecision in Engineering Design*. Department of Mechanical Engineering, California Institute of Technology, 2001, accessed: 12/4/2017. [Online]. Available: http://www.design.caltech.edu/Research/Imprecise/Reading_List/Imprecision_Book.pdf

[79] Y. Akao, S. Mizuno, and K. Ishihara, *The Customer-Driven Approach to Quality Planning and Deployment*, 1st ed., Y. Akao and S. Mizuno, Eds. Asian Productivity Organization, January 1994.

[80] AIAG, "Potential Failure Mode and Effects Analysis (FMEA). Reference Manual," http://www.aiag.org/store/publications/details?ProductCode=FMEA-4, Fourth Edition, 2008, [Online: Accessed 12/4/2017].

[81] Telcordia, "Telcordia Reliability Prediction Procedure, SR-332, Issue 4," http://telecom-info.telcordia.com/site-cgi/ido/docs.cgi?DOCUMENT=sr-332&KEYWORDS=&TITLE=&ID=267585000SEARCH, 2005, [Online: Accessed 12/4/2017].

[82] J. Izadian, "Transistor test-fixture with biasing for millimeter-wave noise measurement," in *29th ARFTG Conference Digest*, vol. 11, June 1987, pp. 28–37.

[83] J. S. Izadian, "Testing transistors at millimeter waves for noise parameters," *Microwaves and RF*, vol. 26, p. 71, oct 1987.

[84] W. Batty, C. E. Christoffersen, A. B. Yakovlev, J. F. Whitaker, A. Mortazawi, A. Al-Zayed, M. Ozkar, S. C. Ortiz, R. M. Reano, K. Yang, L. P. B. Katehi, C. M. Snowden, and M. B. Steer, "Global coupled EM-electrical-thermal simulation and experimental validation for a spatial power combining mmic array," *IEEE Transactions on Microwave Theory and Techniques*, vol. 50, no. 12, pp. 2820–2833, Dec 2002.

[85] W. Batty, C. E. Christoffersen, C. M. Snowden, and M. B. Steer, "Fully physical coupled electro-thermal modeling of power devices and circuits," in *Proc. 13th Physical Simulation of Semicond. Dev. workshop*, 2002.

[86] Ansoft, "A coupled thermal and stress analysis tool for electromagnetic applications," *Microwave Journal*, vol. 47, no. 7, pp. 112–118, July 2004.

[87] B. Schoenlinner, A. Abbaspour-Tamijani, L. C. Kempel, and G. M. Rebeiz, "Switchable low-loss RF MEMS Ka-Band frequency-selective surface," *IEEE Transactions on Microwave Theory and Techniques*, vol. 52, no. 11, pp. 2474–2481, Nov 2004.

[88] M. Kameche and N. V. Drozdovski, "GAs, InP and GaN HEMT-based microwave control devices: What is best and why," *Microwave Journal*, vol. 48, no. 5, pp. 164–173, 2005.

[89] C. S. Lee, S. W. Lee, and S. L. Chuang, "Plot of modal field distribution in rectangular and circular waveguides," *IEEE Transactions on Microwave Theory and Techniques*, vol. 33, no. 3, pp. 271–274, Mar 1985.

[90] S. G. Tantawi, C. D. Nantista, G. B. Bowden, K. S. Fant, N. M. Kroll, A. E. Vlieks, Y.-H. Chin, H. Hayano, V. F. Vogel, , and J. Nielson, "Evaluation of the TE_{12} mode in circular waveguide for low-loss, high-power RF transmission," http://journals.aps.org/prab/pdf/10.1103/PhysRevSTAB.3.082001, 2000, [Online: Accessed 7/3/2017].

[91] M.-C. Yang, J.-H. Li, and K. J. Webb, "Functional waveguide mode transformers," *IEEE Transactions on Microwave Theory and Techniques*, vol. 52, no. 1, pp. 161–169, Jan 2004.

[92] R. B. Dybdal, L. Peters, and W. H. Peake, "Rectangular waveguides with impedance walls," *IEEE Transactions on Microwave Theory and Techniques*, vol. 19, no. 1, pp. 2–8, Jan 1971.

[93] S. S. Bharj and S. Mak, "Waveguide-to-microstrip transition uses evanescent mode," *Microwaves & RF*, vol. 23, pp. 99–100, 134, Jan 1984.

[94] E. V. Jull, W. J. Bleackley, and M. M. Steen, "The design of waveguides with symmetrically placed double ridges (correspondence)," *IEEE Transactions on Microwave Theory and Techniques*, vol. 17, no. 7, pp. 397–399, July 1969.

[95] L.-Y. V. Chen, "K-band spatial combiner using active array modules in an oversized rectangular waveguide," 2003.

[96] H. Thelander, M. DeLisio, and J. Rosenberg, "Shrinking the size and cost of high power at ka-band with grid amplifiers," in *9^{th} Ka and Broadband Communications Conference, Lacco Ameno / Ischia, Italy, (KACONF)*, September 2003, pp. 1–8.

[97] H. T. Than, G. W. Sun, G. S. Cuellar, J. Zeng, N. T. Schultz, M. E. Moya, Y. Chung, B. C. Deckman, and M. P. DeLisio, "A 600-w c-band amplifier using spatially combined gaas fets," in *2011 IEEE Compound Semiconductor Integrated Circuit Symposium (CSICS)*, September 2011, pp. 1–4.

[98] ——, "Design and performance of a 600-w c-band amplifier using spatially combined gaas fets for satellite communications," *IEEE Journal of Solid-State Circuits*, vol. 47, no. 10, pp. 2039–2315, Nov 2012.

[99] P. Kahn, L. Epp, and A. Silva, "A Ka-Band wideband-gap solid-state power amplifier: Architecture identification," http://ipnpr.jpl.nasa.gov/progress_report/42-162/162E.pdf, 2005, [Online: Accessed 7/3/2017].

[100] J. Schellenberg, "The evolution of power combining techniques: From the 60s to today," in *2015 IEEE MTT-S International Microwave Symposium*, May 2015, pp. 1–4.

[101] R. Bhat, A. Chakrabarti, and H. Krishnaswamy, "Large-scale power combining and mixed-signal linearizing architectures for watt-class mmWave CMOS power amplifiers," *IEEE Transactions on Microwave Theory and Techniques*, vol. 63, no. 2, pp. 703–718, Feb 2015.

[102] S. G. Shina, *Six Sigma Electronics Design and Manufacturing*, 1st ed. McGraw-Hill, 2002.

[103] *Handbook on Satellite Communications (HSC)*, 3rd ed. ITU, March 2002, ch. 1, Sec. 1.5, pp. 30-39.

[104] D. Miller and M. Drinkwine, "High Voltage Microwave Devices: An Overview," http://csmantech.org/OldSite/Digests/2003/2003PDF/7-1.pdf, 2003, [Online: Accessed 12/4/2017].

[105] R. A. York, "Some considerations for optimal efficiency and low noise in large power combiners," *IEEE Transactions on Microwave Theory and Techniques*, vol. 49, no. 8, pp. 1477–1482, August 2001.

[106] K. W. Kobayashi, M. Nishimoto, L. T. Tran, H. Wang, J. C. Cowles, T. R. Block, J. H. Elliott, B. R. Allen, A. K. Oki, and D. C. Streit, "A 44-GHz high IP3 InP-HBT amplifier with practical current reuse biasing," *IEEE Transactions on Microwave Theory and Techniques*, vol. 46, no. 12, pp. 2541–2552, Dec 1998.

[107] J. L. B. Walker, Ed., *Handbook of RF and Microwave Power Amplifiers*, 1st ed., ser. The Cambridge RF and Microwave Engineering Series. The Edinburgh Building, Cambridge CB2 8RU, UK: Cambridge University Press, 2012, ch. 6, section 6.3.2, pp. 236-241.

[108] K. M. Passino and S. Yurkovich, *Fuzzy Control*, 1st ed. Section 3.6 pp. 161-168: Addison-Wesley, 1998.

[109] A. Saleh, "Frequency-independent and frequency-dependent nonlinear models of TWT amplifiers," *IEEE Transactions on Communications*, vol. 29, no. 11, pp. 1715–1720, 1981.

[110] A. Ghorbani and M. Sheikhan, "The effect of solid state power amplifiers (SSPAs) nonlinearities on MPSK and M-QAM signal transmission," in *Sixth International Conference on Digital Processing of Signals in Communications*, Sep 1991, pp. 193–197.

[111] C. Rapp, "Effects of HPA-nonlinearity on a 4-DPSK/OFDM-signal for a digital sound broadcasting signal," in *Proceedings Second European Conf. on Sat. Comm. (ESA SP-332), Liege, Belgium*, oct 1991, pp. 179–184.

[112] M. Honkanen and S.-G. Haggman, "New aspects on nonlinear power amplifier modeling in radio communication system simulations," in *IEEE International Symposium on Personal, Indoor and Mobile Radio Communications, PIMRC*, vol. 3, 1997, pp. 844–848.

[113] G. White, A. Burr, and T. Javornik, "Modelling of nonlinear distortion in broadband fixed wireless access systems," *Electronics Letters*, vol. 39, no. 8, pp. 686–687, 2003.

[114] M. O'Droma, S. Meza, and Y. Lei, "New modified Saleh models for memoryless nonlinear power amplifier behavioural modelling," *IEEE Communications Letters*, vol. 13, no. 6, pp. 399–401, 2009.

[115] ——, "Erratum: New modified Saleh models for memoryless nonlinear power amplifier behavioural modelling (IEEE Communications Letters (2009) 13: 6 (399-401))," *IEEE Communications Letters*, vol. 13, no. 12, p. 1007, 2009.

[116] D. Schreurs, M. O'Droma, A. A. Goacher, and M. Gadringer, Eds., *Power Amplifier Behavioral Modeling*, 1st ed., ser. The Cambridge RF and Microwave Engineering series. Cambridge, U.K: Cambridge University Press, 2009, ch. 3, sec. 3.3, pp. 98-99.

[117] Ampleon, "BLM7G1822S-20, 1805 MHz to 2170 MHz, LDMOS 2-stage power MMIC," http://www.ampleon.com/products/mobile-broadband/

1.8-2.0-ghz-transistors/BLM7G1822S-20PB.html, 2015, [Online: Accessed 12/4/2017].

[118] A. Alabadelah, T. Fernandez, A. Mediavilla, B. Nauwelaers, A. Santarelli, D. Schreurs, A. Tazón, and P. A. Traverso, "Nonlinear models of microwave power devices and circuits," http://amsacta.unibo.it/1084/1/GA043204.PDF, 2004, [Online: Accessed 12/4/2017].

[119] P. Aaen, J. Pla, and J. Wood, *Modeling and Characterization of RF and Microwave Power FETs*, 1st ed., ser. The Cambridge RF and Microwave Engineering Series. The Edinburgh Building, Cambridge CB2 8RU, UK: Cambridge University Press, 2007, ch. 2, section 2.4, pp. 61-68.

[120] J. S. Kenney and P. Fedorenko, "Identification of RF power amplifier memory effect origins using third-order intermodulation distortion amplitude and phase asymmetry," in *2006 IEEE MTT-S International Microwave Symposium Digest*, June 2006, pp. 1121–1124.

[121] A. E. Parker and J. G. Rathmell, "Broad-band characterization of FET self-heating," *IEEE Transactions on Microwave Theory and Techniques*, vol. 53, no. 7, pp. 2424–2429, July 2005.

[122] W. H. Hayt and J. E. Kemmerly, *Engineering circuit analysis*, 2nd ed. Tokyo: McGraw-Hill Kogakusha, 1971, ch. 7, pp. 195-228.

[123] NXP, "MW7IC18100, 1990 MHz, 100 W, 28 V GSM/GSM EDGE RF LDMOS Wideband Integrated Power Amplifier," http://www.nxp.com/assets/documents/data/en/data-sheets/MW7IC18100N.pdf, 2009, [Online: Accessed 12/4/2017].

[124] S. Boumaiza and F. M. Ghannouchi, "Thermal memory effects modeling and compensation in RF power amplifiers and predistortion linearizers," *IEEE Transactions on Microwave Theory and Techniques*, vol. 51, no. 12, pp. 2427–2433, Dec 2003.

[125] A. Cann, "Improved nonlinearity model with variable knee sharpness," *IEEE Transactions on Aerospace and Electronic Systems*, vol. 48, no. 4, pp. 3637–3646, 2012.

[126] J. Xia, A. Islam, H. Huang, and S. Boumaiza, "Envelope memory polynomial reformulation for hardware optimization of analog-RF predistortion," *IEEE Microwave and Wireless Components Letters*, vol. 25, no. 6, pp. 415–417, June 2015.

[127] A. Zhu, P. J. Draxler, C. Hsia, T. J. Brazil, D. F. Kimball, and P. M. Asbeck, "Digital predistortion for envelope-tracking power amplifiers using decomposed piecewise Volterra series," *IEEE Transactions on Microwave Theory and Techniques*, vol. 56, no. 10, pp. 2237–2247, Oct 2008.

[128] S. Glock, J. Rascher, B. Sogl, T. Ussmueller, J.-E. Mueller, and R. Weigel, "A memoryless semi-physical power amplifier behavioral model based on the correlation between AM-AM and AM-PM distortions," *IEEE Transactions on Microwave Theory and Techniques*, vol. 63, no. 6, pp. 1826–1835, June 2015.

[129] Y. S. Lee, M. W. Lee, S. H. Kam, and Y. H. Jeong, "A high-linearity wideband power amplifier with cascaded third-order analog predistorters," *IEEE Microwave and Wireless Components Letters*, vol. 20, no. 2, pp. 112–114, Feb 2010.

[130] I. Aoki, S. Kee, R. Magoon, R. Aparicio, F. Bohn, J. Zachan, G. Hatcher, D. McClymont, and A. Hajimiri, "A fully-integrated quad-band GSM/GPRS CMOS power amplifier," *IEEE Journal of Solid-State Circuits*, vol. 43, no. 12, pp. 2747–2758, 2008.

[131] A. Afsahi, A. Behzad, V. Magoon, and L. E. Larson, "Linearized dual-band power amplifiers with integrated baluns in 65 nm CMOS for a 2×2 802.11n MIMO WLAN SoC," *IEEE Journal of Solid-State Circuits*, vol. 45, no. 5, pp. 955–966, May 2010.

[132] J. Fuhrmann, P. Oßmann, K. Dufrêne, H. Pretl, and R. Weigel, "A 28 nm standard CMOS watt-level power amplifier for LTE applications," in *IEEE Topical Conference on Power Amplifiers for Wireless and Radio Applications (PAWR)*, Jan 2015, pp. 1–3.

[133] P. Oßmann, J. Fuhrmann, K. Dufrêne, J. Fritzin, J. Moreira, H. Pretl, and A. Springer, "Design of a fully integrated two-stage watt-level power amplifier using 28-nm CMOS technology," *IEEE Transactions on Microwave Theory and Techniques*, vol. 64, no. 1, pp. 188–199, Jan 2016.

[134] W. Bösch and G. Gatti, "Measurement and simulation of memory effects in predistortion linearizers," *IEEE Transactions on Microwave Theory and Techniques*, vol. 37, no. 12, pp. 1885–1890, Dec 1989.

[135] A. Cann, "Nonlinearity model with variable knee sharpness," *IEEE Transactions on Aerospace and Electronic Systems*, vol. AES-16, no. 6, pp. 874–877, 1980.

[136] M. O'Droma and L. Yiming, "A new Bessel-Fourier memoryless nonlinear power amplifier behavioral model," *IEEE Microwave and Wireless Components Letters*, vol. 23, no. 1, pp. 25–27, 2013.

[137] P. Fisher and S. Al-Sarawi, "Improving the accuracy of SSPA device behavioral modeling," in *International Conference on Information and Communication Technology Research, ICTRC*, May 2015, pp. 278–281.

[138] T. Cunha, P. Lavrador, E. Lima, and J. Pedro, "Rational function-based model with memory for power amplifier behavioral modeling," in *Workshop on Integrated Nonlinear Microwave and Millimetre-Wave Circuits (INMMIC)*, April 2011, pp. 1–4.

[139] M. Rawat, K. Rawat, F. Ghannouchi, S. Bhattacharjee, and H. Leung, "Generalized rational functions for reduced-complexity behavioral modeling and digital predistortion of broadband wireless transmitters," *IEEE Transactions on Instrumentation and Measurement*, vol. 63, no. 2, pp. 485–498, 2014.

[140] A. Harguem, N. Boulejfen, F. Ghannouchi, and A. Gharsallah, "Robust behavioral modeling of dynamic nonlinearities using Gegenbauer polynomials with application to RF power amplifiers," *International Journal of RF and Microwave Computer-Aided Engineering*, vol. 24, no. 2, pp. 268–279, 2014.

[141] C. Jebali, N. Boulejfen, M. Rawat, A. Gharsallah, and F. Ghannouchi, "Modeling of wideband radio frequency power amplifiers using Zernike polynomials," *International Journal of RF and Microwave Computer-Aided Engineering*, vol. 22, no. 3, pp. 289–296, 2012.

[142] N. Safari, P. Fedorenko, J. S. Kenney, and T. Roste, "Spline-based model for digital predistortion of wide-band signals for high power amplifier linearization," in *IEEE International Microwave Symposium*, June 2007, pp. 1441–1444.

[143] S. Loyka, "On the use of Cann's model for nonlinear behavioral-level simulation," *IEEE Transactions on Vehicular Technology*, vol. 49, no. 5, pp. 1982–1985, 2000.

[144] M. Isaksson, D. Wisell, and D. Ronnow, "A comparative analysis of behavioral models for RF power amplifiers," *IEEE Transactions on Microwave Theory and Techniques*, vol. 54, no. 1, pp. 348–359, 2006.

[145] Sirenza Microdevices, "SHF-0189, 0.05 - 6 GHz, 0.5 watt GaAs HFET," http://datasheet.octopart.com/SHF-0189-Sirenza-datasheet-129519.pdf, EDS-101240 Rev E, [Online: Accessed 12/4/2017].

[146] NXP, "MW6S004NT1, Up to 2000 MHz, LDMOS RF Power Field Effect Transistor," http://www.nxp.com/assets/documents/data/en/data-sheets/MW6S004N.pdf, 2009, [Online: Accessed 12/4/2017].

[147] ——, "MMG3005NT1, 800 - 2000 MHz, Heterojunction Bipolar Transistor," http://cache.nxp.com/assets/documents/data/en/data-sheets/MMG3005NT1.pdf, 2014, [Online: Accessed 12/4/2017].

[148] Broadcom, "ALM-31122, 700 MHz - 1 GHz E-pHEMT, 1 watt High Linearity Amplifier," https://www.broadcom.com/products/wireless/amplifiers/linear-power/alm31122, 2014, [Online: Accessed 12/4/2017].

[149] Northrop Grumman, "APN180, 27-31 GHz GaN Power Amplifier," http://www.northropgrumman.com/BusinessVentures/Microelectronics/Products/Documents/pageDocs/APN180.pdf, 2014, [Online: Accessed 12/4/2017].

[150] T. Nojima and T. Konno, "Cuber predistortion linearizer for relay equipment in 800 MHz band land mobile telephone system," *IEEE Transactions on Vehicular Technology*, vol. 34, no. 4, pp. 169–177, Nov 1985.

[151] M. Faulkner, M.Johansson, and W. Yates, "Error sensitivity of power amplifiers using pre-distortion," in *Proceedings 41st IEEE Vehicular Technology Conference*, May 1991, pp. 451–456.

[152] J. Litva and T. K.-Y. Lo, Eds., *Digital Beamforming in Wireless Communications*, 1st ed. Norwood, MA, USA: Artech House, Inc., 1996, ch. 4, sec. 4.4.1, pp. 79-81.

[153] T. Magesacher, P. Singerl, and M. Mataln, "Optimal segmentation for piecewise rf power amplifier models," *IEEE Microwave and Wireless Components Letters*, vol. 26, no. 11, pp. 909–911, Nov 2016.

[154] S. C. Cripps, Ed., *RF power amplifiers for wireless communications*, 2nd ed. Norwood, MA, USA: Artech House, Inc., 2006, ch 14, sec. 14.1, pp. 400.

[155] Sirenza Microdevices, "SHF-0189, Amplifier Application Circuits, DESIGN APPLICATION NOTE — AN-031," http://application-notes.digchip.com/147/147-47818.pdf, EAN-101798 Rev A, [Online: Accessed 12/4/2017].

[156] P. B. Kennington, *High-Linearity RF Power Amplifier Design*, 1st ed. Norwood, MA 02062: Artech House, 2000, ch. 4, section 4.6, ch. 5 & ch. 7.

[157] W. Woo and J. S. Kenney, "A new envelope predistortion linearization architecture for handset power amplifiers," in *Radio and Wireless Conference, 2004 IEEE*, Sept 2004, pp. 175–178.

[158] Maxim, "MAX2010, 500 MHz to 1100 MHz Adjustable RF Predistorter," , 2003, [Online: Accessed 12/4/2017].

[159] AnalogDevices, "AD8302, LF to 2700 MHz RF/IF Gain and Phase Detector," http://www.analog.com/media/cn/technical-documentation/data-sheets/AD8302.pdf, 2002, [Online: Accessed 12/4/2017].

[160] ElmecTechnology, "CDM3005, 3.0 ns LTCC Delay Line," http://www.elmectech.com/images/webE_PDF/CDMwn124009i.pdf, 2002, [Online: Accessed 12/4/2017].

[161] S. M. and H. Lipson, "Distilling free-form natural laws from experimental data," *Science*, vol. 324, no. 5923, pp. 81–85, 2009.

[162] Nutonian. (2017) Eureqa (version 0.98 beta). [Online]. Available: http://www.nutonian.com/products/eureqa/

Index

Biography

Paul Owen Fisher (S'79-M'81) received the B.Eng. degree (with Distinction), in communications engineering, from the Royal Melbourne Institute of Technology (RMIT, now RMIT University), Melbourne, Australia, in 1981, the M.Eng. degree, in radio frequency engineering from the University of Adelaide, Adelaide, Australia in 2003 and is currently pursuing the Ph.D. degree in electrical and electronic engineering from the University of Adelaide, Adelaide, Australia.

He has previously been employed by British Aerospace Dynamics Group, Space Communications Division, Stevenage, UK, Codan Pty. Ltd., Satellite Communications Group, Adelaide, Australia and NEC Australia, Space Communications Sub-division, Radio Group, Melbourne, Australia where he has been involved in a range of engineering design, development and manufacturing projects covering both space and terrestrial segment products related to antennas and electronic modules over L to Ku-Band frequency ranges. Currently he is the Engineering Manager at RF Industries (RFI) in Adelaide, Australia and is involved with the design and development of radio communications products for the Cellular and Land Mobile Radio markets.

Paul Owen Fisher
paul.fisher@adelaide.edu.au
paul.fisher@rfi.com.au

Scientifc Genealogy of
Paul Owen Fisher

Formalised supervisor relationship
Mentoring relationship
Nobel prize

"If I have seen further it is by standing on the shoulders of Giants."
Isaac Newton